THE EFFECTS OF DETAILED ANALYSIS ON THE PREDICTION OF SEISMIC BUILDING POUNDING PERFORMANCE

A thesis submitted in partial fulfilment of the
requirements for the Degree
of Doctor of Philosophy
in the University of Canterbury

by Gregory Lloyd Cole

Primary Supervisor:

Assoc. Prof. Rajesh Dhakal

University of Canterbury

2012

Department of Civil and Natural Resources Engineering
College of Engineering
University of Canterbury
Christchurch, New Zealand

Abstract

Building pounding is a recognised phenomenon where adjacent buildings collide under lateral loading due to insufficient provision of building separation. The consequences of this interaction are known to be complex, and both buildings' responses can be significantly affected. In the absence of extensive experimental data, numerical modelling has been frequently adopted as a means of evaluating building pounding risk during earthquakes. In performing numerical analysis, it becomes necessary to create specialised 'contact' elements to simulate building contact. While many contact elements have been previously proposed, detailed consideration of their inherent assumptions has frequently been overlooked. This thesis considers the significance and consequences of using the Kelvin contact element for a variety of pounding situations and with varying levels of model detail.

Pounding between two adjacent floors (floor/floor collision) is considered as a one dimensional wave propagation problem. By modelling each floor as a flexible rod (termed distributed mass modelling), theoretical relationships for collision force, collision duration and post-collision velocity are derived. This theory is then compared to the predictions made when using the traditionally adopted assumptions of fully rigid colliding floors (termed lumped mass modelling). The post-collision velocities obtained from each method are found to agree only when the axial period of both floors is identical. Relationships between lumped mass and distributed mass models are formed, and an 'equivalent lumped mass' method is developed where distributed mass effects can be emulated without explicit modelling of floor flexibility.

The theoretical solution method is then adapted for use in Non-Linear Time History Analysis (NLTHA) software to model specific pounding situations. Numerical modelling of a single collision is performed to compare these results to the theoretical predictions. Good agreement is found, and the model's complexity is simplified until a sufficiently accurate simulation is performed without overly onerous computational requirements. Five methods are detailed that incorporate energy loss during collision into the distributed mass models and a calibration method is developed that enables researchers to define the level of energy loss that occurs during a single collision.

Using the developed modelling methods, the pounding response of two existing Wellington buildings is predicted. This is first performed using 2D analysis of the stiffest frame from each building. The predicted building pounding damage is categorised into local damage (damage

resulting from the magnitude of the force applied during contact) and global damage (damage due to the change in dynamic building properties resulting from momentum transfer during collision). Local and global damage effects are found to be fundamentally different consequences of collision, with the two categories responding differently to changes in the modelled system. The effects of building separation, scaling of input motion, modelling of soil-structure-interaction, collision damping, and floor rigidity are investigated for the considered system.

3D analysis of the building configuration is then investigated. Additional complications arising from the transverse movement of buildings prior to and during collision are identified and refined modelling methods are developed. The 3D configuration of these buildings causes torsional interaction, despite both buildings being perfectly symmetrical. This torsion is due to the eccentric positioning of the buildings relative to each other, which causes an eccentric contact load when pounding occurs. The 3D models are used to test the effects of building separation, 2D vs. 3D modelling, collision damping, floor rigidity, and the significance of the torsional interactions.

Attention is then focused on collisions between a building's floors and an adjacent building's columns (floor/column collision). Due to the high frequency content of pounding impacts, the significance of using Timoshenko beam theory instead of Euler-Bernoulli theory is assessed. The shear stiffness in the Timoshenko formulation is found to significantly affect the columns' predicted performance, and is used in subsequent modelling. An appropriately accurate method of modelling that minimises computational effort is then developed. The simplified model is used to predict the performance of two three-storey buildings that experience floor/column collision. The effects of floor/column impact are predicted for collisions at mid-height, and near the support of the impacted column. Each of these scenarios investigates the effect of building separation on local damage and global damage.

Finally, a method to model collision between two adjacent walls that collide out-of-plane is developed (wall/wall contact). The adopted contact element properties are selected using analogous situations that have been previously investigated. The method is used to investigate a single collision between two different wall configurations. In the conclusions, the developed modelling methods from all the considered collision configurations are collected and presented in a summary table. It is intended that these recommendations will assist other researchers in selecting appropriate building pounding modelling properties.

Dedication

This thesis is dedicated to my mother, my father, and my girlfriend. It is frighteningly easy to overlook the support provided to me for my academic (and my other) interests, simply because it has always been present. I cannot overstate how much I value your support and love. Thank you Maria, Mike and Jane.

Acknowledgements

The work presented in this thesis could not have been produced without the input from many individuals, companies and communities. So many people have contributed to this work that I cannot fit it on a single page. These acknowledgements are presented in no particular order below:

Many engineering consultancies have provided information that has enriched and informed this thesis. This information includes: proposed pounding analysis methods, detailed documentation of pounding damage, advice on modelling parameters, and access to extensive databases of building information. I am particularly indebted to Paul Brimer of Dunning Thornton Consultants, Noel Evans of Opus Consultants, Des Bull of Holmes Consulting Group, and many engineers in Beca Carter Hollings and Furner for the time and energy donated to my project. I also wish to acknowledge Adrian Humphris from Wellington City Archives for providing details on scores of existing Wellington buildings.

I have been very fortunate in to have had an exemplary team of supervisors to guide this project. To my associate supervisors: Professor Athol Carr for spending many, many days modifying and expanding the code of Ruaumoko specifically for my research, as well as his ongoing insight and support; and Professor Des Bull who has always made time to discuss the engineering issues of the day. Des's mantra of "what is your technical argument?" has become central to the way I approach any engineering disagreement. To my primary supervisor Associate Professor Rajesh Dhakal for his adaptability and expertise. Rajesh has enabled and encouraged me to pursue a topic that was new to us both. Despite this considerable disadvantage, Rajesh has continually worked to familiarise himself with the issues found in pounding analysis. Rajesh has also systematically raised the standards of all publications I have produced. This thesis would be profoundly different without his input.

The funding for this thesis has been provided by the Tertiary Education Commission, the Earthquake Commission and Beca, Carter Hollings and Furner Ltd. Without this generous assistance from all parties, this thesis could not have been realised.

I also wish to acknowledge the people who have supported my efforts over the last four years. To the postgraduate students of the third floor, many of whom I now call friends, thank you for sharing your successes and for your encouragement when times were hard. To my officemates:

Debs, Julia, Ben, Craig and Adam, thank you for answering my sometimes inane questions, and for the random conversations that occur when all day is spent in the same 3 m by 8 m room. “Get cash next pay?” indeed.

Finally, thank you to my flatmates of nearly four years; Hamish, Sarah and the always lovely Jane. To Hamish for proof reading this thesis, and for the discussions solving all the world’s problems- usually with the appreciation of fine beer, wine and/or whiskey. To Sarah for sharing my geeky interests and for challenging (and changing) the way that I think about more than a few things. Most importantly, to Jane for leaving her hometown for me, experiencing the reality of what a PhD is with me, and for loving me. Thank you.

There are many more people that I could name here, but the list must stop somewhere. If I have missed your name, please know that you are not forgotten. I am indebted to you all.

Table of Contents

ABSTRACT ..... **V**

DEDICATION ..... **VII**

ACKNOWLEDGEMENTS ..... **VIII**

TABLE OF CONTENTS ..... **X**

TABLE OF FIGURES ..... **XVIII**

LIST OF TABLES ..... **XXVII**

TABLE OF EQUATIONS ..... **XXIX**

CHAPTER 1 INTRODUCTION **1**

1.1 MOTIVATION 1

1.2 OBJECTIVES 4

1.2.1 Develop Modelling Techniques for Floor/Floor Collision *4*

1.2.2 Develop Modelling Techniques for Floor/Column Collision *5*

1.2.3 Develop Modelling Techniques for Floor/Wall Collision *5*

1.2.4 Predict Damage to New Zealand Buildings *5*

1.3 ISSUES RELATED TO BUILDING POUNDING 6

1.3.1 Pounding of Bridge Decks *6*

1.3.2 Adjacent Building Hazards *7*

1.3.3 Intrabuilding Pounding *7*

1.4 ORGANISATION 8

1.4.1 Relevant Papers by the Author *10*

CHAPTER 2 LITERATURE REVIEW **11**

2.1 OBSERVED POUNDING DAMAGE IN EARTHQUAKES 11

2.1.1 1985 Mexico City Earthquake *11*

2.1.2 1989 Loma Prieta Earthquake *12*

2.1.3 2010 – 2011 Christchurch Earthquakes *13*

2.1.4 Other reports of pounding damage *14*

2.1.5 Discussion *16*

2.1.6 Conclusions *18*

2.2 THE EVOLUTION OF CONTACT ELEMENTS 18

2.2.1 Contact Modelling Methods Adopted from Physics *18*

2.2.2 Pounding Specific Contact Models *21*

2.2.3 Three Dimensional Pounding Specific Contact Models *25*

2.2.4 Pounding-Specific Contact Models between Distributed Masses *26*

2.2.5 The Coefficient of Restitution *27*

2.2.6 Discussion *28*
2.2.7 Conclusions *33*
2.3 Prediction of Separation Distances to Prevent Pounding 33
2.3.1 Common Aspects to Separation Distance Prediction *33*
2.3.2 Conventional Combination Methods *34*
2.3.3 Alternate Combination Methods *35*
2.3.4 Evaluating Combination Method Accuracy *38*
2.3.5 Probabilistic Risk of Pounding *38*
2.3.6 Discussion *39*
2.4 Outcomes of Pounding Analysis using SDOF Buildings 39
2.4.1 SDOF Building Pounding Research *39*
2.4.2 Discussion *44*
2.5 Outcomes of Pounding Analysis using MDOF Buildings 45
2.5.1 Linear-Elastic Building Models *45*
2.5.2 Nonlinear Building Models *47*
2.5.3 3D Pounding Investigations *50*
2.5.4 Soil-Structure Interaction Modelling *52*
2.5.5 Floor/Column Collision Modelling *53*
2.5.6 Analysed Mitigation Methods *55*
2.5.7 Discussion *59*
2.5.8 Conclusions *61*
2.6 Experimental Studies 62
2.6.1 Discussion *66*
2.7 Other Areas Related to Existing Pounding Research 67
2.8 Contributions of the Current Project 67
2.9 Conclusions 68

CHAPTER 3 THE EFFECT OF DIAPHRAGM MASS DISTRIBUTION ON POUNDING MODELS 70

3.1 The Theory of Distributed Mass Collisions 70
3.1.1 Collision of a Distributed Mass Against a Rigid Wall *72*
3.1.2 Simplified Collision Force vs. Building Separation Relationship *76*
3.1.3 Collision of a Distributed Mass Including an Initial Acceleration *78*
3.1.4 Collision of Two Distributed Masses – Mathematical Solution *80*
3.1.5 Collision of Two Distributed Masses – Behaviour During Collision *82*
3.1.6 Secondary Collisions *86*
3.1.7 Wave Propagation in Other Structural Elements *87*
3.1.8 Influence of Strain Rate Effects on Collision *88*
3.1.9 Comparison with Previous Experimental Data *89*
3.2 Comparison of Lumped and Distributed Mass Models 90

3.2.1 Stereo Mechanics and Lumped Mass Models *90*
3.2.2 Model Comparison using the Influence Coefficient *91*
3.2.3 Equivalent Lumped Mass Formulation *94*
3.2.4 Incorporating Inelastic Effects in the Equivalent Lumped Mass Model *96*
3.2.5 Reporting Contact Force in Lumped Mass Models *98*
3.3 Conclusions 99

CHAPTER 4 DEVELOPMENT OF THE UNIAXIAL CONTACT ELEMENT FOR POUNDING ANALYSIS 101

4.1 Parameters Requiring Quantification 101
4.2 Model Optimization over a Single Collision 102
4.2.1 Displacement Response *103*
4.2.2 Collision Force Response *105*
4.2.3 The Role of the Collision Element Stiffness in Contact *106*
4.2.4 Conclusions *107*
4.3 Model Optimization over Excitation History 107
4.3.1 Test Setup *107*
4.3.2 Drift Results *110*
4.3.3 Contact Force Results *112*
4.3.4 Conclusions *115*
4.4 Modelling Collision Plasticity 116
4.4.1 Sources of Energy Loss During Collision *116*
4.4.2 Alternative Mechanisms for Contact Energy Dissipation *117*
4.4.3 Energy Dissipation Models Selected for Comparison *118*
4.4.4 Testing Method for Dissipation Models *118*
4.5 Dissipation Models – Multilinear Element 121
4.5.1 Dependence on Collision Velocity *121*
4.5.2 Dependence on Mass and Axial Period *124*
4.5.3 Dependence on Number of Diaphragm Elements *126*
4.5.4 Assessing Physical Representation of Contact *127*
4.6 Dissipation Models – Damped Kelvin Element 128
4.6.1 Dependence on Collision Velocity *128*
4.6.2 Dependence on Mass and Axial Period *129*
4.6.3 Dependence on Number of Diaphragm Elements *130*
4.6.4 Assessing Physical Representation of Contact *131*
4.7 Dissipation Models – Viscous Diaphragm 132
4.7.1 Dependence on Collision Velocity, Mass and Axial Period *133*
4.7.2 Dependence on Number of Diaphragm Elements *134*
4.7.3 Assessing Physical Representation of Contact *134*
4.8 Dissipation Models – Global Modal Damping 136

4.8.1 Dependence on Collision Velocity *136*
4.9 Dissipation Models – Intervening Objects 138
4.10 Dissipation Model Summary 140
4.11 Method to Define Plasticity Index Relationships 141
4.12 Conclusions 144

CHAPTER 5 MODELLING AND SELECTION OF BUILDINGS FOR DETAILED ANALYSIS 145

5.1 Selected Building Characteristics 145
5.2 2D Building Modelling 146
5.2.1 Building Simplifications for Analysis *146*
5.2.2 Analysis Program *148*
5.2.3 Material Properties *148*
5.2.4 Analysis Properties *149*
5.2.5 Building layout *150*
5.2.6 Concrete Beam Behaviour *153*
5.2.7 Concrete Column Behaviour *154*
5.2.8 Diaphragm Modelling *157*
5.2.9 Member Capacities *158*
5.2.10 Soil Structure Interaction *158*
5.2.11 Ground Motion Records *160*
5.3 3D Building Modelling 164
5.3.1 Building layout *164*
5.3.2 Modelling of Floor Diaphragms *164*
5.3.3 Soil Structure Interaction *165*
5.3.4 Modelling Biaxial Member Capacities *166*
5.3.5 Time step Modifications *166*
5.3.6 Hysteresis Modifications *167*
5.3.7 Ground Motion Scaling Modifications *167*
5.4 Conclusions 169

CHAPTER 6 2D ANALYSIS OF FLOOR/FLOOR POUNDING 170

6.1 Building Properties 170
6.2 Contact Element Properties 171
6.3 Testing Schedule and Naming Conventions 171
6.4 Global Damage vs. Local Damage 172
6.5 Detailed Inspection of Pounding Records 174
6.6 Effect of Building Separation and Input Record 178
6.6.1 Displacement Response *178*
6.6.2 Shear Force and Curvature Ductilities *186*
6.6.3 Collision Force Response *189*

6.7 Effects of Scaling PGA 192
6.8 Effects of SSI 195
6.9 Effects of Collision Damping 197
6.10 Effects of Lumped Mass Modelling 200
6.11 Conclusions 202

CHAPTER 7 DEVELOPMENT OF THE 3D CONTACT ELEMENT 204

7.1 Limitations of 2D Modelling 204
7.2 Additional Requirements of the Elastic 3D Contact Element 205
7.3 Attempted Modelling Methods 208
7.3.1 3D Node/Node Contact Element 209
7.3.2 3D Contact using Extrapolated Shape Functions 211
7.3.3 3D Contact using Distributed Stresses 214
7.4 Assigning Contact Element Stiffness over the Contact Interface 215
7.4.1 Tested Diaphragm Configurations 216
7.4.2 Results 217
7.4.3 Method of Calculating 3D Contact Stiffness 219
7.5 Plasticity in the 3D Contact Element 219
7.6 3D Equivalent Lumped Mass Formulation 221
7.7 Conclusions 221

CHAPTER 8 3D ANALYSIS OF FLOOR/FLOOR POUNDING 223

8.1 Single Collision between Two Floors 223
8.2 Building Properties 228
8.3 Testing Schedule and Naming Conventions 230
8.4 Effects of Building Separation on 3D Models 231
8.4.1 Response of Buildings with No Contact 231
8.4.2 Displacement Sensitivity to Building Separation 234
8.4.3 Global Damage Sensitivity to Building Separation 237
8.4.4 Local Damage Sensitivity to Building Separation 241
8.4.5 Collision Force Response to Individual Collisions 245
8.5 Comparison with 2D Analysis Methods 248
8.5.1 Influence on Displacement Envelopes 250
8.5.2 Influence on Global Damage Demand 252
8.5.3 Influence on Local Damage Demand 253
8.6 Effects of Rigid Diaphragms 254
8.6.1 Influence on Displacement Envelopes 254
8.6.2 Influence on Global Damage Demand 256
8.6.3 Influence on Local Damage Demand 257
8.7 Collision Damping in 3D Models 258

8.7.1 Influence on Displacement Envelopes *259*
8.7.2 Influence on Global Damage Demand *260*
8.7.3 Influence on Local Damage Demand *260*
8.8 Eccentric Pounding Configuration 261
8.8.1 Response of Building 2A with No Contact (NC) *262*
8.8.2 Displacement Sensitivity to Building Separation *264*
8.8.3 Global Damage Sensitivity to Building Separation *266*
8.8.4 Local Damage Sensitivity to Building Separation *266*
8.9 Effects of 2D Analysis for Eccentric Configuration 267
8.9.1 Influence on Displacement Envelopes *267*
8.9.2 Influence on Global Damage Demand *268*
8.9.3 Influence on Local Damage Demand *269*
8.10 Effects of Rigid Diaphragms for Eccentric Configuration 269
8.10.1 Influence on Displacement Envelopes *270*
8.10.2 Influence on Global Damage Demand *271*
8.10.3 Influence on Local Damage Demand *272*
8.11 The Suitability of Modelling Pounding in 2D 272
8.12 Conclusions 273

CHAPTER 9 ANALYSIS OF COLLISIONS WITH COLUMNS 275

9.1 Existing Column/Floor Collision Research 275
9.2 Idealized Floor/Column Response to a Single Collision 276
9.2.1 Euler – Bernoulli and Timoshenko Beam Models *277*
9.2.2 Characterising an Arbitrary Column Impact *278*
9.2.3 Characterising Floor/Column Impact *283*
9.2.4 Prediction of Floor/Column Loads *285*
9.2.5 Accurate Mid-span Model *288*
9.2.6 Accurate Near-base Model *290*
9.3 Simplified Floor/Column Model Development 293
9.3.1 Model Naming Conventions *293*
9.3.2 Mid-span Floor/Column Collision *293*
9.3.3 Near-base Floor/Column Collision *296*
9.3.4 Effect of Differing the Number of Diaphragm Elements *300*
9.3.5 Effect of Shear Stiffness and Rotational Inertia *302*
9.3.6 Reassessing the Definition of Collision Element Stiffness *304*
9.3.7 Transitioning Between Floor/Column and Floor/Floor Collisions *307*
9.3.8 Modelling Column Plasticity *310*
9.3.9 Floor Plasticity in Floor/Column Collisions *311*
9.3.10 Conclusions *311*

9.4 Performance of Column Collision Models in 3D 312
9.4.1 Building Configurations 312
9.5 Floor/Column Models – Mid-span Collision 314
9.5.1 Mid-span Collision Influence on Local Damage 315
9.5.2 Mid-span Collision Influence on Global Damage 320
9.6 Floor/Column Models – Near-floor Collision 321
9.6.1 Near-floor Collision Influence on Local Damage 321
9.6.2 Near-floor Collision Influence on Global Damage 326
9.7 Conclusions 326

CHAPTER 10 ANALYSIS OF COLLISIONS WITH WALLS 328

10.1 Existing Wall Collision Research 329
10.2 Idealized Wall Response to a Single Collision 329
10.2.1 Characterising an Arbitrary Wall Impact 329
10.2.2 Calibration of Wall/Wall Collision Element Stiffness 332
10.2.3 Accurate Equal Wall Model – Stiffness Calibration 333
10.2.4 Accurate Equal Wall Model – Collision Behaviour 337
10.2.5 Accurate Unequal Wall Model – Stiffness Calibration 340
10.2.6 Accurate Unequal Wall Model – Collision Behaviour 342
10.3 Conclusions 344

CHAPTER 11 CONCLUSIONS AND RECOMMENDATIONS 346

11.1 Conclusions and Key Contributions 346
11.1.1 Conclusions 346
11.1.2 Key Contributions and Findings 348
11.2 Recommended Pounding Modelling Techniques 350
11.3 Research Limitations 352
11.4 Avenues for Future Research 353

REFERENCES 356

APPENDIX A THE CHRISTCHURCH EARTHQUAKES 372

APPENDIX B GRAPHICAL RECORDS OF POUNDING DAMAGED BUILDINGS 406

APPENDIX C DERIVATION OF STEREO MECHANICS 417

APPENDIX D SOLUTION OF WAVE EQUATION FOR A DISTRIBUTED MASS VS. A RIGID BARRIER 419

APPENDIX E INITIAL ACCELERATION SOLUTION OF WAVE EQUATION FOR A DISTRIBUTED MASS VS. RIGID BARRIER 421

APPENDIX F SOLUTION OF THE WAVE EQUATION FOR TWO COLLIDING DISTRIBUTED MASSES 423

APPENDIX G CALCULATING VELOCITIES IN A COLLISION OF TWO DISTRIBUTED MASSES CONSIDERING MOMENTUM 426

APPENDIX H SAMPLE CALCULATIONS FOR MODEL PRODUCTION 429

APPENDIX I SAMPLE RUAUMOKO 3D INPUT FILE FOR 2D ANALYSIS 439

APPENDIX J CALCULATION OF FUNDAMENTAL LUMPED PARAMETER MODEL VALUES FOR SSI 446

APPENDIX K RULES FOR NODE/NODE 3D CONTACT ELEMENT 447

APPENDIX L SUPPLEMENTARY FIGURES FOR CHAPTER 9 449

Table of Figures

Figure 1.1 Examples of Christchurch buildings with no separation. 2

Figure 1.2 Examples of Wellington buildings with no separation 2

Figure 1.3 Observed pounding damage. 3

Figure 1.4 A building configuration where only floor/floor contact is possible 5

Figure 1.5 A building configuration where only floor/column contact is possible. 5

Figure 1.6 Damage of concrete slab and hollowcore units resulting from collision of floor units. 8

Figure 2.1 Pounding damage in Mexico City 1985. 12

Figure 2.2 Example of severe pounding damage observed in the 1989 Loma Prieta earthquake. 13

Figure 2.3 Evidence of pounding damage. 15

Figure 2.4 Pounding prone building configurations 17

Figure 2.5 Assumed collision using stereo mechanics 19

Figure 2.6 Assumed collision for Hertzian contact 20

Figure 2.7 Hertz contact element hysteresis 20

Figure 2.8 Kelvin element. 22

Figure 2.9 Multilinear gap element 23

Figure 2.10 Determining whether collision occurs between two rigid floors. 26

Figure 2.11 Zhu et al. contact model between a node and a target surface 26

Figure 2.12 Nodal layout for collision between distributed masses 27

Figure 2.13 Layout of contact element and internal deck elements 27

Figure 2.14 Coefficient of restitution dependence on relative velocity. 28

Figure 2.15 Experiment configurations used to calculate e. 32

Figure 2.16 Calculation of Pseudo Energy Radius using building velocity and building displacement. 37

Figure 2.17 Difference in application of modal combination techniques. 37

Figure 2.18 Numerical model of pounding between multiple buildings and adopted building hysteresis. 41

Figure 2.19 Influence of changing the coefficient of restitution 43

Figure 2.20 Comparison of maximum bridge displacement using full ground motions with calculated characteristic excitation variables. 44

Figure 2.21 Idealisation adopted by Maison and Kasai. 46

Figure 2.22 Example building layout. 48

Figure 2.23 Building configurations tested by Filiatrault. 49

Figure 2.24 L shape arrangement of tested buildings. 50

Figure 2.25 Modelled pounding configuration. 51

Figure 2.26 Soil structure interaction model. 52

Figure 2.27 Floor/column pounding configuration. 54

Figure 2.28 Proposed means of applying linking element between buildings with differing floor heights. 55

Figure 2.29 Proposed 'bumper' wall design to allow zero separation between adjacent buildings. 57

Figure 2.30 Proposed mitigation linking methods. 59

FIGURE 2.31 FILIATRAULT EXPERIMENTAL SETUP. 63
FIGURE 2.32 EXPERIMENTAL SETUP FOR TWO STOREY BUILDINGS. 63
FIGURE 2.33 ZHU SHAKETABLE EXPERIMENTS. 65
FIGURE 2.34 GUO EXPERIMENTAL SETUP. 66
FIGURE 2.35 LINDSAY POUNDING CONTACT CONFIGURATION. 66
FIGURE 3.1 APPROXIMATION OF A FLOOR AS A ROD OF UNIFORM DENSITY 71
FIGURE 3.2 COLLISION OF A DISTRIBUTED MASS AGAINST A RIGID WALL 72
FIGURE 3.3 DIMENSIONLESS DISPLACEMENT DURING A COLLISION. 73
FIGURE 3.4 DIMENSIONLESS PLOTS DURING A COLLISION. 74
FIGURE 3.5 SNAPSHOTS OF A COLLISION BETWEEN A DISTRIBUTED MASS AND A RIGID WALL 75
FIGURE 3.6 SINGLE DEGREE OF FREEDOM OSCILLATOR SEPARATED FROM A RIGID WALL BY A DISTANCE U_{GAP} 77
FIGURE 3.7 RELATIONSHIP BETWEEN COLLISION FORCE AND BUILDING SEPARATION FOR A SINGLE COLLISION OF A SDOF OSCILLATOR 78
FIGURE 3.8 DIMENSIONLESS PLOTS FOR γ = -0.5. 79
FIGURE 3.9 CONSTANT ACCELERATION APPLIED TO A BUILDING WITH AN INFINITELY SMALL INITIAL SEPARATION 80
FIGURE 3.10 COLLISION OF TWO DISTRIBUTED MASSES 81
FIGURE 3.11 DIMENSIONLESS VELOCITY FOR COLLISION OF TWO DISTRIBUTED MASSES 82
FIGURE 3.12 SNAPSHOTS OF A COLLISION BETWEEN TWO DISTRIBUTED MASSES 83
FIGURE 3.13 TIME FOLLOWING COLLISION ASSUMING NO SECONDARY CONTACT 86
FIGURE 3.14 SNAPSHOTS DURING A COLLISION OF A BUILDING FLOOR WITH ANOTHER BUILDING. 88
FIGURE 3.15 INFLUENCE COEFFICIENT, α, IN TERMS OF MASS RATIO AND PERIOD RATIO. 93
FIGURE 3.16 CALCULATION OF THE EFFECTIVE COEFFICIENT OF RESTITUTION 95
FIGURE 4.1 DIFFERENCES BETWEEN THEORETICAL AND NUMERICAL MODELS FOR COLLIDING DIAPHRAGMS. 102
FIGURE 4.2 MODEL DEPENDENCE ON NUMBER OF ELEMENTS PER DIAPHRAGM 102
FIGURE 4.3 DISPLACEMENT RESPONSE OF DIAPHRAGM 2 FOR NUMERICAL MODELLING USING 500, 5 AND 0 AXIAL ELEMENTS PER DIAPHRAGM 104
FIGURE 4.4 CONTACT FORCE DURING DIAPHRAGM COLLISION 106
FIGURE 4.5 MODELLED BUILDING LAYOUT. 108
FIGURE 4.6 HORIZONTAL GROUND EXCITATION OF SCALED INPUT RECORDS. 109
FIGURE 4.7 MODEL CONFIGURATIONS IN TERMS OF NUMBER OF ELEMENT PER DIAPHRAGM 110
FIGURE 4.8 BUILDING 1 ERROR IN DRIFT MAXIMA RELATIVE TO BENCHMARK MODEL 111
FIGURE 4.9 BUILDING 2 ERRORS IN DRIFT MAXIMA RELATIVE TO BENCHMARK MODEL 112
FIGURE 4.10 NORMALISED EL CENTRO COLLISION PROFILES (BENCHMARK MODEL) 113
FIGURE 4.11 COLLISION FORCE COMPARISON FOR 20 ELEMENT MODEL. 114
FIGURE 4.12 COLLISION FORCE COMPARISON FOR ALL TEST CASES 115
FIGURE 4.13 FORCE PROFILES DURING FIRST EL CENTRO ROOF COLLISION. 115
FIGURE 4.14 ELEVATION OF TWO ADJACENT BUILDINGS WITH CRUSHABLE INTERVENING OBJECTS 117
FIGURE 4.15 MULTILINEAR PLASTICITY RESULTS, CASES 1 – 5 122
FIGURE 4.16 AVERAGED PLASTICITY INDEX, CASES 1 – 5 122
FIGURE 4.17 COMPARISON OF PREDICTED AND RECORDED POST COLLISION VELOCITIES, CASES 1 – 5 123

FIGURE 4.18 AVERAGED PLASTICITY INDEX FOR DIFFERENT MASS AND AXIAL PERIOD CONFIGURATIONS 124
FIGURE 4.19 COMPARISON OF PREDICTED AND RECORDED POST COLLISION VELOCITIES, CASES 5 - 10 125
FIGURE 4.20 NORMALISED COLLISION FORCE PROFILES FOR K_R/K_A=1.5, CASES 5 – 10. 125
FIGURE 4.21 EFFECT OF ELEMENT NUMBER ON CONTACT ELEMENT HYSTERESIS. CASE 5. 126
FIGURE 4.22 EFFECT OF ELEMENT NUMBER ON PLASTICITY INDEX 126
FIGURE 4.23 COLLISION FORCE HISTORIES. 127
FIGURE 4.24 DAMPED KELVIN ELEMENT PLASTICITY INDEX 128
FIGURE 4.25 COMPARISON OF PREDICTED AND RECORDED POST COLLISION VELOCITIES 129
FIGURE 4.26 DEPENDENCE OF PLASTICITY INDEX ON MASS RATIO AND AXIAL PERIOD RATIO 130
FIGURE 4.27 PREDICTED POST COLLISION VELOCITIES USING CASE 7 BACKBONE 130
FIGURE 4.28 COMPARISON OF 2 AND 20 ELEMENT PER DIAPHRAGM MODELS 131
FIGURE 4.29 RECORDED CONTACT ELEMENT HYSTERESIS FOR CASE 5 131
FIGURE 4.30 CONTACT FORCE PROFILES. 132
FIGURE 4.31 AXIAL DIAPHRAGM ELEMENT WITH DAMPING 132
FIGURE 4.32 DAMPED DIAPHRAGM PLASTICITY INDEX, CASES 1 – 10 134
FIGURE 4.33 EFFECT OF NUMBER OF DIAPHRAGM ELEMENTS ON CALCULATED PLASTICITY INDEX. CASE 5 134
FIGURE 4.34 RECORDED CONTACT FORCE FOR DAMPED DIAPHRAGM. 135
FIGURE 4.35 AXIAL ELEMENT HYSTERESIS IN DIAPHRAGM 1. 136
FIGURE 4.36 PLASTICITY INDEX DEPENDENCE ON COLLISION VELOCITY 137
FIGURE 4.37 EFFECT OF 5% MODAL DAMPING ON DAMPED DIAPHRAGM PLASTICITY INDEX 137
FIGURE 4.38 COMPARISON OF PREDICTED AND RECORDED POST COLLISION VELOCITIES FOR DAMPED DIAPHRAGM MODEL WITH 5% MODAL DAMPING 138
FIGURE 4.39 STAGES OF A FACADE BEING CRUSHED 139
FIGURE 4.40 ELASTOPLASTIC HYSTERESIS FOR CRUSHING OF FACADE 140
FIGURE 4.41 INITIAL STEPS TO CALIBRATE PLASTICITY INDEX FOR TWO DIAPHRAGMS. 143
FIGURE 5.1COMPARISON OF ORIGINAL BUILDING LAYOUT WITH THE ADOPTED BUILDING MODEL 147
FIGURE 5.2 DAMPING ALTERNATIVES WITHIN RUAUMOKO. 149
FIGURE 5.3 COLLISION ELEMENT HYSTERESIS MODELLING WITHIN NLTHA. 150
FIGURE 5.4 2D MODEL GEOMETRY (FRONT ELEVATION). 151
FIGURE 5.5 BUILDING 1 MEMBER SIZES 151
FIGURE 5.6 BUILDING 2 MEMBER SIZES 151
FIGURE 5.7 MODELLING COLLISIONS WITH SLIGHT FLOOR HEIGHT DIFFERENCES 152
FIGURE 5.8 EQUIVALENT NUMERICAL REPRESENTATION OF COLLISION FOR FLOORS WITH SMALL HEIGHT DIFFERENCE. 152
FIGURE 5.9 BEAM HYSTERESIS USING MODIFIED TAKEDA AND SPECIFIED PARAMETERS 153
FIGURE 5.10 COMPARISON OF ADOPTED HYSTERETIC BACKBONE WITH RESPONSE 2000 FOR TWO BEAM SECTIONS 154
FIGURE 5.11 REVISED TAKEDA HYSTERESIS WITH SPECIFIED PARAMETERS 155
FIGURE 5.12 COMPARISON OF COLUMN MOMENT CAPACITIES FOR TWO MODELLED COLUMNS. 155
FIGURE 5.13 COMPARISON OF COLUMN MOMENT CURVATURE BACKBONES AS A FUNCTION OF AXIAL LOAD. 156
FIGURE 5.14 EFFECTIVE MASS PARTICIPATION IN COLLISIONS. 157

FIGURE 5.15 SOIL STRUCTURE INTERACTION MODEL AT FOUNDATIONS 159
FIGURE 5.16 SCALED EARTHQUAKE SPECTRA WITH MODELLED BUILDING PERIODS 163
FIGURE 5.17 SCALED EARTHQUAKE GROUND MOTIONS USED IN ANALYSIS 163
FIGURE 5.18 3D BUILDING POUNDING LAYOUT 164
FIGURE 5.19 PLAN VIEW OF THE FINITE ELEMENT LAYOUT AT FLOORS 1 AND 2. 165
FIGURE 5.20 TRANSLATIONAL COMPONENTS OF SSI AT THE BUILDING INTERFACE 166
FIGURE 5.21 EARTHQUAKE SPECTRA OF GROUND MOTIONS USED IN 3D MODELLING. 168
FIGURE 6.1 ROOF LEVEL COLLISION IN TA+10_1XPGA 172
FIGURE 6.2 HORIZONTAL MEMBER FORCES AT 6.987 SECONDS (KN). 173
FIGURE 6.3 EFFECT OF ROOF COLLISION ON BUILDING ELEMENTS. 174
FIGURE 6.4 DISPLACEMENT RECORDS FOR EL+NC_1XPGA AND EL+05_1XPGA. 175
FIGURE 6.5 COLLISION FORCE PROFILES FOR EL+05_1XPGA. 177
FIGURE 6.6 EL CENTRO DISPLACEMENT ENVELOPES. 179
FIGURE 6.7 TABAS DISPLACEMENT ENVELOPES 179
FIGURE 6.8 UNION DISPLACEMENT ENVELOPES. 180
FIGURE 6.9 DEFINITIONS OF BUILDING ENVELOPE LABELS 181
FIGURE 6.10 NORMALISED DISPLACEMENTS. 182
FIGURE 6.11 DIMENSIONLESS DISPLACEMENTS. 183
FIGURE 6.12 LEVEL 2 NEGATIVE (LEFT) BUILDING DEFLECTION 184
FIGURE 6.13 LEVEL 3 NORMALISED DEFLECTION ENVELOPES 185
FIGURE 6.14 LEVEL 2 NORMALISED DEFLECTION ENVELOPES 185
FIGURE 6.15 LEVEL 1 NORMALISED DEFLECTION ENVELOPES 185
FIGURE 6.16 MAXIMUM RECORDED SHEAR FORCES FOR EL- RECORD 186
FIGURE 6.17 NORMALISED SHEAR DEMAND. 187
FIGURE 6.18 CORRELATIONS BETWEEN DISPLACEMENT AMPLIFICATION AND SHEAR AMPLIFICATION. 187
FIGURE 6.19 SHEAR NORMALISED BY AVERAGE NC RESPONSE. 188
FIGURE 6.20 EFFECT OF BUILDING SEPARATION ON MAXIMUM COLUMN DUCTILITY 189
FIGURE 6.21 MAXIMUM RECORDED CONTACT FORCE IN TERMS OF BUILDING SEPARATION 189
FIGURE 6.22 EFFECT OF INCREASING BUILDING SEPARATION ON CONTACT FORCE. 190
FIGURE 6.23 COLLISION FORCES PREDICTED USING RELATIVE VELOCITY FROM RECORDS WITHOUT POUNDING 191
FIGURE 6.24 CORRELATIONS BETWEEN GLOBAL DAMAGE AND LOCAL DAMAGE 192
FIGURE 6.25 2XPGA/1XPGA DISPLACEMENT RATIO BY FLOOR LEVEL. 193
FIGURE 6.26 2XPGA MAXIMUM MEMBER DUCTILITIES IN BUILDING 1. 194
FIGURE 6.27 2XPGA/1XPGA DUCTILITY RATIO. 194
FIGURE 6.28 2XPGA/1XPGA CONTACT FORCE. 195
FIGURE 6.29 DISPLACEMENT RATIO OF NOSSI/1XPGA. 195
FIGURE 6.30 SHEAR RATIO OF NOSSI/1XPGA 196
FIGURE 6.31 DUCTILITY RATIO NOSSI/1XPGA 196
FIGURE 6.32 CONTACT FORCE RATIO NOSSI/1XPGA. 197

FIGURE 6.33 PLASTICITY INDEXES FOR MODELLED COLLIDING DIAPHRAGMS 197
FIGURE 6.34 DISPLACEMENT RATIO OF DAMP/1XPGA. 199
FIGURE 6.35 SHEAR RATIO OF DAMP/1XPGA. 199
FIGURE 6.36 CONTACT FORCE RATIO OF DAMP/1XPGA. 200
FIGURE 6.37 DISPLACEMENT RATIO OF LUMP/1XPGA. 200
FIGURE 6.38 SHEAR RATIO OF LUMP/1XPGA. 201
FIGURE 6.39 CONTACT FORCE RATIO OF LUMP/1XPGA. 202
FIGURE 7.1 EFFECT OF 2D MODELLING FOR BUILDINGS OF DIFFERING LENGTH. 204
FIGURE 7.2 DEFINITION OF LOCAL AXES AND COMPONENTS OF THE 3D CONTACT ELEMENT 206
FIGURE 7.3 THEORETICAL FRICTION MODEL FOR Z COMPONENT OF FRICTION. 206
FIGURE 7.4 CONSEQUENCES OF BUILDING OFFSETS AT THE BEGINNING OF A COLLISION. 207
FIGURE 7.5 EQUIVALENT NODAL FORCES FOR HORIZONTAL OFFSET USING NODE\NODE CONTACT ELEMEN 209
FIGURE 7.6 TWO EXAMPLES OF CENTROID CALCULATION FOR NODE/NODE ELEMENT. 210
FIGURE 7.7 NODAL LOADINGS FROM UNIFORM COMPRESSION 210
FIGURE 7.8 STATIC HORIZONTAL STRESSES WITHIN TWO 10 M X 4 M PLATES IN CONTACT. 211
FIGURE 7.9 THREE COLLISION SURFACE ELEMENTS BETWEEN TWO FLOORS 212
FIGURE 7.10 CALCULATION PROCESS FOR CONTACT LOADINGS. 212
FIGURE 7.11 EXTRAPOLATIONS AND EQUIVALENT NODAL FORCES BASED UPON AVAILABLE FINITE ELEMENT DEGREES OF FREEDOM. 213
FIGURE 7.12 CONTACT ELEMENT LAYOUT FOR DISTRIBUTED STRESS ELEMENT 214
FIGURE 7.13 CALCULATION OF CONTACT STRESSES FOR STARRED ELEMENT 214
FIGURE 7.14 COMPARISON OF 2D AND 3D CONTACT MODELS FOR FLOOR/FLOOR COLLISION 215
FIGURE 7.15 TWO METHODS OF APPROXIMATING COLLISION ELEMENT STIFFNESS FOR THE 3D COLLISION ELEMENT. 216
FIGURE 7.16 PLAN VIEW OF TESTED MODEL LAYOUTS. 217
FIGURE 7.17 STRESSES RESULTING FROM REGULAR CONTACT ELEMENT SPACING. 218
FIGURE 7.18 STRESSES RESULTING FROM IRREGULAR CONTACT ELEMENT SPACING. 218
FIGURE 7.19 POSSIBLE IMPLEMENTATIONS OF A 3D VISCOUS DIAPHRAGM MODEL 220
FIGURE 8.1 FINITE ELEMENT LAYOUT FOR FLOOR COLLISION 223
FIGURE 8.2 COLLISION ELEMENT FORCES DURING COLLISION. 224
FIGURE 8.3 DISPLACEMENT RESPONSE AT FOUR INSTANTS DURING COLLISION. 225
FIGURE 8.4 NORMAL EAST-WEST FLOOR STRESSES DURING COLLISION 226
FIGURE 8.5 PLAN VIEW OF TWO FLOORS UNDERGOING AN IDEALISED ECCENTRIC COLLISION. 228
FIGURE 8.6 3D MODEL CONFIGURATION. 229
FIGURE 8.7 DISPLACEMENT ENVELOPES OVER THE HEIGHT OF EACH BUILDING FOR 'NO CONTACT' ANALYSES. 232
FIGURE 8.8 INTERSTOREY SHEAR ENVELOPES OVER HEIGHT OF BUILDING DURING 'NO CONTACT' ANALYSES. 233
FIGURE 8.9 BUILDING DUCTILITIES RECORDED IN NO CONTACT ANALYSES. 234
FIGURE 8.10 BUILDING 1 X DIRECTION DISPLACEMENT AMPLIFICATION DUE TO POUNDING 235
FIGURE 8.11 BUILDING 2 X DIRECTION DISPLACEMENT AMPLIFICATION DUE TO POUNDING 235
FIGURE 8.12 Y DIRECTION DISPLACEMENT AMPLIFICATIONS DUE TO POUNDING 236
FIGURE 8.13 BUILDING 1 LEFT DISPLACEMENT ENVELOPES AT FRONT AND REAR BUILDING FRAMES. 237

FIGURE 8.14 BUILDING 2 RIGHT DISPLACEMENT ENVELOPES AT FRONT AND REAR BUILDING FRAMES. 237
FIGURE 8.15 INTERSTOREY SHEAR AMPLIFICATION IN BUILDING 2. 239
FIGURE 8.16 BEAM DUCTILITY DUE TO MOVEMENT IN THE X DIRECTION 240
FIGURE 8.17 BUILDING 1 DUCTILITIES. 240
FIGURE 8.18 DUCTILITIES RECORDED AT BEAM A AND BEAM B 241
FIGURE 8.19 AVERAGE FORCE MAGNITUDES FOR CONTACT ELEMENT ACTIONS. 242
FIGURE 8.20 AXIAL CONTACT FORCE RESULTS FROM 3DMODEL TESTING 242
FIGURE 8.21 NORMALISED CONTACT FORCE RESPONSE. 243
FIGURE 8.22 MAXIMUM CONTACT FORCE NORMALISED BY THE FORCE PREDICTED USING RECORDS' SPECTRAL VELOCITIES (SV) OR THE NZ LOADING CODE'S PSEUDO SPECTRAL VELOCITY (PSV). 244
FIGURE 8.23 CORRELATIONS BETWEEN GLOBAL AND LOCAL DAMAGE MEASURES 245
FIGURE 8.24 COLLISION PROFILES OF THE SIX LARGEST LEVEL 2 COLLISIONS DURING EL+05_3DMODEL 246
FIGURE 8.25 COLLISION AFFECTED BY DIAPHRAGM ROTATION. 246
FIGURE 8.26 'TOE - TIP' COLLISION WHERE ONLY THE DIAPHRAGM'S TWO CORNERS EXPERIENCE COLLISION. 247
FIGURE 8.27 HORIZONTAL FRICTION FORCES AT LEVEL 2 DURING EL+05_3DMODEL 247
FIGURE 8.28 INDIVIDUAL COLLISION ELEMENT HORIZONTAL FRICTION FORCES IN EL+05_3DMODEL. 248
FIGURE 8.29 VERTICAL FRICTION FORCES AT LEVEL 2 DURING EL+05_3DMODEL 248
FIGURE 8.30 REPRESENTATIONS OF 3D PERFORMANCE IN 2D MODELS 249
FIGURE 8.31 COMPARISON OF 2DSLAVE WITH STANDARD 2D ANALYSIS TECHNIQUES 249
FIGURE 8.32 FRONT FRAME DISPLACEMENT MAGNIFICATIONS IN 2D MODELS AT LEVEL 3. 251
FIGURE 8.33 REAR FRAME DISPLACEMENT DIFFERENCES IN 2D MODELS AT LEVEL 3. 252
FIGURE 8.34 DIFFERENCES IN SHEAR MAXIMA RESULTING FROM 2D MODELLING. 253
FIGURE 8.35 DIFFERENCES IN DUCTILITY MAXIMA RESULTING FROM 2D MODELLING. 253
FIGURE 8.36 COLLISION FORCE SENSITIVITY TO 2D MODELLING APPROACHES. 254
FIGURE 8.37 LEVEL 3 X AXIS DISPLACEMENT ENVELOPE SENSITIVITY TO DIAPHRAGM FLEXIBILITY 255
FIGURE 8.38 LEVEL 3 Y AXIS DISPLACEMENT ENVELOPE SENSITIVITY TO DIAPHRAGM FLEXIBILITY. 255
FIGURE 8.39 EFFECT OF DIAPHRAGM FLEXIBILITY ON INTERSTOREY SHEARS 256
FIGURE 8.40 EFFECT OF DIAPHRAGM FLEXIBILITY ON BUILDING DUCTILITIES 257
FIGURE 8.41 EFFECT OF DIAPHRAGM FLEXIBILITY ON CONTACT FORCE AND FRICTION FORCE 257
FIGURE 8.42 PLASTICITY INDEX BACKBONE CALCULATED FOR THE BUILDING CONFIGURATION *3DMODEL* 258
FIGURE 8.43 LEVEL 3 X AXIS DISPLACEMENT SENSITIVITY TO DIAPHRAGM DAMPING 259
FIGURE 8.44 SHEAR FORCE AMPLIFICATION DUE TO COLLISION DAMPING 260
FIGURE 8.45 DUCTILITY AMPLIFICATION DUE TO COLLISION DAMPING 260
FIGURE 8.46 HORIZONTAL FRICTION FORCE AMPLIFICATION DUE TO COLLISION DAMPING 261
FIGURE 8.47 BUILDING CONFIGURATION SELECTED TO INDUCE ECCENTRIC POUNDING LOAD. 262
FIGURE 8.48 BUILDING 2A DISPLACEMENT ENVELOPES 263
FIGURE 8.49 BUILDING 2A INTERSTOREY SHEAR ENVELOPES 263
FIGURE 8.50 BUILDING 2A MAXIMUM RECORDED DUCTILITIES 263
FIGURE 8.51 FRONT FRAME X AXIS DISPLACEMENT SENSITIVITY TO BUILDING SEPARATION 264

FIGURE 8.52 BUILDING 1 LEFT DISPLACEMENT ENVELOPES AT LEVEL 3. 265
FIGURE 8.53 BUILDING 2A RIGHT DISPLACEMENT ENVELOPES AT LEVEL 3. 265
FIGURE 8.54 Y AXIS MAXIMUM ABSOLUTE DISPLACEMENT AMPLIFICATIONS 266
FIGURE 8.55 NORMALISED CONTACT FORCE IN TEST 3DMODELE. 267
FIGURE 8.56 DISPLACEMENT SENSITIVITY TO 2D MODELLING. 268
FIGURE 8.57 INTERSTOREY SHEAR SENSITIVITY TO 2D MODELLING 268
FIGURE 8.58 DUCTILITY SENSITIVITY TO 2D MODELLING 269
FIGURE 8.59 COLLISION FORCE SENSITIVITY TO 2D MODELLING 269
FIGURE 8.60 X DIRECTION LEVEL 3 DISPLACEMENT AMPLIFICATION FOR TEST 3DRIGIDE 270
FIGURE 8.61 Y DIRECTION DISPLACEMENT SENSITIVITY TO RIGID DIAPHRAGMS 270
FIGURE 8.62 INTERSTOREY SHEAR SENSITIVITY TO RIGID DIAPHRAGM MODELLING 271
FIGURE 8.63 DUCTILITY SENSITIVITY TO RIGID DIAPHRAGM MODELLING. 271
FIGURE 8.64 CONTACT FORCE SENSITIVITY TO RIGID DIAPHRAGM MODELLING 272
FIGURE 9.1 MOMENT/SHEAR DEMAND RATIO DUE TO VARIOUS LOADINGS. 277
FIGURE 9.2 PIN - PIN BEAM SUBJECTED TO A TRANSVERSE IMPULSE 279
FIGURE 9.3 DISPLACEMENT PROFILES AT MAXIMUM DISPLACEMENT AFTER MID-SPAN LOADING. 279
FIGURE 9.4 DISPLACEMENT PROFILES AT MAXIMUM DISPLACEMENT AFTER NEAR SUPPORT LOADING 280
FIGURE 9.5 BEAM DEFLECTIONS DURING THE FIRST 0.013 SECONDS AT THE POINT OF MAXIMUM DEFLECTION 280
FIGURE 9.6 SNAPSHOTS OF BEAM DISPLACEMENTS DURING THE FIRST 1.1 MS OF MID-SPAN LOADING. 281
FIGURE 9.7 3D REPRESENTATION OF DISPLACEMENTS DUE TO MID-SPAN LOADING. 282
FIGURE 9.8 3D REPRESENTATION OF SHEAR LOADS DUE TO MID-SPAN LOADING. 283
FIGURE 9.9 COLUMN/FLOOR TEST MODEL 284
FIGURE 9.10 REACTIONS AND COLUMN STIFFNESS FOR POINT LOAD AT AN ARBITRARY HEIGHT 286
FIGURE 9.11 SIMPLIFIED PREDICTION OF FLOOR/COLUMN LOADINGS FOR THE TOPMOST COLLISION POINT 287
FIGURE 9.12 DEFORMATION OF SPECIFIC COLUMN LOCATIONS. 288
FIGURE 9.13 COLUMN DISPLACEMENTS DURING COLLISION. 289
FIGURE 9.14 COLUMN SHEARS FROM MID-SPAN FLOOR COLLISION. 289
FIGURE 9.15 COLLISION FORCE RESULTING FROM MID-SPAN FLOOR COLLISION 290
FIGURE 9.16 NEAR-BASE DISPLACEMENT PROFILES AT SPECIFIED TIMES. 291
FIGURE 9.17 NEAR-BASE COLUMN SHEAR LOADINGS AT SPECIFIC COLUMN LOCATIONS. 291
FIGURE 9.18 EXAGGERATED COLUMN DEFORMATION RESULTING FROM NEAR-BASE COLLISION 292
FIGURE 9.19 TOTAL COLLISION FORCE RESULTING FROM NEAR-BASE COLLISION 292
FIGURE 9.20 MID-SPAN COLLISION MODEL LAYOUTS 294
FIGURE 9.21 COLUMN SHEAR AND MOMENT VARIATION FOR MID-SPAN COLLISION 295
FIGURE 9.22 MAXIMUM DEFLECTIONS FOR MID-SPAN COLLISION 295
FIGURE 9.23 POST COLLISION DIAPHRAGM VELOCITY AND COLLISION DURATION FOR MID-SPAN COLLISION 296
FIGURE 9.24 COLUMN MASS DISTRIBUTION OPTIONS 297
FIGURE 9.25 IMPORTANT PARAMETER VARIATIONS FOR 10 COLUMN ELEMENT MODELS 298
FIGURE 9.26 IMPORTANT PARAMETERS VARIATIONS FOR 4 COLUMN ELEMENT MODELS 299

FIGURE 9.27 TOP SUPPORT SHEAR LOADING DURING COLLISION 299
FIGURE 9.28 EFFECT OF DIFFERING DIAPHRAGM ELEMENT NUMBER ON MID-SPAN COLLISION 301
FIGURE 9.29 EFFECT OF DIFFERING DIAPHRAGM ELEMENT NUMBER ON NEAR-BASE COLLISION 301
FIGURE 9.30 INFLUENCE OF SHEAR STIFFNESS AND ROTATIONAL INERTIA ON MID-SPAN COLLISION RESULTS 303
FIGURE 9.31 INFLUENCE OF SHEAR STIFFNESS AND ROTATIONAL INERTIA ON NEAR-BASE COLLISION RESULTS 303
FIGURE 9.32 ELEMENT STIFFNESS EVALUATION FOR DETERMINING K_C 304
FIGURE 9.33 COLUMN STIFFNESS TO LOADINGS APPLIED IN MODELLED TESTS 306
FIGURE 9.34 DEFINITIONS OF CONTACT ELEMENTS WITHOUT EXPLICIT COLUMN COLLISION MODELLING. 307
FIGURE 9.35 ELEMENTS IN FLOOR/COLUMN COLLISION WHEN THE FLOORS ARE SLIGHTLY OFFSET. 308
FIGURE 9.36 PLAN VIEW AT IMPACTED FLOOR HEIGHT OF AREAS IN CONTACT DURING FLOOR/FLOOR AND FLOOR/COLUMN COLLISIONS 308
FIGURE 9.37 PLAN VIEW AT IMPACTED FLOOR HEIGHT OF EFFECTIVE SLAB WIDTHS ACTIVATED IN FLOOR/COLUMN COLLISION 309
FIGURE 9.38 TRANSITION BETWEEN FLOOR/COLUMN AND FLOOR/FLOOR COLLISION 310
FIGURE 9.39 PLASTIC HINGE LOCATIONS FOR FLOOR/COLUMN MODELLING 311
FIGURE 9.40 POSSIBLE LOAD TRANSFER MECHANISM WHEN FLOORS ARE SLIGHTLY OFFSET 313
FIGURE 9.41 ELEVATION OF FLOOR/COLUMN COLLISION LOCATIONS. 313
FIGURE 9.42 MID-SPAN FLOOR/COLUMN MODEL CONFIGURATION. 314
FIGURE 9.43 ELEVATION OF COLUMN LABELLING ACCORDING TO FLOOR NUMBER 315
FIGURE 9.44 COLUMN LAYOUT OVER IMPACTED AREA. 315
FIGURE 9.45 SHEAR AMPLIFICATION IN MID-SPAN COLLISION. 316
FIGURE 9.46 SHEAR AMPLIFICATION OF MID-SPAN MODEL 317
FIGURE 9.47 PERCENTAGE OF SHEAR CAPACITY AS A FUNCTION OF FLOOR SEPARATION 318
FIGURE 9.48 NORMALISED SHEAR FORCE IN COLUMNS AT B2L3. 318
FIGURE 9.49 COLUMN DUCTILITY IN MID-SPAN COLLISION. 319
FIGURE 9.50 MAXIMUM COLLISION FORCE RECORDED AT EACH FLOOR. 319
FIGURE 9.51 SHEAR AMPLIFICATION IN NEAR-FLOOR COLLISION. 321
FIGURE 9.52 COLUMN LAYOUTS FOR MID-SPAN AND NEAR-FLOOR MODELS INCLUDING FLOOR MASS 322
FIGURE 9.53 COMPARISON OF MID-SPAN AND NEAR-FLOOR COLUMN SHEAR DEMANDS. 323
FIGURE 9.54 SHEAR AMPLIFICATION OF NEAR-FLOOR MODEL. 323
FIGURE 9.55 PERCENTAGE OF SHEAR CAPACITY AS A FUNCTION OF (NORMALISED) SEPARATION. 324
FIGURE 9.56 COLUMN DUCTILITY IN NEAR-FLOOR COLLISION. 325
FIGURE 9.57 MAXIMUM COLLISION FORCE RECORDED AT EACH FLOOR. 326
FIGURE 10.1 ARBITRARY COLLISION TEST OF HYBRID FINITE ELEMENT 330
FIGURE 10.2 MID-SPAN DISPLACEMENT DUE TO MID-SPAN LOADING 330
FIGURE 10.3 MAXIMUM SHEARS ALONG BEAM AS A RESULT OF MID-SPAN EXCITATION 331
FIGURE 10.4 MAXIMUM MOMENT ENVELOPE DUE TO MID-SPAN EXCITATION 331
FIGURE 10.5 COLLISION ELEMENT TYPES PRESENT WHEN A WALL COLLIDES WITH A LARGE WALL. 332
FIGURE 10.6 FINITE ELEMENT LAYOUT OF THE EQUAL WALL MODEL. 334
FIGURE 10.7 MID-WALL DEFLECTION SENSITIVITY TO SOFT VS. SOFT COLLISION ELEMENT STIFFNESS 336
FIGURE 10.8 TOP-OF-WALL DEFLECTION SENSITIVITY TO SOFT VS. SOFT COLLISION ELEMENT STIFFNESS 336

Figure 10.9 Wall A mid-wall, out-of-plane moment results about the horizontal axis. 337
Figure 10.10 Top-of-wall shear force sensitivity to collision element stiffness 337
Figure 10.11 Wall displacements (m) at time of release. 338
Figure 10.12 Wall displacements (m) at 0.032 and 0.04 seconds after release 338
Figure 10.13 Wall displacements (m) at 0.077 and 0.1 seconds after release 339
Figure 10.14 Element configuration for collision of uneven walls 340
Figure 10.15 Out-of-plane displacement sensitivity to collision element stiffness 341
Figure 10.16 Horizontal shears at mid-height of Building A's right wall 341
Figure 10.17 Horizontal moments in Building B. 342
Figure 10.18 Snapshots of collision of two unequal walls at 0.023 and 0.065 seconds 343
Figure 10.19 Snapshots of collision of two unequal walls at 0.105 and 0.121 344
Figure 11.1 Summary of relevant parameters in for various forms of building collision 352

List of Tables

TABLE 2.1 REPORTS OF POUNDING DAMAGE FROM NON POUNDING-SPECIFIC SURVEYS 15
TABLE 2.2 SUMMARY OF CONTACT METHODS' CHARACTERISTICS 29
TABLE 3.1 DISTRIBUTED MASS MOMENTUM DURING COLLISION 84
TABLE 3.2 ASSESSING APPLICABILITY OF PREVIOUS BRIDGE AND BUILDING EXPERIMENTAL DATA 89
TABLE 3.3 DEFINITION OF α BASED UPON MASS APPROXIMATION 92
TABLE 4.1 PROPERTIES OF COLLIDING DIAPHRAGMS 103
TABLE 4.2 MODELLED BUILDING PROPERTIES 108
TABLE 4.3 DEFINITION OF LUMPED MASS COLLISION ELEMENT STIFFNESS. 109
TABLE 4.4 PROPERTIES OF TEST CASES 1 - 5 120
TABLE 4.5 PROPERTIES OF TEST CASES 6 - 10 121
TABLE 4.6 DAMPING METHOD SUMMARY 141
TABLE 5.1 ADOPTED BUILDING PROPERTIES 148
TABLE 5.2 SOIL PROPERTIES FOR SSI MODELLING 160
TABLE 5.3 GROUND MOTION CHARACTERISTICS (1/25 YEAR RETURN PERIOD) 162
TABLE 5.4 RECORDED PERIODS OF 3D BUILDING MODELS 168
TABLE 6.1 COLLIDING FLOOR PROPERTIES 170
TABLE 6.2 CALCULATED FLOOR COLLISION PROPERTIES 171
TABLE 6.3 VALUES USED IN CHAPTER 6 TEST NAMES 172
TABLE 6.4 EFFECT OF VISCOUS DIAPHRAGM ON THE EFFECTIVE COEFFICIENT OF RESTITUTION 198
TABLE 7.1 RELATIVE BUILDING DEFORMATIONS BY AVERAGE DRIFT AND BUILDING HEIGHT (MM). 208
TABLE 8.1 TESTED DIAPHRAGM PROPERTIES 224
TABLE 8.2 3D MODEL COLLIDING FLOOR PROPERTIES 229
TABLE 8.3 CALCULATED FLOOR COLLISION PROPERTIES 230
TABLE 8.4 FUNDAMENTAL PERIODS OF BUILDING 1 & BUILDING 2 UNDER 2D AND 3D MODELLING ASSUMPTIONS 230
TABLE 8.5 REQUIRED SEPARATIONS TO PREVENT POUNDING (MM) 235
TABLE 8.6 DAMPED 3D DIAPHRAGM PROPERTIES 259
TABLE 8.7 ECCENTRIC POUNDING 3D MODEL COLLIDING FLOOR PROPERTIES 262
TABLE 8.8 ECCENTRIC POUNDING CALCULATED FLOOR COLLISION PROPERTIES 262
TABLE 8.9 COMPARISON OF 2D MODELS' SUITABILITY FOR REPRESENTING POUNDING RESPONSE 273
TABLE 9.1 PREDICTED PROPERTIES OF ACCURATE MODELS 286
TABLE 9.2 PREDICTED FLOOR/COLUMN COLLISION PROPERTIES BASED UPON LOADING POINT 293
TABLE 9.3 TEST MODEL VALUES FOR MID-SPAN FLOOR/COLUMN COLLISION 294
TABLE 9.4 TESTED NEAR-BASE MODELS 298
TABLE 9.5 IMPULSE ERROR FROM SIMPLIFIED NEAR-BASE MODELS 300
TABLE 9.6 EQUIVALENT VALUE OF γ IF COLLISION ELEMENT STIFFNESS WAS SET USING $\Gamma = 1$ 305
TABLE 9.7 COMPARATIVE STIFFNESSES OF COLLISION ELEMENTS AND IMPACTED COLUMN 306
TABLE 9.8 CHARACTERISTICS OF FLOOR/COLUMN AND FLOOR/FLOOR COLLISIONS 310

TABLE 9.9 SEPARATIONS REQUIRED TO PREVENT POUNDING IN ANALYSED RECORDS (MM) 314
TABLE 10.1 PROPERTIES OF ARBITRARY COLLISION TEST 330
TABLE 10.2 RECOMMENDED CONTACT ELEMENT STIFFNESSES BASED ON CONTACT CLASSIFICATION 333
TABLE 10.3 SHARED BUILDING PROPERTIES FOR EQUAL WALL COLLISION 334
TABLE 10.4 DIFFERING BUILDING PROPERTIES FOR EQUAL WALL COLLISION 334
TABLE 11.1 SUMMARY OF RECOMMENDED MODELLING METHODS FOR VARIOUS BUILDING CONFIGURATIONS 351

Table of Equations

Many equations are used in this thesis, and individual equations are frequently referenced from other chapters. A table of equations is provided here to enable quick reference to this information.

2.1 19
2.2 19
2.3 19
2.4 20
2.5 20
2.6 21
2.7 21
2.8 22
2.9 22
2.10 22
2.11 22
2.12 23
2.13 24
2.14 24
2.15 24
2.16 25
2.17 25
2.18 25
2.19 25
2.20 27
2.21 33
2.22 33
2.23 33
2.24 33
2.25 34
2.26 35
2.27 35
2.28 35
2.29 36
2.30 36
2.31 42
2.32 42
2.33 42
3.1 71
3.2 72
3.3 72
3.4 72
3.5 72
3.6 73
3.7 73
3.8 73
3.9 73
3.10 73
3.11 75
3.12 76
3.13 76
3.14 76
3.15 77
3.16 77
3.17 77
3.18 77
3.19 78
3.20 79
3.21 81
3.22 81
3.23 81
3.24 83
3.25 83
3.26 84
3.27 84
3.28 85
3.29 85
3.30 85
3.31 86
3.32 87
3.33 87
3.34 91
3.35 91
3.36 94
3.37 94
3.38 95
3.39 95
3.40 95
3.41 96
3.42 97
3.43 97
3.44 97
3.45 98
3.46 99
3.47 99
4.1 119
4.2 119
4.3 133
4.4 133
5.1 162
8.1 243
9.1 277
9.2 278
9.3 285
9.4 286
9.5 286
9.6 286
9.7 287
9.8 305
9.9 306
9.10 307
9.11 308

Chapter 1 Introduction

Related papers

Cole, G. L., Dhakal, R. P., Carr, A. J. and Bull, D. K. (2010). *Interbuilding pounding damage observed in the 2010 Darfield earthquake*. Bulletin of the New Zealand Society for Earthquake Engineering 43(4): 382 - 386.

1.1 Motivation

When structural engineers undertake a seismic design for a building, assumptions are made by necessity. As a design advances, the engineer progressively challenges these assumptions to ensure they are valid for the situation under consideration. Nevertheless, assumptions can be and have been overlooked by both individuals and the wider engineering community over considerable periods of time. Historically, engineers usually assumed that buildings would respond to earthquake ground motions without interference from surrounding objects. Unfortunately, in reality this assumption has frequently been invalid at the time of construction, or has become invalid as the surrounding land was developed. Today, many buildings face the risk of collision with other neighbouring buildings during a seismic event. These collisions cause additional loadings to all involved buildings in ways that were never considered during design. This phenomenon is known as 'interbuilding pounding'.

Pounding occurs when adjacent buildings respond differently to an earthquake ground motion. If the relative movement of two adjacent buildings exceeds their initial separation, pounding occurs. Relative movement between buildings is commonly expected during earthquakes due to differences in building deformation modes, elastic building period, and the change in period that occurs as a building sustains inelastic deformations.

Many countries, including New Zealand, have a substantial number of existing buildings that are susceptible to pounding during an earthquake. Building owners' desire to utilise all available land as rentable space has frequently resulted in buildings with little or no separation. Small building separations are particularly common in central urban areas where land is at a premium. Typical examples are displayed for Christchurch city and Wellington city in Figure 1.1 and Figure 1.2. New Zealand legislation has required minimum separation distances to property boundaries since at least 1976 (NZS4203 1976), however in many instances the regulations have not been strictly enforced.

Figure 1.1 Examples of Christchurch buildings with no separation. Note these photos were taken before the 2010 – 2011 Christchurch earthquakes. The damage sustained to these buildings during the earthquakes has resulted in the demolition of at least three of these buildings.

Figure 1.2 Examples of Wellington buildings with no separation

Building pounding damage is known to often occur in large magnitude earthquakes. Brief acknowledgements of observed pounding damage have been noted in many recent earthquakes, including: Gisborne, New Zealand (Evans and Wells 2008); L'Aquila, Italy (AIR 2009); and Wenchuan, China (Wang and Chau 2008). However, detailed reports on specific buildings' pounding damage are rare, due to the wider subject areas of the reconnaissance teams. Moderate to severe building damage is often observed in these events (Figure 1.3). Few building collapses are attributed to pounding. However, this may be partially attributed to the destruction of

structural elements, including those with any evidence of pounding, which occurs during any collapse.

Figure 1.3 Observed pounding damage. Left: Wenchuan earthquake (image reproduced from Wang and Chau 2008). Right: L'Aquila earthquake (image reproduced from AIR 2009)

During the production of this thesis two major earthquakes occurred near Christchurch New Zealand, where this research was undertaken. Christchurch experienced a M_w 7.1 quake on the 4th of September 2010, and a M_w 6.3 quake on the 22nd of February 2011. These events were tragic and have devastated the city's infrastructure; however, they have also provided opportunities to specifically investigate pounding damage. The findings of these investigations are presented in Appendix A.

The existence of a sizable building stock outside of Christchurch with the potential for pounding, and the known possible severity of pounding damage have raised a number of important issues for New Zealand authorities. These include: is pounding damage likely to cause partial or complete building failure to other New Zealand buildings? Are there situations where pounding damage would be negligible? Can we predict pounding damage? Are there cost-effective mitigation methods? Currently, informed answers to many of these questions do not exist.

The personal motivation for this project originates from the 2004 Building Act. This legislation requires territorial authorities to adopt policies regarding the treatment of 'Earthquake Prone Buildings'. Earthquake Prone Buildings (EPBs) refer to buildings that are likely to collapse during a moderate earthquake and cause human injury or death, or damage to other buildings. Existing EPBs must first be identified, and then mitigated according to the local territorial authorities regulations. In order to assist the identification of EPBs, the New Zealand Society of Earthquake Engineers (NZSEE) produced recommendations for the assessment and improvement of existing New Zealand buildings (NZSEE 1996). These recommendations have

been widely adopted by New Zealand territorial authorities and structural engineers who assess existing buildings.

The recommendations identify pounding as a potential critical structural weakness (the other critical structural weaknesses are: short columns, plan irregularity and vertical irregularity). However, the recommendations provide little guidance on how pounding should be assessed and mitigated. Appendix 4D of the recommendations states *'It is expected that as further research on pounding is undertaken more appropriate and practical means to evaluate and mitigate pounding will become available'* (NZSEE 1996). Currently, New Zealand engineers are required to consider pounding effects with almost no guidance on how the consideration should be undertaken.

After spending six months performing evaluating EPBs in Wellington city for a national consulting company, the author sought to address this gap in engineering knowledge. Specifically, the means to model common New Zealand building configurations with pounding potential were of interest. This dissertation presents the results of investigations into multiple pounding modelling methods, which culminates in recommendations regarding how pounding can be accurately represented with numerical models.

1.2 Objectives

Due to the considerations presented above, four objectives were identified for investigation:

1.2.1 Develop Modelling Techniques for Floor/Floor Collision

Almost all previous pounding research has been concerned with the increase in building deflections and shears arising from momentum transfer during collisions. To date, the specific mechanisms involved in contact have not been considered in detail. Floor/floor collision describes contact between two buildings where all floors impact against other floors (Figure 1.4). In this project, collision between two floors is initially investigated in isolation to determine the floors' typical behaviour during and after collision. Simplified modelling techniques are then used to accurately represent this behaviour in subsequent analysis. Modelling is first performed in two dimensions, but is extended to three dimensions after considering the complications it causes. Multiple chapters are dedicated to methodically developing the floor/floor contact model in order to present the key ideas common to the subsequent models.

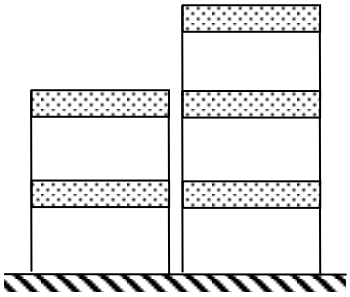

Figure 1.4 A building configuration where only floor/floor contact is possible

1.2.2 Develop Modelling Techniques for Floor/Column Collision

The factors governing the response of columns in floor/column collisions are then presented. Floor/column collision occurs when one building's floor impacts the adjacent building's columns (Figure 1.5). Floor/column contact is more complex than floor/floor contact because the column experiences flexure and shear loading instead of axial loading. Furthermore, the nature of the loading depends upon the point of collision within the column's span. The general response of columns to sudden impact is investigated and simplified methods of floor/column analysis then developed for modelling.

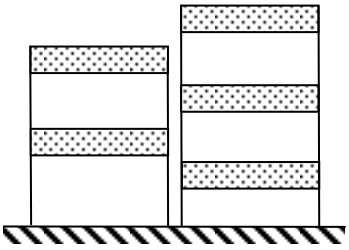

Figure 1.5 A building configuration where only floor/column contact is possible. Alternatively, if the vertical elements at the collision interface were walls, floor/wall collision would occur.

1.2.3 Develop Modelling Techniques for Floor/Wall Collision

To the author's knowledge, this third collision scenario has never been investigated. Collisions between walls and other structural elements are considered so that universal modelling techniques can be developed for any form of collision with a wall. The degree of complexity increases from that of floor/column collision due to plate bending within the wall. As out-of-plane wall contact involves three dimensional response, no 2D analysis is performed. Once again, modelling methods are developed to accurately represent floor/wall collision.

1.2.4 Predict Damage to New Zealand Buildings

As each contact method is developed, the new analysis tools are applied to a single building configuration that is modified to suit the specific components that are being tested. The buildings used in this configuration are adapted from existing, low rise New Zealand buildings. In this work, older low rise buildings are targeted since they represent a considerable portion of the

existing building stock with pounding potential. However, the developed methods could also be used to model high rise structures if required.

1.3 Issues Related to Building Pounding

There are a number of issues that are related to building pounding and yet predominantly lie outside the scope of this dissertation. In order to provide a wider context for the subject area, three issues are briefly described below.

1.3.1 Pounding of Bridge Decks

Pounding of bridge decks has also been frequently observed during large seismic events (Hao 1998; Bi et al. 2011). Piers supporting the decks may respond differently to earthquake ground motions, causing relative movement between decks. Pounding occurs when this relative movement exceeds the constructed deck separation. Collision between adjacent deck elements causes extensive local damage and may even cause deck unseating.

The differences in bridge and building pounding arise from their differing geometries. Firstly, bridges present substantially different length scales to buildings. Bridges with pounding susceptibility can be hundreds to thousands of meters long. In contrast, buildings with pounding susceptibility commonly have plan dimensions between 100 and 10 meters along any one boundary. The larger length scale of bridges increases the significance of any non-uniform ground excitation. Differences in ground motions at the base of piers can result from the speed of earthquake shockwaves, local site amplification and even the local soil structure interaction at each pier (Bi et al. 2011). These effects can substantially affect the decks' responses, causing further relative movements.

The second major distinction between collision of bridge decks and collision of buildings is the number of 'floors'. In terms of pounding response, bridge decks are essentially equivalent to long, one storey buildings. Adjacent decks always align at joints since traffic travels over these points. Thus, when collision occurs between decks, the loadings are predominantly carried within these decks (and into the bridge abutments). In contrast, buildings require loadings to be transferred to the ground through lateral load carrying elements (i.e. columns or walls). The additional loadings from pounding collision must be carried in shear and flexure through the structural system, potentially over multiple storeys. This factor is particularly important when floor to wall or floor to column collision occurs.

In this dissertation, bridge pounding is only discussed when it has direct relevance to building pounding. Most of this discussion occurs in the literature review.

1.3.2 Adjacent Building Hazards

Interbuilding pounding may be considered as a subset of 'adjacent building hazards', where adjacent building hazards describe damage caused to one building as a direct result of the behaviour of an adjacent building. Two other adjacent building hazards resulting from seismic excitation are considered here; adjacent building failure, and interbuilding soil structure interaction.

Adjacent building failure describes when one building is substantially damaged by the collapse of an adjacent building. For example, a collapsing multi-storey masonry building can 'rain' bricks on an adjacent single storey building. Damage from adjacent building failures have been frequently observed in moderate to severe earthquakes in New Zealand (Evans and Wells 2008; Cole et al. 2012). However, to date the issue has received little attention. Adjacent building failure is discussed further in Appendix A.

Interbuilding soil structure interaction creates additional complexity in adjacent building interactions. Building interactions may be affected by the presence of adjacent buildings even if pounding does not occur, due to the effects each building causes on the local soil (Chouw and Schmid 1995; Rahman 1999). These effects are complicated and lie outside the scope of this thesis. The influence of interbuilding soil structure interaction is discussed in Chapter 2 (Literature Review) and Chapter 5 (Modelling and Selection of Buildings for Detailed Analysis).

1.3.3 Intrabuilding Pounding

The term 'pounding' can be used to describe high energy collision between two or more objects of any description. When buildings are considered, pounding may be classified as either occurring within a single building (intrabuilding pounding) or between adjacent buildings (interbuilding pounding). While this dissertation focuses on interbuilding pounding, serious repercussions also may arise from intrabuilding pounding. Figure 1.6 demonstrates the internal building damage caused by pounding during an earthquake at an internal seismic isolation joint. The photo displays the top of a second storey flooring slab after the carpet has been removed. The hollowcore unit and the supporting beam are separated by a 25 mm thick polystyrene section. Relative movement during the earthquake has destroyed a significant portion of the end of the hollowcore unit and its in situ slab above. The resulting gap after the earthquake is approximately 50 mm. The damage to the hollowcore has almost resulted in the collapse of the

flooring unit. In the photo, the unit is supported only by two prestressing strands, as the surrounding concrete was destroyed.

Figure 1.6 Damage of concrete slab and hollowcore units resulting from collision of floor units. Photo credit: Holmes Consulting Group Ltd.

While intrabuilding pounding is potentially very serious, almost no research has specifically addressed this form of damage. Unfortunately, this subject is also outside the scope of this dissertation and is only discussed further in terms of recommended future research (Chapter 11).

1.4 Organisation

The thesis is divided into eleven chapters. Each chapter presents a specific topic, but may not necessarily function as a standalone document. The thesis is organised as outlined below;

Chapter 2 presents a study of the literature to date that deals with pounding analysis. The review emphasizes methods to model the contact between buildings. However, the wider subject field is also considered to provide the reader with a greater understanding of the current state of the art in building pounding.

Chapter 3 begins the detailed investigation into floor/floor contact. While previous research has considered each colliding floor to be perfectly rigid, the contact of building diaphragms is instead modelled as a one dimensional wave propagation problem. Wave propagation contact is

compared to existing modelling assumptions and the relationship between the two differing predictions is derived. Scenarios where wave propagation may be significant are presented.

Chapter 4 develops simplified methods to adequately model diaphragm wave propagation while minimising computational expense. Energy loss during collision is considered and further adaptations of the model are investigated. Chapter 4 concludes with a floor/floor contact model that can be used for two dimensional analysis.

Chapter 5 describes the building configuration selected for use in subsequent modelling. The simplifications made to enable this modelling are outlined and discussed. The selection of various analysis properties and member hystereses are also discussed in terms of the specific requirements of pounding modelling.

Chapter 6 uses the adopted model to investigate the influence of various parameters with 2D analysis. The effects of increasing building separation, changing ground motion intensity and removing soil structure interaction are investigated using the newly developed contact models.

Chapter 7 discusses the shortcomings of 2D modelling and considers the additional effects of three dimensional collisions. The transverse building movement and contact friction are found to complicate the numerical representation of collision. Multiple analysis methods are proposed to deal with these issues and one method is selected for use in modelling of 3D floor/floor collision in Chapter 8.

Chapter 8 concludes the work solely concerned with floor/floor contact. Three dimensional analyses of low rise buildings are compared to the corresponding two dimensional results. The effects of diaphragm rigidity, collision specific damping, and building torsion are also examined in terms of local and global building damage.

Chapter 9 considers floor/column collision in a similar manner to that of floor/floor collision in Chapter 3 to Chapter 8. Timoshenko beam theory is presented and used to develop a simplified model for 2D and 3D analysis. The influence of floor/column collision is presented by direct comparison with floor/floor models.

Chapter 10 presents a similar structure to Chapter 9, but in the context of collision with walls. Wall collisions are examined and simplified models are produced to allow reasonable modelling of wall behaviour during collision.

Finally, **Chapter 11** outlines the important contributions of the thesis, and the work that remains to be undertaken.

1.4.1 Relevant Papers by the Author

Where applicable, chapter headings are immediately followed by a list of papers by the author. These papers are directly related to the chapter in question. Some papers may be referenced in multiple chapters, and are provided to inform readers how the thesis links to the author's other publications. The thesis is a complete document and does not require the reader to read the indicated papers.

Chapter 2 Literature Review

Related Papers

Cole, G. L., Dhakal, R. P., Carr, A. J. and Bull, D. K. (2010). *Building pounding state of the art: Identifying structures vulnerable to pounding damage*. New Zealand Society for Earthquake Engineering Annual Conference (NZSEE 2010). Wellington, New Zealand: paper P11.

Cole, G. L., R. P. Dhakal, Carr, A. J. and Bull, D. K. (2010). *Comparing Contact Elements' Abilities to Model Critical Pounding Problems*. Asia Conference on Earthquake Engineering (ACEE 2010). Bangkok, Thailand.

While still a relatively niche topic, building pounding has been the subject of hundreds of academic publications. To present this information, this review categorises the existing research in six sub categories. Section 2.1 presents the published observations of pounding damage. Section 2.2 focuses specifically on the methods that are presently available to numerically model impact. Analysis methods are then considered in order of increasing complexity (Sections 2.3 - 2.5). Section 2.6 details pounding specific experimental testing. The remaining sections briefly describe other pounding topics outside this review and assess the position of this project in the context of the existing research.

Section 2.2 describes the subject material most directly relevant to this project. The other sections provide important contextual information about existing pounding research; however, a detailed understanding of their contents is not strictly required to understand the work presented in subsequent chapters.

2.1 Observed Pounding Damage in Earthquakes

Pounding research has been primarily motivated by the pounding damage observed in previous earthquakes. To the author's knowledge, two papers have specifically investigated pounding damage after moderate to major seismic events (excluding papers by the author). These papers are individually described in Sections 2.1.1 and 2.1.2. The pounding observed in the 2010 – 2011 Christchurch earthquakes is briefly described in Section 2.1.3, and is discussed in detail in Appendix A. Other documentation of pounding damage is presented in Section 2.1.4. The remaining sections discuss and draw conclusions on the severity of the pounding hazard.

2.1.1 1985 Mexico City Earthquake

The first known pounding specific study was performed by Bertero (1986) following the M_w 8.0 Mexico City earthquake. Three types of pounding damage were identified;

1. pounding between adjacent units of the same building separated by construction joints,

2. pounding between units of the same building or adjacent different buildings that are widely separated but connected by one or more bridges, and
3. pounding between adjacent different buildings

Adjacent different buildings are noted as the most prone configurations for collapse (Figure 2.1). Consecutive buildings units were observed to have serious pounding damage, however no collapses were recorded. Pounding of linking bridges was not found to have caused any building collapse, however some of the affected buildings did require demolition.

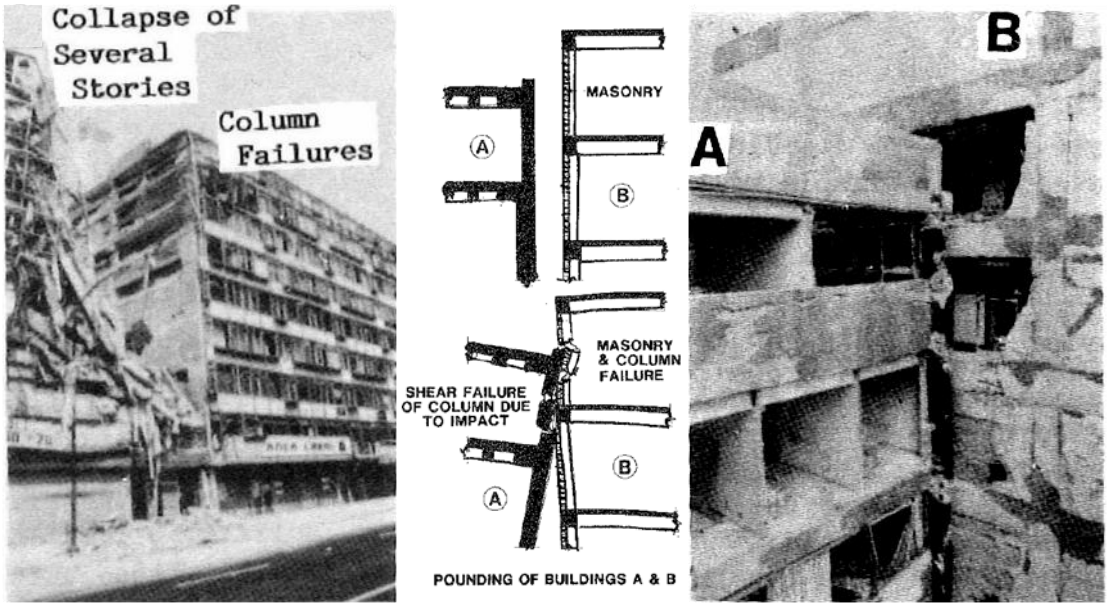

Figure 2.1 Pounding damage in Mexico City 1985. Left: partial collapse due to interstorey collision. Centre, right: schematic and details of interstorey pounding causing masonry and column failure between two buildings (figures reproduced from Bertero 1986).

Bertero concluded that; *'(1) In the centre of Mexico City there are a large number of adjacent buildings (units of the same building or different buildings) which are very close to each other (clear separation not exceeding 10 cm). (2) The percentage of these buildings that suffered severe damage due to pounding was very small. In spite of this the number of adjacent buildings that suffered severe non-structural damages and structural local failures and dramatic partial collapse is large and may in fact be the highest in the recorded history of earthquake damage'*.

2.1.2 1989 Loma Prieta Earthquake

Pounding damage was also specifically investigated in the M_w 6.9 1989 Loma Prieta earthquake (Kasai et al. 1992; Kasai et al. 1996b; Kasai and Maison 1997). These papers state over 500 buildings were affected by over 200 instances of pounding. However, approximately 50 of these instances are included based on speculated performance, without direct evidence of pounding's role in the building damage. 38 instances of pounding damage were associated with severe

pounding damage, where one or both buildings were rendered unusable requiring repair (Figure 2.2).

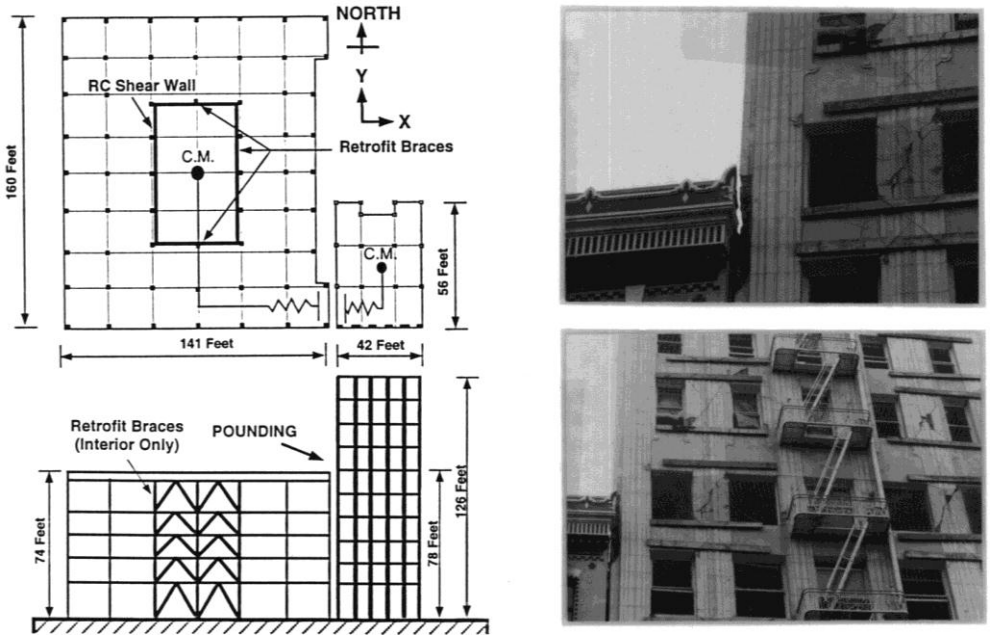

Figure 2.2 Example of severe pounding damage observed in the 1989 Loma Prieta earthquake. Note that the large diagonal shear cracks form in only one direction in the taller building's vertical elements (which indicates that this damage may have been caused by pounding). Image reproduced from Kasai (1996b)

Kasai et al. noted the following trends;

1. Pounding damage primarily occurred in multi-storey masonry buildings constructed prior to the 1930s. More modern buildings were found to generally perform well.
2. Soft soil stiffness was speculated as being a contributory factor to pounding damage.
3. Buildings with party walls performed poorly. Buildings with unconnected adjacent party walls frequently caused permanent relative deflections, while common party walls caused significant local damage at the connections between the buildings. One instance is detailed where the common party wall caused the disconnection of a timber roof diaphragm.
4. Floor/column collisions and pounding promoted by torsion were both found to increase pounding damage.
5. The 1989 Loma Prieta earthquake caused relatively low building excitations, much more extensive pounding damage was predicted for a larger future event.

2.1.3 2010 – 2011 Christchurch Earthquakes

Pounding specific studies were performed by the author after the M_w 7.1 2010 Darfield earthquake (Cole et al. 2010), and the M_w 6.3 2011 Christchurch earthquake (Cole et al. 2012).

Extensive details of the findings of these studies are presented in Appendix A, however it is appropriate to provide a brief summary here alongside the other existing studies.

After each earthquake, a street survey of pounding damage was performed. Following the Darfield event, this survey was opportunistic and general observations about pounding characteristics were presented. Following the Christchurch earthquake, a street by street survey was performed in Christchurch's Central Business District (CBD). The following trends were reported:

1. Pounding was observed in the Darfield and Christchurch earthquakes to occur rarely when compared to the total earthquake-affected building stock. However, damage that was specifically attributable to building pounding was observed in each event.
2. Pounding in the Darfield event severely affected only unreinforced masonry buildings.
3. Minor 'non-structural' elements between buildings, such as building flashings, can significantly damage important structural elements if they are not appropriately designed.
4. Pounding damage from each earthquake was assessed in terms of previously identified factors that increase pounding vulnerability (see Section 2.1.5). In both events, floor/column pounding and brittle materials were found to be the most common factors present where significant pounding damage occurred.

While the pounding studies for the above earthquakes are detailed, they represent a very small sample size of major earthquakes. Additional information on the typical severity of pounding damage in a major earthquake can be found using earthquake reconnaissance reports.

2.1.4 Other reports of pounding damage

Table 2.1 details earthquakes where pounding damage has been reported in non pounding-specific studies. In these publications, pounding damage is usually described in a few brief sentences. The table may not be comprehensive, but it has been compiled from multiple sources discovered during the production of this dissertation. A selection of pounding damage photos from these earthquakes are presented in Figure 2.3. A much larger collection of pounding damage photos is also presented in Appendix B.

Table 2.1 Reports of pounding damage from non pounding-specific surveys

Earthquake year and location	*M_w*	*No. of pounding instances*	*Paper focus*	*Reference*
1925 Santa Barbara	*6.8*	*1*	*Seismic design*	*(Ford 1926)*
1964 Alaska	*9.2*	*1*	*Seismic design*	*(Arnold 1989)**
1968 Tokachi-Oki	*8.3*	*2*	*Case study*	*(Takeyama 1973)**
1971 San Fernando	*6.6*	*1*	*Case study*	*(Bertero and Collins 1973)*
1972 Managua	*6.2*	*2*	*EQ reconnaissance*	*(Berg and Degenkolb 1973)**
1976 Guatemala	*7.5*	*'large'*	*EQ reconnaissance*	*(Sozen and Roesset 1976)**
1976 Friuli	*6.4*	*1*	*EQ reconnaissance*	*(Stratta and Wyllie 1979)**
1977 Romania	*7.4*	*~15*	*EQ reconnaissance*	*(ICCPDC et al. 1978)**
1985 Mexico City	*8.0*	****	*EQ reconnaissance*	*(Rosenblueth and Meli 1986)*
1999 Izmit	*7.4*	*4*	*EQ reconnaissance*	*(AIR 1999)* *(Gillies et al. 2001)*
2006 Yogyakarta	*6.3*	*1*	*EQ reconnaissance*	*(Elanshai et al. 2007)*
2007 Peru	*8.0*	*3*	*Six case studies*	*(Yu and Gonzalez 2008)*
2007 Gisborne	*6.6*	*1*	*EQ reconnaissance*	*(Evans and Wells 2008)*
2008 Wenchuan	*7.9*	*2*	*Analysis paper*	*(Wang and Chau 2008)*
2009 L'Aquila	*6.3*	*1*	*EQ reconnaissance*	*(AIR 2009)*

** papers cited in Anagnostopoulos (1995), but unavailable to the author*

*** pounding damage present in 40 % of collapsed or seriously damaged buildings*

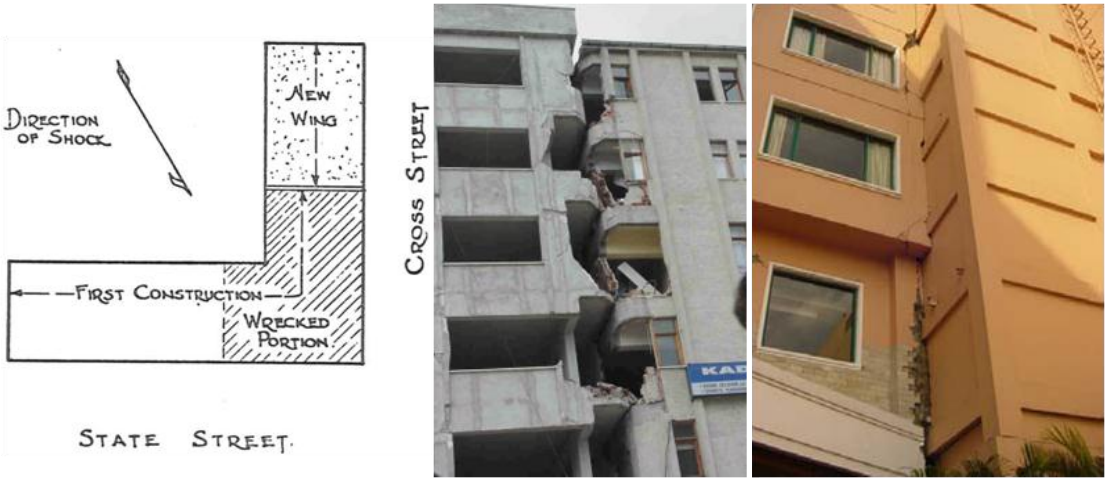

Figure 2.3 Evidence of pounding damage. Left: San Fernando (Bertero and Collins 1973). Centre: Izmit (AIR 1999). Right: Yogyakarta (Elanshai et al. 2007)

The earthquake reconnaissance reports do not generally state how frequently pounding was observed in the inspected cities, but usually describe pounding because it occurred in a specific scenario selected for further study. Similarly, the case studies describe pounding because it happened to be present in the considered scenario, rather than the case study being specifically

selected because of pounding damage. The incidental way pounding evidence is presented in these reports suggests that much pounding damage goes unreported. However, widespread significant pounding damage is not likely to have occurred in earthquakes that have detailed reconnaissance reports. This is because if pounding damage was commonly observed, it can be reasonably expected that the paper authors would have commented to that effect.

Perhaps the most commonly referenced observation of structural pounding is that of Rosenblueth and Meli (1986). Rosenblueth and Meli reported on the general performance of buildings in the 1985 Mexico City earthquake, however the section regarding pounding damage states; *'In over 40 percent of collapsed or seriously damaged buildings, there was pounding with adjacent structures. Sometimes pounding caused minor local damage. In 15 percent of all cases it led to collapse'*. Many subsequent papers, including Bertero's paper described in Section 2.1.1, quote these statistics to emphasize the significance of the pounding hazard. However, the specific wording of the section was subsequently challenged by Anagnostopoulos (1996), who received the following clarification from Meli; *'In 15% of all buildings with major damage or collapse (not only collapse) evidence of pounding was found. Not necessarily pounding was the main cause of collapse. Probably only 20-30% of these cases pounding could have been a significant factor in the structural damage'*. Anagnostopoulos then argues that the low occurrence of collapse resulting from pounding could be used to justify removing code requirements for separation between buildings.

2.1.5 Discussion

Common building configurations that are susceptible to pounding were identified in both pounding-centric studies (Bertero 1986; Kasai et al. 1996b). From these reports, Jeng and Tzeng (2000) identified five types of pounding damage that are directly attributable to the configurations of the affected buildings. Other buildings with similar configurations can thus be identified as prone to pounding. The configurations are (see also Figure 2.4):

1. **Floor/column or floor/wall pounding**. Pounding between buildings with floors at differing heights causes floor/column or floor/wall collisions, inducing high shear and flexural stresses in the vertical structural elements. Collision of this form can lead to failure of the vertical elements, which may trigger local or global collapse of one or both buildings
2. **Adjacent buildings with greatly differing mass**. Momentum is transferred between buildings during collision. When a massive building collides with a significantly smaller

building, this transfer can greatly increase the velocity of the smaller building, resulting in much greater displacement envelopes.

3. **Building subject to torsional actions arising from pounding**. While two adjacent buildings may not be prone to torsional response, their configurations relative to each other may induce torsional loading when contact occurs.
4. **Similar buildings in a row with no separation**. Buildings in contact transfer momentum during collision. When multiple buildings transfer their momentum in one direction along the row, this momentum accumulates in the building at the end of the row. The increased momentum increases the building velocity, which increases the maximum displacement of the building. As the earthquake reverses directions, both buildings at either end of the row have their actions increased.
5. **Buildings with significantly differing total height**. When a smaller building collides with a much taller building, the sudden change in momentum of the taller building's lower floors can greatly increase the shear force in the floors above.

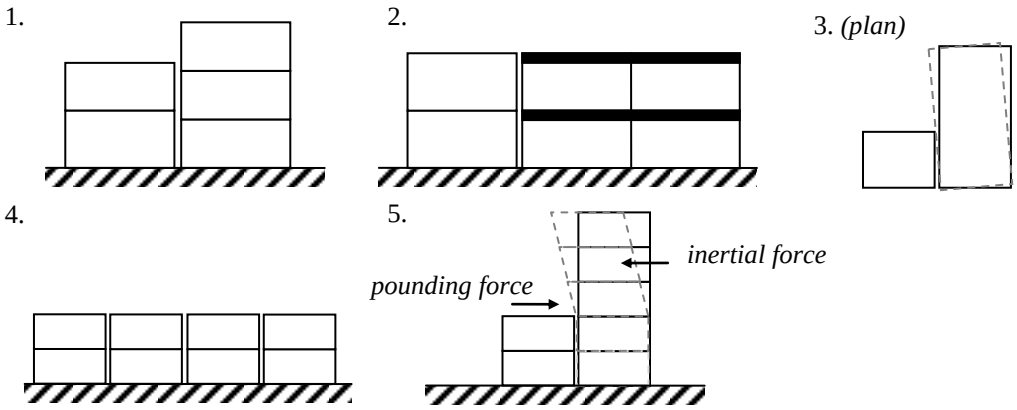

Figure 2.4 Pounding prone building configurations

A sixth factor can also be identified that greatly increases pounding susceptibility; the ductility of each structure. Collisions of buildings made of unreinforced masonry are highly brittle and are much more prone to local brittle failures that can lead to partial or total collapse (refer Figure 2.1 and Figure 2.3). However, buildings with a high level of ductility can absorb more damage resulting from a high energy collision, and thus are much more resilient to pounding damage.

When the likelihood of pounding damage in an earthquake is considered, little scientific data exists. However, the reports of observed pounding damage do present consistent themes. Severe pounding damage occurs rarely and usually presents with at least one of the above pounding prone characteristics. Minor pounding damage occurs much more frequently, however its damage does not affect the life safety of occupants in the building. It must be noted that minor

pounding damage does endanger people near the buildings during an earthquake as materials spalling at the point of impact is common during collision.

In light of the presented evidence, an argument similar to that of Anagnostopoulos (1996) can be made for disregarding pounding as a minor hazard. However, in the view of the author, such an approach is short sighted. While modern buildings may not be at great risk from pounding, many existing buildings have been constructed with configurations similar to those described above. Methods to safeguard these buildings require accurate modelling techniques to represent their behaviour. In this way, building configurations can be evaluated for their risk of pounding damage and mitigation methods' effectiveness may be assessed.

2.1.6 Conclusions

The following conclusions are drawn based upon the review performed in Section 2.1

1. Severe pounding damage resulting in collapse is rare but has occurred in multiple earthquakes.
2. Systematic assessment of pounding damage after an earthquake is also rare. The true extent of the pounding hazard can only be approximately quantified.
3. Six factors have been identified that greatly increase the risk of significant damage resulting from pounding.
4. Methods to analyse pounding damage are required to help evaluate the pounding risks of existing buildings.

2.2 The Evolution of Contact Elements

Whenever numerical models are used that simulate building contact, some technique must be employed to represent this contact within the model. The selection of this contact modelling method introduces new assumptions to the analysis, which can have significant effects on the entire model. This section presents the contact modelling methods that are currently available for pounding analysis.

2.2.1 Contact Modelling Methods Adopted from Physics

The behaviour of colliding objects received attention in the discipline of physics before building pounding was identified as a credible problem. This section briefly outlines the theory of physics based models that have been adopted in pounding analyses.

Many physicists' methods to model contact are concisely summarised in a text on impact by Goldsmith (1960). Three relevant methods are presented here:

1. Stereo mechanics
2. The Hertzian contact element
3. Lagrange multipliers

Stereo mechanics predicts the post collision velocity of two colliding point masses by considering conservation of momentum over the course of the collision (Figure 2.5).

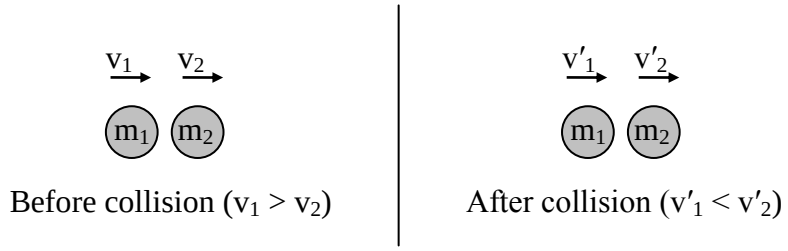

Figure 2.5 Assumed collision using stereo mechanics

The post collision velocities are;

$$v_1' = v_1 - (1+e)\frac{m_2}{m_2 + m_1}(v_1 - v_2) \qquad (2.1)$$

$$v_2' = v_2 - (1+e)\frac{m_1}{m_1 + m_2}(v_2 - v_1) \qquad (2.2)$$

where v = initial velocity, v′ = post collision velocity, m = particle mass and e = the coefficient of restitution. The coefficient of restitution is a measure of energy loss during the collision. When e = 1 the collision is completely elastic, while e = 0 causes a completely plastic collision which results in $v'_1 = v'_2$. A detailed derivation of these equations is presented in Appendix C. Stereo mechanics equations do not provide any prediction of the time a collision takes, and is typically assumed to occur instantaneously. Stereo mechanics is used in building pounding analysis by applying Equation 2.1 and Equation 2.2 to floor nodes when they come into contact.

Hertzian contact (or the Hertz element) was developed using significantly different assumptions. Collision between one flat and one parabolic surface is predicted by considering the potential energy of the deforming parabolic surface (Figure 2.6). Some other surface geometries can also be treated in a similar manner. The mathematical solution of the resulting equation provides the contact force as a function of the parabolic surface deformation (Figure 2.7):

$$F = \beta x^{\frac{3}{2}} \qquad (2.3)$$

Figure 2.6 Assumed collision for Hertzian contact

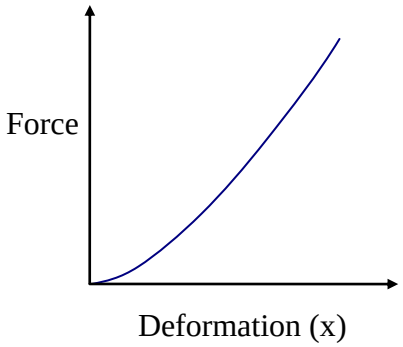

Figure 2.7 Hertz contact element hysteresis (compressive displacements and forces shown as positive)

where β is a constant that depends on the geometry and materials of the colliding objects. For example, for the collision between two spheres;

$$\beta = \frac{4}{3\pi\left(\frac{1-\nu_1^{\,2}}{\pi E_1}+\frac{1-\nu_2^{\,2}}{\pi E_2}\right)}\left(\frac{R_1 R_2}{R_1+R_2}\right) \qquad (2.4)$$

where ν = Poisson's ratio, E = Young's modulus, R = sphere radius and the subscripts distinguish sphere 1 from sphere 2. In building pounding analyses, Equation 2.3 can be used as a conditional spring between two colliding objects to simulate collision.

Finally, Lagrange multipliers is a mathematical method that can be use used to maximise (or minimise) a function given a specific constraint. To model impact, the equation expressing the total energy of the colliding system is minimised subject to the constraint that two colliding objects cannot overlap. Different implementations of this method have been used to model pounding (Papadrakakis et al. 1991; Lavan 2009); however, the general process is outlined below for an elastic undamped system. The total energy of the elastic undamped system, Π, is equal to the system's internal strain energy plus the system's kinetic energy, less the work of any externally applied loads:

$$\Pi = \frac{1}{2}\{u\}^T[K]\{u\}+\frac{1}{2}\{\dot{u}\}^T[M]\{\dot{u}\}-\{P\}^T\{u\} \qquad (2.5)$$

where u = nodal displacement, K = stiffness matrix, M = mass matrix and P = external force vector. The augmented expression including the displacement constraint is:

$$L(u,\dot{u},\lambda) = \frac{1}{2}\{u\}^T[K]\{u\} + \frac{1}{2}\{\dot{u}\}^T[M]\{\dot{u}\} - \{P\}^T\{u\} + \{\lambda\}^T\left|[X]\{u\} + u_{gap}\right| \quad (2.6)$$

where $[X]\{u\} + u_{gap}$ is the separation between two potentially colliding objects at a given point in time, and λ = Lagrange multiplier vector. Equation 2.6 is solved by finding the local minima in terms of all dependent variables. Thus:

$$\nabla_{u,\dot{u},\lambda} L(u,\dot{u},\lambda) = 0 \quad (2.7)$$

These equations can be solved for u at any time a collision occurs.

The axial flexibility of colliding objects is also considered in the Goldsmith text. Axial collision between two rods is described for collision of both two flat ended and two rounded rods (the latter using the Hertz element at the point of contact). These considerations are important precursors to some of the methods presented in this thesis.

2.2.2 Pounding Specific Contact Models

A number of contact models have also been developed specifically for numerical modelling of pounding. This section presents specific modelling schemes that assume collision occurs between two rigid objects. The influence of object flexibility during collision is addressed in Section 2.2.4.

The simplest pounding contact element is known as the Kelvin, or Kelvin-Voight, element (Figure 2.8). This element is frequently used in pounding modelling (Anagnostopoulos 1988; Anagnostopoulos and Spiliopoulos 1992; Maison and Kasai 1992; Watanabe and Kawashima 2004), and consists of a linear spring and a viscous damping element (a dashpot) in parallel. These elements only activate once a specified separation is exceeded (i.e. when $u_1(t) - u_2(t) \geq u_{gap}$). A large spring stiffness is used to minimise the amount of object overlap that occurs when the specified initial separation (u_{gap}) is closed, thus modelling contact. Ideally this stiffness would be infinite, since that would prevent any material overlap. However, numerical analysis typically cannot handle such rapid changes in stiffness. Instead, a 'sufficiently large' stiffness is selected.

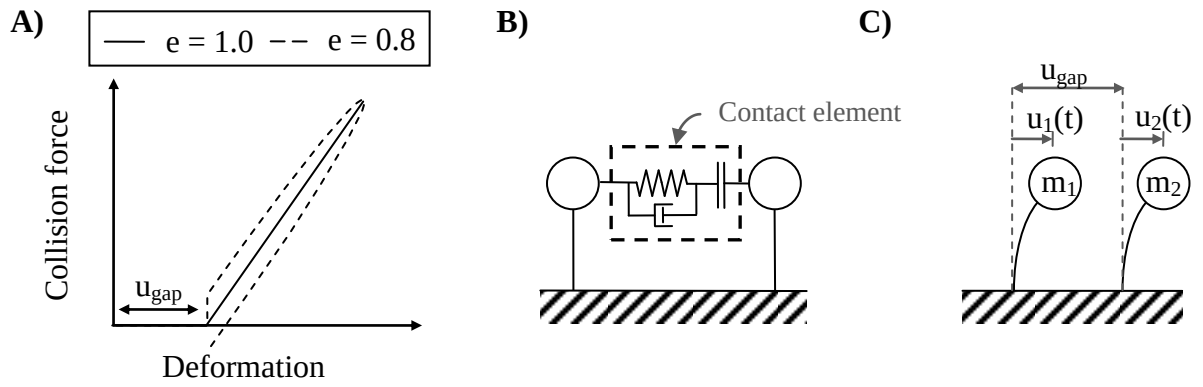

Figure 2.8 Kelvin element. A) element hysteresis (compressive displacements and forces shown as positive), B) element components, C) Nodal properties

The mathematical formulation for the Kelvin element can be expressed as:

$$F(t) = \begin{cases} kx(t) + c\dot{x}(t) & \text{if } x(t) \le 0 \\ 0 & \text{if } x(t) > 0 \end{cases} \qquad (2.8)$$

where (refer to Figure 2.8C for definitions of u_1, u_2 and u_{gap});

$$x(t) = u_2(t) - u_1(t) + u_{gap} \qquad (2.9)$$

To use the Kelvin element, three properties must be specified; the spring stiffness, damping constant and the initial separation between the colliding objects. The initial separation is physically measurable and easily determined, however the other properties require further information. Anagnostopoulos (1988, 2004) related the damping constant to the spring stiffness and the coefficient of restitution;

$$c = 2\zeta\sqrt{k\frac{m_1 m_2}{m_1 + m_2}} \qquad (2.10)$$

$$\zeta = -\frac{\ln(e)}{\sqrt{\pi^2 + [\ln(e)]^2}} \qquad (2.11)$$

This was achieved by equating the post collision velocities calculated using stereo mechanics to those found using the Kelvin element. The collision spring stiffness is less specifically defined. When modelling single degree of freedom oscillators, Anagnostopoulos (1988) adopted a collision spring stiffness 20 times larger than the model's largest interstorey stiffness. Varying this stiffness by up to a factor of 10 was found to not notably change the oscillators' displacement results. Similar results were noted by Maison and Kasai (1992). Sinclair (1993)

also notes similar results, with the notable exception of the impact elements' contact force. The contact force was found to be highly sensitive to the Kelvin element stiffness.

An alternative energy dissipation method for the Kelvin element, termed the multilinear gap element, was proposed by Valles and Reinhorn (1997). This element dissipates energy by defining two contact stiffnesses, and does not use any viscous damping (Figure 2.9). When the collision force increases, the collision force is calculated using an approach stiffness (k_a), while a decreasing collision force uses a larger restitution stiffness (k_r). Hysteretic energy is lost and can be calculated from the enclosed area that is bordered by the force/displacement relationship of the element.

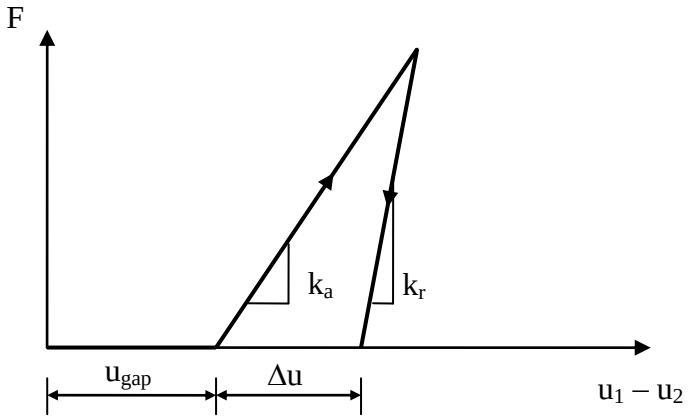

Figure 2.9 Multilinear gap element

This element can be mathematically presented as:

$$F(t) = \begin{cases} k_a x(t) & \text{if } x \le 0, \dot{x}(t) > 0 \\ \max\begin{cases} k_r\left(x(t) - \Delta u\right) \\ 0 \end{cases} & \text{if } x \le 0, \dot{x}(t) \le 0 \\ 0 & \text{if } x > 0 \end{cases} \qquad (2.12)$$

where x is defined in Equation 2.9. Hysteresis of this form results in zero contact force before the two buildings have completely separated. The remaining displacement is shown in Figure 2.9 as Δu. Physically, Δu can be interpreted as the increase in the gap between the buildings due to spalling cover concrete and plastic deformation. If this is the case then u_{gap} must be updated for the next collision ($u'_{gap} = u_{gap} + \Delta u$). Alternatively u_{gap} can be kept constant and Δu is viewed as simply a means to achieve collision damping. It is believed that this element has never been tested, and no relationship between the energy dissipated by this contact and the coefficient of restitution has been published to date.

Muthukumar and DesRoches (2004), and Jankowski (2004) both note a considerable disadvantage of the Kelvin element: tensile forces can be induced when contact occurs (Figure 2.8A). Any tensile force in the contact element occurs towards the end of a collision when the damping force produces a tensile force that is greater than the compressive spring force. A tensile contact force is physically inaccurate and is a shortcoming of the element. This shortcoming can be addressed with minor modifications to the element (for example, Shakya et al. 2008), however it must be noted that Equation 2.11 is invalid for these new models.

Jankowski (2004; 2005) presented a modification to the Hertz element which incorporated plasticity into the collision, termed the 'nonlinear viscoelastic element'. Inelasticity was introduced with the following piecewise relation;

$$F(t)=\begin{cases}\beta x^{\frac{3}{2}}(t)+c(t)\dot{x}(t) & \text{if } x\le 0, \dot{x}(t)>0\\ \beta x^{\frac{3}{2}}(t) & \text{if } x\le 0, \dot{x}(t)\le 0\\ 0 & \text{if } x>0\end{cases} \qquad (2.13)$$

where

$$c(t)=2\zeta\sqrt{\beta\sqrt{x(t)}\frac{m_1 m_2}{m_1+m_2}} \qquad (2.14)$$

A relationship between the coefficient of restitution (e), and the damping coefficient (c) was later published (Jankowski 2006);

$$\zeta=\frac{9\sqrt{5}}{2}\frac{1-e^2}{e(e(9\pi-16)+16)} \qquad (2.15)$$

Equation 2.15 is noted to be an approximation of the actual relationship between these two parameters. However, the equation is almost identical to the numerically calculated function.

A second damping scheme for the Hertz element was proposed for pounding analyses by Muthukumar and DesRoches (2006). The element had been previously adopted in robotics and multibody systems analyses and is termed the 'Hertzdamp' element. The element was defined as:

$$F(t) = \begin{cases} \beta x^{\frac{3}{2}}(t) + c(t)\dot{x}(t) & \text{if } x \le 0 \\ 0 & \text{if } x > 0 \end{cases} \qquad (2.16)$$

where

$$c(t) = \zeta x^{\frac{3}{2}} \qquad (2.17)$$

$$\zeta = \frac{3\beta(1-e^2)}{4\dot{x}(t_0)} \qquad (2.18)$$

and $\dot{x}(t_0)$ is the relative velocity at the onset of collision (Equation 2.9). In 2009, Ye et al. demonstrated that Equation 2.18 is an approximation of the actual relationship between ζ and e, and that this formula produces significantly inaccurate values when $e < 0.8$. A revised approximation was also proposed:

$$\zeta = \frac{8\beta(1-e)}{5e\dot{x}(t_0)} \qquad (2.19)$$

This relationship is shown to be valid for $e \ge 0.4$.

2.2.3 Three Dimensional Pounding Specific Contact Models

Methods to model three dimensional pounding effects generally require further information about each collision. These methods are considered separately here. Papadrakakis et al. (1996) created a Lagrange Multiplier formulation for use in three dimensional modelling. A modified method was subsequently presented by Mouzakis and Papadrakakis (2004), which replaced the Lagrange Multipliers with calculations based on stereo mechanics. Both methods use the colliding objects' plan geometry to determine whether any collision has occurred (Figure 2.10). The calculations used in this formulation are too onerous to present here, however the method models stereo mechanics, object geometry, and friction during contact. These mechanisms are used to determine the post collision velocity and displacement of both objects for the time step following contact. Rigid diaphragms are a necessary assumption for the use of this method.

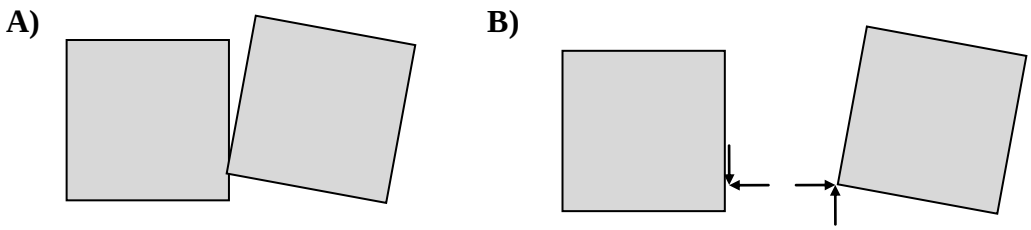

Figure 2.10 Determining whether collision occurs between two rigid floors. A) plan floor geometry at time of contact. B) equivalent force representation

Another three dimensional contact model was produced by Zhu et al. (2002), which was developed for collision between bridge decks. The element considers a collision between a node and a surface (Figure 2.11). The orientation of the force is determined by the orientation of the contactor node (point k in Figure 2.11). The Kelvin element is used in this location and equivalent forces are calculated at the four corners of the target surface (points a, b, c, and d). Like the other 3D models in this section, this process assumes that the target surface is perfectly rigid. Friction forces are also modelled up to the magnitude of static friction. After this point, the element simulates the relative sliding of the two colliding objects. To date, this element has not been used in building pounding analyses.

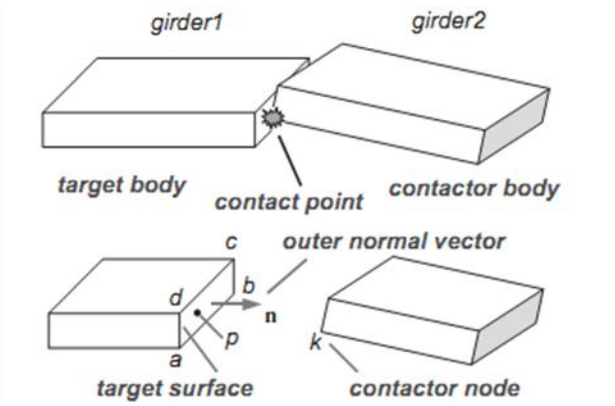

Figure 2.11 Zhu et al. contact model between a node and a target surface. Image reproduced from Zhu et al. (2002).

2.2.4 Pounding-Specific Contact Models between Distributed Masses

The performance of a contact model is also dependent upon the internal modelling of each colliding object. The contact models presented in Sections 2.2.2 and 2.2.3 implicitly assume collision of rigid objects. The effect of this assumption has been previously investigated for bridge pounding. Watanabe and Kawashima (2004) modelled deck flexibility during collision by considering collision as a wave propagation problem. A single collision between two identical decks was numerically modelled. In order to model the wave propagation, five, ten and twenty axial elements were modelled in each bridge deck during various analyses (Figure 2.12). An elastic Kelvin element was used to model contact, with the contact element stiffness defined in terms of the adjacent deck element stiffness (Figure 2.13).

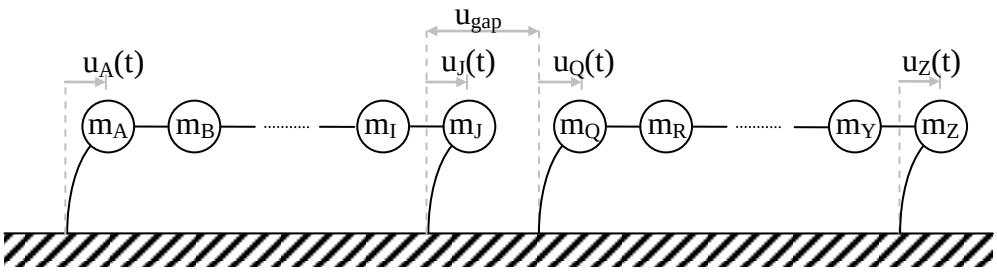

where $m_1 = \sum_{i=A}^{J} m_i$ and $m_2 = \sum_{i=Q}^{Z} m_i$

Figure 2.12 Nodal layout for collision between distributed masses

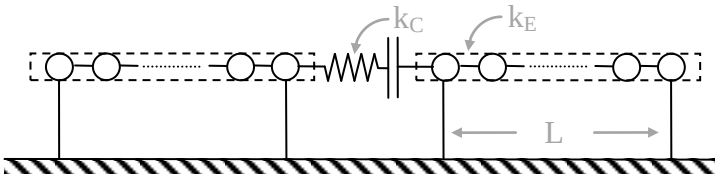

Figure 2.13 Layout of contact element and internal deck elements

This relationship is formulated as;

$$\gamma = \frac{k_C}{k_E} = \frac{k_C L}{nEA} \qquad (2.20)$$

where E = Young's modulus of elasticity, A = bridge deck cross sectional area, L = bridge deck length, and n = the number of elements within the deck. By comparing numerical simulation with the theoretical response, Watanabe and Kawashima determined that the most accurate collision modelling is obtained using $\gamma \approx 1.0$. Watanabe and Kawashima further demonstrated that modelling collision with the assumption of rigid decks can significantly change the predicted collision response. The effects of diaphragm flexibility on pounding building systems are considered in detail in Chapter 3.

2.2.5 The Coefficient of Restitution

The coefficient of restitution is a key parameter in many contact models, but has received little specific study. Various researchers have adopted or reported values of e between 0.4 (Zhu et al. 2002) and 1.0 (Conoscente et al. 1992). The coefficient of restitution is usually selected between 0.75 and 0.5 and a number of researchers have specifically adopted e = 0.65 (Jankowski 2005). Recently, Jankowski (2010) investigated the influence of impact velocity on the coefficient of restitution. Almost all prior pounding analyses have assumed that the coefficient of restitution is constant throughout the duration of any analysis. However Jankowski recalls that experimental studies in the physics discipline showed that the coefficient of restitution is dependent on the relative velocity (Goldsmith 1960). Jankowski performed similar experiments on common

building materials. The experiment involved dropping a ball of the tested material from different heights. The ball was dropped onto a fixed flat surface of the same material, and the ball's pre and post collision velocities were recorded. These velocities were then used to determine the coefficient of restitution of each impact (Figure 2.14).

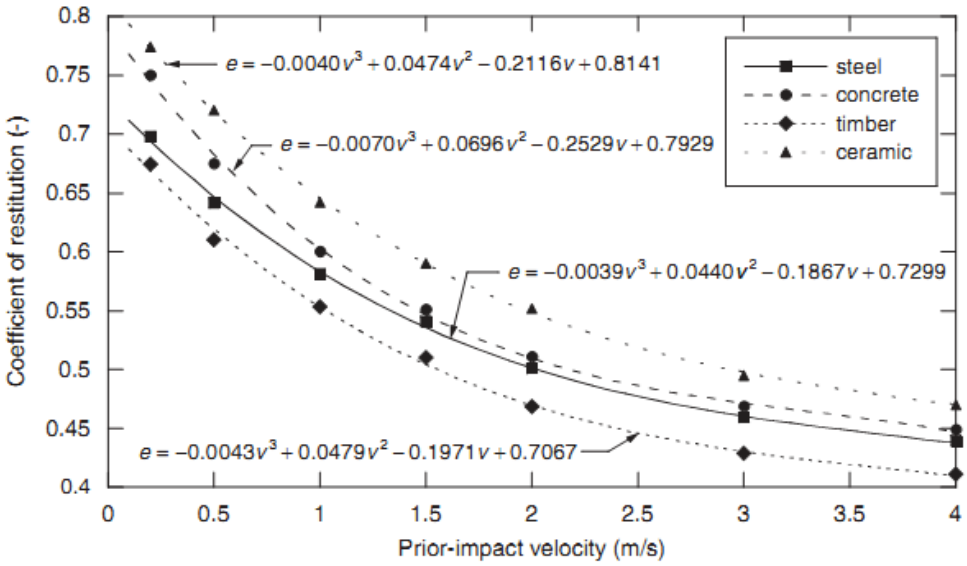

Figure 2.14 Coefficient of restitution dependence on relative velocity. Image reproduced from Jankowski (2010).

To test these results, Jankowski performed a small scale shaketable experiment. The experimental displacements were predicted using two modelling approaches; a constant coefficient of restitution, and a coefficient of restitution varying according to Figure 2.14. The variable coefficient of restitution was shown to be slightly more accurate than the constant coefficient (the weighted error function reduced by 2.1 percentage points over the course of the tested record). It was noted that a larger scale experiment is required for further verification.

The coefficient of restitution has not received further attention partially because displacement results have been reported as being reasonably insensitive to small changes in the property (Papadrakakis et al. 1991; Anagnostopoulos and Spiliopoulos 1992; Azevedo and Bento 1996). However, Anagnostopoulos notes that collision force and floor acceleration properties are much more dependent upon this property. Furthermore, Dimitrakopoulos et al. (2010b) have also shown that these findings are at least partially dependent upon the chosen excitation frequency (refer Figure 2.19). The justification for the selection of the coefficient of restitution's value is discussed further in Section 2.2.6.

2.2.6 Discussion

While a reasonably wide array of contact element options are available, it is still difficult to accurately model collision. The strengths and weaknesses of each modelling method are

presented in Table 2.2. The ability of the methods to be incorporated into existing non-linear time history programs is also qualitatively assessed (see the key at the end of Table 2.2).

Table 2.2 Summary of contact methods' characteristics

Advantages	Disadvantages
Stereo mechanics *	
Small calibration requirements – only the coefficient of restitution needs to be specified.	**Difficult to implement** – stereo mechanics is defined in terms of velocities, however numerical time history programs are typically defined in terms of accelerations. Thus implementation in a program requires specialised coding. **No force data** – the collision force cannot be measured from stereo mechanics .
Hertz element **	
Continuous function – the element is more numerically stable because the force relation is continuous.	**Parameters undefined** – the parameter β was initially intended for modelling rounded surfaces. No rational definition of β exists for modelling building pounding. This also means that recorded collision forces are not reliable. **No force data** – The recorded forces in this element are dependent upon the element stiffness. A larger stiffness results in a shorter collision with larger peak collision velocities. Reliable force data cannot be obtained unless β is rationally defined.
Lagrange multiplier *	
No calibration requirements – no additional parameters are required to run a model.	**Difficult to implement** – Lagrangian multipliers use a modified equation of dynamic equilibrium. This means that specialised coding is required to implement this method in a numerical time history program. **No force data** – Force data can be calculated but will be governed by the time step of the analyses if the floors are modelled as rigid. Investigations using flexible floor diaphragms have not been investigated to date.
Kelvin **	
Conceptually simple – the Kelvin element is convenient due to its simple componentry. **Popular** – many programs already support this element since the coding of the element is relatively simple.	**Parameters undefined** – the Kelvin stiffness is still reasonably arbitrarily chosen. A large stiffness is desired to minimise material overlap, however this must be balanced with numerical stability of the program. Numerical instability increases with sudden and drastic changes in stiffness. **No force data** – the reported collision force is dependent upon the collision element stiffness, which is reasonably arbitrarily assigned. **Physically unrealistic** – the Kelvin element does not accurately represent the physical phenomenon. The maximum stiffness of the element is governed by numerical stability rather than physical considerations. Unrealistic tensile contact forces can also when using this element.

Multilinear **	
Conceptually simple – the multilinear element requires definition of only two stiffnesses.	**Parameters undefined** – No guidance on k_a or k_r is currently available. Furthermore, no relationships or recommendations on the ratio k_r/k_a exist. This ratio governs the energy dissipation of the element. **No force data** – as per Kelvin element **Physically unrealistic** – The hysteresis of each contact changes the gap between the buildings (Δu). This gap change is completely arbitrary since it has not been calibrated to any physical phenomena.
Nonlinear viscoelastic **	
Continuous function – this element has one force discontinuity which occurs when the damping is removed (see Equation 2.13). This element is less numerically stable than the Hertz element, but more stable than the Kelvin element.	As per Hertz element.
Hertzdamp **	
As per Hertz element.	As per Hertz element.
Papadrakakis 3D contact *	
Models 3D contact – allows the modelling of contact friction in addition to axial contact. **Low calibration required** – only the coefficient of restitution and the coefficient of friction need to be specified.	**Assumes rigid boundary** – No flexibility in the surface of the colliding objects is modelled. Thus contact always occurs at one colliding object's corner. **Difficult to implement** – stereo mechanics used is in the axial definition of this element providing similar issues to that described for the stereo mechanics element. Furthermore, the geometry of both colliding objects is required for calculation of the contact. This information is frequently not easily accessible in numerical programs. **No force data** – the collision force cannot be measured from stereo mechanics .
Zhu 3D contact *	
Models 3D contact – allows the modelling of contact friction in addition to axial contact.	**Assumes rigid boundary** – As per the Papadrakakis 3D contact element. **Difficult to implement** – this element is easier to implement than Papadrakakis' model. However, geometry information is still required that is frequently not easily accessible in numerical programs. **Parameters undefined** – the axial component of this element uses the Kelvin element. Thus the disadvantages of the Kelvin element are also present here. **No force data** – as per Kelvin element. **Physically unrealistic** – as per Kelvin element.

* *Contact method cannot be easily added to programs.*

** *Contact method can be added to other programs with a small amount of effort.*

*** *Contact method already exists in multiple programs and can be added to other programs with a small amount of effort.*

In addition to the tabulated disadvantages, almost all implementations of the available elements have used a constant, and rather arbitrarily selected, coefficient of restitution. These values have been justified by comparison to similar situations where more detailed research has been performed.

Jankowski (2005) presented a summary of four situations that were considered to be analogous to building pounding; metal spheres dropped onto metal plates, a concrete striker hitting the end of a prestressed concrete pile, the collision of two steel small scale bridge decks, and the collision of two small scale steel towers. Unfortunately, these situations present a number of characteristics that are not present in building pounding. As shown in Figure 2.15, all scenarios except the bridge decks use a hemispherical or near hemispherical contacts, which were intentionally installed by the experimenters. Use of this type of contact has continued in recent experimental studies (Guo et al. 2008; Guo et al. 2009). As discussed in Section 2.2.1, hemispherical contacts produce a nonlinear contact relationship that is caused by the rounded contact surface. These tests cause contact force relationships similar to the Hertz element because of the contact surface's design. The primary mechanism that is activated in the collision is thus notably different to that expected in floor/floor contact.

The model bridge decks are the most similar configuration to floor/floor collision (Zhu et al. 2002). However, the reported value of the coefficient of restitution ($e = 0.4$) is significantly lower than conventional expectation. Very little specific information is presented for any contributing reasons for this result and the low value of restitution is not specifically discussed. Additionally, the previously reported velocity dependence of the coefficient of restitution (Section 2.2.5) leaves significant uncertainty regarding this parameter. It should be noted that the experiments testing velocity dependence were performed with a spherical contact.

The Kelvin element is used in all modelling performed in this thesis. This is selected because of the element's simplicity and manipulability. The alternative to the Kelvin element is the Hertz element. However, the advantages of the Hertz element are outweighed by the lack of clarity regarding the definition of β. The highlighted shortcomings of the Kelvin element are addressed in subsequent chapters.

Data on the force of the collision is consistently unavailable. In many instances this absence of information may be acceptable. However, if damage at the collision interface is to be considered, the collision force is significant. This aspect is related to colliding object flexibility and is also investigated further in the following chapters.

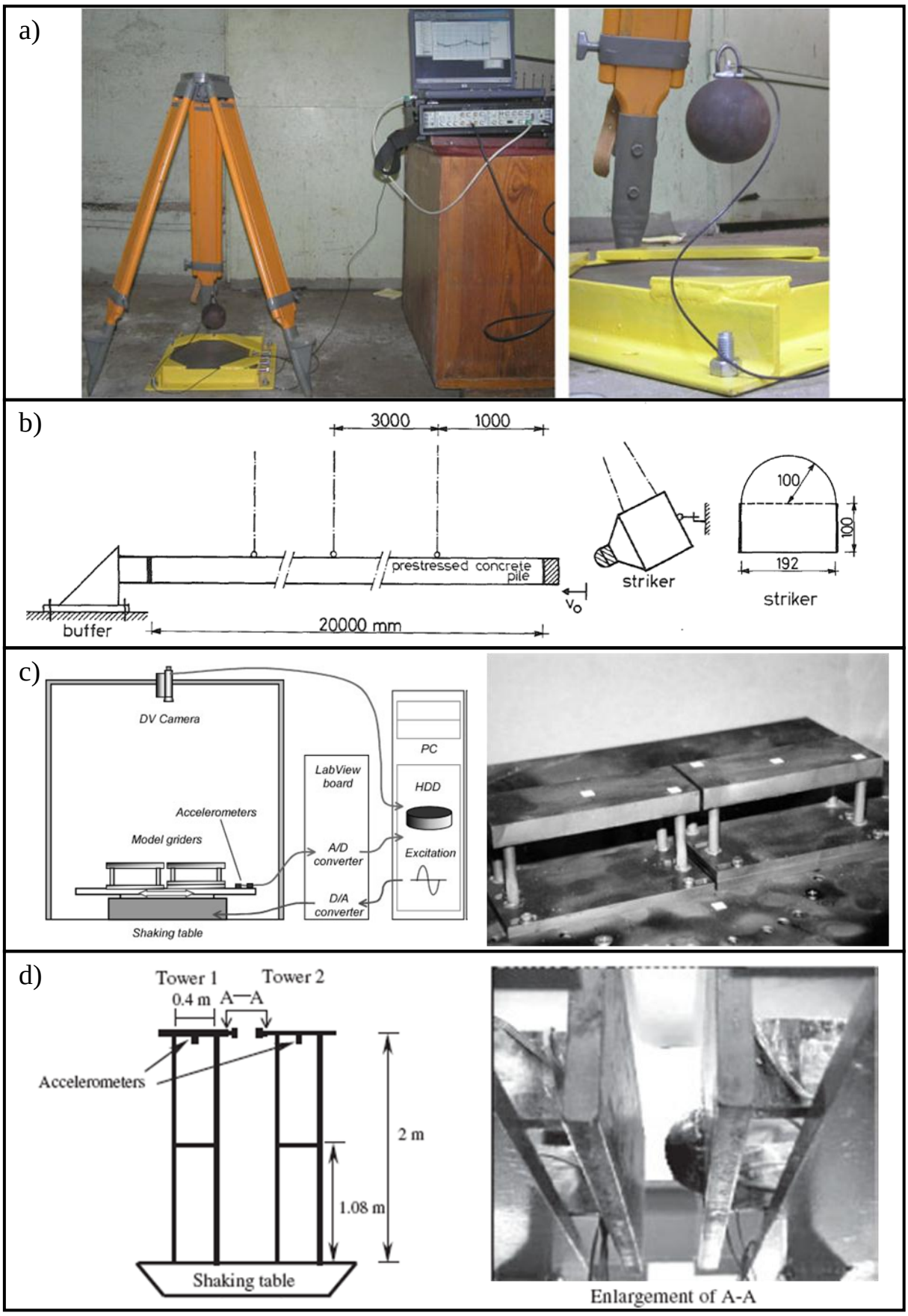

Figure 2.15 Experiment configurations used to calculate e. a) sphere vs. plate (Jankowski 2010). b) striker vs. pile (van Mier et al. 1991). c) model bridges (Zhu et al. 2002). d) Model towers (Chau et al. 2003). Images reproduced from their respective papers

2.2.7 Conclusions

The following conclusions are drawn based on the contact element review presented in Section 2.2.

1. Nine existing contact models are described and analysed in terms of their current capabilities. All of these contact models have drawbacks which currently limit the understanding of building contact. Specifically, meaningful information on the contact force is currently unavailable.
2. The currently available elements are considered to be sufficiently accurate if only building displacements and interstorey shears are of interest. This is because these parameters have been found to be insensitive to the parameters that are not currently well defined.
3. The Kelvin element has been adopted for the majority of modelling performed in this thesis.

2.3 Prediction of Separation Distances to Prevent Pounding

The simplest method to prevent pounding damage is to provide sufficient separation between adjacent buildings to avoid any contact during an earthquake. This approach requires a rational method to calculate the necessary separation, but does not require simulation of building contact. This means that the elements presented in Section 2.2 are not required for this type of modelling. Methods to predict the required building separation have been recently summarized by Lopez-Garcia and Soong (2009). The information presented in this section adopts a similar format and similar terminology to this paper.

2.3.1 Common Aspects to Separation Distance Prediction

To date, predictions of required building separations have used combinations of the expected maximum displacements of individual buildings. This is usually done using the following relationships:

$$u_{rel}(t) = u_1(t) - u_2(t) \tag{2.21}$$

$$X_1 = \max[u_1(t)] \tag{2.22}$$

$$X_2 = \max[u_2(t)] \tag{2.23}$$

$$X_{rel} = \max[u_{rel}(t)] \tag{2.24}$$

where u_1 and u_2 are the displacements of Building 1 and Building 2 at a given point in time (see Figure 2.8C), and u_{rel} is the relative displacement between these buildings. For a given ground motion, the relative displacement of two buildings is a function of time. The separation required to prevent pounding for this ground motion is equal to the maximum relative displacement recorded during the ground motion (Equation 2.24). However, approximate values of X_{rel} can be obtained by using various combinations of the maximum individual buildings' displacements (Equation 2.22 and Equation 2.23). When the two buildings are different heights, X_1 and X_2 correspond to the building displacements at the height of the shorter building. Existing research has focused on methods that predict X_{rel} based on a simplified Complete Quadratic Combination (CQC). The simplified CQC considers only the fundamental mode of each building when calculating each building's maximum displacement:

$$S_{req} = X_{rel} \approx \sqrt{X_1^{\,2} + X_2^{\,2} - 2\rho \times X_1 X_2} \qquad (2.25)$$

where ρ = the correlation coefficient between the two buildings and S_{req} = the minimum separation required to prevent pounding. Equation 2.25 was proposed for building separation prediction by Jeng et al. (1992) and is identified as the Double Difference Combination rule (DDC). The majority of research in this area has focused on ways to define the correlation coefficient, ρ.

2.3.2 Conventional Combination Methods

Combination methods have been previously developed in other research fields. Perhaps the most common use of combination techniques is found in modal analysis, where a building's response is obtained by combining the results of individual modes. The two simplest and most well known of these methods are absolute combination (ABS) and square root sum-of-the-squares (SRSS) combination. These methods can be obtained by substituting $\rho = -1$ or $\rho = 0$ into Equation 2.25, respectively. The ABS combination always over predicts the necessary building separation since the method assumes that both buildings' maximum deflections occur at the same time, and act in the opposite directions (towards each other). SRSS is found to be a more accurate method; however, SRSS can be either conservative (over predicting minimum separations) or unconservative depending on the specific circumstances. SRSS is typically used by researchers as a baseline to allow comparison to any alternative method.

2.3.3 Alternate Combination Methods

This section primarily describes the available combination methods that have been developed specifically for modelling of building separation. Evaluation of these methods' is considered in detail in the following section.

Jeng et al. (1992) first proposed using an existing correlation coefficient to evaluate building separation, which was derived using white noise excitation. This method was subsequently tested and recommended for use in the National Building Code of Canada by Filiatrault (Filiatrault et al. 1994; Filiatrault and Cervantes 1995). The correlation coefficient is calculated using:

$$\rho = \frac{8\sqrt{\xi_1\xi_2}\left(\xi_1 + \xi_2\frac{T_1}{T_2}\right)\left(\frac{T_1}{T_2}\right)^{\frac{3}{2}}}{\left[1-\left(\frac{T_1}{T_2}\right)^2\right]^2 + 4\xi_1\xi_2\left[1+\left(\frac{T_1}{T_2}\right)^2\right]\left(\frac{T_1}{T_2}\right) + 4\left(\xi_1^{\,2} + \xi_2^{\,2}\right)\left(\frac{T_1}{T_2}\right)^2} \qquad (2.26)$$

where T = building fundamental period and ξ = building damping ratios. This approach assumes that the considered buildings' deformations can be approximately predicted by the buildings' elastic properties. If the building's damping ratios are set to be equal, ρ approaches 1.0 when T_1/T_2 approaches 1.0. In an elastic system with SDOF oscillators this situation produces $S_{req} = 0$, which corresponds to completely in phase movement of the two buildings.

The research group that proposed Equation 2.26 subsequently developed a method to include the effects of building inelasticity in the correlation coefficient (Kasai et al. 1996a). This was achieved by empirically relating effective elastic properties to building displacement ductility. The effective values depend on the adopted inelastic hysteresis for the building. For a bi-linear building hysteresis the effective parameters were calibrated using a post-elastic stiffness 5% that of the elastic stiffness. The resulting relationships are:

$$T_{eff} = T\left[1 + 0.09(\mu - 1)\right] \qquad (2.27)$$

$$\xi_{eff} = \xi + 0.084(\mu - 1)^{1.3} \qquad (2.28)$$

These effective parameters were then used in Equation 2.26 to calculate the correlation coefficient. The same research group (Jeng and Kasai 1996; Jagiasi and Kasai 1996) also investigated the effects of travelling waves (the delay in seismic impulse between foundations caused by the propagation of the ground motion along the ground surface). This was done by

making additional modifications to Equation 2.26. The vast majority of building pounding configurations was found to be insensitive to wave propagation effects.

Penzien (1997) developed a separate method to create effective elastic properties for defining building separation. This method uses a secant stiffness to represent an assumed bilinear building hysteresis, and represents the building damping through calculation of the hysteresis' equivalent viscous damping. Some numerical modification is made to these formulae to account for the likely level of hysteretic damping when the maximum relative displacement occurs, (which does not necessarily occur at the same time as the maximum deformation of either building). The proposed parameters are:

$$T_{eff} = T\sqrt{\frac{\mu}{1.54 + \alpha(\mu - 1.54)}} \tag{2.29}$$

$$\xi_{eff} = \xi + \frac{2}{\pi}\left(\frac{1.54(\mu - 1.54)(1-\alpha)}{\mu(1.54 + \alpha(\mu - 1.54))}\right) \tag{2.30}$$

where α = the ratio of post-elastic stiffness to elastic stiffness.

A third simplified method was developed using the Pseudo Energy Radius (PER) (Valles-Mattox and Reinhorn 1996; Valles and Reinhorn 1997). The method modified Equation 2.26 to use the maximum PER for each building, rather than the maximum displacement. The PER produces an effective building displacement and is found by taking the vector sum of two perpendicular component vectors. These are; the building velocity divided by the building's circular natural frequency, and the building displacement (Figure 2.16). This method uses numerical simulation with filtered white noise ground motions to calculate the required ρ (i.e. the numerical results for S_{req} were used to back calculate the required ρ for a variety of building properties). The required value of ρ is then presented in multiple plots for the considered building configurations. It was also suggested that the PER could be used to evaluate the effect of pounding on buildings that are almost sufficiently separated to prevent collision. However, no examples using this method have been published to date.

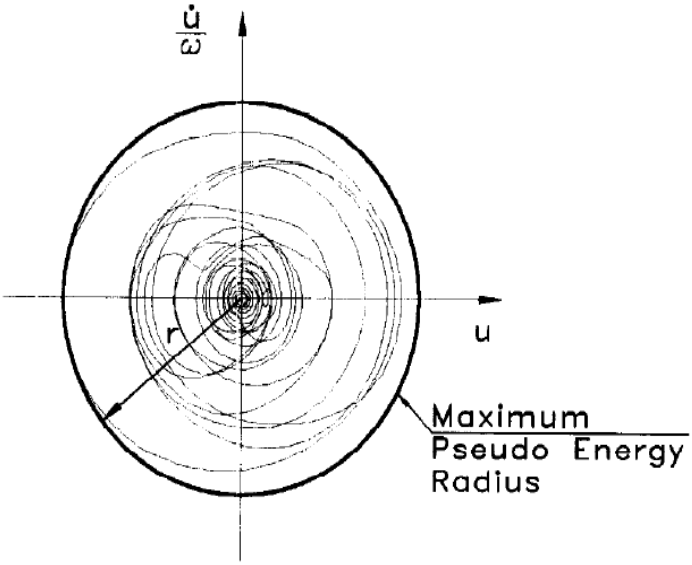

Figure 2.16 Calculation of Pseudo Energy Radius using building velocity and building displacement. Image reproduced from Valles-Mattox and Reinhorn 1996.

Other researchers have used the full Complete Quadratic Combination (CQC) method in order to include the effects of higher modes in the calculation of required separation distance (Hong et al. 2003; Wang and Hong 2006). This research found that combining modes to calculate minimum separation involves a different mechanism to that used in normal modal combinations. This difference comes from building separation being a one-sided crossing problem (where only actions toward the adjacent building should be included in the building separation calculation), while standard building actions are two-sided crossing problems (where a mode's actions in either direction contribute to the overall combined action). This difference is illustrated in Figure 2.17.

Standard action combination
Two-sided crossing problem

Separation displacement combination
One-sided crossing problem

Figure 2.17 Difference in application of modal combination techniques.

The researchers also considered the effect of uncertainty in building parameters by using probability distributions to define each building's period and damping ratio. These distributions effects were modelled using linear elastic buildings and the resulting separations were compared to the predictions using the CQC method. Generally, the CQC method was found to overestimate separation distance when the building's period ratio was within 0.75-1.25, but underestimate separation distance when the buildings periods were well separated. Part of this research team (Hao and Zhang 1999) also investigated the effect of travelling waves on the prediction of

separation distance. In this research, it was found that specific configurations of low rise buildings can be significantly affected by travelling waves.

2.3.4 Evaluating Combination Method Accuracy

All of the methods proposed in the previous section were evaluated for prediction accuracy by their respective authors. However, attention is focused here on independent evaluations performed by other researchers. Specifically, the ability of the presented models to predict inelastic building's required separations is evaluated.

Lin and Weng (2001) investigated the effectiveness of the ABS and SRSS methods in terms of their application in the 1997 Uniform Building Code (UBC). The 1997 UBC code uses a combination of the ABS and SRSS methods to specify minimum building separation. Multi-storey buildings were modelled assuming elasto-plastic interstorey hysteresis, to approximate the response of steel moment resisting frame systems. These building were subjected to 1000 artificial earthquake records to determine the probability of building pounding occurring over their 50 year building life. The method adopted in the UBC is found to provide poor estimates of the required building separation. This resulted in inconsistent probabilities of pounding occurrence. This means that buildings designed to this code are at varying risk of pounding, depending upon the buildings' specific configuration.

Lopez-Garcia and Soong assessed the various methods proposed or nominated by Filiatrault, Kasai, and Penzien (Garcia 2004; Lopez-Garcia and Soong 2009). A modified method based on that proposed by Valles was also tested. The tests used 1000 randomly generated seismic excitations for each building configuration. Building inelasticity was modelled using a bi-linear hysteresis with a post-elastic stiffness 5% that of the elastic stiffness. The period and inelasticity of each building were included as input parameters. Lopez-Garcia and Soong found that none of the listed methods could consistently provide accurate, or acceptably conservative, results. It was concluded that when inelastic buildings were modelled, none of the considered methods could provide any more accuracy that that obtained using SRSS.

2.3.5 Probabilistic Risk of Pounding

Recently, the risk of pounding for a specified building configuration has been address using probabilistic risk assessments (Tubaldi et al. 2012). The proposed method uses linear-elastic SDOF oscillators to predict the probability of pounding for a given peak ground acceleration and building configuration. While some example analyses are performed, ways to use the resulting probabilistic risks are not discussed. In its current form, the proposed technique is not strictly a

method to specify minimum building separation. Nevertheless, it is expected that the ongoing research in this area will produce such methods in the future.

2.3.6 Discussion

As seen in Section 2.3.4, simple prediction methods for the inelastic response of buildings have so far not adequately encapsulated the building response. While the method suggested by Hong et al. (2003) was not evaluated in Section 2.3.4, it also considers purely elastic building response and is thus similarly limited. As is discussed further in Section 2.5.3, the effect of soil structure interaction is also likely to play a significant role in determining the required building separation. Nevertheless, the ability to calculate the required building separation for a given earthquake intensity would be very useful for code specifications. It is conceivable that further research in this area will produce such a tool.

2.4 Outcomes of Pounding Analysis using SDOF Buildings

The simplest method of modelling contact between two buildings involves simplifying each building as much as possible. This process results in each building being modelled as a Single Degree of Freedom (SDOF) oscillator. Such simplification assumes that building performance can be appropriately predicted using the fundamental period of the structure, which is governed by the modelled building mass and stiffness. The SDOF approach is desirable in pounding research because it greatly reduces the number of variables that affect building response.

2.4.1 SDOF Building Pounding Research

SDOF analyses can be used to create analytical solutions for pounding in very specific circumstances. Davis (1992) investigated the performance of a SDOF oscillator colliding against a completely rigid surface using the Hertz element. These analyses used a constant sinusoidal oscillation as an input ground motion and studied the steady state response of the oscillator. An analytical solution for the steady state contact velocity was produced for the case of a completely rigid contact element. Davis found that complex steady state behaviours may occur, and sometimes no readily recognisable steady state behaviour could be observed. The paper also notes that pounding can cause an effective ‘period shift’ of the oscillator’s natural period, changing the frequency of the input oscillations at which the maximum SDOF collision velocity is achieved.

Chau and Wei (2001) extended Davis’s work by considering the steady state response of two colliding oscillators under constant sinusoidal excitation. The analytical solution produced in this paper provides the steady state relative contact velocity between the two oscillators. The

maximum contact velocity is found in terms of the period of the excitation, and is found to sometimes occur at periods less than that of either oscillator. This effect is noted as being potentially detrimental to buildings since the addition of a neighbouring building may cause an existing building to 'period shift' into a range of higher spectral acceleration during an earthquake.

While not strictly SDOF, Wang and Chau (2008) further investigated the effect of pounding between elastic buildings by including torsion interactions. Analyses were performed with each building containing a single translational, and a single rotational degree of freedom. Wang and Chau show that torsional actions can significantly increase the relative impact velocity when an eccentric (or offset) collision occurs. Reducing the building offset is also noted to not always reduce the buildings' relative impact velocity.

Very similar conclusions regarding torsion were reported earlier by Leibovich et al. (1996), who also modelled both torsion and translation for single floored buildings. A subsequent paper on this topic is known to exist (Leibovich and Rutenberg 1998), but could not be obtained by the author.

SDOF pounding analyses have also been employed to model larger numbers of buildings in a row (Figure 2.18). Anagnostopoulos (1988) modelled pounding of up to five SDOF buildings. Each building was found to be predominantly influenced by only its immediately adjacent neighbour on each side. This result has been used to subsequently justify modelling pounding in configurations of two buildings (one sided impact) or three buildings (two sided impact), rather than modelling entire rows of buildings. Buildings with one sided impact (for example, a building at the end of a row) were found to generally incur greater displacements as the result of pounding, while buildings with two sided impact (buildings in the centre of a row with no building separation) generally recorded decreased displacements. The paper also states that buildings with large differences in mass cause more pronounced pounding effects for the lighter structure.

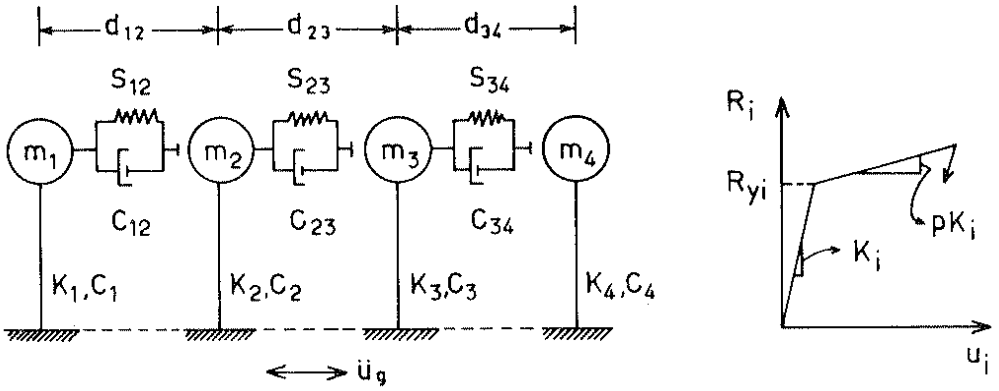

Figure 2.18 Numerical model of pounding between multiple buildings and adopted building hysteresis. Image reproduced from Anagnostopoulos (1988).

Athanassiadou et al. (1994) included travelling wave effects for modelling up to eight buildings in a row. The effect of the travelling wave was shown to be relatively minor. The analyses also report the amplified displacement of end buildings with one sided impact, and the reduction of internal, two sided impact buildings. Stiff buildings are found to be the most affected by pounding irrespective of their location, with stiff buildings that suffer one sided impact being the most adversely affected. Small building separations (~10 mm) between buildings with similar dynamic properties were determined to be sufficient to 'drastically reduce' pounding effects.

Jankowski (2006) used two SDOF oscillators to create pounding force 'spectra'. This was done by setting the base properties of each oscillator and then varying each oscillator's period. Jankowski produced the collision force in terms of both oscillator periods, creating three dimensional plots. The effects of gap, oscillator mass, oscillator ductility and travelling waves were investigated. Increasing the gap of oscillators reduced the number of configurations that experienced pounding. However, when pounding did occur, the contact force was largely unaffected.

Dimitrakopoulos et al. (2009a; 2009b; 2010a; 2010b) considered the pounding of up to three SDOF oscillators using dimensional analysis, and provides an explanation for the apparently contradictory conclusions drawn by other researchers (see also Section 2.5.7). The method relies on the pounding effect of an earthquake record being approximated as a single sine or cosine wave. The wave parameters are calculated from the record (namely, wave amplitude and frequency). When it exists, the wave parameters are determined from the earthquake record's dominant single pulse. This approach is valid for many near fault records. All other records have characteristic wave forms derived from a mean Fourier spectrum period and the excitation's peak ground acceleration (Dimitrakopoulos et al. 2009a). Once this characterisation is made, Dimitrakopoulos presents all independent variables and then performs a dimensional analysis to nondimensionalise these terms (shown here for the case with two elastic SDOF oscillators);

$$u_{max} = f\left(\omega_0, \omega_1, \xi_0, \xi_1, m_0, m_1, a_p, \omega_p, \delta, \varepsilon_N\right) \tag{2.31}$$

$$\frac{u_{max}\omega_p^{\,2}}{a_p} = \varphi\left(\frac{\omega_0}{\omega_p}, \frac{\omega_0}{\omega_1}, \frac{m_0}{m_1}, \frac{\delta\omega_p^{\,2}}{a_p}, \varepsilon_N\right) \tag{2.32}$$

or

$$\Pi_u = \varphi\left(\Pi_{\omega p}, \Pi_\omega, \Pi_m, \Pi_\delta, \Pi_\varepsilon\right) \tag{2.33}$$

where u_{max} = maximum displacement of oscillator 0; ω = the circular natural frequency, ξ = damping ratio and m = mass of oscillators; subscripts 0 and 1 identify the two oscillators; a_p and ω_p = the acceleration amplitude and frequency of the wave pulse; δ = the oscillator separation; and ε_N = the coefficient of restitution. Building damping parameters (ξ) do not appear in Equation 2.32 or Equation 2.33 because they have been assumed to be constant ($\xi_0=\xi_1=0.05$) (Dimitrakopoulos et al. 2009b). Dimitrakopoulos shows that the response of Π_u is 'self-similar'. These means that if two different models have different properties, but possess the same independent non-dimensional numbers ($\Pi_{\omega p}$, Π_ω, Π_m, Π_δ, Π_ε), they will produce the same non-dimensional results (i.e. Π_u). This result is shown to be more beneficial than the common methods used to express the consequences of pounding interaction, such as amplification factors (for example, $u_{max}/u_{max\ (no\ pounding)}$). This is because the existing methods do not possess self-similarity.

Dimitrakopoulos investigated the effects of the relevant non-dimensional numbers using Lagrange multipliers to simulate contact for three scenarios; pounding of an oscillator against a rigid wall, pounding of two oscillators, and pounding of three oscillators when the properties of the two external oscillators are equal. Considering the single oscillator case, Dimitrakopoulos shows that increasing the coefficient of restitution does not always increase the response of the pounding oscillator (Figure 2.19). For example, decreasing the value of the coefficient of restitution (ε_N) causes a reduction in maximum oscillator displacement when $\Pi_{\omega p} = 0.4$, but an increase in displacement when $\Pi_{\omega p} = 1.2$. These results are in agreement with separate analyses by the author in Chapter 3.

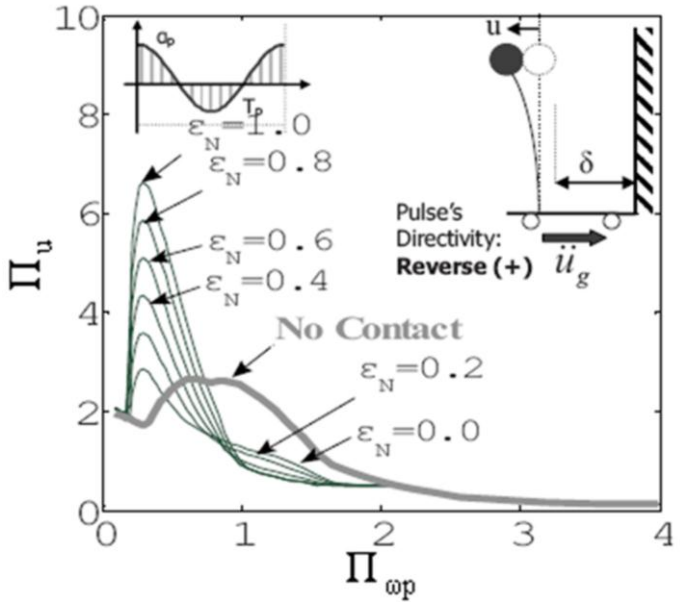

Figure 2.19 Influence of changing the coefficient of restitution (Π_δ=0.5; Π_m and Π_ω do not exist since there is only one oscillator). Image reproduced from Dimitrakopoulos et al. (2010b)

When two oscillators were modelled, the effects of relative stiffness and relative mass between the oscillators were investigated. Amplification or deamplification of the stiffer and the more flexible oscillator was shown to be dependent upon $\Pi_{\omega p}$ (amongst other dimensionless terms). $\Pi_{\omega p}$ includes properties from the ground motion (namely ω_p), which means the response of the collision is also dependent on the ground motion. In general terms, for small $\Pi_{\omega p}$ the response of the more flexible oscillator is amplified, while larger values of $\Pi_{\omega p}$ amplify the response of the stiffer structure (compared to non contact oscillation). The specific properties that cause displacement amplification are dependent on the specific dimensionless numbers of the considered system.

The dimensionless parameters are proposed as an explanation for why apparently contradictory statements appear in different researcher's pounding parameter studies. It is possible for a researcher to perform many analyses but still remain within a relatively small range of other important parameters. For example, the mass and gap of the structure may be varied, however if $\Pi_{\omega p}$ remains reasonably constant, then the observed trends are produced from only one spectral region and thus are not necessarily applicable to other situations.

Dimitrakopoulos also extended the dimensional analysis treatment from completely linear elastic structures to elasto-plastic and bilinear structural systems (Dimitrakopoulos et al. 2010a). The nonlinear systems increase the number of dimensionless numbers that are needed to completely describe the system. This increases the amount of dimensional space that must be evaluated if a complete characterisation of the pounding problem is desired.

In addition to the assumptions inherent in SDOF analysis, the major assumption in this research is the characterisation of a total earthquake record using only a single sine or cosine acceleration pulse. This assumption was checked for a bridge configuration using a combination of elastic and bilinear springs (Dimitrakopoulos et al. 2010a). A total of 62 Greek earthquake records were analysed to produce Figure 2.20. A completely linear relationship in this figure would imply complete equivalence between the simplified and the actual ground motions. Dimitrakopoulos concludes that the adopted characterisation sufficiently captures the fundamental aspects of the ground motions.

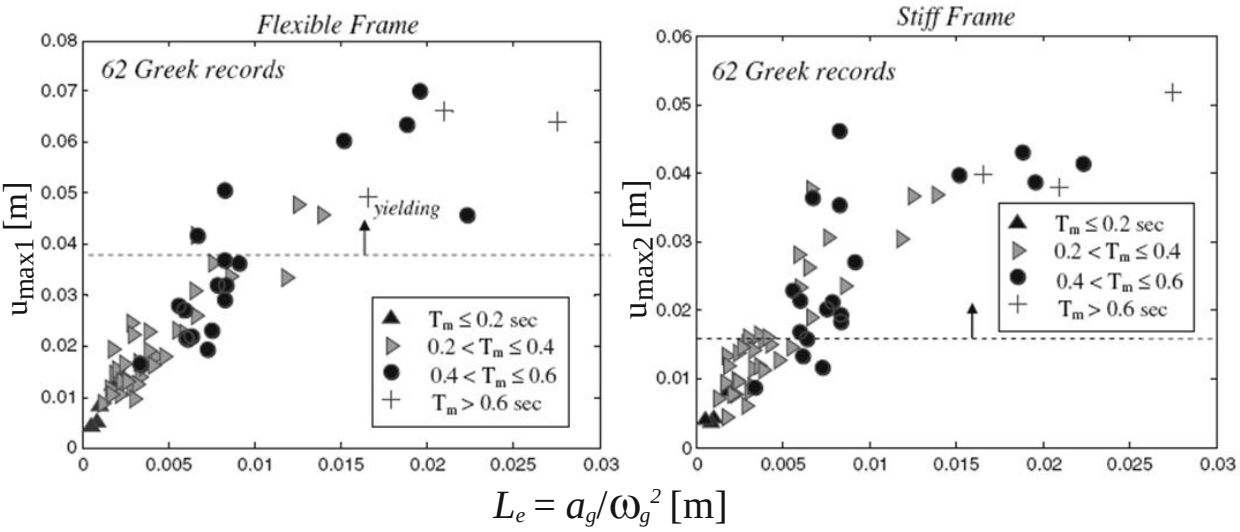

Figure 2.20 Comparison of maximum bridge displacement using full ground motions with calculated characteristic excitation variables. Images reproduced from Dimitrakopoulos et al. (2010a)

Research by others who have drawn similar conclusions to those presented in this section are not explicitly detailed here. These papers include contributions from Govil and Singhal (1991), and Pantelides and Ma (1996, 1998).

2.4.2 Discussion

Unfortunately many applications of SDOF building pounding results are limited. While analytical solutions have been produced, their limiting assumptions do not represent any common scenario where pounding may be anticipated. However, SDOF modelling of multiple buildings with pounding potential or torsional pounding effects does provide fundamental insights into pounding. SDOF modelling can thus be considered an effective means of performing initial sensitivity studies on aspects of pounding behaviour. Given the ready availability of computers with powerful computational abilities, more detailed investigation is usually possible for deeper understanding of the phenomenon under consideration.

The dimensional analysis of pounding structures contains important lessons for a wide range of pounding research, including the work undertaken in this thesis. It is important to be aware of all parameters that govern pounding response. However, it is noted that the goals of the work undertaken in subsequent chapters is different to that of Dimitrakopoulos. This work does not attempt to parametrically characterise pounding for all possible building scenarios. Furthermore, the adopted models feature many degrees of freedom in each building, and a complete dimensional analysis would require consideration of (and development of dimensionless numbers for) every degree of freedom's mass and natural frequency. Performing a complete study of these parameters is not practically feasible. The dimensionless numbers determined by Dimitrakopoulos et al. do succinctly describe a pounding system, and their merits are considered further in Section 6.6.1.

2.5 Outcomes of Pounding Analysis using MDOF Buildings

The most sophisticated pounding models involve explicit modelling of contact and detailed modelling of each building involved in collision. Multi degree of freedom (MDOF) building models enable more detailed characterisations of these buildings. MDOF building modelling involves using one or more degrees of freedom to represent each floor of each building. This allows parameters such as interstorey shear and interstorey drift to be recorded. During the last 20 years, MDOF building modelling has been the most common method used for pounding analyses. As a result, the research presented here is categorised by the characteristics of the adopted modelling techniques, and the focus of the research. These topics are: linear-elastic building models, non-linear building models, 3D pounding investigations, soil structure interaction modelling, floor/column collision modelling, and analysed mitigation methods. They are presented in turn below. A discussion on various aspects of the presented work is also presented in Section 2.5.7.

2.5.1 Linear-Elastic Building Models

This section details building models that does not model inelasticity in either building. Note that some of these models do include inelasticity in the collision between the buildings (i.e. the adopted coefficient of restitution is less than 1.0).

One of the earliest MDOF models considered pounding as a pseudo-static loading (Stavroulakis and Abdalla 1991). Each building had an upper triangular (such as that used for equivalent static earthquake loading in NZS1170.5 (2004)) lateral load distribution applied towards the adjacent building. The system was mathematically represented as a quadratic programming problem and then solved by minimising the energy in the system. The presented results examined collision

between 6, 9 and 12 storey buildings. The results were presented in terms of contact forces at each building storey, and the contact forces were shown to be highly dependent upon initial building separation. This method was acknowledged as being highly idealised and was presented as a first attempt at understanding the pounding phenomenon.

Maison and Kasai (1990) modelled pounding by evaluating the building's dynamic performance depending on its current state (pounding or not pounding). Two buildings of differing height were modelled that were susceptible to pounding. The smaller building was assumed to be completely rigid, so only the larger building's performance was considered. When no building contact was detected, the larger building's movement was calculated using decoupled modes and incremental analysis. When the building's deflection caused collision at the top of the smaller building (which was assumed to be the only point of contact), a second state was introduced. In this state, the collision force was calculated using a spring with stiffness in the order of the building's floor stiffness. The spring was connected between the impacted floor and a rigid node representing the smaller building's roof. This new model was again solved using decoupled modes and incremental analysis. When the building's deflection reduces to the point where no collision occurs, the model reverts to the original building state. These two states were used as appropriate to model the building over the duration of the earthquake. The code to perform this modelling was named SLAM and was developed as an extension to the software program ETABs. The program was subsequently improved (Maison and Kasai 1992) to model the collision between two MDOF buildings and was renamed SLAM2 (Figure 2.21).

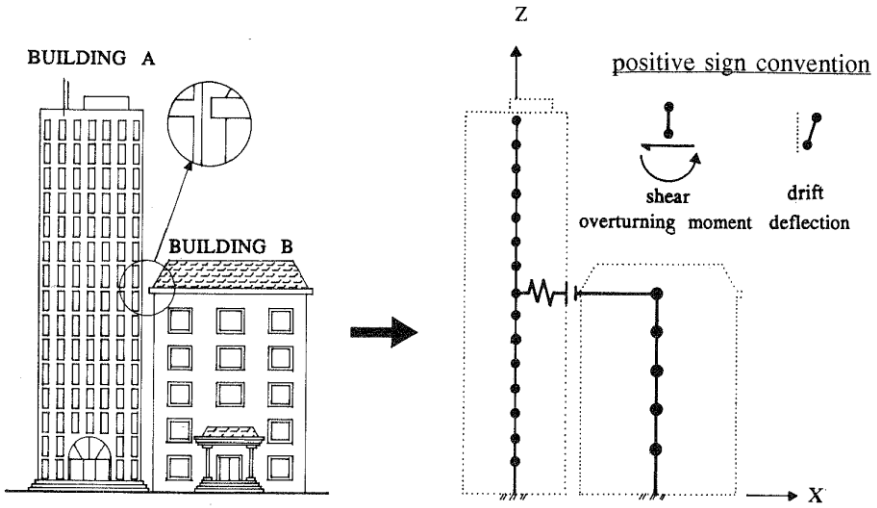

Figure 2.21 Idealisation adopted by Maison and Kasai. Image reproduced from Maison and Kasai (1992)

Both versions of SLAM were used to perform various example and parametric analyses. Analyses of a 15 storey building pounding with a rigid building of 4, 8 12 or 15 storeys was performed using SLAM. It was concluded that neglecting the effects of pounding leads to

unconservative design, especially in the floors above the point of collision. Analyses using SLAM2 considered collision between a 15 storey building and an 8 storey building, using a variety of building properties. Increasing building mass was reported to increase the response of the other building and building actions were observed to return to the 'no pounding' case as the building separation increases. However, relationships between response amplification and building separation were found to be nonlinear and did not affect all building actions equally. Finally, the effect of varying contact stiffness and collision specific damping was found to be relatively minor providing 'realistic' values are adopted.

A similar method was adopted by Conoscente et al. (1992). Here buildings were analysed using modal decoupling and contact was simulated using stereo mechanics. This allowed modelling of collision at any floor. The method was applied to the collision of two 15 storey buildings with 20% mass difference and 20% period difference. Interstorey shears up to 2.8 times greater than the corresponding shears without pounding were reported.

Papadrakakis et al. (1991) also performed sample analyses but used Lagrange multipliers for two 5 storey buildings. Two coefficients of restitution were tested under sinusoidal excitation and were found not to cause significant changes in the displacement response. It was also noted that pounding reduced the actions of the building closest to resonance, while increasing the other building's actions. A single inelastic building configuration was also presented in these results.

2.5.2 Nonlinear Building Models

While elastic building analyses are simpler to perform, they are unlikely to accurately represent many building pounding scenarios. This is because major earthquake ground motions usually cause damage and inelastic actions within buildings. Analytical models that have attempted to capture these inelastic building pounding responses are presented chronologically below.

Perhaps the most citied analytical pounding studies to date were performed by Anagnostopoulos and Spiliopoulos (Anagnostopoulos and Spiliopoulos 1992; Spiliopoulos and Anagnostopoulos 1992). In these tests the Kelvin element was used to model contact between 5 and 10 storey buildings with bilinear interstorey hysteresis (Figure 2.22). Soil flexibility was also modelled using a rotational spring and dashpot system.

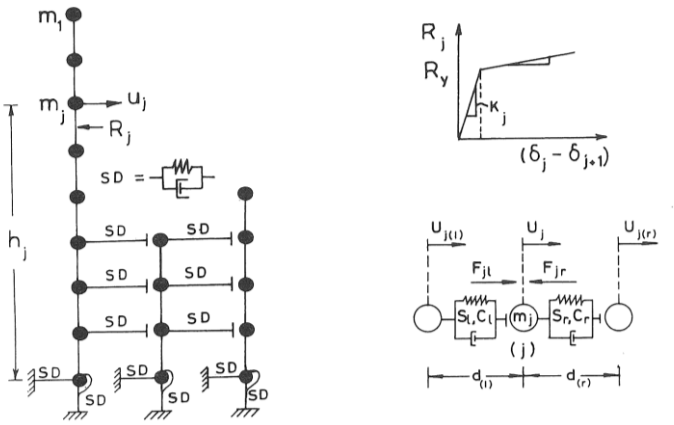

Figure 2.22 Example building layout. Image reproduced from Anagnostopoulos and Spiliopoulos (1992).

Results are presented in terms of the amplification of interstorey shear and interstorey displacement ductility. Pounding was modelled in configurations of two and three buildings. The effects of collision between buildings with changing height, building separation, building mass and collision element properties were investigated. Anagnostopoulos and Spiliopoulos conclude the following: building actions can be either increased or decreased by pounding depending on each building's mass and period; when two buildings have similar mass, the actions of the stiffer building are generally amplified; collision between buildings of differing height can cause "serious problems"; and, displacement ductility is insensitive to the stiffness of the Kelvin element. Anagnostopoulos and Spiliopoulos also note that high response amplifications do not occur when buildings' height, period and mass are similar. This is used to argue that building separation requirements could be relaxed under certain conditions.

Sinclair (1993) investigated 6 and 12 storey reinforced concrete frame buildings using the Hertz contact element. Sinclair reports that the change in frame response is highly variable depending upon the adopted ground motion. It was found that the largest response amplifications (compared to that recorded when no pounding occurred) were observed when applying design basis earthquakes, rather than maximum credible earthquakes. This was partly attributed to a previous observation made by Jeng et al. (1992): *'When a building is initially vibrating with a relatively small amplitude, and is then subjected to relatively high earthquake excitation, the forced vibration dominates the response. Thus, two buildings tend to vibrate in-phase driven by earthquake input. In contrast, when the building is initially vibrating with a relatively large amplitude, (after a period of high excitation), and is then subjected to relatively low earthquake excitation, the free vibration dominates the response'*. Significant amplifications in building response for buildings of differing height were also observed, in agreement with Anagnostopoulos and Spiliopoulos (1992).

Carr and Moss (1994) used Sinclair's models to further investigate a 12 storey vs. 6 storey building configuration with various building separations. Carr and Moss observe that collisions occur at all floors for small building separations, but as building separation increases, the lower floors do not experience impact. Increases in interstorey shears due to pounding are also recorded.

Filiatrault et al. (1994) performed numerical simulations using elasto-plastic building hystereses and an elastic Kelvin element. Collision between three storey and eight storey buildings with differing lateral restraint systems were investigated (Figure 2.23). Filiatrault observed that when two buildings have no separation, impacts occur at time intervals of approximately half the mean of the building's periods. Increasing the gap is noted to reduce the number of impacts but not necessarily reduce the severity of pounding's consequences.

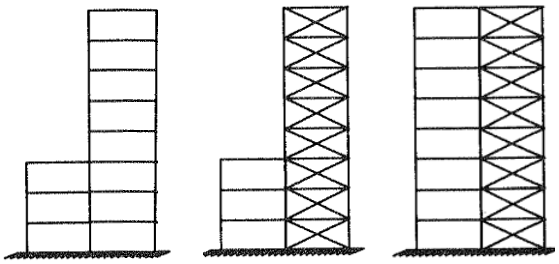

Figure 2.23 Building configurations tested by Filiatrault. Images reproduced from Filiatrault et al. (1994).

In a report created at the University of Liege (ULIEGE 2007), building pounding was modelled using multilinear building hysteresis and Kelvin contact elements. In these investigations, multiple pounding configurations were modelled to assess possible mitigation methods. Before mitigation methods were investigated, analyses of the response of buildings with equal height and buildings with unequal height were documented in reasonable detail. Three configurations of pounding were investigated between two buildings with similar height and plan geometry. The configurations were observed to not generally cause collapse unless other building deficiencies were present. Two configurations of buildings with greatly differing height were then investigated, and two types of response were identified. When the taller building dominated the response, it imposed high loadings over the height of the smaller building. When the smaller building dominated the response (such as when the smaller building was a wall structure), the actions above the topmost point of contact were significantly increased in the taller building. This report also contains a 70 page state of the art review of pounding literature.

Research by others who have drawn similar conclusions to those presented in this section are not explicitly detailed here. These papers include contributions from Azevedo and Bento (1996), and Mahmoud and Jankowski (2009).

2.5.3 3D Pounding Investigations

Amongst other things, 3D modelling of pounding allows the quantification of torsional actions on a pounding system. The effect of friction during contact has also usually been investigated. However, the extra computational expense of 3D analysis mean few investigations have been performed to date.

Papadrakakis et al. (1996) investigated the effects of modelling pounding in 3D using Lagrange multipliers to model contact between elastic two storey buildings. Two elastic building configurations were tested: two adjacent buildings, and three buildings arranged in an L shape (Figure 2.24). These building configurations were modelled with and without mass eccentricity within each building, and the results were reported in terms of building strain energy. Three dimensional response is noted to differ from two dimensional prediction, with the 3D modelling predicting up to 40% greater building actions.

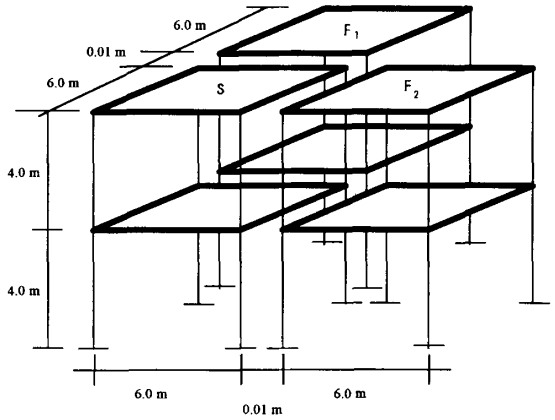

Figure 2.24 L shape arrangement of tested buildings. Image reproduced from Papadrakakis et al. (1996)

Mouzakis and Papadrakakis (2004) presented another 3D modelling method using stereo mechanics and modelling collision friction (see Section 2.2.3), which was used to investigate the performance of inelastic buildings. Two building configurations were investigated; collision between two five storey buildings, and collision between a five storey and a two storey building. For the considered configurations, changing the coefficient of friction was found to not noticeably affect the stiffer building, but could significantly affect the displacements of the more flexible building. The displacement results of pounding models that included contact friction were also reported to be insensitive to whether the buildings were model elastically or inelastically.

Jankowski (2008) used 3D modelling to investigate a building configuration where one building was significantly stiffer and more massive than the adjacent building. In these analyses, the 2D Hertz element was adopted, and friction between the buildings was also modelled during contact.

A sensitivity study was performed which investigated the building separation, the smaller building's mass, the smaller building's stiffness, and the smaller building's yield load. The smaller building, but not the larger building, was found to be sensitive to these changes in the longitudinal, transverse and torsional directions.

Jankowski (2009) subsequently investigated a specific case of pounding damage: a seismically separated staircase structure that suffered significant damage as a result of pounding during the 1971 San Fernando earthquake (Figure 2.25). The staircase collided with a significantly larger main building, which Jankowski modelled using over 10,000 finite elements. Contact was modelled using Lagrange multipliers and contact friction was also simulated. The building configuration was modelled using the actual building separation, and again with sufficient separation to prevent pounding. The effect of pounding was found to be notable on the staircase structure but almost imperceptible on the main building in the longitudinal, transverse, torsional and vertical directions.

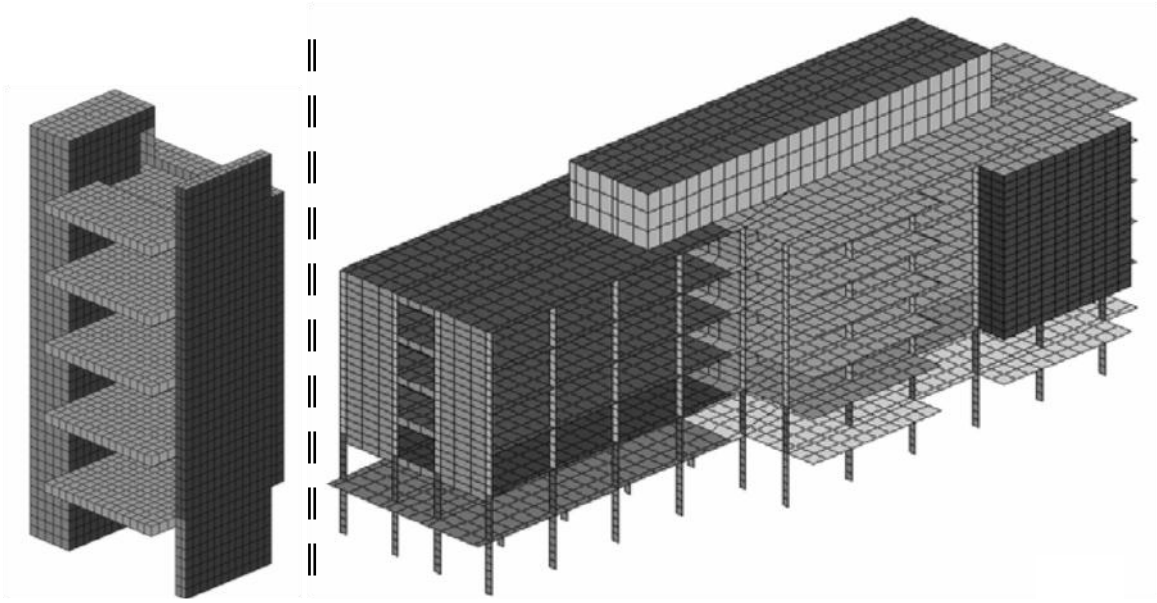

Figure 2.25 Modelled pounding configuration. Left: staircase. Right: main building (not to scale). Images reproduced from Jankowski (2009).

This same building configuration was again investigated considering the effects of spatially varying earthquake motion (Jankowski 2012). Providing slightly different ground motions to different foundations was found to notably affect the response of both buildings. It is concluded that spatially varying earthquake motions can be significant for buildings with large plan dimensions.

Research by others who have drawn similar conclusions to those presented in this section are not explicitly detailed here. These papers include contributions from Raheem (2006).

2.5.4 Soil-Structure Interaction Modelling

While other researchers have included some form of soil modelling (Papadrakakis et al. 1991; Anagnostopoulos and Spiliopoulos 1992), this section details studies that have focused on the influence of soil structure interaction (SSI) on pounding.

Schmid and Chouw (1992) investigated the effect of SSI by modelling a soil and building system with boundary elements and finite elements. Two buildings comprised of elastic structural elements were connected to a soil modelled as an elastic halfspace (Figure 2.26). Structural components were modelled as finite elements while the soil was modelled using boundary elements. Analyses were performed by alternating between the time and the Laplace domains as necessary, and contact was modelled by changing the problem's boundary conditions when contact was observed. Collision between a three storey and a single storey building was simulated. The analysed buildings' dynamic properties were shown to significantly change when SSI was included in the modelling, which substantially changed the predicted pounding response of the buildings. SSI was noted to generally increase building displacements, increasing the chance of pounding damage. Chouw and Schmid (1995) also note that each building's response is also affected by the adjacent building even when contact does not occur. This is due to the soil's response being affected by the presence of each building. This interaction is termed Structure-Soil-Structure Interaction (SSSI).

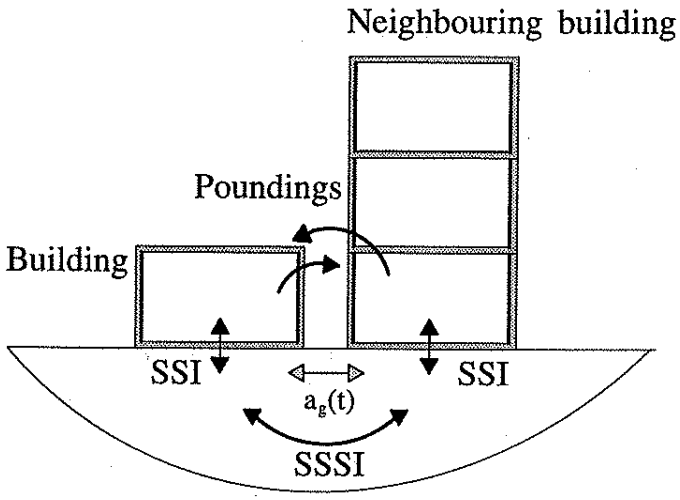

Figure 2.26 Soil structure interaction model. Image reproduced from Chouw and Schmid (1995)

Chouw (2002a; 2002b) also investigated the influence of near-source earthquakes on the response of pounding buildings modelled with SSSI. A Laplace model, similar to that used in Chouw and Schmid (1995), was used to investigate pounding between two well separated buildings that had a connecting bridge at the third floor level. The near-source earthquake characteristics are found to cause greater responses in longer period buildings. This effect is

further amplified by SSI since SSI typically lengthens the buildings' fundamental periods. These effects increase the risk of building pounding for many building configurations. Chouw concludes that further research in this area is required to determine the governing parameters of this type of configuration.

The effects of soil on pounding analyses have also been investigated using simplified soil models (Rahman 1999; Rahman et al. 2000; 2001). In these analyses, soil flexibility was simulated using lumped parameter models. SSSI effects, termed "through-soil coupling" was also modelled using an elastic beam with uniformly distributed soil springs. This element was applied between the two buildings' nearest foundations. Soil flexibility was again found to significantly affect building response, and hence affect the prediction of pounding response. Through-soil coupling is shown to amplify or deamplify response depending on the specific situation. Generally, through-soil coupling effects were found to be less pronounced than soil flexibility effects; however the predicted impact forces on the buildings were noted to change when through-soil coupling was included in the models.

Shakya et al. also used lump parameter modelling of SSI to investigate the influence of soil flexibility (Shakya et al. 2008; Shakya and Wijeyewickrema 2009). In these analyses, three building configurations were investigated (9 storey vs. 10 storey vs. 9 storey, 9 storey vs. 10 storey, and 5 storey vs. 5 storey). In all configurations, floor/column pounding occurred between the buildings. Shakya compared the performance of fixed and flexible soil conditions for two near-source and two far-source earthquakes. Near field earthquakes were found to excite the buildings significantly more than the far field earthquakes, and pounding was found to reduce the deflections of all buildings. Soil flexibility was also observed to generally reduce the interstorey shear demands and impact forces, when compared to the fixed base models. In these analyses, no explicit SSSI modelling was performed.

2.5.5 Floor/Column Collision Modelling

While other research (Papadrakakis et al. 1991; Sinclair 1993; Filiatrault et al. 1994; Shakya et al. 2008; (Shakya and Wijeyewickrema 2009) has performed some analysis of floor/column collision, the only known dedicated investigations of the phenomenon have been performed by Karayannis and Favvata.

Karayannis and Favvata (2005a; 2005b) investigated the performance of modern concrete columns when tall multi-storey buildings were subjected to direct collision from a significantly shorter adjacent building (Figure 2.27). Impact was modelled between the top of the smaller

building, and the corresponding column in the taller building. Detailed modelling of the impacted column was performed in order to accurately simulate its performance. The impacted column used fibre models to simulate the response of individual bars and layers of concrete at selected sections. Methods to distribute the inelastic column behaviour along a specified length of the column were also adopted. The effects of building separation, the overall height of the taller building, and the location of the collision on the column (1/3rd column height, 2/3^{rds} column height and floor/floor collision) were investigated. Floor/column collision was found to greatly load the impacted column, with ductility demands frequently exceeding available capacity. Furthermore, all pounding simulations exceeded column shear capacity in the impacted columns. Increasing building separation was found to decrease ductility demands, but not shear demands. Karayannis and Favvata conclude that non-conservative buildings may be designed if floor/column pounding is present but neglected.

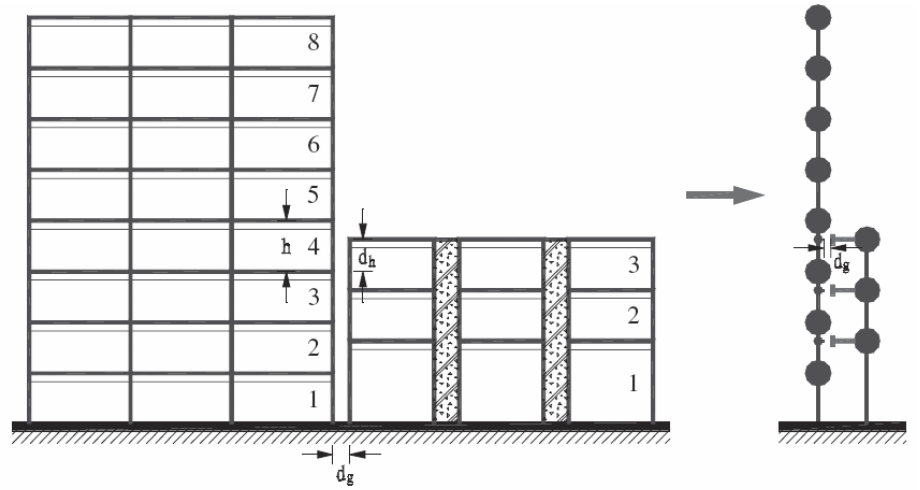

Figure 2.27 Floor/column pounding configuration. Image reproduced from Karayannis and Favvata (2005a)

Favvata and Karayannis (2008) also investigated predicting pounding damage using pushover analyses on two adjacent buildings. The tested configuration investigated floor/column pounding between an eight storey and a three storey building. Pushover analyses were applied to one or both buildings and the results were compared to the dynamic responses from earlier work (Karayannis and Favvata 2005b). Multiple loading patterns were trialled and the predictions were assessed using the resulting interstorey drifts and shear capacities of the impacted column. The loading patterns, and the selection of which building to apply loading to, significantly affected the predicted structural responses. It was concluded that further investigation of predictions using pushover analyses is warranted.

2.5.6 Analysed Mitigation Methods

Mitigation of pounding effects has been extensively researched over the past 20 years. This research is presented here in approximately chronological order.

Westermo (1989) investigated four configurations of 2D elastic buildings which were linked with axial springs (pin ended beams). Each configuration was subjected to harmonic and earthquake ground motions and the base shears, relative deflections, and link forces were reported. Westermo concludes that linking buildings appears to be a viable solution in some situations, such as when both buildings possess similar dynamic properties. However, the need for more detailed inelastic study was also emphasised.

Lavelle and Sues (1992) investigated the feasibility of a variety of linking elements that were applied at the top of two buildings with significantly varying overall heights (Figure 2.28). A variety of linking devices are proposed (yielding or bilinear hysteretic, visco-elastic, friction, viscous, or magnetic damping), however, only two are analysed in detail: a bilinear link, and a bilinear link in parallel with a viscous damper. Lavelle and Sues also note many restraints that affect any retrofit of buildings (limited construction space, required compatibility with existing structural systems, and large energy dissipation requirements over short displacements).

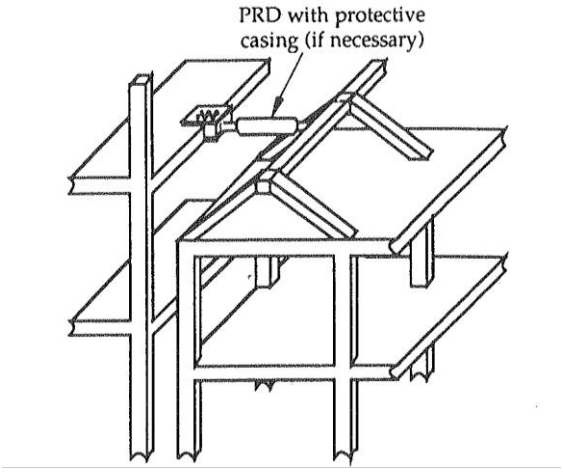

Figure 2.28 Proposed means of applying linking element between buildings with differing floor heights. PRD = Pounding Reduction Device. Image reproduced from Lavelle and Sues (1992)

The tested devices were modelled using Monte Carlo simulation of 64 artificially generated ground motions. Both devices were found to reduce the local demand at the point of potential impact (measured using mean impact velocity, mean total impact energy, and floor acceleration spectra), however the global response (the overall interstorey response) of each building was not significantly reduced. Specifically, the taller building was found to frequently respond more in its second mode as a result of the linking. It is concluded that linking elements can reduce

localised pounding damage while not adversely affecting the global structural response of either building.

Filiatrault and Folz (1992) investigated friction dampers between two configurations of two six storey buildings, and two configurations of three vs. eight storey buildings. Each configuration was tested for three ground motions. It was found that a single linking element at the roof between the six storey buildings reduced the effects of pounding in many situations. However, increases in building demands were also recorded in some instances. The three vs. eight storey buildings' responses were "completely altered" when connection was made between the buildings' third storey.

Spiliopoulos and Anagnostopoulos (1992) investigated the use of three types of mitigation measures. Firstly, placing a filler material between adjacent buildings was considered. The material was assumed to be elastic with a cubic force-displacement relationship. This infill was found to not produce any consistent reduction in building response, and sometimes even increased building demands. However, a reduction in floor accelerations was consistently observed. Elastic permanent connections between the top of the buildings was also investigated. By performing frequency analyses on two SDOF buildings connected with an elastic spring, it was shown that reduction in one building's actions always causes an increase in the other's actions. It was concluded that neither of these mitigation methods are suitable. The third method involved providing 'bumper' walls which were designed to withstand pounding impacts (Figure 2.29). An impact was simulated on the bumper walls using an estimated representative relative velocity. Since the resulting concrete stresses were within the available concrete capacity, bumper walls were recommended for further investigation.

Bumper walls were subsequently developed further (Anagnostopoulos and Karamaneas 2008a; Anagnostopoulos and Karamaneas 2008b). This was done by modelling a new five storey building next to an existing five storey building with zero building separation. This configuration would have experienced floor/column pounding if the bumper walls were not used. The bumper wall was tested for three earthquake records. Global damage in both buildings was found to increase slightly (when compared to the no pounding models) with ~0-25% increase in beam rotation ductility demands. The largest recorded collision was then modelled in more detail to determine the local damage at the point of impact. The calculated stresses were deemed damaging but repairable without any catastrophic failure. The bumper walls were noted not to prevent large accelerations in the impacted floors, but were concluded to be a technically feasible pounding mitigation measure.

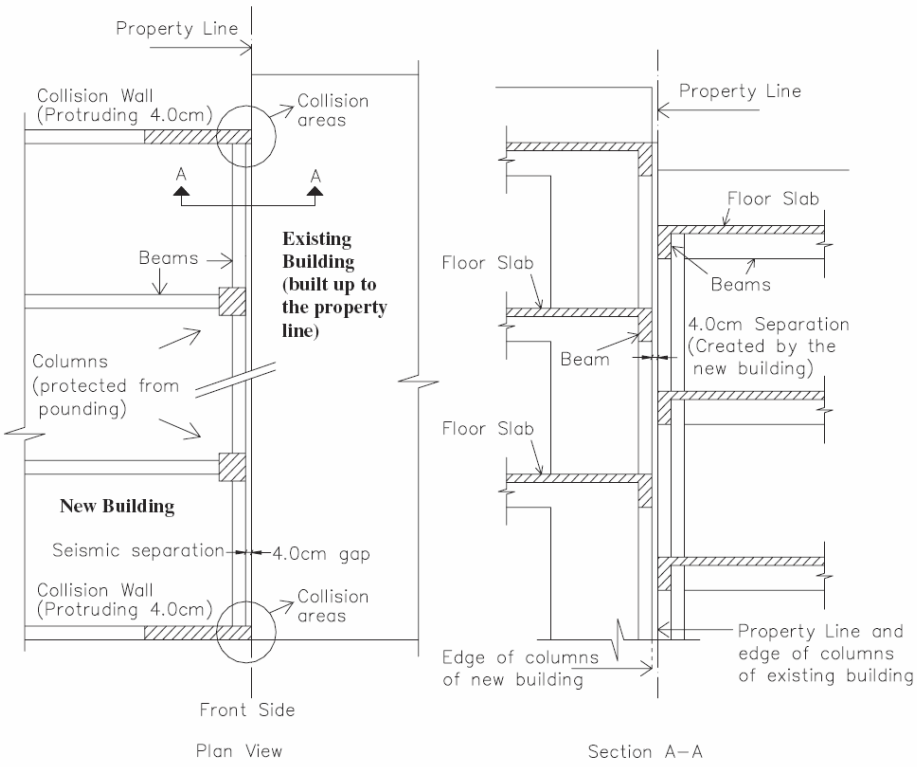

Figure 2.29 Proposed 'bumper' wall design to allow zero separation between adjacent buildings. Image reproduced from Anagnostopoulos and Karamaneas (2008b)

Luco and De Barros (1998) investigated providing viscous dampers linking two elastic buildings at every available floor. In these analyses it was assumed that sufficient separation was available to install the dampers, and that no pounding occurred once the devices were installed (i.e. the adjacent buildings never physically impact in the analyses). By performing frequency analyses, optimum damping values for a range of building properties were produced. An example analysis of a 10 storey building connected to a five storey building with optimised dampers was performed. The buildings were subjected to the El Centro ground motion and significant reductions in both building's interstorey shears and displacements were reported (compared to the values obtained without damping or building pounding). It was concluded that these dampers can be applied to prevent pounding in certain situations.

Salem and Feng (2008) performed 1/6th scale shaketable tests between elastic steel buildings. A flexible eight storey building and a stiff three storey building were tested with viscous dampers linking their third floors. This configuration was subjected to two ground motions and the floor accelerations, interstorey drifts, and impact forces were recorded. The dampers were found to reduce floor accelerations and interstorey drifts when compared to the cases with pounding but without dampers. Damping was noted to be more effective when some initial building separation was present. Analytical investigations were also performed to investigate the inelastic

performance of the buildings (Salem 2006), from which a design guide for the addition of damping elements was proposed.

Tande and Shinde (2008) investigated adding viscoelastic dampers at each level between two 20 storey elastic buildings. Damper stiffness was selected to be the largest stiffness that did not substantially change either building's modes. The viscous properties were then calibrated to minimise building displacement. Roof displacements and base shears were successfully reduced using this procedure. It was also shown that dampers are not required at all levels to achieve similar levels of damping.

The ULIEGE (2007) report investigated various mitigation techniques for a number of building configuration types. Two configurations with equal building heights (seven storey frame vs. frame, and seven storey frame vs. wall) were investigated with three types of mitigation (elastic links, viscous dampers, and viscoelastic dampers) for a single ground motion. Effective mitigation was achieved for the frame vs. frame configuration using either viscous or viscoelastic dampers. However, the frame vs. wall configuration could not be effectively mitigated.

Two configurations of buildings with differing heights were then investigated. Pounding between a 7 storey frame and a 15 storey frame was first investigated using five mitigation methods (soft infill material and tension only links, in addition to those mentioned previously). Viscoelastic and viscous dampers were found to improve building performance; however this improvement was not sufficient to prevent failure of the taller building. When the seven storey building was changed to a wall structure, no effective pounding configuration could be found. It was concluded that substantial retrofit of the taller structure would be required in addition to any pounding mitigation measure.

Finally, mitigation of floor/column collision between a four storey and a three storey building was investigated. All mitigation techniques used inclined members to link the floors (Figure 2.30). Elastic links, viscous dampers and viscoelastic dampers were tested. Axial links were found to increase the stiffer building's response, and viscous dampers were found to be ineffective. However, viscoelastic dampers were found to successfully reduce shear demands to within building capacity for the considered configuration. From these analyses, various mitigation methods were recommended depending on the specific building configuration.

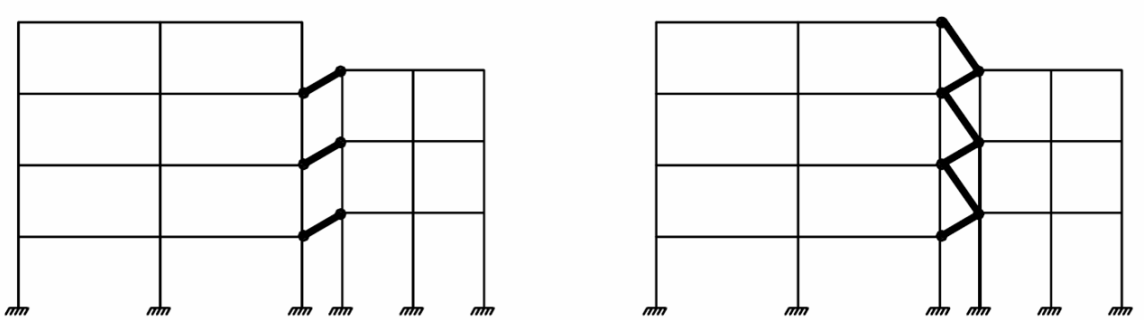

Figure 2.30 Proposed mitigation linking methods. Image reproduced from ULIEGE (2007)

Ohami et al. (2008) investigated pounding mitigation by designing a new building to connect to an older adjacent and seismically vulnerable building. Two ten storey structural systems (frame and wall) were considered for connection with an existing five storey building. In addition, rigid links and viscous dampers were investigated as linking elements. Each configuration was subjected to three ground motions, and interstorey drift and beam ductility were recorded. No effective mitigation could be produced for the ten storey frame; however, the ten storey wall building could prevent collapse of the five storey building when linked with either connecting element.

Recently, Hadi and Uz (2009) investigated viscous dampers between all floors of two adjacent buildings. In these analyses pounding is assumed not to occur (when the buildings are connected with dampers, the buildings' displacements are assumed to be sufficiently small to prevent any contact). Four building configurations (10 storey vs. 5 storey, 15 storey vs. 10 storey, 20 storey vs. 20 storey, and 20 storey vs. significantly stiffer 20 storey) and four ground motions were considered. In all cases damping was found to be beneficial compared to the no pounding, no link case. Placement of the dampers at only select floors is also investigated and was found to be comparable to the full damping method. However, the required placement of these dampers was found to be dependent upon the specific building configuration.

2.5.7 Discussion

This section discusses the various aspects of the responses reported throughout Section 2.5. The various subtopics are ordered in roughly the same manner as they were presented in the text.

Elastic MDOF systems have very limited applicability in pounding assessment. This is because potential building failure is the primary consequence that is of interest, which only occurs under post-elastic conditions. Nevertheless, elastic analyses can provide trends and relationships of how changing building conditions may affect pounding. Like SDOF systems, elastic analysis should only be considered a starting point for more detailed study.

In both the elastic and inelastic building models, most investigations have focused on global damage to the impacted buildings. Global building response describes the performance of elements that are not directly impacted during a collision. Examples of global response include interstorey shear, beam ductilities and floor displacements. In contrast, local damage deals with forces that are directly caused by the impact. Local response includes; impact force, impacted column shears (in floor/column collision), and impacted floor accelerations. Typically researchers have used interstorey shears and maximum building displacements as damage measures. This is perhaps unsurprising since detailed evaluation of the contact element (and hence accurate prediction of contact force) is missing from nearly all these papers. While global building response and damage is useful, understanding of local damage is also essential to the understanding and mitigation of pounding response. The differences between global and local damage is considered further in Section 6.4.

The comparatively few publications addressing either SSI or floor/column collision show how frequently these aspects of pounding are overlooked. However, both these factors have critical repercussions for pounding buildings. In particular, an informed recommendation for modelling SSI in pounding situations would be immensely useful. Fortunately, floor/column pounding is starting to receive greater attention. Hopefully this will result in further development of simplified modelling methods and mitigation techniques.

Individual researchers have frequently been very positive about the outcomes of their suggested mitigation methods. However, their use is greatly restricted by practical limitations. As stated by Spiliopoulos and Anagnostopoulos (1992), linking adjacent buildings change both building's performance. This raises many legal issues when the buildings are owned by different parties. Furthermore, application of such methods requires a detailed knowledge of the dynamic performance of multiple buildings, which is a sizeable and time consuming task. Practical issues such as the minimum building separation required to install specific mitigation measures is also frequently overlooked.

Other mitigation methods assume that one of the considered buildings is yet to be built (Anagnostopoulos and Karamaneas 2008a; Ohami et al. 2008), which are obviously not applicable for existing buildings with pounding potential. However, linking damping schemes (and other mitigation methods) have been consistently reported as being able to reduce pounding to within building capacities. These methods should therefore be applicable to existing building configurations with pounding potential if detailed modelling, legal agreement and installation can be achieved. Perhaps the simplest mitigation method (which has been suggested by others) is

to stiffen, or apply additional damping within each building. This approach has the advantage of not requiring any adjacent building calculations (apart from an estimate of maximum building displacement).

In many of the considered topics in Section 2.5, conflicting conclusions have been drawn by different researchers. As a result, overarching universal conclusions are difficult to make. The ULIEGE report (2007) attempted to catalogue the various conflicting and agreeing conclusions; however, the report finds that the frequently differing basic assumptions between the various models prevent any meaningful comparison. It is concluded that '*the only common conclusion is that the effect of pounding on the response of the structure is a very complex one, depending on various parameters describing the structures and the characteristics of the ground motions.'* These findings can be at least partially explained by the huge parametric space pounding inhabits (see Section 2.4.2).

Nevertheless, universal truths about pounding response are possible to find. For example, a column is much more likely to fail in shear if it is impacted directly than if the impact occurs at the floor level immediately above. When reading conclusions about pounding analysis, it is important to always keep the tested building configuration in mind, since application to other building configurations can frequently be invalid. The conclusions drawn in the following section should therefore only be applied in the most general of senses.

2.5.8 Conclusions

The following conclusions are drawn based on the literature review detailed in Section 2.5. It is emphasised that these conclusions are general trends only (see Section 2.5.7).

1. The maximum displacement of two colliding buildings may be amplified or deamplified compared to the displacement of the same buildings without collision. Any amplification of response is dependent upon the buildings' configuration and the specific earthquake record.
2. Buildings with floor/floor collisions between buildings of similar height, mass and stiffness do not usually suffer catastrophic collapse due to pounding unless other significant structural weaknesses are present.
3. Buildings' dynamic characteristics can be substantively changed by pounding. An effective 'period shift' can move a building from one spectral range to another, where higher excitation may occur.

4. Buildings with greatly differing overall heights frequently suffer major shear amplification immediately above the topmost point of contact. The small building can also be significantly overloaded by this impact.
5. The performance of many buildings in a row may be suitably approximated by modelling just the buildings immediately adjacent to the building under consideration.
6. SSI considerably changes the response of pounding buildings, due to the change in dynamic characteristics in each building.
7. Floor/column pounding is a particularly critical form of pounding. Shear failure of columns is highly likely if they are directly impacted during an earthquake.
8. Linking adjacent buildings changes the performance of both buildings, but can reduce the effects of pounding to acceptable levels. Other mitigation methods are also available when constructing new buildings near other existing buildings.

2.6 Experimental Studies

This section focuses on experimental studies of colliding structures. Building and bridge experiments are considered in turn. Experimental studies that are focused on the force response of a single collision are detailed in Section 2.2.5.

Experimental shaketable testing has been performed in comparatively few instances. Filiatrault modelled the elastic pounding interaction of two steel frames subjected to ten seconds of El Centro ground motion (Filiatrault et al. 1995; Filiatrault et al. 1996). An eight storey and a three building were modelled for pounding with no building separation and 15 mm separation in separate tests (Figure 2.31). Impact was caused at each floor level by placing aluminium load cells with known axial stiffness between the buildings. Both separations showed significant increases in recorded accelerations at the third floor.

The results of the shake table tests were then emulated using various analysis packages (SLAM2 and PC-ANSR). In these analysis packages, the contact element was set as the load cell stiffness. It was concluded that PC-ANSR can accurately predict displacements and impact forces of the shaketable when calibrated dynamic properties are used. However, floor accelerations could not be accurately predicted. SLAM2 was found to be less accurate but required significantly less computation. It was concluded that SLAM2 provides a simple and reasonably accurate prediction of elastic pounding between adjacent buildings.

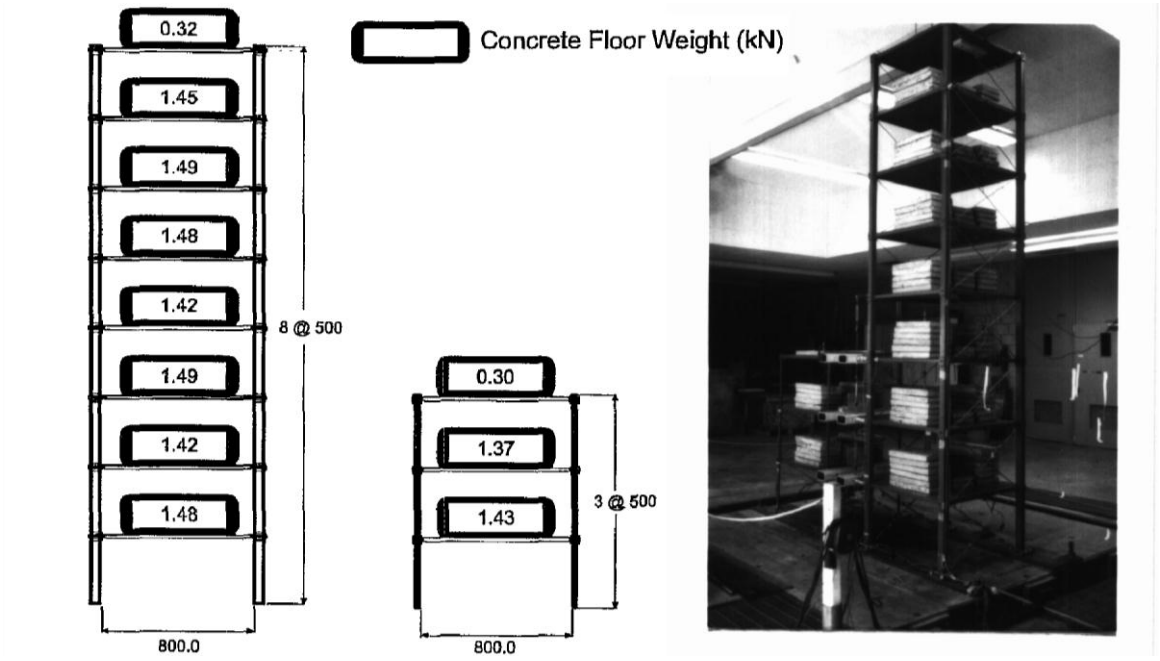

Figure 2.31 Filiatrault experimental setup. Image reproduced from Filiatrault et al. (1996)

Papadrakakis and Mouzakis (1995) investigated pounding between two Reinforced Concrete (RC), two storey buildings. In these tests a period difference was created between the two buildings by using differing column sizes and differing floor masses (Figure 2.32).

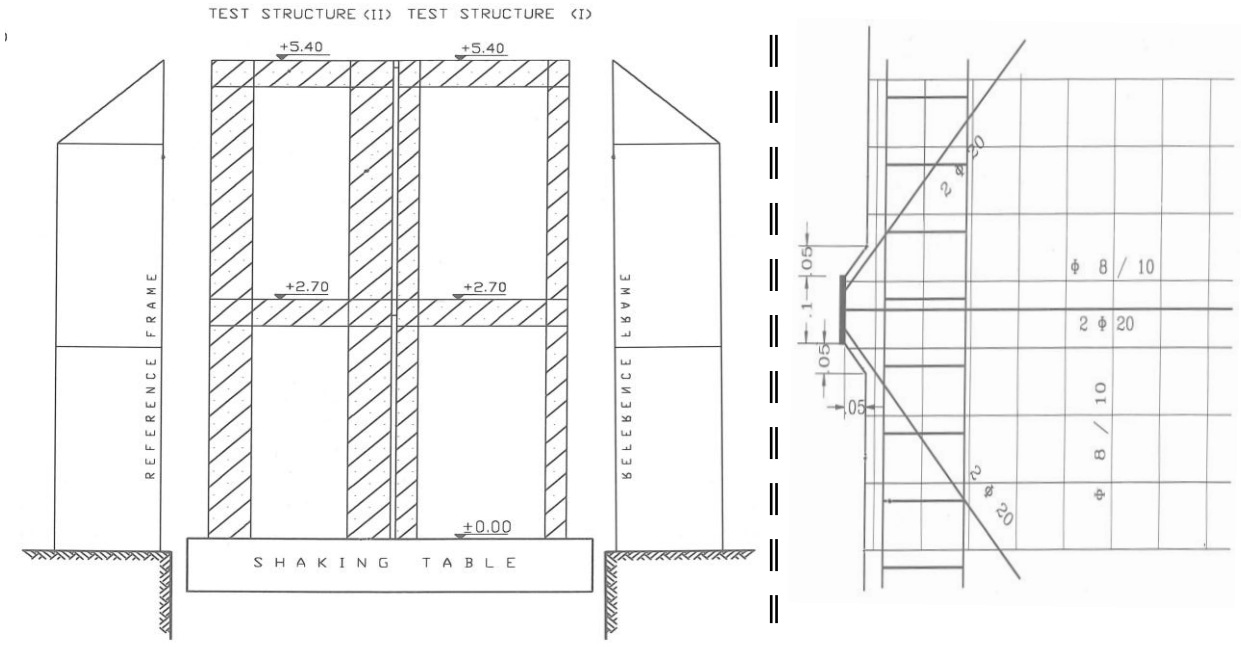

Figure 2.32 Experimental setup for two storey buildings. Left: elevation of experimental setup. Right: plan view of contact point on the right hand building's floor. Images reproduced from Papadrakakis and Mouzakis (1995)

The right hand building's floors were specifically designed to cause contact at the centre of the floors at both Level 1 and Level 2. The configuration was first tested without pounding, and then tested with no building separation. Floor accelerations and absolute displacements were recorded. The buildings were excited using a ramped sinusoidal displacement pattern at the

resonant frequency of the more flexible building. Pounding was observed to reduce the flexible building's displacements while increasing the stiff building's displacements. These responses are then analytically simulated using a Lagrange multiplier method (Papadrakakis et al. 1991), which assumes perfectly elastic contact. It is concluded that the analytical model provides "good" agreement with the experimental results.

Chau et al. (2003) undertook experiments to verify the previously derived analytical solution for two elastic SDOF oscillators colliding with a Hertzian element (Chau and Wei 2001). Hertzian collision properties were created by using a hemisphere as the contact point (refer Figure 2.15d). Two steel, single floor towers were subjected to sinusoidal ground motions to obtain the buildings' steady state response. The separation required to prevent pounding was found to be greatest when the ground frequency matched the fundamental period of the more flexible building. The experimental results were compared to analytical and numerical predictions. Numerical investigations found that the impact velocity is not very sensitive to contact plasticity, while theory is found to agree 'qualitatively' with the experimental impact velocity and required building separation.

Chau et al. (2004) also investigated the effects of mass eccentricity on the SDOF oscillator system. For these tests, the contact was changed to a hemisphere contact at either end of the building width. Increasing mass eccentricity is found to increase both the torsional and the translational interactions of the two buildings. It is concluded that torsional interaction adds significantly more complexity to the pounding system.

Other shake table testing has been performed on two $1/10^{th}$ scale steel frames (Rezavani and Moghadam 2004; Rezavandi and Moghadam 2007). Pounding between a three storey and a six storey building was tested using sinusoidal and earthquake ground motions. Three mitigation methods were also tested; polystyrene infill, rigid links at level three, and rigid links at levels one and three. Polystyrene infill was found to reduce floor accelerations, while third floor building connection reduced building acceleration and displacement responses. Connecting at multiple levels was not found to provide any additional benefit. Analytical models using SAP2000 were compared to the experimental data; however, the analytical predictions differ significantly from the recorded responses.

Salem and Feng (2008) also used shaketable testing to test linking viscous elements between buildings. This work was discussed previously in Section 2.5.6.

Bridge experimental testing is also relevant to building pounding problems since the collision conditions can be very similar. Zhu et al. (2002) tested small scale models of bridges to investigate the accuracy of numerical analysis performed using their 3D contact element (refer Section 2.2.3). Two configurations were tested: a deck colliding with an abutment, and two decks which collide due to the difference in pier lateral stiffness. The tests used sinusoidal excitation to cause collision with the 2 kg bridge decks (Figure 2.33). This excitation was initially applied along the longitudinal direction of the decks to create 1D motion, and then applied at an angle to induce deck rotation as a result of collision.

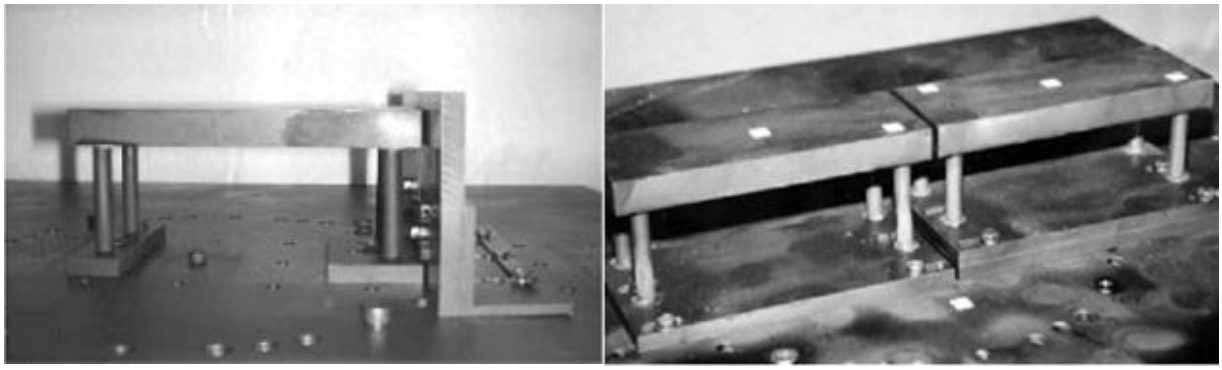

Figure 2.33 Zhu shaketable experiments. Left: Deck vs. abutment. Right: Collision between decks. Images reproduced from Zhu et al. (2002).

The experiments were used to calculate the coefficient of restitution in the longitudinal and tangential directions, in addition to the static and dynamic coefficients of friction. These parameters were then incorporated into the numerical analyses. The analyses were found to provide good agreement with the experimental displacement results, which was considered suitable verification of the analysis method.

Guo et al. (2008; 2009) performed 1/20th scale testing of bridge decks based on the standard drawings of highway bridges of China. These tests were used to compare the predictions of the Kelvin Voight and the nonlinear viscoelastic elements, and to investigate the effectiveness of magnetorheological (MR) dampers. The deck mass was provided by concrete blocks, however the collision points were restricted to semi-circular steel contacts (Figure 2.34). Experiments were run for three earthquake records under the following conditions: no pounding, pounding, and pounding potential with MR dampers installed. The setting of these dampers included passive-off, passive-on and semiactive.

The experimental data was compared to predictions of the two considered collision elements after each element's collision parameters had been calibrated from the results. The displacement and acceleration predictions were found to be approximately equal between the two calibrated modelling methods. In general, displacement and acceleration results were well predicted.

Semiactive MR damping is also noted as being effective at reducing accelerations, provided that the damping prevents deck collision.

Figure 2.34 Guo experimental setup. Left: Deck configuration. Right: Point of contact detail. Images reproduced from Guo et al. (2009).

Recently, Lindsay et al. (2011) have reported on small scale (10 kg bridge decks) bridge pounding shake table testing. The decks were constructed using Polyvinyl-Chloride (PVC) with a circular disk contact area (Figure 2.35). Lindsay et al. reports the experimentally determined coefficient of restitution as a function of the collision velocity, and also presents collision force vs. time plots. The collision force results are compared to analyses performed using a calibrated nonlinear viscoelastic element. Lindsay concludes that further testing is necessary to investigate the limitations of the presented model.

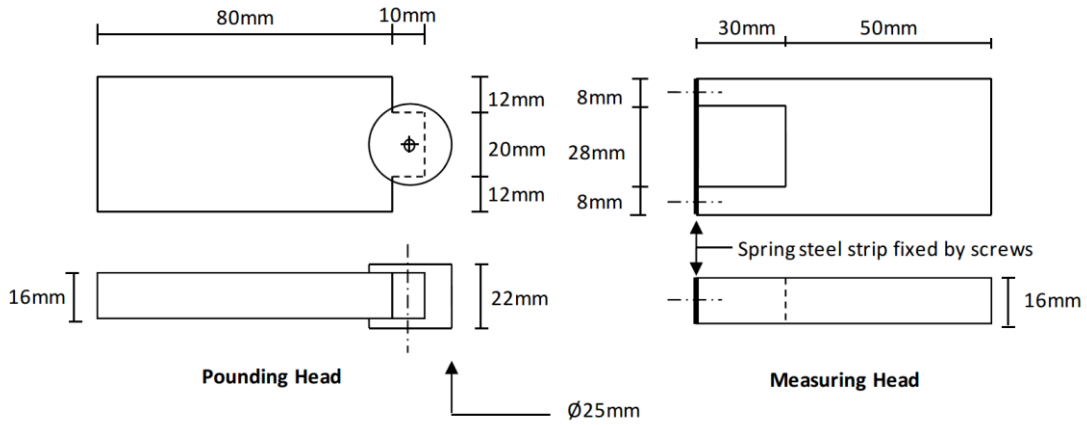

Figure 2.35 Lindsay pounding contact configuration. Image reproduced from Lindsay et al. 2011.

2.6.1 Discussion

As was also observed in Section 2.2.6, experimental tests of pounding usually use custom contact areas to model impact. The reasoning for doing this is understandable (it typically allows measurement of the collision forces), but ultimately it provides little useful information. This is because the specialised contact areas change the nature of the collision and do not exist in actual building pounding situations. The testing of Zhu et al. doesn't use a customised contact area, but

also does not report any contact force results. However, experimental testing to date does confirm that elastic displacement pounding response can be reasonably well predicted, even without accurate calculation of the coefficient of restitution.

2.7 Other Areas Related to Existing Pounding Research

While this chapter considers much of the currently available literature on pounding, some topics have been intentionally omitted. This has been done because of the lack of direct relevance to the situation considered in this project. Nevertheless, they are briefly mentioned here with references for the interested reader.

Bridge pounding – As described in Section 1.3.1, bridge pounding has been frequently reported after major earthquakes. While this phenomenon shares similarities with building pounding, the differing height-to-length aspect ratio, and the lack of multiple storeys changes much of the way these structures perform. Examples of recent investigations include; Chouw and Hao (2005), Matsumoto and Kawashima (2008), and Bi et al. (2011).

Pounding of base isolated buildings – Isolated buildings have also been recently considered for pounding potential. Specifically, the effects of running out of seismic separation between the isolated structure and the surrounding foundation have been considered. Examples of recent investigations include; Komodromos et al. (2007), Polycarpou et al. (2008), and Masroor and Mosqueda (2012).

2.8 Contributions of the Current Project

This project differs in a number of ways to previous research:

1. Particular attention is focused on understanding the physical process governing a single collision. This understanding enables a straightforward calibration of contact element and building properties so that collision force and related local damage can be evaluated.
2. The performance of low rise buildings is considered in detail here, whereas most previous work has focused on six storey buildings or greater.
3. A unified modelling approach is developed for floor/floor, floor/column and floor/wall analysis. Almost all previous research has considered the analysis of these configurations in isolation.
4. The detail at which all developed contact elements are assessed extends beyond anything that is available in the current literature.

2.9 Conclusions

The following conclusions are drawn based on the literature review presented in Chapter 2.

1. Severe pounding damage resulting in collapse is rare but has occurred in multiple earthquakes. Six factors have been identified that greatly increase the risk of collapse due to pounding.
2. Prediction methods for the required separation to prevent collision between inelastic buildings have so far been unable to produce results with consistently acceptable accuracy. The currently proposed methods are approximately as accurate as the traditional Square-Root-Sum-of-the-Squares (SRSS) method.
3. The currently available contact elements are considered to be sufficiently accurate if only building displacements and interstorey shears are of interest. This is because these parameters have been found to be insensitive to the parameters that are not currently well defined.
4. Characteristics of the ground motion can greatly change predicted pounding performance. Much of the existing research has attempted parametric analysis of building properties to attempt to fully characterise pounding interaction. However, frequently these investigations have used ground motions with similar or unevaluated properties. This is one reason why conflicting conclusions are found between different researchers.
5. The maximum displacement of two colliding buildings may be amplified or deamplified compared to the displacement of buildings that do not collide. Any amplification of response is dependent upon the buildings' configuration and the specific earthquake record.
6. SSI considerably changes the response of pounding buildings. This is primarily due to the change in dynamic characteristics caused by SSI for each building.
7. Floor/column pounding is a particularly critical form of pounding. Shear failure of columns is highly likely if they are directly impacted during an earthquake.
8. Linking adjacent buildings changes the performance of both buildings, but can reduce the effects of pounding to acceptable levels. Other mitigation methods are also available when constructing new buildings near other existing buildings.
9. In pounding specific studies, no generally applicable experimental contact force data has been presented to date. Nearly all existing experimental analyses adopted customised contact surfaces in order to be able to measure the contact force. However, the contact force is dependent upon these contact conditions. This issue has frequently been

overlooked because the contact surface changes typically do not significantly affect the buildings' predicted displacement responses.

Chapter 3 The Effect of Diaphragm Mass Distribution on Pounding Models

Related Papers

Cole GL, Dhakal RP, Carr AJ, and Bull DK (2009), *The Effect of Diaphragm Wave Propagation on the Analysis of Pounding Structures*. Computational Methods in Structural Dynamics and Earthquake Engineering 2009: Rhodes, Greece.

Cole GL, Dhakal RP, Carr AJ, and Bull DK (2009), *The Significance of Lumped or Distributed Mass Assumptions on the Analysis of Pounding Structures.* 13th Asia Pacific Vibration Conference, 2009: Christchurch, New Zealand.

Cole GL, Dhakal RP, Carr AJ, and Bull DK (2011), *An Investigation of the Effects of Mass Distribution on Pounding Structures*. Earthquake Engineering & Structural Dynamics, 2011. 40(6): 641-659.

While previous pounding research has generally considered each floor as a single point of mass, in reality floors are three dimensional objects with mass distributed throughout their respective volumes. In order to better understand floor/floor collision, more detailed modelling of each floor is necessary. If it is assumed that buildings can be accurately modelled in 2D, then floors may be considered to be 'rods' with distributed mass and axial flexibility. The response of such rods can be expressed analytically.

This chapter investigates collision between floors that are modelled as distributed masses with axial flexibility. The work extends the findings Watanabe and Kawashima (2004) which were presented in Section 2.2.4. The theoretical performance of colliding distributed masses is presented and is then compared to lumped mass alternatives. Derivations for the collision of distributed masses have also been presented elsewhere (Goldsmith 1960); however their explanations are typically complex and specific concerns regarding pounding performance are not presented. A simple alternate derivation is presented by Watanabe and Kawashima (2004). These alternate formulations cover the situations presented in Sections 3.1.1 and 3.1.4.

3.1 The Theory of Distributed Mass Collisions

Typically, the majority of a building storey's mass is located at the level of the floor slab. This mass can be roughly approximated as being uniformly distributed over the area of the floor (Figure 3.1).

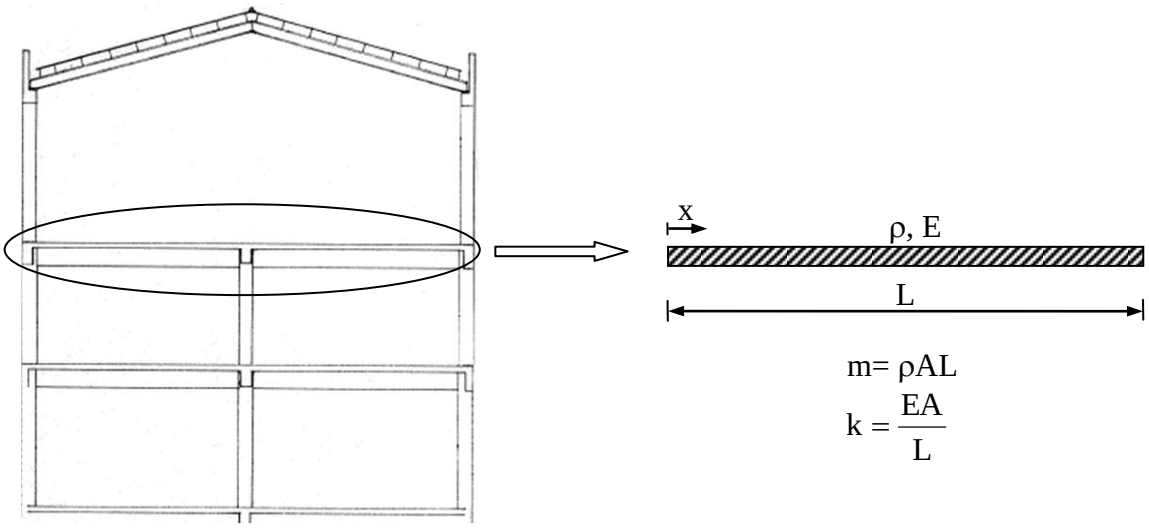

Figure 3.1 Approximation of a floor as a rod of uniform density

In this figure, m = floor mass, k = axial stiffness, ρ = mass density, A = cross sectional area, E = Young's modulus and L = floor length. Five simplifying assumptions are made:

1. The diaphragm is modelled as a rod with distributed mass and uniform cross section throughout its length
2. The modulus of elasticity and volumetric density of the rod are uniform over its length
3. The collision response is one dimensional. That is, stresses are only induced in the axial direction.
4. No other elements act on the rod. Thus any connecting frames, walls or other floors are disregarded.
5. The collision occurs at time t_0, at which point all displacements over the length of the rod are defined as zero.

The axial behaviour of a rod of uniform weight (also known as a distributed mass) is governed by the one dimensional wave equation.

$$\frac{\partial^2 u(x,t)}{\partial t^2} = \nu^2 \frac{\partial^2 u(x,t)}{\partial x^2} \qquad \text{where } \nu^2 = \frac{E}{\rho} \qquad (3.1)$$

where u = displacement at point x and ν = wave velocity, which is the speed at which a wave propagates along the mass. Collision can be modelled by appropriate selection of boundary conditions. As Equation 3.1 is a second order Partial Differential Equation (PDE) in both time and space, two boundary conditions and two initial conditions are required. In order to determine the boundary conditions for the collision of two distributed masses, the collision of a single distributed mass with a rigid wall is considered first.

3.1.1 Collision of a Distributed Mass Against a Rigid Wall

Figure 3.2 illustrates the collision of a distributed mass with a rigid wall. The entire length of the distributed mass moves at a velocity v_0 at the onset of the collision.

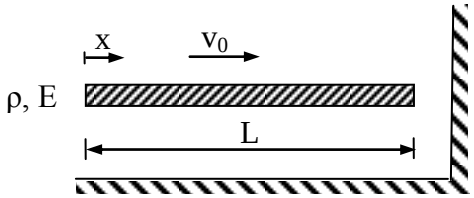

Figure 3.2 Collision of a distributed mass against a rigid wall

The boundary conditions for this configuration are known;

$$E\frac{\partial u(0,t)}{\partial x} = 0 \qquad u(L,t) = 0 \tag{3.2}$$

This mathematically represents the zero stress state of the free end and the zero movement of the collision end during the collision. The initial conditions are;

$$u(x,0) = 0 \qquad \frac{\partial u(x,0)}{\partial t} = v_0 \tag{3.3}$$

which reflect the stated conditions of zero displacement and constant velocity at point of impact, respectively. The wave equation is solved using separation of variables and its solution is shown below. A full derivation is presented in Appendix D. The complete solution for u over the duration of the collision is:

$$u(x,t) = \sum_{n=1}^{\infty} \frac{8v_0 L(-1)^{n+1}}{(2n-1)^2 \pi^2 \nu} \cos\left(\frac{(2n-1)\pi}{2L} x\right) \sin\left(\frac{(2n-1)\pi}{2L} \nu t\right) \tag{3.4}$$

The duration of the collision, $T_{contact}$, can be obtained from this result by taking the fundamental mode (n = 1) and determining the time when the sine term is equal to π.

$$T_{contact} = \frac{2L}{\nu} \tag{3.5}$$

Equation 3.5 is also the *axial natural period* of the distributed mass. The axial natural period has a similar meaning to the natural period of a single degree of freedom oscillator. If a distributed mass is disturbed and then allowed to oscillate freely, it will oscillate every $T_{contact}$ seconds. This property is used in subsequent sections.

Equation 3.4 can be simplified by adopting dimensionless input parameters:

$$T = \frac{v}{L}t \qquad X = \frac{x}{L} \tag{3.6}$$

where T = dimensionless time and ranges between 0 and 2, and X = dimensionless space and ranges between 0 and 1. For example, T = 1 corresponds to half way through the collision and X = 1 corresponds to the collision interface (i.e. x = L). Displacement (u), velocity (v), acceleration (a) and internal stress (f) can be presented in terms of dimensionless functions. Inspections of the below equations show all these values to be linearly dependent upon the initial velocity:

$$u(X,T) = \frac{v_0 L}{v} U(X,T) \tag{3.7}$$

$$v(X,T) = v_0 V(X,T) \tag{3.8}$$

$$a(X,T) = \frac{v_0 v}{L} A(X,T) \tag{3.9}$$

$$f(X,T) = \frac{E v_0}{v} F(X,T) \tag{3.10}$$

where U: $0 \rightarrow 1$, V: $-1 \rightarrow 1$, A: $-\infty \rightarrow 0$, and F: $-1 \rightarrow 0$. Appendix D contains the full expressions for these functions, however their shapes are presented in Figure 3.3 and Figure 3.4.

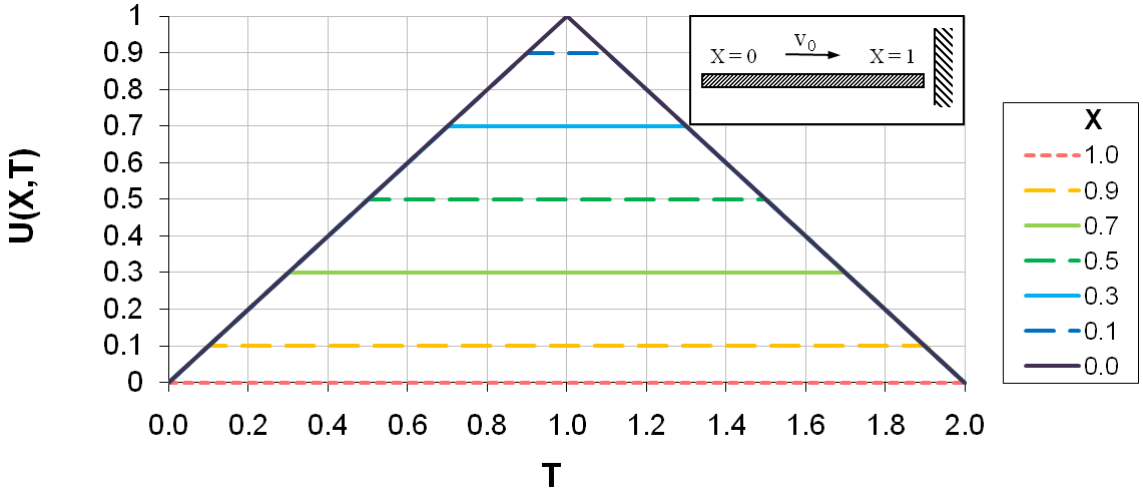

Figure 3.3 Dimensionless displacement during a collision.

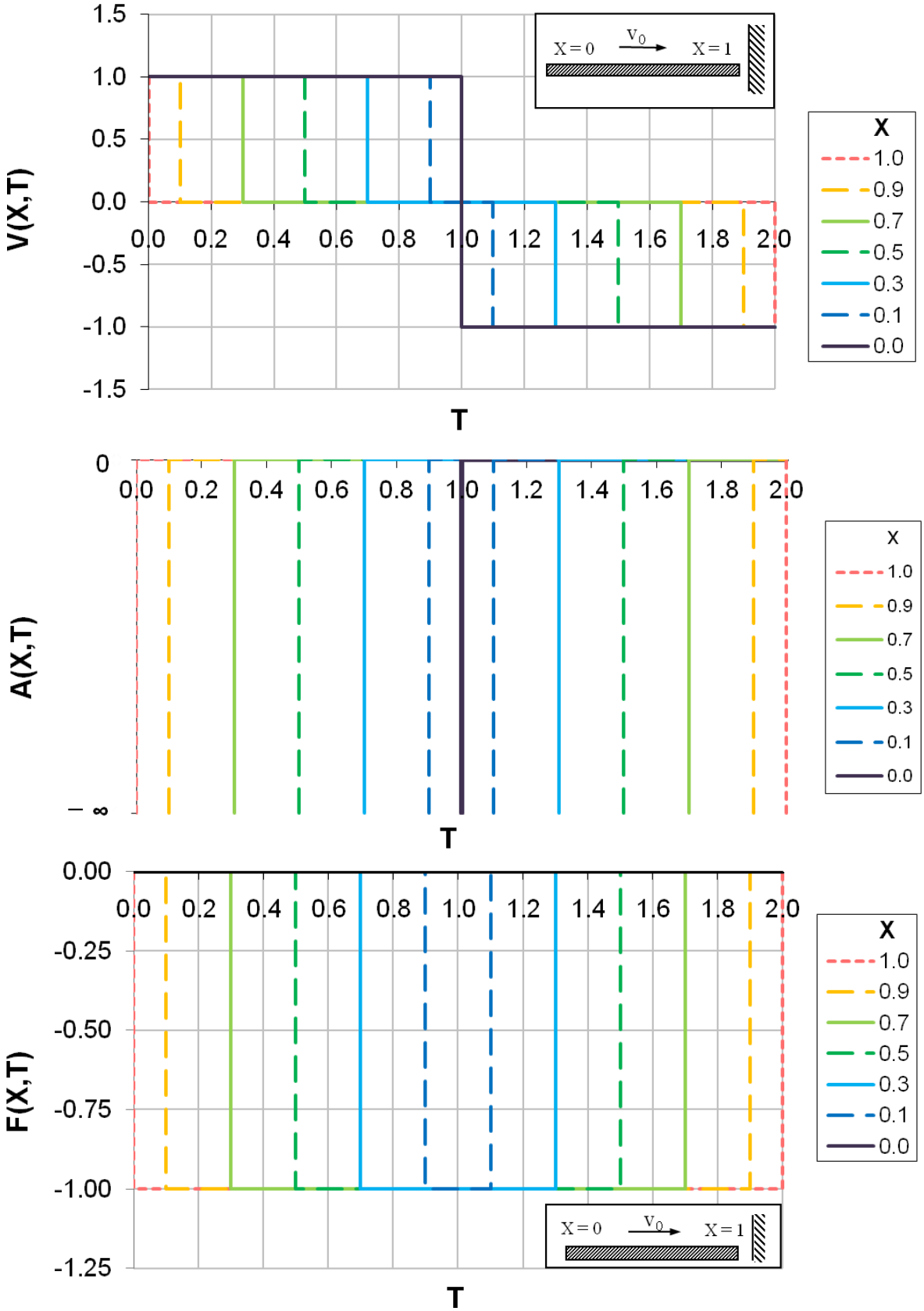

Figure 3.4 Dimensionless plots during a collision. Top: dimensionless velocity. Centre: dimensionless acceleration. Bottom: dimensionless stress

This behaviour can be more readily understood by considering five points along the diaphragm at different instances in time (Figure 3.5). Three states within the distributed mass can be identified:

1. Particles move at the initial velocity, v_0, prior to the impact wave reaching that position (Figure 3.5a).

2. Particles are instantly stopped and do not move once the impact wave has passed, but undergo a constant compressive stress(Figure 3.5b-d).

3. Particles move at v_0 in the opposite direction when the reflected wave reaches that point. The compressive stress is cancelled by the reflecting wave and the point returns to a zero stress state. As the post collision velocity is equal and opposite to the pre-collision velocity, momentum is conserved over the course of the collision (Figure 3.5e-i).

Note that that a particle's velocity only changes when the wave front passes through its location. This property is utilised in subsequent sections.

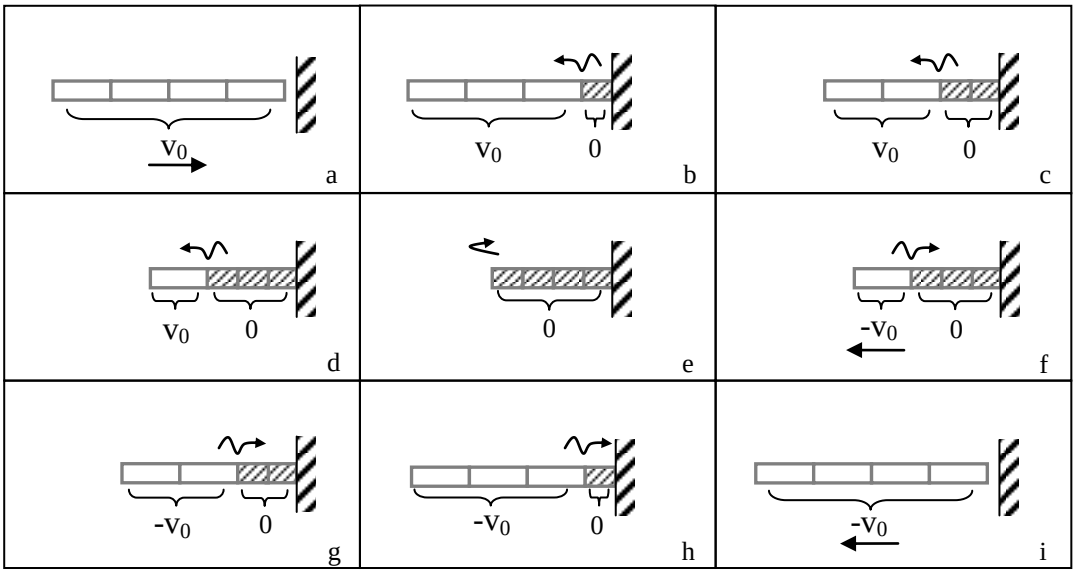

Figure 3.5 Snapshots of a collision between a distributed mass and a rigid wall

At any time when an instant change in velocity occurs, an infinite acceleration occurs. At first inspection there appears to be an incompatibility between the infinite accelerations and the finite stresses. One might argue the following:

$$F = ma = fA$$

$$a = f \times \frac{A}{m} \qquad (3.11)$$

$$\therefore f \to \infty \text{ since } a \to \infty$$

where F = force, a = acceleration, A = cross sectional area, m = mass, and f = stress. Equation 3.11 is valid for discrete mass cases, however the modelled mass in this case is distributed. Thus $m = \rho AL$ and cannot be accurately assumed to be lumped at one point. This means Newton's

second law is not applicable as currently stated. The internal stress in the distributed mass is a constant compression, and is caused by the impact. This can therefore be termed the 'contact stress' or the 'contact force'. Knowing that the absolute value of the dimensionless stress is either 0.0 or 1.0, the contact stress is:

$$f_{contact} = \frac{Ev_0}{v} \times F(X,T) = \sqrt{\rho E} v_0 \times 1.0 \qquad (3.12)$$

Taking the example of a possible building configuration; floor velocity = 1 m/s, floor length = 40 m, effective density = 80 kN/m^3 ≈ 8000 kg/m^3 (100 mm thick concrete slab plus superimposed dead load), and elastic modulus = 25 GN/m^2, a representative collision stress and contact duration can be estimated as:

$$\begin{aligned} f_{contact} &= \sqrt{25\times10^9 \times 8000} \times 1 = 14\times10^6 \text{ Pa} \\ &= \quad 14\,\text{MPa} \end{aligned} \qquad (3.13)$$

$$T_{contact} = \frac{2\times 40}{\sqrt{\frac{25\times10^9}{8000}}} = 0.045 \text{ s} \qquad (3.14)$$

where the contact surface is assumed to be flat and vertical. Equations 3.11 and 3.14 illustrate a notable advantage of the wave equation over stereo mechanics and other lumped mass models (Section 2.2.2). The contact duration cannot be determined when considering lumped masses, since the length of the mass used in these models is assumed to be zero, and thus the collision is assumed to be instantaneous.

3.1.2 Simplified Collision Force vs. Building Separation Relationship

A simplified relationship between contact force and building separation can be inferred from Equation 3.12. Since contact force is directly proportional to the impact velocity, the relative magnitude of the collision force can be approximated as a function of building separation. This is done by considering the response of an elastic SDOF oscillator colliding with a rigid wall (Figure 3.6). In this model, the oscillator is excited by being released from an initial displacement of u_0. A SDOF model is adopted here (instead of a distributed mass) because its motion is simpler to describe, and in this particular case, the use of a SDOF oscillator does not affect the outcome of the analysis. This is because the investigated properties all use pre-collision conditions.

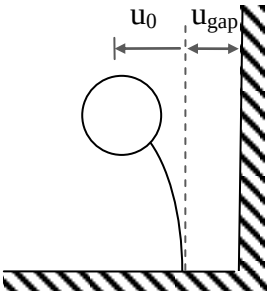

Figure 3.6 Single degree of freedom oscillator separated from a rigid wall by a distance u_{gap}

The displacement (u) and velocity ($\dot{u}$) of the oscillator before collision are:

$$u = u_0 \cos\left(2\pi \frac{t}{T}\right) \tag{3.15}$$

$$\dot{u} = -\frac{2\pi}{T} u_0 \sin\left(2\pi \frac{t}{T}\right) = \dot{u}_{max} \sin\left(2\pi \frac{t}{T}\right) \tag{3.16}$$

The oscillator velocity and displacement may be related by equating for t

$$\left|\frac{\dot{u}}{\dot{u}_{max}}\right| = \sin\left(\cos^{-1}\left(\frac{u}{u_0}\right)\right) = \sqrt{1-\left(\frac{u}{u_0}\right)^2} \tag{3.17}$$

Collision between the SDOF oscillator and the rigid wall occurs when $u = u_{gap}$. At this time the velocity of the SDOF oscillator is $\dot{u}$. Thus the impact velocity is $\dot{u}_{impact} = \dot{u}(t)$ when $u(t) = u_{gap}$. Since collision force is directly proportional to impact velocity, $F/F_{max} = \dot{u}_{impact}/\dot{u}_{max}$, where F = the collision force for a specific gap and F_{max} = the collision force when there is no gap (since maximum velocity occurs when u = 0). Furthermore since the system is elastic, u_0 also provides the maximum displacement for the no pounding case. Thus $u_0 = u_{np}$, where np indicates the required gap for 'no pounding' to occur. Equation 3.17 may be therefore rewritten as:

$$\frac{F}{F_{max}} = \sqrt{1-\left(\frac{u_{gap}}{u_{np}}\right)^2} \tag{3.18}$$

Figure 3.7 displays the resulting relationship. This relationship will change when ground motions are used to excite the oscillator since the oscillator's velocity will not be related to its displacement in the manner described above. However, Figure 3.7 does provide an important conceptual understanding of the way collision force may reduce with increasing building separation. This theory is compared to analytical findings in later chapters.

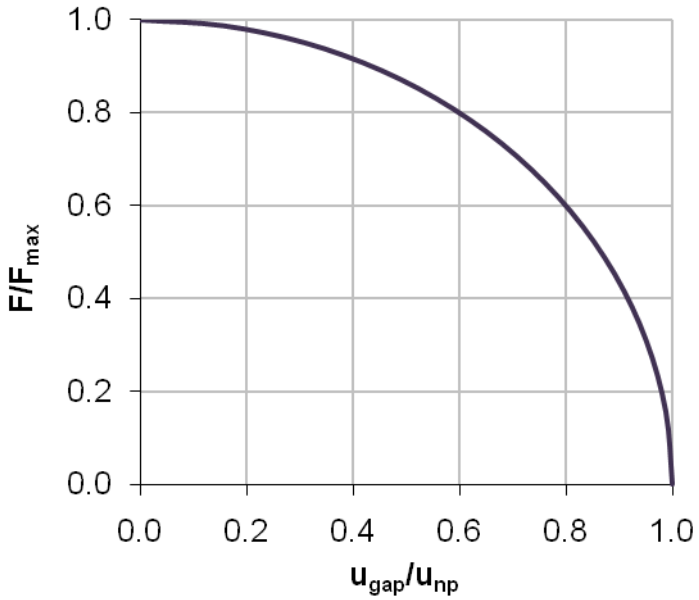

Figure 3.7 Relationship between collision force and building separation for a single collision of a SDOF oscillator

3.1.3 Collision of a Distributed Mass Including an Initial Acceleration

The initial conditions of the previous section assume a uniform velocity and no acceleration at the onset of collision. Addition of a constant acceleration over the duration of the collision increases the solution's complexity but will be briefly considered here. It must be noted that this derivation is not strictly mathematically correct (in a general solution process, a second order in time PDE cannot have an acceleration initial condition, since this causes the deflections to not be uniquely defined). However, in this particular case, comparison with numerical tests showed complete agreement. The solution is therefore considered to be valid. The derivation is presented in Appendix E. The dimensionless solution is now also dependent on a new dimensionless number, termed γ.

$$\gamma = \frac{a_0 L}{v v_0} \tag{3.19}$$

where a_0 = the constant acceleration during impact. Equation 3.19 is a measure of the relative influence of the constant acceleration and the initial velocity in the mass. If $a_0 = 0$, then $\gamma = 0$ and it has no influence on the solution. Dimensionless velocity and stress is plotted for $\gamma = -0.5$ in Figure 3.8. These values may be converted to dimensioned values using Equations 3.8 and 3.10.

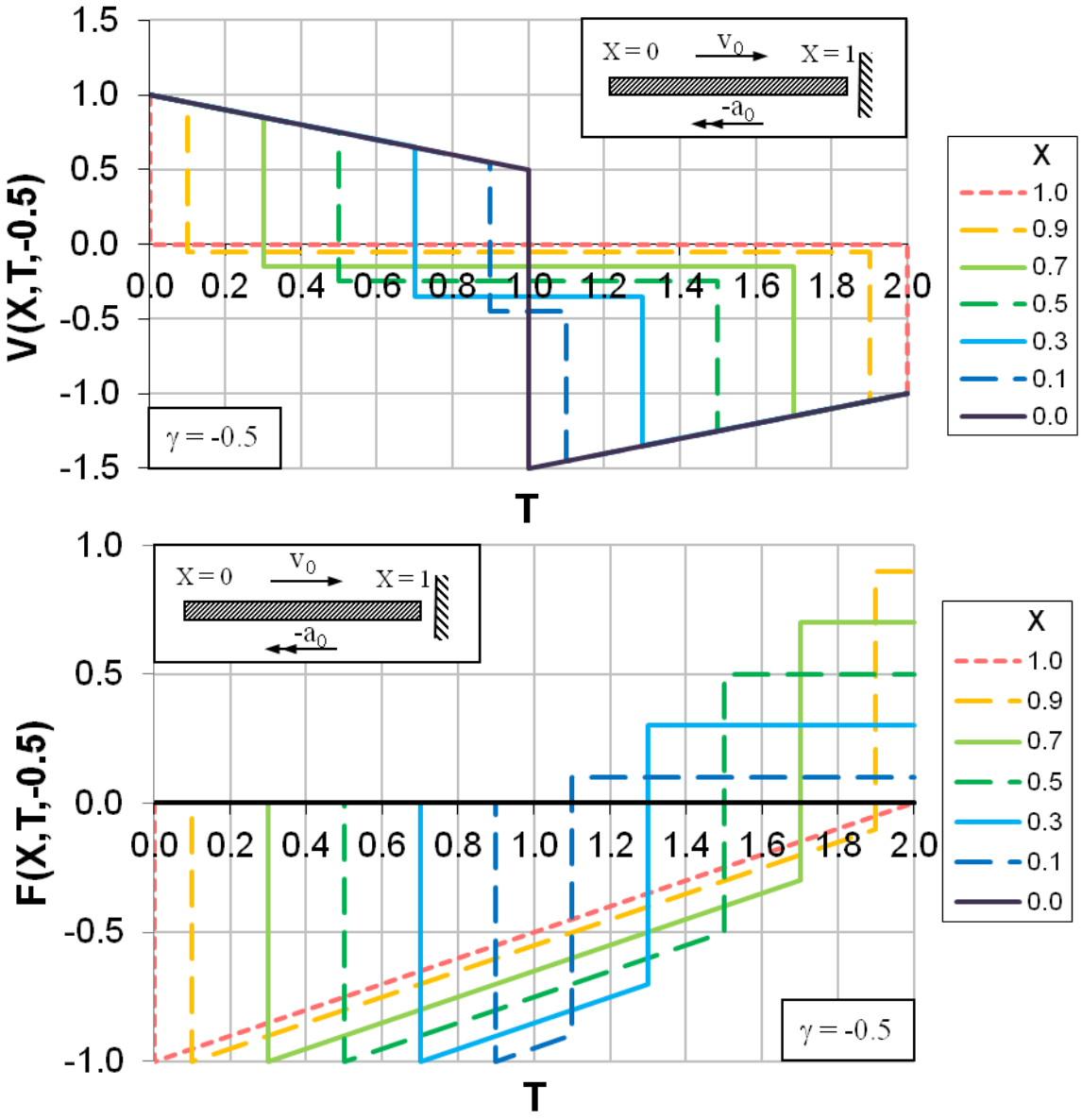

Figure 3.8 Dimensionless plots for γ = -0.5. Top: Dimensionless velocity. Bottom: Dimensionless stress

When $\gamma \leq 0$, the maximum contact stress (i.e. the stress at X = 1) can still be calculated by Equation 3.12. This is because the maximum stress occurs at the beginning of the collision, before the constant acceleration has had an effect. However, a positive value of γ causes larger stresses later in the collision. This stress can be calculated by using a modified initial velocity:

$$v' = v_0 + a_0 T_{contact} \qquad (3.20)$$

Where $T_{contact}$ can be found by determining when a positive stress occurs at X = 1. At X= 1, a positive (tensile) stress indicates that the boundary condition u(x,t) = 0 is restraining the distributed mass's edge from leaving the rigid boundary. This means the boundary condition is no longer valid and the collision has finished. When $0.5 < \gamma \leq -0.5$, $T_{contact}$ may be found using Equation 3.5. Ballpark values of γ may be found by using the properties of concrete adopted in

Equation 3.13 (thus the wave velocity (v) is 3200 ms^{-1}). Assuming a diaphragm length of less than 50 m, the diaphragm acceleration must be orders of magnitude larger than the impact velocity in order for $|\gamma| > 0.5$. If $|\gamma|$ is greater than 0.5, the acceleration changes the duration of contact. For example, if $\gamma < -0.5$, then the velocity change caused by the acceleration over the duration of the collision is sufficient to move the mass away from the rigid boundary before T = 2. Similarly, $\gamma > 0.5$ will cause the mass to remain in contact with the boundary after the collision has ended.

Collisions where $|\gamma| > 0.5$ do sometimes occur during pounding analyses. For example, consider a building and a rigid wall that is separated by an infinitesimal initial gap. The building consists of two columns supporting a distributed mass (Figure 3.9). If a constant acceleration is applied as shown, the building will contact the wall without any significant relative velocity (due to the size of the separation). In this circumstance wave propagation does not determine the duration of the collision. Instead the contact is determined by the duration of the applied acceleration.

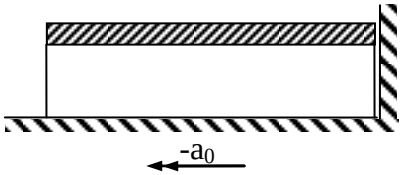

Figure 3.9 Constant acceleration applied to a building with an infinitely small initial separation

While the above example is highly idealised, long contact durations can be observed between buildings with very small initial separations and at points in an excitation where the ground motion is sufficiently strong to dominate the motion of both buildings. Long contacts are hereby termed ‘continuous contacts’ to distinguish them from the type of contact described in Section 3.1.1.

3.1.4 Collision of Two Distributed Masses – Mathematical Solution

The presentation of the behaviour of two colliding distributed masses can be achieved in a number of ways. This section provides a description of the mathematical solution method which provides dimensionless solutions. This method is consistent with the derivations presented in previous sections. A second solution method is then adopted in Section 3.1.5 because its approach enables a more intuitive understanding of the collision process.

The mathematical solution for the collision of two distributed masses requires a new boundary condition during the collision. As previously shown for the solution of the single distributed mass, a particle’s velocity only changes when a wave front passes through its location. At the

collision interface (the location of contact between the two distributed masses), the wave front passes only at the first instant and the last instant of collision. This means that the velocity of the collision interface must be constant throughout the duration of the collision. This constant interface velocity is hereby termed 'v_c'. Furthermore, since both distributed masses are in contact for the duration of the collision, the collision interface velocity must be the same in each mass. This velocity can be calculated by applying Newton's second law.

$$A_1 f_1 + A_2 f_2 = 0 \tag{3.21}$$

where the subscripts are as defined in Figure 3.10.

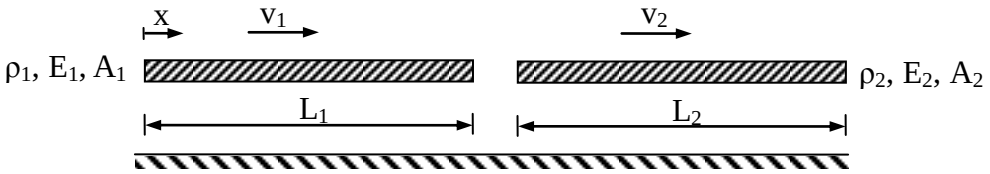

Figure 3.10 Collision of two distributed masses

The stress in a distributed mass is known for the single mass case (Equation 3.10). As the collision interface is moving at a constant velocity, its solution can be found by modifying the initial velocity to be an initial velocity *relative to the velocity of the collision interface*. Thus:

$$\begin{aligned} &\frac{A_1 E_1 (v_1 - v_c)}{v_1} + \frac{A_2 E_2 (v_2 - v_c)}{v_2} = 0 \\ &v_c = \frac{A_1\sqrt{\rho_1 E_1}\, v_1 + A_2\sqrt{\rho_2 E_2}\, v_2}{A_1\sqrt{\rho_1 E_1} + A_2\sqrt{\rho_2 E_2}} \end{aligned} \tag{3.22}$$

where v_c is the velocity of the collision interface. This boundary condition allows the independent solution of each mass's response. In this way, the mass's response can be equivalently viewed as a single distributed mass colliding with a rigid wall that moves at a constant velocity v_c. A full derivation, including conversions to dimensionless numbers, is presented in Appendix F. The two masses' velocities are presented below to illustrate their response. Velocity can be more simply characterised in dimensionless formulations:

$$v_m(X_m, T_m, \Psi_m) = v_{0,m} V_m(X_m, T_m, \Psi_m) \tag{3.23}$$

where $v_{0,m}$ = initial velocity of mass m and $v_m(X_m, T_m, \Psi_m)$ = velocity of mass m throughout time T_m and space X_m (Ψ_m is constant over the course of a collision). Velocity results are dependent upon a new dimensionless number; $\Psi_m = v_c/v_{0,m}$ which is a relative measure of the influence of

the interface velocity on the response of the mass. The dimensionless function V_m is presented for an example collision of two distributed masses where $\Psi_1 = 0.735$ and $\Psi_2 = 1.47$ in Figure 3.11. If $\Psi_1 = 0$, then $V_1(X_1,T_1,0)$ is the same as $V(X,T)$ in Figure 3.4. Note the collision finishes before $T_2 = 2$. This is because time is scaled differently in the two graphs, and the collision finishes when $T_1 = 2$.

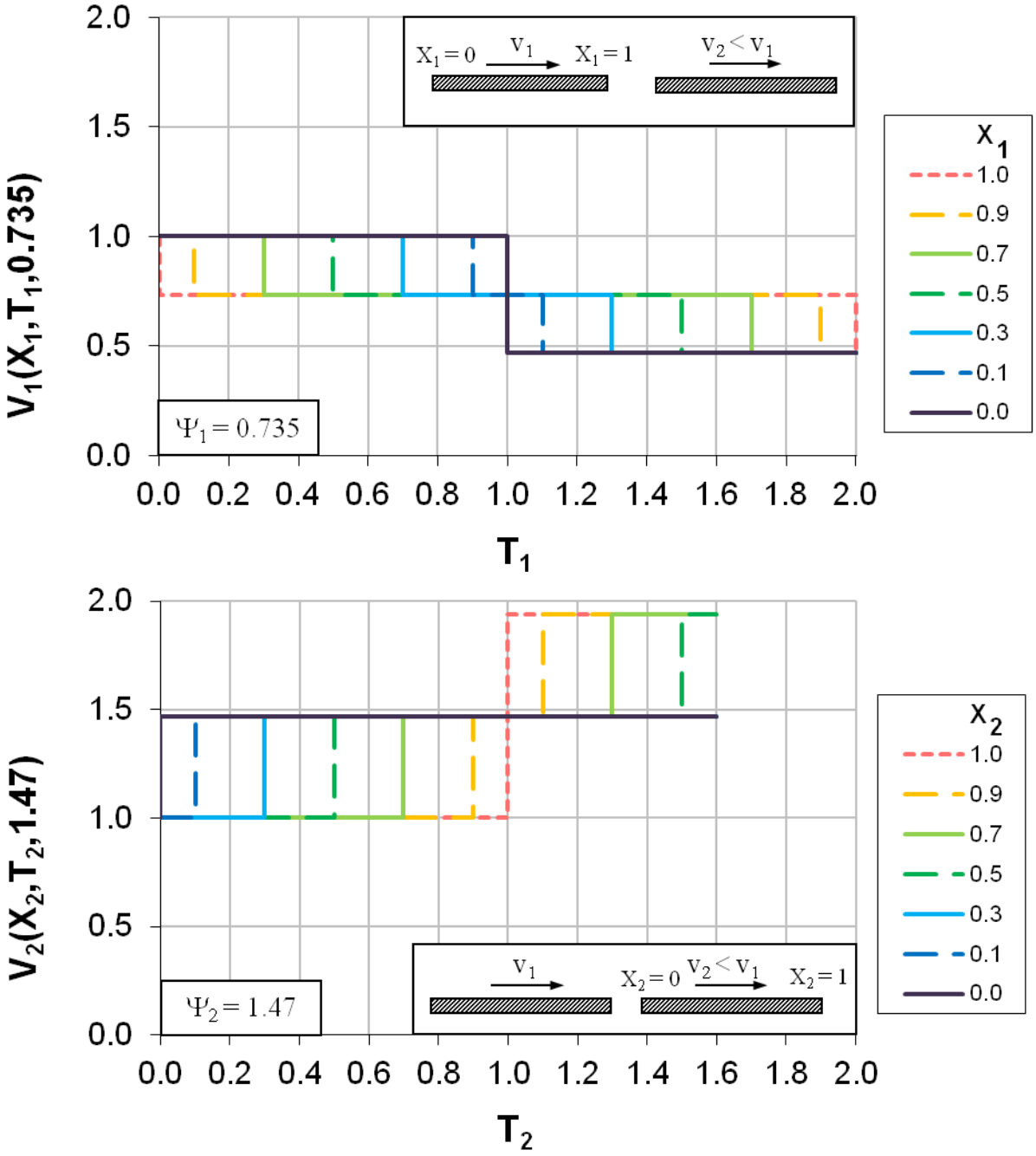

Figure 3.11 Dimensionless velocity for collision of two distributed masses

3.1.5 Collision of Two Distributed Masses – Behaviour During Collision

The velocities of two colliding distributed masses can be more readily understood by considering select instants during the collision (Figure 3.12).

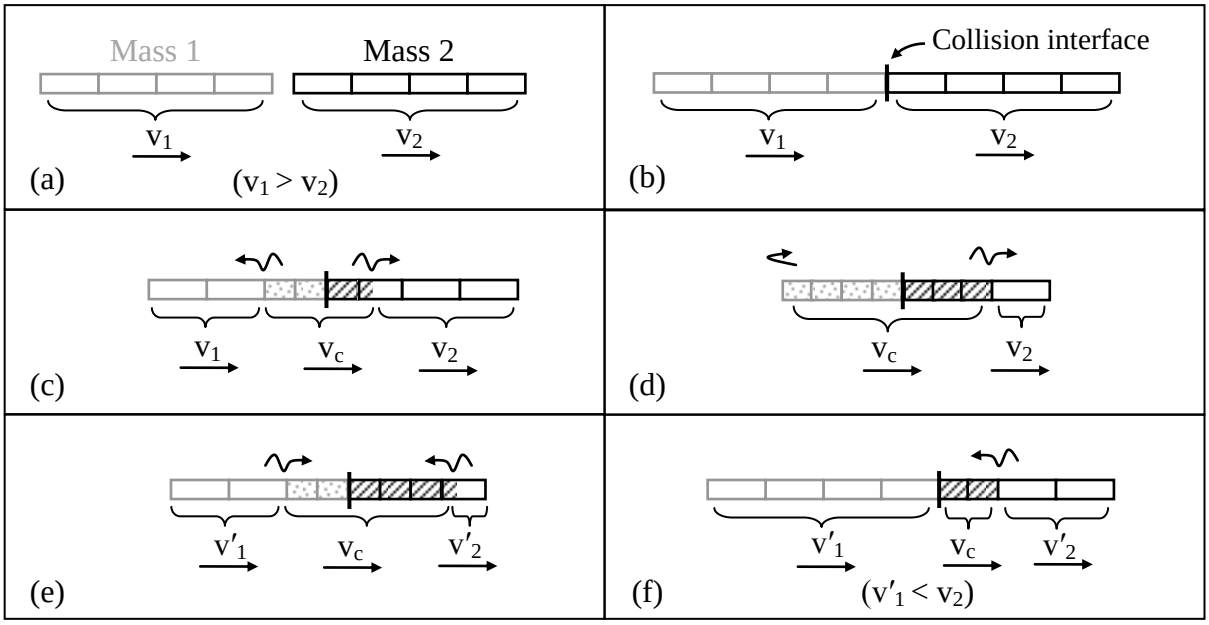

Figure 3.12 Snapshots of a collision between two distributed masses

Figure 3.12 presents very similar behaviour to that described in Figure 3.5. Each distributed mass has a wave front propagate to its free end and reflect back to the collision interface, and the collision is completed when the first wave front returns to the collision interface. Most of the velocities shown here are known (v_1, v_2, v_c). v'_1 and v'_2 can be found using the previously presented dimensionless plots; however, in this section they are calculated by considering conservation of momentum. These calculations are simplified using convenient substitutions. For example, the axial period of each colliding mass (Equation 3.5) can be expressed in terms of its mass and axial stiffness:

$$T_{contact} = \frac{2L}{v} = \frac{2L}{\sqrt{\frac{E}{\rho}}} = 2\sqrt{\frac{m}{k}} \qquad (3.24)$$

The axial period of distributed mass 1 and 2 can be thus expressed as:

$$T_n = 2\sqrt{\frac{m_n}{k_n}} \quad \text{where } n = 1,2 \qquad (3.25)$$

Where $m = \rho AL$ and $k = EA/L$, as shown in Figure 3.1. Note T_n no longer has the same definition as in Section 3.1.4. As dimensionless time is not discussed any further in this or subsequent sections, T_n is redefined as axial period of distributed mass n.

The collision velocity, v_c, (see Equation 3.22) can also be presented in terms of mass and axial period:

$$v_c = \frac{\frac{m_1}{m_2} v_1 + \frac{T_1}{T_2} v_2}{\frac{m_1}{m_2} + \frac{T_1}{T_2}} \qquad (3.26)$$

The collision velocity is governed by the velocity of each mass, the axial period ratio, and the mass ratio. To calculate v'_1 and v'_2, consider three instances from Figure 3.12, as presented in Table 3.1. The proportion of Mass 2 moving at a given velocity is governed by the ratio of the two colliding diaphragms' axial periods. For example in Table 3.1, $T_1 = ¾T_2$. Thus when all of Mass 1 moves at v_c, only three quarters of Mass 2 moves at velocity v_c, while the remaining quarter travels at v_2 (Table 3.1d).

Table 3.1 Distributed mass momentum during collision

	Diaphragm velocity	Mass 1 momentum	Mass 2 momentum
b	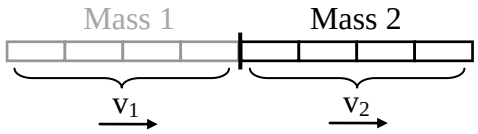	$p_{1b} = m_1 v_1$	$p_{2b} = m_2 v_2$
d	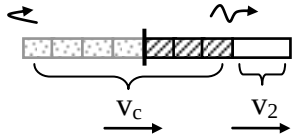	$p_{1d} = m_1 v_c$	$p_{2d} = m_2\left(\frac{T_1}{T_2} v_c + \left(1 - \frac{T_1}{T_2}\right) v_2\right)$
f	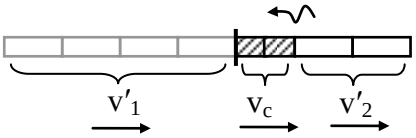	$p_{1f} = m_1 v'_1$	$p_{2f} = \left(2\left(1 - \frac{T_1}{T_2}\right) v_c + \left(2\frac{T_1}{T_2} - 1\right) v'_2\right)$

When the two masses are in contact, the change in momentum of Mass 1 (Δp_1) is equal and opposite to the change in momentum of Mass 2 (Δp_2). Substitution into just the first half of the collision ($p_{1d} - p_{1b} = p_{2b} - p_{2d}$) produces the relationship for v_c stated in Equation 3.26. Similarly by using $p_{1f} - p_{1d} = p_{2d} - p_{2f}$, v_c can also be found in terms of the final velocities v'_1 and v'_2. By equating the two expressions for v_c, an expression directly relating final velocity to initial velocity is found. Further details are presented in Appendix G:

$$v'_1 = v_1 + 2\frac{1}{1 + \frac{m_1 T_2}{m_2 T_1}}(v_2 - v_1) \qquad (3.27)$$

The expression for Mass 2's 'post collision' velocity (v'_2) is similar but has the subscripts 1 and 2 exchanged. However, as shown in Table 3.1f, different segments of Mass 2 have different velocities at the end of the collision. This causes Mass 2 to continue to oscillate after the collision is completed. The average velocity of Mass 2 (v''_2) is defined as the average velocity the diaphragm moves at as a whole after the collision. In contrast, v'_2 is the velocity in a section of the mass which is caused by the propagation and reflection of the compression wave. For example, in Table 3.1f, v'_2 is the velocity of only the uncompressed mass; while v''_2 is the average velocity found when considering all of Mass 2 (and is not shown in the figure). The average velocity is found by considering conservation of momentum of the entire length of Mass 2 after it separates from Mass 1;

$$m_2 v''_2 = m_2\left(2\left(1-\frac{T_1}{T_2}\right)v_c + \left(2\frac{T_1}{T_2}-1\right)v'_2\right)$$

$$v''_2 = v_2 + 2\frac{1}{\frac{T_2}{T_1}+\frac{m_2}{m_1}}\left(v_1 - v_2\right) \qquad (3.28)$$

This complication does not occur in Mass 1 since at the end of collision all parts of Mass 1 move at v'_1 (Table 3.1f). Thus the overall diaphragm velocity is equal to v'_1. For the remainder of the thesis, v''_2 shall be referred to as v'_2. This is because the original definition of v'_2 is only an intermediate step in the derivation, and relabeling provides consistency of nomenclature in the following sections. Note the mass labelling must be assigned using the criteria $T_2 \geq T_1$, in order to make Equations 3.27 and 3.28 valid.

It is also useful to express the collision force at the interface in terms of each mass's velocity, axial period and mass. This can be achieved by using the expressions for the stress of the distributed masses:

$$F = f_1 A_1 = f_2 A_2 = \frac{A_1 E_1\left(v_1 - v_c\right)}{v_1} \qquad (3.29)$$

After various substitutions, the following result is obtained:

$$F = 2\frac{v_1 - v_2}{\frac{T_1}{m_1}+\frac{T_2}{m_2}} \qquad (3.30)$$

To the author's knowledge, this is the first time a theoretically derived formula for collision force has been presented in building pounding research. It is acknowledged that the coefficient of restitution is likely to affect the collision force away from the contact. However, the force at the collision interface is anticipated to start at the calculated value and then decay over time. Note the collision force does not have a subscript. This is because the force is equal in both diaphragms. For comparison, the collision force for a single diaphragm colliding with a rigid wall is (from Equation 3.12):

$$F = 2\frac{m}{T}v_0 \qquad (3.31)$$

3.1.6 Secondary Collisions

Under certain conditions, it is possible for a secondary collision to occur at the end of the first (primary) collision. Consider Figure 3.13, which shows the velocities in each distributed mass in the time immediately following collision.

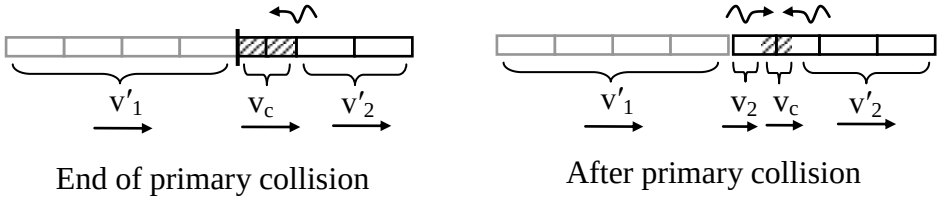

Figure 3.13 Time following collision assuming no secondary contact

Mass 2 is compressed when the primary collision is completed. As Mass 1 'separates' from Mass 2, the compressed end of Mass 2 begins to expand. If the velocity of the expanding end is less than that of v'_1, then the two masses remain in contact and a secondary collision occurs.

The circumstances that will lead to a secondary collision can be predicted using the previously presented relationships. Suppose that no secondary collision occurs. When the compressed end expands, it moves at velocity v_2. This is because the compression wave caused by the primary collision is completely negated by the tension wave caused by the masses' separation. This tension wave changes the velocity of the end of the rod back to its original state (i.e. v_2). As the velocity after collision in Mass 1 is known (v'_1), a condition for secondary collision can be stated; if $v'_1 > v_2$ then a secondary collision will occur. Substituting from Equation 3.27 provides this relation in terms of initial velocities. A secondary collision will occur if:

$$v_1 + 2\frac{1}{1+\frac{m_1 T_2}{m_2 T_1}}(v_2 - v_1) > v_2$$

$$\left(1 - 2\frac{1}{1+\frac{m_1 T_2}{m_2 T_1}}\right) v_1 > \left(1 - 2\frac{1}{1+\frac{m_1 T_2}{m_2 T_1}}\right) v_2 \qquad (3.32)$$

The common term in this equation can be positive or negative, depending on the masses properties. Due to the mathematical consequences of dividing by a negative number, this generates two possible conditions. A secondary collision will occur if:

$$v_1 > v_2 \text{ and } \left(1 - 2\frac{1}{1+\frac{m_1 T_2}{m_2 T_1}}\right) > 0$$

or

$$v_1 < v_2 \text{ and } \left(1 - 2\frac{1}{1+\frac{m_1 T_2}{m_2 T_1}}\right) < 0$$

However, the primary collision requires that v_1 must be greater than v_2. Therefore the first condition on the top line is always met, and the first condition on the bottom line is never met. Further simplification of the top line's second condition provides:

$$\frac{m_1 T_2}{m_2 T_1} > 1 \qquad (3.33)$$

While this secondary collision will result in further energy transfer between the two masses, it is not considered any further in this study. This is because secondary collision is significantly smaller than primary collision (the relative collision velocity of the secondary collision, $v_2 - v'_1$, is by definition smaller than the initial relative collision velocity, $v_2 - v_1$). Furthermore, other aspects of the model will more significantly affect the overall collision mechanism, such as the assumption of a perfectly elastic collision response.

3.1.7 Wave Propagation in Other Structural Elements

The modelling of colliding buildings as two distributed masses assumes that these collisions are not significantly affected by wave propagation through other structural elements. Specifically,

the influence of wave propagation through building columns has not been considered. The implications of this assumption are briefly considered here.

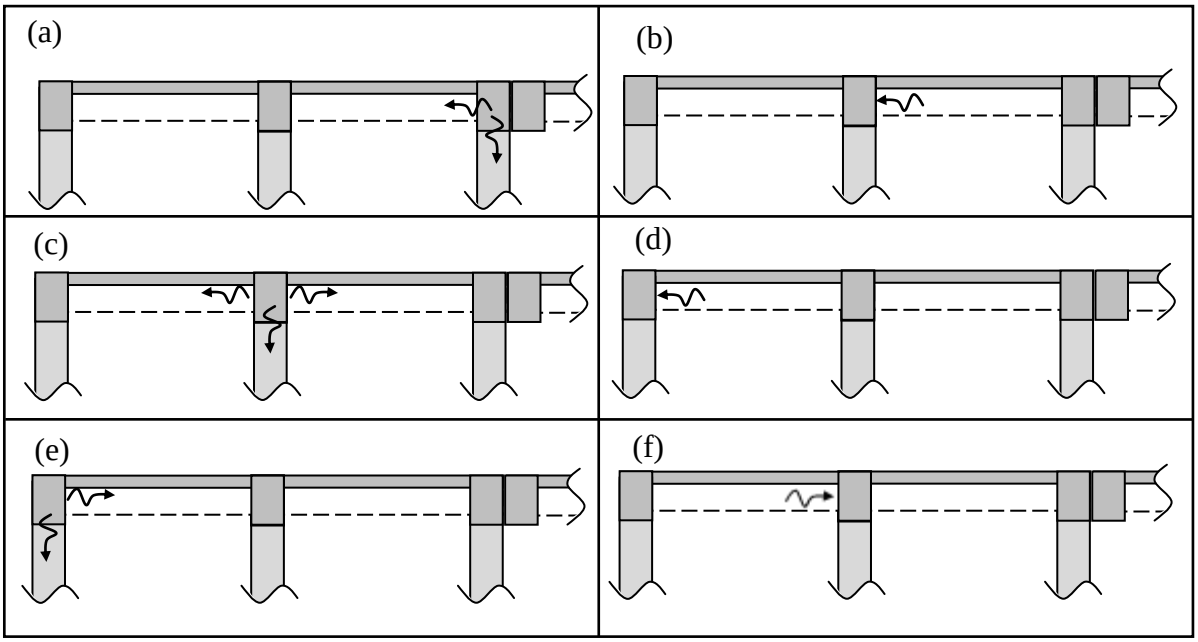

Figure 3.14 Snapshots during a collision of a building floor with another building.

Qualitative understanding of the influence of other structural elements may be gained by considering the collision of two building floors in more detail. Figure 3.14 presents snapshots during a collision of two buildings' floors. The left hand building's floor is presented while the right hand building is truncated for clarity. At time (a), the collision has just begun, and stress waves propagate down the closest column and along the building floor. A second splitting occurs after time (b), as shown in time (c), and a similar situation occurs at time (e) and again after time (f). At any time that any of these new wavefronts reflect back to the collision interface, they will affect the collision force.

Subsequent chapters include columns in the modelling, and the effect of these columns is considered. However, they are not modelled as distributed masses and thus may not accurately capture the actual structural response. While it is believed that these effects will be relatively minor, it is acknowledged that the effects have not been extensively investigated and may present a source of error.

3.1.8 Influence of Strain Rate Effects on Collision

The rate that concrete is loaded is known to affect the stiffness and strength of that concrete. When floor/floor collision occurs, a very high strain rate results. It may therefore be expected that the failure load and axial stiffness of concrete diaphragms will require adjustment for strain rate effects. In distributed mass collision, the therotical solution shows that points within each

mass go instantaneously from a completely unstressed to a completely stressed state. This implies an infinite strain rate with infantessimal duration. It is suspected that this effect will be minor on the overall collision properties; however, a strain rate law could be simply added by other reasearchers. This would involve modifying the Young's modulus and compressive strength capacity of each diaphragm using any selected strain rate law. It is noted that these adjustments will produce incorrect building diaphragm axial stiffnesses under low strain rates, however this error is highly unlikely to affect the overall building response. If the equivalent lumped mass model (as presented in Section 3.2.3) is used, the modified Young's modulus would affect the axial period duration which will in turn change the modelling parameters calculation in Equation 3.37 to Equation 3.40.

3.1.9 Comparison with Previous Experimental Data

It is desirable to verify the theory presented in this chapter with experimental testing. Physical testing lies outside the scope of this project; however, other researchers have previously produced results which could provide such verification. Use of the experimental data presented in Section 2.2.6 and Section 2.6 is considered in Table 3.2.

Table 3.2 Assessing applicability of previous bridge and building experimental data

Reference	***Is collision force reported?***	***Are the boundary conditions compatible with the presented theory?***	***Difference in boundary conditions***
Van Mier et al. 1991	*Yes*	*No*	*The distributed mass is fully fixed at one end and the impact hammer is a lumped mass*
Papadrakakis and Mouzakis 1995	*No*	*Yes*	*-*
Filiatrault et al. 1996	*Yes*	*No*	*The dimensions of the model means the mass is not distributed over any substantial distance. Furthermore, the load cell used to record the collision force is placed between the colliding floors and is comparatively flexible. This stiffness is the critical factor that governs the collision duration and force (rather than the process of wave propagation).*
Zhu et al. 2002	*No*	*No*	*While the shape of the bridge decks are directly applicable to the presented theory, the scaling of the bridge reduces the collision duration. The resulting short collision duration would require force measurement equipment that is accurate at very small (~0.0001 second) time resolutions.*
Chau et al. 2003	*No*	*No*	*A hemispherical contact is used between the buildings, and the scale of the model causes similar problems to that stated for Zhu et al.*

Rezavandi and Moghadam 2007	*No*	*Yes*	*-*
Guo et al. 2009	*No**	*No*	*Rounded contact points change the expected collision force profile, and the scaling causes problems similar to that state Zhu et al.*
Lindsay et al. 2011	*Yes*	*No*	*The properties of the equipment used to measure the collision force has affected the recorded collision force response. Scaling has also cause problems, as described for Zhu et al.*

** One collision force is reported, however the measurement of this collision is unclear, and the supporting information is insufficient for verifying calculation.*

None of the previously presented experiments adequately record data that is applicable to the collision of distributed masses. However, experiments performed by physicists are more directly relevant. Goldsmith (1960) reports the results of multiple experiments where collisions between distributed masses occurred. The axial stresses resulting from collision were compared to theoretical predictions and found to agree within acceptable tolerances. One of these experiments involved the collision of 10 ft long, 3/8 in diameter steel rods, while another investigated the collision of rectangular glass rods. The original data cannot be presented here since the original papers are 1950s conference papers, or 1950s papers written in German, and cannot be accessed. For the purposes of this project, the reported results of others are accepted as sufficient verification for the presented theory.

3.2 Comparison of Lumped and Distributed Mass Models

The theory presented in the previous sections of this chapter is based on different assumptions to most of those presented in Section 2.2. It is useful to make a distinction here between two types of models. The collision elements presented in Sections 2.2.1 to 2.2.3 assume the colliding objects are axially rigid and do not internally oscillate. These elements are termed *lumped mass models*, because the colliding objects act as if all their mass was located at one point. However, the model presented in Section 2.2.4 by Watanabe and Kawashima, and the theory presented in this chapter are termed *distributed mass models*. This is because the colliding object's mass and axial flexibility are assigned throughout the length of the object. The differences between these two modelling assumptions are investigated in this section.

3.2.1 Stereo Mechanics and Lumped Mass Models

When numerical analyses are performed, the response of lumped masses undergoing collision is primarily controlled by the selected collision element. However, in most cases, the post collision velocities can be accurately predicted by stereo mechanics. This is because the assumptions

made when deriving stereo mechanics formula are almost the same as the assumptions used when creating lumped mass contact elements. Specifically, stereo mechanics will produce the same post collision velocities as lumped mass models if:

1. There is no acceleration in either mass at the onset of collision.
2. No other external load is applied to either mass during the collision.
3. Any collision damping is calibrated to the coefficient of restitution (see Section 2.2).
4. The collision element stiffness is sufficiently large to cause a near instantaneous collision.

When modelling the collision of two buildings, the first two conditions are not commonly met. Both colliding floors are likely to have some acceleration at the time of collision, and building columns or walls will also exert some force on the floors during the collision. Nevertheless, these effects are typically minor. The second two conditions are usually met. Collision damping is usually intentionally calibrated to the coefficient of restitution, and the element stiffness is selected to minimise object overlap during collision which also reduces collision duration.

Using stereo mechanics to characterise the behaviour of lumped mass models provides a simple means to compare the effects of lumped and distributed mass models. This method is adopted below.

3.2.2 Model Comparison using the Influence Coefficient

If a collision between lumped masses is assumed to be fully elastic (e = 1.0), a direct comparison may be made between the post collision velocities of lumped and distributed masses. Equations 3.27 and 3.28 show remarkable similarities with Equations 2.1 and 2.2. Both models can be expressed in terms of the general equations:

$$v_1' = v_1 - 2\alpha_1(v_1 - v_2) \tag{3.34}$$

$$v_2' = v_2 - 2\alpha_2(v_2 - v_1) \tag{3.35}$$

where α is defined in Table 3.3. The value of α ranges between 0 and 1. When $\alpha = 0$ then $v'_1 = v_1$, causing no change in velocity. Thus α may be considered as an 'influence coefficient' which indicates the degree of velocity change caused by a collision. A greater value of α indicates a greater velocity change in the distributed mass as a result of collision, and thus the mass has a greater vulnerability to damage due to pounding. Recall that T_1/T_2 is always less than or equal to 1.0 due to the restrictions resulting from Equation 3.28. The value of α is the same

for both mass formulations (i.e. lumped and distributed mass models) only if $T_1 = T_2$. This corresponds to the case when Mass 2 does not oscillate after impact (refer to Table 3.1f). The values of α are displayed for the likely range of mass ratio and period ratio in Figure 3.15.

Table 3.3 Definition of α based upon mass approximation

	Lumped mass	**Distributed mass ($T_1 \leq T_2$)**
α_1	$\frac{1}{1+\frac{m_1}{m_2}}$	$\frac{1}{1+\frac{m_1 T_2}{m_2 T_1}}$
α_2	$\frac{1}{1+\frac{m_2}{m_1}}$	$\frac{1}{\frac{T_2}{T_1}+\frac{m_2}{m_1}}$

The distributed mass formulation cannot produce a greater value of α than the lumped mass model. As the collision period ratio (T_1/T_2) is reduced, α is also reduced. This is because less energy is transferred between the diaphragms. The 'lost' energy is stored instead as strain energy in Mass 2, causing internal oscillation after contact. As the mass ratio increases, α_1 reduces while α_2 increases. This behaviour supports previous researchers' findings that building pounding can significantly damage the lighter building when one building is greatly heavier than the other (Jeng and Tzeng 2000; Anagnostopoulos and Spiliopoulos 1992). Mass ratio and collision period ratio are not actually independent parameters (refer Equation 3.25). The figures could instead be presented using mass ratio and axial stiffness ratio. However, the present formulation allows much more intuitive interpretation of results. Note also that the distributed mass calculation of α_1 contains the same term as found in the condition for secondary collisions (Equation 3.33). This means that secondary collisions will occur when $\alpha_1 < 0.5$.

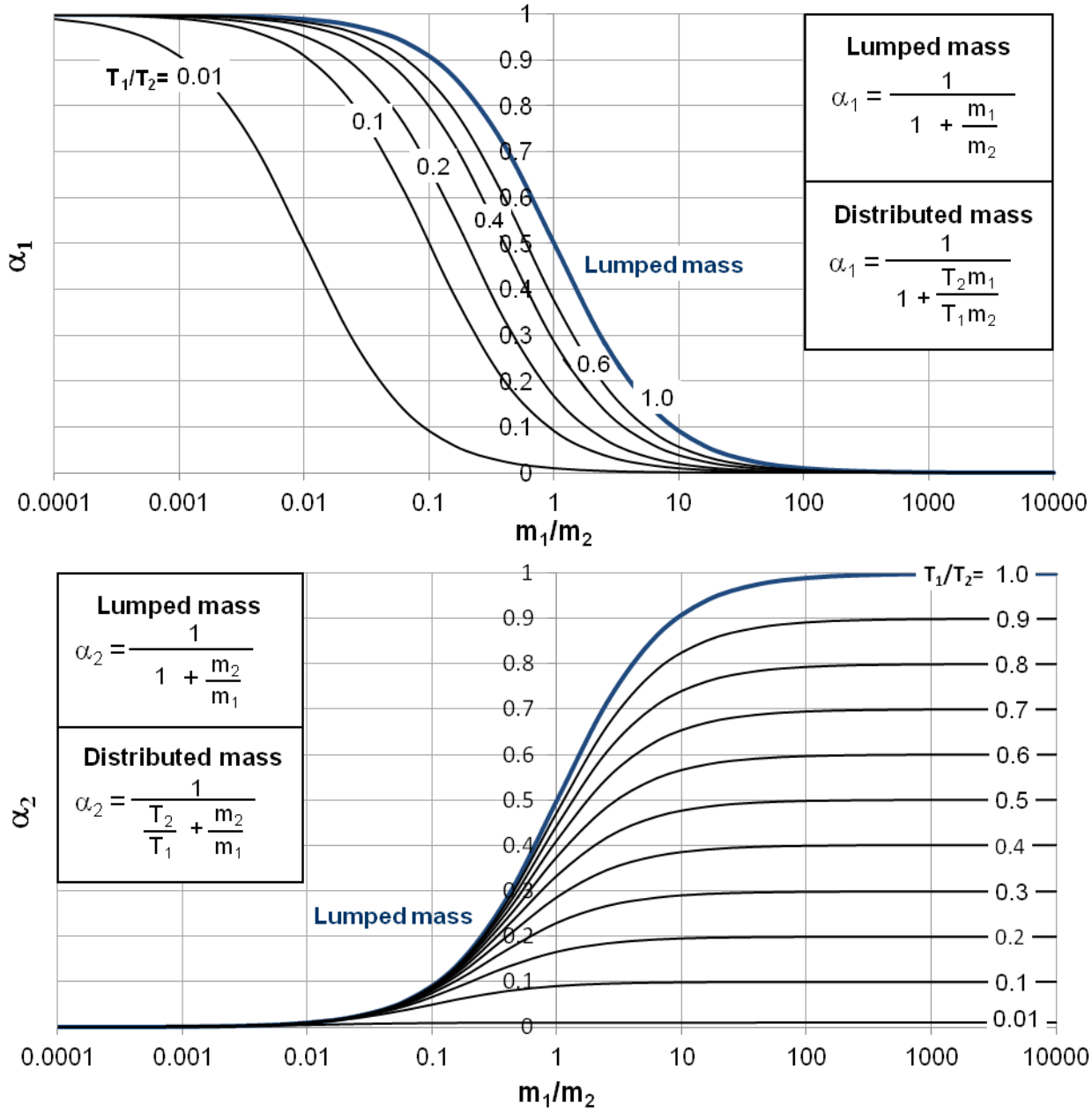

Figure 3.15 Influence coefficient, α, in terms of mass ratio and period ratio. Lumped mass results are identical to the distributed mass results with T_1/T_2 = 1.0.

The influence coefficient (α) provides previously unrealised insight into the collision process. Specifically, it provides a means of identifying when distributed mass effects are likely to be important. In some circumstances reference to Figure 3.15 alone may be sufficient to show that lumped mass modelling is suitable for the modelling of a specific building configuration. Using α as a measure of how much pounding influences the velocity of a structure is also informative. Mass 1 is almost entirely unaffected by a collision if $m_1/m_2 > 20$ while Mass 2 is similarly unaffected if $m_1/m_2 < 0.05$. Thus buildings that are significantly more massive than their neighbours suffer very little change in velocity if collision does occur. However, local damage may still be present as a result of the force of any collision. In such circumstances, pounding

analysis may still be required if the collision force or the performance of the other building is a concern.

3.2.3 Equivalent Lumped Mass Formulation

The relationship between the post collision velocity calculated using stereo mechanics, and α changes slightly if the collision is not elastic:

$$v_1' = v_1 - (1+e)\alpha_1(v_1 - v_2) \tag{3.36}$$

Since distributed mass modelling results in some energy loss during collision (Section 3.2.2), the coefficient of restitution can be calibrated to provide the same post collision velocities as the distributed mass formulation. This is achieved by equating Equation 3.36 (using the lumped mass's α_1) and Equation 3.34 (using the distributed mass's α_1):

$$\begin{aligned} (1+e_{eff})\frac{1}{1+\frac{m_1}{m_2}} &= \frac{2}{1+\frac{m_1 T_2}{m_2 T_1}} \\ e_{eff} &= 2\left(\frac{1+\frac{m_1}{m_2}}{1+\frac{m_1 T_2}{m_2 T_1}}\right) - 1 \end{aligned} \tag{3.37}$$

Where e_{eff} is termed the effective coefficient of restitution. The effective coefficient produces the same post collision velocity as an elastic collision between the two distributed masses. The same effective coefficient is found if the equations for Mass 2 are used in the derivation. It is possible for Equation 3.37 to produce effective coefficients of restitution that are less than 0 (Figure 3.16). However, this result is unlikely to occur for real building configurations, due to the usual range of mass and axial stiffness ratios. If a negative value for e_{eff} is calculated, another modelling approach must be used. This is because the coefficient of restitution generally forms a logarithmic relationship to the collision element damping ratio (refer Equation 2.11).

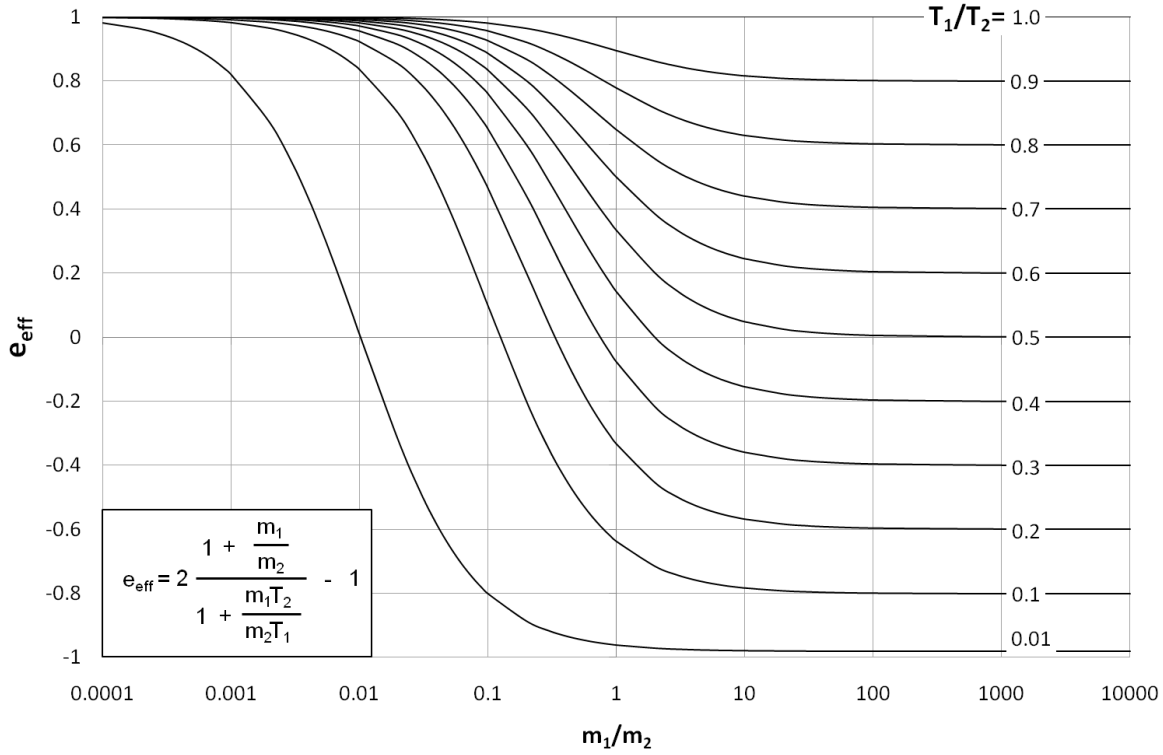

Figure 3.16 calculation of the effective coefficient of restitution

The duration of the collision for the lumped mass model can also be calibrated to the theoretical collision duration. This is achieved by modifying the contact element stiffness, which affects contact duration. When using the Kelvin element, the duration of a lumped mass collision is (Anagnostopoulos 2004);

$$T = \frac{\pi}{\omega_d} = \frac{\pi}{\sqrt{k_C \frac{m_1 + m_2}{m_1 m_2}\left(1-\zeta^2\right)}} \tag{3.38}$$

The theoretical duration of the collision for two distributed masses is T_1. Substituting and rearranging of the collision element stiffness (k_C) produces;

$$k_C = \frac{\frac{m_1 m_2}{m_1 + m_2}\left(\frac{\pi}{T_1}\right)^2}{1-\zeta^2} \tag{3.39}$$

where ζ is:

$$\zeta = \frac{-\ln\left(e_{eff}\right)}{\sqrt{\pi^2 + \left[\ln\left(e_{eff}\right)\right]^2}} \tag{3.40}$$

And where the relationship between ζ and the damping constand in the element (c) was presented previously in Equation 2.10. A Kelvin element using the above values produces the same post collision velocity in each mass and has the same collision duration as the theory presented in Section 3.1.5. Note however that a different collision force profile and magnitude will be recorded. This is because the Kelvin element cannot replicate the collision force response without the explicit modelling of the distributed masses. This model is adopted in specific tests presented in the following chapters. The Hertzdamp model (refer Section 2.2.2) could have its parameters calibrated in a similar manner, however its derivation is considerably more complicated due to the element's non-linear stiffness and damping. The Hertzdamp model calibration is not attempted in this thesis.

3.2.4 Incorporating Inelastic Effects in the Equivalent Lumped Mass Model

This section proposes a method by which inelastic effects may be modelled in a distributed mass collision. When considering lumped masses, the coefficient of restitution represents the linear combination of two extreme states; completely elastic collision and completely plastic collision. Here the post collision velocity of Mass 1 is considered. When two lumped masses undergo completely elastic collision, both momentum and kinetic energy are conserved. Mass 1's post collision velocity can be calculated using the theory presented previously (Equation 3.34). Similarly, a completely plastic collision between two lumped masses causes both masses to move at the same velocity. This velocity can be calculated by considering conservation of momentum alone, since $v'_1 = v'_2$;

$$v'_1 = \frac{v_1 m_1 + v_2 m_2}{m_1 + m_2} = v_1 - \frac{1}{1 + \frac{m_1}{m_2}}\left(v_1 - v_2\right) \qquad (3.41)$$

Equation 3.34 and Equation 3.41 can be linearly combined so that when e = 1, only Equation 3.34 contributes to the post collision velocity. Similarly when e = 0, only Equation 3.41 contributes to the post collision velocity. This is achieved by multiplying the two equations by the coefficients (e) and (1 - e), respectively. Thus the inelastic expression for the coefficient of restitution is calculated as;

$$v_1' = e\left(v_1 - 2\frac{1}{1+\frac{m_1}{m_2}}(v_1 - v_2) \right) + (1-e)\left(v_1 - \frac{1}{1+\frac{m_1}{m_2}}(v_1 - v_2) \right) \qquad (3.42)$$
$$= v_1 - \frac{(1+e)}{1+\frac{m_1}{m_2}}(v_1 - v_2)$$

This expression matches Equation 2.1 and is thus one of the equations of stereo mechanics. Now consider the distributed mass case. Inelasticity can be incorporated into the distributed mass model by following the same method. A new parameter is introduced to describe the inelasticity of the distributed mass collision. The parameter is an index indicating the level of plasticity in a distributed mass collision and is thus termed the plasticity index, r. The fully elastic post collision velocities of both masses are already known (Equation 3.34). The fully plastic collision causes the same post collision velocities as the lumped mass model, by the same considerations as presented in the previous paragraph (Equation 3.41). The general distributed mass expression is thus;

$$v_1' = r\left(v_1 - \frac{2}{1+\frac{T_2 m_1}{T_1 m_2}}(v_1 - v_2) \right) + (1-r)\left(v_1 - \frac{1}{1+\frac{m_1}{m_2}}(v_1 - v_2) \right) \qquad (3.43)$$
$$v_1' = v_1 - \left(\frac{2r}{1+\frac{T_2 m_1}{T_1 m_2}} + \frac{1-r}{1+\frac{m_1}{m_2}} \right)(v_1 - v_2)$$

The expression for distributed Mass 2 is similar;

$$v_2' = v_2 - \left(\frac{2r}{\frac{T_2}{T_1}+\frac{m_2}{m_1}} + \frac{1-r}{1+\frac{m_2}{m_1}} \right)(v_2 - v_1) \qquad (3.44)$$

When r = 1 the collision is completely elastic, and when r = 0 the collision is completely plastic. Finally, the effective coefficient of restitution can be related to the plasticity index by equating Equations 3.42 and 3.43;

$$e_{eff} = r\left(2\frac{\left(\frac{m_1}{m_2}+1\right)}{\frac{T_2 m_1}{T_1 m_2}+1} - 1 \right) = r \times \left[\text{elastic } e_{eff}\right] \qquad (3.45)$$

Equation 3.45 can also be derived using the expressions for Mass 2. Comparing Equation 3.45 with Equation 3.37 shows that the plasticity index creates a linear scaling of the elastic effective coefficient of restitution. When r = 0, e_{eff} is also zero, regardless of the properties of either distributed mass. The inelastic version of Figure 3.16 is thus the same as the existing version, but the vertical axis is scaled between r and -r.

When the level of plasticity increases, the duration of the collision also increases. This means Equations 3.38 and 3.39 are no longer strictly valid for the equivalent lumped mass model. Ideally when the plasticity index increases, collision stiffness must decrease in order to change the collision duration. However, the way that contact duration increases with increasing plasticity is not known. In the absence of further information, Equations 3.38 and 3.39 remain a reasonable approximation for inelastic collision duration.

Note that the meaning of the plasticity index is similar, but not identical, to the coefficient of restitution. Appropriate values of r will not necessarily be the same as the commonly used values for e.

3.2.5 Reporting Contact Force in Lumped Mass Models

Previous researchers have reported maximum collision force values when using lumped mass models (Jankowski 2006; Shakya et al. 2008). Usually in these instances, conclusions have been drawn on the relative increase or decrease of the maximum collision force when a parameter was changed. This practise is critiqued by assessing the performance of the Kelvin element during a collision.

A collision between two lumped masses causes an impulse on each mass. The impulse can be calculated if the pre collision velocity of each mass is known. This is because the post collision velocity can be calculated using stereo mechanic (impulse = change in the object's momentum over the course of the collision). The impulse acting on an object can also be calculated by integrating the applied force over time. In the case of a numerically modelled collision, the force applied to each object during collision is equal to the force in the collision element. Using results

reported by Anagnostopoulos (2004) for the Kelvin element, and considering the elastic case, the collision force is:

$$F = k_c(u_1 - u_2) = k_c \frac{(v_1 - v_2)}{\sqrt{k_c \frac{(m_1 + m_2)}{m_1 m_2}}} \sin\left(\sqrt{k_c \frac{(m_1 + m_2)}{m_1 m_2}} t\right) \qquad (3.46)$$

The maximum force is found when the sin term equals 1.0 (when $t = T_{contact}/2$). Thus:

$$F_{max} = (v_1 - v_2)\sqrt{k_c \frac{m_1 m_2}{m_1 + m_2}} \qquad (3.47)$$

The modelled collision force and collision duration (Equation 3.38) are both proportional to the contact stiffness of the element ($F_{max} \propto k_c^{1/2}$, $T \propto k_c^{-1/2}$), which was arbitrarily selected in previous research. The magnitudes of many reported collision force results are thus highly suspect. However, the force relationship described in Equation 3.47 correctly identifies collision force as being proportional to velocity. Thus previous researchers' claims regarding increases or decreases of force magnitude are likely to still be valid (such as 'reducing one building's stiffness resulted in higher collision forces in the tested model'). The proportionalities between F_{max} and k_c, and between T and k_c are the same for inelastic collisions, although their proofs are more complicated.

Similar force expressions have not been formally derived for the Hertz element and its derivative elements. However, it is believed that similar expressions would be found for these elements too. In all instances, the selection of collision element stiffness affects the recorded maximum collision force, and overall contact duration. Particular care must be taken when selecting collision element parameters if realistic collision forces are desired.

3.3 Conclusions

The following conclusions are drawn from the investigations and theory presented in Chapter 3.

1. Building floors can be approximated as rods of uniform density. When collision occurs between two floors, their responses can be predicted by the one dimensional wave equation.
2. Secondary collisions can affect the overall collision behaviour. Secondary collisions can be predicted and are smaller than primary collisions.

3. Floor accelerations that are present at the time of collision can also affect the overall collision behaviour. The significance of accelerations is determined in part by the ratio of relative acceleration and relative velocity at the start of collision. In large magnitude (high velocity) collisions, floor accelerations are unlikely to be significant.
4. Lumped mass models are identified as collisions between perfectly rigid floors, or floors with all mass modelled at a single point
5. The performance of lumped mass models and distributed mass models can be assessed by comparing the post collision velocities predicted by stereo mechanics and the one dimensional wave equation, respectively.
6. An equivalent lumped mass formulation was developed that produces the post collision velocities predicted by the wave equation for collisions between lumped masses. This element is tested in subsequent chapters.
7. The plasticity of a collision between distributed masses may be measured using the plasticity index, which is the distributed mass equivalent to the lumped mass coefficient of restitution.

Chapter 4 Development of the Uniaxial Contact Element for Pounding Analysis

Related Papers

Cole GL, Dhakal RP, Carr AJ, and Bull DK (2009), *The Effect of Diaphragm Wave Propagation on the Analysis of Pounding Structures*. Computational Methods in Structural Dynamics and Earthquake Engineering 2009: Rhodes, Greece.

Cole GL, Dhakal RP, Carr AJ, and Bull DK (2011), *An Investigation of the Effects of Mass Distribution on Pounding Structures*. Earthquake Engineering & Structural Dynamics, 2011. 40(6)

The theory described in the previous chapter may be applied in Non-Linear Time History Analyses (NLTHA) of building pounding. However, a number of issues arise when converting this theory into a suitable numerical model. This chapter investigates the most appropriate means of modelling collision between floors of adjacent buildings in *Ruaumoko*, a NLTHA program developed at the University of Canterbury (Carr 2007). The modelling method is developed incrementally. Initially, a single elastic collision is considered in isolation (Section 4.2). The influences of collision element changes are then investigated for a simple building configuration (Section 4.3). Finally, methods to incorporate inelasticity into the collision are explored (Section 4.4 – Section 4.11). A more thorough investigation of the effects of pounding on a more realistic building configuration is presented in Chapter 6.

4.1 Parameters Requiring Quantification

Numerical modelling of colliding distributed masses cannot perfectly represent the theoretical solution. For example, uniform mass distribution was assumed while developing the previously presented theory. However, a uniform distribution of mass cannot be applied in the available NLTHA programs (Figure 4.1). Furthermore, contact between the edges of the colliding masses requires the use of a collision element. As previously discussed (Section 2.2), the Kelvin contact element is adopted for use in all subsequent analyses because of its simplicity and availability. However the properties of this element require quantification. When an elastic collision is numerically modelled, two additional properties are required: the number of masses present in each colliding floor, and the collision element stiffness. These properties are investigated in the following sections. Note that the term ‘diaphragm’ is frequently adopted in this chapter. For the purposes of the discussions in this thesis, ‘diaphragm’ has the same definition as ‘distributed mass’ (refer Section 3.1).

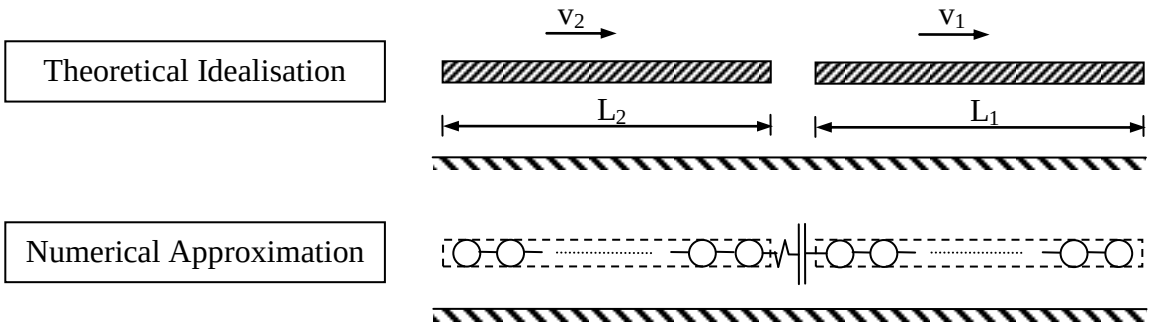

Figure 4.1 Differences between theoretical and numerical models for colliding diaphragms.

As previously discussed, Watanabe and Kawashima (2004) investigated appropriate selection of collision stiffness for models with 5, 10 and 20 elements in each diaphragm (refer Section 2.2.4). This investigation recommended $\gamma = 1.0$ for single collisions between bridge decks, allowing the calculation of the collision stiffness using Equation 2.20. However, as the selection of this property is so central to this thesis, a more detailed investigation is performed to verify these findings.

4.2 Model Optimization over a Single Collision

NLTHA model responses were tested for a single collision by changing the number of elements used to represent each diaphragm. Three models are presented in this section; 0, 5 and 500 elements per diaphragm. This corresponds to 1, 6 and 501 massed nodes per diaphragm, respectively. These three points refer to the convergence of numerical and theoretical results (500 elements), the minimum number of nodes tested by Watanabe (5 elements), and the standard practice for modelling of pounding (0 elements, lumped mass at node). The model layout is presented in Figure 4.2. Low stiffness springs connecting the diaphragm to the ground have been omitted for clarity in this figure. These springs are necessary for the model to run, but have sufficiently small stiffness to not affect the recorded response.

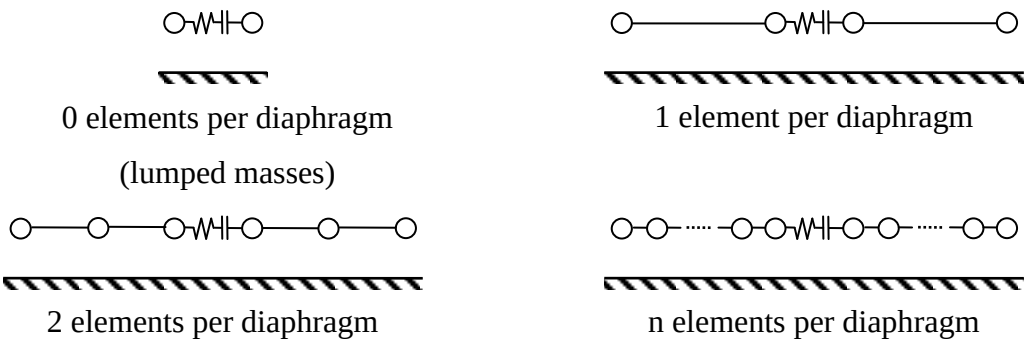

Figure 4.2 Model dependence on number of elements per diaphragm

To determine the most appropriate collision element stiffness, each model is run with three different values of γ. Each model is run with three collision element stiffnesses (using $\gamma = 10, 1, 0.1$). The properties of the two colliding diaphragms are presented in Table 4.1. These

properties have been relatively arbitrarily selected since they are directly compared to the previously presented theory (which is valid for any mass and diaphragm stiffness). More practical values are adopted in subsequent sections. The performance of each analysis is assessed based on the displacement and contact force response recorded during the collision. These response measures are considered in turn in the following sections.

Table 4.1 Properties of colliding diaphragms

Property	***Diaphragm 1***	***Diaphragm 2***	***Ratio***
Mass	*42.3 Tonne*	*56.4 Tonne*	*0.75:1*
Axial stiffness	*5,017,000 kN/m*	*5,017,000 kN/m*	*1:1*
Axial period	*0.00581 seconds*	*0.00671 seconds*	*0.857:1*
Distributed mass α	*0.533*	*0.400*	-
Lumped mass α	*0.571*	*0.428*	-
Initial velocity	*-13.3 m/s*	*10 m/s*	-
Distributed mass v' (Equation 3.34)	*11.6 m/s*	*-8.67 m/s*	-
Lumped mass v' (Equation 3.34)	*13.3 m/s*	*-10 m/s*	-

4.2.1 Displacement Response

The collision displacement response of both ends of Diaphragm 2 (from Figure 4.1) is displayed in Figure 4.3. Note that because the diaphragms are numbered in terms of increasing axial period, Diaphragm 2 is located to the left of Diaphragm 1 in these tests. The collision begins at 0.00052 seconds and finishes at 0.0063 seconds. As the axial collision period of Diaphragm 1 is smaller than that of Diaphragm 2, axial oscillation occurs in Diaphragm 2 after the collision. Points C and D on Diaphragm 1 are not presented in the figure for clarity.

The 500 element model (Figure 4.3, top) shows almost complete independence from the contact element stiffness, and all values of γ adequately match the theoretical behaviour. The effects of γ are much more pronounced in the 5 element model (Figure 4.3, middle). $\gamma = 10$ provides the most accurate displacement history, including the response of the oscillating diaphragm post collision. The average post collision velocities also agree with that of distributed mass theory (Equation 3.28). $\gamma = 1.0$ provides similar results, however $\gamma = 0.1$ produces a much longer collision, and displays a significantly larger maximum displacement. This corresponds to a larger overlap of the two diaphragms during collision, which is undesirable.

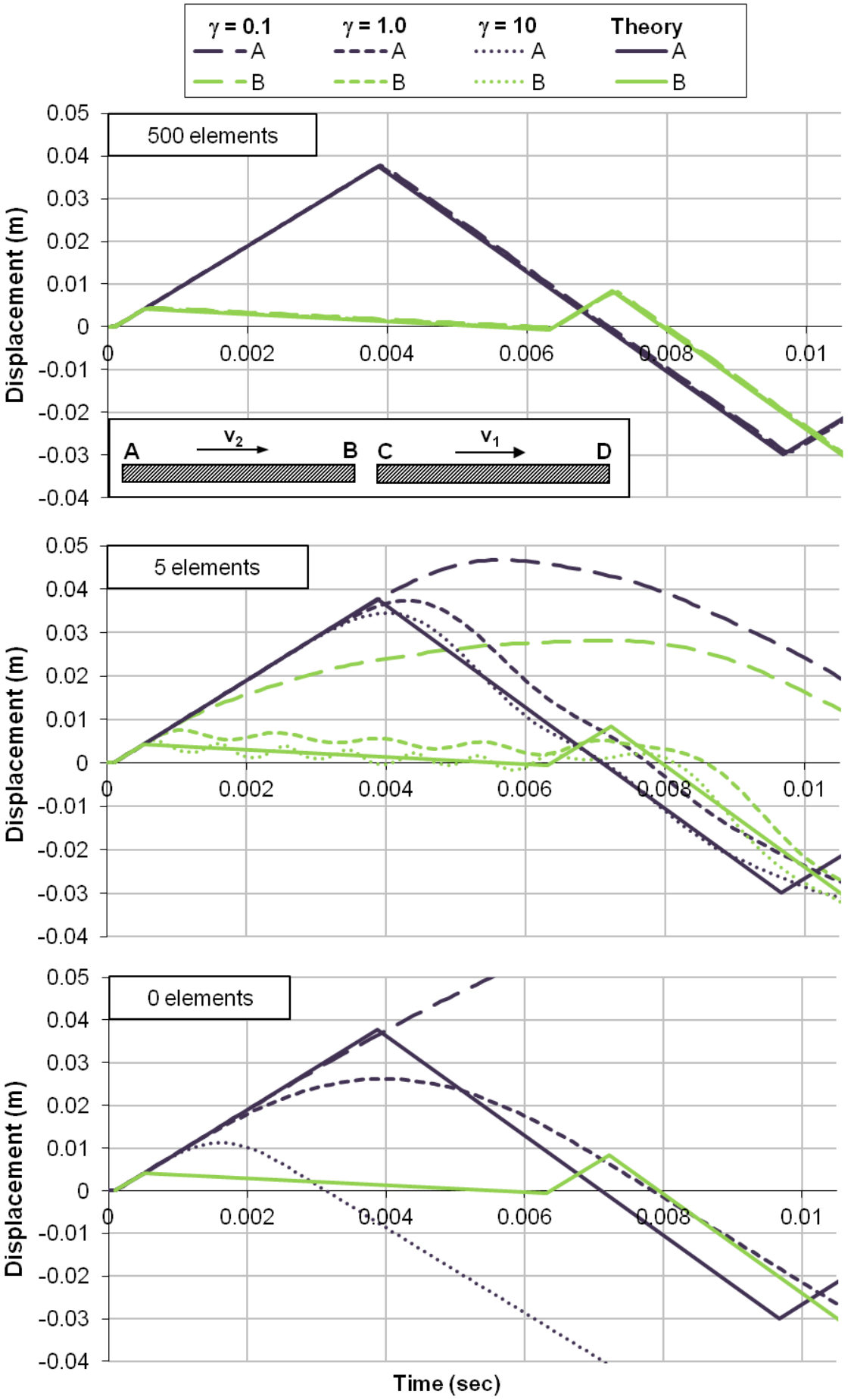

Figure 4.3 Displacement response of diaphragm 2 for numerical modelling using 500, 5 and 0 axial elements per diaphragm

The 0 element model is more difficult to interpret (Figure 4.3, bottom). As shown in Figure 4.2, in the 0 element case there is only one node and thus points A and B cannot be distinguished. While the theoretical displacement is shown for both ends of Diaphragm 2, the most desirable displacement performance may depend on the particular modelling situation. However, this distinction is largely academic, as both ends' displacements are approximated poorly. Note the value of γ is taken as the ratio of the collision element stiffness and the total diaphragm stiffness, since no axial diaphragm springs exist in the model (and thus $n = 0$ in Equation 2.20). Post collision velocities do not match distributed mass theory but instead match the predictions of stereo mechanics. In the 0 element model, the post collision velocity is independent of the collision stiffness.

4.2.2 Collision Force Response

Figure 4.4 presents the collision force histories over the course of the collision. In the 500 element case, the result for $\gamma = 0.1$ is very similar to the theoretical force, with the contact duration overestimated by 2%. The response to $\gamma = 1.0$ is very similar to that of $\gamma = 0.1$. When $\gamma = 10$ however, the higher levels of contact stiffness result in greater oscillation about the theoretical force. This is because the large contact element stiffness 'overloads' the adjacent axial springs when contact is first made. These springs then require time to oscillate to equilibrium (this equilibrium is the compression force predicted for distributed mass theory). These results concur with the observations of Watanabe and Kawashima. Additionally, very small time steps are required to sufficiently capture the collision force spikes when large collision stiffnesses are used.

The force response changes dramatically for the 5 element case. $\gamma = 0.1$ now causes an overly soft collision as the contact duration is substantially over predicted. However, the maximum recorded collision force is similar to that predicted by theory. The most accurate collision force response is observed when $\gamma = 1.0$, although accurate estimation of the collision force requires some form of averaging and the contact duration is still overestimated by 18%. $\gamma = 10$ appears to cause five separate collisions. This is again due to the extra oscillation in each diaphragm that is caused by the high collision element stiffness.

The results for the 0 element case show considerable deviation from distributed mass theory. This is again attributable to the model representing lumped mass collision. The collision forces do not oscillate wildly like previous figures, which is due to the lack of internal diaphragm vibration.

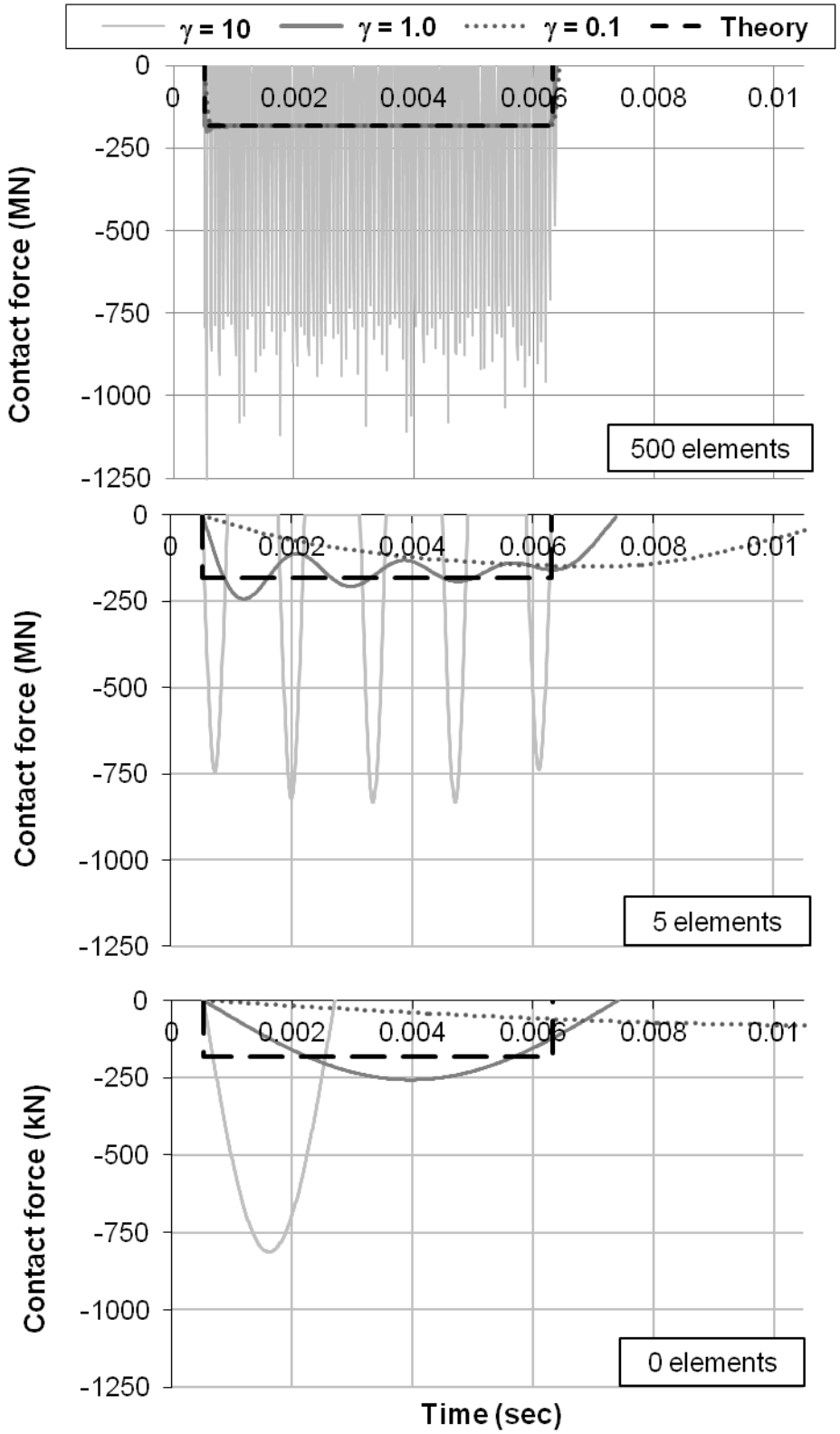

Figure 4.4 Contact force during diaphragm collision

4.2.3 The Role of the Collision Element Stiffness in Contact

Section 4.2.1 and Section 4.2.2 illustrate the conflicting requirements of the collision element. The element must be sufficiently stiff to avoid material overlap, but sufficiently soft to avoid creating large oscillations in the adjacent axial elements (observed in Section 4.2.2 as oscillation in the collision force). While not explicitly shown in the above sections, overly stiff contact

elements also affect the numerical stability of the numerical analysis. Other researchers have also identified this conflict (Zhu et al. 2002; Watanabe and Kawashima 2004) when looking at colliding bridge decks. Selection of the contact element stiffness is therefore a trade off between these requirements. Based upon the results of Section 4.2.1 and Section 4.2.2, $\gamma = 1.0$ is considered the most appropriate method to assign contact element stiffness. This conclusion is in agreement with the findings of Watanabe and Kawashima (2004).

4.2.4 Conclusions

The general behaviour of colliding diaphragms described in Section 4.2 is summarised below.

1. Larger values of γ produce more accurate displacement histories. This is because larger stiffnesses allow less overlap of the two contact surfaces.
2. Smaller values of γ produce less oscillatory contact forces but also longer contact duration.
3. Increasing the number of elements in a diaphragm increases the accuracy of the simulation due to the more uniform distribution of mass. Lowering the number of elements results in longer collision duration and higher displacement sensitivity to γ.
4. When at least one element is present in each diaphragm, $\gamma = 1$ appears to be the most appropriate selection. This finding supports that of Watanabe and Kawashima.
5. The response for the 0 element diaphragm case is fundamentally different because the axial properties of the diaphragm cannot be modelled and thus wave propagation cannot occur. Points 1 and 2 are not strictly valid for single node diaphragms.

4.3 Model Optimization over Excitation History

Non-linear time history modelling of pounding involves many more factors than just the behaviour of colliding diaphragms during impact. The building models and earthquake records both determine the performance of buildings irrespective of whether pounding occurs. To more accurately determine the influence of the selected type of diaphragm modelling on the overall response of two colliding buildings, a simplified building pounding scenario is modelled.

4.3.1 Test Setup

Two simplified buildings, each with two storeys, are modelled for three excitations. General building dimensions and key properties are presented in Figure 4.5 and Table 4.2, respectively. The lengths of these buildings were selected based on common geometries of Wellington buildings, while the width loosely corresponds to the expected distance between seismic frames. Seismic weights of 6 kPa (smaller building) and 8 kPa (larger building) were assigned based on

the range of typical office building weights produced by NZS1170.5 (2004). Interstorey stiffnesses were then assigned to produce the desired building periods. Building periods were selected as 0.2 seconds (smaller building) and 0.3 seconds (larger building) to ensure relative motion between the two buildings. A building separation of 8 mm was assigned to ensure pounding occurred.

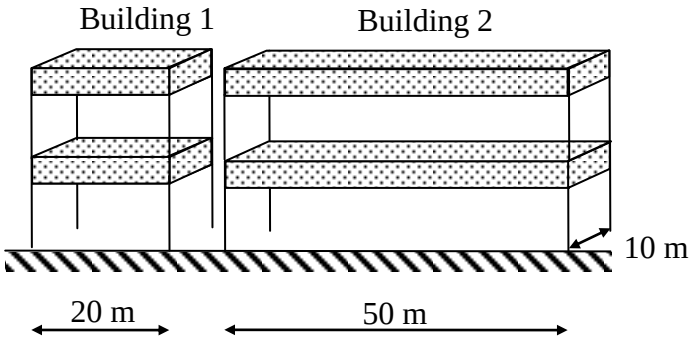

Figure 4.5 Modelled building layout. Plan dimensions to scale (excluding building separation)

Table 4.2 Modelled Building properties

	Building 1	***Building 2***	***Ratio***
Floor seismic weight	*1,600 kN*	*3,000 kN*	*0.53:1*
Interstorey stiffness	*420,000 kN/m*	*350,000 kN/m*	*1.2:1*
Diaphragm stiffness (k_D)	*1,881,300 kN/m*	*752,520 kN/m*	*2.5:1*
Structure period	*0.2 sec*	*0.3 sec*	*0.67:1*
Axial collision period (T)	*0.019 sec*	*0.04 sec*	*0.48:1*
Lumped mass α (Table 3.3)	*0.652*	*0.348*	-
Distributed mass α (Table 3.3)	*0.464*	*0.248*	-
Storey yield	*2400 kN*	*1400 kN*	*1.7:1*

El Centro (East-West, 1940), Mexico City (East-West, 1985) and Loma Prieta (North-South, 1989) earthquake components were adopted as input records (Figure 4.6). Each of these records was reduced to ten seconds of high intensity ground motion to shorten the required computation time. The intensities of each record were also modified to adjust each building's inelastic response. The scaling factors for El Centro, Mexico City, and Loma Prieta are 1.0, 2.0 and 1.0, respectively. After scaling, El Centro induces little inelastic interstorey deformation, while Loma Prieta causes a significant inelastic displacement early in the record. Mexico City causes moderate inelastic deformation.

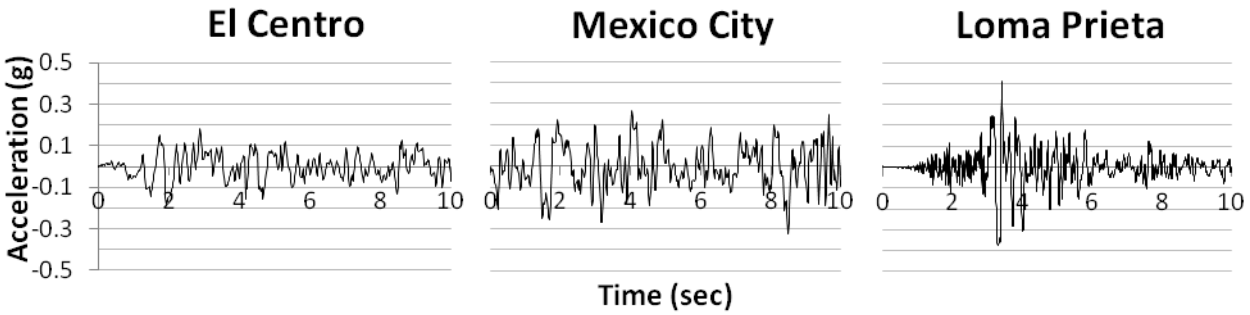

Figure 4.6 Horizontal ground excitation of scaled input records.

Ten tests were run for each excitation (Table 4.3). Four of these tests used lumped mass models, while the remaining six tests used distributed masses. The contact element stiffness for distributed mass modelling was calculated using $\gamma = 1$. However, a rational choice for the number of elements in each diaphragm was still required. The six distributed mass tests used 1, 2, 3, 4, 5 and 20 axial elements per diaphragm, respectively. The 20 element test was used as the benchmark for all other tests. Five elements and less were tested since the five element model performed suitably well in the single collision modelling (Section 4.3). Additional floor elements add accuracy, but can also notably increase computation time. This is because the maximum permissible time step is often sensitive to the contact element's stiffness, which is in turn affected by the number of diaphragm elements (Equation 2.20). The number of elements in each diaphragm also affects the model configuration (Figure 4.7). The benchmark test used a time step of 10^{-7} seconds while all other tests used 10^{-6} seconds. These values were determined by reducing the time step until the energy calculated by the equation of dynamic equilibrium for a given configuration equalled that of the input energy from each input record. The time steps could have been increased incrementally for models with fewer elements per diaphragm, however in these tests the time step was held constant for consistency.

Table 4.3 Definition of lumped mass collision element stiffness. k_D = diaphragm element stiffness

	Distributed mass						*Lumped mass*			
Test name	***Benchmark***	***5***	***4***	***3***	***2***	***1***	***0(10)***	***0(1)***	***0(0.1)***	***0(equiv)***
elements per diaphragm	*20*	*5*	*4*	*3*	*2*	*1*	*0*	*0*	*0*	*0*
Element stiffness, k_c=	k_D	k_D	k_D	k_D	k_D	k_D	$10k_D$	k_D	$0.1k_D$	*Equation* 2.20

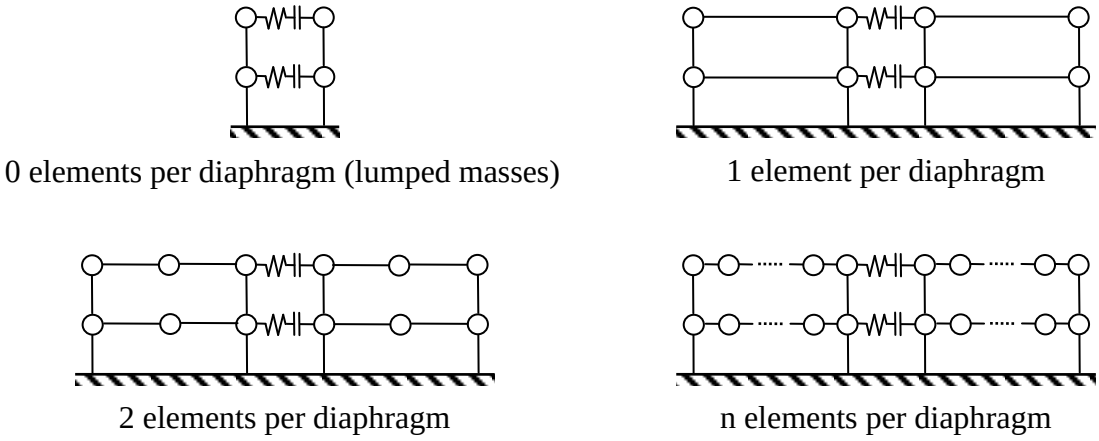

Figure 4.7 Model configurations in terms of number of element per diaphragm

When considering lumped masses, the number of elements in each diaphragm was fixed at zero. However, only vague guidelines exist to calculate the collision element stiffness (k_C), which is usually described in terms of the diaphragm stiffness (k_D). Three values of k_C were tested for the lumped mass models, in addition to the equivalent lumped mass formulation. Note the diaphragm axial stiffness (k_D) used in Table 4.3 was taken as the larger value from Table 4.2.

4.3.2 Drift Results

The resulting drift envelopes for Building 1 and Building 2 are presented in Figure 4.8 and Figure 4.9, respectively. The drifts are presented as a percentage error from that of the benchmark result; i.e. the result obtained from 20 elements per diaphragm model. The figures present two series for each earthquake; the first series shows the displacement envelope for leftward building movement in each inset diagram, while the second series shows the corresponding movement to the right. A negative error value signifies that the test recorded a smaller magnitude than the benchmark test.

All traditional lumped mass models are found to have at least 10 % error, regardless of the location of the recorded drift. Surprisingly, the lumped masses frequently underestimate the response. This result shows that a lower value of α (or equivalently, a lower value of e) does not necessarily reduce the global damage caused by pounding on a structure, which agrees with findings by Dimitrakopoulos et al. (refer Section 2.4.1). The equivalent lumped mass formulation, test 0(equiv), provides a significant increase in accuracy and is approximately as accurate as the one element per diaphragm case. Drift error does exceed 10 % for one excitation in the second storey of Building 2, but all other drift recordings show marked improvement in accuracy.

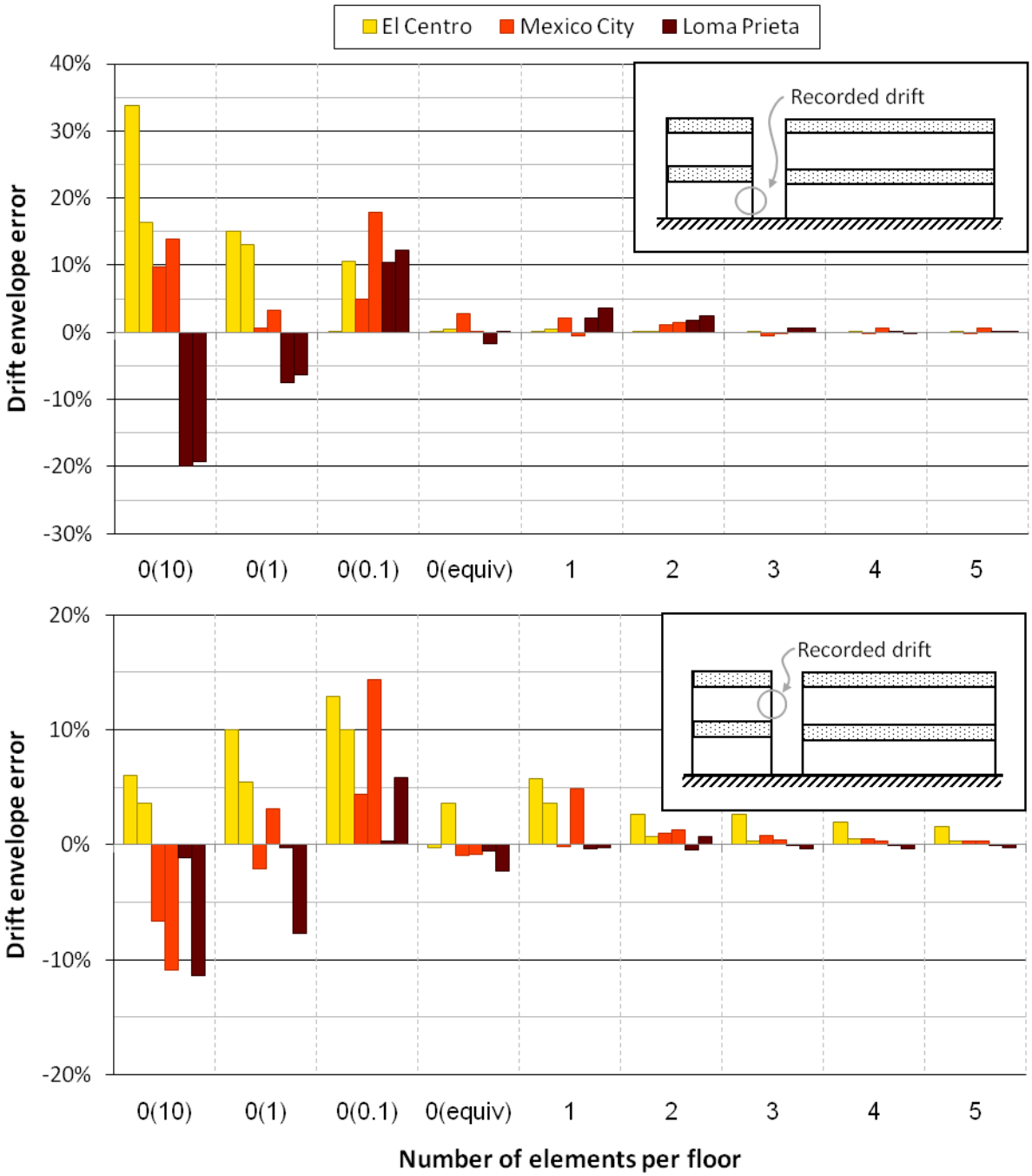

Figure 4.8 Building 1 error in drift maxima relative to benchmark model

However, the equivalent lumped mass formulation cannot as accurately represent the opposite ends of either building (refer to the inset diagrams in Figure 4.8 or Figure 4.9). This is due to the perfectly rigid diaphragm model. The rigid diaphragm reduces the shear demands of the columns at the collision interface as the contact loading is directly applied to all columns that are connected to that diaphragm. The figures also illustrate that increasing the number of diaphragm elements progressively increases the displacement envelope accuracy. If two or more elements are used per diaphragm, then nearly all recorded errors are less than 5% (only one error exceeded 5% with a value of 6.2%).

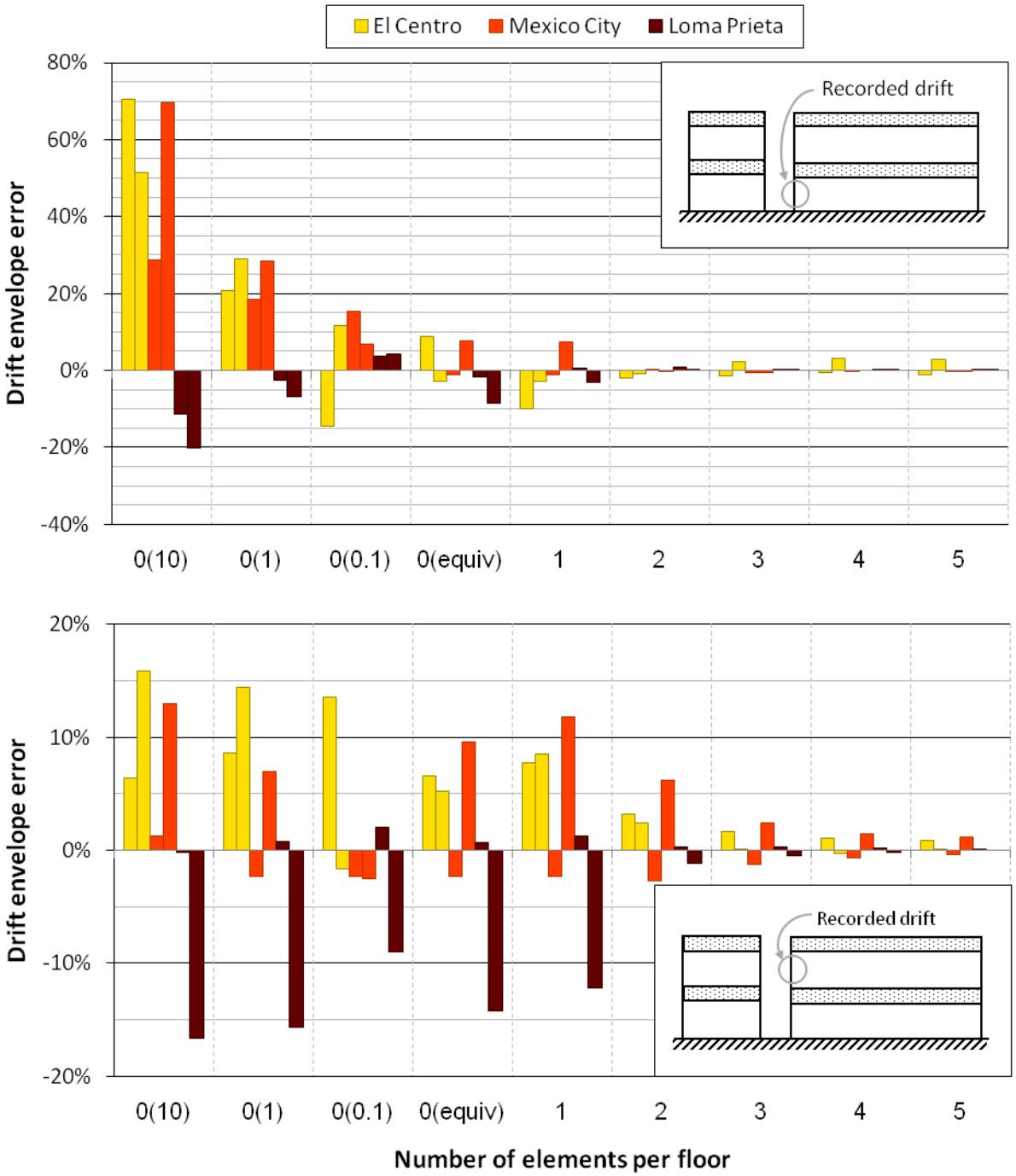

Figure 4.9 Building 2 errors in drift maxima relative to benchmark model

4.3.3 Contact Force Results

The accuracy of the tested models can also be assessed by inspecting the contact force. Figure 4.10 presents the normalised contact force profiles of every collision recorded in the benchmark model. The presented collisions were recorded at the buildings' roof during the El Centro record. The collision force is normalised by the force predicted using Equation 3.30, and time is normalised by the predicted collision duration (the minimum axial period of the two colliding diaphragms). The dashed line indicates the theoretical collision profile between two diaphragms with constant velocity.

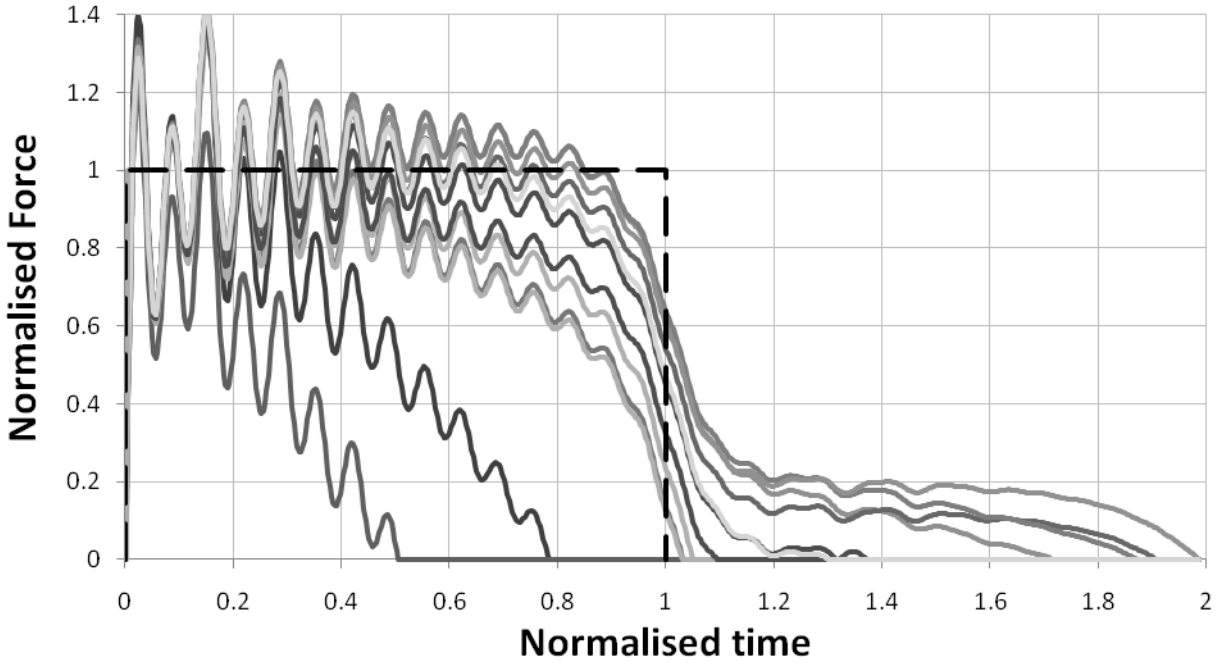

Figure 4.10 Normalised El Centro collision profiles (benchmark model). Each solid line represents the contact force during a different collision. The dashed line indicates the theoretically predicted force for all collisions.

Initially, the collision force is observed to oscillate around the theoretical value. However, the influence of relative strength of the diaphragms' accelerations (Section 3.1.3) is observed later in the collision. The collisions that finish at 0.5 and 0.76 times the collision duration are dominated by negative relative accelerations that oppose the collision. In the twelve collisions recorded in the El Centro record, no substantial increase in collision force is caused by positive relative accelerations. This can be attributed to the buildings' columns applying forces to both diaphragms that oppose the motion causing these collisions.

The collisions appear to last up to twice as long as the predicted contact duration. However, this behaviour is expected since the criterion for secondary conditions (Equation 3.33) is met in this building configuration (refer Table 4.2). The magnitudes of the secondary collisions recorded in the El Centro record are approximately 20% that of the primary collision, and the secondary collision appears to have approximately the same contact duration.

In order to compare the recorded collision forces with those predicted by Equation 3.30, the force magnitude for each recorded collision was calculated by averaging the first local maximum and the first local minimum in the force collision (i.e. the peak at time 0.05 and the trough at time 0.1 in Figure 4.10). The predicted collision force and the averaged collision force (termed the recorded collision force) are compared in Figure 4.11. A positive error indicates that Equation 3.30 overestimated the contact force. 10% error is adopted as the acceptable threshold of accuracy. This threshold is consistent with the generally adopted accuracy in a variety of engineering applications. The criterion is illustrated with darker lines on the 10% error threshold.

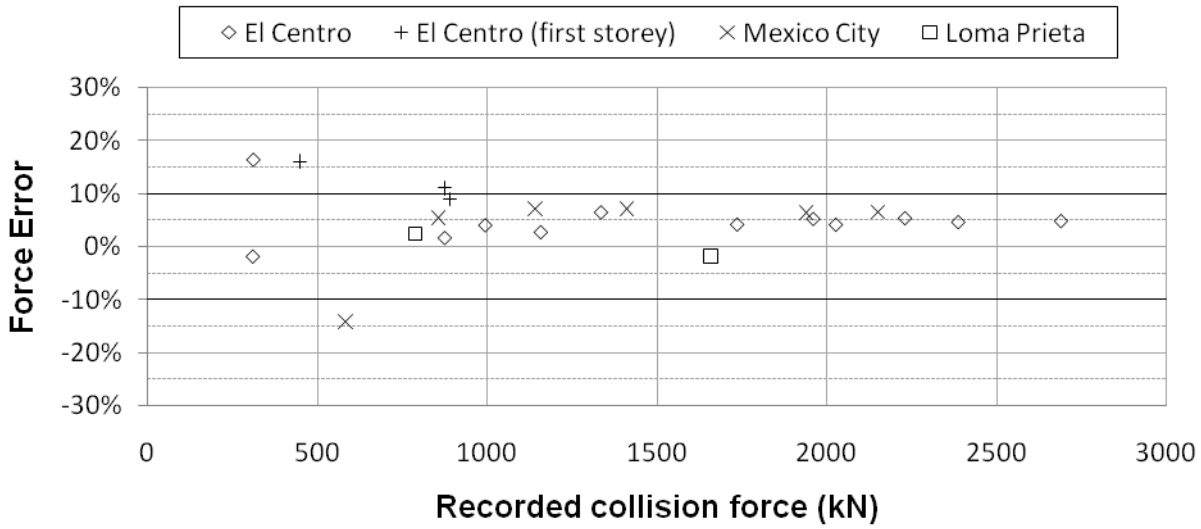

Figure 4.11 Collision force comparison for 20 element model. Note force error is calculated as the percentage error between the predicted and the recorded collision force

All three excitations present similar collision force accuracy. El Centro was the only excitation to experience collision at the first floor. First floor collisions appear to be not as accurately predicted by Equation 3.30. Figure 4.11 demonstrates that the accuracy of Equation 3.30 is affected by the magnitude of the collision force. The drop in accuracy at lower force magnitudes can be primarily attributed to the greater influence of the accelerations in each floor at the onset of collision. Overall, Equation 3.30 is shown to be very accurate when using the 20 element model.

The accuracy of Equation 3.30 is then assessed for the other test cases (Figure 4.12). Each test is compared to the recorded collision force from the 20 element model. The presented results show all collisions from the El Centro excitation only. If no collision was recorded, the error has been reported as -100%. A positive error indicates that Equation 3.30 overestimated the collision force.

Significantly more scatter is present in Figure 4.12. This scatter is not surprising since inadequate modelling of earlier collisions in the record affects the pre collision velocities of subsequent collisions. This means collision force predictions are likely to get progressively less accurate as the record continues. The accuracy of Equation 3.30 increases with increasing model complexity. Ignoring the traditional models [0(10), 0(1) and 0(0.1)], all results >1000 kN are within 15% of the theoretically calculated results, and all except two of these results are within 10%. Furthermore the collision force is accurately calculated for major collisions (>2000 kN) in all tests. Equation 3.30 is therefore a universally useful tool for predicting the maximum collision force magnitudes when two diaphragms collide.

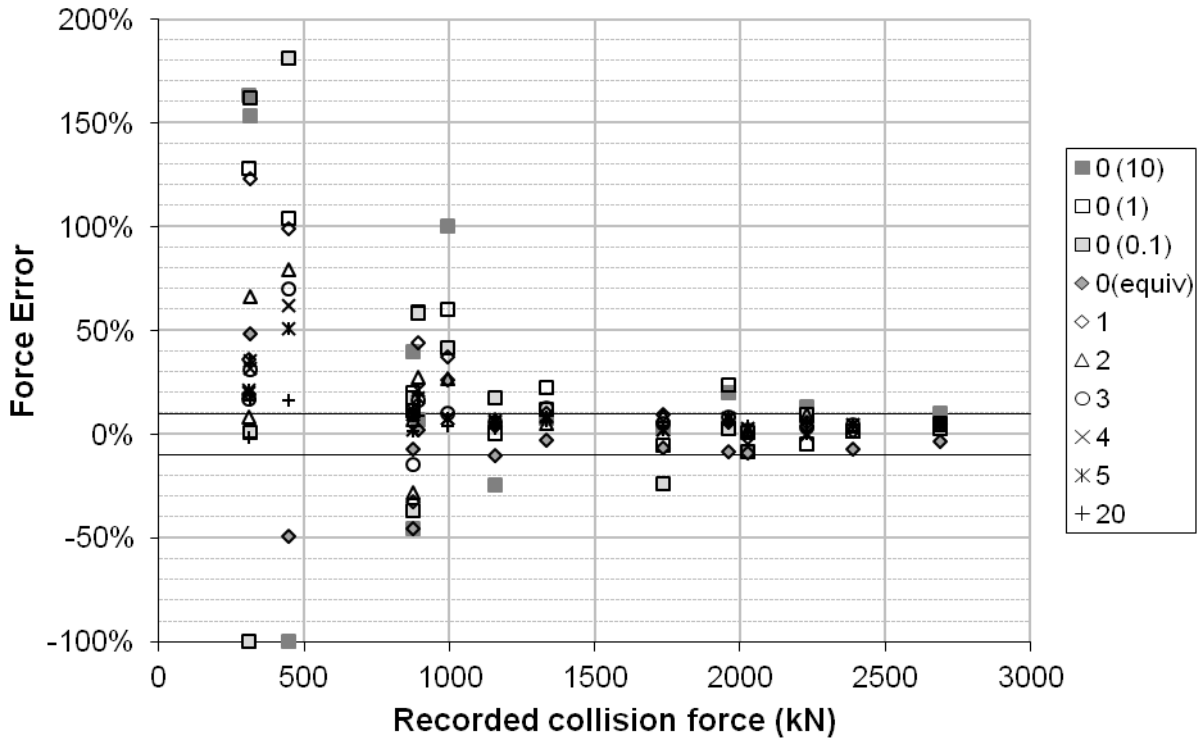

Figure 4.12 Collision force comparison for all test cases

Finally, the collision force profiles for the first roof collision in the El Centro record is presented in Figure 4.13. Tests 0(10), 0(1) and 0(0.1) are not shown but are similar to the profiles presented previously in Figure 4.4. All the distributed mass collision profiles reasonably approximate the theoretical collision.

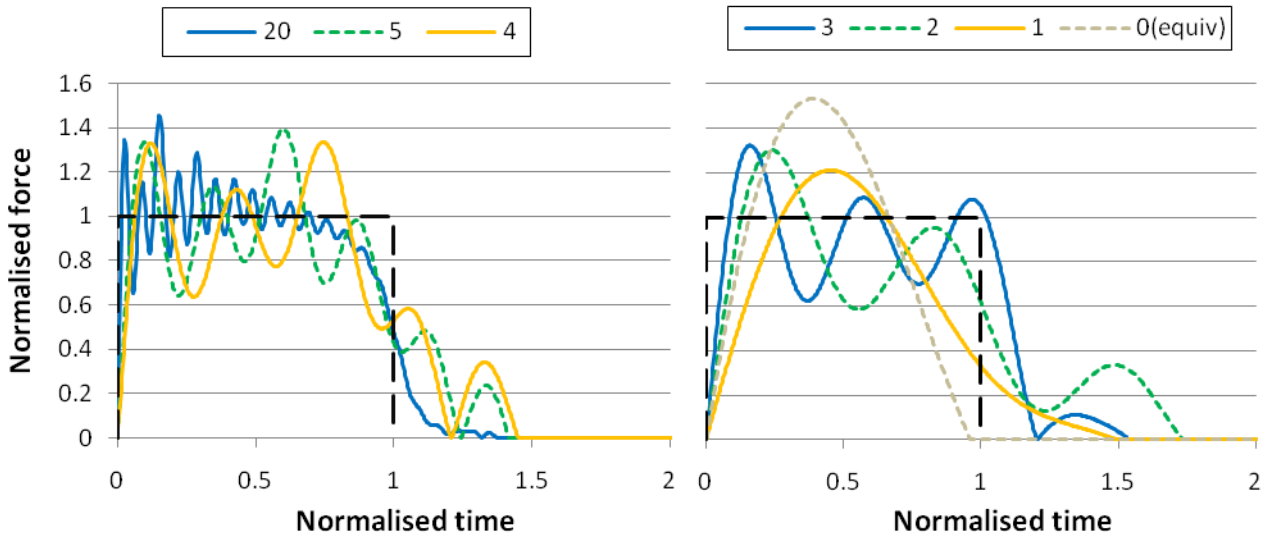

Figure 4.13 Force profiles during first El Centro roof collision. Theoretical response is shown with a dashed black line

4.3.4 Conclusions

Based on the results of the tests in Section 4.3, the following conclusions are drawn:

1. The traditional methods of modelling floor/floor contact can cause significant inaccuracy in recorded drifts since they do not accurately model the energy lost to axial diaphragm oscillation.
2. Significantly more accuracy may be achieved in lumped mass models if the equivalent lumped mass formulation is adopted. However, some inaccuracy is still likely.
3. At least two axial elements per diaphragm is recommended to suitably model the influence of diaphragm flexibility on floor/floor collisions. Additional accuracy may be achieved by using additional diaphragm elements. The two element model is selected since all but one of the reported drift errors were less than 5%, and collision force was acceptably predicted for the largest collisions in each record.

4.4 Modelling Collision Plasticity

The findings presented thus far in this chapter have assumed that two adjacent building diaphragms impact with no energy dissipation and with no resistance from any other factor. While this is an appropriate starting point, the above effects can considerably affect the nature of the pounding response. Attention is now turned to sources of external resistance and energy dissipation, and methods to model their effects during diaphragm collision. This section considers only floor/floor contact. Energy dissipation in floor/column or floor/wall collisions is discussed in their corresponding chapters.

4.4.1 Sources of Energy Loss During Collision

Many physical processes exist that are not currently modelled when collision occurs. These processes include energy dissipation from sound, heat, local destruction of areas sustaining contact and internal damage to the diaphragm (for example, concrete micro cracking). Further sources of energy dissipation arise when objects other than the primary building structure are considered. These include crushing accumulated debris between buildings, crushing of secondary structural elements contacts (for example, façade panels), or crushing of any other external objects (Figure 4.14). Additional energy dissipation may occur due to the layout of diaphragms within each building, since shockwaves do not necessarily reflect back to the collision interface. Energy dissipation within the diaphragm will also be affected by penetrations, the shape of the diaphragm and the movement of building contents during the collision (live loads).

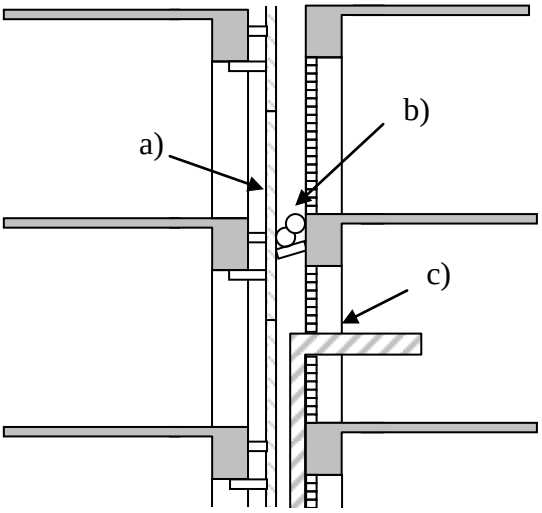

Figure 4.14 Elevation of two adjacent buildings with crushable intervening objects a) facade b) accumulated debris and c) building services

It is apparent that many complex processes may influence the amount of energy that is dissipated in a collision. However since many of these processes are not readily quantifiable, previous collision models have adopted highly idealised energy dissipation models.

4.4.2 Alternative Mechanisms for Contact Energy Dissipation

The remaining sections in this chapter investigate the viable alternatives that may be used to analytically remove energy from both buildings during the course of collision. These options are critiqued to determine which model would be the most useful for modelling energy dissipation when a collision between two diaphragms occurs. Existing contact element models (Section 2.2) have commonly adopted one of two kinds of energy dissipation; viscous dampers, and hysteretic damping. These methods concentrate all energy dissipation within the contact element itself. Two further modelling methods are considered here:

1. **energy dissipation within the diaphragm during collision**. As distributed mass models specifically simulate the axial compression of each diaphragm, energy dissipation can also be incorporated into this process. Energy dissipation may be achieved using viscous or hysteretic damping within the diaphragm itself. Such an approach can be used instead of, or in addition to, the contact element damping mentioned above.
2. **modelling of the crushing of any intervening objects**. Hysteresis loops can alternatively be generated by considering any deformable or destroyable components between two diaphragms. The performance of these objects can be approximated provided their strengths and stiffnesses can be determined.

4.4.3 Energy Dissipation Models Selected for Comparison

A total of five energy dissipation models are investigated for their suitability in simulating diaphragm collisions:

1. Multilinear element. [Section 4.5]
2. Damped Kelvin element. [Section 4.6]
3. Viscous diaphragm. [Section 4.7]
4. Global model damping. [Section 4.8]
5. Hysteretic simulation of destructible elements. [Section 4.9]

While the first two methods already exist, their performance must be reassessed for the collision of distributed masses. This is because collision elements react differently when each diaphragm is not perfectly rigid. For example, the force response of the Kelvin element during contact was shown to be highly sensitive to the number of elements in each diaphragm (Figure 4.4). The consequences of this change in collision modelling for the above methods are presented in subsequent sections.

Global model damping was not mentioned in Section 4.4.2. This is because it is not a collision-specific method of energy dissipation. Global damping refers to the damping that is applied to the modes of the model during the modal analysis. This damping is then present throughout the duration of the ground motion. Lumped mass modelling neglects this effect as the collision is assumed to be almost instantaneous. However, global model damping affects distributed mass collisions because the collision occurs over a finite period of time (see Equation 3.25). The effect of this damping contribution is thus investigated.

4.4.4 Testing Method for Dissipation Models

The methods described in the previous section are assessed using two criteria: whether the proposed method provides physically realistic results, and whether the proposed method can be consistently applied to different building configurations. The second criterion can be explained using an existing solution for lumped mass modelling. The Kelvin element provides a consistent level of energy dissipation because its percentage of critical damping (ζ) was related to the coefficient of restitution (Equation 2.10). This allows the post collision velocity to be calculated regardless of the colliding objects' properties. In the following sections, relationships between the relevant energy dissipation measure and the plasticity index (refer Section 3.2.4) are sought.

It should be noted that while plasticity index consistency is desirable from an analytical perspective, it is not necessarily physically realistic. For example, consider the crushing of the building services pipe shown in Figure 4.14. The amount of energy dissipated is highly dependent upon collision velocity. Assuming the initial collision is sufficiently strong, the pipe will be completely crushed the first time the building makes contact. Once the pipe is crushed, it will contribute negligible energy dissipation in subsequent collisions. Thus two collisions of the same velocity may produce two different plasticity indexes. For this reason, the assessment of the crushing hysteresis is approached differently and is described in Section 4.9. In this thesis, relationships between energy dissipation measures and the plasticity index are sought so that the models are as accessible as the equivalent stereo mechanics formulation for lumped mass models.

An energy dissipation model is considered 'consistent' if the same plasticity index is calculated for multiple values of a particular variable. For example, an energy dissipation model may be consistent with respect to velocity, but inconsistent with respect to diaphragm mass. The plasticity index is calculated using NLTHA and rearranging Equations 3.43 and 3.44:

$$r_1 = \frac{\frac{v'_1 - v_1}{v_2 - v_1} - \frac{1}{1+\frac{m_1}{m_2}}}{\frac{2}{1+\frac{T_2 m_1}{T_1 m_2}} - \frac{1}{1+\frac{m_1}{m_2}}} \tag{4.1}$$

$$r_2 = \frac{\frac{v'_2 - v_2}{v_1 - v_2} - \frac{1}{1+\frac{m_2}{m_1}}}{\frac{2}{\frac{T_2}{T_1}+\frac{m_2}{m_1}} - \frac{1}{1+\frac{m_2}{m_1}}} \tag{4.2}$$

Thus, for a specific configuration, the plasticity indexes calculated by Equations 4.1 and 4.2 change only due to the pre and post collision velocities since diaphragm mass and axial period remaining constant. The calculation of the plasticity index provides three further 'common sense' checks that must be met for the calculated values to be valid. These checks arise from the definition of the plasticity index (refer Section 3.2.4):

1. The values of the calculated plasticity index should always be between zero and one ($0 \leq r \leq 1$).
2. The diaphragms' plasticity indexes should always be equal ($r_1 = r_2$)
3. When the collision element is elastic, the plasticity index should be one (when elastic, $r = 1$)

Ten test cases are used to investigate consistency of various parameters (Table 4.4 and Table 4.5). Cases 1 – 5 test consistency with respect to collision velocity, and use identical model properties. Cases 6 – 10 test consistency in terms of diaphragm mass and axial period. Cases 6 – 8 maintain a constant mass ratio and axial period ratio, while Cases 9 – 10 vary each of these parameters in turn.

Table 4.4 Properties of test cases 1 - 5

Case no	***1***	***2***	***3***	***4***	***5***
Diaphragm 1 Initial velocity (m/s)	*2*	*1*	*10*	*5*	*10*
Diaphragm 2 Initial velocity (m/s)	*1.9*	*-1*	*5*	*-10*	*-10*
Relative velocity (m/s)	*0.1*	*2*	*5*	*15*	*20*

Case 1 – 5 common properties	***Diaphragm 1***	***Diaphragm 2***	***Ratio***
Mass (Tonne)	*102*	*122*	*0.833:1*
Axial stiffness (kN/m)	*5,016,800*	*5,016,800*	*1:1*
Axial period (sec)	*0.00902*	*0.00988*	*0.913:1*
Distributed mass α	*0.522*	*0.436*	*-*

Table 4.5 Properties of test cases 6 - 10

Case no	*6*	*7*	*8*	*9*	*10*
Diaphragm 1					
Mass (Tonne)	*10.2*	*102*	*204*	*102*	*102*
Axial stiffness (kN/m)	*2,508,400*	*5,016,800*	*5,016,800*	*5,016,800*	*5,016,800*
Axial period (sec)	*0.00403*	*0.00902*	*0.01275*	*0.00902*	*0.00902*
Distributed mass α	*0.586*	*0.586*	*0.586*	*0.739*	*0.656*
Initial velocity (m/s)	*10*	*10*	*5*	*10*	*10*
Diaphragm 2					
Mass (Tonne)	*20.4*	*204*	*408*	*408*	*204*
Axial stiffness (kN/m)	*2,508,400*	*5,016,800*	*5,016,800*	*10,033,600*	*9,121,454*
Axial period (sec)	*0.0057*	*0.01275*	*0.01803*	*0.01275*	*0.00946*
Distributed mass α	*0.293*	*0.293*	*0.293*	*0.185*	*0.328*
Initial velocity (m/s)	*-10*	*-10*	*0*	*-10*	*-10*
Ratios					
Mass	*0.5:1*	*0.5:1*	*0.5:1*	*0.25:1*	*0.5:1*
Axial stiffness	*1:1*	*1:1*	*1:1*	*0.5:1*	*0.55:1*
Axial period	*0.707:1*	*0.707:1*	*0.707:1*	*0.707:1*	*0.953:1*

The model configurations used in these tests are based on that shown in Figure 4.2. The two elements per diaphragm model is tested first, in accordance with the conclusions drawn from the elastic model tests (Section 4.3.4).

4.5 Dissipation Models – Multilinear Element

As discussed in Section 2.2.2, the multilinear element provides energy dissipation by defining a restitution stiffness (k_r) that is greater than the approach stiffness (k_a). The energy lost in a single collision is controlled by modifying the ratio of these stiffnesses ($k_r/k_a \geq 1.0$). The plasticity index is now calculated for stiffness ratios of 1, 2, 5, 10 and 20.

4.5.1 Dependence on Collision Velocity

Figure 4.15 displays the plasticity index results for Case 1 – Case 5. Many of the series cannot be differentiated in the figure, since they produce almost identical results. These series also appear to meet the three common sense conditions for the plasticity index from Section 4.4.3. However, Case 1 and Case 3 show varying degrees of disagreement. This can be explained by considering the magnitudes of the initial relative velocity and total velocities of each diaphragm. For example, Case 1 has a relative velocity of 0.1 m/s, however each diaphragm is moving at approximately ten times this velocity when collision occurs. This configuration creates a high level of sensitivity in the plasticity index. This sensitivity is not necessarily a problem since the

plasticity index may be calculated with the modeller's choice of initial velocities (so long as they cause collision). If the overly sensitive Case 1 and Case 3 are ignored, plasticity index is observed to be independent of collision velocity.

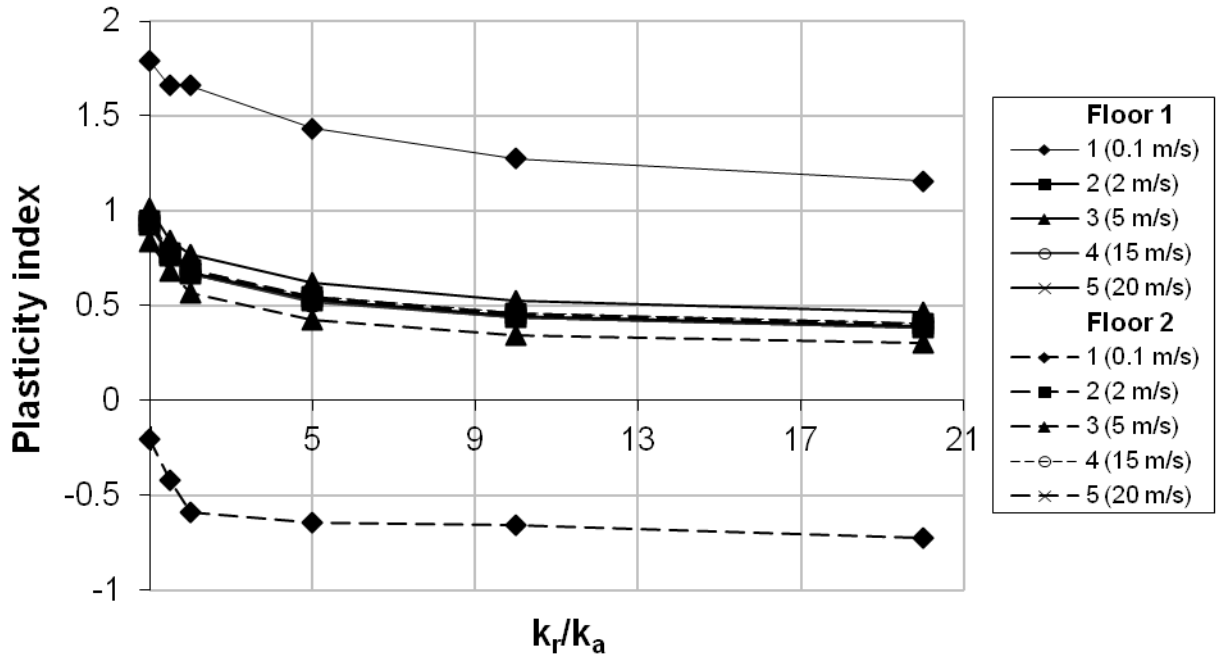

Figure 4.15 Multilinear plasticity results, Cases 1 – 5

The objective of this modelling is to produce a single backbone curve that defines the relationship between the stiffness ratio (k_r/k_a) and the plasticity index. While Cases 2, 4 and 5 present very similar plasticity index values between the two diaphragms, minor variations do exist. These errors are caused by the simplifications that have been incorporated into the model (such as the use of two elements per diaphragm). The accuracy of the results in Figure 4.15 may be improved by averaging the results of each diaphragm (Figure 4.16).

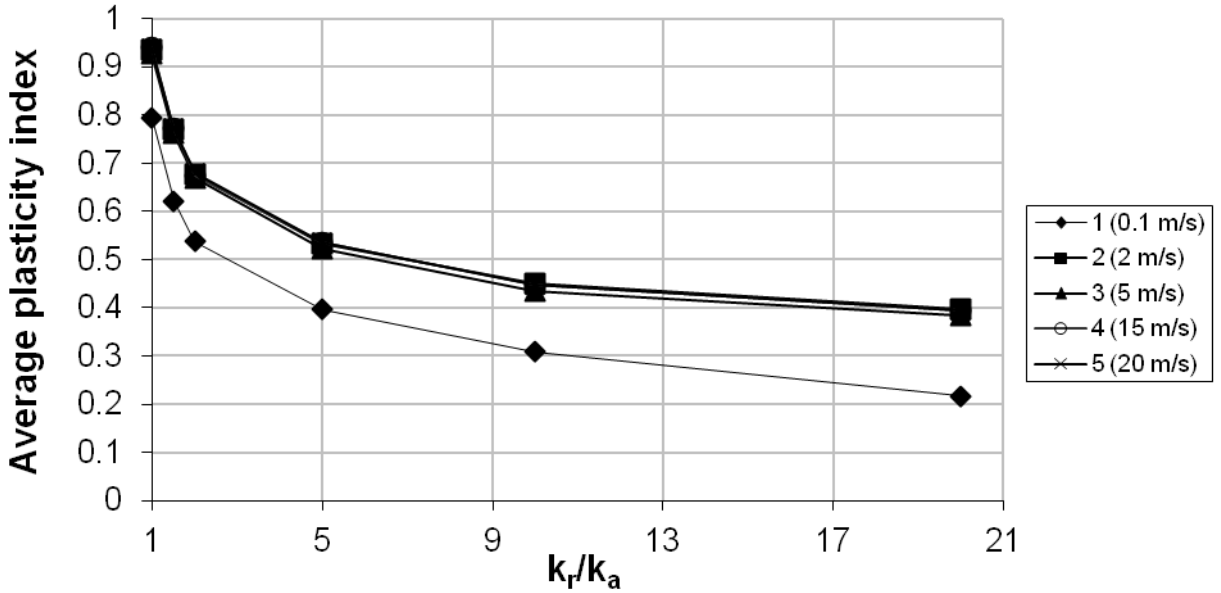

Figure 4.16 Averaged plasticity index, Cases 1 – 5

At k_r/k_a = 1, the hysteresis is identical to the elastic Kelvin element. However, the plasticity index at this stiffness ratio is not reported as 1.0. This is again due to the inaccuracies inherent to NLTHA which cannot be easily overcome. While this discrepancy is undesirable, it is not considered to render this method invalid. This is because the typically specified plasticity index is expected to be between 0.8 and 0.6. If a value close to 1.0 was desired, the modeller could add elements to each diaphragm to improve the accuracy of the modelling. This discrepancy also provides an indication of the coarseness of the adopted model.

The results presented in Figure 4.16 can be used to define a relationship between plasticity index and stiffness ratio. The averaged values recorded from Case 5 are adopted as the 'backbone' curve describing this relationship. Case 5 is selected since it produced the least discrepancy between the two diaphragms' calculated plasticity index values. Note these values are almost identical to Case 2 and Case 4. The backbone curve is tested by comparing post collision velocities. Velocities recorded in the numerical models are compared to the post collision velocities calculated using the backbone curve as input for the plasticity index in Equations 3.43 and 3.44 (Figure 4.17). The calculated results are in very close agreement with the numerical results. This shows that while Case 1 and Case 3 may not be suitable for defining r, their post collision velocities can be accurately predicted using the r values calibrated using other cases. Thus post collision velocity can be reliably predicted for a model configuration once the backbone relationship is determined.

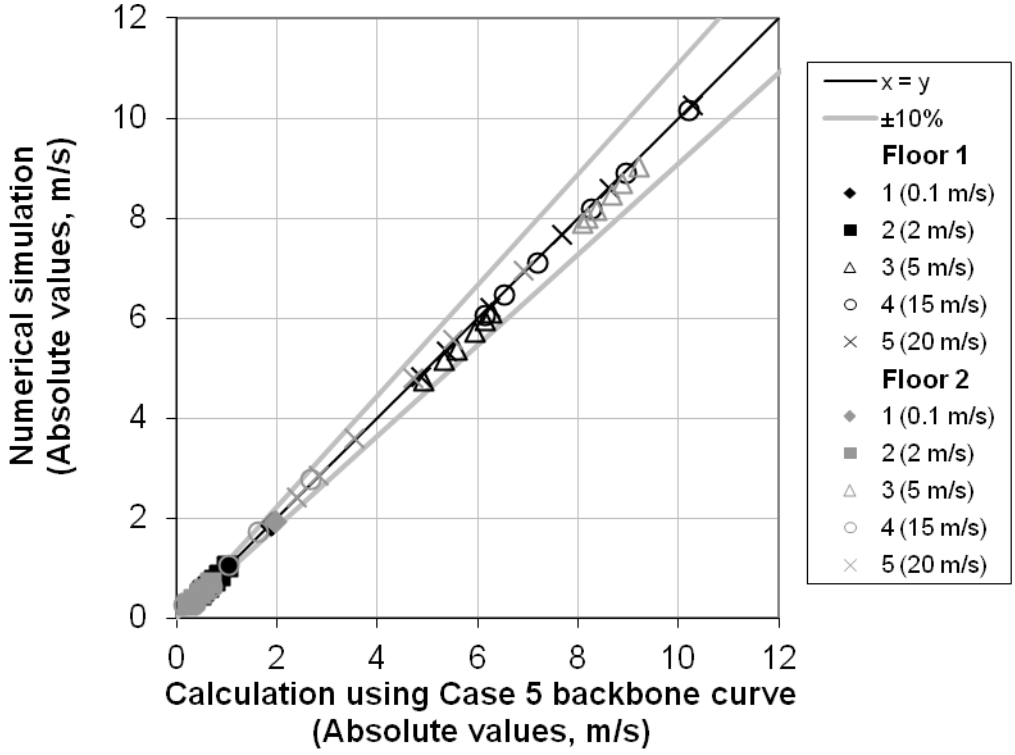

Figure 4.17 Comparison of predicted and recorded post collision velocities, cases 1 – 5

4.5.2 Dependence on Mass and Axial Period

The cases presented above provided a backbone for one particular diaphragm configuration. In order to determine whether this backbone is applicable to all possible diaphragm collisions, the diaphragms' masses and axial periods are varied in Cases 6 – 10. Since Equations 3.43 and 3.44 are dependent on the ratio of mass and the ratio of axial period, these ratios are kept constant in Cases 6 – 8 (but are varied in Case 9 and Case 10). Figure 4.18 presents the diaphragms' averaged plasticity indexes for the five cases. Case 5 is also included for comparison

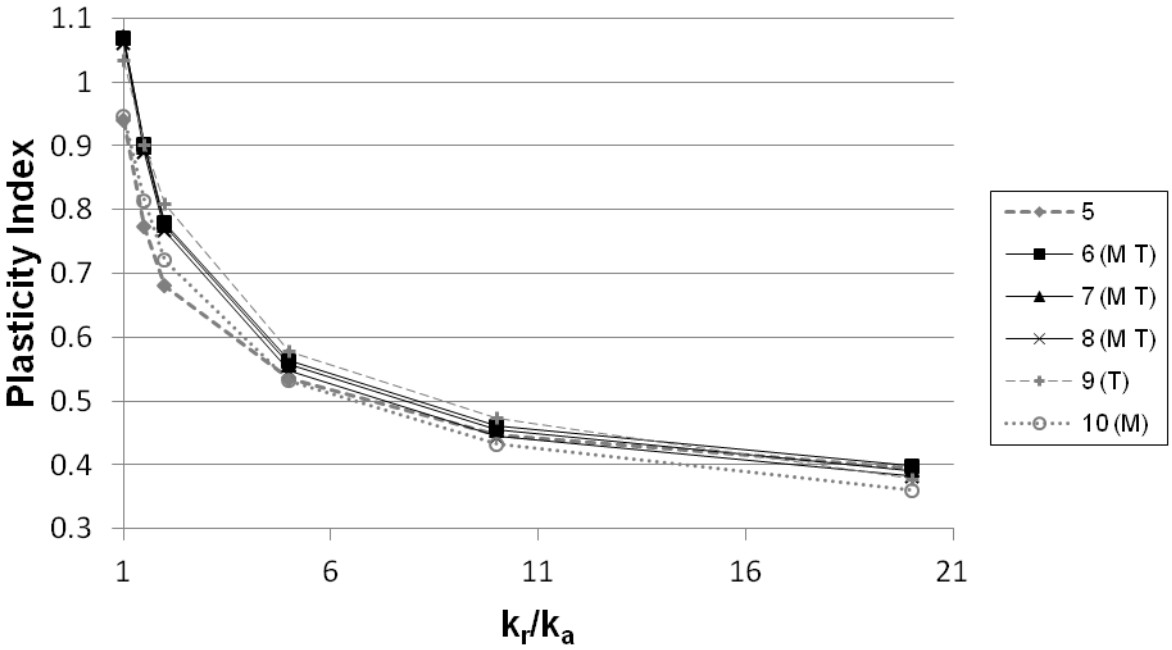

Figure 4.18 Averaged plasticity index for different mass and axial period configurations

Figure 4.18 indentifies the series with a common mass ratio with an M and a common axial period with a T. While all series present similar relationships between plasticity index and stiffness ratio, the shape of this relationship changes when either the mass ratio or the period ratio changes. This means that a new relationship between plasticity index and stiffness ratio must be recalculated whenever a model uses a different mass ratio or axial plasticity ratio. This finding is confirmed by using Case 7's backbone curve to predict the post collision velocities of Cases 5 – 10 (Figure 4.19).

Cases which do not share Case 7's mass and period ratios predict post collision velocities which differ to that of the recorded velocities by over 10% in multiple locations. The reason for the differing relationships between plasticity index and stiffness ratio may be better understood by inspecting the collision element's force history during collision (Figure 4.20).

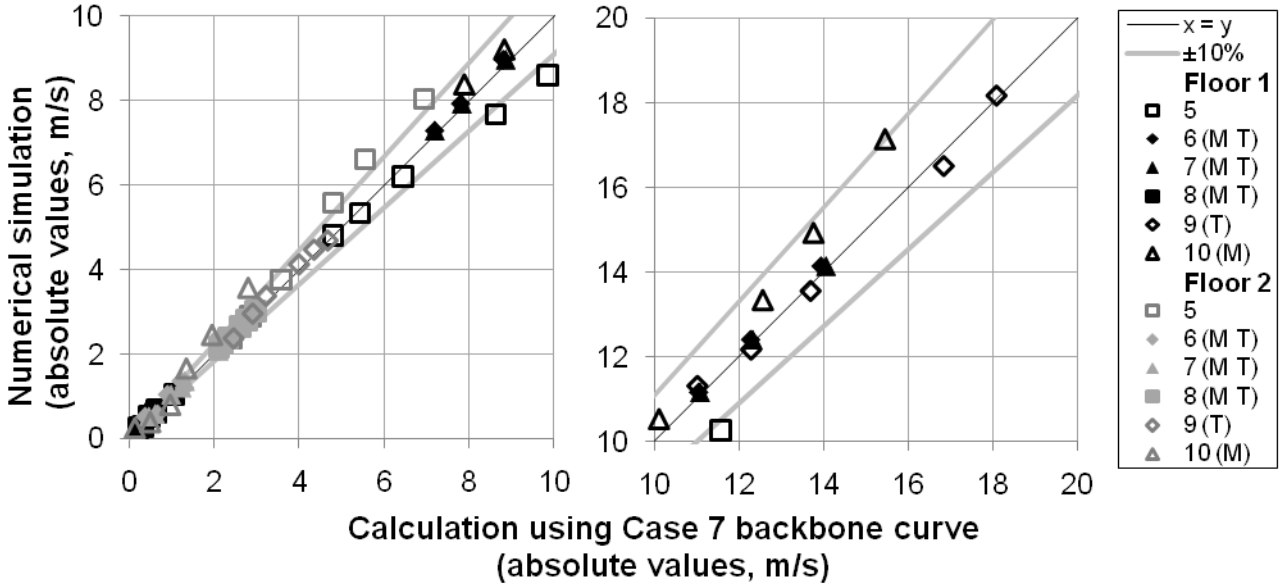

Figure 4.19 Comparison of predicted and recorded post collision velocities, Cases 5 - 10

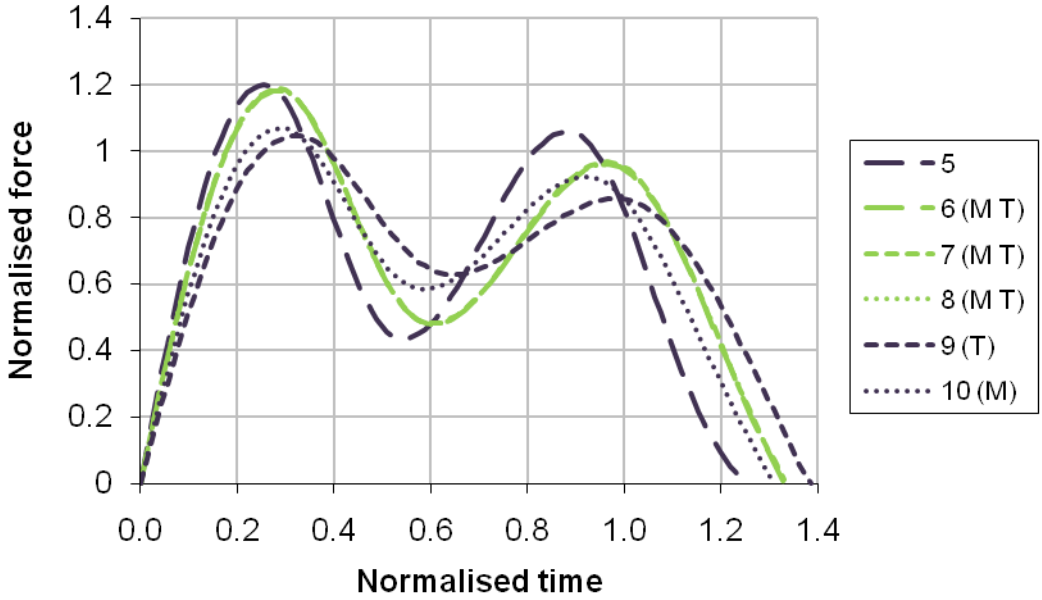

Figure 4.20 Normalised collision force profiles for k_r/k_a=1.5, Cases 5 – 10. Force normalised by calculated collision force (assuming elastic collision). Time normalised by calculated collision duration.

Figure 4.20 uses lighter colours to present the cases with common mass and period ratios, while all other series use dark lines. Cases 6 – 8 are difficult to differentiate since they produce near identical force profiles. The force profile changes when either the mass ratio or the period ratio changes. This is because the level of oscillation in each diaphragm also changes with these properties. It would be possible to perform a full parametric investigation to define a relationship between stiffness ratio and plasticity index for all practical values of axial period ratio and mass ratio. However, such analyses are not performed in this thesis. The reason for this will become apparent in the next section.

4.5.3 Dependence on Number of Diaphragm Elements

When collision damping is used, post collision velocity may also be affected by the number of elements in each diaphragm. This is because greater numbers of diaphragm elements result in more high frequency axial modes, which in turn cause more oscillation in the contact element. The two diaphragm element hysteresis is also much softer since it has one tenth the initial stiffness to that of the 20 element diaphragms (Figure 4.21). These factors also change the relationship between the plasticity index and the stiffness ratio (Figure 4.22). Note that the 2D element's more accurate modelling of the diaphragms means a stiffness ratio of 1.0 results in a plasticity index of 1.0.

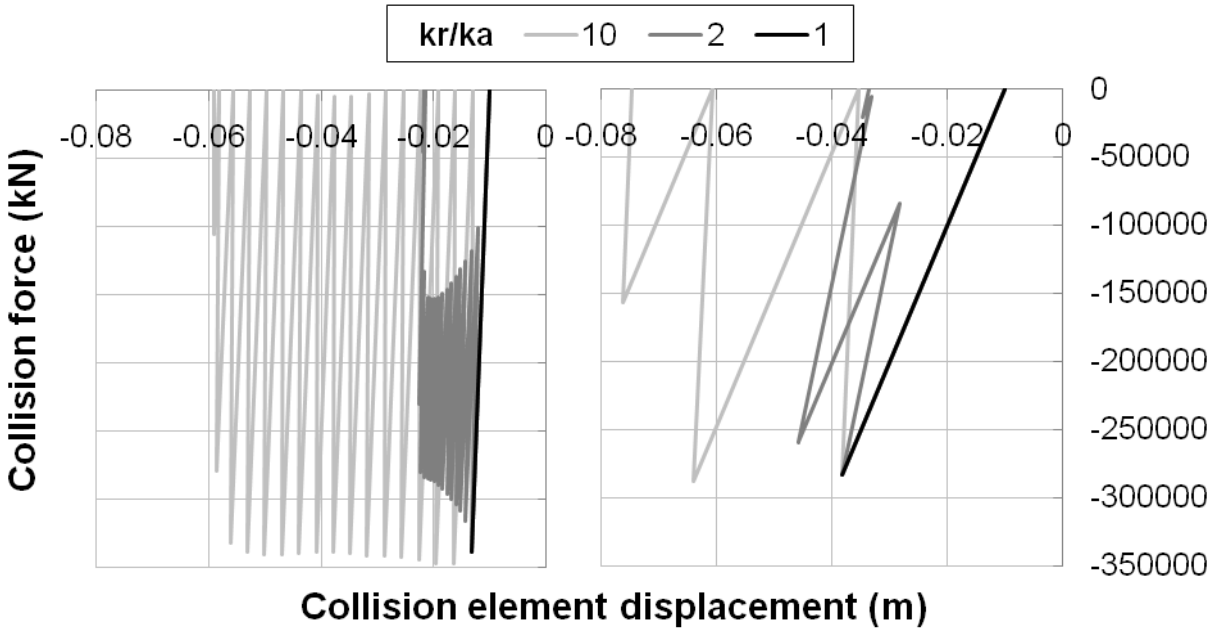

Figure 4.21 Effect of element number on contact element hysteresis. Case 5. Left: 20 elements per diaphragm. Right: 2 elements per diaphragm.

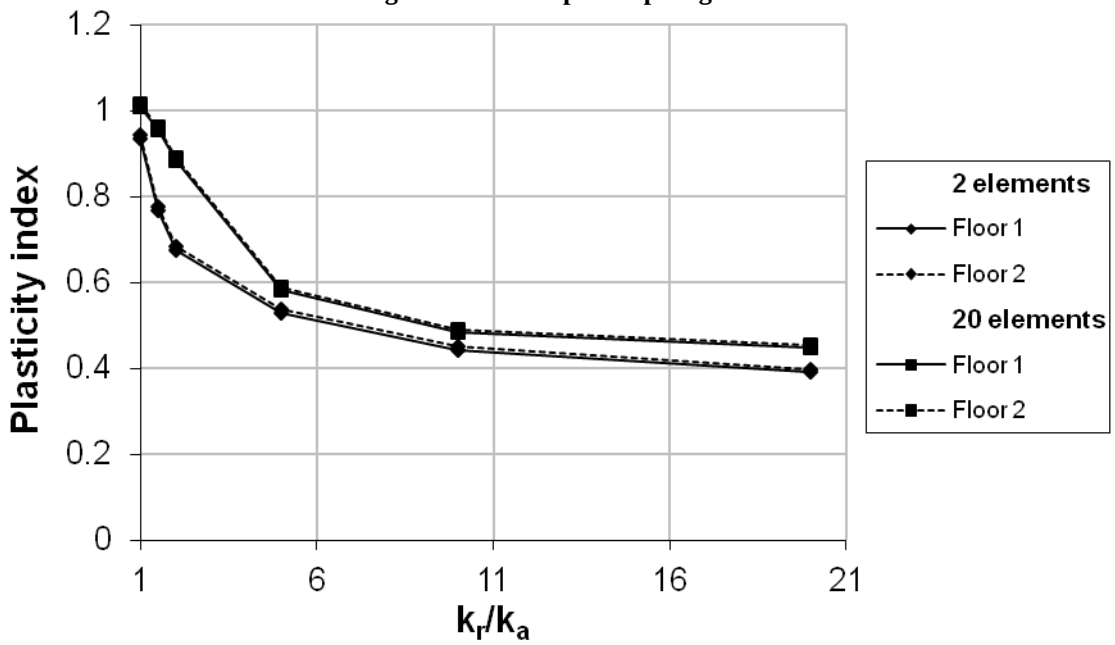

Figure 4.22 Effect of element number on plasticity index

The plasticity index's dependence on the number of diaphragm elements greatly increases its parametric space. This additional parameter makes calculation of every possible backbone impractical. Instead, a method to calculate the backbone of a diaphragm configuration is presented in a subsequent section (Section 4.11).

4.5.4 Assessing Physical Representation of Contact

To assess the physical realism of the multilinear element, the element's hysteresis (Figure 4.21) and force profiles (Figure 4.23) are scrutinized. The hystereses presented in Figure 4.21 show significant inelastic displacement in the collision elements during collision. For example, in the two elements per diaphragm case, $k_r/k_a = 10$ produces approximately three times more compression in the collision element than $k_r/k_a = 1$. This increased displacement causes significantly more object overlap, which is undesirable. As discussed in Section 2.2.2 this hysteresis also causes further interpretation problems, since the collision force can be zero even when the contact element displacement is less than the initial separation, and thus still considered to be 'in contact'. This behaviour can be interpreted two possible ways: the building separation is increasing with each collision, or the loss of force is an acceptable numerical anomaly. Neither of these consequences accurately reflects the physical behaviour of a general collision.

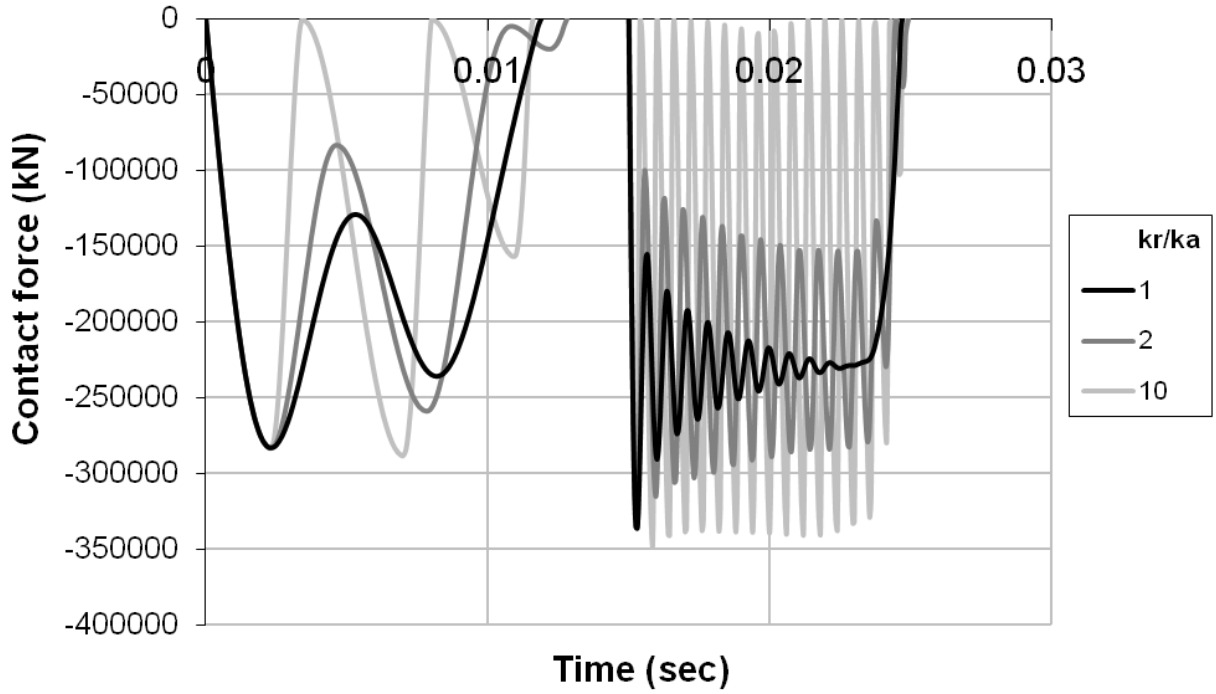

Figure 4.23 Collision force histories. First collision 2 elements per diaphragm, second collision 20 elements per diaphragm.

Figure 4.23 illustrates the collision profile of two collisions, the first collision has two axial elements per diaphragm, while the collision starting at 0.015 seconds has 20 elements per diaphragm. These two collisions actually took place in different analyses but have been

presented in a single graph for convenience. As k_r/k_a increases, the oscillation in the collision force also increases. As previously discussed (Section 4.2.2), this oscillation is numerically undesirable and does not represent any physical phenomenon. The multilinear element therefore provides a less realistic and less desirable force profile as the stiffness ratio increases.

4.6 Dissipation Models – Damped Kelvin Element

The inelastic Kelvin element discussed in Section 2.2.2 is now tested for distributed collision. In this element, the level of energy is controlled by the percentage of critical damping adopted in the contact element (Equation 2.10). Note that this value is calculated using the total mass of each diaphragm, not the mass of each nearest node. This definition for critical damping is adopted because it allows a consistent interpretation regardless of the number of nodes in each diaphragm. This approach is also consistent with the interpretation used in lumped mass models. Plasticity index values were calculated for the following percentages of critical damping; 0, 25, 50, 75, 100 and 120%.

4.6.1 Dependence on Collision Velocity

The averaged plasticity indexes are presented in Figure 4.24 for Case 1 – Case 5 (refer Table 4.4). The relationship between percentage of critical damping and plasticity index is almost completely linear. To test the robustness of the abilities of Equations 3.43 and 3.44 to predict post collision velocity, Case 3 is used for the backbone curve. Case 3 had the largest difference between r_1 and r_2 excluding Case 1. Case 1 is not used since Case 1 produced nonsensical results (such as a negative plasticity index at $\zeta = 120\%$). The comparison between predicted and recorded post collision velocities is presented in Figure 4.25.

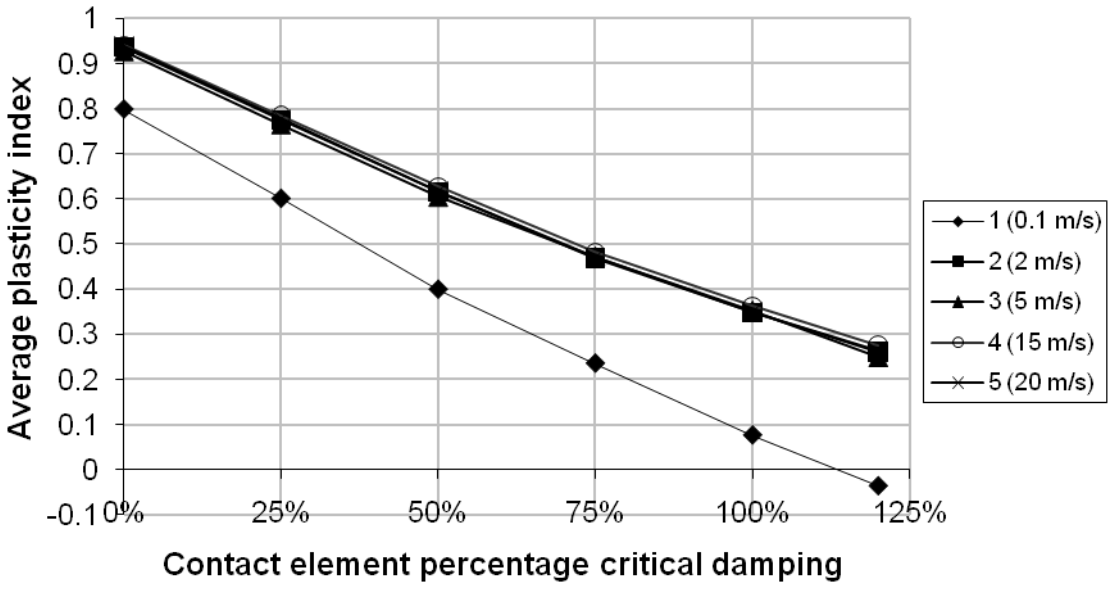

Figure 4.24 Damped Kelvin element plasticity index

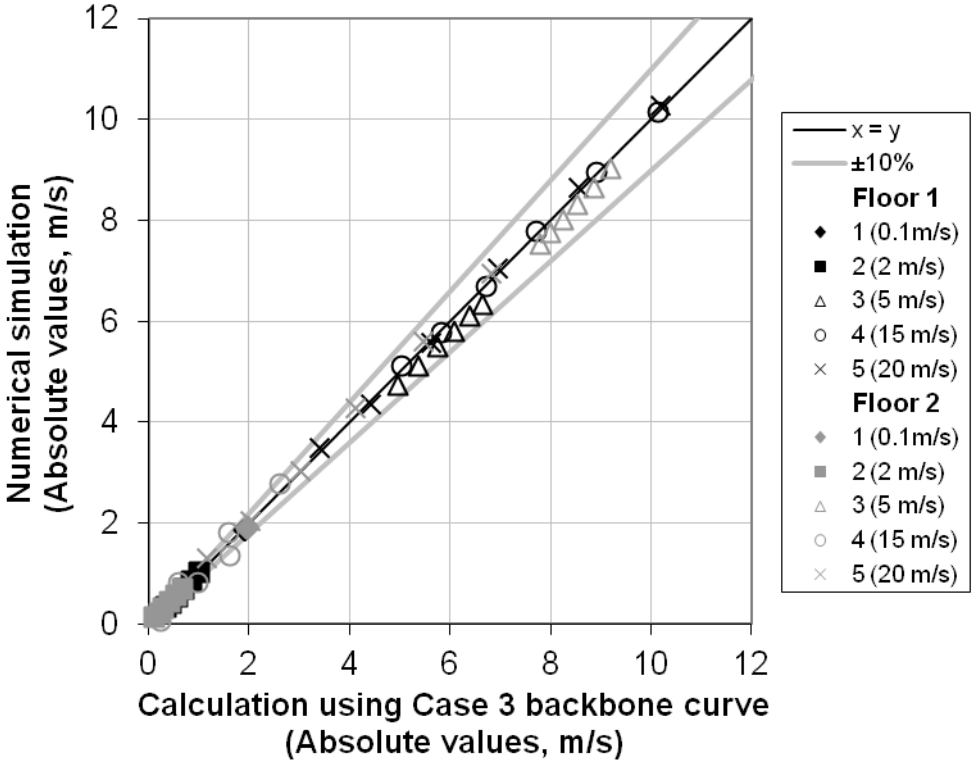

Figure 4.25 Comparison of predicted and recorded post collision velocities

The error in Figure 4.25 is slightly bigger than was observed when the more accurate Case 5 was used for the multilinear element. Six results show more than 10% error. The procedure presented later in this chapter (Section 4.11) is recommended to minimise these inaccuracies in modelling. The consistency of the results presented in Figure 4.24 and Figure 4.25 also show that the Kelvin element plasticity index is consistent with respect to collision velocity.

4.6.2 Dependence on Mass and Axial Period

The average plasticity index values for Cases 6 – 10 (refer Table 4.5) are presented in Figure 4.26. These results show the same trends as the multilinear element (i.e. the plasticity index is dependent on both the mass ratio and axial period ratio). This is also reflected in the predicted post collision velocities using Case 7 (Figure 4.27). Cases 6, 7 and 8 are accurately predicted, but Cases 9 and 10 are not. Once again, a near linear relationship between the plasticity index and percentage of critical damping is observed.

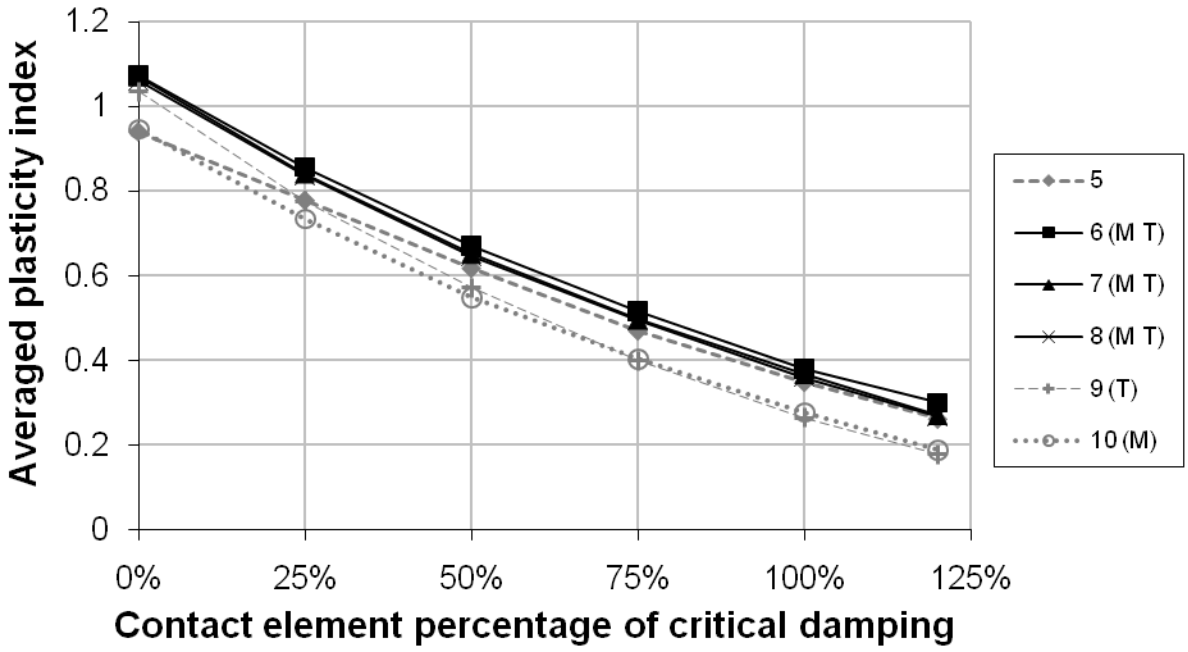

Figure 4.26 Dependence of plasticity index on mass ratio and axial period ratio

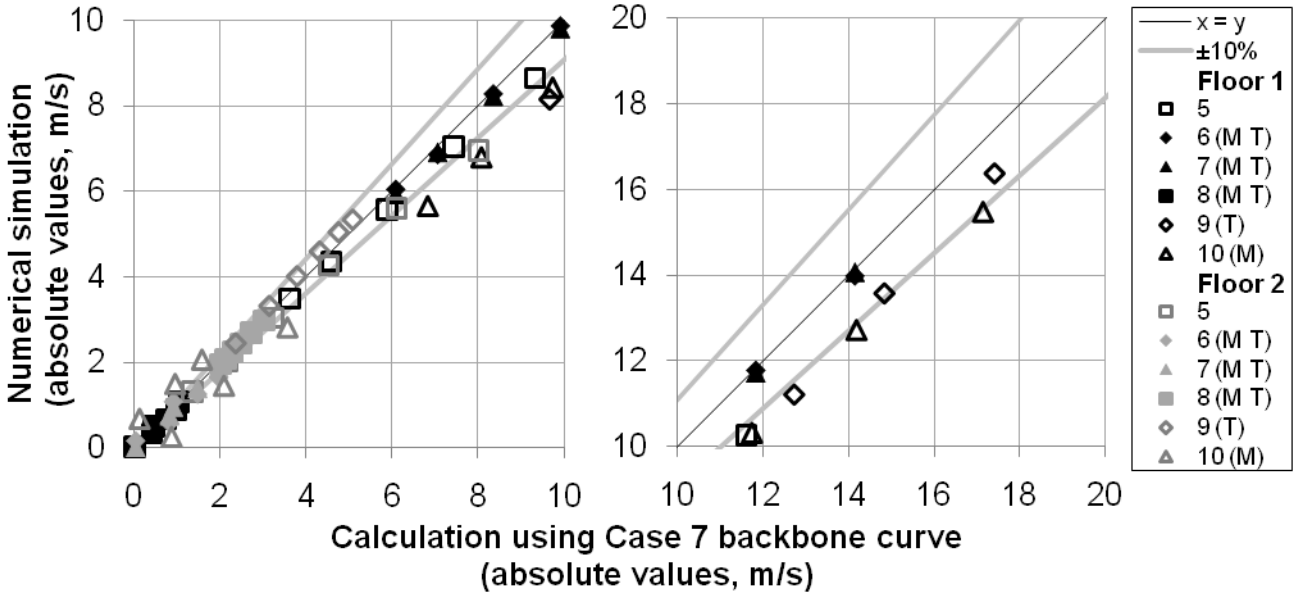

Figure 4.27 Predicted post collision velocities using Case 7 backbone

4.6.3 Dependence on Number of Diaphragm Elements

Figure 4.28 compares the plasticity index values between the two element and the 20 element models. Significantly less energy is dissipated in diaphragms with more elements. The reason for this can be observed in the contact element's hysteresis (Figure 4.29).

The area enclosed in the hysteresis loop of the 20 element case is much less that of the corresponding 2 element case. The influence of the damping level on the effective stiffness is also notable in Figure 4.29. This is because the maximum relative velocity occurs at the beginning of a collision, so the maximum damping force occurs immediately upon impact. As

previously noted, sudden jumps in force are difficult for NLTHA programs to simulate. It is therefore recommended that high levels of damping (such as 100%) be avoided where possible.

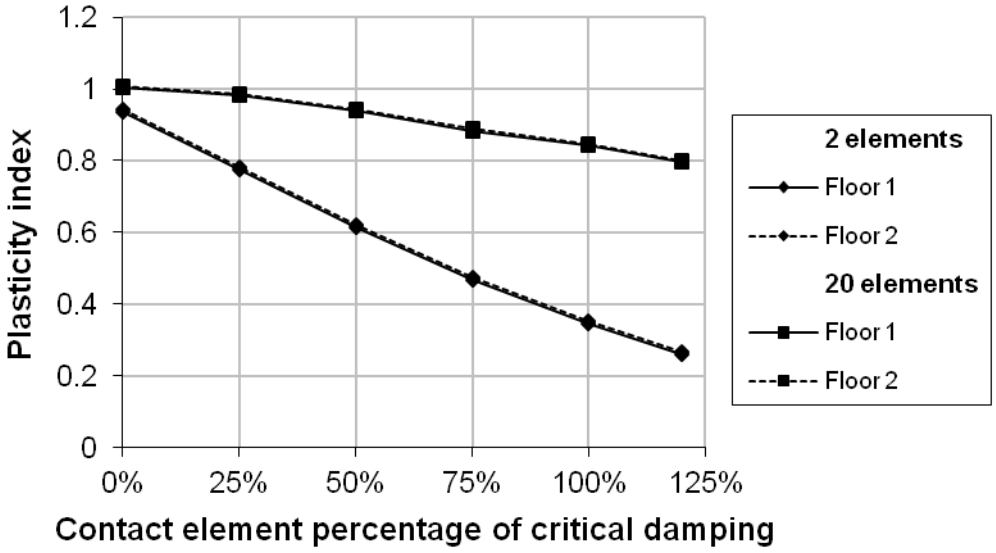

Figure 4.28 Comparison of 2 and 20 element per diaphragm models

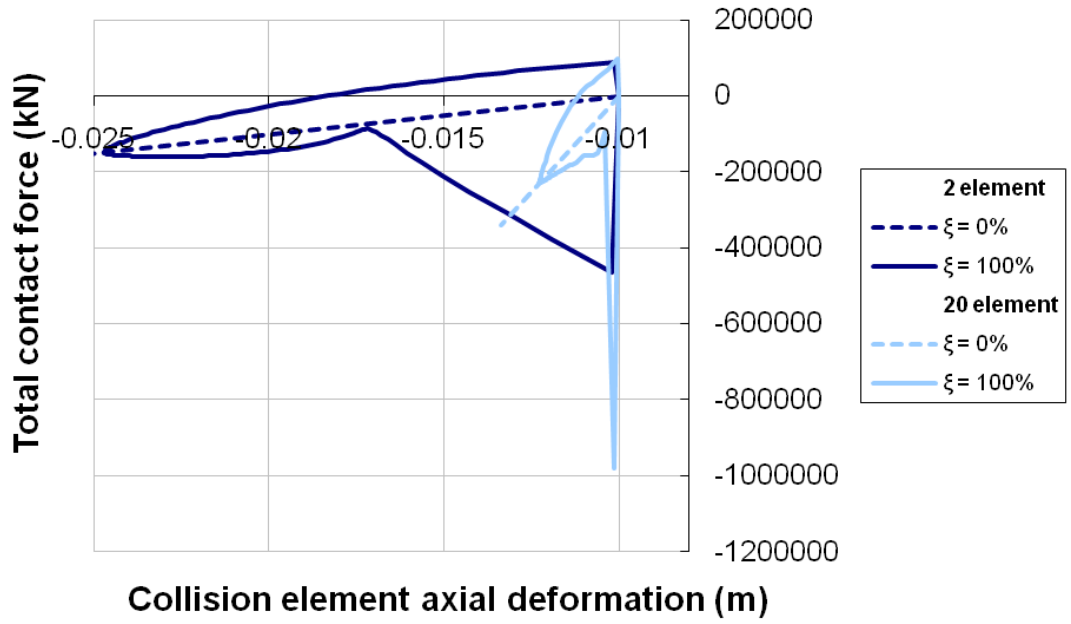

Figure 4.29 Recorded contact element hysteresis for case 5 (initial separation 0.01m).

4.6.4 Assessing Physical Representation of Contact

The collision force history for 2 element and 20 element models are presented in Figure 4.30. The presented collisions show the force history recorded in Case 5.

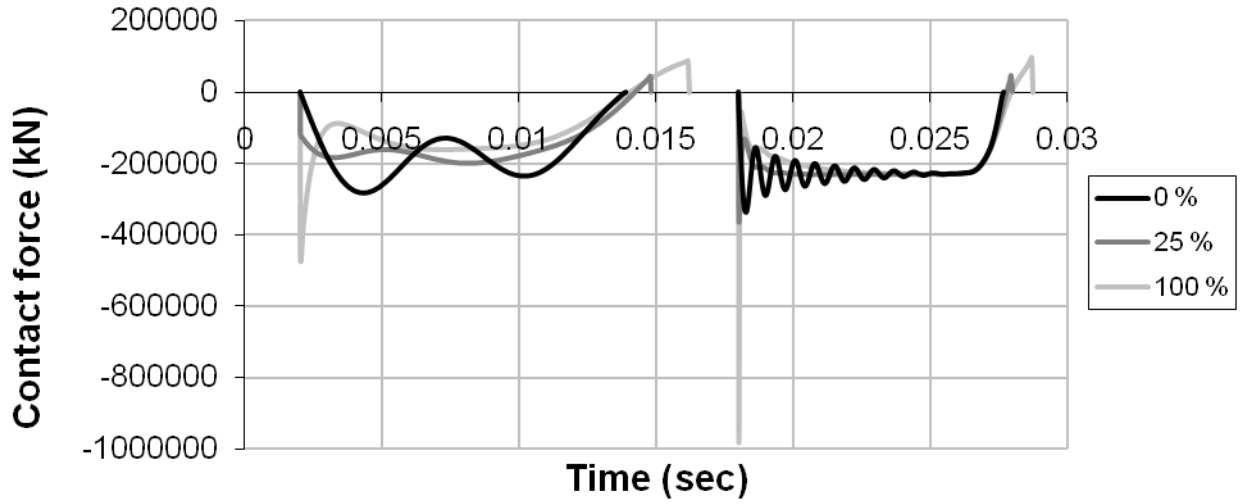

Figure 4.30 Contact force profiles. First collision 2 elements per diaphragm. Second collision 20 elements per diaphragm

Two collisions are presented on a single plot for convenience, the first uses two elements per diaphragm while the second has 20 elements per diaphragm. In addition to the high initial force discussed above, one other undesirable trait is observed: the tensile force that occurs at the end of a collision. As previously discussed in Section 2.2.2, this indicates a 'sticky' contact which is highly unlikely to be present in real life. The tensile force may be removed by using a viscous damper that only acts in compression; however this will also decrease the element's damping effectiveness. Even if a compression-only damper is used, the initial high force will still be present. This element therefore does not provide a desirable collision force profile, and is particularly poorly performing if a high percentage of critical damping is specified.

4.7 Dissipation Models – Viscous Diaphragm

In this model, viscosity is introduced to the diaphragm instead of the collision element. The level of energy dissipation is again controlled by the percentage of critical damping. However, as multiple dampers now exist within each diaphragm, a rational means of calculating this critical damping must first be determined. When existing buildings are modelled, the layout of the diaphragm nodes is determined by column joints and other factors. This means that an even nodal distribution is unlikely. Thus the method needs to be able to account for non-uniform mass distribution. Consider the general diaphragm element presented in Figure 4.31.

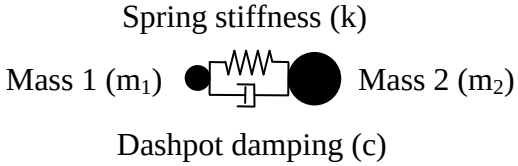

Figure 4.31 Axial diaphragm element with damping

The element has two linking components (a spring and a dashpot) and two masses. The relative movement between the two masses is of interest here, and can be directly obtained from the displacement (extension) history of the linking spring (or the dashpot). The displacement of the spring element in time can be viewed as a single degree of freedom oscillation. It is this oscillation from which the damping is calibrated. The damping of a single degree of freedom oscillator is;

$$c = 2\zeta\sqrt{m_{eff}k} \tag{4.3}$$

Where the effective mass, m_{eff}, is obtained from the axial mode obtained from modal analysis:

$$m_{eff} = \frac{1}{\frac{1}{m_1} + \frac{1}{m_2}} \tag{4.4}$$

Derivation of this term may be found in Anagnostopoulos (2004). Note that substitution of Equation 4.4 into Equation 4.3 produces the damping of the Kelvin element (Equation 2.10). However, the above formulation differs to the Kelvin element because of the definition of m_1 and m_2. In the present formulation m_1 and m_2 are the masses of nodes within the diaphragm, whereas in the Kelvin element m_1 and m_2 describe the total mass of diaphragm one and two, respectively. Using Equations 4.3 and 4.4, plasticity index values were calculated for the following percentages of critical damping: 0, 25, 50, 75, 100 and 120%.

4.7.1 Dependence on Collision Velocity, Mass and Axial Period

Since the general form of the plasticity index is now understood, all ten cases are presented in Figure 4.32. This element produces consistent plasticity values for different velocities in a given configuration (Cases 1 – 5), and for other configurations providing the mass ratio and axial period ratio are kept constant.

For the first time, the plasticity index is observed to reach a local minimum. This is potentially a concern if, say, a plasticity index of 0.4 is desired. The lower bound is suspected to be caused by the dampers in each diaphragm increasing the overall resistance of the diaphragms, which causes less diaphragm contraction and thus lowers the overall energy dissipation. The prediction of post collision velocities by Equations 3.43 and 3.44 are again very well correlated to the recorded post collision velocities. This correlation is not shown but is similar to Figure 4.25 and Figure 4.27.

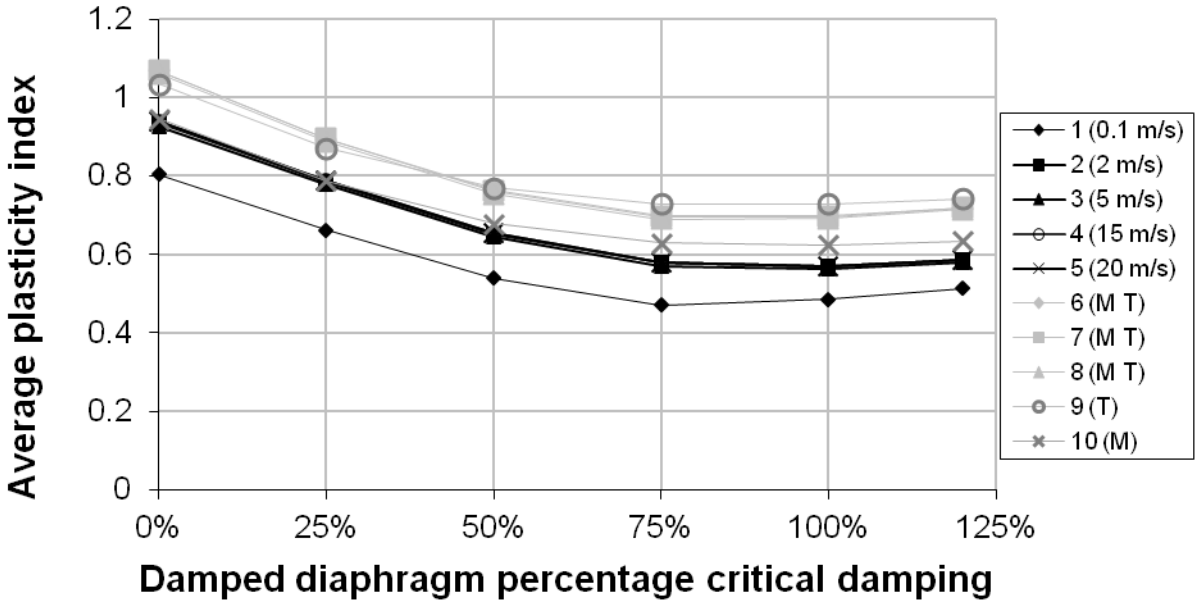

Figure 4.32 Damped diaphragm plasticity index, cases 1 – 10

4.7.2 Dependence on Number of Diaphragm Elements

Figure 4.33 presents Case 5 for two elements and twenty elements per diaphragm. When additional diaphragm elements are added, significantly more damping is required to achieve lower plasticity index values. While it cannot be seen in this figure, the 20 element case also presents a local minimum. However, this minimum occurs at approximately 2000% of critical damping. At this point, the recorded plasticity index is 0.14. Once again, the plasticity is found to be dependent upon the number of elements.

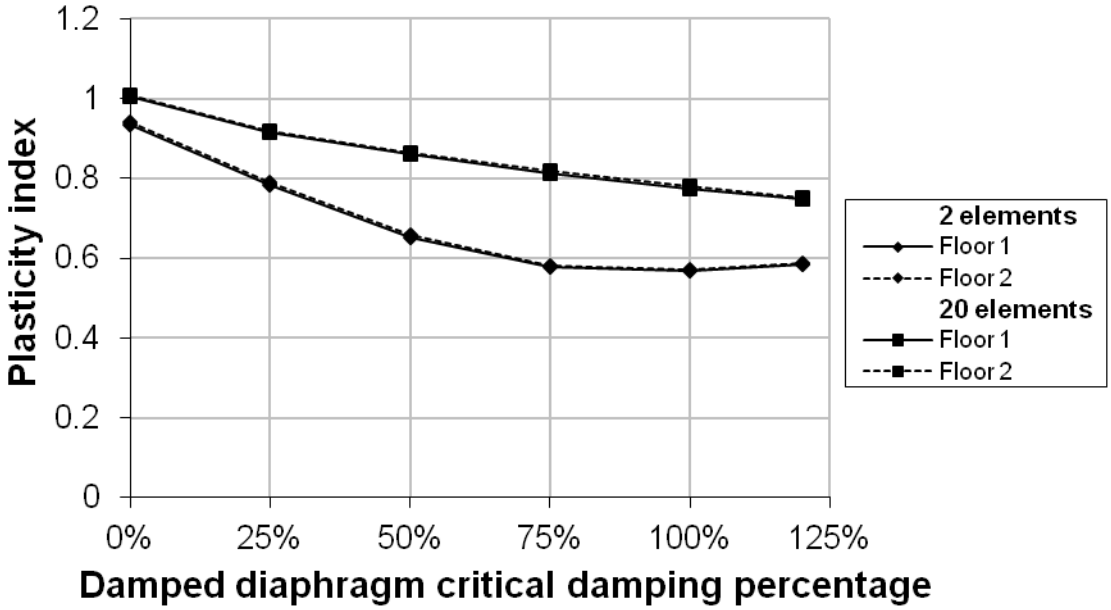

Figure 4.33 Effect of number of diaphragm elements on calculated plasticity index. Case 5

4.7.3 Assessing Physical Representation of Contact

The damped diaphragm method produces a reasonably credible contact force history (Figure 4.34). No tensile forces or overly large oscillations are generated. Increasing the damping in the

twenty element case does cause an increase in the minimum recorded force; however this is damped out during the collision. The oscillation is also considerably less than that observed in the damped Kelvin element (refer Figure 4.30). Surprisingly, increasing the diaphragm damping reduces the length of the contact; this is likely due to the increase in effective stiffness of the diaphragm caused by the damper elements.

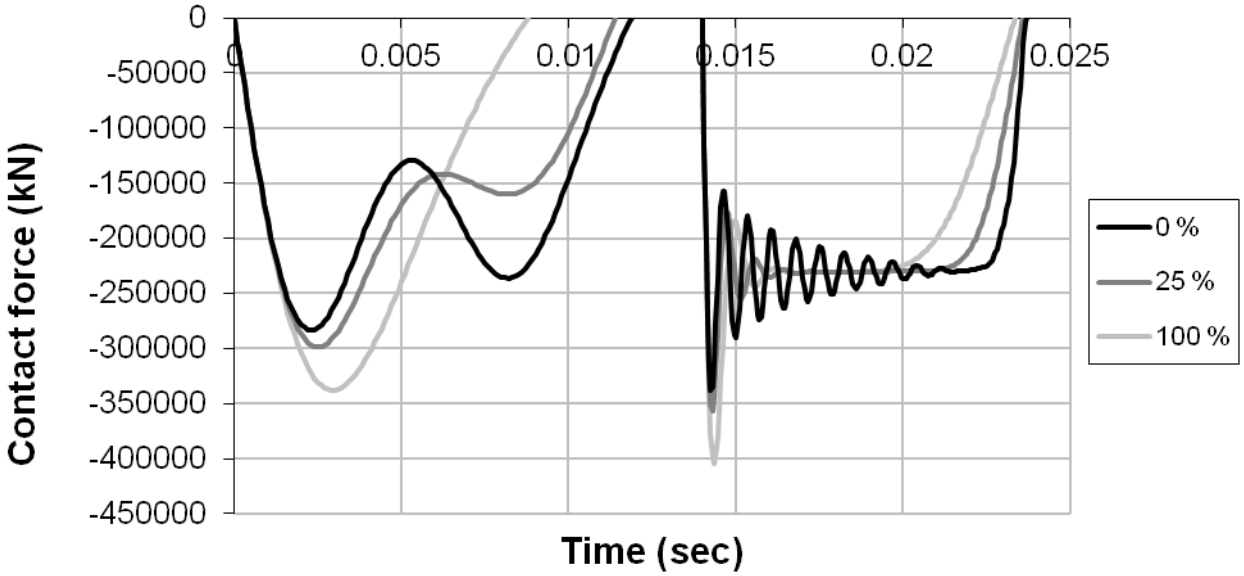

Figure 4.34 Recorded contact force for damped diaphragm. First collision: 2 elements, second collision: 20 elements

The hysteretic performance of the combined axial spring and viscous damper diaphragm element is displayed for the 2 and 20 element models in Figure 4.35. In this figure, 'near' refers to the axial element in Diaphragm 1 that is nearest to the collision element, and 'far' refers to the axial element furthest from the collision element. The results for the 'far' element in the 20 element case is difficult to identify since it has a significantly smaller magnitude (-50,000 kN). The damped diaphragm appears to be a physically reasonable modelling approach.

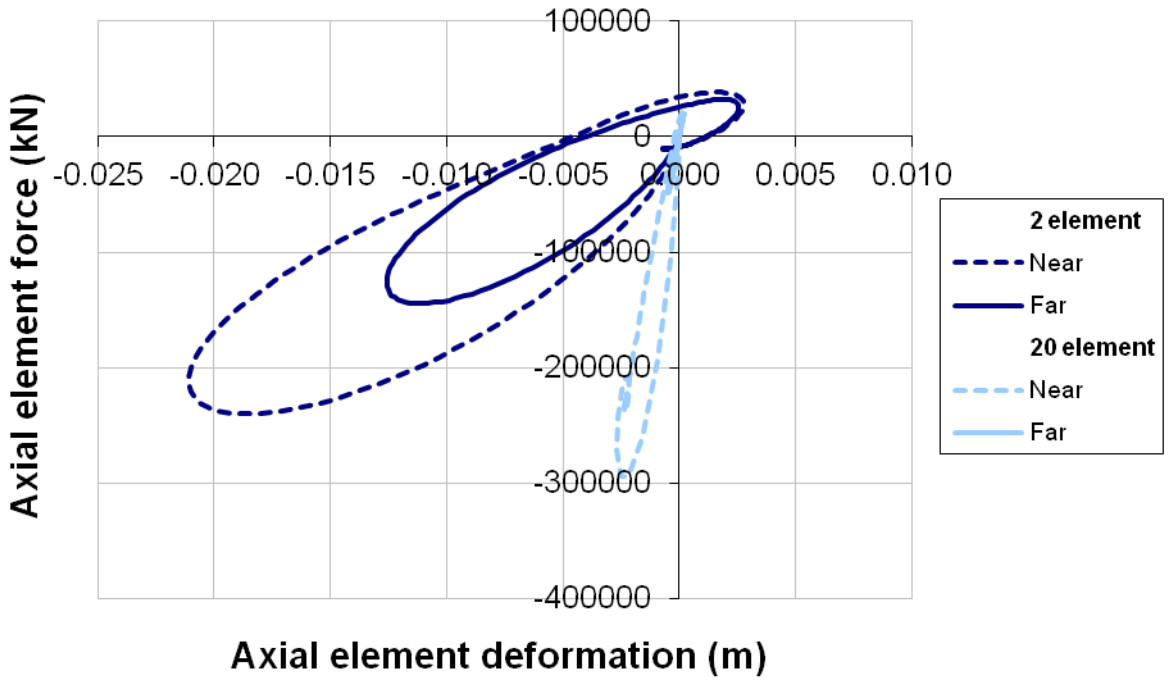

Figure 4.35 Axial element hysteresis in Diaphragm 1. Case 5 with 50% damping

4.8 Dissipation Models – Global Modal Damping

Modal damping also affects the post collision velocity due to its actions over the course of the collision. For the purposes of this section, modal damping is defined as uniform damping of all modes at the specified percentage. Rayleigh damping and other damping schemes would provide different results but have not been investigated here. These effects of damping scheme selection is discussed further in Section 5.2.4

4.8.1 Dependence on Collision Velocity

Modal damping acts in a very different manner than the localised elements shown in previous sections. The resulting plasticity index behaviour also changes. Figure 4.36 displays the plasticity index calculated for each colliding floor. The floors' plasticity index values are observed to diverge as the global damping increases. This trend is particularly notable in Case 1 and Case 3. This poor performance can be explained by examining the energy damping mechanism. Modal damping removes energy from any node in a model that has velocity. This means that a collision with global damping does not dissipate energy proportionally to the *relative* collision velocity, as seen in all the previous tests. Instead, energy is dissipated proportionally to the *absolute* velocity of each diaphragm. This behaviour is undesirable, so modal damping is not recommended as a means to dissipate energy during contact.

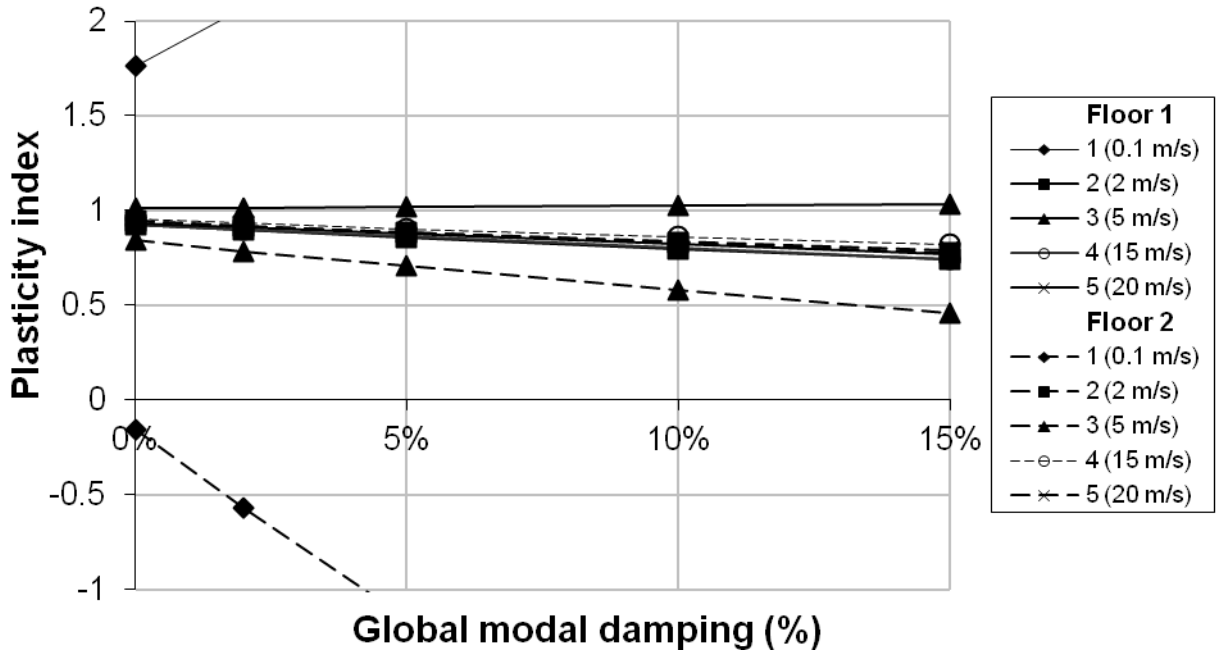

Figure 4.36 Plasticity index dependence on collision velocity

However, some global damping is likely to be present in any numerical model. This is because global damping is the most common method used to represent the energy dissipation that happens throughout a structure during an earthquake. Thus, it is likely that any pounding model will have some global damping in addition to one of the previously tested models. The effect of adding 5% global damping to the viscous diaphragm model is investigated in Figure 4.37 and Figure 4.38.

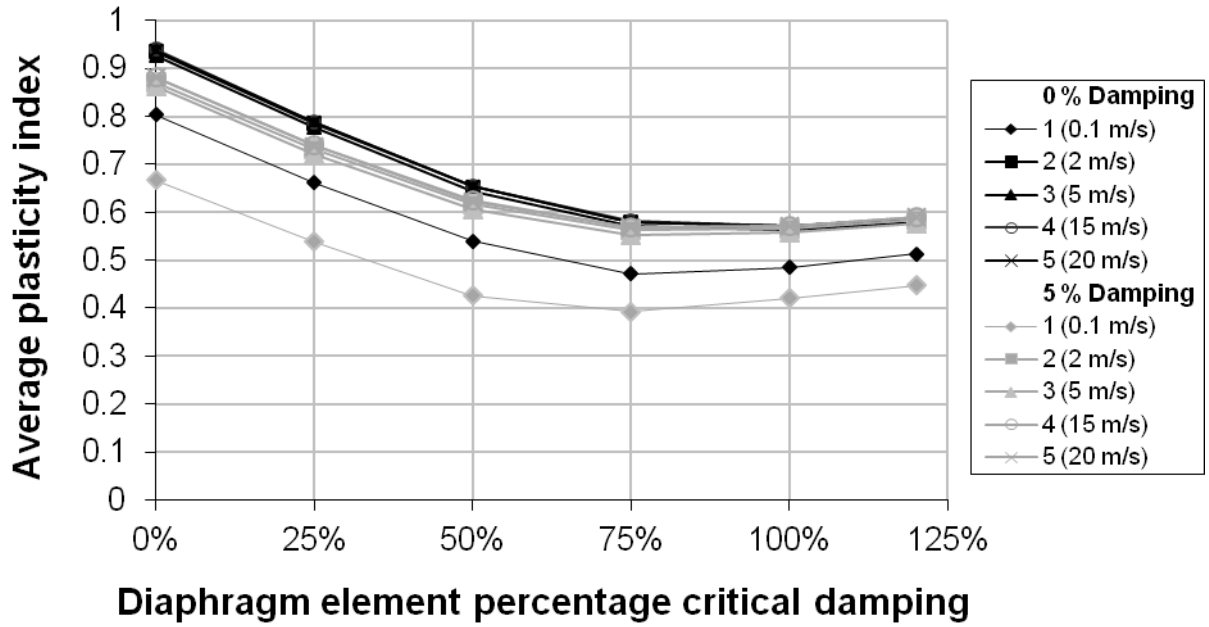

Figure 4.37 Effect of 5% modal damping on damped diaphragm plasticity index

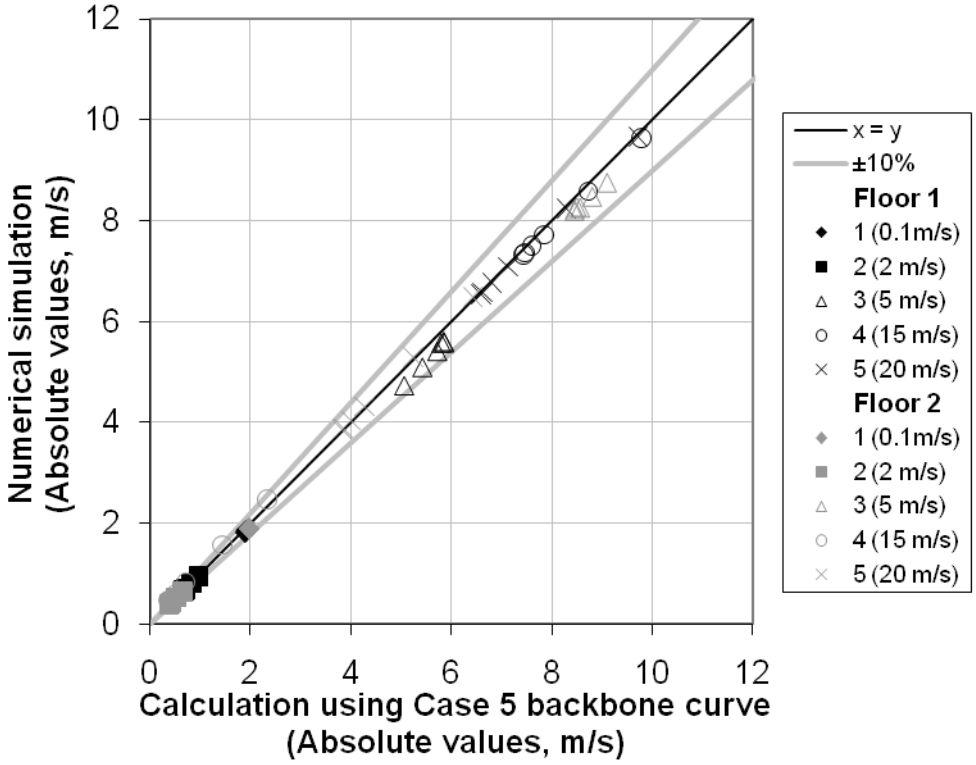

Figure 4.38 Comparison of predicted and recorded post collision velocities for damped diaphragm model with 5% modal damping

The effects of modal damping on plasticity index reduce with increasing diaphragm damping. At 120% critical diaphragm element damping, the modal damping results have almost completely converged with the undamped results. The reason for this convergence is unknown. 5% modal damping is observed to only slightly affect the accuracy of the predicted post collision velocities (Figure 4.38).

The inclusion of modal damping in models with distributed mass collision may be either ignored or incorporated into plasticity models. A model that ignores modal damping would not use global damping in the calibration of plasticity index, despite modal damping being used in any subsequent analysis with the adopted plasticity index. Ignoring global damping's effect on collision is consistent with current pounding modelling techniques. However, including global damping in calibrations for the plasticity index produces more accurate predictions for post collision velocities. In this thesis, global damping is not included in any plasticity index calculations. This choice provides consistency with the elastic pounding models, which assume a plasticity index of 1.0 despite global damping being present.

4.9 Dissipation Models – Intervening Objects

As noted in Section 4.4.2, intervening objects have the potential to affect the response of buildings during collision. In many instances, these effects can be directly incorporated into

contact models. For example, Figure 4.39 shows a facade located between two diaphragms. Figure 4.40 displays a simplified elasto-plastic hysteresis for the collision of these two diaphragms in an earthquake. Here u_{gap} denotes the separation between the two building diaphragms and u'_{gap} denotes the separation between the outside of the façade and the opposing diaphragm. Three distinct phases exist;

1. An elastic and plastic phase associated with the crushing of the supports of the façade, such as metal cleats or the bolts used in the fixings. At the end of phase one the façade has been moved so that no gap exists between the façade and either diaphragm (Figure 4.39b). A relatively large plastic deformation can occur depending on the separation of the façade to its supporting structure. The flexibility ($1/k_1$) of this segment (Figure 4.40) is equal to the flexibility of the affected facade supports plus $1/k_2$, while the strength (F_1) is equal to the combined support yielding strength.
2. An elastic and plastic phase associated with the crushing of the façade mullion itself. The mullion is generally stronger than its supports, thus yielding occurs at a higher force (Figure 4.39c). The flexibility of this segment ($1/k_2$) is equal to the mullion flexibility plus $1/k_3$, and F_2 is equal to the mullion crushing strength.
3. The third phase models the collision of the two diaphragms with insignificant further contribution from the façade. Note, however, that $u_{gap} \neq u'_{gap} + \Delta u_1 + \Delta u_2$, due to the elastic recovery of the facade. The final stiffness (k_3) set as a 'sufficiently large' value to minimise diaphragm overlap (see Section 4.2 for further details).

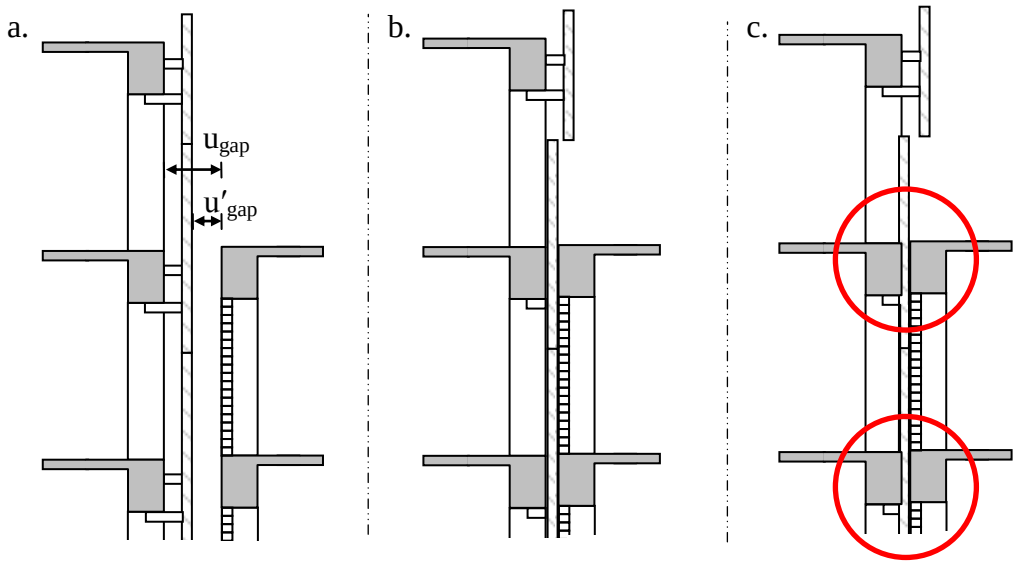

Figure 4.39 Stages of a facade being crushed. a) prior to collision. b) crushing of facade support. c) crushing of mullions

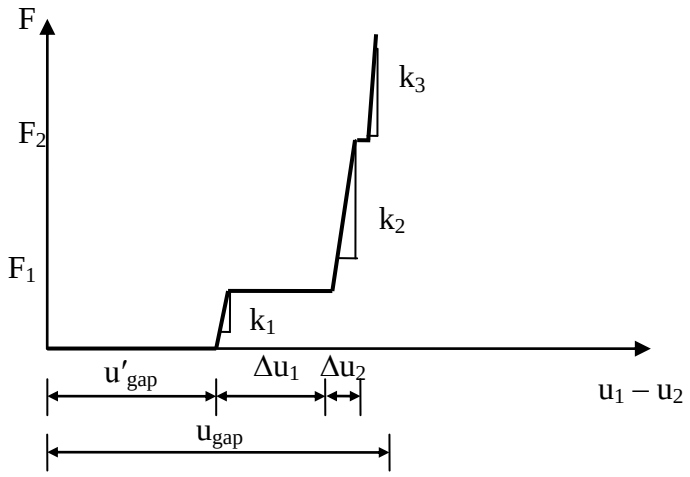

Figure 4.40 Elastoplastic hysteresis for crushing of facade

If the buildings start to separate at any point during the collision, elastic recovery will occur. Any further collisions now must overcome a greater separation equal to u'_{gap} plus the previous plastic deformations. Once the plastic deformations have occurred once, no further plastic deformation occurs in later collisions. However, collision stiffness would equal k_1 for $F < F_1$, k_2 for $F_1 \leq F < F_2$, and k_3 for $F \geq F_2$.

Similar hysteresis can be described for the other deformable objects that may be present between buildings. Some, such as accumulated debris, may suddenly dislodge and create a larger building separation. The significance of these local effects will largely depend on the relative building velocities. It is likely that the energy dissipated by such considerations is entirely negligible. Specifically, the hysteretic energy loss occurs only once, (for example, the façade can only be completely plastically crushed once). However, the increase in separation of the two diaphragms is much more likely to be important. It would certainly be incorrect to model the two diaphragms without the façade and separated by a gap u'_{gap}.

The wide variety of effects that intervening objects may have on collisions is too large to be considered in detail here. In common circumstances, a reasonable elasto-plastic approximation of the strength and stiffness of the intervening objects is likely to be adequate for analytical modelling. It is recommended that this modelling be undertaken in addition to one of the other collision damping models, since they represent different processes. If such modelling is not possible in the chosen NLTHA program, it is considered that most intervening objects may be ignored without significant error being introduced to the model.

4.10 Dissipation Model Summary

The characteristics of the various contact damping methods are summarised in Table 4.6.

Table 4.6 Damping method summary

Damping method	*Method to measure energy loss*	*Collision increases gap*	*Known disadvantages*
Multilinear hysteresis	Plasticity index	Always or never	UFP
Damped Kelvin	Plasticity index	Never	UFP
Viscous diaphragm	Plasticity index	Never	LB
Global modal damping	Plasticity index	Never	AWM
Intervening objects	-	Once	HSC

UFP Damping method has an Unrealistic Force Profile

LB Plasticity index has a Lower Bound greater than 0

AWM Damping method Affects the Whole Model, not just the collision

HSC Damping method is Highly Specific to building Configuration

As the table indicates, all methods present drawbacks. All methods except for intervening object modelling also produce post collision velocities that can be predicted using the plasticity index. These methods can provide a consistent measure of energy loss, however it is emphasised that this does not necessarily mean that they are modelling collision damping in a realistic manner. The primary advantage of these methods is their analytical convenience. To determine their applicability to actual collision scenarios requires a large amount of laboratory testing that is not performed here. The above methods provide an approach that is consistent with the calibration of the lumped mass coefficient of restitution.

Intervening object modelling is likely to be the most appropriate method if there are known elements that will be crushed before two diaphragms can collide. However, additional damping is also likely to be required. Note that while multilinear hysteresis can be set to increase the separation with each collision, this is not likely to be realistic and is best avoided entirely. If collision force profiles are of interest, the viscous diaphragm is likely to be the most suitable option, since it provides the most sensible force profile. In the absence of further information any model could be justified depending on the specific circumstances being considered. However, the viscous diaphragm presents the most realistic collision response, and is the most generally recommendable method.

4.11 Method to Define Plasticity Index Relationships

The multilinear, damped Kelvin, and viscous diaphragm elements have been shown to be dependent upon mass ratio, axial period ratio, and the number of elements in each diaphragm. However, once an analytical model is created, a unique relationship can be defined that is valid for collisions of any relative velocity. This relationship can be defined by calibrating the

damping relationship for any colliding diaphragms prior to running the pounding analysis. A method to do this is presented below (see also Figure 4.41):

1. Reproduce the two diaphragms and the contact element in a separate model. Each diaphragm's axial stiffnesses, nodal masses and geometry should be kept identical to the original model. The contact element's properties should also be kept constant. If the viscous diaphragm is being used, also include these damping elements.
2. Add a very low stiffness spring to connect each diaphragm to the ground. This step is necessary in order for most NLTHA programs to run. The stiffness of these springs should be sufficiently small to produce negligible effects on the post collision velocity.
3. Apply a force history to each node in one diaphragm. These forces should be scaled according to each node's mass, thus creating a uniform acceleration at each node. The force should be applied with a large magnitude but short duration so that a large (say 5 m/s) velocity can be achieved in the diaphragm. Ensure that no force is being applied to the diaphragm when the collision occurs. This can be controlled by adjusting the initial separation in the contact element.
4. Record the pre-collision and post-collision velocities of each diaphragm. This can be achieved by calculating the total momentum in each diaphragm immediately before and immediately after collision. The average velocity is then found by dividing by the total mass of the considered diaphragm.
5. Calculate the value of r_1 and r_2 using Equations 4.1 and 4.2. Plot these values as shown in Figure 4.16.
6. Repeat steps 3 – 5 while adjusting the parameter that controls damping. For example, when testing the multilinear element, k_r/k_a was modified. In that calibration, six analyses were performed (k_r/k_a = 1, 2, 5, 10 and 20) to adequately define the backbone curve; however more may be required if extra accuracy is sought.
7. Repeat steps 1 - 6 for any other diaphragms that may collide during the original model's analysis.

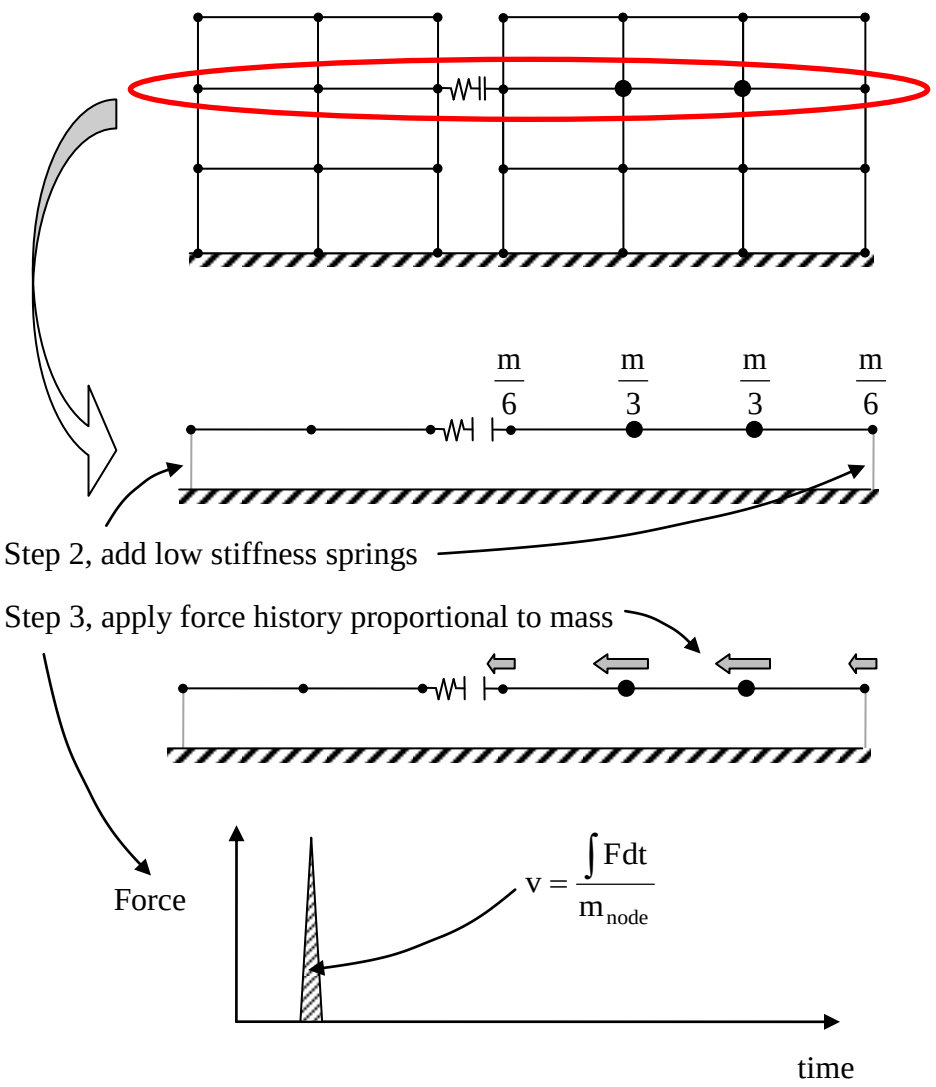

Figure 4.41 Initial steps to calibrate plasticity index for two diaphragms.

Note that even if intervening objects are to be modelled in the collision, they should not be used when defining the plasticity index relationship.

The presented approach also has other advantages. For example, two element per diaphragm modelling is known to have some error when emulating the collision of two distributed masses. This can be seen in any of the plasticity index plots (for example, Figure 4.35) where the elastic version of the tested two element model does not produce a plasticity index of 1. However if a plasticity index is specified, this error is avoided since the system has been specifically calibrated. On the other hand, if the theory presented in the previous chapter is in any way incorrect or incomplete, then a systematic error may be introduced to the model. For example, Equations 3.43 and 3.44 do not include the effects of secondary collisions. Thus any models calibrated using these equations also neglect these effects.

4.12 Conclusions

The following conclusions are drawn from the investigations performed in Chapter 4.

1. When at least one element is present in each diaphragm, $\gamma = 1$ appears to be the most appropriate selection for collision element stiffness. Thus k_c = the softer of the two adjacent diaphragm axial stiffnesses
2. Lumped mass floor/floor modelling methods can cause significant inaccuracy in recorded drifts since they do not accurately model the energy lost to axial diaphragm oscillation.
3. Significantly more accuracy may be achieved in lumped mass models if the equivalent lumped mass formulation is adopted.
4. At least two axial elements per diaphragm is recommended to accurately model the influence of diaphragm flexibility on floor/floor collisions.
5. The multilinear, damped Kelvin and viscous diaphragm damping models are all effective at dissipating energy during collision. However, all also present drawbacks. It is recommended that a damping method be chosen to suit the needs of the modeller. In typical modelling situations, viscous diaphragm damping is considered to be the most realistic method.
6. Modal damping is not recommended as a means to specifically control damping in a collision. However, low levels of modal damping do not significantly affect collision damping results.
7. Intervening objects may be specifically modelled for more accurate results. However, these effects are not expected be significant on most analyses.
8. A method to calculate the plasticity index for a specific building configuration has been produced and will be used in subsequent chapters.

Chapter 5 Modelling and Selection of Buildings for Detailed Analysis

Related papers

Cole G, Dhakal R, Carr AJ, and Bull D (2010), *Distributed Mass Effects on Building Pounding Analysis*, in 9th US National and 10th Canadian Conference on Earthquake Engineering. 2010: Toronto, Canada

Cole, G., Dhakal, R., Carr, A. J. and Bull, D. (2012). *The influence of pounding on member demands in low rise buildings*. New Zealand Society for Earthquake Engineering Annual Conference (NZSEE 2012). Christchurch, New Zealand**:** paper 026.

In order to illustrate the effectiveness of the contact element model proposed in this dissertation, two existing buildings were selected for detailed modelling and analysis. While these buildings have been modelled as realistically as practically feasible, some simplification was inevitable. This chapter outlines the selection criteria for the modelled buildings and provides details of the adopted building modelling methods. This section is intended to contain sufficient detail to allow the interested reader to reproduce the adopted modelling method for any future projects.

5.1 Selected Building Characteristics

Two buildings from Wellington, New Zealand were selected for modelling. Wellington was selected since it is located in an area of high seismic activity and since it is known to have many buildings that could suffer from pounding in a major earthquake. In particular, Wellington contains many older two to three storey buildings with little or no building separation. These buildings can be loosely categorised as buildings with favourable geometry (such as low total height, no major building irregularities) but primitive earthquake restraint systems (unreinforced masonry, pre 1970's reinforced concrete frames or masonry infilled panels). While many researchers have focused on the effects of pounding on modern high rise buildings, the assessment of these types of existing buildings has been largely overlooked. Two buildings with 'typical' 1960s construction were thus selected for detailed modelling.

In order to adequately model the selected building type, detailed drawings were sought from Wellington City Archives (WCA). With the generous help of WCA staff, original drawings of two suitable buildings were obtained. Both buildings contain masonry infilled reinforced concrete frame systems and are still currently in use. As the two selected buildings are not situated next to each other, the modelled situation does not actually represent an existing pounding hazard. However, the adopted models do represent a common scenario in New Zealand where pounding may occur.

While existing buildings were sought to ensure realistic building performance, a number of major simplifying assumptions have been made to facilitate modelling. For example, the masonry infill is assumed to be seismically isolated from the reinforced concrete frame. Wherever major simplifying assumptions are made in a model they are noted in the accompanying text.

5.2 2D Building Modelling

The modelling methods detailed in this section relate to the 2D models used in Chapter 6. Many of these details are also used in the 3D models. However, since 3D modelling presents unique challenges, Section 5.3 specifically outlines the changes required for the 3D cases.

5.2.1 Building Simplifications for Analysis

Figure 5.1 compares the model geometry adopted for one of the modelled buildings with the collected building drawing data. A number of gross assumptions are apparent; the wall located at the bottom floor has been removed, the parapets are excluded, the total height of the building has been modified, and the facade infill at levels two and three are not modelled in any way. The reasons and consequences of each of these assumptions are assessed below.

On first inspection, the removal of the level 1 wall appears to be a rather unjustifiable change to the building layout. However, the goal of the presented modelling is not to accurately represent this particular building, but to realistically model buildings of a certain era and form (see Section 5.1). The reason for this wall's presence is the earth embankment at the end of the building's boundary. Comparison with other frames within the building shows very similar column and beam strengths and stiffnesses between ground and first floor levels. No other frames include solid walls of this form. It is thus considered that this wall was added simply as a barrier to the earth embankment and had this embankment not been present, the surrounding frame would have been constructed in the same manner without the concrete walls.

Decisions to not model the parapets and to change the third floor interstorey height were made to ensure that floor/floor collisions with the other modelled building were possible. If the original building height was kept, floor/floor collisions would still occur, however, the load path would include the in situ concrete infill located at the roof level. While this effect may be interesting to investigate, it complicates the basic phenomenon that is of interest here. The location of the neighbouring building's roof can be observed in the overlay in Figure 5.1, since its height is the same as the presented model's roof height. While the stiffness of the parapets are not included,

their weights are included to provide a more accurate assessment of seismic mass. Other minor adjustments to the overall building geometry have also been made to simplify the models.

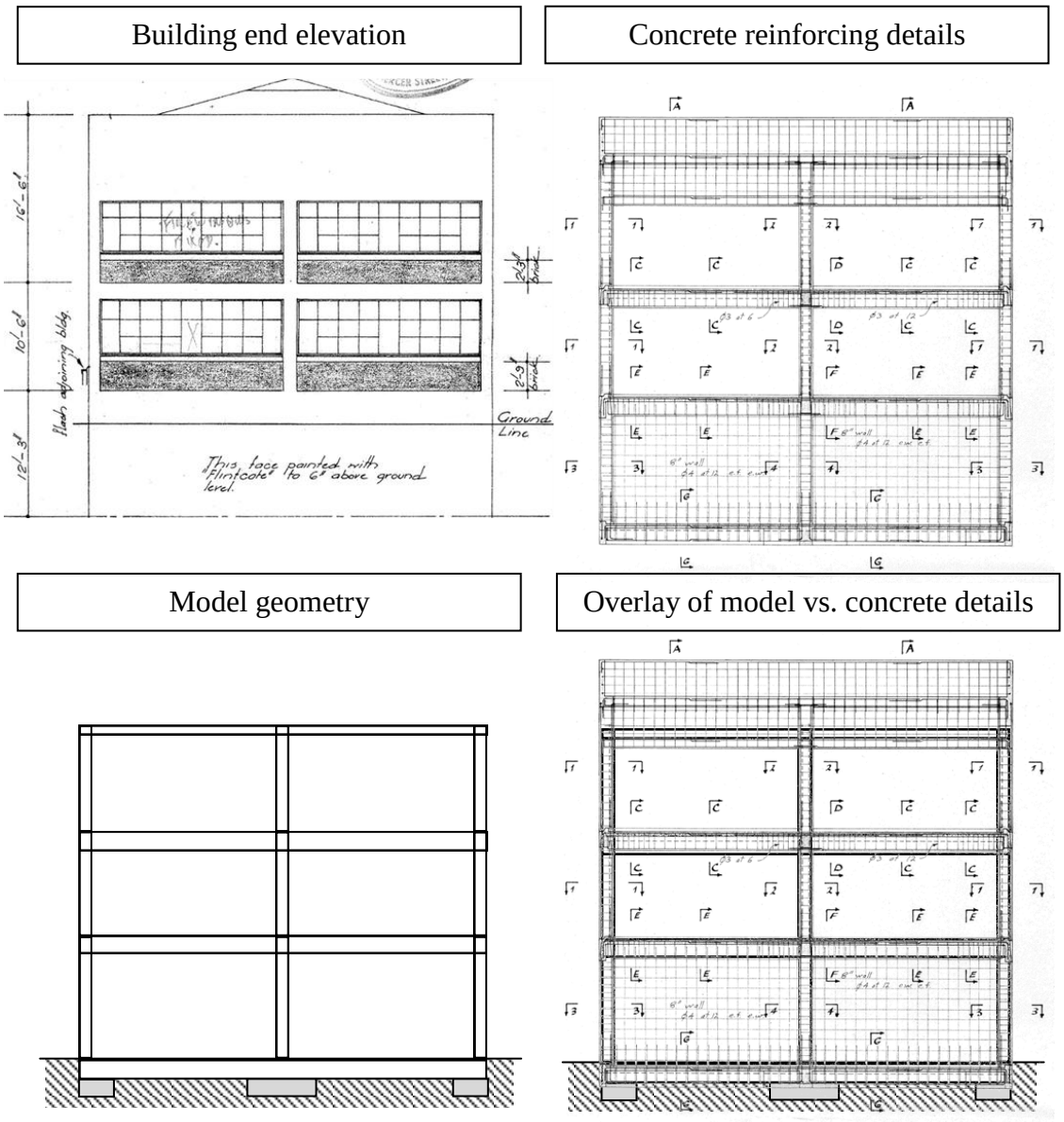

Figure 5.1Comparison of original building layout with the adopted building model

Finally, the facade infill located at levels two and three is assumed to provide no seismic resistance to the frame. This implies that the facade is seismically separated from its surrounding frame. In reality such separation is unlikely. However, in a moderate to major earthquake, glazing can be reasonably expected to break and not provide any significant stiffness contribution. It is also noted that neglecting stiffness contributions from the facade is a very common (albeit frequently incorrect) assumption. Since including these effects adds a further layer of complexity not related to the pounding phenomenon, they are excluded in the analyses presented here.

It is noted that many of the assumptions made here do not significantly differ from standard practises used when making 2D models. However, they are explicitly detailed here to appropriately document the adopted modelling method. Similar adjustments have also been made for Building 2, which is not discussed in detail here.

5.2.2 Analysis Program

Almost all analysis presented in this dissertation has been performed using Ruaumoko. As previously mentioned (Chapter 4), Ruaumoko is a non-linear time history analysis program which was developed at the University of Canterbury. This program has been adopted since it has the necessary analysis capabilities, and since the program could be indirectly modified via discussion with the program's creator. It is acknowledged that other software tools exist that could perform these analyses (for example; LS-DYNA, DRAIN-2DX, SAP, ABAQUS). Some of these other programs may be even more suited to specific analysis tasks; however Ruaumoko is used throughout this project to provide consistency in the reported results.

5.2.3 Material Properties

The aim of modelling existing buildings is to reasonably simulate the buildings in their current state. Material properties such as concrete compressive strength change over time. To account for these changes the recommendations of the NZSEE guidelines (NZSEE 1996), and current New Zealand standards were adopted. As the NZSEE guidelines are over 10 years old, some sections recommend methods from superseded standards. In these places, the methods from the newer standards were adopted when deemed appropriate. Appendix H shows in more detail the calculations performed and reference standards used for the modelling of one frame. The adopted properties are summarised in Table 5.1.

Table 5.1 Adopted building properties

Property	***Value***
Reinforcing steel yield stress	*300 MPa*
Reinforcing steel Young's modulus	*200 GPa*
Concrete compression strength	*45 MPa*
Concrete Young's modulus (strength)	*29 GPa*
Concrete Young's modulus (stiffness)	*32 GPa*

The concrete values are equal to or greater than both the values used when the buildings were designed, and the values used in current design standards for new buildings. This reflects the additional concrete strength and stiffness that is expected to have accrued over the past 50 years.

5.2.4 Analysis Properties

General model properties, such as analysis time step or the model damping scheme, can also have a significant effect on the resulting pounding response. In this thesis, uniform modal damping is applied using the Wilson and Penzien damping model (1972). This damping model is more computationally expensive than the more common Rayleigh damping model since uniform damping creates a fully populated damping matrix, whereas Rayleigh's damping matrix is banded. However, the extra computational cost is necessary to more appropriately model the amount of modal damping that is activated when diaphragm oscillation occurs. Figure 5.2 illustrates the percentage of critical damping applied across all structure modes in a model when the first two modes (at 0.48 Hz and 0.95 Hz) are set at 5% critical damping. The diaphragms' axial natural frequencies are always very much greater than either building's fundamental frequencies. If Rayleigh damping is adopted, this means the diaphragm's axial modes may be very highly damped. For example, if the axial mode frequency is assumed to be 20 times the fundamental frequency (9.6 Hz), then the damping of the axial mode exceeds 130%. However, if uniform damping is adopted, the damping of any mode may be explicitly controlled. In this project, modelling is performed with 5% uniform modal damping.

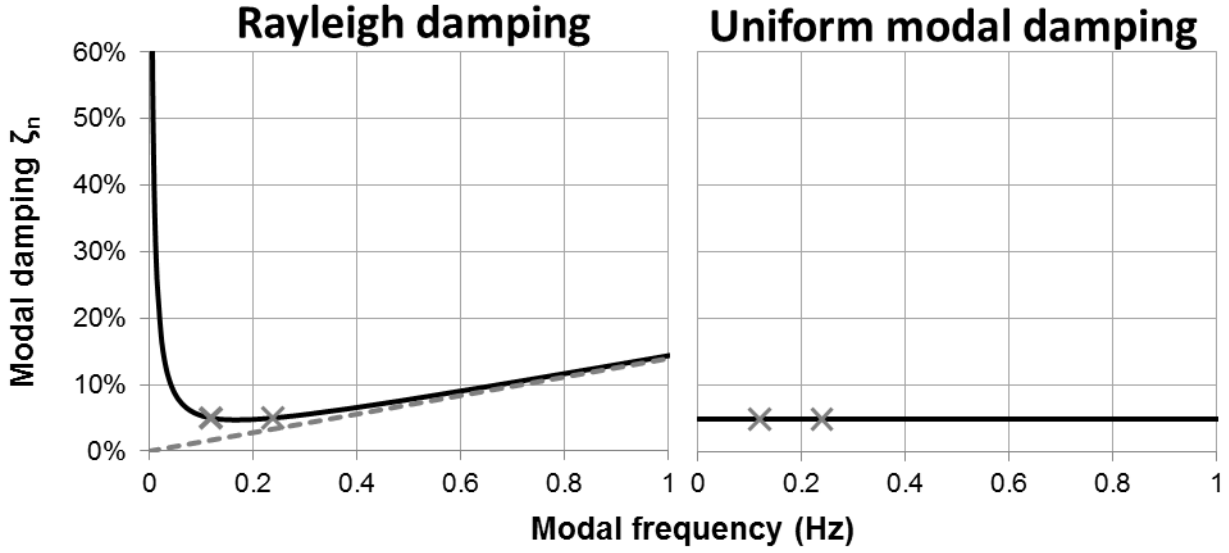

Figure 5.2 Damping alternatives within Ruaumoko. 5% damping specified at indicated frequencies. Dashed line indicates the infinite asymptote of the Rayleigh function.

Special consideration of the numerical time step is also required when performing pounding analyses. While standard NLTHA typically adopts time steps of about 0.01 seconds, pounding analyses simulate a response that occurs on a much smaller timescale. Watanabe and Kawashima (2004) recommended that the time step used in analysis should be shorter than the collision duration. However, little further guidance is currently available.

As noted in Section 4.3.1, the maximum permissible time step is at least partially dependent upon the collision element stiffness. The reason for this is shown in Figure 5.3. Element forces are calculated after each time step, which results in an imperfect representation of the contact element hysteresis. For example, three consecutive steps are shown at the beginning of a collision in Figure 5.3. At step 1, collision has not occurred while step 2 calculates a large collision force due to the very high contact element stiffness. A linear change in force is assumed over the time between steps 1 and 2. This causes the hysteretic energy of the element to also be misrepresented over this time step. When collision element separation occurs (steps 9 to 11) another sudden jump in stiffness occurs. The resulting enclosed space on the hysteretic loop represents the unintentionally lost energy. As shown in Figure 5.3, increasing the collision element stiffness increases this effect, while reducing the time step is the simplest method to reduce the effect.

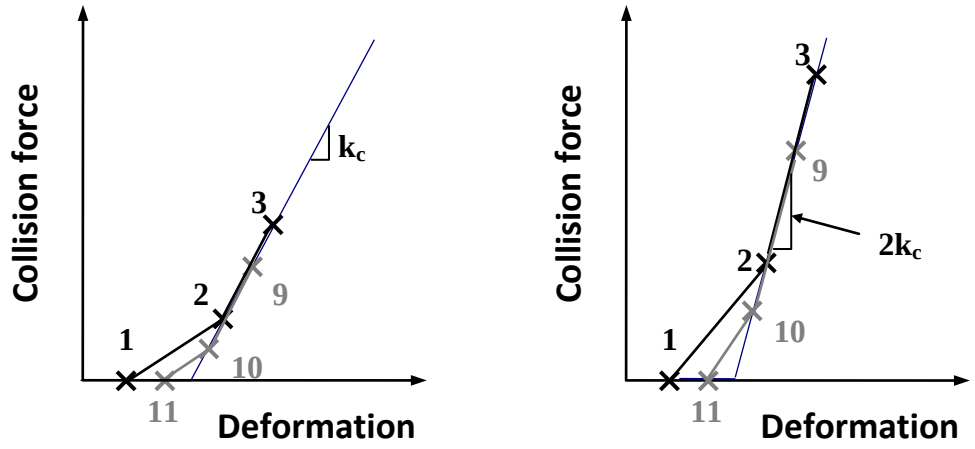

Figure 5.3 Collision element hysteresis modelling within NLTHA. Left: Collision element stiffness k_c. Right: collision element stiffness $2k_c$

In the subsequent analyses, a time step of 10^{-4} seconds is adopted. This value was determined by reducing the time step until an acceptable energy loss occurred over the course of the collision. The adopted time step caused an overall energy loss of 1.2% in the checked analysis.

An example analysis input file is provided in Appendix I to provide further details about the modelling method. Note that while this model is 2D, the input file is formatted for (and was performed in) Ruaumoko 3D.

5.2.5 Building layout

Basic building properties are presented here to provide some familiarity with the adopted model. The 2D model geometry is presented in Figure 5.4, while member sizes are presented in Figure 5.5 and Figure 5.6. The presented frames have been reproduced from the external frames of each of the selected buildings. Soil structure interaction is omitted from these figures for clarity. Further details of the model layout and properties are included in Appendix I. The heights of

Floors 1 and 2 differ between the two buildings (Floor 1 difference; 76 mm, Floor 2 difference; 77 mm). To model the collision at these locations, another node is added (Figure 5.7).

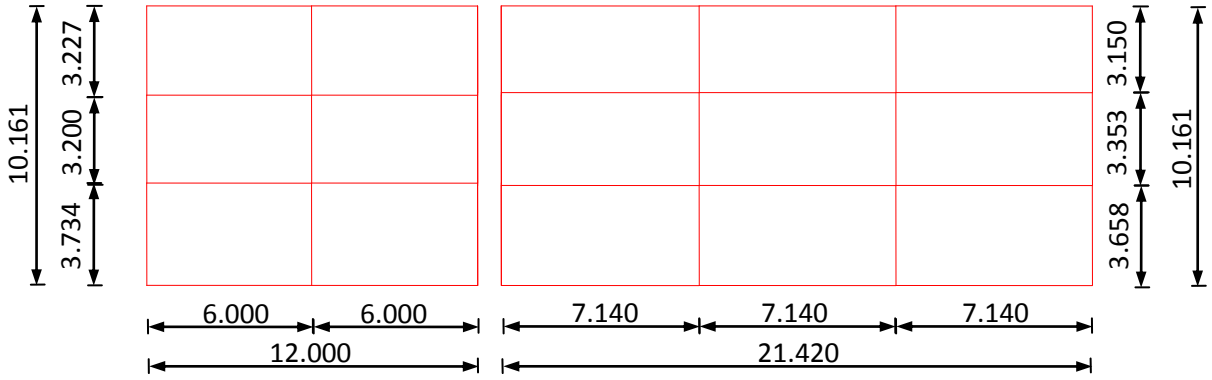

Figure 5.4 2D model geometry (front elevation). Units shown in meters.

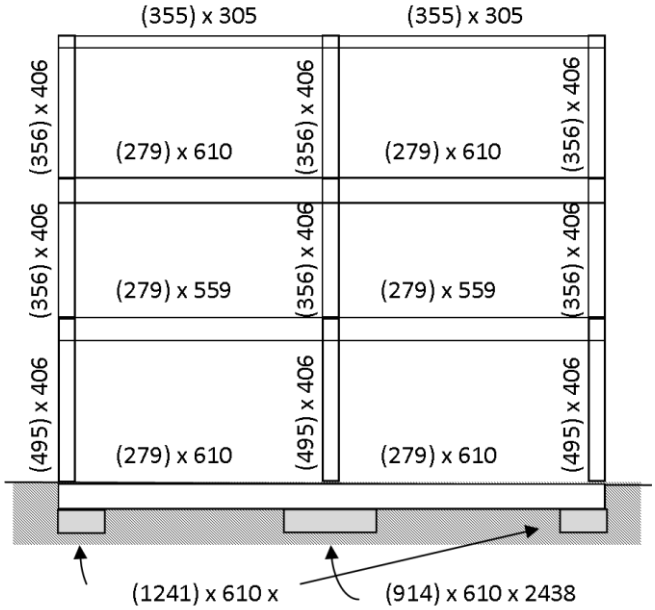

Figure 5.5 Building 1 member sizes (bracketed numbers refer to 'into the page' dimensions)

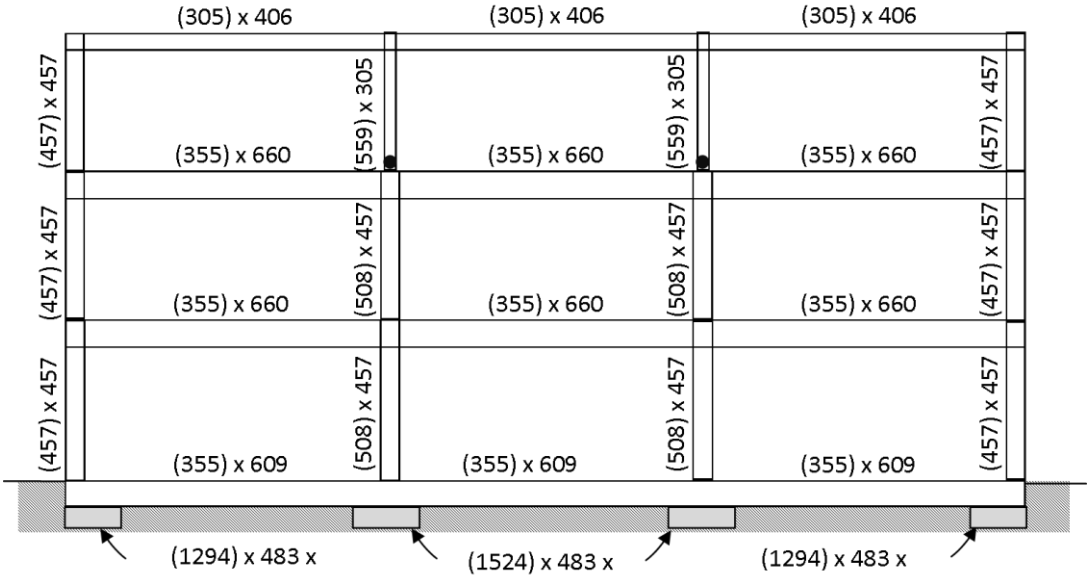

Figure 5.6 Building 2 member sizes (bracketed numbers refer to 'into the page' dimensions). Pinned connections marked with dots.

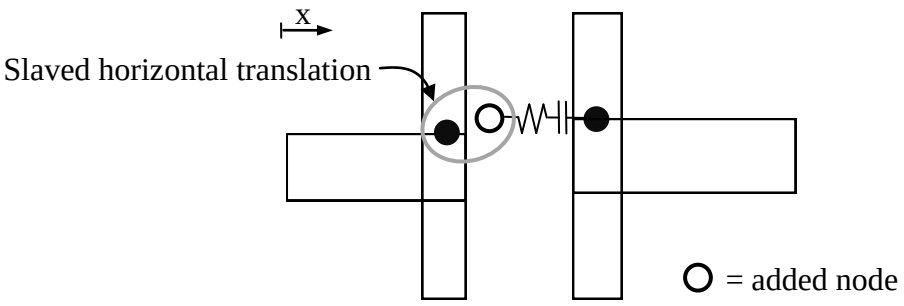

Figure 5.7 Modelling collisions with slight floor height differences.

The added node is located at the same height as one building's node, but is horizontally slaved to the other building's node (its remaining degrees of freedom are fixed). This means the horizontal collision force is transferred without inducing a moment from the floor height difference. The moment resulting from this eccentricity is intentionally removed since the induced moment is considered to be a secondary effect, and its inclusion would require a detailed assessment of the beam-column joints' rotational inertias. Figure 5.8 presents an alternative method that does incorporate the floor height difference explicitly in the model. Note that the two additional nodes in this model are not connected to the other column members but are rigidly linked to their respective beam-column joint nodes. In actual floor collisions of this nature, it is expected that the local damage at the collision interface will also influence the actions induced in these locations. The method suggested in Figure 5.8 is not used in this thesis.

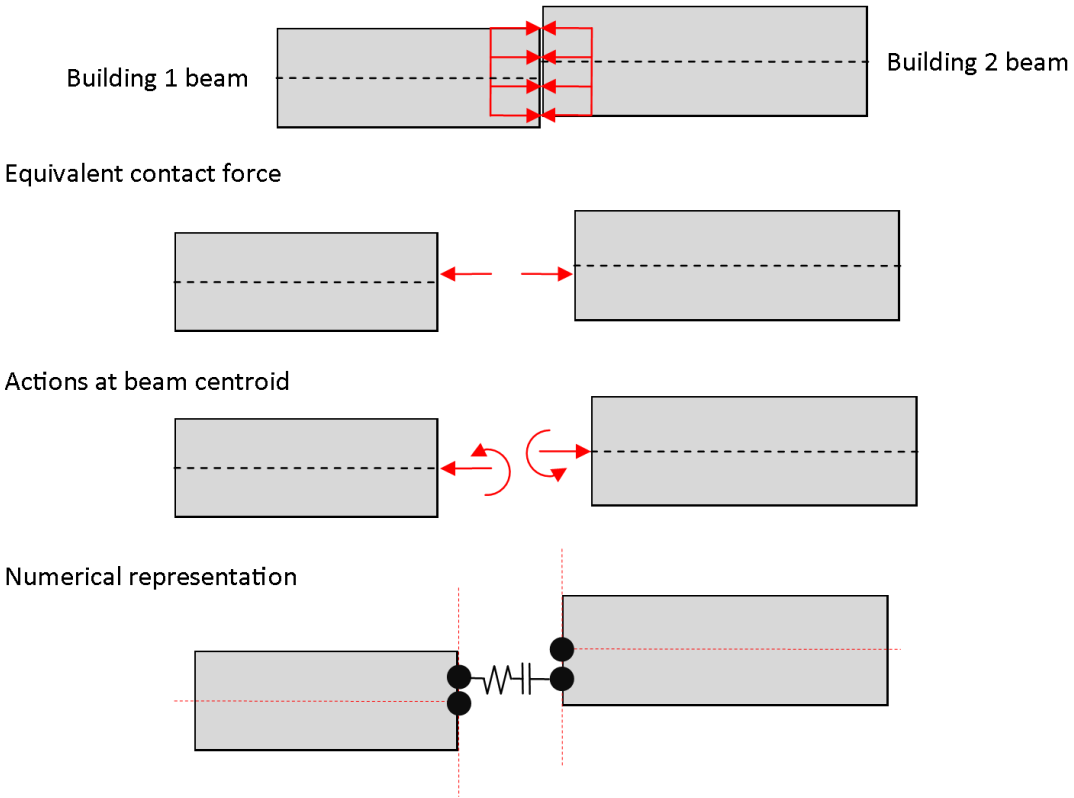

Figure 5.8 Equivalent numerical representation of collision for floors with small height difference. Beam centroids are assumed to be located at half beam depth.

5.2.6 Concrete Beam Behaviour

The behaviour of concrete beams has been modelled primarily using the New Zealand concrete standard (NZS3101 2006). Following this standard, flexural stiffness and strength of beam members have been modified to include contributions from the floor slab (Appendix H). Beam flexural hysteresis is modelled using the Modified Takeda law with $\alpha = 0.5$ and $\beta = 0$, as recommended by Dong (2003) for sections without calibration by experimental testing (Figure 5.9). These recommendations were made for concrete sections with deformed longitudinal reinforcing steel. However, the age of the buildings under consideration means the longitudinal reinforcement is not likely to be deformed. Use of round reinforcing is much more likely. While other more accurate hysteresis laws exist for round reinforcing, these are more complicated and require many parameters to be calibrated. No recommendations for the post elastic stiffness were made by Dong, so this stiffness was set at 0.01 times the initial stiffness. No allowance for axial/flexural interaction was made for the beam members. While this is a common assumption, it could be argued that it is not valid for pounding analyses due to the large axial forces that occur in the slab and beams when collisions occurs. However the collision duration (discussed in Section 3.1.5) is significantly smaller than the time frame over which flexural damage occurs in a beam, so this effect will not be considered here. Nevertheless, future investigation into this effect may be useful. Since beam hysteresis is not the primary focus of this work, the Modified Takeda law is considered to be sufficiently accurate for the testing performed here.

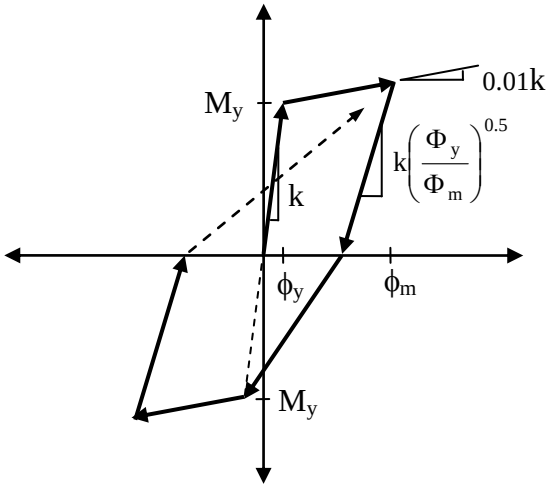

Figure 5.9 Beam hysteresis using modified Takeda and specified parameters

The suitability of the beam hysteretic model was checked using Response 2000 (Bentz 2000), a computer program developed at the University of Toronto which calculates section moment curvature relationships based on modified compression field theory. Figure 5.10 compares the adopted backbone curve with the section response predicted by Response 2000 for two

arbitrarily selected beam sections. Both pre-yield, and post-yield stiffnesses reasonably approximate the behaviour of the sections. Note the Ruaumoko model's flexural stiffness (EI) uses the 'stiffness' Young's modulus from Table 5.1 and 0.4 times I_{gross}, in accordance with the relevant standards. However, Response 2000 calculates the Young's modulus from the concrete characteristic strength, and the second moment of area is calculated using fibre analysis. Despite these differences, the elastic stiffnesses compare very favourably. The good agreement with yield moment is expected since Response 2000 was used to calculate the yield moments for the Ruaumoko models.

Yield curvatures predicted in Ruaumoko are typically approximately 50% the values predicted by Response 2000. This accuracy is acceptable for defining the backbone of the hysteresis. However, this also has a significant effect on the reported ductilities. Since curvature ductility uses the yield curvature on the denominator, curvature ductilities using the adopted hystereses in Ruaumoko are double that of Response 2000. To counter this effect, beam curvature ductilities are halved before reporting. Note this is not necessary for column ductilities due to their differing hysteresis parameters.

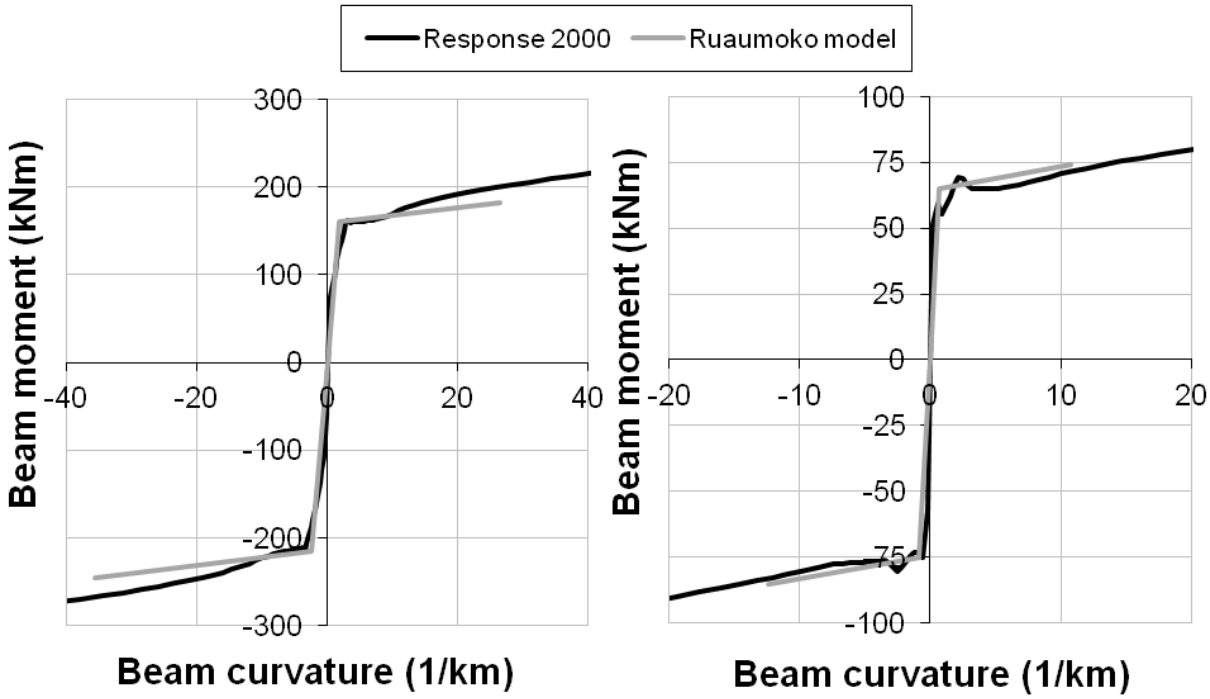

Figure 5.10 Comparison of adopted hysteretic backbone with Response 2000 for two beam sections

5.2.7 Concrete Column Behaviour

Modelling of columns is more complicated than beam modelling due to the changing axial loading that occurs within columns during a ground motion. The column flexural hysteretic response was modelled in Ruaumoko using the revised Takeda hysteresis (Figure 5.11).

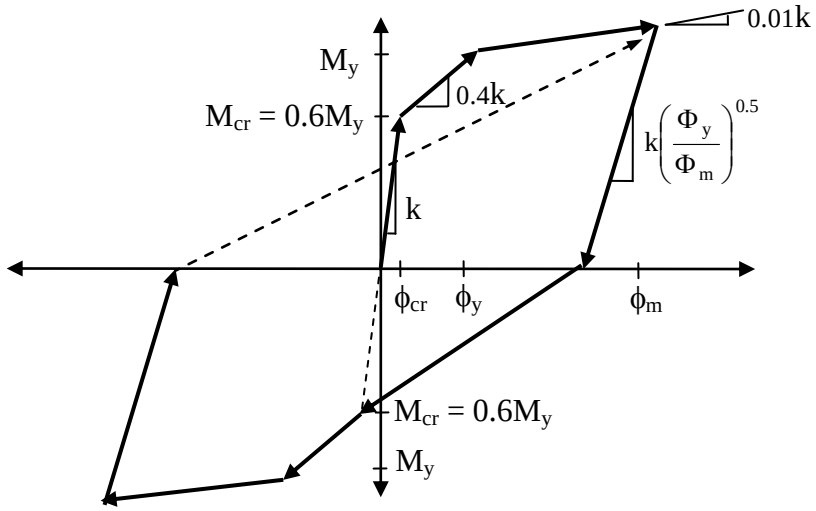

Figure 5.11 Revised Takeda hysteresis with specified parameters

This model is similar to the modified Takeda hysteresis used for beams, however a stiffness change between cracking and yielding is now also included. This additional detail is necessary because of the influence of the axial loading of the columns. Where applicable, the adopted values for the hysteretic parameters are kept the same as was used in the beam model. Two additional parameters are required; the moment at which cracking occurs, and the stiffness between cracking and yielding. These parameters were set at $0.6M_y$ and 0.4k after calibration with modelling of multiple columns' flexural behaviour at the column balance point in Response 2000 (Figure 5.12). While these models do introduce some error at lower loadings, they were considered to be suitably accurate for pounding modelling.

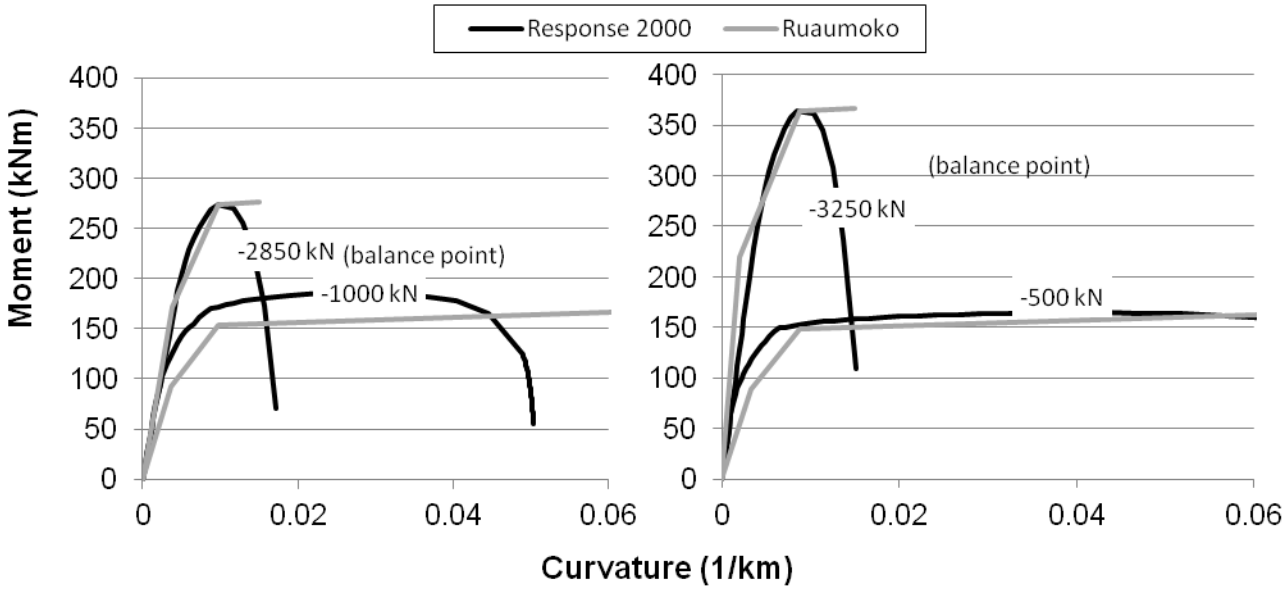

Figure 5.12 Comparison of column moment capacities for two modelled columns.

Unfortunately additional errors have occurred when applying this calibration due to an inconsistency between the theory and application of Ruaumoko's flexural-axial (M-N) interaction subroutines. The calibration was performed using the theory for M-N interaction

provided in Ruaumoko's manuals. However, when tested later Ruaumoko was found to produce a different M-N curve. This has resulted in columns' moment capacities being consistently underestimated, while the columns' stiffnesses were overestimated. The effect of this error is presented for one column in Figure 5.13.

The stiffness difference increases with increasing axial load. This is because the flexural stiffness is adjusted to achieve the required yield moment for a given axial load (which keeps the yield curvature constant). The yield curvature is calculated using the axial load from the static analysis that is performed before an earthquake history is applied. However, since the yield moment was underestimated in the static case, the yield curvature is also underestimated. Fortunately the range of axial loads typically ranged between 0 and -500 kN, so this error is not as amplified as it might otherwise have been.

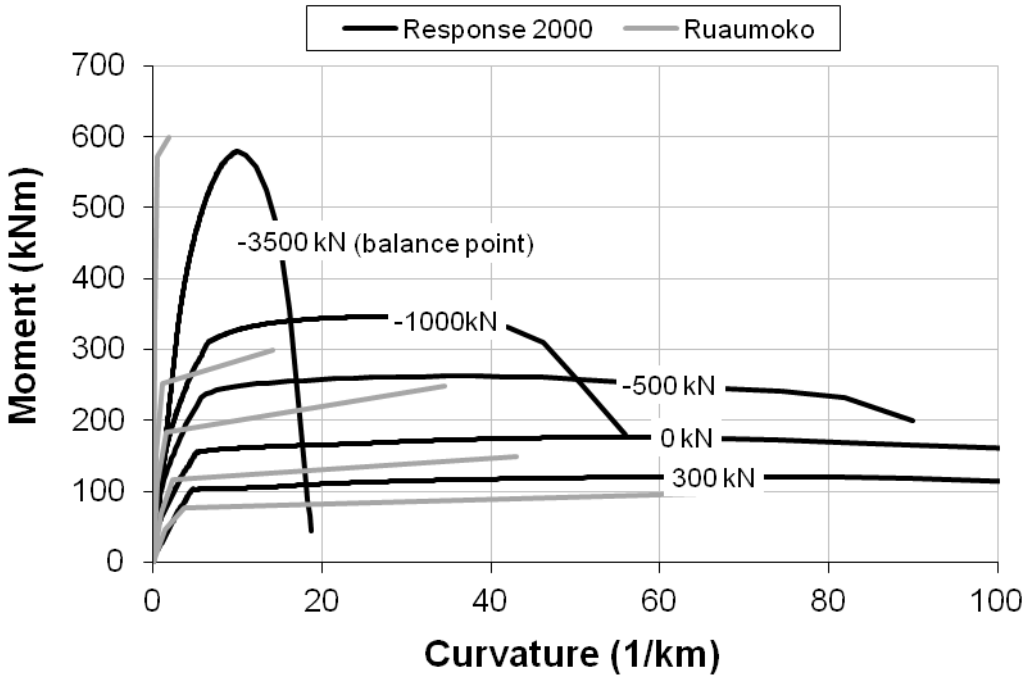

Figure 5.13 Comparison of column moment curvature backbones as a function of axial load.

If the M-N relationship had been tested before its use, it may have been possible to recalibrate the input parameters to attain a more realistic response. However, the above errors were only discovered after a sizable number of simulations had already been run. While the errors are unfortunate and will change the performance of each building, they are not considered to affect the pounding mechanism. As pounding damage is the primary interest of this modelling, reanalysing the existing data was not deemed worthwhile. In order to allow comparison with the remaining analyses, the column modelling method was not changed after discovering this error.

5.2.8 Diaphragm Modelling

When modelling buildings without pounding, diaphragm modelling is usually comparatively simple. Frequently any diaphragms are considered to be completely rigid, which simplifies the analysis by removing the diaphragms' axial modes. However, as the diaphragm is directly involved in floor/floor pounding, more detailed modelling is warranted in these analyses. Specifically, the diaphragm mass and axial stiffness require quantification.

The role of the diaphragm mass is particularly hard to define because the mass involved in a collision can significantly vary from the diaphragm's seismic mass. This problem can be illustrated by considering the plan layout of the two selected buildings (Figure 5.14). When a collision occurs, the collision force experienced by each building is equal and opposite. As shown in Chapter 3, this force is dependent on the amount of mass in each colliding floor (Equation 3.30). Thus appropriate modelling of the collision requires that the assumed tributary width is equal in each building. However, if the two buildings use different spacings between columns, using the common tributary width method is very difficult. This is because any modification to the seismic mass also requires modification to the interstorey stiffness to preserve the fundamental characteristics of the building (such as building period). This problem is even more severe at the other end of the buildings presented in Figure 5.14, since the overhanging floor is likely to contribute to the collision force, but would not be included in normal tributary width calculations.

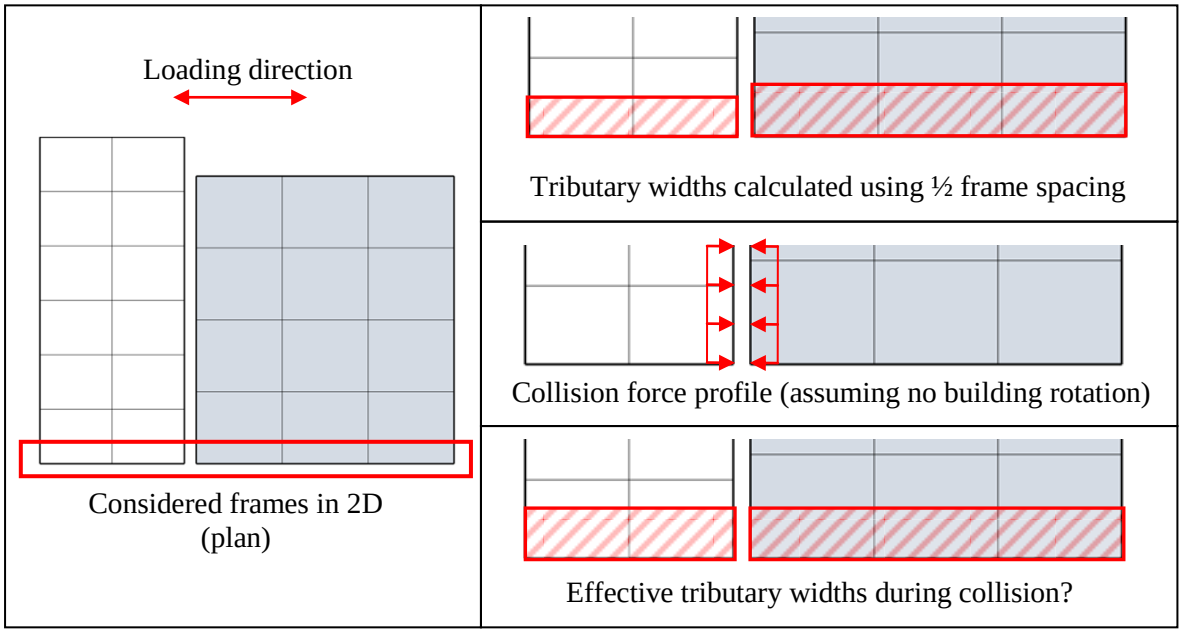

Figure 5.14 Effective mass participation in collisions. Lines denote locations of frames

One alternate method of dealing with this issue in 2D is to model each building in its entirety. This requires adding all columns' stiffnesses at each gridline and representing the entire building

as a single frame. This modelling method may be suitable when both buildings are predominantly regular, with no major stiffness concentrations in the building (i.e. there is no major sources of torsion). However modelling of this form becomes difficult if post elastic behaviour is to be included, since beam and column strengths can significantly vary between adjacent frames.

In the presented 2D analyses, the tributary widths are selected in the usual fashion without any consideration for the effect of pounding. 2D modelling of both buildings in their entirety is then considered alongside 3D modelling in Chapter 8. This is done to highlight the effects of the various assumptions in comparison to the 3D models. Building 1 is modelled with two diaphragm elements per floor, and Building 2 is modelled with three diaphragm elements per floor. This selection is primarily governed by the locations of the columns within each building.

Diaphragm axial stiffness is added to the corresponding axial beam stiffness since the diaphragm is compressed when collision occurs. The diaphragm's activated cross sectional area is assumed to be the building's tributary width times the slab depth. The axial performance of the diaphragm is assumed to be perfectly linearly elastic.

5.2.9 Member Capacities

Two measures of member capacity are assessed after modelling: curvature ductility and shear capacity. Shear capacities are calculated using the New Zealand Concrete Structures Standard (NZS3101 2006). Curvature ductility limits have been adopted from Walker and Dhakal (2009), which recommend a beam curvature limit of $\mu_\phi = 9$ and column curvature limit of $\mu_\phi = 12$ for limited ductile concrete members. These limits represent the expected ductility capacities of beams and columns designed as 'limited ductile' plastic hinge regions, as defined in NZS3101 (2006). Column ductility capacity is greater than beam ductility capacity due to the differing detailing requirements specified in NZS3101. These detailing requirements will not have been strictly adhered to in the modelled buildings since they were designed prior to this code; however, the limits are considered to be suitable for the purposes of the modelling performed here.

5.2.10 Soil Structure Interaction

As previously noted, soil structure interaction (SSI) can notably affect the displacements of buildings (refer Section 2.5.4). Since pounding is caused by the relative displacements between two buildings, soil structure interaction is likely to influence pounding and its effects. With this in mind, a simple soil structure interaction model was sought for use in the numerical models.

The ‘fundamental lumped parameter model’ (Wolf 1994) was selected to model each pad foundation in each building. This model simulates the movement of a rigid disk on an elastic halfspace using viscous dampers, elastic springs and additional masses. The area of the rigid disk is used to approximate the area of the buildings’ pad foundations (Figure 5.15). The model has five parameters for each foundation and includes a ‘monkey tail’, an additional mass which is attached to the foundation node by a damper. The model is applied separately in the horizontal, vertical and rational directions (Figure 5.15 displays the layout for the vertical displacements only).

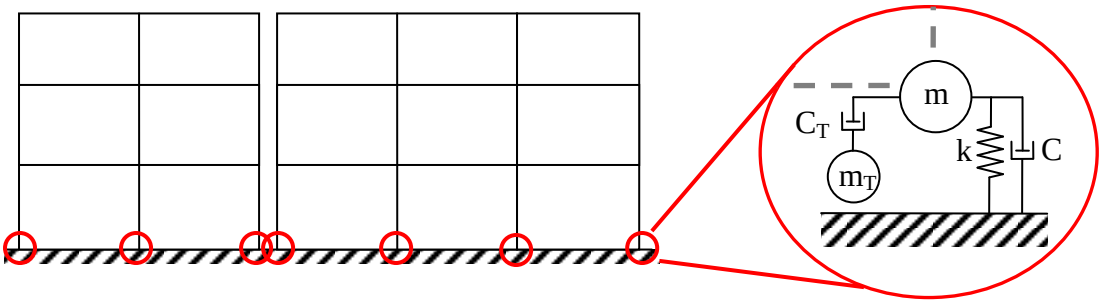

Figure 5.15 Soil structure interaction model at foundations

Horizontal SSI effects were not included in the 2D modelling. This is because the tested models have building separations of 0 – 20 mm, and the effect of crushing this much soil between the adjacent building’s foundations is considered to be negligible. Through-soil coupling similar to that used by Rahman (1999) (refer Section 2.5.4) could have been used in addition to the above method. However, in the opinion of the author, the application of through-soil coupling still requires further verification. Moreover, implementation of through-soil coupling would produce further parameters for calibration that are not the primary focus of this thesis. The small mass of the considered buildings will also reduce any effect this level of modelling would produce.

The lumped parameter model’s parameters are calculated from soil properties and the equivalent rigid disk radius. The required soil properties are: density, shear stiffness and Poisson’s ratio. Soil properties were obtained through using bore logs from one of the selected buildings, and conversations with practising geotechnical engineers from Beca, Carter, Hollings and Ferner Ltd, who are familiar with Wellington soils. These properties are summarised in Table 5.2.

Table 5.2 Soil properties for SSI modelling

Property	*Value*	*Calculation method*	*Source*
Shear stiffness G_{max}	*175 MPa*	*$G_{max} = 325N_{60}^{0.68}$ [In Kips]**	*Bore log*
Soil density ρ	*1937 kg/m^3*	-	*Beca*
Poisson's Ratio ν	*0.3*	-	*Beca*
Shear wave velocity c_s	*290 m/s*	$c_s = \sqrt{\frac{G_{\max}}{\rho}}$	-

** Formula obtained from Kramer (1996)*

The equations used to calculate the parameters in Figure 5.15 are presented in Appendix J. Modelling soil as an elastic half space, which effectively assumes an infinite depth of soil, may be seen as being incompatible with the shallow soil class adopted in the following section. However, in this case the elastic halfspace is deemed to be applicable since the modelled buildings are relatively light weight (due to their low number of storeys). Furthermore, no information on the likely depth to bedrock was obtained (the bore samples stopped at 20 m without hitting solid rock). More complicated SSI models exist that can take bedrock into account, but they also require further information.

5.2.11 Ground Motion Records

Three excitation records are used in the pounding analyses; El Centro (Imperial Valley, 1940), Tabas (Iran, 1978), and La Union (Mexico, 1985). These particular records are adopted because they are considered to possess similar characteristics to a major rupture of the Wellington fault. The records have been scaled according to NZS1170.5 (2004). This scaling requires selection of a soil class. The soil class (type C) was selected based upon the soil type of Te Aro, a central Wellington suburb with many buildings with pounding potential. Based on building locations and available Wellington City Archives data, this soil class is believed to also be consistent with the soil types of the two selected buildings.

Because pounding requires the modelling of at least two buildings, judgement is required in the scaling process. This is because the two buildings may have differing natural periods and ductilities, which are both required inputs in ground motion scaling. In order to perform the scaling, the following building characterisations have been made;

1. **Natural period** - Ground motion scaling requires the knowledge of the fundamental period of each direction of each building in order to determine the frequency range of interest. The period of each building will obviously vary but as this study focuses on less than four storey structures, the periods are expected to be 0.4 seconds or less. The New

Zealand standard states for periods less than 0.4 seconds the frequency range shall be calculated using 0.4 seconds. This result is therefore considered consistent for the modelled buildings.

2. **Ductility** – The structural performance parameter also requires a specific value for the building's ductility. In this study $\mu = 1$ has been adopted. This is because the non-linear nature of the buildings is explicitly modelled, and thus reducing the input seismisity for ductility would 'double count' the effects of building inelasticity. If the ductility was instead set at $\mu = 1.25$ (nominally ductile), the final scaling of the spectra would change by 4 % ($\mu = 2$ would change the spectra by 15 %).

Unless specifically stated otherwise, the ground motions are scaled for the 1/25 year event. This is magnitude of a 'service level' motion in the current New Zealand standard (NZS1170.5) and is roughly equivalent to the 'ultimate' design criteria when the buildings were constructed in the 1960s (Fenwick and MacRae 2009). In the early 1960s, buildings were constructed using the 1935 New Zealand building code, which used the working stress design method. Fenwick and MacRae converted the working stress method to an equivalent limit state formulation to allow comparison with current New Zealand codes. They found that the 1935 code produced an equivalent horizontal seismic shear of $0.104W_t$, where W_t is the seismic weight of the considered structure. The 1/25 year horizontal seismic shear in the current New Zealand standard is $0.1W_t$.

The use of the selected ground motion for the 1/25 year design earthquake magnitude technically does not meet the New Zealand standard. The standard states that the record scaling factor, k_1, may not be less than 0.33 (i.e. the scaled magnitude of the record must not be less than 0.33 times the original magnitude). It is understood that this requirement is present to ensure the scaled motions have similar characteristics (such as frequency content) to the type of earthquake that naturally occurs at that magnitude and distance. In this case however, the selected earthquakes original magnitudes are approximately in the order of a 1/500 year event. This leads to k_1 values of less than 0.33 for the Tabas and El Centro earthquakes (0.12 and 0.29 respectively). Despite failing this criterion, these earthquakes are still used. Since the analyses rely on comparisons between the pounding and no pounding building configurations, this is not considered to significantly affect the results presented in the following chapters.

The ground motion records have also been truncated to minimise computational time. 12 to 16 seconds of each record is used. The duration of the record is determined by the length of high level excitation. This selection could be considered inappropriate given the previous findings of Sinclair (1993) and Jeng et al. (1992), who claimed the most adverse pounding effects do not

occur at the time of maximum excitation (see Section 2.5.2). However, the selected sections of ground motion include both high amplitude and low amplitude regions over their respective time scales, and are therefore deemed appropriate for the modelling undertaken here.

All two dimensional analyses use the primary component of the ground motions, however the secondary ground motion's components were also scaled in anticipation of three dimensional analysis. Vertical earthquake components are not considered in the analyses since they are not a primary contributor to pounding interactions. Characteristics of the ground motions are presented in Figure 5.16, Figure 5.17 and Table 5.3. PGA and PGV refer to the records' Peak Ground Acceleration and Peak Ground Velocity, respectively. T_m is the mean period calculated from the Fourier transform of each record, as recommended by Dimitrakopoulos (2009);

$$T_m = \frac{\sum_i C_i^{\,2}\left(1/f_i\right)}{\sum_i C_i^{\,2}} \qquad (5.1)$$

Where C_i = the Fourier amplitude and f_i = frequency of data point i. ω_m is also presented in Table 5.3 and represents mean circular angular frequency. $\omega_m = 2\pi/T_m$ and is included as this value is used to non dimensionalise some pounding parameters.

Table 5.3 Ground motion characteristics (1/25 year return period)

Record	***Component***	***PGA***	***PGV***	***T_m***	***ω_m***
		g	*m/s*	*Seconds*	*rad s^{-1}*
El Centro	*Primary*	*0.131*	*0.136*	*0.609*	*10.32*
	Secondary	*0.081*	*0.169*	*0.717*	*8.77*
La Union	*Primary*	*0.103*	*0.120*	*0.567*	*11.08*
	Secondary	*0.089*	*0.077*	*0.370*	*17.00*
Tabas	*Primary*	*0.136*	*0.105*	*0.457*	*13.75*
	Secondary	*0.117*	*0.108*	*0.511*	*12.29*

Hao and Zhang (1999) have suggested that the wave propagation of the seismic impulse can be significant for the response of low rise buildings. However, in that study the considered buildings were modelled perfectly elastically. The inelasticity of the buildings (which changes the dynamic properties of both buildings), and the small building widths modelled here minimise any effects that may arise from this ground wave propagation. Consequently, no seismic wave propagation effects are modelled. This approach is also in line with the conclusions of related

studies in this area by others (Athanassiadou et al. 1994; Jeng and Kasai 1996; Jagiasi and Kasai 1996).

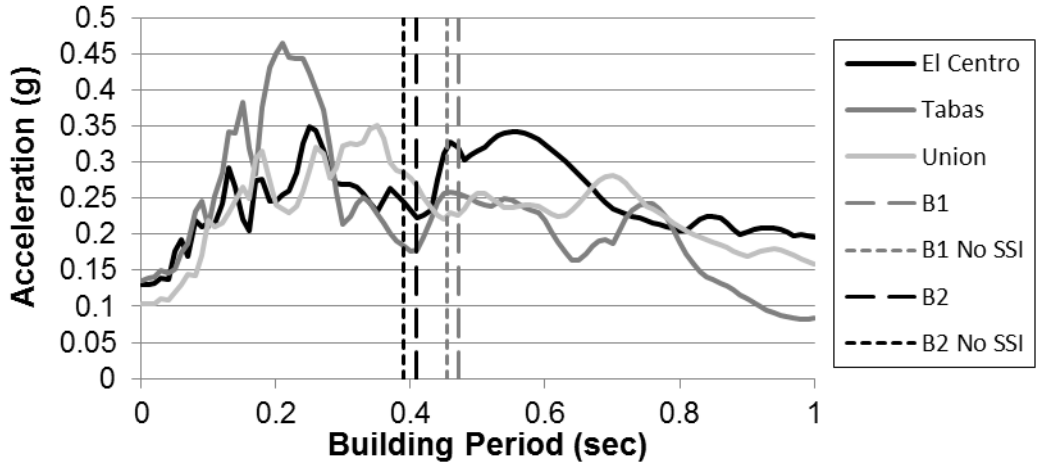

Figure 5.16 Scaled earthquake spectra with modelled building periods. B1 = Building 1. 'No SSI' models use fully fixed foundations (refer Section 6.8).

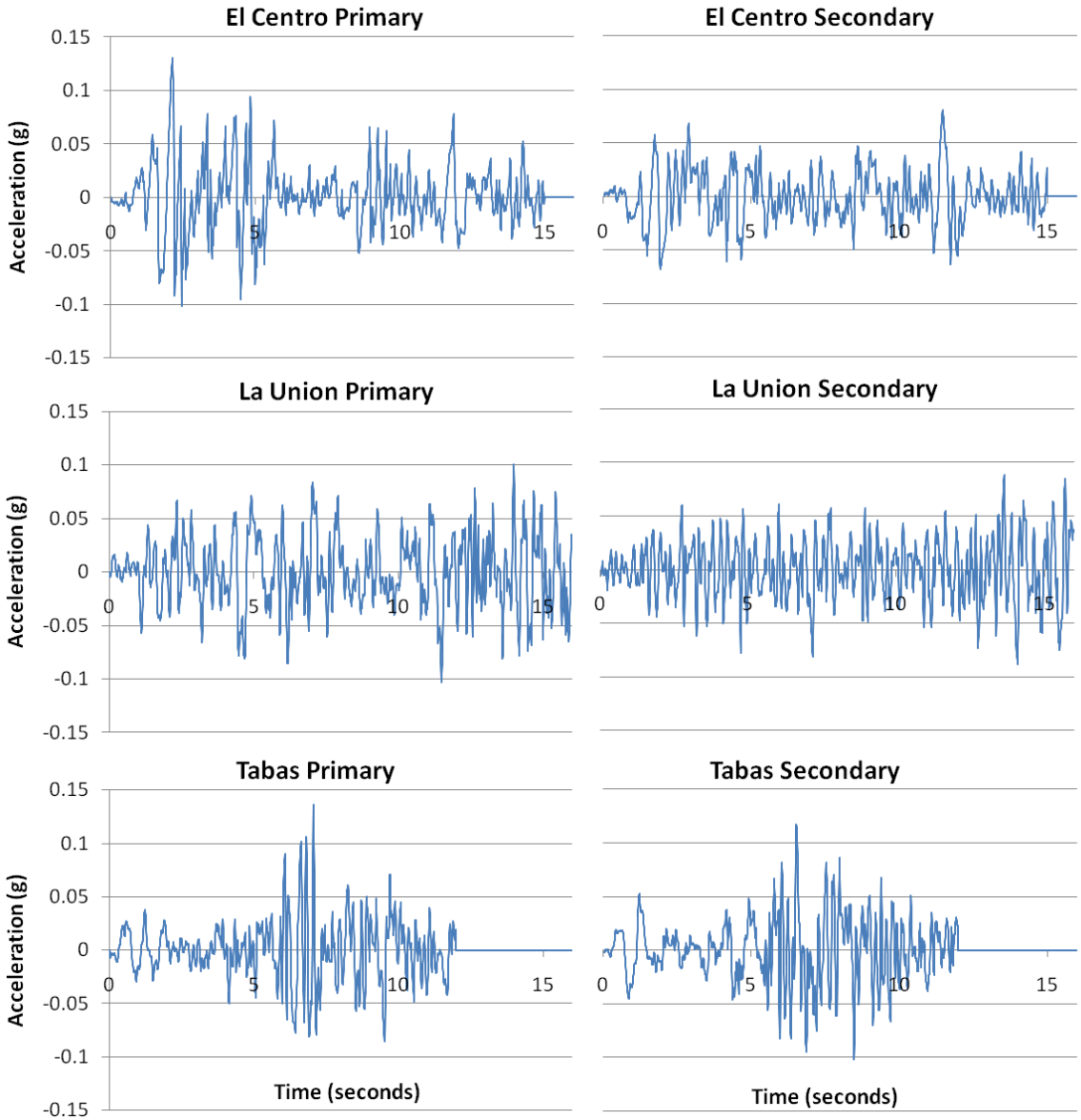

Figure 5.17 Scaled earthquake ground motions used in analysis

5.3 3D Building Modelling

The following sections outline the additional modelling parameters required in 3D and the differences in modelling approach between the 3D and 2D models. If an aspect of the modelling is not covered below, it can be assumed to be the same as described in the 2D modelling section (Section 5.2).

5.3.1 Building layout

Figure 5.18 presents an overview of the building layout for the 3D analyses. Each building's floors and roof are modelled using triangle and quadrilateral finite elements. Figure 5.18 presents the default building configuration used in Chapter 8. Note that the right building (Building 2) is not as long as the left building (Building 1). The building lengths differ by approximately 3 metres and is representative of configurations frequently observed in Wellington.

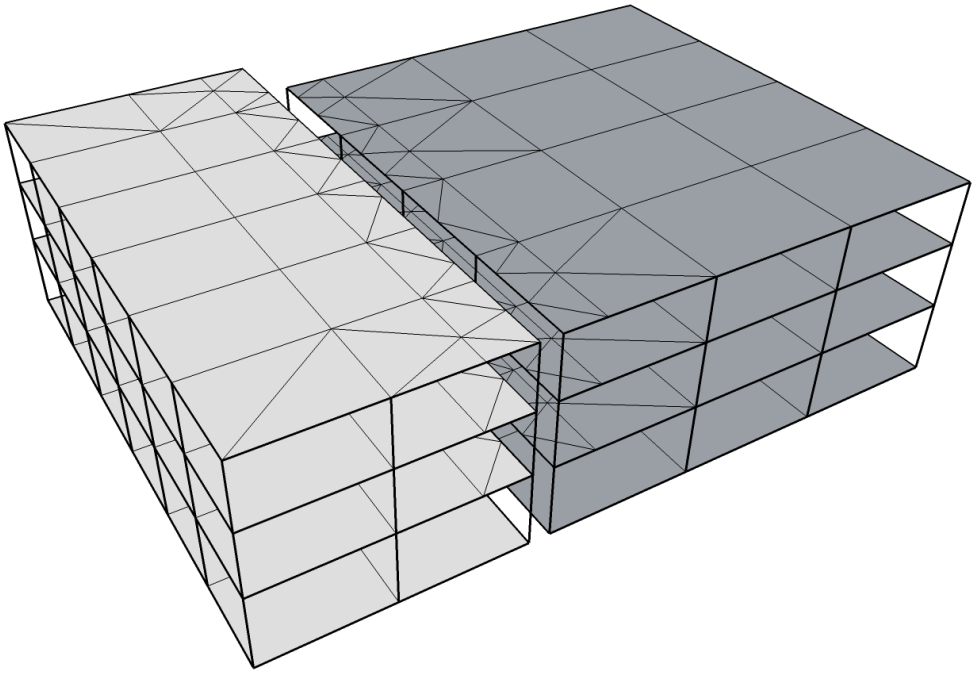

Figure 5.18 3D building pounding layout

5.3.2 Modelling of Floor Diaphragms

The floors and roof of each building are modelled with a combination of finite element triangles and quadrilaterals. These elements provide axial (in-plane) stiffness but do not model any plate (out-of-plane) stiffness. The triangle finite elements are six degree of freedom CST (Constant Strain Triangle) elements while the quadrilateral elements are eight degree of freedom, isoparametric finite elements. These elements do not possess in-plane rotational degrees of freedom. The significance of this property is discussed in Section 7.3.1 and Section 7.4.1. At the ground, 1st and 2nd floor levels, the finite elements are used to explicitly represent the 130 mm concrete diaphragm. At roof level, the finite elements are modelled as 0.5 mm steel. Roof

diaphragm elements are included at this location because no roof cross bracing was present in either building. Not modelling the roofing at all caused unrealistic flexibility along some portions of the wall. In reality sheet metal roofing would be corrugated; however this complication is not considered here.

Triangular finite elements are required due to the layout of the contact elements between the buildings (Figure 5.19). The layout of the finite elements in each building is determined by the locations of columns and beams in that building. However, every node along the building interface requires a contact element connecting it to the corresponding location on the opposite building. Furthermore, elements must be arranged to avoid poorly performing elongated finite elements. In one instance, the two buildings' gridlines are offset by 171 mm. This separation is too small to model with the adopted finite element mesh and is instead dealt with in the manner described for vertical offsets in Section 5.2.5 (Figure 5.7).

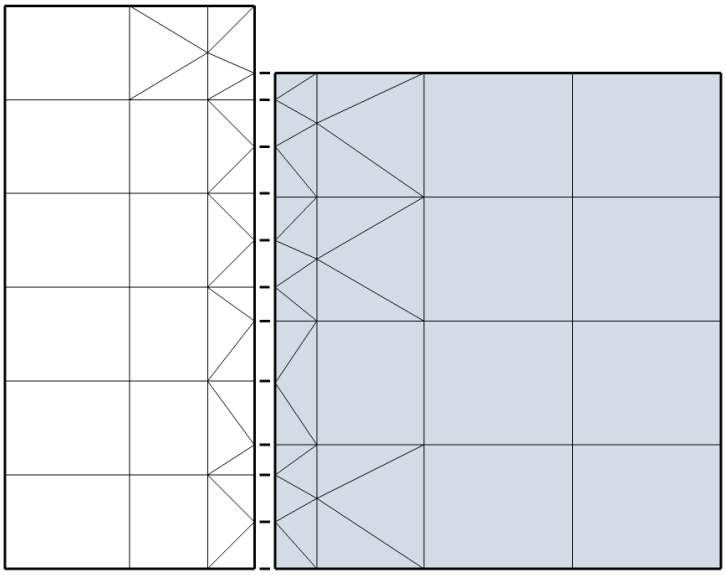

Figure 5.19 Plan view of the finite element layout at floors 1 and 2. Locations of contact elements are indicted with horizontal black lines between the buildings.

The adopted mesh is comparatively coarse. This approach was selected to limit the required analysis computation time, while still providing an acceptably accurate displacement response in each floor. However, a more refined mesh would be required if an accurate representation of in plane stresses was desired.

5.3.3 Soil Structure Interaction

The modelling of soil structure interaction in 3D essentially emulates the 2D approach. No soil structure interaction is modelled in the horizontal plane. In the 2D modelling this assumption is interpreted as not allowing interbuilding axial horizontal soil crushing, while allowing shear soil deformation to occur. This corresponds to the X and Z components in Figure 5.20, respectively.

In the 3D analyses however, the horizontal Y direction SSI component would cause soil shear deformations between the buildings (Figure 5.20). This is analogous to the vertical (Z direction) component. Soil structure interaction is still not modelled in the Y direction despite this contradiction. It is considered that the level of detail this modelling represents is not justified given the known level of crudeness in the adopted SSI model. Furthermore, significant relative horizontal movement of adjacent foundations is not expected and has not been reported in any literature on pounding to date. It must be acknowledged that the interactions shown in Figure 5.20 are only convenient shorthand to describe the interaction between the buildings. In reality, each building's foundations will be affected by many aspects of the neighbouring building. SSI modelling for pounding analyses remains a subject requiring significant future research.

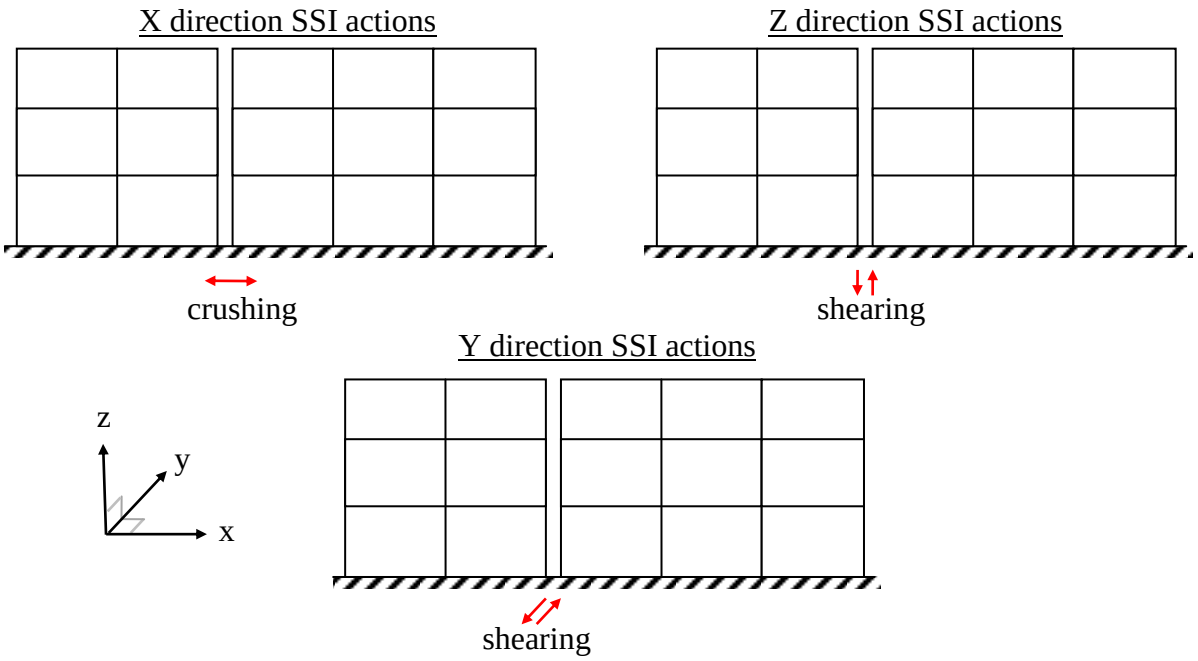

Figure 5.20 Translational components of SSI at the building interface. Only SSI between the two foundations nearest the building interface is shown here (SSI between other foundations is ommitted for clarity).

5.3.4 Modelling Biaxial Member Capacities

No biaxial moment interaction has been modelled in the presented analyses. While biaxial moment interaction was initially intended, it was found to destabilise the analysis solution and significantly increase computation time. As this was not a primary parameter of interest, the model was simplified to prevent these instabilities.

5.3.5 Time step Modifications

As discussed in Section 5.2.4, the adopted time step can be dependent upon the contact element stiffness. The change in contact element stiffness for the 3D models also required adjustment of the analysis time step. A time step of $5x10^{-5}$ seconds was adopted, which resulted in an energy

loss of <1% over the course of the ground motion. This time step is half that adopted in the 2D analyses. The method of assigning contact element stiffness in 3D is presented in Section 7.4.

5.3.6 Hysteresis Modifications

As noted in Section 5.2.7, the flexural-axial (M-N) column interactions were found to introduce error into the 2D analyses. This source of error was removed from the 3D analyses by adopting a different modelling approach. Column flexural capacities were calculated based upon their static axial loading. This approach allowed the columns to be modelled using beam elements within Ruaumoko. While investigating model instability, the columns were further simplified by adopting the same flexural hysteresis as the beams elements (Section 5.2.6). While it is believed that the original hysteresis was not the cause of the instability problems, the beam hysteresis model was kept to guarantee model stability. In most instances, column yield curvatures were found to be suitably predicted by the new hysteresis, so no modification of column ductility was necessary. However, columns with axial loads of less than 50 kN performed in a similar manner as presented for beams in Section 5.2.6. The ductilities of columns with less than 50 kN static axial loading were thus halved before reporting.

Modifications were also made to the way the maximum beam ductilities were recorded within a collision. Roof beam members recorded ductilities of up to 15 in the 3D 'no pounding' analyses. These ductilities greatly exceeded the ductilities reported by other beams. After inspection of the individual elements, it was found that the roof element flexural capacities were approximately one tenth that of the beams located at lower floors. These roof elements do not significantly contribute to the seismic resistance of the frame. Furthermore, these elements are also supported by other elements, such as the building infill, so their catastrophic failure is unlikely. The purpose of reporting ductilities is to provide information on the seismic capacity of the frame. The roof beams are thus disregarded when reporting maximum beam ductility results.

5.3.7 Ground Motion Scaling Modifications

After initial testing, the fundamental periods of the 3D models were found to be outside the initial assumptions made when scaling the ground motions (Table 5.4).

Table 5.4 Recorded periods of 3D building models

Building	*Component*	*Fundamental period*	*Assumed period*	*Change in scaling factor (from 2D)*		
		Seconds	*Seconds*	*Tabas*	Centro	Union
Building 1	*x direction*	*0.662*	*0.4*	*+10%*	-8%	0%
	y direction	*0.573*				
	rotation	*0.665*				
Building 2	*x direction*	*0.488*	*0.4*	*-6%*	-5%	1%
	y direction	*0.449*				
	rotation	*0.452*				

New ground motion scaling factors were calculated for both buildings using their revised periods. As only one ground motion scaling factor can be used in an analysis, only one building's scaling factors could be adopted. Usually this selection would be based upon the building of greater interest. However, since both buildings are of interest in this particular study, Building 1's factors were arbitrarily selected. Use of Building 2's properties change the record scaling by less than 5% for all ground motions except the Tabas record (with 9%). All 3D modelling used both X and Y ground motion components, where the X direction was subjected to the primary component.

Subsequent model changes further adjusted both building's fundamental periods. However, this period shift caused only a 3% change in ground motion scaling. This change was deemed insignificant and was not incorporated into the modelling. The values presented in Table 5.4 show the change in scaling factors from that used in the 2D modelling. A comparison of scaled earthquake spectra and building period is presented in Figure 5.21.

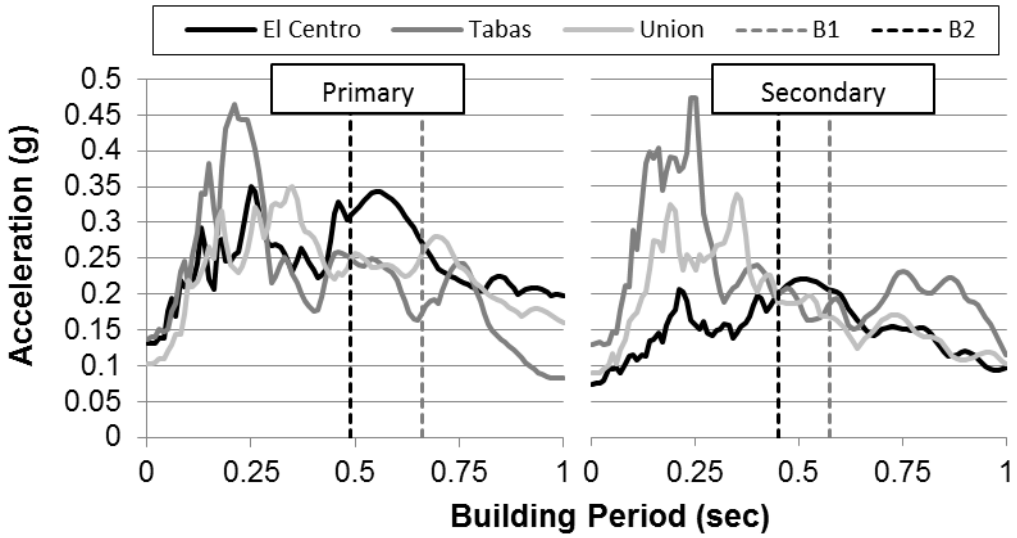

Figure 5.21 Earthquake spectra of ground motions used in 3D modelling. B1 indicates Building 1.

The reported fundamental building periods are larger than is generally expected for three storey buildings. Three storey masonry buildings are usually expected to have periods less than 0.4 seconds. However, the modelling approach adopted here assumes the masonry does not interact with the surrounding concrete frame during an earthquake. These models are therefore more appropriately characterised as Reinforced Concrete Moment Resisting Frames (RCMRF). The approximate empirical formula for RCMRF in the NZSEE building guidelines (NZSEE 1996) predicts a fundamental period of 0.51 seconds for both buildings. Furthermore, some additional period elongation can be attributed to the soil structure interaction. With these considerations, the building fundamental periods fall within expected bounds.

5.4 Conclusions

The following conclusions are drawn from the issues presented in Chapter 5.

1. Many existing low rise New Zealand building configurations present potential pounding risks. To model this risk, two existing Wellington 1960's buildings have been selected for 2D and 3D modelling. Both buildings have masonry infill structural systems.
2. The adopted modelling method requires multiple approximations and assumptions to be made about each building's performance. Some of these simplifications mean the models may no longer accurately reflect the original buildings. However, both buildings are considered to be suitably characteristic of the building type under investigation.
3. Multiple modelling parameters require reassessment when considering pounding. Specifically, the adopted time step and modal damping scheme can significantly influence model predictions. Rayleigh modal damping is not recommended when modelling pounding.
4. Special considerations for ground motion scaling are also required in pounding analyses. When one building is of specific interest, that building's parameters are recommended for scaling the ground motion. In the following 2D analyses, the building's properties which affect ground motion scaling happen to coincide. In the 3D analyses, Building 1's properties have been arbitrarily selected.

Chapter 6 2D Analysis of Floor/Floor Pounding

Related Papers

Cole, G., Dhakal, R., Carr, A. J. and Bull, D. (2012). The influence of pounding on member demands in low rise buildings. *New Zealand Society for Earthquake Engineering Annual Conference (NZSEE 2012)*. Christchurch, New Zealand**:** paper 026.

The effects of the modelling techniques developed in Chapter 4 are now investigated using the detailed 2D model described in Chapter 5. The purpose of this chapter is not to attempt to parametrically characterise pounding. Instead one building configuration is examined in detail to provide further understanding of the factors governing collision. These investigations are also used as a baseline for comparison with analyses performed in subsequent chapters.

6.1 Building Properties

Before presenting results, the expected pounding response is assessed based upon the considerations of previous chapters. Table 6.1 presents the properties of each building's diaphragms that affect post collision velocity. Building 2 is the more massive building and weighs almost twice that of Building 1 at all floors except the roof. At all levels Building 1's axial period is less than Building 2's. Building 1's axial periods therefore determine the collision durations, which range between 0.012 and 0.018 seconds. The fundamental period of Building 1 and Building 2 was recorded as 0.471 and 0.408 seconds, respectively. It is noted that these values lie outside the range assumed when the earthquake scaling was performed (Section 5.2.11). However, the change in scaling factors was found to be minimal (approximately 5%) and was not adjusted.

Table 6.1 Colliding floor properties

	Building 1			***Building 2***			***Ratio***	
Level	***Mass***	***Axial Stiffness***	***Axial Period***	***Mass***	***Axial Stiffness***	***Axial Period***	***Mass***	***Axial Period***
	Tonne	*kN/m*	*sec*	*Tonne*	*kN/m*	*sec*	*-*	*-*
Roof	*22.1*	*284,000*	*0.018*	*17.1*	*182,000*	*0.019*	*1.29:1*	*0.912:1*
Level 2	*44.3*	*1,124,000*	*0.013*	*90.7*	*845,000*	*0.021*	*0.488:1*	*0.606:1*
Level 1	*37.4*	*1,095,000*	*0.012*	*92.8*	*845,000*	*0.021*	*0.403:1*	*0.558:1*

Table 6.1's values are used in the equations presented in Chapter 3 to calculate various collision properties (Table 6.2). Distributed mass values are of interest here since the diaphragm flexibility is explicitly modelled. As previously discussed (refer Section 3.2.2), a higher value for α indicates a larger velocity change due to pounding. The calculated effective coefficients of

restitution are also notable since each floor produces a different value. This shows that the influence of floor flexibility is not consistent between different floor configurations. The roof level is predicted to include secondary collisions (by Equation 3.33).

Table 6.2 Calculated floor collision properties

	Building 1		***Building 2***		***Collision Properties***	
Level	***Lumped Mass α***	***Distributed Mass α***	***Lumped Mass α***	***Distributed Mass α***	***e_{eff}***	***Secondary collisions***
Roof	*0.436*	*0.414*	*0.564*	*0.535*	*0.897*	*Yes*
Level 2	*0.672*	*0.554*	*0.328*	*0.270*	*0.648*	*No*
Level 1	*0.713*	*0.580*	*0.287*	*0.234*	*0.628*	*No*

6.2 Contact Element Properties

Unless otherwise stated, the analyses performed in this section assume perfectly elastic collisions. This assumption allows the effect of diaphragm oscillation to be more directly observed, and avoids the acknowledged uncertainty in the commonly adopted values of coefficient of restitution (and plasticity index). However, it is acknowledged that this approach will introduce more error into the performed analyses. In order to gauge the effect of this assumption, element damping is investigated later in the chapter.

6.3 Testing Schedule and Naming Conventions

Within this chapter, the following naming convention is used to identify tests:

[*Earthquake record*] [*Earthquake direction*] [*Separation (mm)*]_[*Test*]

The possible values for these fields are presented in Table 6.3. The five tests are:

1. *1xPGA* – 'Default' test using the 1/25 year PGA described in Section 5.2.11. [Section 6.6]
2. *2xPGA* – Test using twice the above PGA for the input excitation. [Section 6.7]
3. *NoSSI* – Testing with foundations fully fixed (i.e. no Soil Structure Interaction) [Section 6.8]
4. *DAMP* – Testing using contact inelasticity, using the method described in Section 4.7. [Section 6.9]
5. *LUMP* – Testing using lumped mass diaphragms (i.e. no axial diaphragm oscillation). [Section 6.10]

If the separation field is stated as NC, then sufficiently large separations were set to ensure no pounding occurs in the record. Earthquake direction is recorded because directivity can significantly affect the response of pounding buildings (Dimitrakopoulos et al. 2009b). Earthquake direction is reversed in Ruaumoko by applying a negative scaling factor to the ground motion. For symmetric buildings, reversing the earthquake direction is equivalent to reversing the building order.

Table 6.3 Values used in Chapter 6 test names

Earthquake record	*Earthquake direction*	*Separation (mm)*	*Test*
EL (El Centro)	*+*	*NC*	*1xPGA*
TA (Tabas)	*-*	*0 - 20*	*2xPGA*
UN (Union)			*NoSSI*
			DAMP
			LUMP

6.4 Global Damage vs. Local Damage

As previously discussed (refer Section 2.5.7), pounding can cause local damage and global damage. As this definition is used throughout the remainder of the dissertation, the definition is restated here. *Global building damage* describes the damage of elements that are not directly impacted during a collision. Examples of global damage include interstorey shear, beam ductilities and floor displacements. In contrast, local damage deals with forces that are directly caused by the impact. *Local damage* includes; impact force, impacted column shears (in floor/column collision), and impacted floor accelerations.

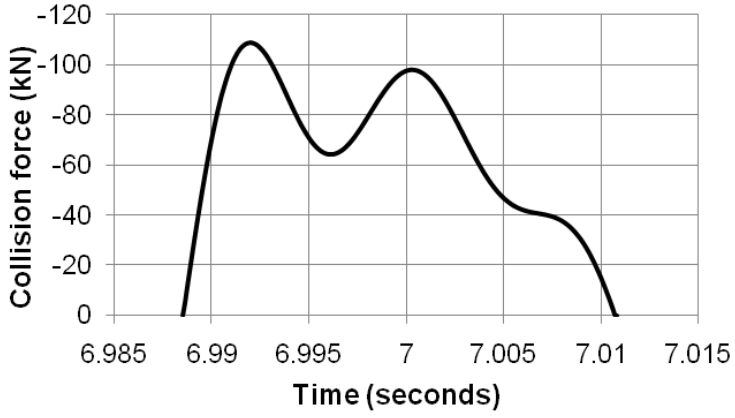

Figure 6.1 Roof level collision in TA+10_1xPGA

The relationship between these two forms of damage is investigated below by examining the forces within each building before, during, and after a single collision. The *TA+10_1xPGA* record is selected for this examination since its first collision occurs only at the roof level, which allows the effects of a single level's collision to be isolated. The first collision occurs

approximately seven seconds into the record and its collision force response is shown in Figure 6.1.

Figure 6.2 shows both building's horizontal forces during an instant of *TA+10_1xPGA* (diaphragm members display axial forces, while column members show shear forces). The presented forces were recorded at 6.987 seconds, just before the first collision takes place. The figure also shows the displaced shape of the buildings at 6.987 seconds. Displacements have been magnified 30 times to effectively illustrate these deformations.

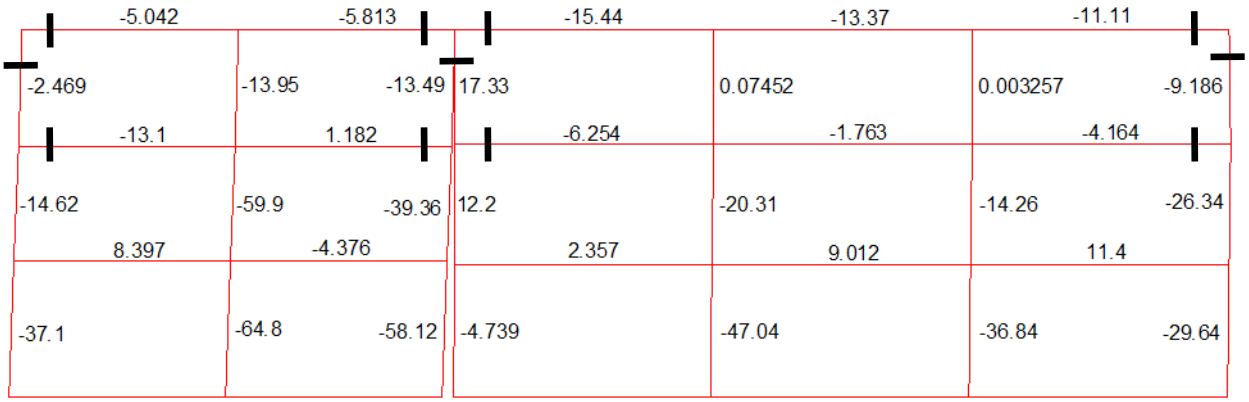

Figure 6.2 Horizontal member forces at 6.987 seconds (kN). Black rectangles indicate record points

Significant differences in column shear force are observed between adjacent columns within the same floor and building in Figure 6.2. This is primarily due to the static gravity load acting on the system. Up to 15 kN of beam/diaphragm axial load was also observed at this time. This is partially due to the static loading, and partially due to the differing stiffness between the external and internal columns.

Figure 6.3 shows the response of the 12 recorded locations throughout the course of the collision. Two points are considered in each building. The black line indicates the node nearest to the collision interface in the stated floor of the stated building, while the grey line indicates the node furthest from the collision interface. Each of these points has two series. The solid line represents *TA+10_1xPGA*, while the dashed line represents *TA+NC_1xPGA*. During collision (between the vertical dashed lines), the collision force primarily affects the roof diaphragms where the collision takes place. A small amount of load is also transferred to Level 2 of the buildings. This load is transferred through the columns and occurs over a significantly longer time than the collision duration. This process shows that while local damage (such as the force in the colliding diaphragms) and global damage (shear and flexure loadings in columns and beams) are related, this relationship is complex. It is therefore expected that factors that are significant to local damage may not be significant to global damage, and vice versa.

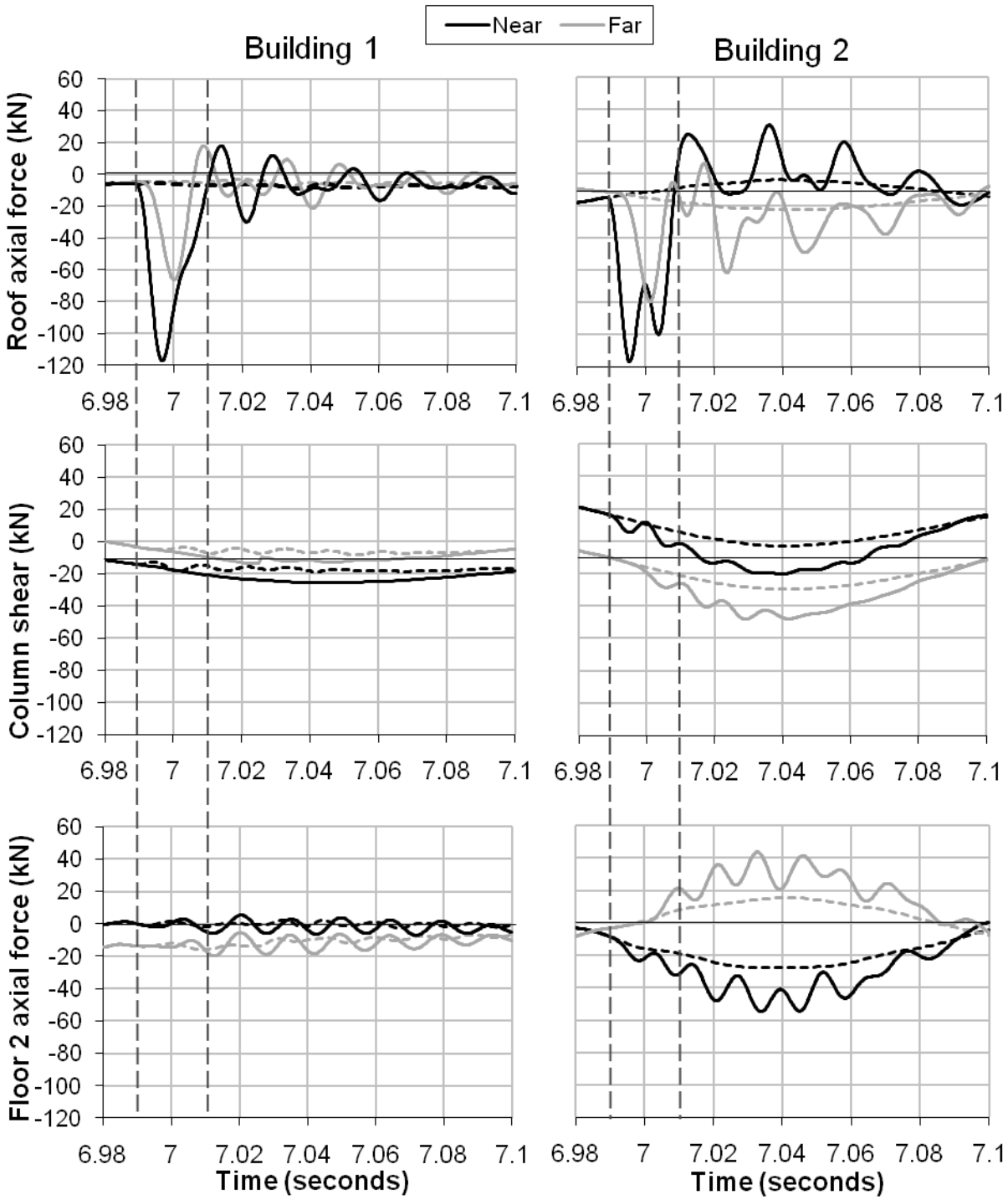

Figure 6.3 Effect of roof collision on building elements. Solid line: response with collision. Dashed line: no collision response. Vertical lines, beginning and end of collision.

6.5 Detailed Inspection of Pounding Records

While later sections present results based on record maxima and minima, a better understanding may be achieved by inspecting a few records in detail. Two records are considered here, El Centro with a sufficient gap to prevent any pounding (*EL+NC_1xPGA*), and El Centro with 5 mm separation (*EL+05_1xPGA*). Figure 6.4 presents five seconds of the displacement response of Levels 1, 2 and 3. These displacements were recorded at the nodes located at the building

interface (i.e. the nodes located nearest to the adjacent building). Effects occurring outside the presented five seconds are discussed in the body text where appropriate.

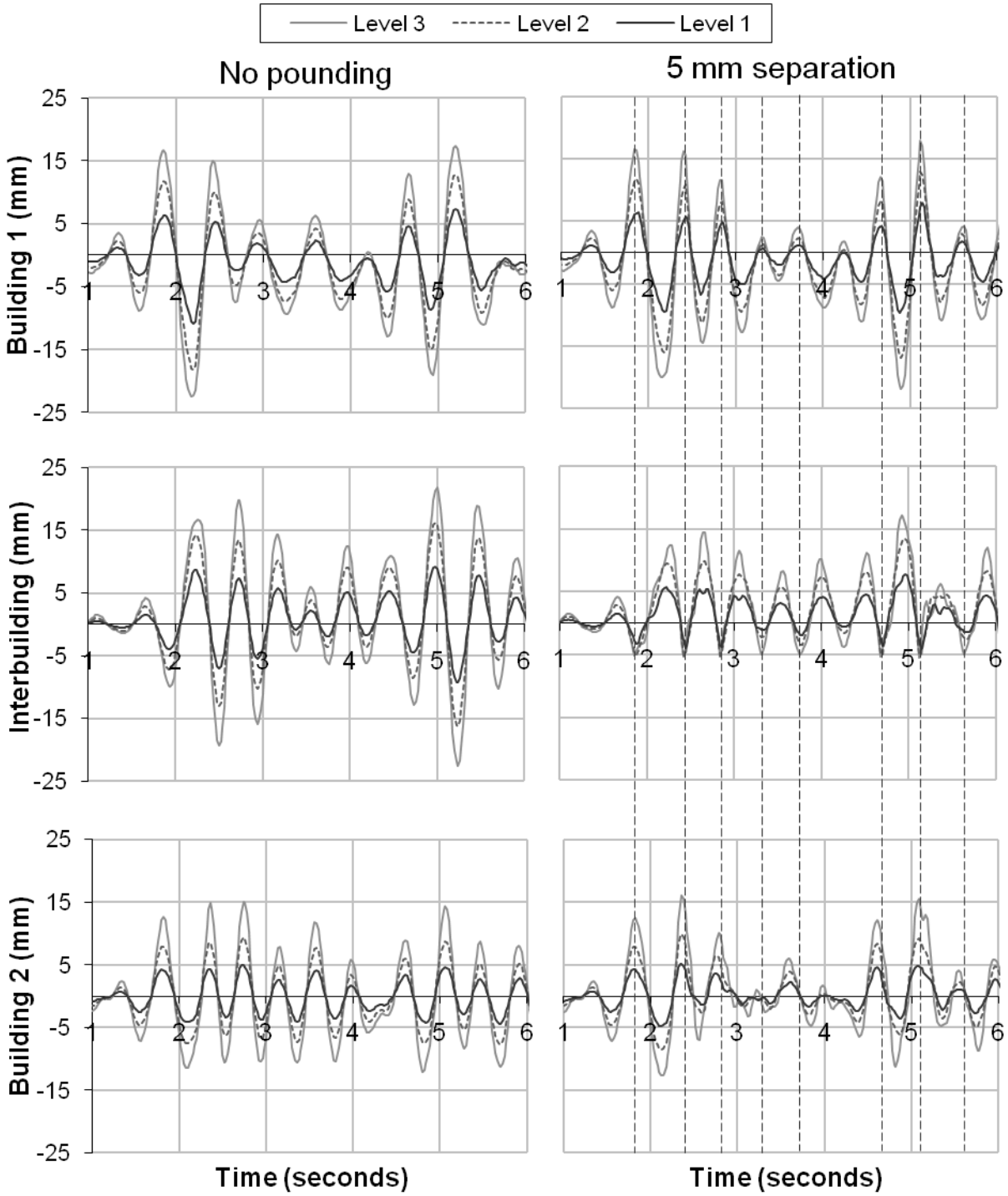

Figure 6.4 Displacement records for EL+NC_1xPGA and EL+05_1xPGA. Dashed vertical lines indicate collision

The displacements in Figure 6.4 are presented for each building. The interbuilding displacements are also presented, and are found by subtracting the displacement of a level in Building 1 from the corresponding level in Building 2. The no pounding case is considered first. Building 1 and Building 2 respond in a similar manner, both are dominated by their first mode with roof

deflections of roughly 15 mm. The first mode can be identified by observing that the lower floors are displacing in the same pattern as the roof, with lower magnitudes.

The interbuilding displacements show all three floors achieving displacements that are less than -5 mm. This could suggest that all three floors will collide in the test using 5 mm separation; however, *EL+05_1xPGA* records show no collisions at the first floor. This is due to the change in displacement response of the higher floors (collisions are indicated with dashed vertical lines). Collision times are observable in the interbuilding results of *EL+05_1xPGA* when a displacement of -5 mm or less is achieved. In the figure, the time between collisions is highly regular (approximately 0.45 seconds). However, this regularity disappears when the excitation intensity reduces later in the record. Both buildings still vibrate predominantly in their first mode. This is unexpected since applying a large force at roof level would usually excite higher building modes.

Comparison of the two records shows a remarkable similarity in displacement response of Building 1 despite the effects of pounding. Large amplifications of Building 1's displacements occur at approximately 2 and 5 seconds in both records. Building 2 presents more sensitivity, particularly between 3 and 4.5 seconds. This response does appear to conflict with the predictions of pounding susceptibility made in Table 6.2 (recall that larger values of α indicate greater susceptibility to pounding). However, one record does not provide sufficient data to draw meaningful comparisons on this issue.

Collision force profiles for Level 2 and Level 3 (the roof) in test *EL+05_1xPGA* are presented in Figure 6.5. The left column of the figure presents the recorded collision force and duration, while the right column scales these values using the theoretical collision force and duration (Equations 3.30 and 3.25, respectively). The agreement between theoretical and recorded collision force magnitudes is very favourable, despite the wide range of these values (theoretical collision force magnitudes are equal to -1 on the dimensionless plots).

Figure 6.5 shows that Level 2's collision forces are more than twice that of the Level 3 forces. This is because significantly more mass and stiffness is present at Level 2 (refer Table 6.2). The lower mass and axial stiffness commonly present at the roof level in low rise buildings may be a significant mitigating factor when pounding occurs. Smaller roof masses reduce the momentum in a collision, while lower floor stiffnesses increase the duration of the collision. Both these effects reduce the magnitude of the collision force. It is possible that the effect of pounding may be overstated in Section 4.3 for buildings of this type of configuration. However, further

investigation into typical building roof configurations would be necessary to quantify these effects.

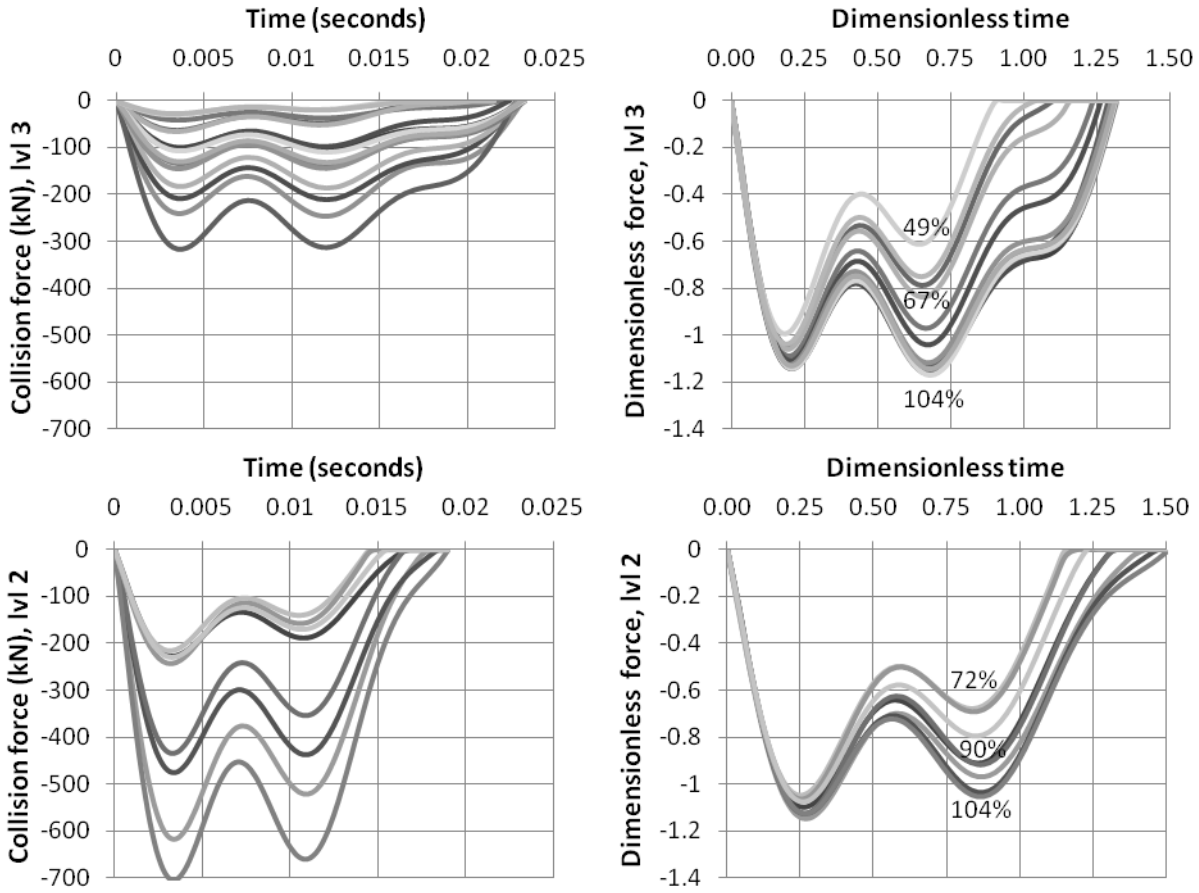

Figure 6.5 Collision force profiles for EL+05_1xPGA. Left: unscaled. Right: scaled. Top: Level 3 collision. Bottom: Level 2 collision. Data labels report percentage of theoretical impulse over collision duration.

As stated in Table 6.2, evidence of secondary collisions should be present at Level 3, but not Level 2. This does appear to be reflected in Figure 6.5. Level 3 force profiles show three oscillations within the force profile, while the Level 2 profiles show just two distinct peaks. The dimensionless time scaling shows Level 3's collision duration lasting to approximately 1.25, when a value closer to 2.0 is expected (refer Figure 4.10). Furthermore, Level 2's dimensionless collision duration lasts consistently longer (1.5) that Level 3's collisions. However, the force profiles are similar to that observed in the two element model in Figure 4.13 (the currently considered model shows collision between a two-element and a three-element diaphragm), so this effect could be reduced if further diaphragm elements were used. It is expected that more diaphragm elements would increase the collision duration at Level 3 and decrease the collision duration at Level 2 due to the more accurate representation of distributed mass collision.

Finally, the scaled plots in Figure 6.5 also state the recorded impulse of certain collisions. Values are presented as percentages of the theoretical impulse. Recorded impulse is calculated by integrating the force history over the duration of the collision, and ranges from 49% to 104% of

the theoretical values. These values are considered lie within expected bounds. The lower impulse values show evidence of negative accelerations (see Section 3.1.3), which are not considered in the theoretical calculations. Level 2 and Level 3 both record up to 104% of theoretical impulse; however, larger values are more frequently recorded at Level 3 (half recorded collisions >100% theoretical impulse) than Level 2 (one quarter of recorded collision >100% theoretical impulse). This may be taken as a further indication of secondary collisions occurring at Level 3, although it is acknowledged that this evidence only is far from conclusive.

6.6 Effect of Building Separation and Input Record

The influence of the input excitation is investigated using the *1xPGA* model defined in Section 6.3. El Centro, Tabas and Union records are applied in positive and negative directions for the following separations; NC, 0, 5, 10, and 15 mm, where NC refers to the no contact model. In total, thirty models were run. Comparisons between different excitations are assessed in terms of displacement, shear, ductility and collision force response below. The best means of presenting these results is also investigated in these sections.

6.6.1 Displacement Response

The displacement envelopes of each building for all thirty records are presented in Figure 6.6 to Figure 6.8. The horizontal axis presents the deformation in millimetres, while the vertical axis displays the height in meters. The heights of each storey are indicated with markers. Comparing building displacements between earthquake records demonstrates how complex pounding processes can be. The only reasonably consistent pounding result is that positive (right) displacements of Building 1 are deamplified. All other displacement envelope results are highly dependent upon both the excitation record, and its direction of amplification.

Consistent trends related to increasing building separation are also difficult to identify. While 0 mm building separation usually causes the greatest deviations from the NC results, this is not the case for *UN+_1xPGA* records (Figure 6.8). It is also observed that multiple records predict displacement amplification for some building separations, but displacement deamplification for other separations (for example, B2TA+ in Figure 6.7).

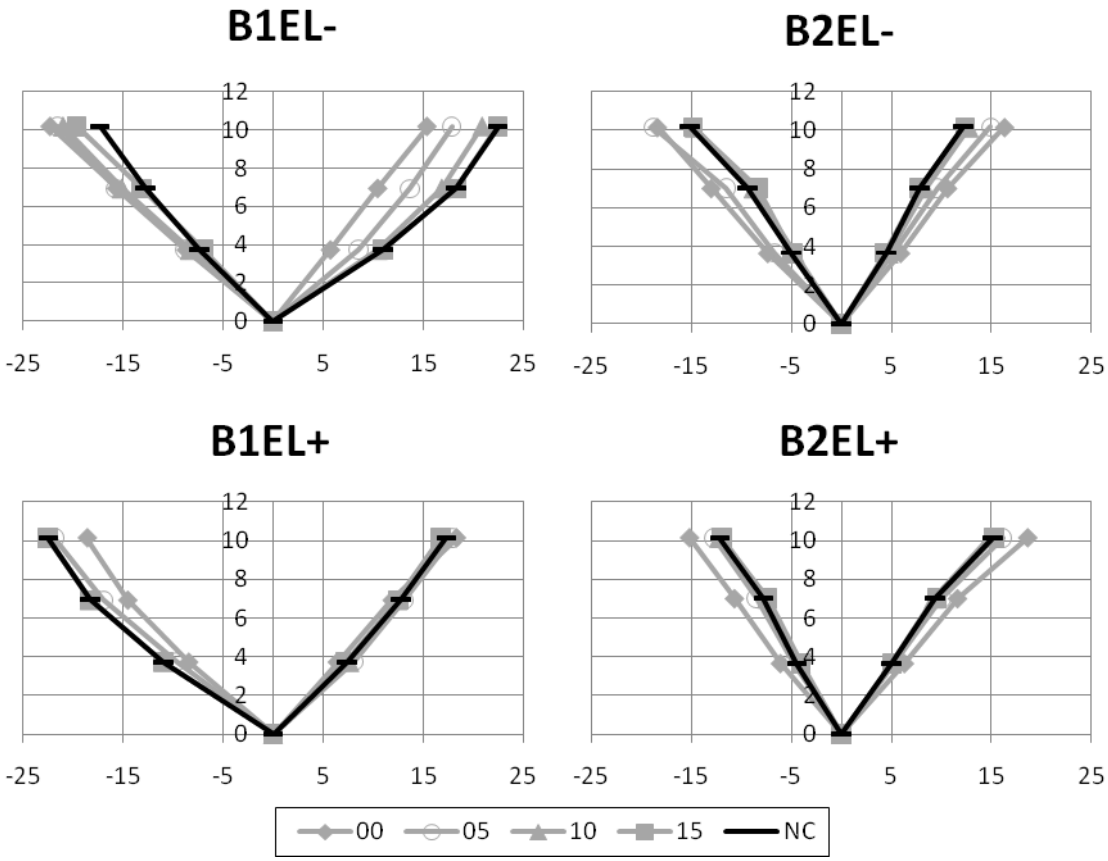

Figure 6.6 El Centro displacement envelopes. Horizontal axis: deformation (mm). Vertical axis, height above ground (m). Left: Building 1 (B1). Right: Building 2 (B2)

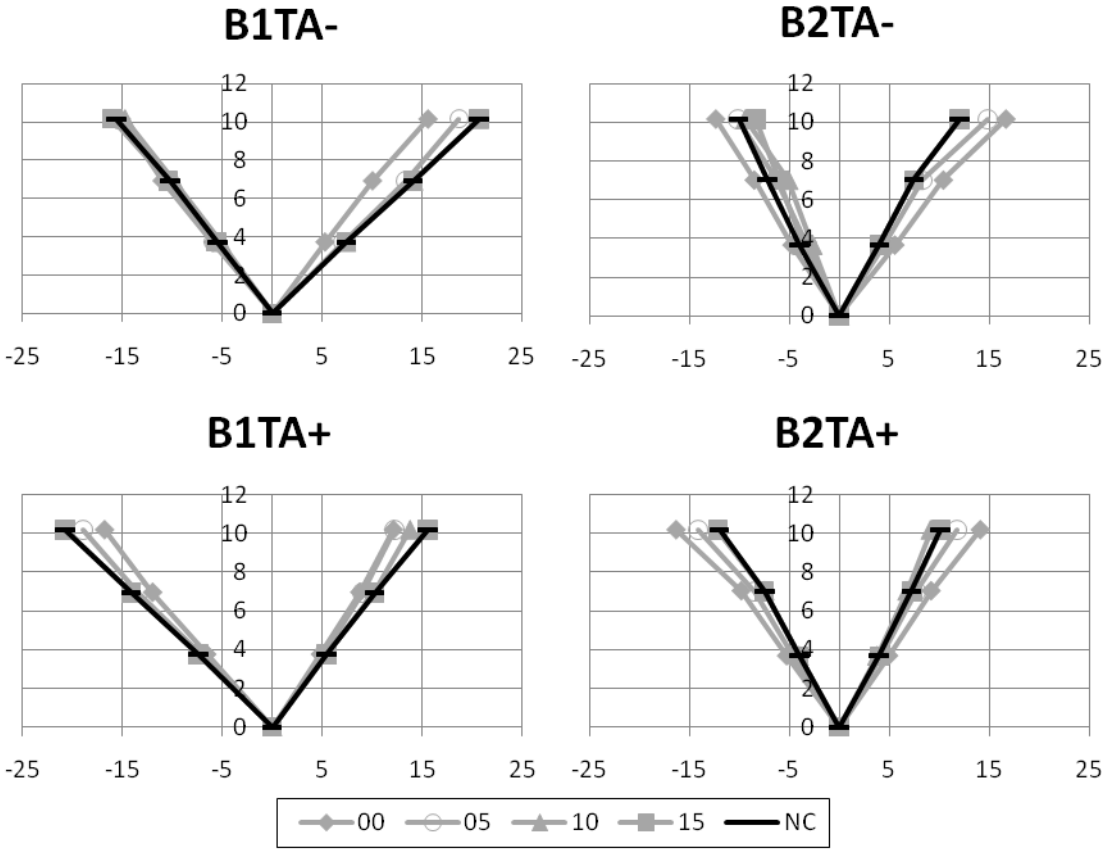

Figure 6.7 Tabas displacement envelopes. Horizontal axis: deformation (mm). Vertical axis, height above ground (m). Left: Building 1 (B1). Right: Building 2 (B2)

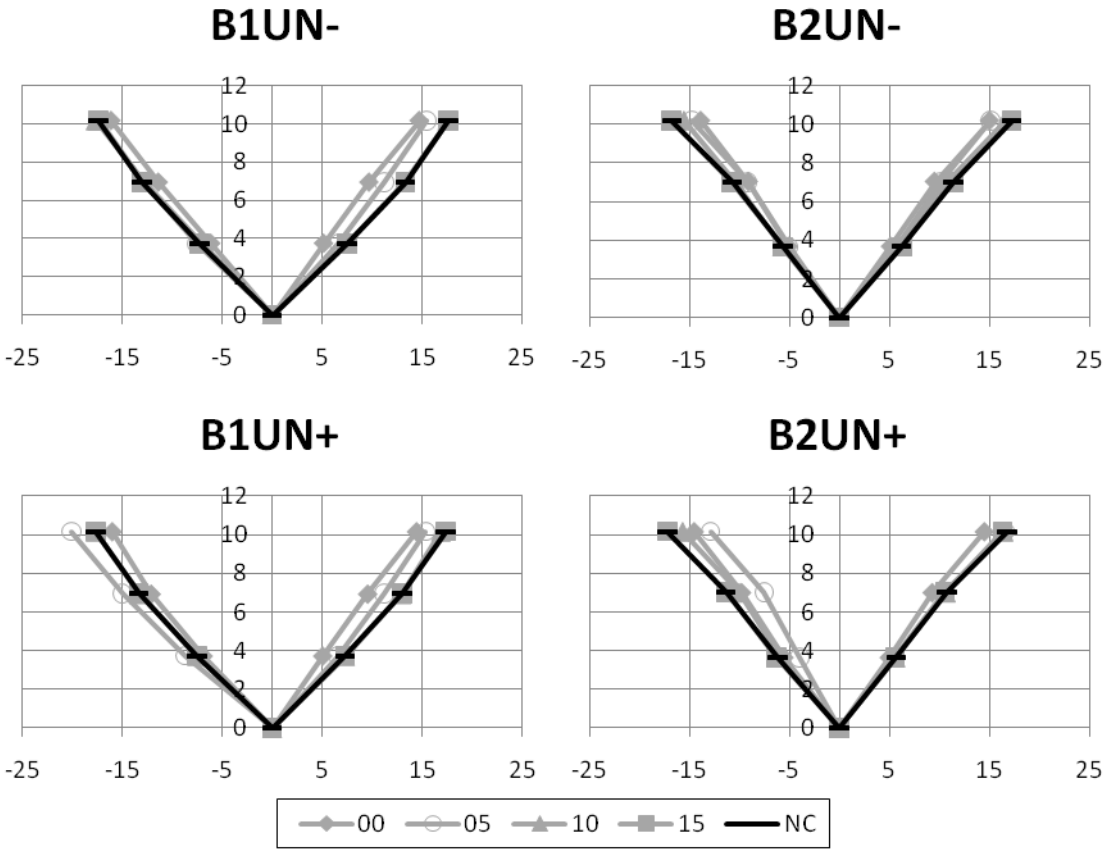

Figure 6.8 Union displacement envelopes. Horizontal axis: deformation (mm). Vertical axis, height above ground (m). Left: Building 1 (B1). Right: Building 2 (B2)

In an attempt to gain further understanding from these results, some basic data manipulation was performed. Previous researchers have typically presented results that have been normalised by the NC deflections. As discussed in Section 2.4.1, Dimitrakopoulos et al. suggested an alternative non dimensionalisation method and used it to great effect on SDOF pounding analyses. Each of these modelling methods is considered in turn.

Displacements are first normalised by the no contact deflections. Presentation of this data uses four displacement envelopes; B1Left, B1Right, B2Left and B2Right (Figure 6.9). These envelopes correspond to left and right deflection of Building 1 and Building 2 respectively. Figure 6.10 presents normalised displacement results for these envelopes. Values less than 1.0 indicate a deamplification due to pounding, while values greater than 1.0 indicate amplification. Pounding can be seen to change the recorded displacement envelopes by up to ±50%. However, these amplifications are highly dependent upon the input excitation. All levels are affected by pounding to approximately the same extent. The normalisation of recorded displacements by the NC displacements is advantageous since it provides more direct information on the parameter of interest (i.e. does pounding amplify the response?). The disadvantage of this method is that four graphs are required to show the four displacement envelopes (two per building) for each record.

In comparison, the raw data could be presented on two graphs per record. The normalised displacements could be simplified by reporting only the maximum absolute deflections of each building. However, more detail is presented here to provide a more thorough overview of the results.

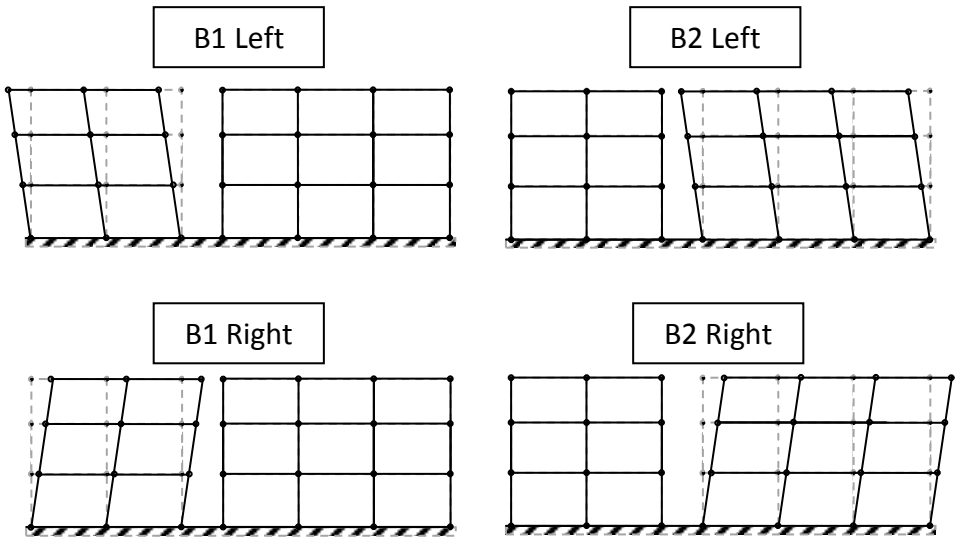

Figure 6.9 Definitions of building envelope labels

The dimensionless displacements are presented in Figure 6.11. The horizontal axis presents Π_u, as defined in Equation 2.32 and Equation 2.33. The advantage of this data transformation in SDOF systems is *self-similarity* (for a given set of dimensionless numbers, the reported results are constant). These dimensionless numbers depend upon the model configuration, and properties of the applied excitation. However the detailed model presented here (Figure 6.11) shows different displacement profiles for different directions of earthquakes, despite their identical dimensionless numbers. This break from self-similarity is attributed to the assumption that an entire ground motion record can be modelled as a single wave pulse (see Section 2.4). It is considered that the dimensionless values proposed by Dimitrakopoulos are not suitable for the modelling presented here. This is because dimensionless presentation requires more data manipulation and this manipulation actually produces results that are more difficult to interpret (compared to Figure 6.10). It is also likely that little application for the dimensionless numbers approach will be found in multi degree of freedom systems, due to the high number of parameters that would require dimensionless characterisation.

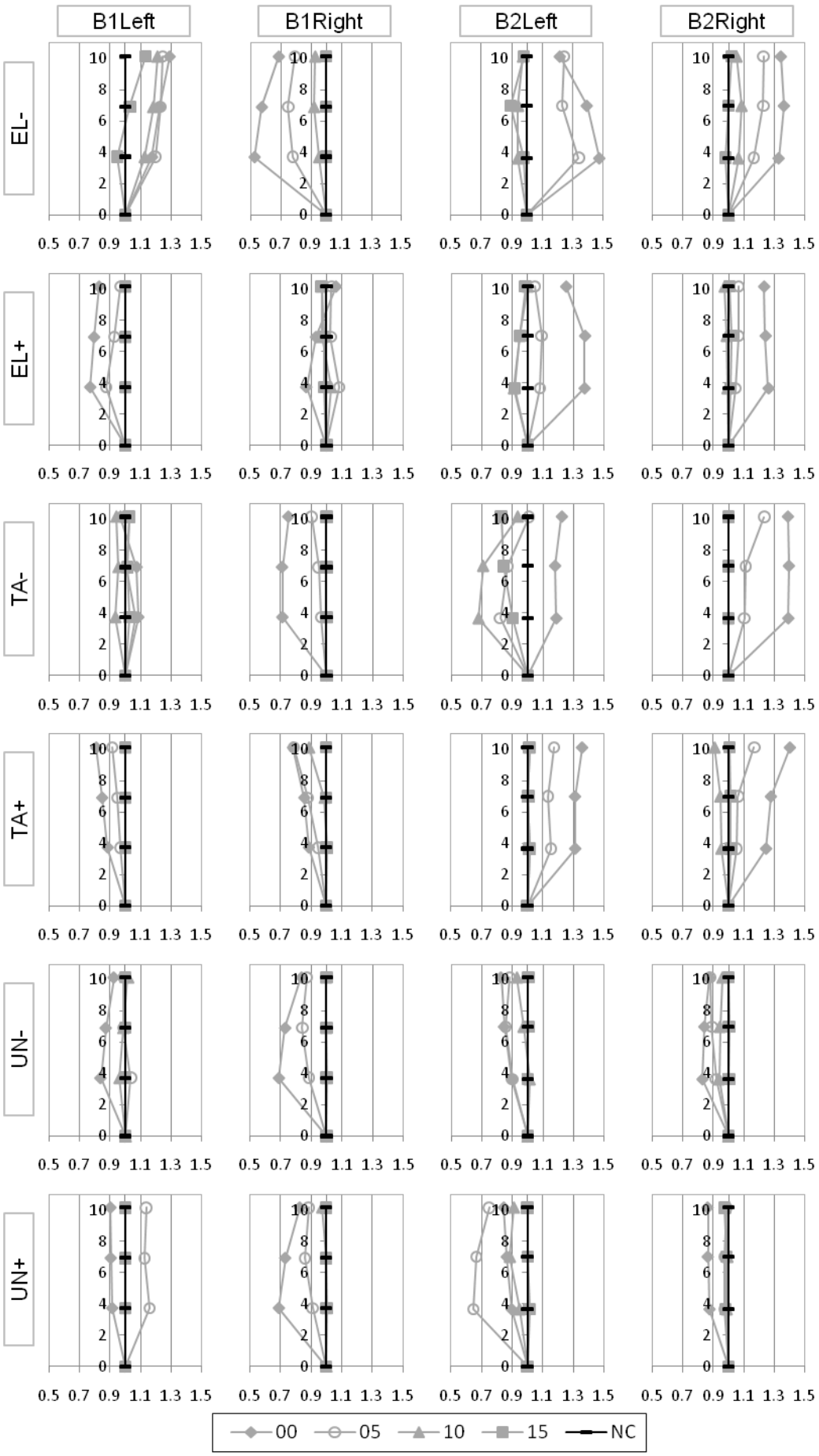

Figure 6.10 Normalised displacements. Vertical axis: height (m). Horizontal axis: displacement/NC displacement.

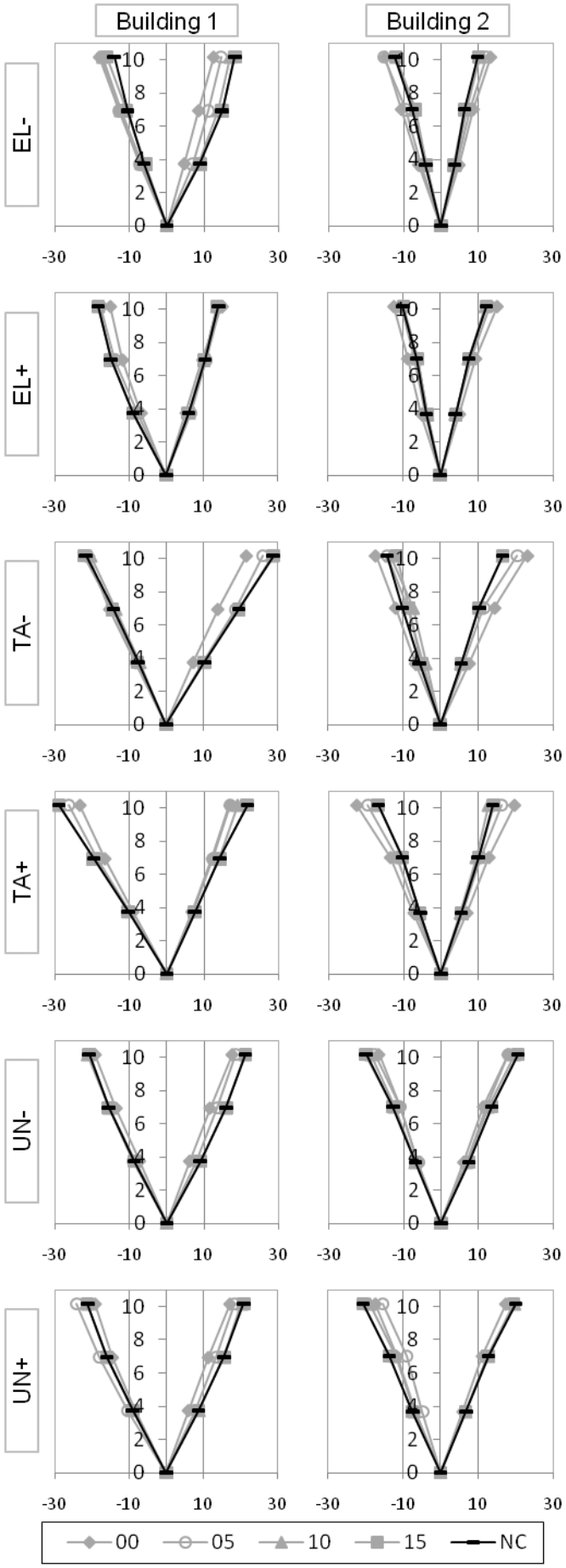

Figure 6.11 Dimensionless displacements. Vertical axis: height (m). Horizontal axis: Dimensionless displacement, Π_u.

Finally, an alternate presentation method for the normalised displacements is used to assess the effect of building separation. Figure 6.12 presents the displacement envelope for negative (left) deflection of Building 2 at Level 2 (i.e. deflection towards Building 1). The record and deflection location was selected since it shows the most displacement sensitivity to the specified building separation. Building separation can be observed to significantly affect the recorded displacement if the results from an individual earthquake records are compared. For example, consider the TA- record; at separations of 0 mm and 10 mm, the maximum recorded displacement is 117% and 70% that of NC, respectively. However, if all available records are considered at once, the influence of building separation is much less pronounced.

The variation between records is investigated further by comparing the zero separation (00) case with the NC case across all displacement envelopes, and at all three floor levels (Figure 6.13 to Figure 6.15). These displacements have been normalised by the average of the NC results. Consider the maximum value of the NC displacements compared to the maximum 00 separation case for any displacement envelope. Only three envelopes across all the presented results record a maximum displacement for the 00 case that exceeds the NC case by more than 10%. Meanwhile, the differences between individual NC records differ by at least 20%. These observations suggest that building displacements are more sensitive to the selected earthquake record than the occurrence of pounding, even though the records were scaled to maintain a constant Peak Spectral Acceleration (PSA) in the buildings. Naturally, these results are only valid for the considered building configuration. Further testing would be necessary to determine whether this trend is generally applicable to buildings that experience pounding.

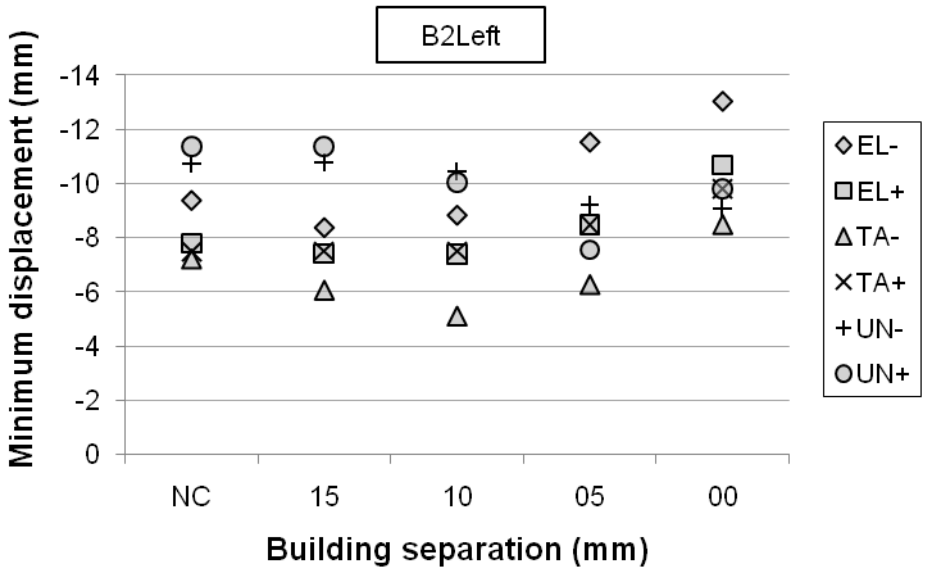

Figure 6.12 Level 2 negative (left) building deflection

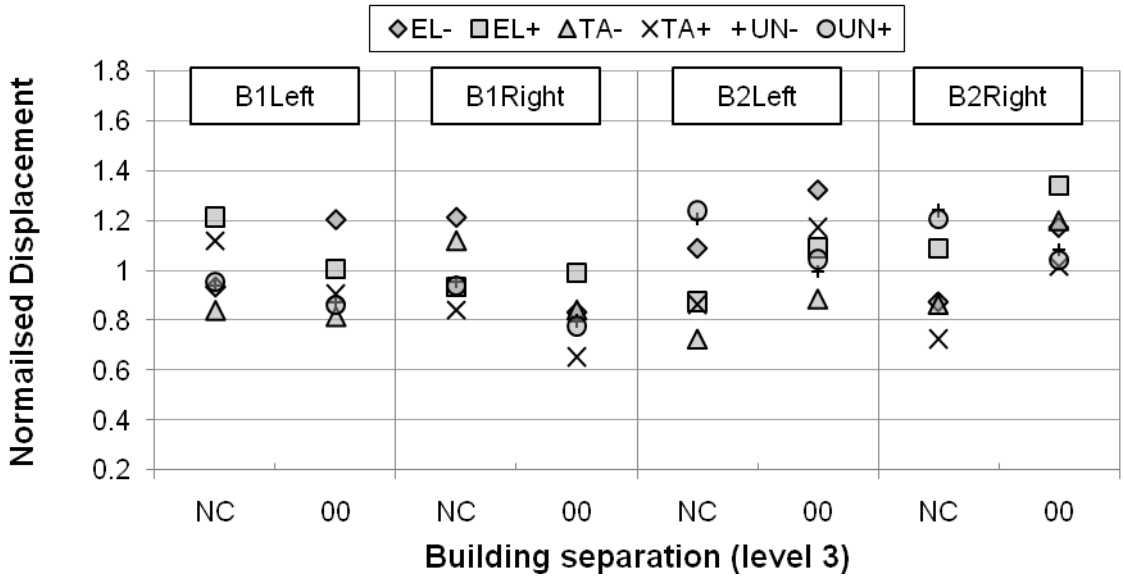

Figure 6.13 Level 3 normalised deflection envelopes

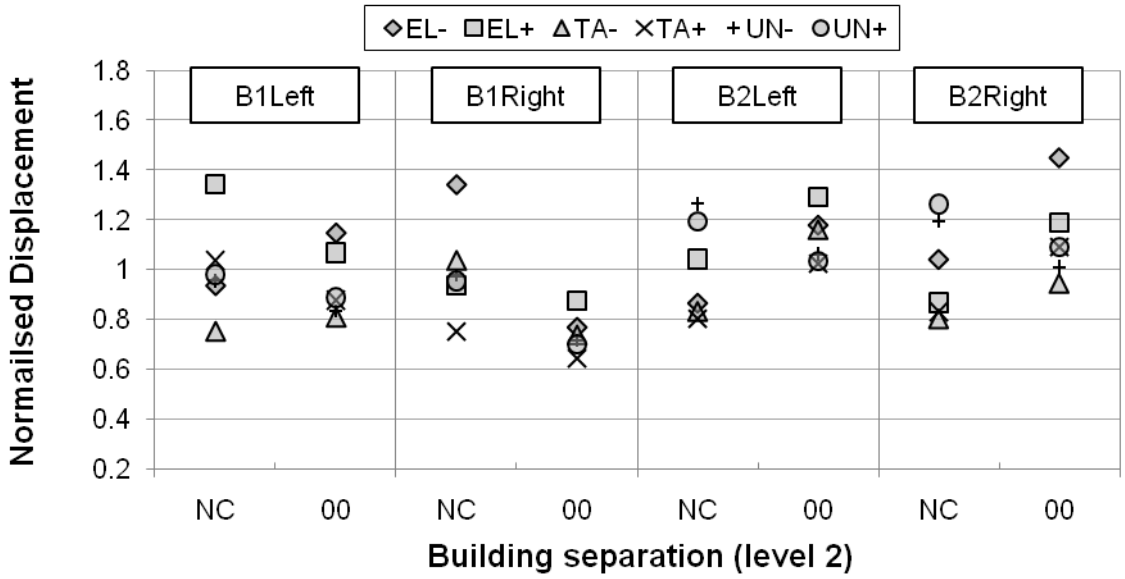

Figure 6.14 Level 2 normalised deflection envelopes

Figure 6.15 Level 1 normalised deflection envelopes

6.6.2 Shear Force and Curvature Ductilities

Attention is now directed to measures of global building demand (refer Section 6.4). Interstorey shear force is considered first since it is more easily characterised. While displacements have been reported in terms of left and right envelopes, shear values are reported using only the total maximum magnitudes. This is done since column shear demands are not direction specific, and presentation of this form reduces the amount of data. Figure 6.16 displays sample shears for the EL- record.

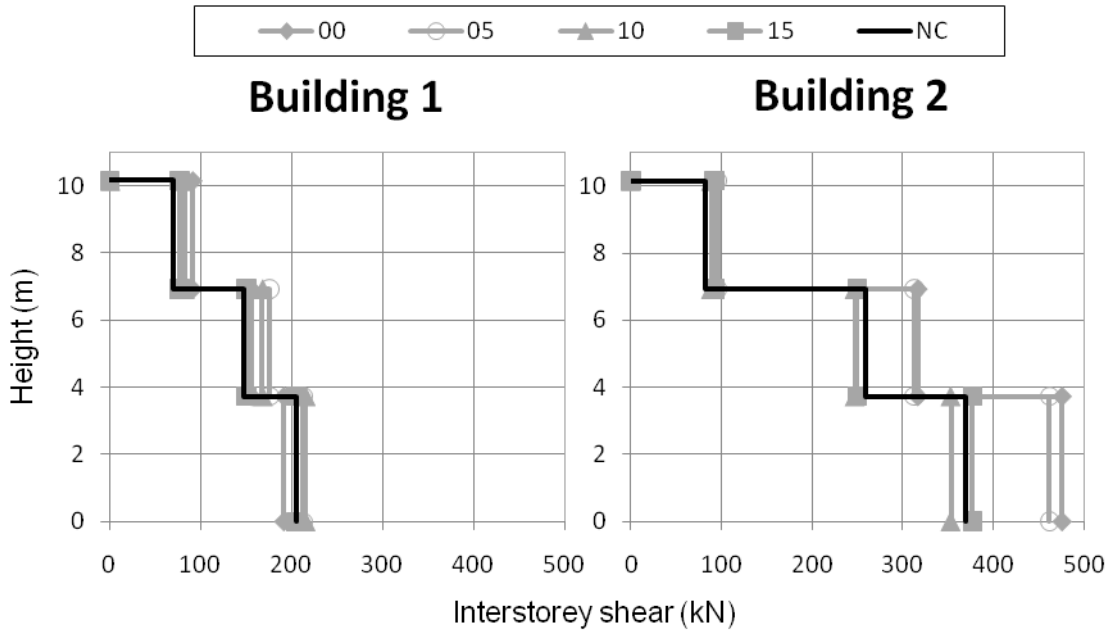

Figure 6.16 Maximum recorded shear forces for EL- record

The effects of pounding are very different between the two buildings. Building 1 is marginally affected, while Building 2's base shear increases by approximately 25%. Furthermore, Building 1's shear sensitivity is approximately constant at all three floors, whereas Building 2's sensitivity is much more pronounced at the lower levels. A normalised shear amplification summary of all thirty records is presented in Figure 6.17. In these plots, the amount of building separation is not identified. All shear magnifications are shown on a single plot of each building in order to view the range of shear magnifications. While the maximum normalised displacement magnifications (Figure 6.10) are larger than that of the shear magnifications, comparison of averaged values reveals more sensitivity within the shear results. On average, both buildings' roof shears are magnified by 10%. A maximum shear amplification of 35% was recorded. The general trends of these amplifications are consistent with the descriptions of Figure 6.16 (which considered only the EL- ground motion).

The suitability of building displacement as a predictor of global damage is assessed in Figure 6.18. Here the horizontal axis presents the maximum displacement amplification of one level of one building, while the vertical axis shows the corresponding level shear amplification (amplifications are normalised by their respective NC values). 0 and 10 mm separations of all six ground motions are included in the figure. No strong correlations are present (correlation coefficients range between 0.31 and 0.84). Displacement envelopes are thus useful for understanding the response of each building but do not provide meaningful information on the amplification of global building demands. Level 1's displacements are not directly proportional to Level 1's shears since some inelastic action in these columns has occurred.

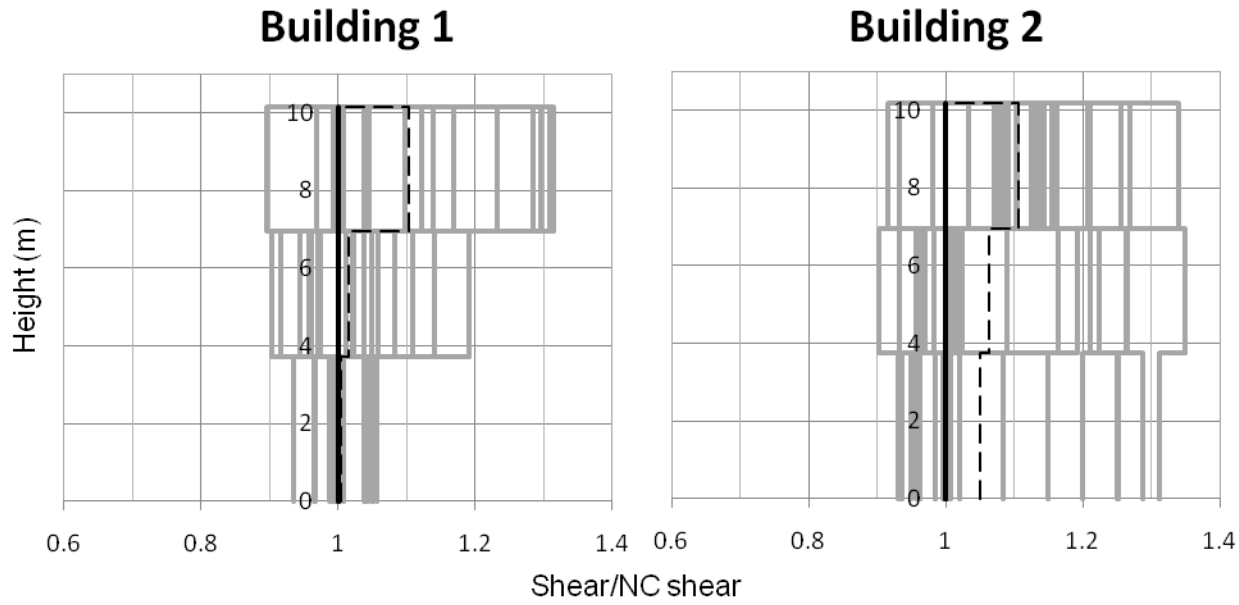

Figure 6.17 Normalised shear demand. Mean values indicated with dashed black lines

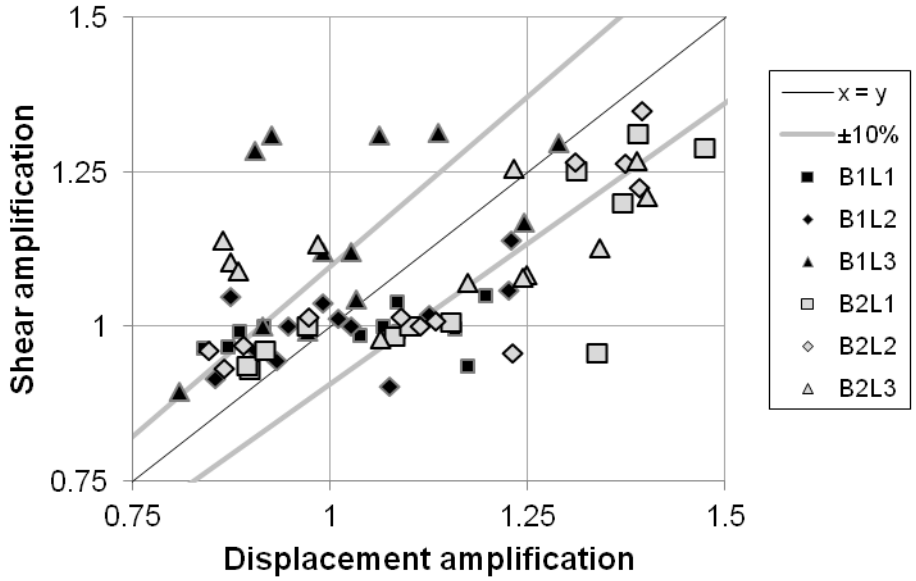

Figure 6.18 Correlations between displacement amplification and shear amplification. B1L1 refers to Building 1, Level 1

Attention is now focused on the influence of separation on shear amplification. Generally speaking, shears were found to decrease in Building 2 as separations increased, while Building 1's shears remained reasonably constant for all separations. The influence of individual separations on maximum shear force is presented in Figure 6.19. In this figure, the separation causing the maximum amplification is presented. The separation corresponding to this amplification is indicated on the horizontal axis of the figure. Amplifications of shears are notably different from displacement amplifications (refer Figure 6.13). Shears are consistently amplified due to pounding, with these amplifications frequently exceeding 20%. Unlike displacement results, the variation of shear amplification between the pounding and no pounding records is much more pronounced than the variation between individual records.

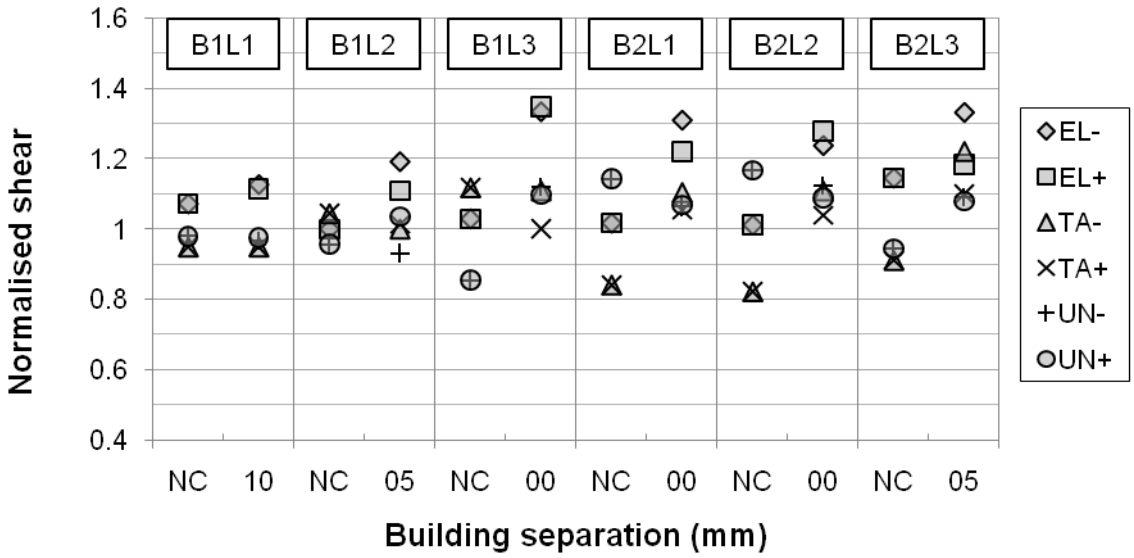

Figure 6.19 Shear normalised by average NC response. Separation causing highest amplification presented. B1L1 = Building 1, Level 1

Curvature member ductilities show similar trends to the interstorey shears, but are generally found to be more sensitive to system changes. This sensitivity is considered to be caused by the significantly lower post elastic stiffnesses in each member. Figure 6.20 presents the maximum ductility observed in all column members during a record. Beam ductilities present similar trends with a maximum recorded ductility of 3. Note that ductilities less than 1.0 are not recorded by default in Ruaumoko, so some data points are missing. All ductilities remain within the acceptable capacities defined in Section 5.2.9. Decreasing building separation consistently reduces column ductility demand in Building 1, while generally increasing Building 2's column demand.

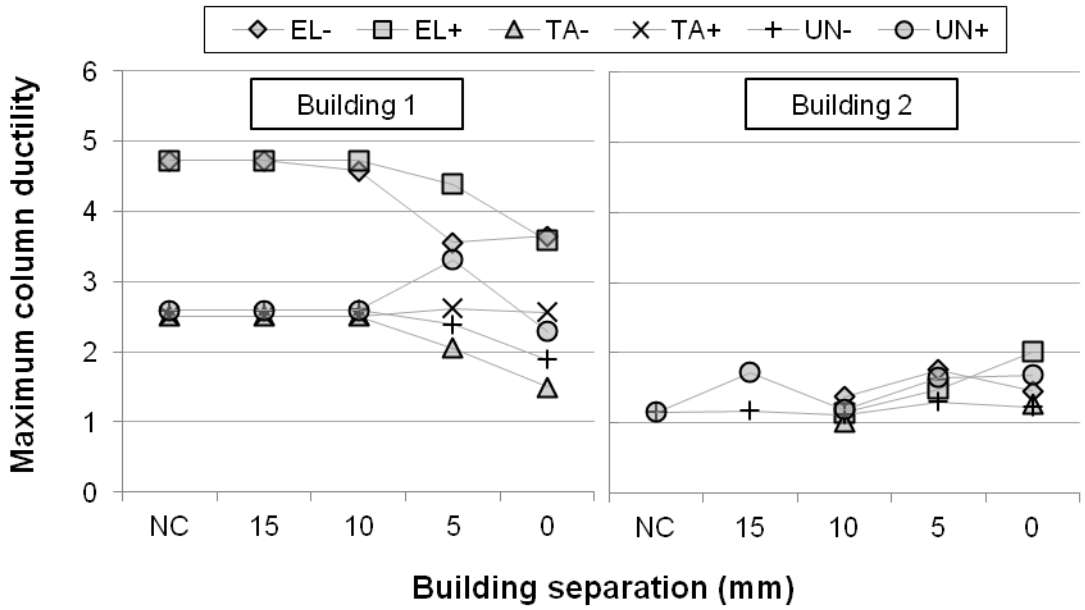

Figure 6.20 Effect of building separation on maximum column ductility

6.6.3 Collision Force Response

Figure 6.21 presents the maximum collision force recorded at each building level during each pounding record. Typically, the contact force recorded in a model is different to that obtained using Equation 3.30 to calculate the collision force (for example, Figure 4.13). However, Figure 6.5 has shown that for this particular building configuration either method produces near identical collision force values. In this chapter the reported collision force values are obtained from the record since this data requires less post processing. Level 2 generally records the highest collision forces, since this is the level with the largest mass. Predictably, Level 1 and Level 2 do not experience collision at larger building separations. In fact, Level 1 only experiences collision in the 0 mm separation case. Level 2 does not experience collision in many of the excitations when the separation is 15 mm.

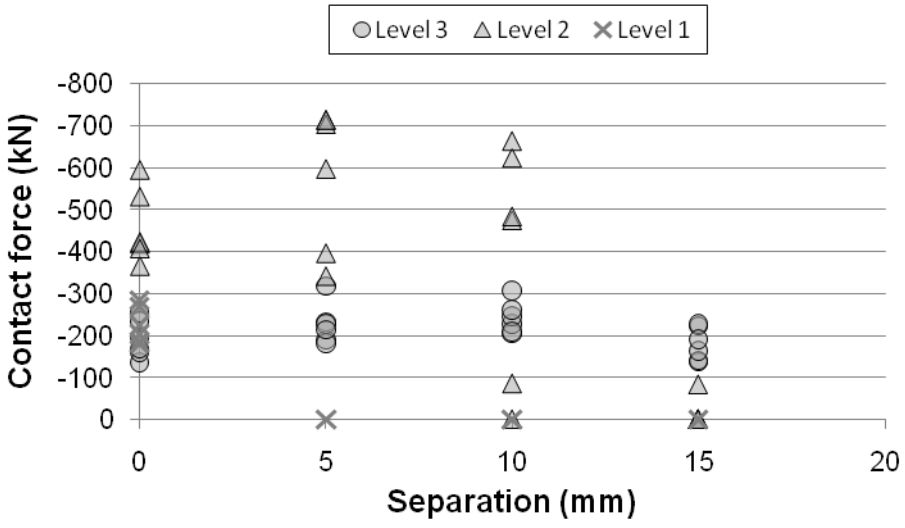

Figure 6.21 Maximum recorded contact force in terms of building separation

The relationship between contact force and building separations is more directly investigated in Figure 6.22. In the figure, the results are compared to the simplistic model presented in Section 3.1.2. Building separations are normalised by the relative displacement of the considered floor recorded in the NC model. Thus Level 1's normalising displacement is less than the corresponding displacement for Level 2. These displacements also change between records, which distributes the normalised displacements between 0 and 1.0 (despite the use of discrete building separations in Figure 6.21). The maximum collision force is normalised by the maximum collision force recorded in the zero separation model. Level 1 and Level 2 report zero maximum collision forces for separations that are less than the minimum separation required for no pounding (i.e. less than a normalised separation of 1.0). This is because the buildings' displacement responses change in the pounding models, which sometimes cause less displacement to occur at these lower levels. The maximum collision force initially increases until the separation is approximately half the no contact separation. This increase is expected since the two buildings have more time to oscillate independently before collision and thus larger collision velocities result when the buildings do experience contact.

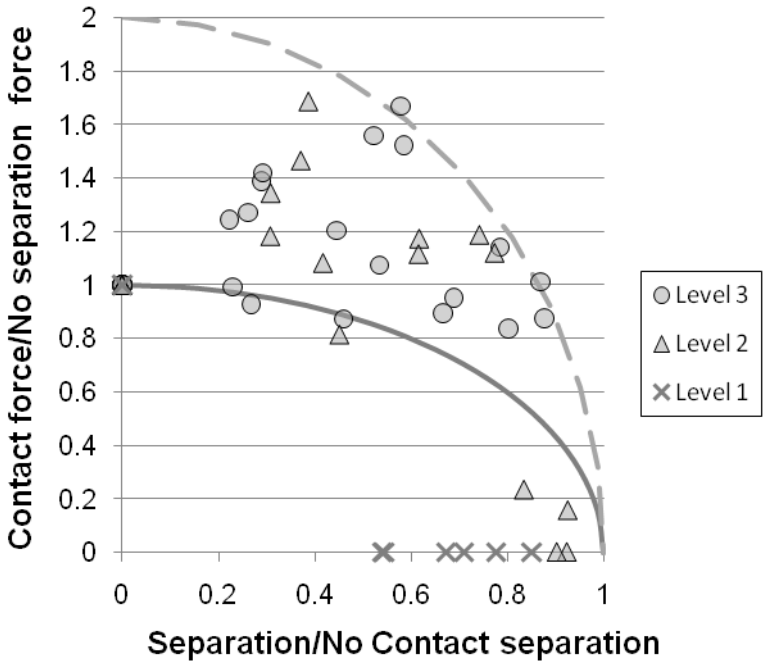

Figure 6.22 Effect of increasing building separation on contact force. Solid line: relationship predicted by Equation 3.17. Broken line: Equation 3.17 x 2

The model proposed in Section 3.1.2 (shown as a solid line in Figure 6.22) is not expected to be very accurate since fundamental aspects of pounding are not accounted for. Nevertheless, in this instance, doubling Section 3.1.2's model accurately predicts the maximum collision force profile between normalised separation values of 0.5 and 1.0. While the presented data comes from a relatively small sample size, it suggests that increasing separation does not notably decrease

collision force unless the gap is at least 90% of the separation required to prevent any pounding. The reported collision force insensitivity to building separation is in agreement with related studies by Jankowski (2006).

When the calculations to create Figure 6.22 were performed, the maximum collision forces were observed to be reliably predicted using Equation 3.30 and approximated floor velocities. Floor velocities were initially predicted by using the maximum recorded relative floor velocity (regardless of whether contact actually occurred at this time). Figure 6.23 presents a comparison of the maximum recorded collision force against predictions of collision force using the NC records' maximum relative velocities. This comparison tests whether collision forces can be reasonably predicted without any explicit modelling of contact. The results in Figure 6.23 are normalised by the recorded collision force. A normalised collision force of less than 1.0 indicates the predicted collision force (using Equation 3.30) exceeded the recorded collision force. Despite the crudeness of this method, the predictions show surprising consistency, albeit in a slightly conservative manner. Most recorded collisions range between 0.6 to 1.05 times the predicted collisions. Crucially, the predicted collision force is not grossly underestimated by this method. These results suggest that approximate magnitudes of collision forces can be suitably predicted without specific modelling of pounding. Prediction of Level 3's collision forces is the most accurate, while Level 1's predictions are the least accurate. Level 1's inaccuracies appear to be caused by the accelerations in each floor at the time of collision. Simplified prediction methods for contact force are investigated further using 3D modelling in Section 8.4.4.

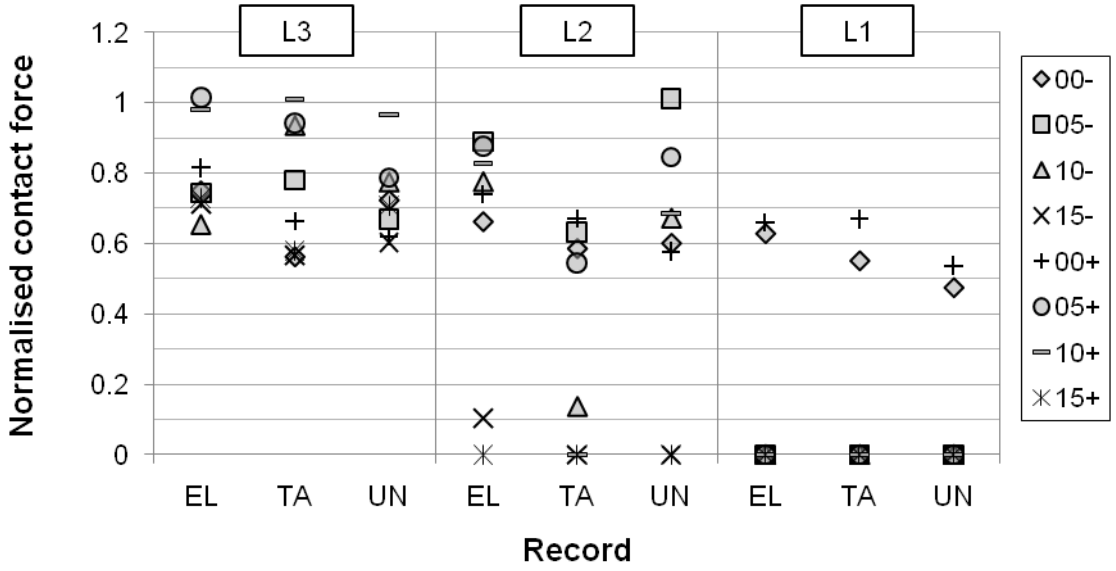

Figure 6.23 Collision forces predicted using relative velocity from records without pounding

Finally, the interaction between global and local pounding damage is investigated by comparing the two damage measures. Figure 6.24 displays the recorded maximum shear forces of each

building level plotted against the maximum recorded collision force for each building level. While collision force is reasonably sensitive to record and building separation changes, interstorey shear remains comparatively constant. No strong correlations are observed between the damage measures. Local and global damage are therefore considered to be independent from each other.

Figure 6.24 Correlations between global damage and local damage

6.7 Effects of Scaling PGA

Dimitrakopoulos et al. (2009b) have shown for elastic systems that if the building separation and the magnitude of an excitation are doubled, the resulting actions on both buildings are also doubled. This is because all the dimensionless numbers defining the problem remain constant (refer Equation 2.32). When inelastic systems are modelled, this relationship will change. Displacements in particular are likely to increase by a factor greater than 2 due to the reduced stiffness of each building. Nevertheless, Dimitrakopoulos' finding is tested here for the currently considered building configuration, which contains many sources of inelasticity (Figure 6.25). Test *2xPGA* uses double the Peak Ground Acceleration (PGA) and double the initial separation of the corresponding *1xPGA* case. To reduce the total amount of computation, the following separations are tested for the *2xPGA* case: 0, 10, 20 and NC. Note that these tests correspond to the *1xPGA* tests with 0, 5, 10 and NC separations respectively. When comparisons are made between the two testing schemes, the *2xPGA* separations are used for labelling.

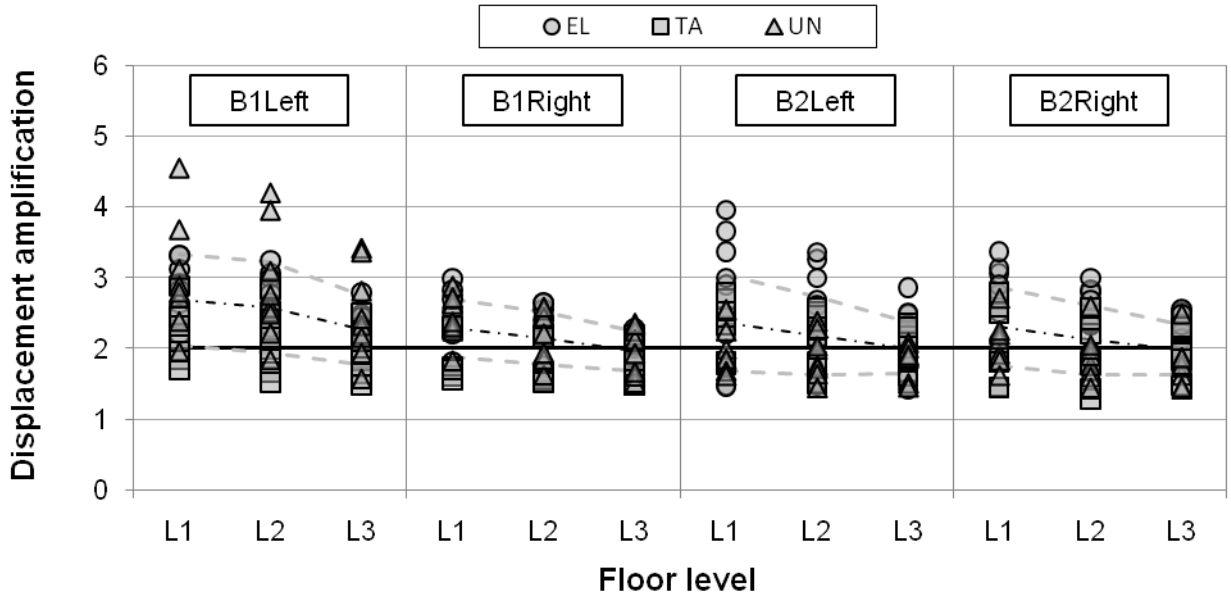

Figure 6.25 2xPGA/1xPGA displacement ratio by floor level. Mean and mean ± one standard deviation shown on figure. Black line indicates expected amplification for an elastic system

As expected, the displacements are generally amplified by factors greater than 2. Level 3's displacements in both buildings are amplified by an average of approximately 2 (or 2.3 for B1Left). This in agreement with predictions by Dimitrakopoulos et al. (2009b) for elastic systems. However, the amplification and standard deviations of lower floors progressively increase. The greater amplification and variance of lower floors can be attributed to the decrease in stiffness at these levels due to member yielding. The displacement amplifications showed no notable trends with respect to building separation. In the tested models, assuming *2xPGA* doubled the displacements of *1xPGA* would produce unconservative design.

The interstorey shear forces were significantly less amplified. Shear amplifications ranged between 0.99 and 1.99. This reduced amplification in shear is expected because shear is dependent upon member end moments. The increased excitation has caused many members to yield at both ends, which effectively limits the shear demand of the member. Maximum beam and column curvature ductilities are more important building demand parameters, since exceeding ductility capacity of a member is the most likely failure mechanism. The maximum *2xPGA* curvature ductilities reported in Building 1's beams and Building 1's columns are presented in Figure 6.26. The curvature capacities are also shown, as presented in Section 5.2.9. Building 1's member capacities are exceeded for all Union and El Centro records. One Tabas record also predicted failure (*TA+00_2xPGA*). Ductility demand shows a weak correlation to the building separation, with smaller separations causing higher ductilities in Building 1. Building 2's absolute ductilities are not presented here, but do not show any consistent relationship with

building separation and do not exceed the available capacity (Building 2 maximum beam ductility = 6.6 and maximum column ductility = 7.4).

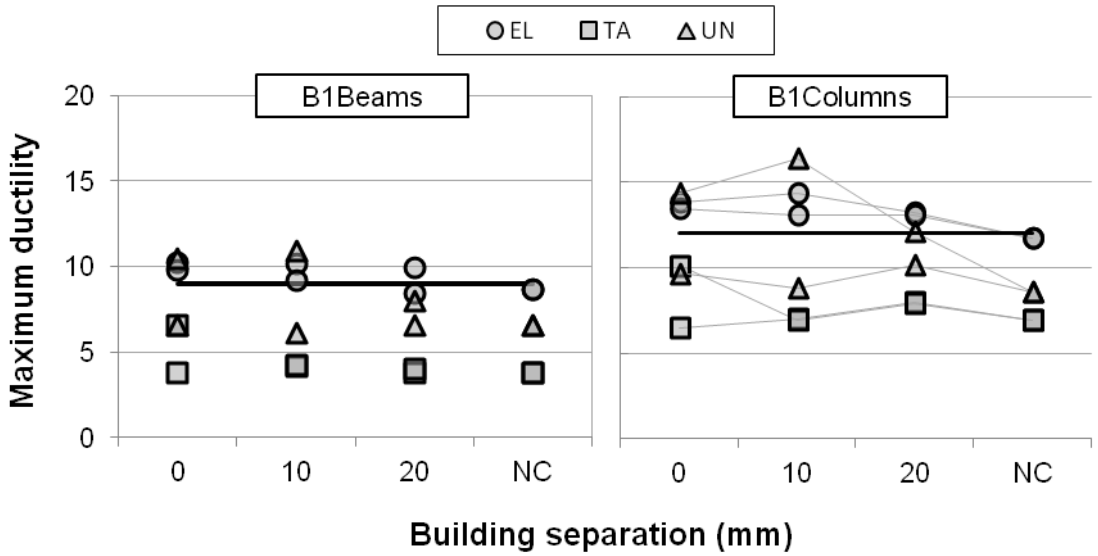

Figure 6.26 2xPGA maximum member ductilities in Building 1. Black line indicates capacity

The ductility amplification from the *1xPGA* tests also varies between the two buildings. Building 1's ductility amplification increases with decreasing separation, while Building 2's ductilities present no clear trend. Note some data could not be used since the ductilities were less than 1.0 for the *1xPGA* case. Despite the two-fold increase in ground motion intensity, most ductilities have been amplified by a factor of approximately 3 to 5; hence these results do not agree with Dimitrakopoulos' predictions for elastic systems.

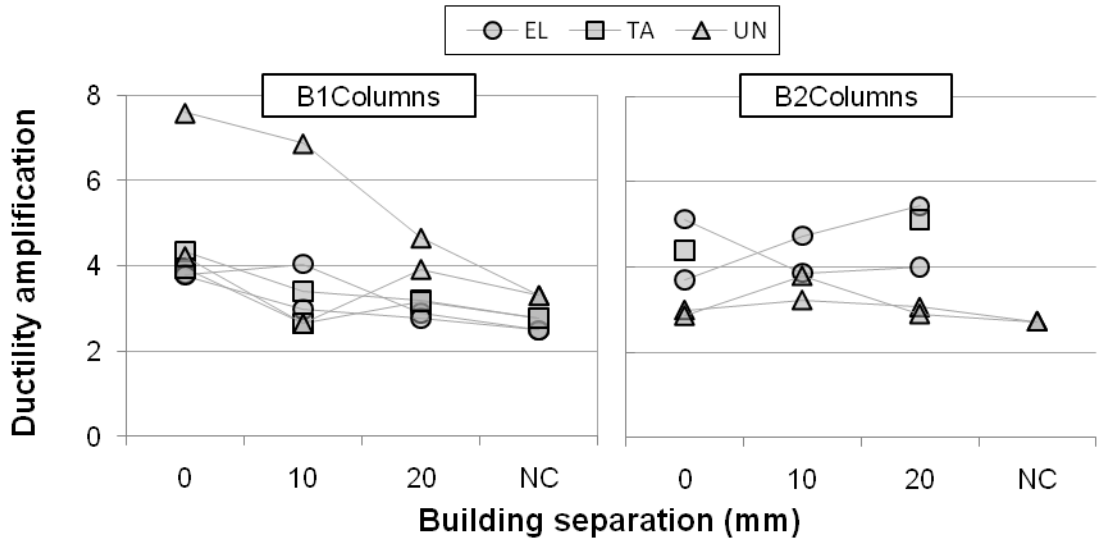

Figure 6.27 2xPGA/1xPGA ductility ratio. Left: Building 1 columns. Right: Building 2 columns

As can be seen in Figure 6.28, the contact force amplification is highly dependent upon floor level. Level 3's contact forces are roughly double that of the *1xPGA* testing, however the lower levels show significantly greater amplifications. This is again attributed to the yielding of Level

1 columns. Thus an inelastic building's shear, ductility and collision force demands cannot be accurately predicted by linearly scaling responses at lower level excitations.

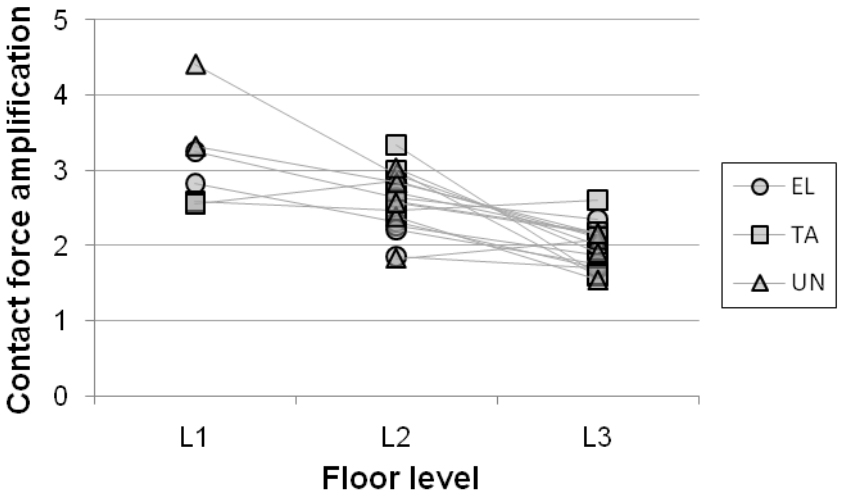

Figure 6.28 2xPGA/1xPGA contact force.

6.8 Effects of SSI

The influence of soil structure interaction is assessed below. This is achieved by re-running *1xPGA* models with fully fixed foundations instead of the models described in Section 5.2.10. These models are labelled as *NoSSI*. To reduce the required computation, only the following separations are tested: 0, 10 and NC. Note that results are presented in terms of *NoSSI/1xPGA*, which shows the deamplifications caused by not modelling SSI. Results are presented in this manner (rather than *1xPGA/NoSSI*, which would show the amplification due to SSI effects) to allow direct comparison with the preceding and following sections. The change in building period due to the foundation fixity can be observed in Figure 5.16.

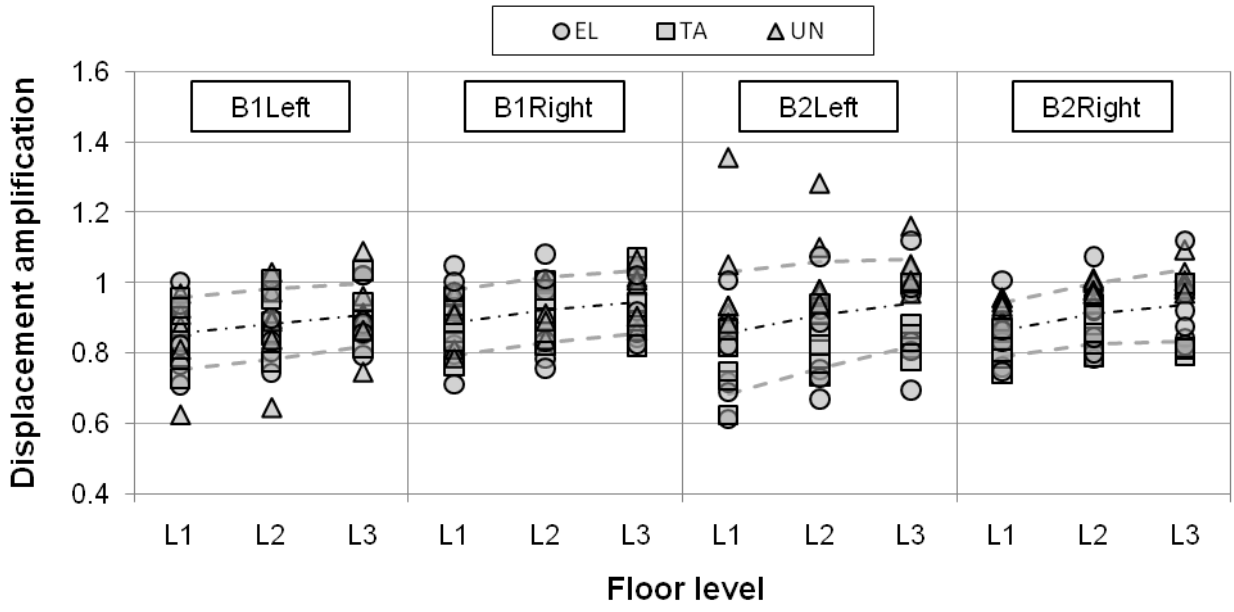

Figure 6.29 Displacement ratio of NoSSI/1xPGA. Line series indicate mean and standard deviation.

Figure 6.29 presents the displacement amplification from the NoSSI case. The lower floors' displacements are deamplified more than the higher floors. Removing SSI from the model reduces the buildings' displacement envelopes by up to 40%. SSI thus has a significant effect on the displacement of the presented model.

Shear (Figure 6.30) shows remarkable insensitivity to the SSI modelling. This suggests that the additional displacement is primarily due to foundation flexibility, rather than an increase in spectral acceleration of the buildings due to period shift. Yielding of members at either end was found to occur only in isolated columns and is not considered to have significantly contributed to the reported shear insensitivity. Ductility amplification (Figure 6.31) is significantly more sensitive and can be either amplified or deamplified by SSI. Note curvature ductilities of less than 1.0 were included in the calculations to create this figure. This was done by manually extracting the maximum recorded curvature from each record file. This method has not been repeated in other sections of this chapter due to its time consuming nature.

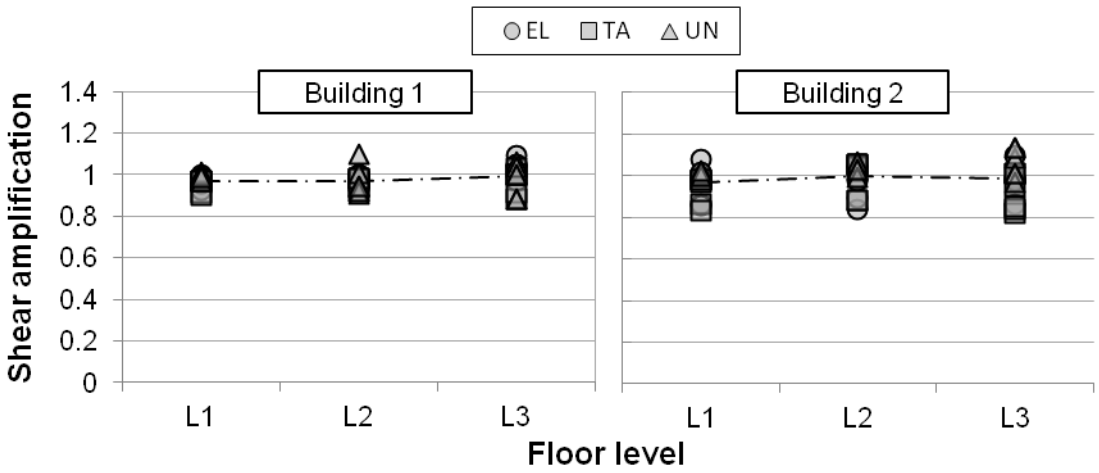

Figure 6.30 Shear ratio of NoSSI/1xPGA

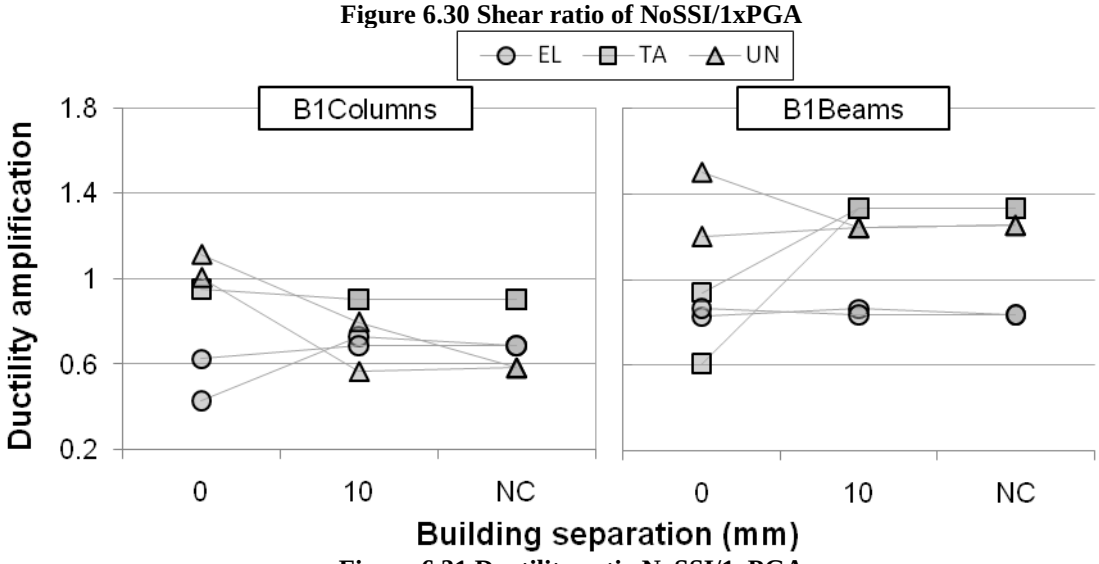

Figure 6.31 Ductility ratio NoSSI/1xPGA

As shown in Figure 6.32, contact force amplifications of ± 20% can result from the change in ground conditions. Collision force is observed to be more sensitive to SSI effects than the interstorey shear, but is less sensitive than building displacement. This is because the collision force is a function of relative floor velocity, which is more sensitive to foundation changes than interstorey drift (and thus interstorey shear) but less sensitive than overall building displacement. The maximum relative floor velocity that caused collision at Level 1 and Level 2 both reduced by over 10% in *NoSSI*.

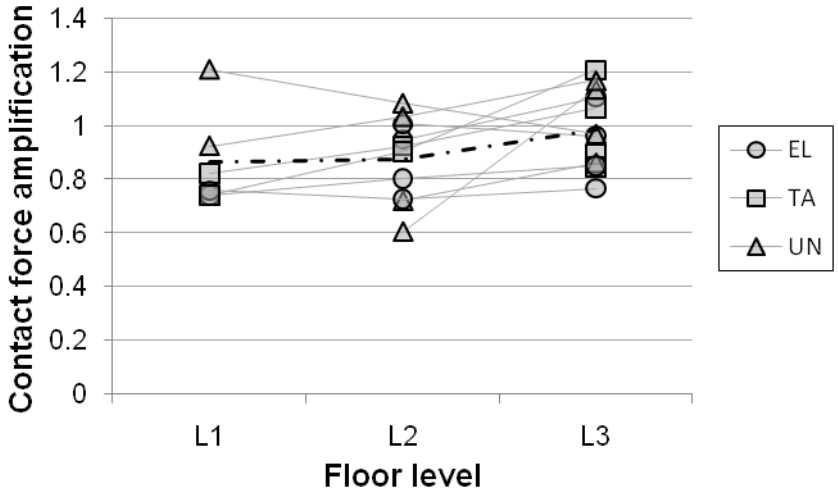

Figure 6.32 Contact force ratio NoSSI/1xPGA. Mean indicated with black line

6.9 Effects of Collision Damping

The effect of contact-specific damping is tested by adding viscous diaphragm elements from Section 4.7, which are calibrated using the method proposed in Section 4.11. These tests are labelled *DAMP*. Plasticity indexes (as defined by Equation 3.43) for each floor level are presented in Figure 6.33.

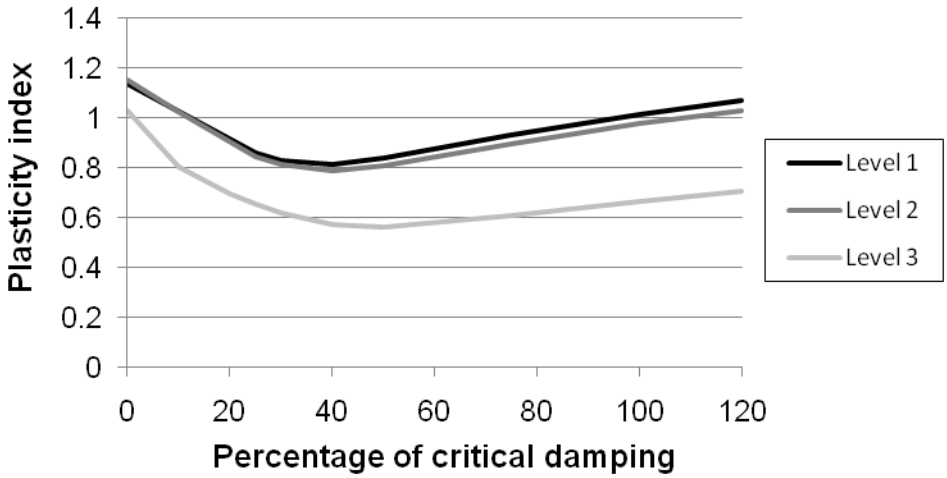

Figure 6.33 Plasticity indexes for modelled colliding diaphragms

The plasticity index relationships of Level 1 and Level 2 are very similar. This is not surprising as the mass and axial period ratios between the two buildings' diaphragms are reasonably similar

at Level 1 and Level 2 (see Table 6.1). As previously discussed, there is very little evidence available to guide the selection of an appropriate plasticity index value. In this model, a consistent plasticity index was sought for all three levels. As seen in Figure 6.33, this value will need to be at least 0.82, since this is the minimum obtained plasticity index for Level 1. This value is larger than that typically used in lumped mass coefficients of restitution models. Nevertheless, it is possible that this value may be comparable to the lumped mass models. This is because the axial oscillation of each diaphragm is already 'removing' a considerable portion of the collision energy. A comparison between plasticity index and coefficient of restitution can be quantified by using Equation 3.45, and is shown in Table 6.4. The second column of the table displays the effective coefficient of restitution for two distributed masses if r = 1. The third column provides the corresponding values when r = 0.85, while the forth column presents the required percentage of critical damping to achieve r = 0.85 from Figure 6.33. Since other researchers have typically used e ≈ 0.65 for lumped mass modelling, r = 0.85 is considered to be suitably comparable (refer column 3). Thus r = 0.85 is adopted for the *DAMP* tests. Even though a consistent method of assigning energy loss for each diaphragm level has been adopted, the value of the effective coefficient of restitution changes notably between levels. This provides further evidence that more thorough research into the mechanisms of energy dissipation during collision is required. In order to reduce the computation time for the testing, only the following separations were tested: 0, 5, 10 and NC.

Table 6.4 Effect of viscous diaphragm on the effective coefficient of restitution

Floor number	e_{eff} *(elastic, r = 1)*	e_{eff} *(r = 0.85)*	ζ *(%) for r = 0.85*
3	0.897	0.762	7.24
2	0.648	0.551	24.8
1	0.629	0.534	27.0

The effect of diaphragm damping on displacement envelope is presented in Figure 6.34. The NC results are not presented in Figure 6.34 since no difference is observed between the *DAMP* and *1xPGA* models when no collision occurs. The amplifications (i.e. the differences from 1.0) are considerably less than that reported for *NoSSI*. The largest reported difference varies by only 6%. Building displacements are slightly more sensitive to diaphragm damping when smaller building separations are tested. This may be attributed to the greater number of collisions that occur, which removes more energy from the system. No correlation was observed between the building level (L1, L2, L3) and displacement amplification.

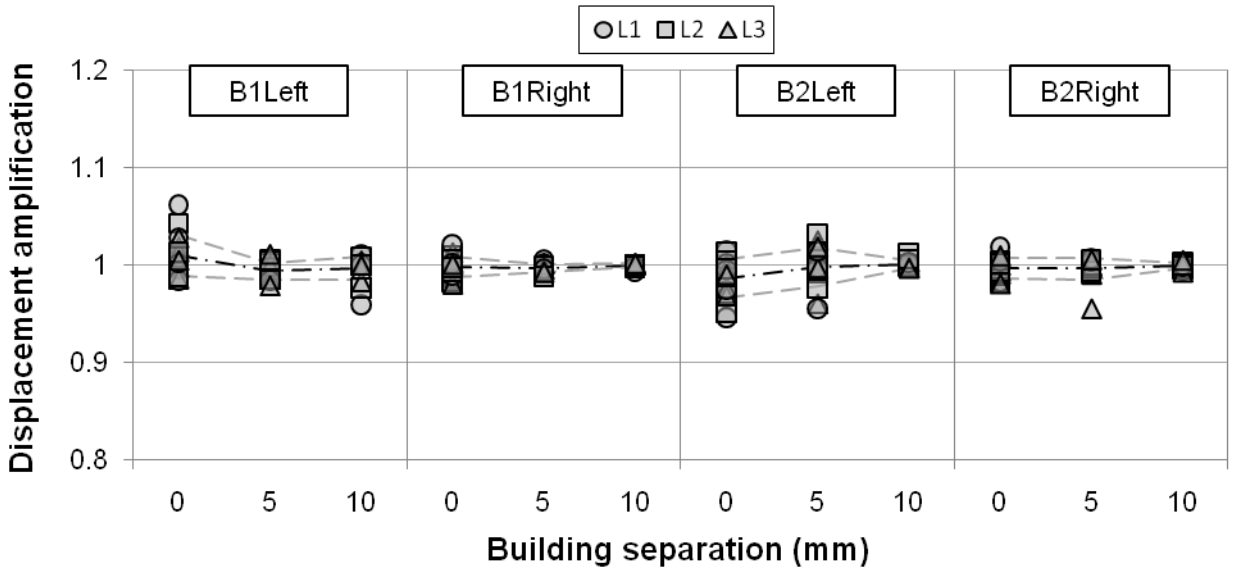

Figure 6.34 Displacement ratio of DAMP/1xPGA. Lines indicate mean and standard deviation

The relationships between shear amplification and separation are very similar to that of the displacement amplification (i.e. Figure 6.34) and are not shown here. Interstorey shear is instead presented in terms of its floor level (Figure 6.35). Level 1 shears were the least affected by diaphragm damping. This is attributable to the large NC base shears (in comparison to the smaller NC shears at roof level). With one exception, shear amplification/deamplification does not exceed 6%. Ductility amplification was also recorded, but is not presented here. Two records amplified the maximum recorded ductility by more than 30%, however the majority of amplifications range between 1.0 and 1.1. The average ductility amplification was 1.04. Thus, diaphragm damping has not significantly affected the global response of the buildings in the presented model.

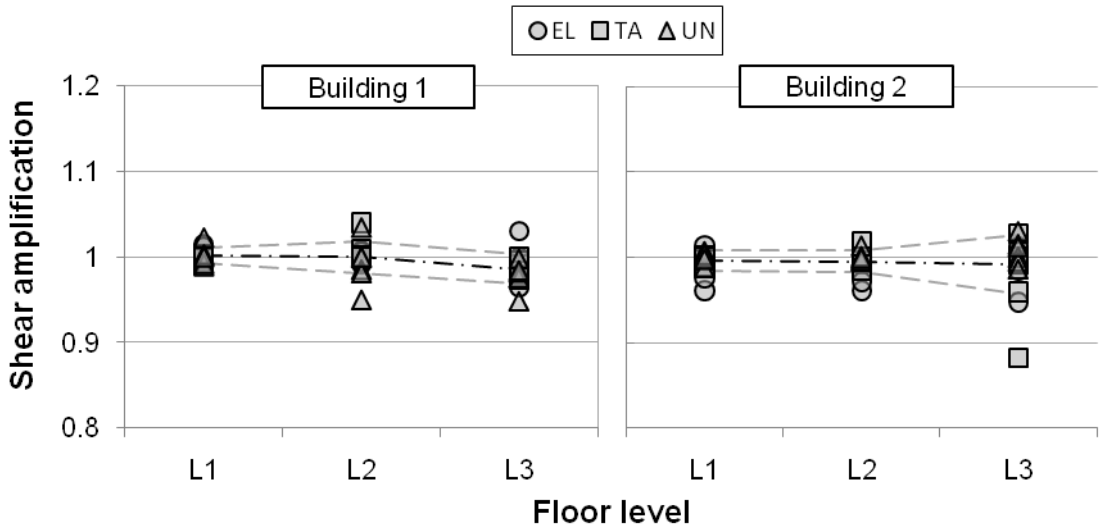

Figure 6.35 Shear ratio of DAMP/1xPGA. Lines indicate means and standard deviation

Local damage measures are much more sensitive to diaphragm damping. Figure 6.36 presents contact force amplification in terms of building level and separation. Lower floors are magnified

notably more than the higher floors (average magnifications: Level 1; 12%, Level 2; 7%, Level 3; 2%). Some contact force increase was expected due to the increase in diaphragm resistance that is caused by the diaphragms' viscous dampers. It is possible that the lower levels were amplified more due to higher levels of viscous damping (refer column 4, Table 6.4). As was also observed in the displacement results, much greater variation in amplifications are recorded at smaller separations.

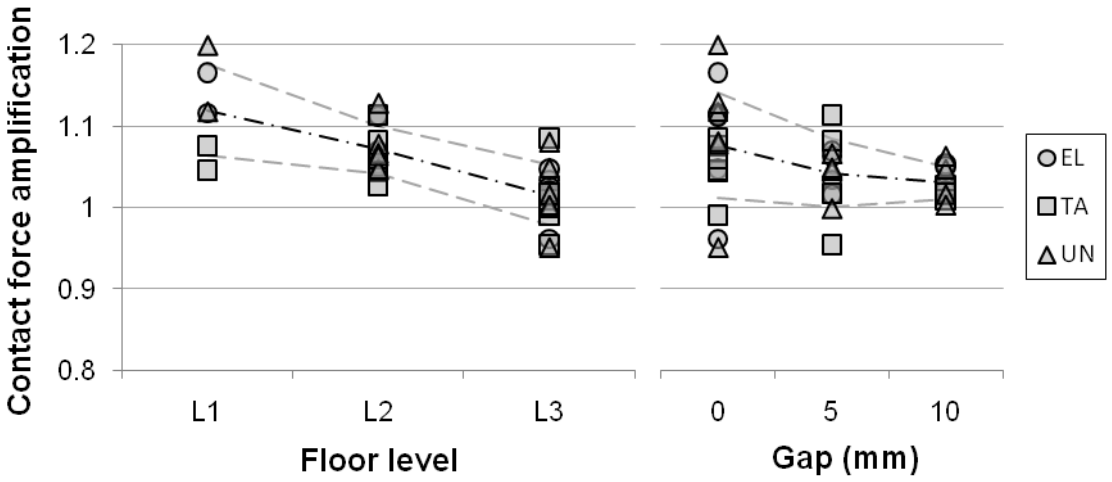

Figure 6.36 Contact force ratio of DAMP/1xPGA. Lines indicate mean and standard deviation

6.10 Effects of Lumped Mass Modelling

Finally, the effect of not modelling any axial compression in the diaphragms was investigated. In these tests (labelled *LUMP*), horizontal movement of nodes within a diaphragm were slaved together, preventing axial oscillation. In the *LUMP* tests, the axial stiffness of the collision elements was equal to the values used in *1xPGA*. This means that the collision element has twice the axial stiffness of Building 1's diaphragms at each floor level. Thus, if the notation used in Section 4.3 was adopted, these tests would be labelled 0(2).

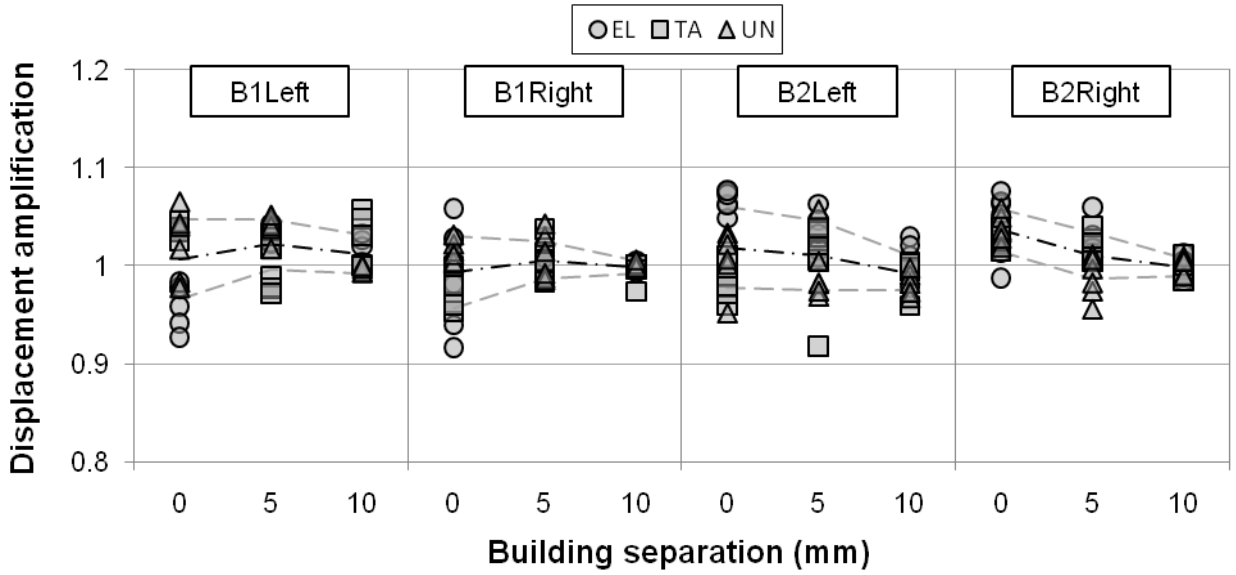

Figure 6.37 Displacement ratio of LUMP/1xPGA. Lines indicate mean and standard deviation

Minor changes in the displacement envelope are observed in Figure 6.37, with no displacement amplification exceeding 10%. As observed in the previous section, the variance (or range) of amplifications generally reduces with increasing gap. Buildings without contact (NC test) recorded negligible amplification (maximum discrepancy 1.3%) and are not shown in the figure.

Interstorey shear is affected to a slightly greater extent (Figure 6.38). The shear force amplification exceeds 10% in one case. However, these effects are still small enough to be neglected. The variation in amplification also increases with increasing building level. Curvature ductility is affected to a greater extent, with a maximum amplification of 40%. However, these ductilities are amplified by only 5% on average. Therefore, overall building response does not seem to be significantly affected by the adopted diaphragm model in the current analysis.

This lack of global damage sensitivity is surprising given the results of Section 4.3.2, where lumped mass modelling caused significant changes in recorded response. This apparent change in behaviour can be at least partially explained by comparing the change in each floor's influence coefficient, α between lumped mass and distributed mass models (refer Table 4.1 and Table 6.2). In Section 4.3.2, all influence coefficients changes by 40% between models. In the present analyses this changes was 20% at Level 1 and Level 2, and only 5% at roof level. This smaller change indicates a smaller sensitivity to the adopted modelling method, which is reflected in the above results.

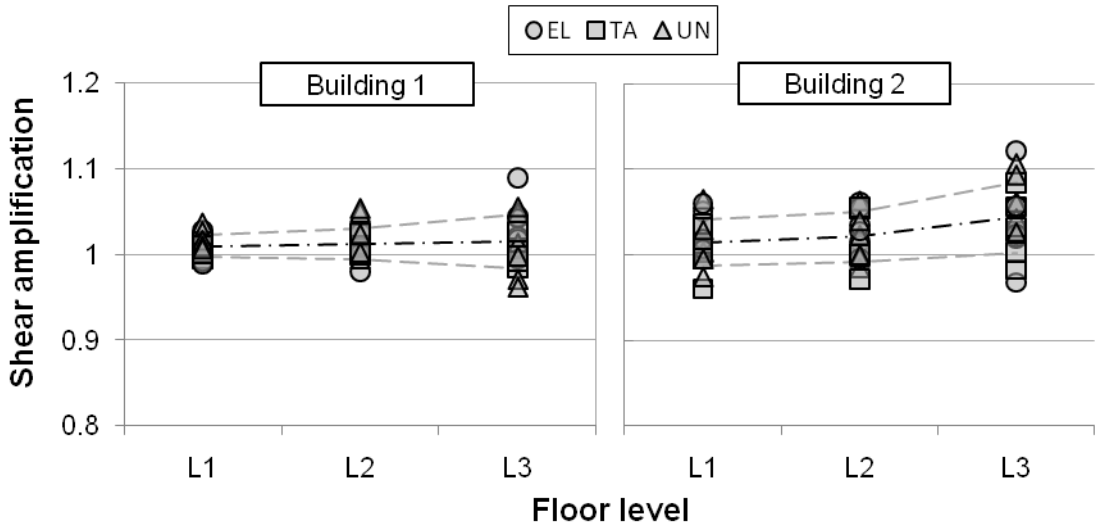

Figure 6.38 Shear ratio of LUMP/1xPGA. Lines indicate mean and standard deviation

The contact force is notably more sensitive to the model changes (Figure 6.39). This is because the collision element stiffness has not been calibrated for the model. The recorded collision force in the LUMP model is therefore unreliable. If accurate collision force magnitudes were required

from this analysis, it is expected these could be obtained using Equation 3.30 with the recorded relative velocities at the onset of collision.

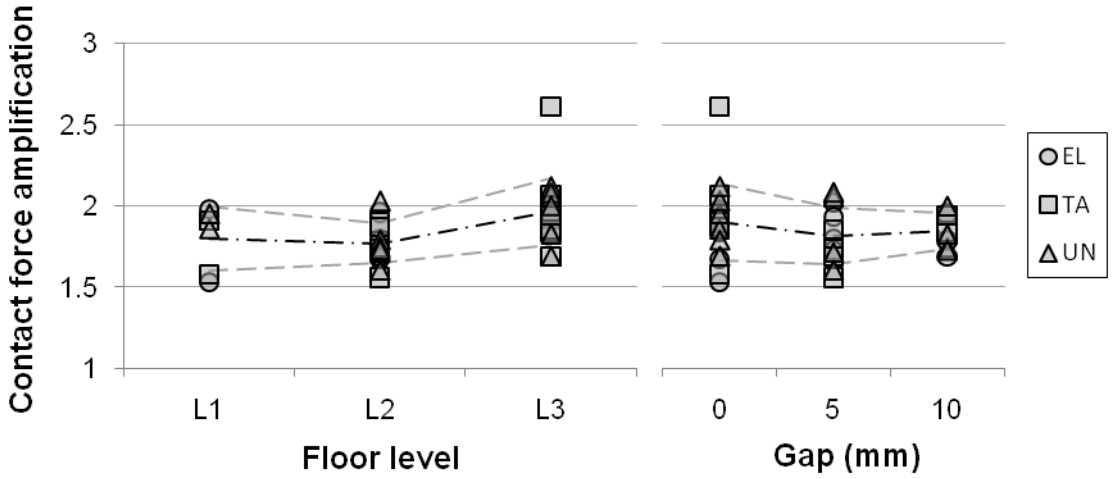

Figure 6.39 Contact force ratio of LUMP/1xPGA. Lines indicate mean and standard deviation

6.11 Conclusions

The following conclusions are drawn from the investigations performed in Chapter 6.

1. The local and global responses to a single collision are related by the load paths formed during collision. In the presented tests however, the maxima of these responses are not correlated in any meaningful way.
2. The amplification of displacement response is also highly complex. Amplification of building responses due to pounding depends on properties of each building in addition to the earthquake excitation.
3. Responses of pounding buildings are most easily interpreted when normalised by their respective 'no contact' values. The non-dimensionalisation proposed by Dimitrakopoulos et al. does not assist the interpretation of multi degree of freedom pounding models. This is because the number of relevant parameters is not meaningfully reduced despite the process requiring additional data manipulation.
4. The amplification of displacement results due to pounding is observed to be less sensitive than the selection of the earthquake record. This trend is not present in the interstorey shear results.
5. Interstorey shears were observed to increase by an average of 10%, and a maximum of 30%, at roof level when pounding occurred. Lower amplifications of shear were observed at lower floor levels.
6. The effect of building separation on the magnitude of collision force can be crudely approximated by using Equation 3.17. As building separation increases, collision force

was observed to increase by up to 70%. At roof level, a separation of 85% that required to avoid any building contact still causes a very similar force magnitude to buildings with no building separation.

7. No correlation between collision force and interstorey shear was found in the modelled building configuration. If both damage measures are of interest, their behaviours must be evaluated separately.
8. In the presented model, the maximum collision force could be crudely predicted using the 'no contact' record's maximum relative velocity. This result suggests that ballpark collision forces may be predicted without any explicit modelling of pounding. Further testing of this result using other building is recommended.
9. Scaling of inelastic building response cannot be performed in the same manner as elastic pounding configurations. Linear scaling of response provides unconservative estimates of all damage parameters.
10. Soil structure interaction is observed to significantly affect building displacements. Contact force magnitudes changed by approximately 10% when SSI was removed. However, interstorey shear was not significantly affected, with an average change in recorded shear of 3%.
11. The effect of damping diaphragms was most pronounced in the first floor's collision force magnitudes. Shear force and displacements were generally unaffected. Greater variations in result amplifications were recorded for shear, displacement and collision force when smaller building separations were used.
12. In the presented model, the effect of more accurate diaphragm modelling is less significant than the effect of modelling soil structure interaction. Any modelling of diaphragm oscillation must therefore also take adequate steps to model SSI effects.

Chapter 7 Development of the 3D Contact Element

While two dimensional modelling of pounding is useful for preliminary investigation, it overlooks many possible three dimensional complications. In order to investigate the significance of three dimensional effects on pounding, a method to model these interactions must be developed. This chapter presents the details of the adopted 3D pounding modelling method. Limitations of 2D models are scrutinized and multiple alternative 3D contact elements are developed and critiqued. One element is then selected and its properties are calibrated for the testing performed in the following chapter.

7.1 Limitations of 2D Modelling

Modelling pounding in 2D requires a number of assumptions regarding both building's performances. Neither building is able to rotate in plan or able to move perpendicular to the collision surface. This second condition also prevents the modelling of any friction during collision in this direction. 2D modelling is also poorly suited for modelling buildings of differing lengths (Figure 7.1).

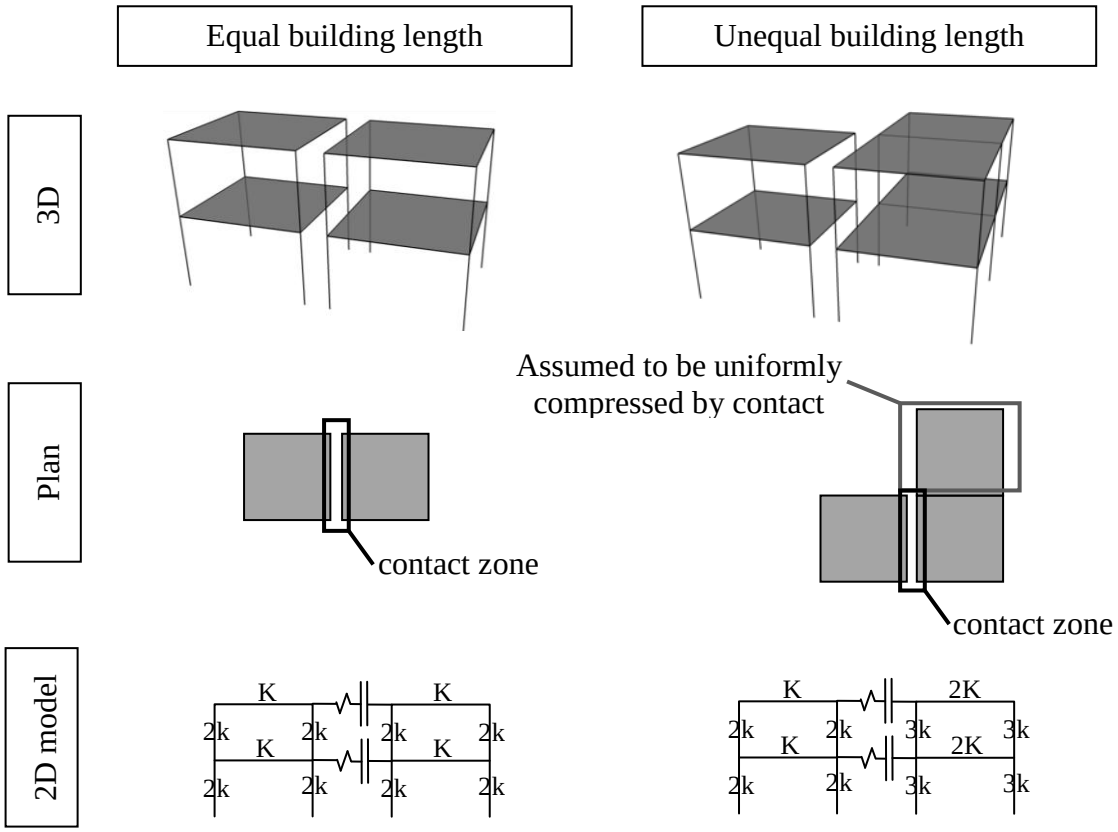

Figure 7.1 Effect of 2D modelling for buildings of differing length. All column stiffnesses = k, all square floor area segment stiffness = K

In Chapter 6, the adopted 2D model only included one external frame in each building. As noted at the time (Figure 5.14), this solution was only approximate. Furthermore, this simplification

requires favourable building geometry, which is not always present. Collisions between buildings with differing lengths can be represented in 2D by modelling each frame individually and linking the frames with springs simulating the building diaphragm. However, such an approach does not include the torsional aspects of this interaction, and requires almost as much modelling detail as required for 3D analysis.

It is possible that in many cases the errors introduced by the 2D assumptions are negligible. However, for this to be proved, comparison with 3D analysis is necessary. A modelling method for collisions in 3D is therefore required.

7.2 Additional Requirements of the Elastic 3D Contact Element

The addition of another horizontal degree of freedom adds other complications to the 3D contact. To simplify the considerations presented in this section, the 3D contact element is initially considered to be entirely elastic (collision plasticity is discussed in Section 7.5). 3D elastic collisions are complicated in two ways; frictional forces may be generated during contact, and transverse building deformations can change the locations of the collision forces within the collision zone (see Figure 7.1). Each of these effects is considered below.

The 2D modelling presented in previous chapters actually features a one dimensional contact element (an axial spring which is activated under certain conditions). While it is possible to model contact friction in a 2D analysis, there is little value in adding this complication. This is because 2D models typically represent elevations of each building's cross section, so any contact friction would be applied vertically as a result of relative vertical movement at the contacting surfaces. Any significant relative vertical movement at the contact is highly unlikely because of the high axial stiffnesses in the vertical elements (i.e. columns and walls). In fact, many analyses omit vertical degrees of freedom entirely. However, when 3D analysis is performed, friction forces can also be generated in the horizontal plane, along the contact surface. Relative horizontal movement between buildings is much more severe than the vertical component. When two buildings come into contact, any relative movement is restrained by the friction of the contact. In 3D pounding analyses, this phenomenon requires suitable representation.

The horizontal friction forces can be incorporated into the Kelvin contact in a relatively straight forward manner. The 3D contact element that was already available in Ruaumoko 3D models friction in the following manner:

1. Record any initial offset in the local y – z plane when collision is initiated (Figure 7.2).

2. Calculate friction forces in the y – z plane using the x axis stiffness (i.e. $k_x=k_y=k_z$). For example, friction force in the z direction is calculated as $F_z=k_z(u_z - u_{z,\ initial})$, where u_z is the element's internal deformation in the local z direction.
3. Friction force magnitudes are restricted to a 'yield' force of $F_{y,z\ max} = \mu F_x$ where μ = the coefficient of friction and F_x = the axial force in the contact element. If the yield force is exceeded, the contacted surfaces slide relative to each other.

The assignment of $k_x=k_y=k_z$ is appropriate because like contact, theoretical frictional forces can suddenly change without any change in the corresponding displacement (Figure 7.3). In the presented work $\mu = 0.4$ was adopted for concrete to concrete friction (Pallett 2002).

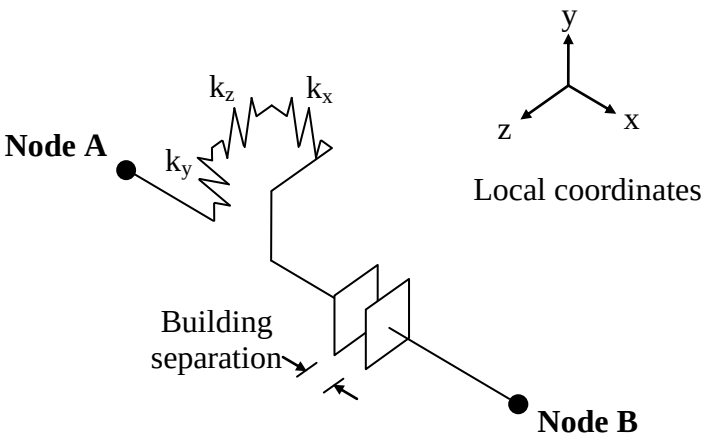

Figure 7.2 Definition of local axes and components of the 3D contact element

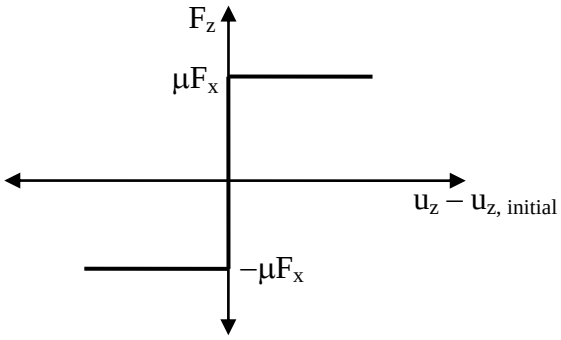

Figure 7.3 Theoretical friction model for z component of friction.

The second complication also results from the relative movement of the buildings. When a collision occurs, the buildings' floors may be offset from each other due to their individual responses to the ground motion (Figure 7.4). However, the contact elements are defined by the static configurations of the buildings before the ground motion is applied. This contact element geometry can cause the collision force to be applied to some areas that do not actually experience collision. Conversely, other areas which do experience contact may have no force applied. If all relative movement occurs in the direction of the contact elements, this corresponds

to the parallel translation case shown in Figure 7.4, and the collision forces are correctly assigned to both buildings. However, any other collision scenario introduces error into the model.

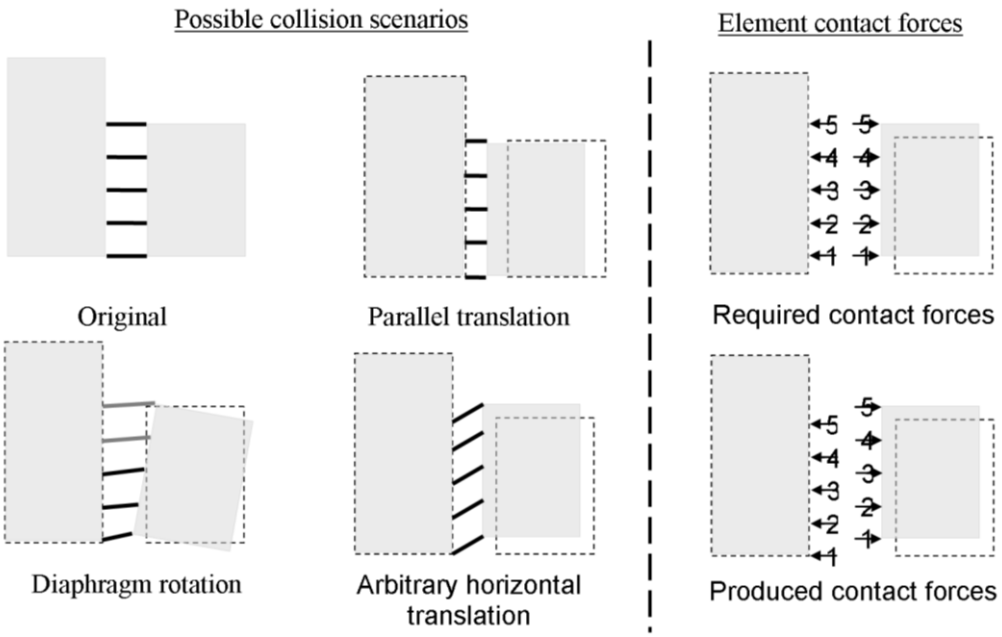

Figure 7.4 Consequences of building offsets at the beginning of a collision. Black lines indicate locations of collision elements. Left: Plan view of potential collision scenarios. Right: Contact forces produced using the standard Kelvin contact element in Ruaumoko.

Figure 7.4 also highlights a second numerical issue. Consider the contact elements (the black lines) in the 'arbitrary horizontal translation' scenario. All of the contact elements have significantly different orientations to that of the original configuration. If large displacement analysis is being used (where element orientation changes the stiffness matrix formulation), an axial force in the contact elements would result in tangential force components in the colliding floors (i.e. forces in the direction perpendicular to the original contact element orientation). This response is certainly incorrect, since tangential contact forces should only be induced by friction. This issue can be addressed by disabling large displacement analysis for the contact elements; however, care must be taken in the way that this is implemented. For the analyses presented in this project, small displacement theory is assumed. This is considered acceptable since the buildings are only three storeys high and do not experience overly large deflections.

The first problem of correctly identifying where contact forces should be applied is more difficult to resolve. The 3D contact elements proposed by other researchers (Section 2.2.3) all assume the colliding diaphragms are rigid. This assumption is obviously incompatible with the goals of this thesis, where diaphragm flexibility is one of the primary properties of interest. A new model which can model diaphragm flexibility and incorporate the effects of offset building collisions is therefore desirable.

In order to further understand the likely magnitude of such building offsets, rough estimates are made from a highly idealised scenario. Suppose two buildings with interstorey heights of 3.6 m present a pounding risk. Table 7.1 presents the floor offsets at the top of these buildings considering a range of building storeys. The buildings are assumed to achieve constant drifts between 0.25-2% over the full height of both buildings. The figures in brackets are based on both buildings reaching their full drift at the same time, while deforming in opposite directions (for example 1% building drift assumes Building 1 deforms to +1 % while Building 2 deforms to -1 %). The other set of figures state the Square Root Sum of the Squares (SRSS) combination of the two absolute deformations. The SRSS combination produces a more likely relative lateral deformation, for the reasons previously discussed in Section 2.2.

Table 7.1 Relative building deformations by average drift and building height (mm). Plain numbers: SQSS combination. Bracketed numbers: Absolute combination

Building Drift (%)	0.25	0.5	1	1.5	2
Number of storeys					
1	13 (18)	25 (36)	51 (72)	76 (108)	102 (144)
2	25 (36)	51 (72)	102 (144)	153 (216)	204 (288)
3	38 (54)	76 (108)	153 (216)	229 (324)	305 (432)
4	51 (72)	102 (144)	204 (288)	305 (432)	407 (576)
5	64 (90)	127 (180)	255 (360)	382 (540)	509 (720)
6	76 (108)	153 (216)	305 (432)	458 (648)	611 (864)

For buildings of three storeys or less, the building offset is unlikely to be significant when compared to the coarseness of the finite element mesh. Ultimately this reasoning leads to the adoption of a 3D contact element that does not explicitly model offsets at the time of collision. This is because the added complication of this effect outweighed the minor benefits that would be achieved in the modelling. However, during this process multiple elements were developed and tested for their suitability. These elements are presented in the following section.

7.3 Attempted Modelling Methods

During the course of investigating alternatives for the 3D contact element, three elements were developed to varying degrees. The elements were developed to deal with the issues arising from building offset during collision. All elements were intended to incorporate the friction model presented in Section 7.2, which is omitted from the following descriptions. While the presented elements were not used in any analyses, they are presented here to document the discovered

shortcomings in the elements and to enable others to continue the elements' development in the future.

7.3.1 3D Node/Node Contact Element

The node/node contact element attempts to model the changing location of collision by applying an additional moment at one or both of the nodes defining the contact element (i.e. Node A and/or Node B in Figure 7.2). The additional moment creates an equivalent force at the node instead of applying the actual force at the point of contact (Figure 7.5). Vertical relative movement is assumed to be negligible and is not modelled.

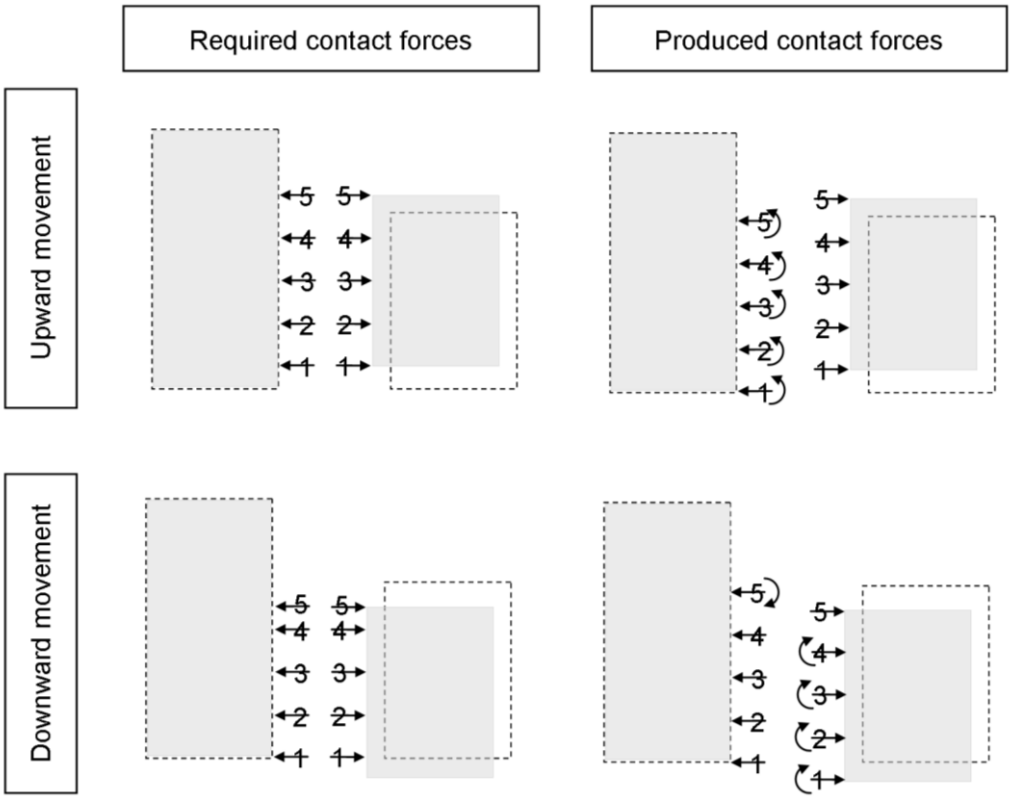

Figure 7.5 Equivalent nodal forces for horizontal offset using node\node contact element

This approach required calculation of a new parameter in each collision element: the distance to the centroid of the collision force. This centroid was calculated based on the building offset and the distance from the edge of the considered object to the contact element node. Furthermore, since this element was intended for general use in 3D pounding analyses, floor/column and floor/wall collisions were also considered. A suite of rules were then created to determine the force centroid based upon the edge distances and the building offset (Appendix J). Two examples are presented in Figure 7.6 for collision between a column and the edge of a floor slab. If the building offset was sufficiently large, a collision may be completely avoided.

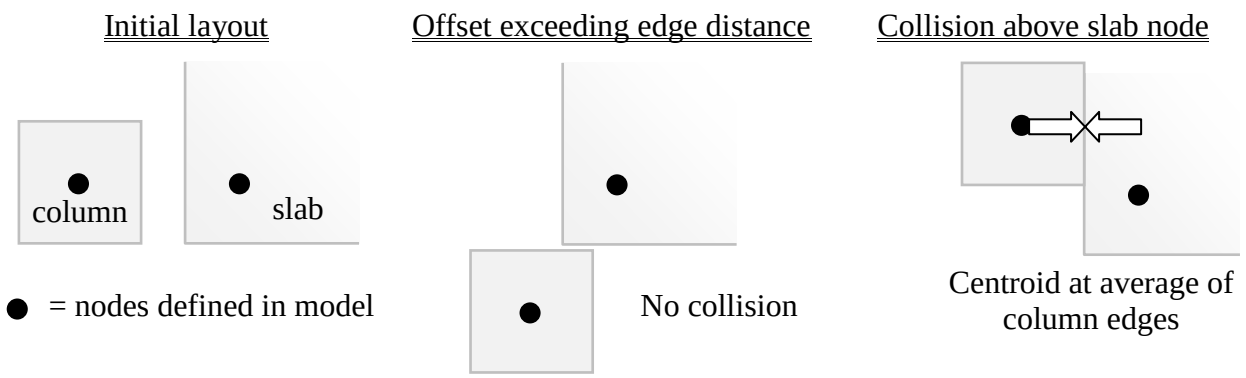

Figure 7.6 Two examples of centroid calculation for node/node element. Collision between a column and a floor slab corner is considered.

The creation of this element appears relatively simple, however the rules used to determine the size and location of the additional moments were found to be unrealistic. For example, consider the produced contact forces in Figure 7.4. The moments applied at the floor nodes do not reflect the physical reality of contact (since impact causes compression over the area of contact, rather than moments at discrete points). This modelling method therefore requires a means of converting the moments into distributed loads along each building edge. Further information about this contact element is available in Appendix K, which presents the rules used for calculating the contact force centroid.

Further complications occur when the nodes defining a floor slab's finite elements coincide with the nodes of contact elements. Many commonly used finite elements, including the finite elements adopted for modelling in Chapter 8, have been developed with only translational degrees of freedom. This means that the in-plane rotation of the nodes defining the element do not contribute to the element's internal stresses. Hence these elements cannot convert the concentrated moments into distributed loading on the building edge. However, if finite elements that have these rotational degrees of freedom (such as the 12 degree of freedom Hybrid Stress finite element in Ruaumoko) are used, this in turn places additional requirements back onto the contact elements. This can be illustrated by considering a static loading of uniform compression between two structural elements (Figure 7.7).

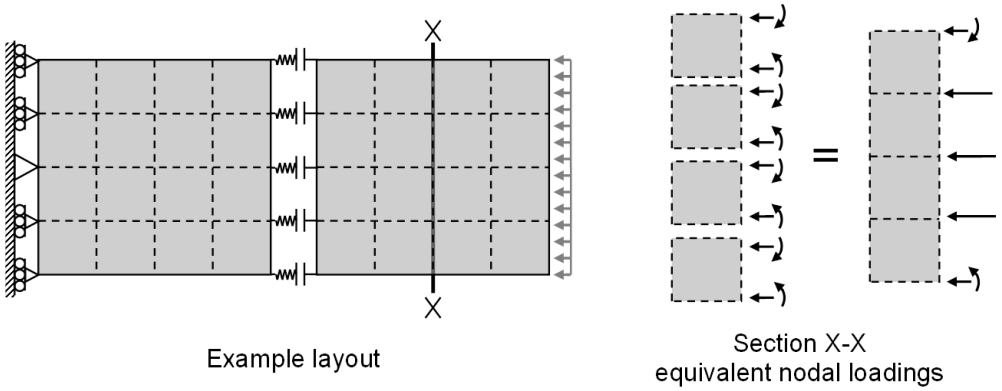

Figure 7.7 Nodal loadings from uniform compression

If Poisson's ratio effects are ignored, the horizontal loading distribution is known throughout both sections, as shown in Figure 7.7 for section X-X. The equivalent nodal loadings for each finite element are also shown. The problem arises when the stresses are transferred through the collision elements. Since there is no lateral movement, no nodal moments are expected to be induced by the contact elements. However, the equivalent nodal loadings require a moment to be applied at the top and bottom nodes of the section. This conflict can be avoided by using lower order finite elements that do not include rotational degrees of freedom, however this option negates the advantage of the node\node contact element. This is because the element, by design, requires nodal rotations to be available to apply moments at each node within the contact element. The consequences of ignoring this conflict are presented in Figure 7.8 for two 10 m x 4 m diaphragms under a 1000 kPa uniform compression. The areas of greatest interest coincide with the areas of greatest error. This behaviour renders the node\node contact element unusable.

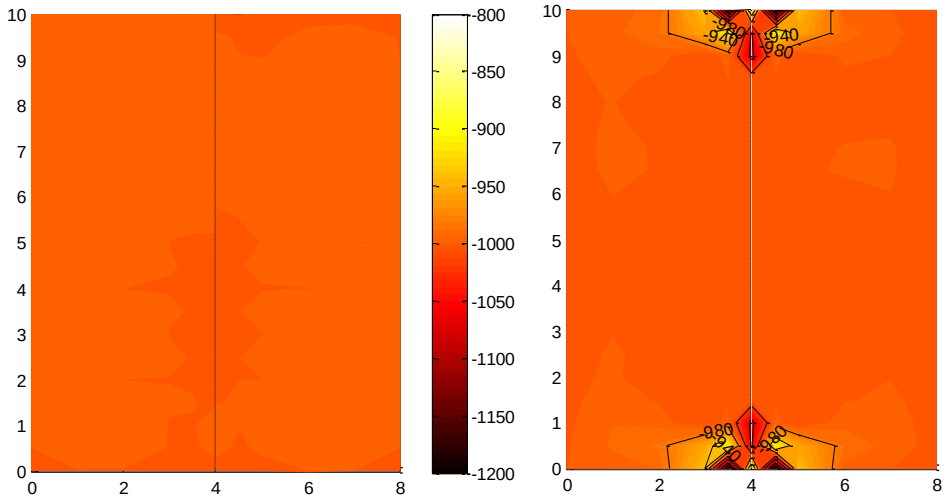

Figure 7.8 Static horizontal stresses within two 10 m x 4 m plates in contact. Left: Results using rigid springs between contacting nodes (matching theoretical solution). Right: Results using proposed element.

The problems found when using this element result from considering contact only at the nodes. In reality, contact between two floors causes distributed stresses along the surface undergoing contact. This situation was addressed in the second 3D contact model which considers contact as a collision surface, and more accurately reflects the physical process of collision.

7.3.2 3D Contact using Extrapolated Shape Functions

Consider two floors, each subdivided into finite elements (Figure 7.9). Contact between the two objects can be modelled using a series of two dimensional contact elements. These contact elements are activated when a prescribed gap is closed and produce linearly varying loadings. This loading is applied to both adjacent floor finite elements. If lateral movement has occurred before the collision, the linearly varying load is determined by extrapolating the known shape functions of each floor finite element border. This process is illustrated for the two 'starred'

finite elements from Figure 7.9 in Figure 7.10. Note that the contact elements themselves are omitted in Figure 7.10 for clarity.

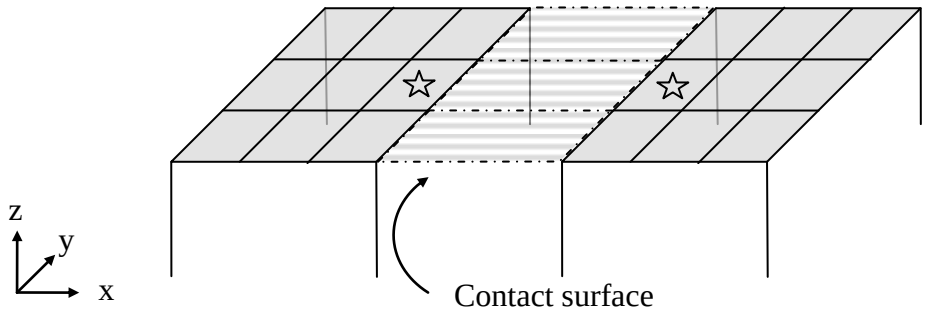

Figure 7.9 Three collision surface elements between two floors

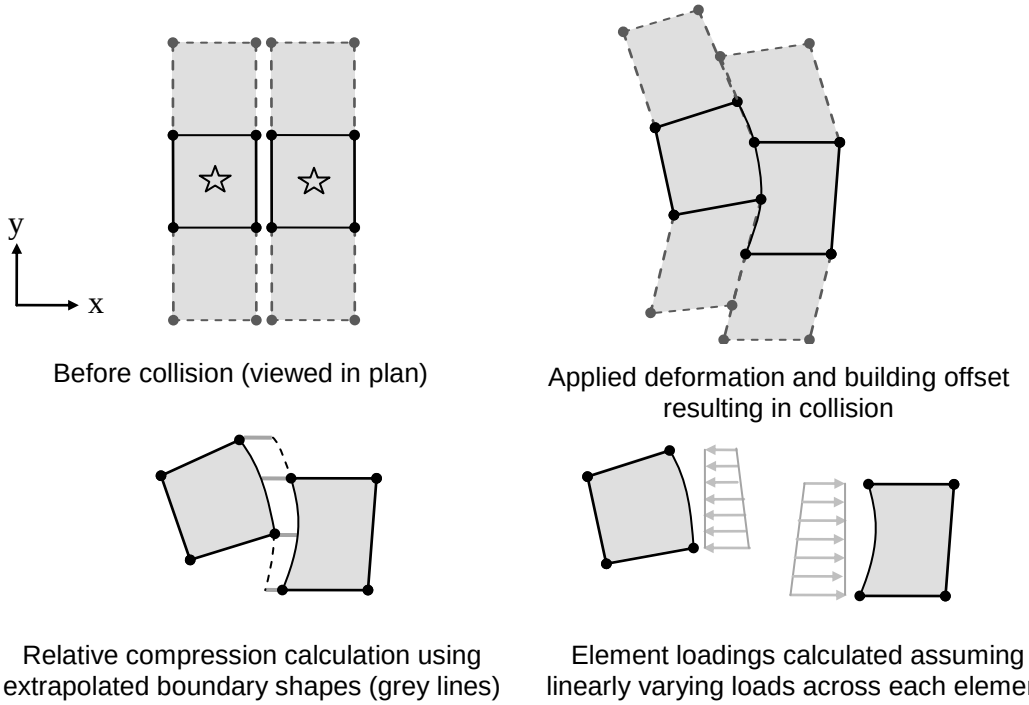

Figure 7.10 Calculation process for contact loadings. Deformations have been greatly exaggerated to illustrate the process.

The magnitudes of the linearly varying contact loadings are calculated at the four nodes defining the collision element. These values are directly proportional to the compression at each node. This means the contact element still requires the Kelvin hysteresis, however the hysteresis is now used to calculate distributed stresses rather than contact forces.

The primary feature of this contact element is the use of extrapolated boundary shapes to calculate the predicted compression between the two colliding finite elements. The manner of this extrapolation can depend on the number of degrees of freedom in each adjacent floor finite element. If each finite element has only translational degrees of freedom, then only linear extrapolation is possible. However, in contrast to the previously proposed element, rotational degrees of freedom are not necessarily a requirement of this element. Because this element

includes two nodes on each floor's contact boundary, internal forces can be transferred to the two ends of the element without requiring nodal moments (Figure 7.11). If both of the bordering finite elements also possess rotational degrees of freedom, further accuracy can be achieved by using the rotations to define cubic boundary shapes. The relative movement between the two objects is now also cubic, which increases the accuracy of the predicted loading. The equivalent nodal forces, including moments, can be calculated using the appropriate Fixed End Moments (FEM) for a standard Euler-Bernoulli beam.

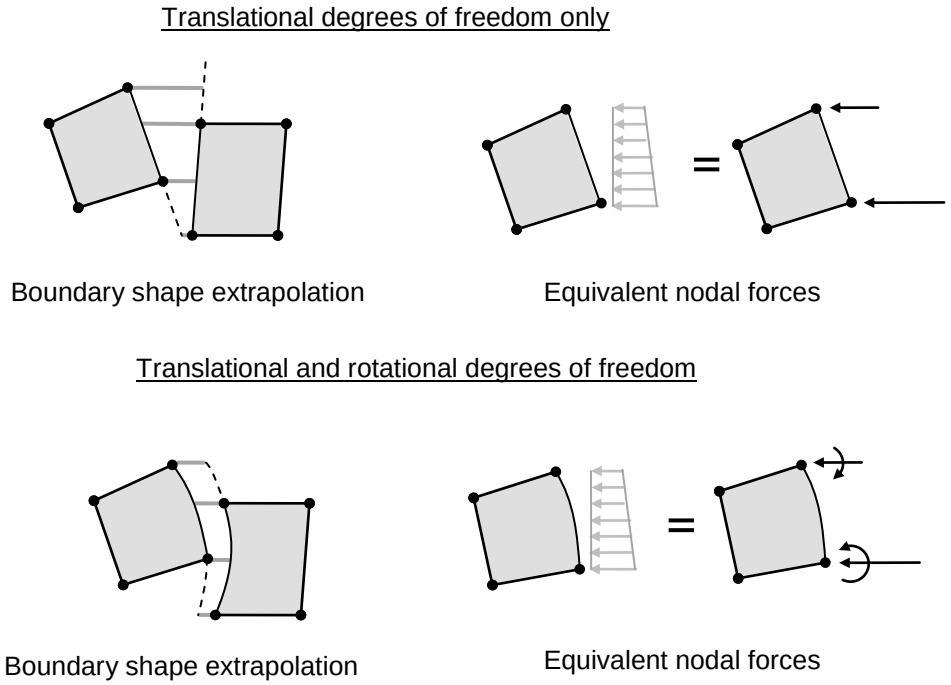

Figure 7.11 Extrapolations and equivalent nodal forces based upon available finite element degrees of freedom.

The use of extrapolations requires careful examination. The loadings presented in Figure 7.10 are not equal and opposite. However, the total loading across the entire contact surface (for example, all contact elements in Figure 7.9) is almost equal and opposite. If the extrapolation of each boundary shape completely predicted the behaviour of the adjacent elements above and below the four nodes of the collision element, then global force equilibrium would be maintained. However, as this is not typically the case, some error is introduced by each extrapolation.

Development of this element was discontinued when tensile contact forces were predicted for parts of a contact surface during static compression of two diaphragms. Tensile forces are not physically realistic since the actual contact surfaces would separate in this circumstance. The predicted tensile forces were located in the extrapolated portions of the contact element shape functions. The added complication of developing algorithms to deal with any predicted tensile loads was deemed to be unnecessarily onerous given the minimal gains in accuracy that were to

be achieved. An easier approach was instead investigated which did not require the use of extrapolated shape functions.

7.3.3 3D Contact using Distributed Stresses

The final model is similar to that presented in the previous section, however instead of extrapolating boundary shapes, the element only calculates stresses over the length that the two boundaries overlap. This removes the errors that result from extrapolation schemes, but also increases the number of contact elements required to 3n - 2 elements, where n is the number of finite elements bordering the contact surface on one of the colliding floors (Figure 7.12). In contrast, the extrapolated shape element required only n contact elements. Figure 7.12 represents the elements as arrows for clarity, however the contact element shape comprises four nodes, effectively connecting two boundary edges.

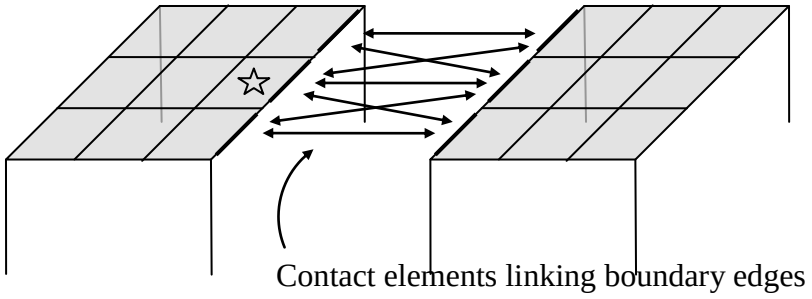

Figure 7.12 Contact element layout for distributed stress element

The calculation of stresses is illustrated in Figure 7.13. Nodal forces are calculated from each element's nodal Fixed End Moments (FEM). The inclusion of rotational degrees of freedom in the contact element depends on the type of the surrounding finite elements.

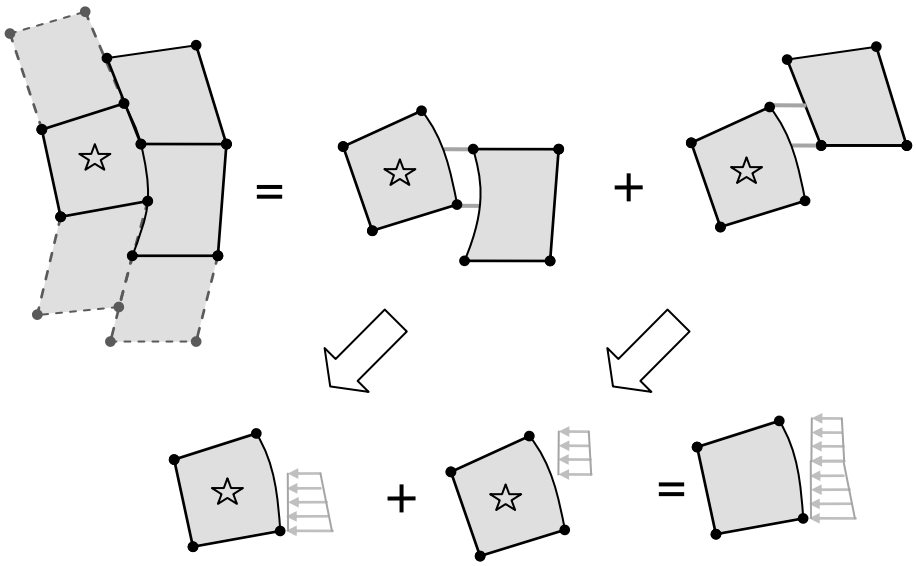

Figure 7.13 Calculation of contact stresses for starred element

While it is believed that this element would work, it has not been developed further. This is because the accuracy increases resulting from the use of this element was considered to be outweighed by the amount of effort required to add the element within Ruaumoko 3D. This element may be worth developing further if interactions between taller buildings were of interest (where larger building offsets could be reasonably expected).

7.4 Assigning Contact Element Stiffness over the Contact Interface

While the physical complications arising from considering 3D contact have been considered (Section 7.2), a method for quantifying the relevant contact element parameters is still required. The selected 3D contact model uses a simple combination of the 2D contact element from Chapter 4, and friction (Section 7.2). However, a means to consistently quantify the 3D contact element's stiffness has not been presented. The underlying principles used in 2D analyses (Section 4.2) can also be used for 3D modelling; however, in 3D analysis, the distribution of contact element stiffnesses across the contact interface also requires consideration (Figure 7.14).

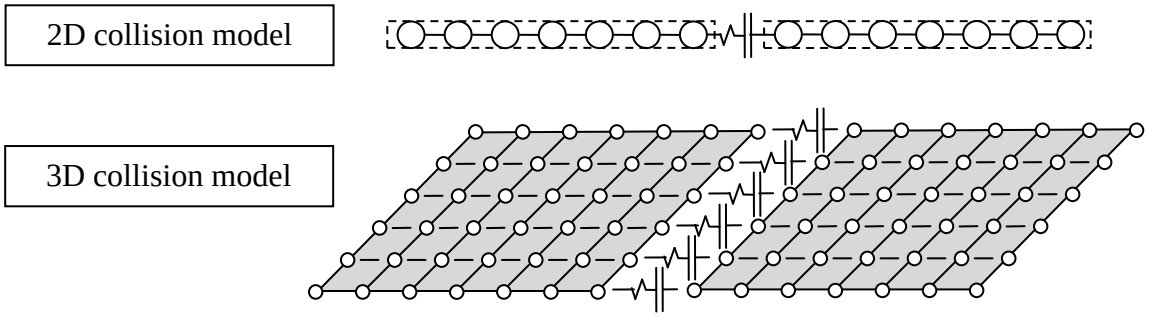

Figure 7.14 Comparison of 2D and 3D contact models for floor/floor collision

Two methods of assigning contact element stiffness are presented here: equal stiffness at all contact elements, and stiffness assigned using tributary area. The methods for calculating these stiffnesses are presented below and illustrated in Figure 7.15.

Equal Stiffness – in this case, the combined contact element stiffness is calculated first. The total contact element stiffness is taken as K = EA/L, where L = the adjacent element length and A = the *overall diaphragm width* multiplied by the diaphragm depth (or thickness). Individual contact element stiffnesses are then assigned by dividing by the number of collision elements. The collision element stiffness is calculated for each diaphragm, and the lesser value is adopted.

Tributary Area – the tributary area stiffness method does not require the combined contact element stiffness. Each element's stiffness is individually assigned using k = EA/L, where L = the adjacent element length and A = the *average adjacent element width* multiplied by the

diaphragm depth. The collision element stiffness is calculated for each diaphragm, and the lesser value is adopted.

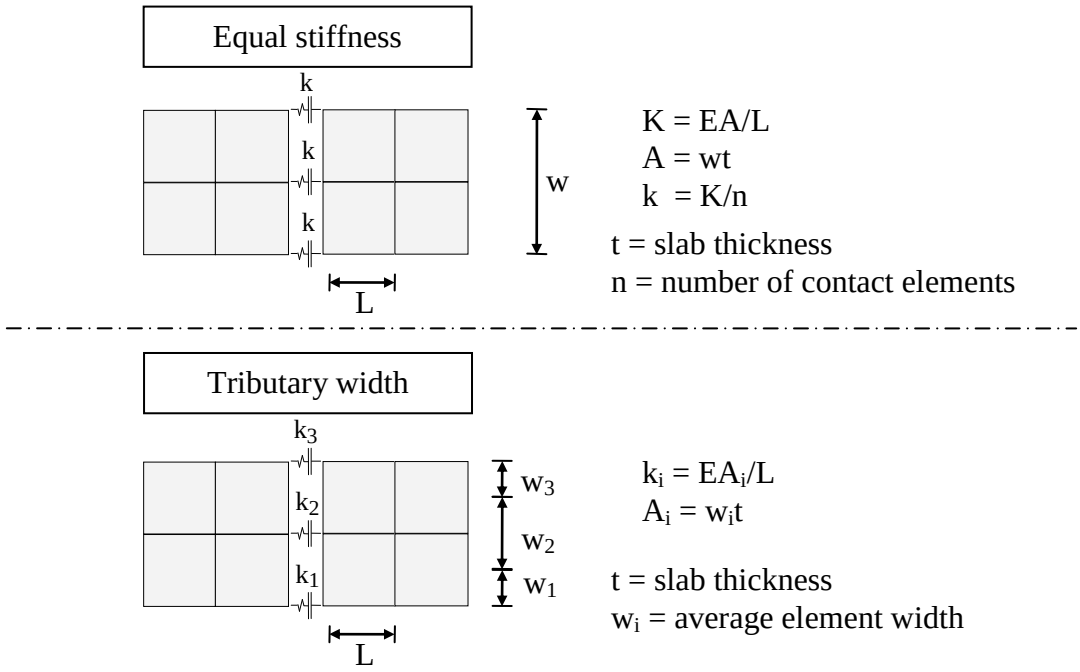

Figure 7.15 Two methods of approximating collision element stiffness for the 3D collision element.

7.4.1 Tested Diaphragm Configurations

The two methods are assessed by comparing the static response of two 10 m by 10 m diaphragms that are initially in contact and then are subjected to a uniform compression. Two configurations of diaphragm are modelled. The first model has all contact elements evenly spaced, while the second model has irregular spacing of contact elements (Figure 7.16). The first model represents the most ideal layout of finite elements, while the second model checks the contact element irregularity that inevitably arises when modelling two buildings of differing proportions. Note that these finite elements do not have in-plane rotational degrees of freedom. This means that the moment requirements (on the topmost and bottommost nodes) presented in Figure 7.7 are not applicable.

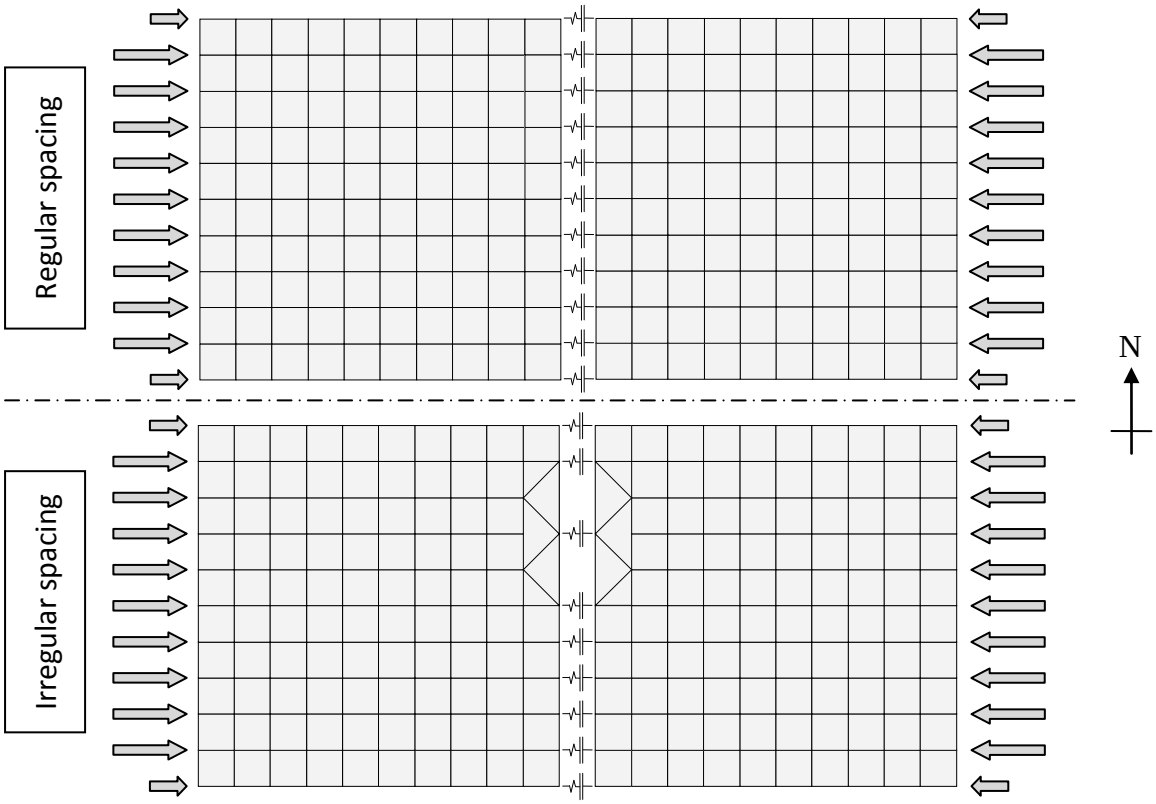

Figure 7.16 Plan view of tested model layouts. Top: regular contact element spacing. Bottom: irregular contact element spacing. Shaded areas indicate locations of finite elements.

7.4.2 Results

Figure 7.17 presents the normal stresses on the left (west) diaphragm shown in Figure 7.16 for regular contact element spacing, while Figure 7.18 presents the corresponding information for the irregular element spacing. The right diaphragm is not presented since it always perfectly mirrors the left diaphragm due to the models' symmetry. A total compression of 1000 kN is applied in each model. The expected resulting normal stresses are 628 kPa in the East – West direction and 0 kPa in the North – South direction. Figure 7.17 shows that the tributary width and equal stiffness methods to be accurate to within 0.04% and 7.5%, respectively. Furthermore, the equal stiffness method records deviations from theory around the irregularly spaced elements. Tributary width is clearly a more accurate method, and is adopted for all subsequent analyses.

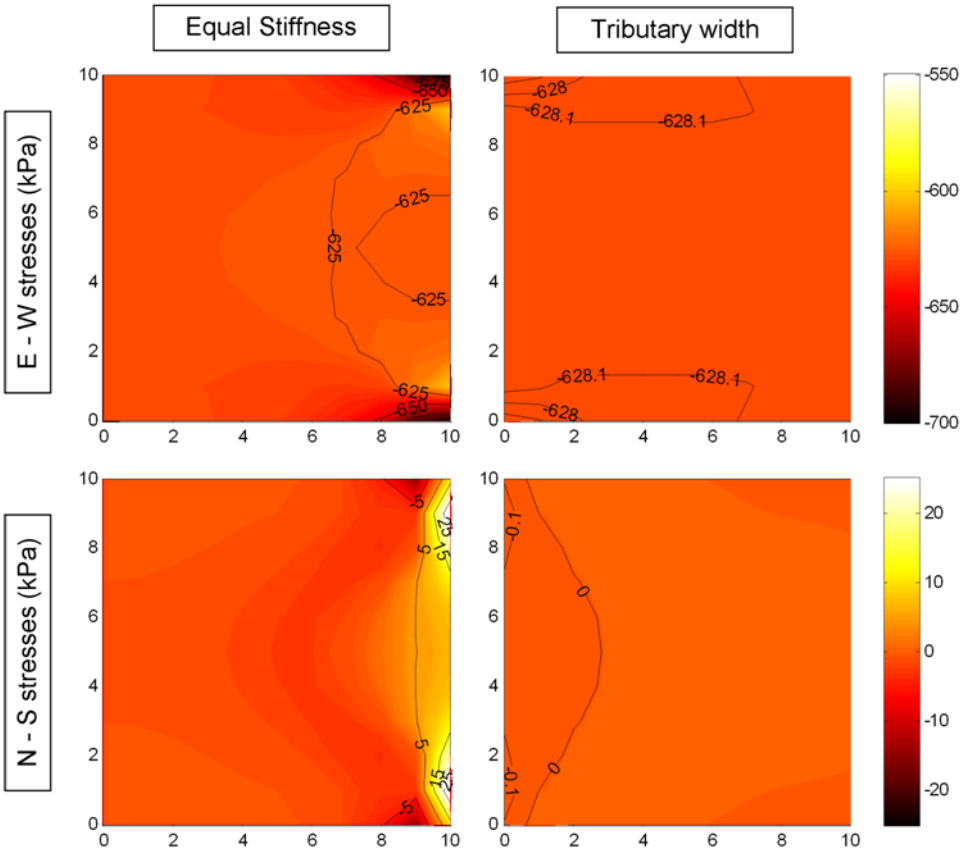

Figure 7.17 Stresses resulting from regular contact element spacing. The internal stresses of the diaphragm are presented in plan. Left: Equal Stiffness. Right: Tributary width. Top: East-West stresses. Bottom: North - South stresses.

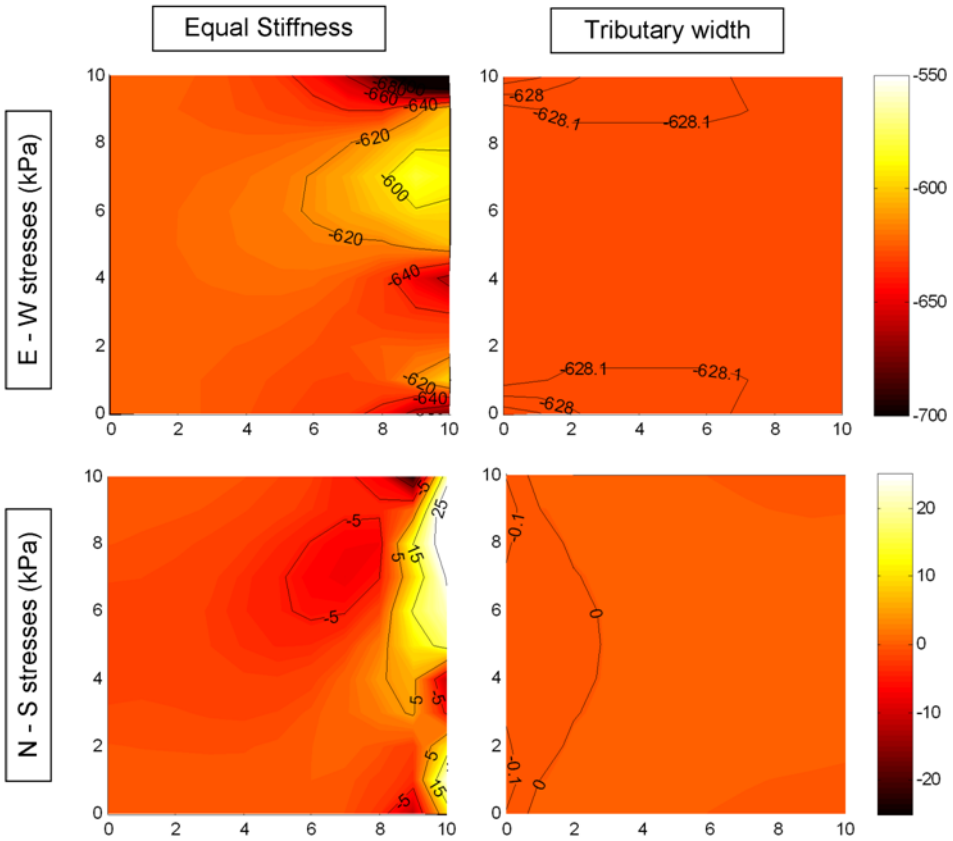

Figure 7.18 Stresses resulting from irregular contact element spacing. The internal stresses of the diaphragm are presented in plan. Left: Equal Stiffness. Right: Tributary width. Top: East-West stresses. Bottom: North - South stresses.

7.4.3 Method of Calculating 3D Contact Stiffness

In the presented 3D pounding modelling, contact stiffnesses were calculated using the following process:

1. Calculate adjacent floor element stiffnesses using the tributary width method. These stiffnesses are calculated at each node that is connected to a contact element.
2. If beams are connected to the considered node and are also oriented in a way that will result in their axial compression during a collision, these axial stiffnesses are added to the floor element stiffnesses.
3. The contact element stiffness is then set as the lower stiffness that has been calculated at either end of the element (i.e. the lower of the stiffnesses calculated at Node A and Node B in Figure 7.2 is adopted).

Axial beam stiffnesses should not be ignored as they can contribute a significant proportion of the calculated stiffness.

7.5 Plasticity in the 3D Contact Element

With some adaptations, the 2D contact elements' various energy dissipation measures can also be applied in 3D analysis. Recall the five models investigated in Chapter 4:

1. Multilinear element
2. Damped Kelvin element
3. Viscous diaphragm
4. Global modal damping
5. Intervening objects

The global modal damping and intervening objects methods require no modification for 3D contact. Similarly, the multilinear element and damped Kelvin element require only a consistent method of application at each contact element on a given floor. When considering the multilinear element, this can be achieved by applying the same value of energy dissipation measure (k_r/k_a) at these contacts. Some care is required in the calculation of the critical damping when using the damped Kelvin element. This is discussed further in Section 8.7. Application of the viscous diaphragm in 3D requires even more detailed consideration. In the 2D analyses, the viscous diaphragm method added viscous dampers to all the diaphragm elements. Extending this process to 3D has a number of possible interpretations (Figure 7.19).

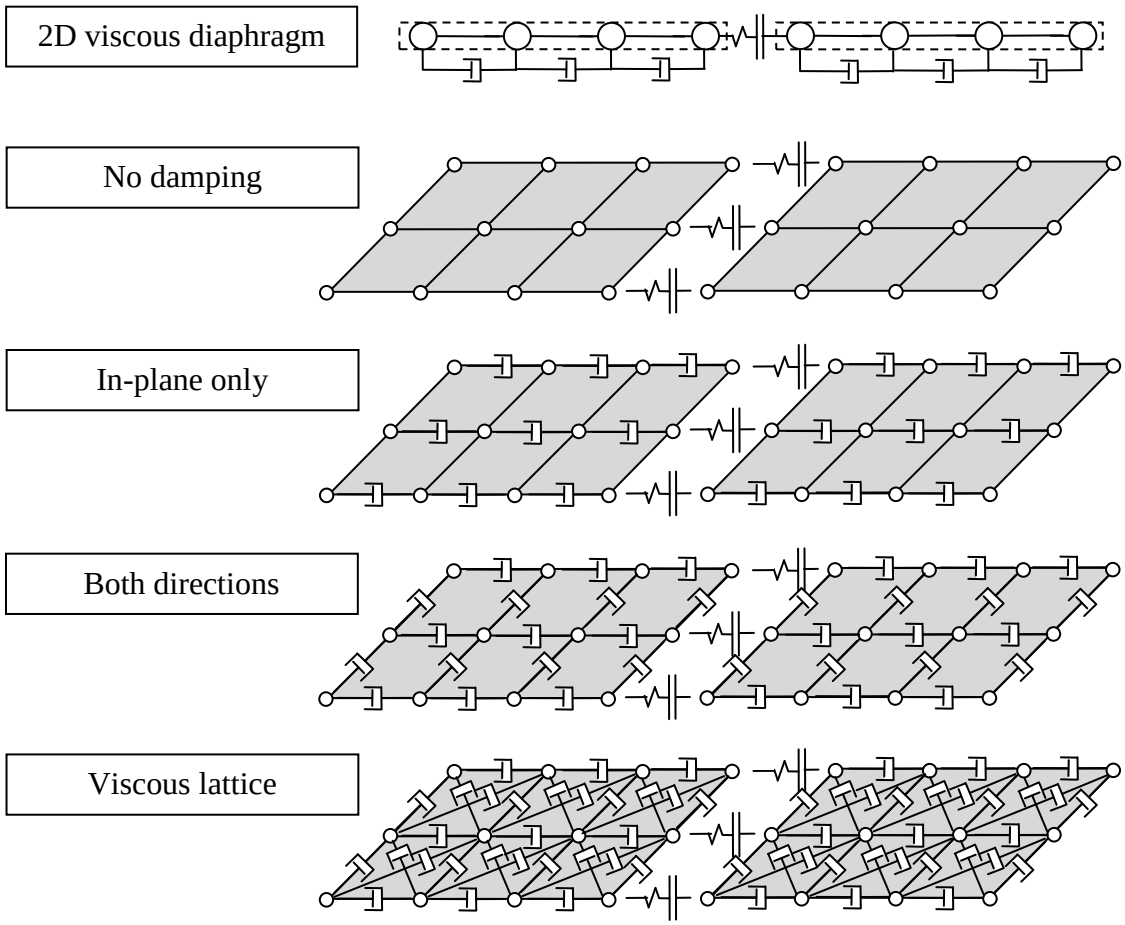

Figure 7.19 Possible implementations of a 3D viscous diaphragm model

The viscous lattice (or possibly even a viscous finite element) is the most literal adaptation of the principle adopted in the 2D analyses. However, this also brings considerably more elements and complication to the method. Furthermore, an effective stiffness and mass must be defined for each damper (refer Equation 4.3). On the other hand if 'in-plane only' damping is adopted, the diaphragms' properties would differ depending on the direction of loading. Such an approach could significantly influence the response of configurations such as the uneven building length scenario of Figure 7.1. It is considered that damping in both directions, without the lattice element is a reasonable compromise. This approach still requires considerable extra effort, as the effective stiffness and mass of each damper must be calculated according to Equation 4.3.

When defining the backbone curve of the plasticity index (Section 4.11), the applied initial velocity should be in the same orientation as the contact elements. Depending upon the building configuration, some out of plane interaction may also occur. This is an inevitable consequence of the 3D modelling.

As with the 2D analyses performed in Chapter 6, the 3D analyses performed in Chapter 8 are performed assuming an elastic collision. The effect of collision plasticity (using the damped Kelvin element) is the subject of one suite of tests (see Section 8.7).

7.6 3D Equivalent Lumped Mass Formulation

The assumptions made during the 2D development of the equivalent lumped mass formulation (Section 3.2.3) do not easily translate to 3D. This is because the 3D analysis requires multiple collision elements across a single floor, whereas 2D analysis only required the definition of a single element. An equivalent lumped mass formulation could be performed in 3D by calculating the element stiffness and damping initially assuming a single contact element, and then assigning these stiffnesses to the various contact elements in proportion to their tributary widths. However, this method has not been tested here. It is speculated that such an approach may provide inaccurate results when contact occurs along a small fraction of the overall collision interface.

It is doubtful that many modellers would desire a 3D equivalent lumped mass formulation. 3D modelling of pounding is currently performed only in very rare circumstances. It is expected that any modeller who is interested in this level of detail will also wish to more accurately model the flexibility of the diaphragm. With these considerations in mind, no further testing of any 3D equivalent lumped mass formulation has been performed.

7.7 Conclusions

The following conclusions are drawn based on the investigations performed in Chapter 7.

1. 2D modelling is unlikely to accurately represent some pounding situations, particularly if one building is considerably longer than the other.
2. Modelling pounding in 3D introduces additional complications due to the relative horizontal movement of the building perpendicular to the direction causing collision. This results in friction forces during contact, and causes difficulty in modelling the exact location of the contact forces.
3. The modelling performed in this thesis of buildings with three storeys or less is unlikely to be significantly affected by the comparatively minor changes in contact force location. This assumption is to be confirmed in the testing performed in Chapter 8.
4. Three contact element models which explicitly model the changes in contact force location were developed to varying degrees. While none of these models are adopted, they may be of use to other researchers in the future.
5. Assigning collision element stiffness over the length of a collision surface is found to be most appropriately calibrated using the tributary width method, including any beams that will be axially compressed.
6. Plasticity in a 3D collision can be modelled but has not been adopted for the default model used in Chapter 8.

7. A 3D equivalent lumped mass formulation has not been developed since it is considered to be largely redundant.

Chapter 8 3D Analysis of Floor/Floor Pounding

The effects of the modelling techniques developed in Chapter 7 are now investigated using the detailed 3D model described in Chapter 5. As stated in the 2D analyses, the purpose of this work is not to attempt to parametrically characterise pounding. Instead one building configuration is examined in detail to provide further understanding of the factors governing collision, and to further illustrate the effects of the proposed contact elements. Firstly, a single collision between two floors is investigated. 2D predictions using the theory developed in Chapter 3 are compared to the results obtained for 3D collisions (Section 8.1). Subsequent sections investigate building displacements, global damage, and local damage for the complete building models described in Chapter 5.

8.1 Single Collision between Two Floors

This section considers the collision between only the first floors of Chapter 5's 3D building models. The layout of this configuration is presented in Figure 8.1. This finite element mesh has been generated to ensure each major gridline has a collision element connecting it to the adjacent building. Further elements have been added at certain points to ensure elongated finite elements (which perform poorly) are avoided. The finite element mesh has been kept coarse to minimise computation time. The accuracy of this approach is considered in this section. Note that while all beams in these floors are also modelled, they are not shown in the figure.

The properties and predicted collision characteristics of both floors are presented in Table 8.1. The axial stiffness of each diaphragm was calculated by recording the displacement of the diaphragm when applied with a uniform (East-West) compression. All calculated values are based upon the assumption that both diaphragms are uniformly compressed during collision. The model geometry shows this assumption is incorrect since the buildings' North-South lengths differ. The significance of this difference is one of the aspects tested here.

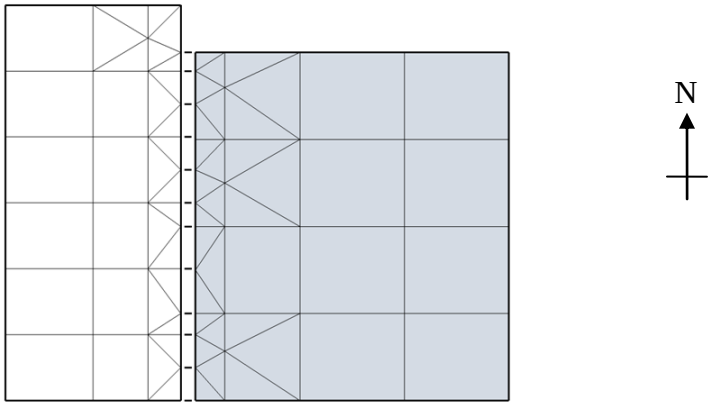

Figure 8.1 Finite element layout for floor collision

Table 8.1 Tested diaphragm properties

Property	*Diaphragm 1*	*Diaphragm 2*	*Ratio*
Mass	*305 Tonne*	*444 Tonne*	*0.69:1*
Axial stiffness	*12,200,000 kN/m*	*6,300,000 kN/m*	*1.94:1*
Axial period	*0.0100 seconds*	*0.0168 seconds*	*0.60:1*
Distributed mass α	*0.464*	*0.319*	-
Lumped mass α	*0.593*	*0.407*	-
Initial velocity	*0 m/s*	*-0.992 m/s*	-
Collision force (Equation 3.30)	*28,000 kN*		-
Distributed mass v' (Equation 3.34)	*-0.921 m/s*	*-0.359 m/s*	-
Lumped mass v' (Equation 3.34)	*-1.18 m/s*	*-0.185 m/s*	-

A collision was generated using the same process as described in Section 4.11, which resulted in a collision after 0.03134 seconds. The collision force in the 12 contact elements is presented in Figure 8.2. In this figure, the contact elements identified by their shade. The darkest line represents the southernmost contact element. The lines progressively lighten moving from South to North (refer Figure 8.1).

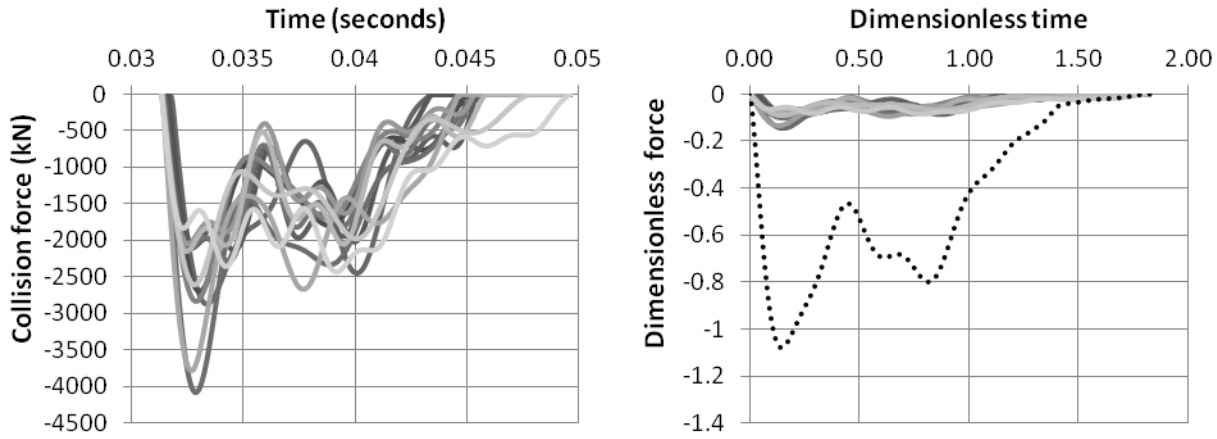

Figure 8.2 Collision element forces during collision. Left: unscaled response. Darkest line indicates the southernmost collision element, lightest line indicates the northernmost collision element. Right: Response divided by the predicted outcome (28,000 kN). Summed force response shown with dotted line.

The collision force is well characterised by the calculated collision force and collision period (Table 8.1). Individual contact elements respond differently due to the differing stiffnesses in their immediate surroundings. However, all present similar shapes to those seen in 2D analyses (for example, Figure 4.13). Note that like the results of Figure 4.13, secondary collisions are predicted for this collision since the distributed mass α_1 is less than 0.5. This property extends the collision duration.

The collision process may be further understood by inspecting the displacements and internal stresses of the diaphragms during the collision. This information is presented in Figure 8.3 and Figure 8.4, respectively.

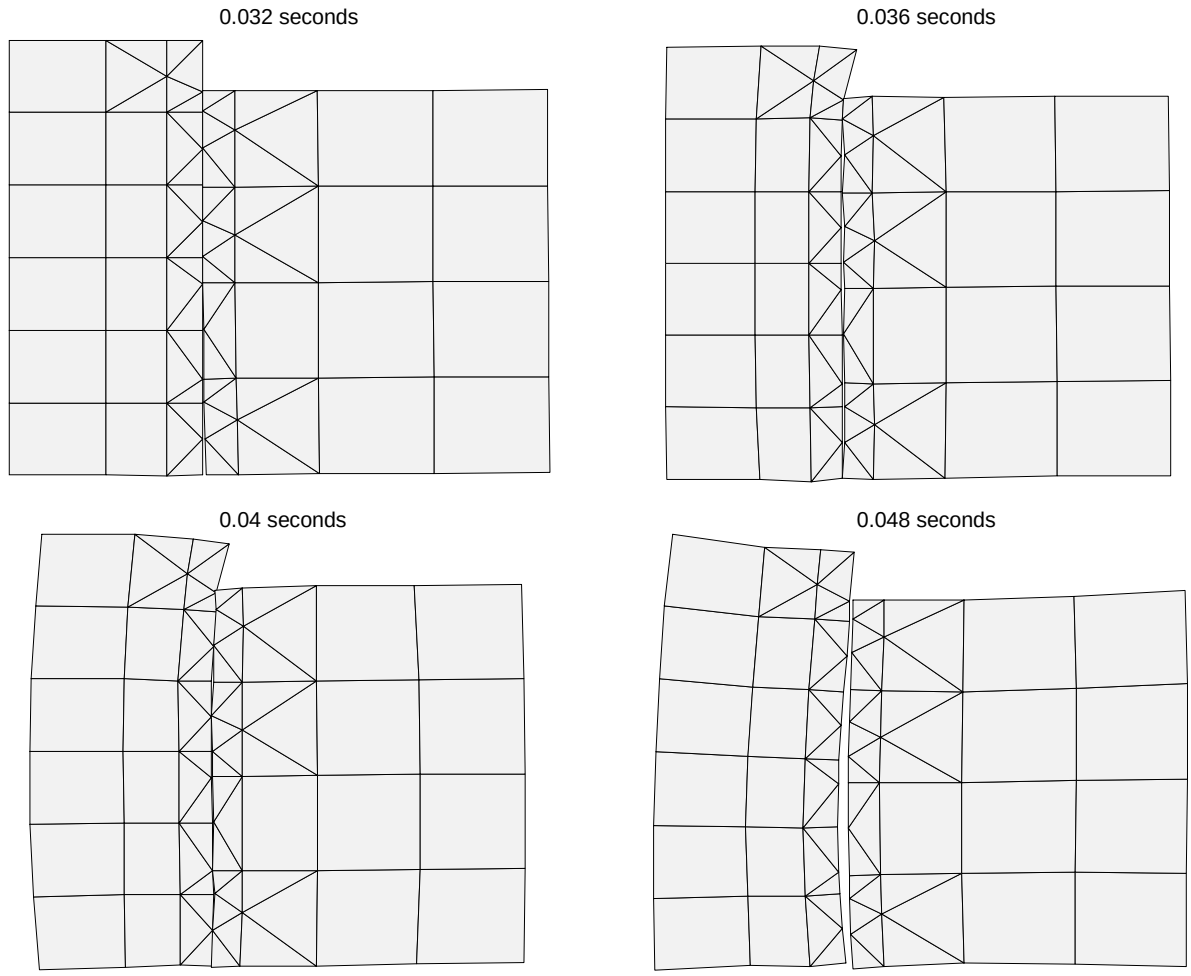

Figure 8.3 Displacement response at four instants during collision. Displacements are magnified 500 times.

Figure 8.3 is considered first. The presented diaphragm displacements are magnified 500 times and show sufficient detail to also see the effect of Poisson's ratio. At 0.032 seconds, the contact elements have just started to be loaded and no notable deformation has occurred.

At 0.036 seconds, the west diaphragm is almost uniformly compressed over the collision interface. At this time, the effects of the western floor's northern 'overhang' are restricted to just the north-eastern corner of the diaphragm. However, by 0.04 seconds, these effects can be observed over the length of the western diaphragm. The western face is in tension while the collision interface (the eastern face) is subject to compression. By 0.048 seconds, the collision is almost complete. Although it cannot be seen in the figure, the northernmost collision element is still activated (the initial separation shown in the figure has been modified for clarity). At this point both diaphragms are in tension. This is indicated by the north-south contraction in the centre of each diaphragm due to Poisson's ratio. Theory only predicts tension in the eastern

diaphragm due to the expected oscillation after collision. The western diaphragm's tensile stresses are attributed to a combination of the overhang and the inconsistent diaphragm stiffness caused by the diaphragm's supporting beams.

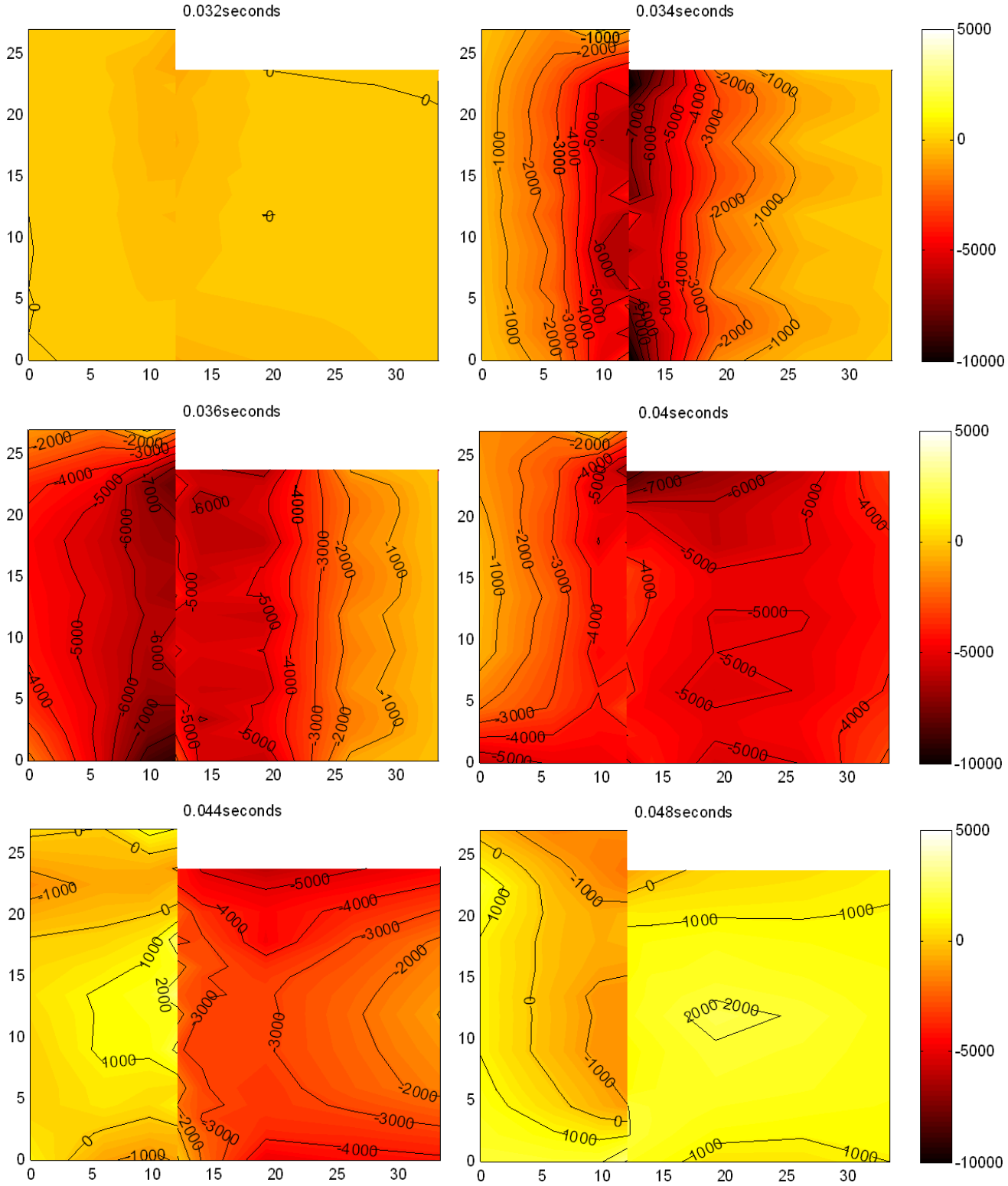

Figure 8.4 Normal East-West floor stresses during collision. Axes show distance (m). Floor stresses are presented in kPa.

The East-West normal stress distributions are presented in Figure 8.4. As previously noted, the adopted mesh size is not detailed enough to provide accurate values of stress in the floors. However, general trends can still be observed and explained. Initially, localised stress concentrations are observed at the corners of the collision interface (0.034 – 0.036 seconds). This is attributed to the stiff beams running East-West in these locations. Additionally, the overhang will have some effect on the northern edge.

The propagation of the stress wave front can be observed in each building. A uniform compression of 8-9 MPa (depending on the definition of the cross section area in the Eastern diaphragm) is expected in each building. The average magnitude of the compressive wave may be approximated by taking a North-South section through the centre of each diaphragm. With this method, both diaphragms report approximately 5 MPa compression. Some load is also transferred by the diaphragms' beams. Nevertheless, some load discrepancy is apparent here.

The later stages of the collision (0.044 seconds onwards) show significant differences in stress along the collision interface. This is a result of building separation which has begun to occur along the interface. The North-South normal stresses and shear stresses are not presented here, but both show stress concentrations at the building overhang.

The post collision velocities of the east and west diaphragms were recorded as -0.927 m/s and -0.350 m/s, respectively. These values are in excellent agreement with those predicted by distributed mass theory (Table 8.1), but differ significantly from the lumped mass predictions. In this case, 2D distributed mass analysis of the collision provides suitably accurate results. It is expected that 2D collision force and collision duration will frequently provide reasonable approximation for buildings of a wide range of differing geometries. If the two buildings do not have any significant torsion at the onset of a collision, the previously presented theory can be used to describe the dominant process of the collision (Figure 8.5). If the effect of the uncompressed section of the larger diaphragm is ignored, the diaphragm floor response is directly analogous to Figure 3.12.

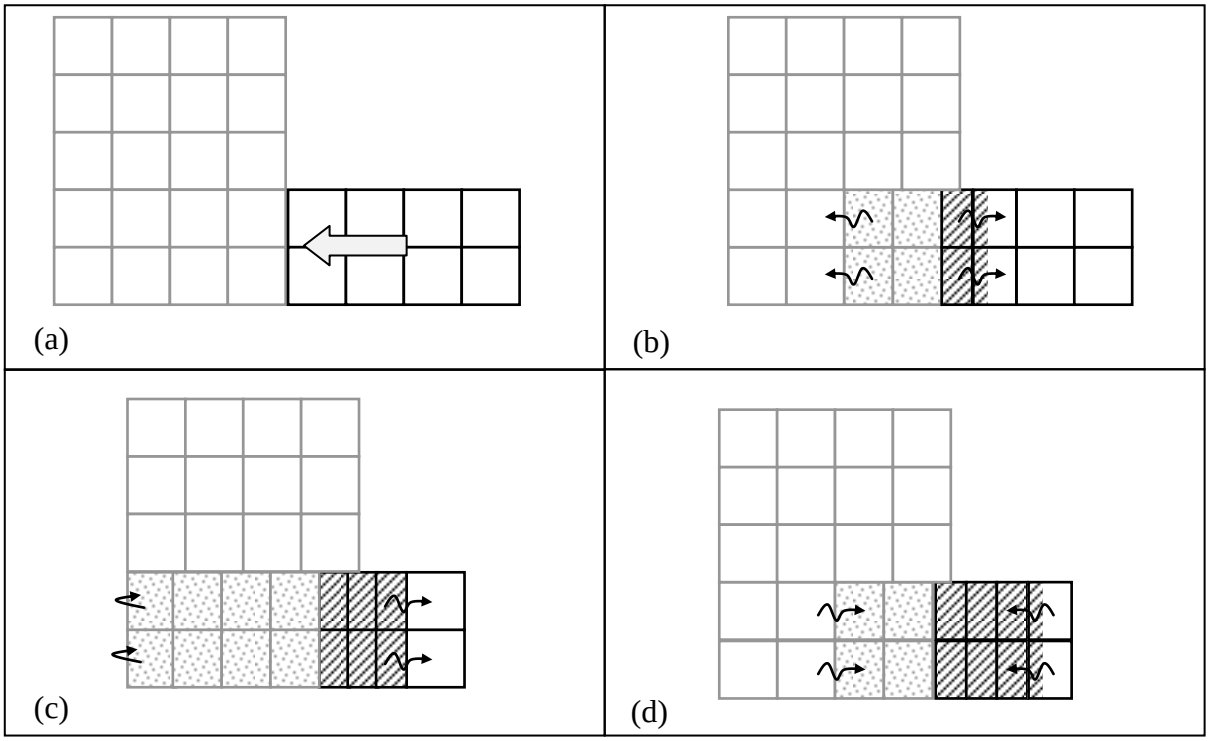

Figure 8.5 Plan view of two floors undergoing an idealised eccentric collision. Interaction from the untouched section of diaphragm is assumed to be negligible. The propagation of the idealised compression wave is shown in parts b – d.

2D collision theory (Equation 3.30 and 3.25) requires information about the total mass and stiffness of each diaphragm. However, in the above scenario, collision only affects a part of the larger diaphragm. The 2D inputs are still valid because the typical diaphragm mass and stiffness distribution is relatively uniform. This means each diaphragm's wave speed is almost constant wherever a collision may occur. Thus the diaphragm's response to collision along a fraction of the interface is similar to that of a complete interface collision. However, the post collision response of one or both buildings is likely to be partially torsional, due to the eccentric collision load. This will complicate the global response of the buildings to the collision, and may introduce a torsional component to any subsequent collision. These complications require 3D modelling to be adequately represented.

8.2 Building Properties

The subsequent sections present results based upon 3D analysis of two three storey buildings (Figure 8.6). Note both Building 1 (shown on the left) and Building 2 have no internal columns between Level 2 and the roof, (this is likely to be due to the light weight roof not requiring any central support). Figure 8.6 also identifies the direction of the global X, Y and Z axes. These definitions are used throughout the remainder of this chapter to describe the direction of various actions. The geometry of these buidings in the XZ plane is consistent with that shown in Figure 5.4. In the Y direction, Building 1 has six 4.5 m wide bays and Building 2 has four 5.943 m wide bays. This leaves an overlap of 3.228 m at the back of the two buildings.

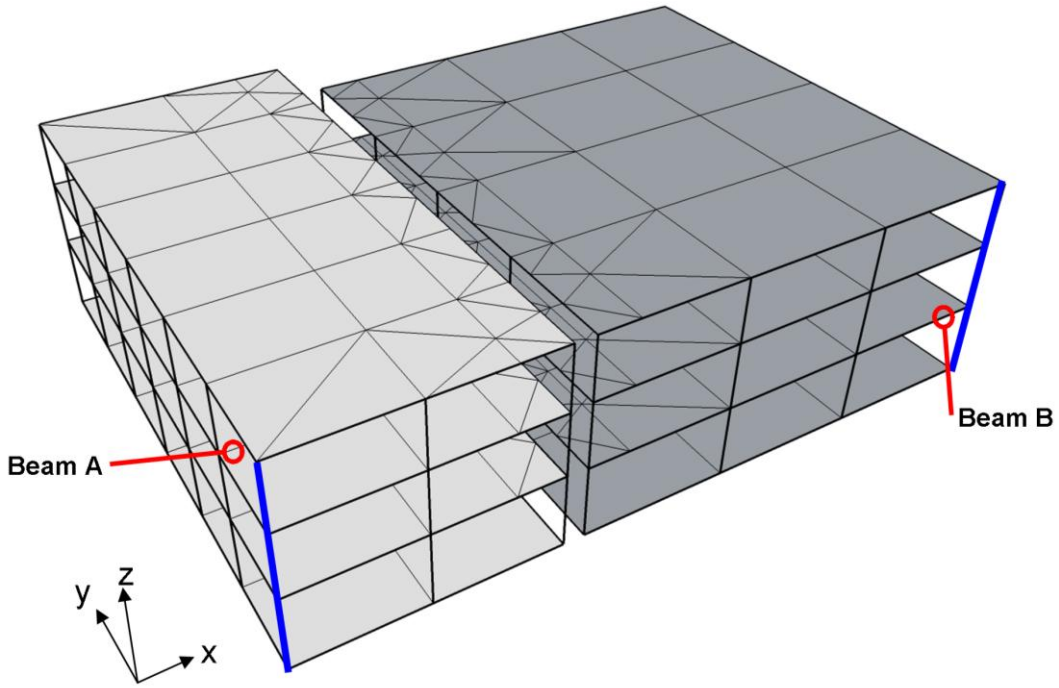

Figure 8.6 3D model configuration. Thick lines indicate points where floor displacement measurements were recorded. Circled members indicate locations of ductility recordings. Note also the definition of global axes.

Table 8.2 and Table 8.3 show the buildings' properties and calculations that directly affect post collision velocity of each floor. The axial periods of Building 1's floors are less than that of Building 2, and therefore govern the expected collision duration. Comparison of the distributed mass 'α's (Table 8.3) predicts that Building 2's roof should be more affected by collision than Building 1 (since Building 2's 'α's are larger). At Level 1 and Level 2, Building 1 is expected to be marginally more sensitive to collision, although this difference should be less pronounced. The effective coefficients of restitution are also noteworthy. At Level 1 and Level 2, e_{eff} is approximately 0.56. This means that the post collision vibrations in Building 2's floors are predicted to absorb more energy than is typically modelled for all collision energy dissipation in a lumped mass model (since typically e ≈ 0.65). Secondary collisions are also expected at all levels.

Table 8.2 3D model colliding floor properties

	Building 1			*Building 2*			*Ratio*	
Level	***Mass***	***Axial Stiffness***	***Axial Period***	***Mass***	***Axial Stiffness***	***Axial Period***	***Mass***	***Axial Period***
	Tonne	*kN/m*	*sec*	*Tonne*	*kN/m*	*sec*	*-*	*-*
Roof	*150*	*927,196*	*0.022*	*60*	*346,279*	*0.024*	*2.51:1*	*0.94:1*
Level 2	*338*	*11,958,185*	*0.010*	*460*	*5,963,474*	*0.017*	*0.73:1*	*0.60:1*
Level 1	*321*	*12,184,738*	*0.010*	*461*	*6,272,241*	*0.017*	*0.70:1*	*0.60:1*

Table 8.3 Calculated floor collision properties

	Building 1		Building 2		Collision Properties	
Level	**Lumped Mass α**	**Distributed Mass α**	**Lumped Mass α**	**Distributed Mass α**	**e_{eff}**	**Secondary collisions**
Roof	*0.285*	*0.272*	*0.715*	*0.683*	*0.910*	*Yes*
Level 2	*0.576*	*0.450*	*0.424*	*0.331*	*0.561*	*Yes*
Level 1	*0.590*	*0.461*	*0.410*	*0.321*	*0.564*	*Yes*

The floor properties used in the single collision analysis (Section 8.1) were selected from the properties of Level 1 in Table 8.2. The single collision floor masses slightly differ between the two models because column masses were not included in the single floor collision.

The properties of the 3D models may also be directly compared to the 2D model (Chapter 6). Comparison of Table 8.2 with Table 6.1 shows axial periods differ by 20 – 30%. Similar differences appear in the fundamental periods of each building (Table 8.4). Major differences in the building period significantly change the buildings performance during a ground motion. This means that while Chapter 6's reported trends are valid in isolation, they cannot be used to provide meaningful comparisons to 3D analyses performed here. The differences in dynamic properties essentially means Chapter 6's 2D analyses are different buildings to the ones modelled in 3D here. Instead additional 2D analyses are performed in this chapter modelling all elements in both buildings (compared to Chapter 6's single frame from each building). This is done to explicitly illustrate the differences between 2D and 3D modelling of pounding.

Table 8.4 Fundamental periods of Building 1 & Building 2 under 2D and 3D modelling assumptions

	2D period *(seconds)*	***3D period (x direction)*** *(seconds)*
Building 1	*0.471*	*0.662*
Building 2	*0.408*	*0.488*

8.3 Testing Schedule and Naming Conventions

When necessary, the performed tests are identified using the format presented in Section 6.3. Eight tests are performed in this chapter:

1. *3DModel* – Default tests using 3D analysis. These tests investigate the effects of building separation. The results are also used as a benchmark for comparison with subsequent tests. [Section 8.4]

2. *2DFlex* – Buildings are constrained to only move in the XZ plane, and nodes at the same X and Z ordinates are connected via the intervening floor stiffness. These tests investigate how much model simplification affects pounding response. [Section 8.5]
3. *2DSlave* – Buildings are constrained to only move in the XZ plane, and nodes at the same X and Z ordinates are constrained (or slaved) to move completely in unison. The distinction between *2DSlave* and *2DFlex* is explained further in Section 8.5. [Section 8.5]
4. *3DRigid* – 3D analysis with the diaphragms modelled as completely rigid objects. [Section 8.6]
5. *3DDamp* – 3D analysis with additional contact damping. [Section 8.7]
6. *3DModelE* – 3D analysis of modified building configuration to encourage eccentric collision. [Section 8.8]
7. *2DSlaveE* – Modelling as per *2DSlave* for the eccentric model. [Section 8.9]
8. *3DRigidE* – Modelling as per *3DRigid* for the eccentric model. [Section 8.10]

The 2D analyses performed in Chapter 6 varied separations between 0 and 25 mm. Tested 3D model building separations range from 0 to 45 mm. This increase is necessary to get sufficient separations to prevent pounding contact. In addition to the above separations, no contact (NC) analyses are performed to obtain building response when pounding does not occur. All 3D tests include both X and Y components of the tested ground motions (see Section 5.3.7). Note that when a "-" ground motion is used, both X and Y ground motion components are reversed.

8.4 Effects of Building Separation on 3D Models

Building separation effects are investigated using *3DModel*. The NC responses are presented first to show the performance of the buildings under the various ground motions. Pounding analyses are then compared to these building parameters to illustrate their sensitivity to contact.

8.4.1 Response of Buildings with No Contact

Figure 8.7 presents the maximum displacement envelopes for each of the six tested ground motions. Floor displacements have been recorded at the floor nodes indicated in Figure 8.6. Floor displacements were also recorded at the rear frames and were found to be in almost identical to the front frames. The X and Y directions correspond to displacements across and along the buildings respectively, as defined in Figure 8.6. Both buildings' envelopes correspond well to first mode shapes, as is expected for low rise buildings. The roof level of both buildings shows additional drifts in the X direction. This can be attributed to the internal columns which extend from the ground level to Level 2, causing a stiffness irregularity between Level 2 and Level 3 (the roof). This effect is not observed in the stiffer Y direction (the relative stiffness of

the X and Y directions can be evaluated using Table 5.4, smaller periods indicates greater stiffness since the mass is constant).

Analytical validation of the transverse movement between floors can also be obtained from this figure. Table 7.1 provided approximate estimates of relative movement to justify not modelling the results of this effect. These estimates are reassessed here. If the minimum displacement of one building's floor is subtracted from the maximum displacement of the other building's floor, a conservative relative transverse movement can be calculated (at a given floor level, and for a given ground motion). Using this process, 39 mm maximum relative movement was recorded at Level 3. This is only 0.16% of the smaller building length, which justifies the omission of collision force location modelling methods (see Section 7.3). When compared to Table 7.1, this suggests that the effective building drifts of the buildings Y axis were approximately 0.25%.

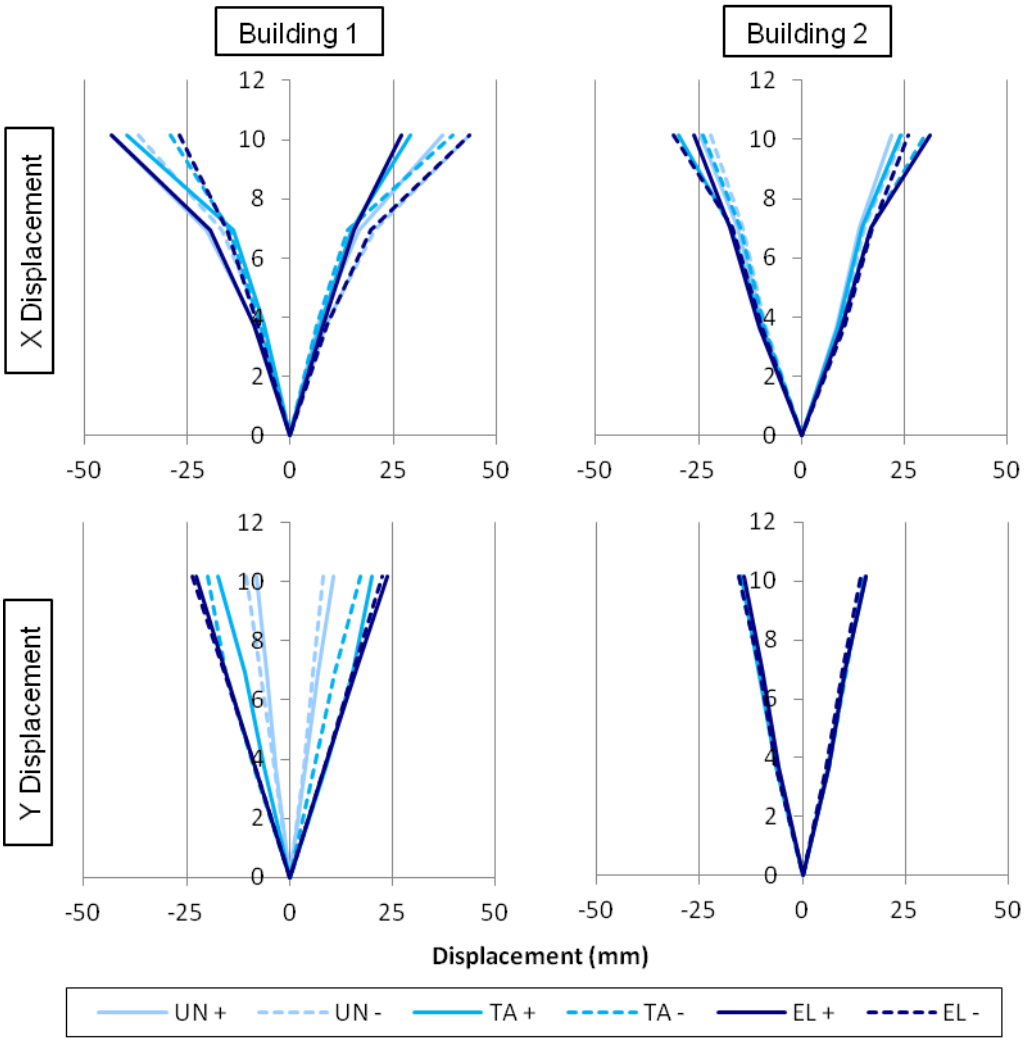

Figure 8.7 Displacement envelopes over the height of each building for 'No Contact' analyses. Vertical axis displays height above ground level in meters.

Interstorey shears of both buildings are also presented for the X and Y directions in Figure 8.8. Only three ground motions are presented since the '+' earthquake directions cause the same interstorey shears as the '-' earthquake records.

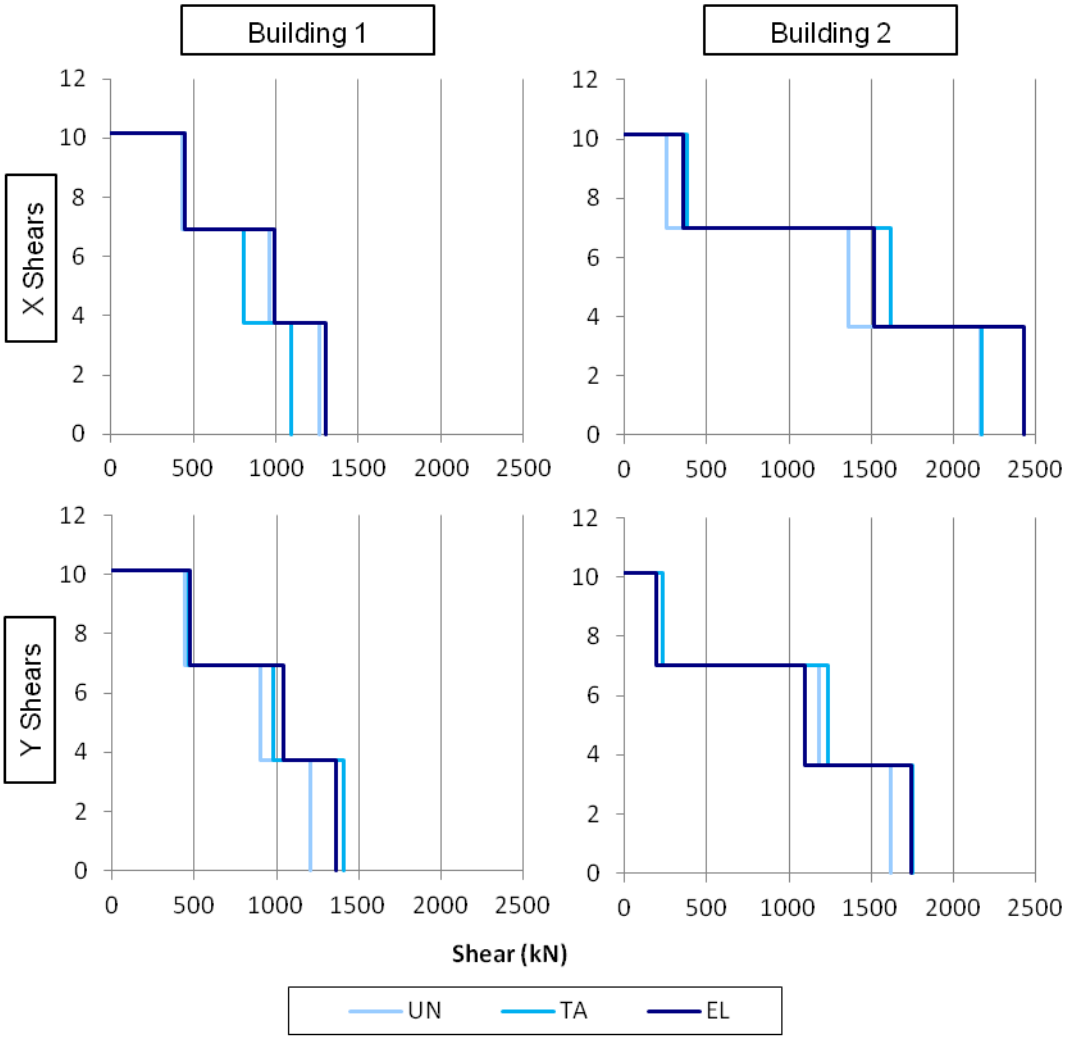

Figure 8.8 Interstorey shear envelopes over height of building during 'No Contact' analyses. Vertical axis displays height above ground level in meters.

Building 2 records greater interstorey shears due to its greater total mass. Despite the earthquake's primary excitation being applied in the X direction, Building 1's shears in the Y direction are greater than those in the X direction. This is attributed to the roof columns' geometries, which have greater moment capacity in the Y direction (many columns have rectangular sections, result in differing X and Y stiffnesses and moment capacities). In the X direction, the roof columns yield at lower levels, restricting the maximum shear force. The ductilities reported in the X direction of the roof level columns are much greater than those reported in the Y direction. This indicates that the X direction is more greatly excited than the Y direction, which is expected since this direction has been excited using the primary component of the ground motions.

Maximum beam and column ductilities (subject to the restriction presented in Section 5.3.6) are presented in Figure 8.9. The ductility of two specific beams are also included to indicate the change in loading of individual members. The locations of these beams are indicated in Figure 8.6. No member's ductility capacity has been exceeded (refer Section 5.2.9). Beam A's ductility is near the maximum ductility for '-' earthquakes while Beam B's ductility is similarly near the maximum for '+' records. This pattern is largely coincidence since the – and + are convenient indicators of direction rather than a fundamental property of the ground motions. However, difference in reported ductility due to the direction change is expected. Ground motion records usually apply asymmetric loadings to buildings, which results in a greater maximum demands in one direction (for example, westerly shear loading may be greater than the easterly loading). Furthermore, gravity loadings (self-weight) are included in the modelling, which may either reduce or increase seismic loads depending on the location of the considered member. Thus while reversing the earthquake orientation does not change the maximum reported building ductilities, the maximum ductilities of individual elements do change. No ductilities are reported for Building 2's columns or Y frame beams since these members did not yield in the NC records.

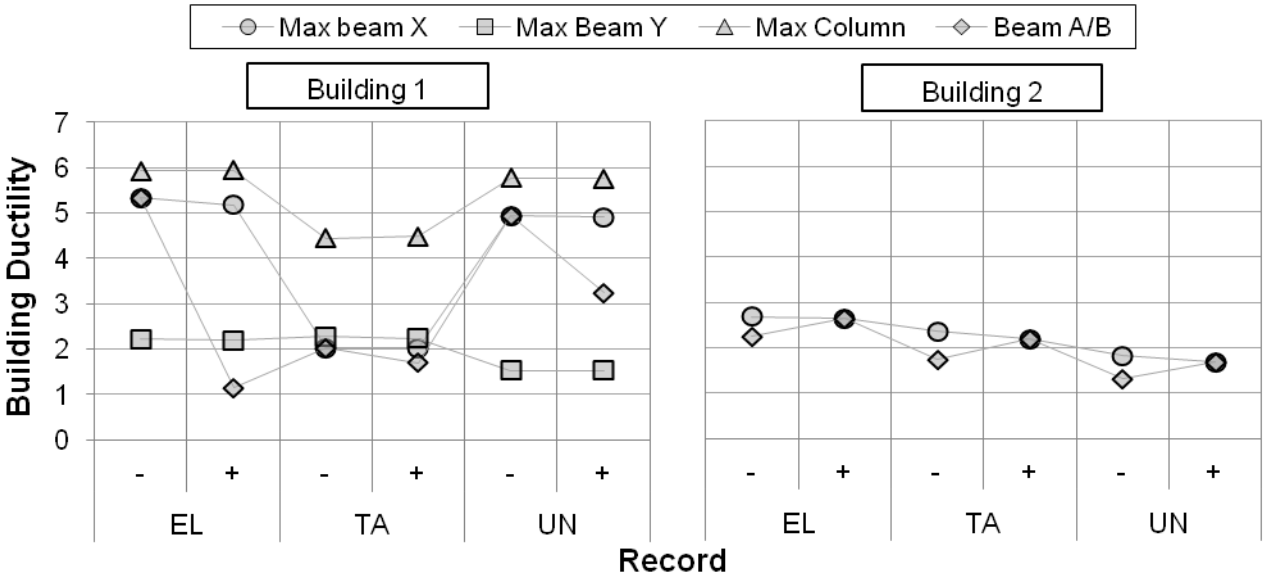

Figure 8.9 Building ductilities recorded in No Contact analyses. X beams refer to members aligned with the global X axis and while Y beams correspond to the Y axis.

8.4.2 Displacement Sensitivity to Building Separation

The effects of pounding on building displacements are assessed at the roof level using the nodes indicated in Figure 8.6. In this section results are normalised by the NC record's responses, while the building separations are normalised by the minimum separation required to achieve a NC response. These minimum separations are stated in Table 8.5 for each ground motion. Figure 8.10 and Figure 8.11 present the displacement amplifications as a result of pounding.

Table 8.5 Required separations to prevent pounding (mm)

	'+' orientation	*'-' orientation*
El Centro (EL)	*63.2*	*43.6*
Tabas (TA)	*50.6*	*49.2*
La Union (UN)	*56.8*	*38.7*

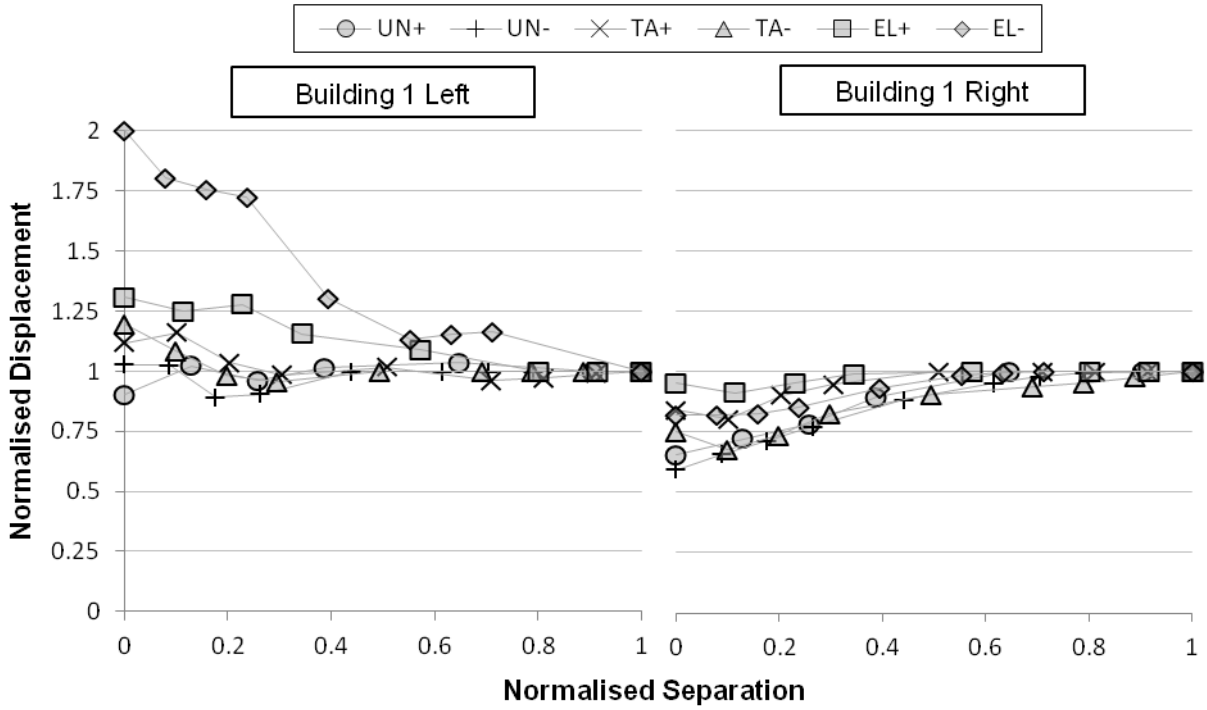

Figure 8.10 Building 1 X direction displacement amplification due to pounding

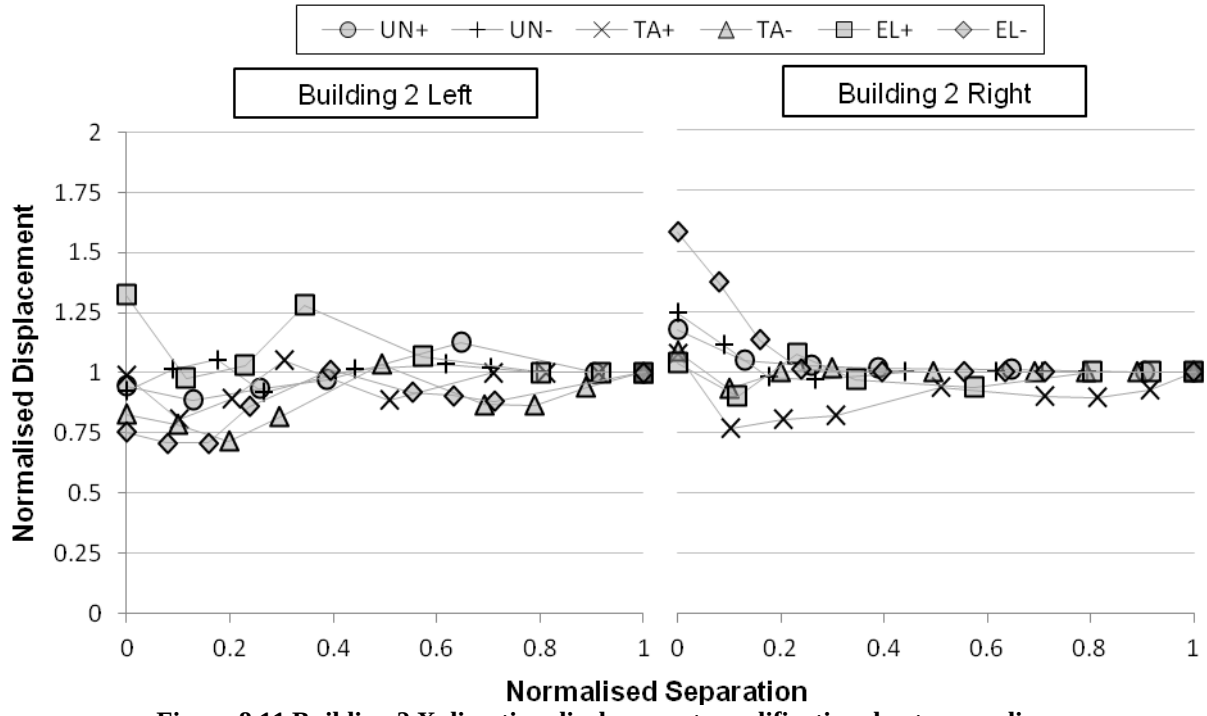

Figure 8.11 Building 2 X direction displacement amplification due to pounding

The presented trends are similar to those discussed for the 2D model in Section 6.6.1, although the maximum recorded amplifications have increased. Amplifications are generally largest at

zero separation and decrease with increasing separation. For normalised separations greater than 0.5, X displacement envelopes differ by less than 17%. The influence of pounding on the Y direction displacements is more muted. The maximum absolute Y direction displacements are presented in Figure 8.12 and differ by less than 20%. For normalised separations of greater than 0.5, Y displacement envelopes differ by less than 10%.

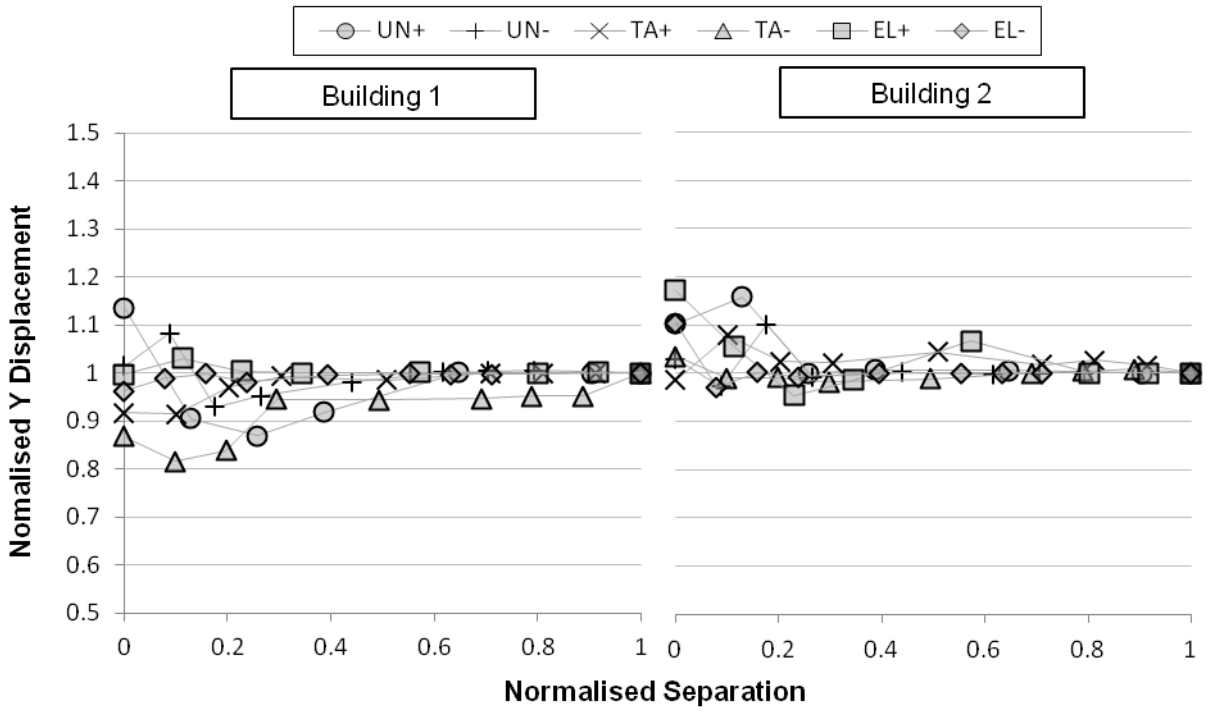

Figure 8.12 Y direction displacement amplifications due to pounding

The building displacements of both the front and the rear frames of the modelled buildings are presented in Figure 8.13 and Figure 8.14. In these figures, the difference in maximum displacements is of interest, since this indicates greater building rotation. Both modelled buildings are perfectly symmetric, so torsion is only generated through pounding. Only four building separations (shown in boxes inset in the figure) are presented for clarity.

Both building's rotations decrease roughly linearly with increasing building separation. For example, consider the EL+ record in Figure 8.13. At 0 mm separation, the difference in frame displacements is 14 mm. As separation increases this difference reduces to 5, 6 and 3 mm, respectively. By 25 mm separation, most records show little building rotation. These results show that torsion can be induced by the pounding configuration even when both buildings are perfectly symmetrical. 'Building 1 Right' and 'Building 2 Left' are not presented here but show similar trends.

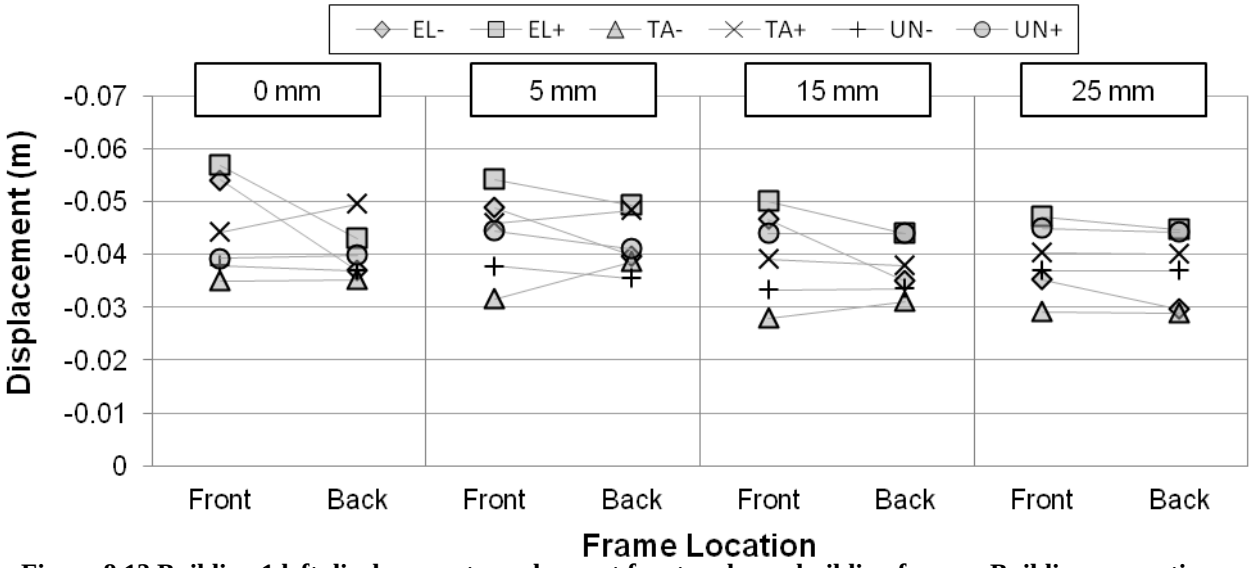

Figure 8.13 Building 1 left displacement envelopes at front and rear building frames. Building separations indicated with boxed numbers

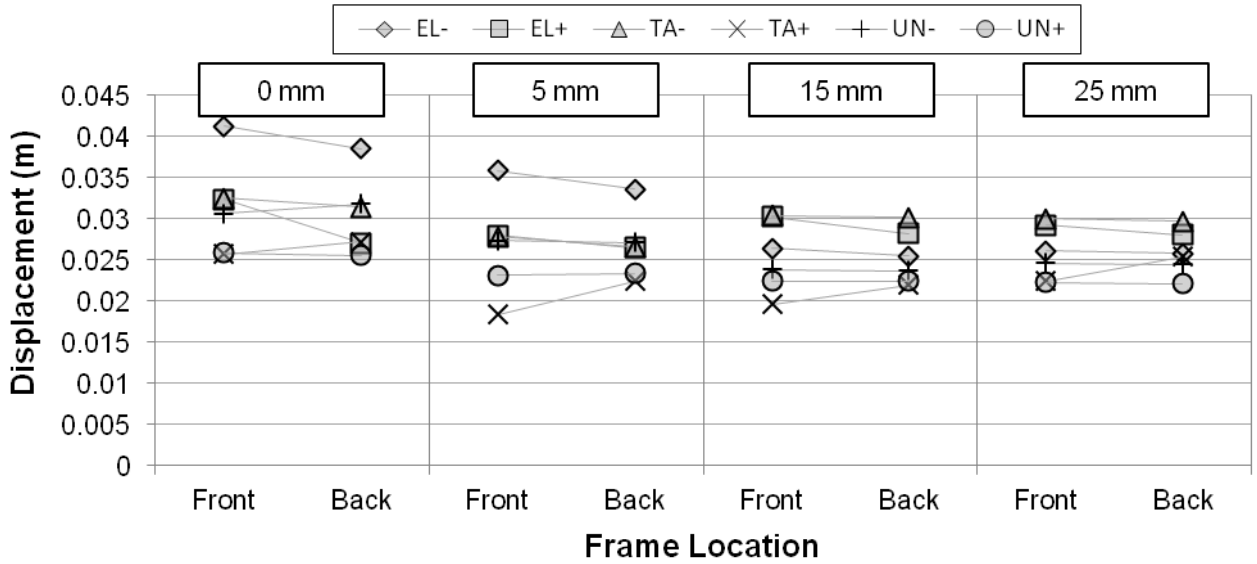

Figure 8.14 Building 2 right displacement envelopes at front and rear building frames. Building separations indicated with boxed numbers

8.4.3 Global Damage Sensitivity to Building Separation

The significance of 3D modelling on global building demand is assessed using interstorey shears and member ductilities. Interpretation of interstorey shear amplifications is difficult since many elements yield during the performed analyses. Building 2's shear amplifications are presented here since no column yielding occurred in the building during the NC analyses. During the pounding analyses yielding did occur in Level 3 columns; however in all cases except one (*EL-00_3DModel*), this was limited to the four corner columns. This yielding has therefore made little difference to the total interstorey shear.

Figure 8.15 presents the interstorey shear amplification of Building 2 due to pounding. Greater shear amplifications occur in the higher stories. At roof level shear demands reach up to twice that of the NC demand. This effect is partially caused by the larger magnitudes of shear force

that occur at the lower levels (requiring a larger shear change to cause the same percentage increase). At Level 2, shears are amplified by up to a maximum of 38% while Level 1 shears are predominantly deamplified. In the no contact records, Level 3 experiences particularly low interstorey shear demands (≈200 kN) in the Y direction. Amplifications in the Y direction are approximately equal to that in the X direction at all levels. Once again pounding is shown to be able to both amplify and deamplify building demands depending on the specific model configuration. Increasing the separation of the buildings generally reduces the shear amplifications.

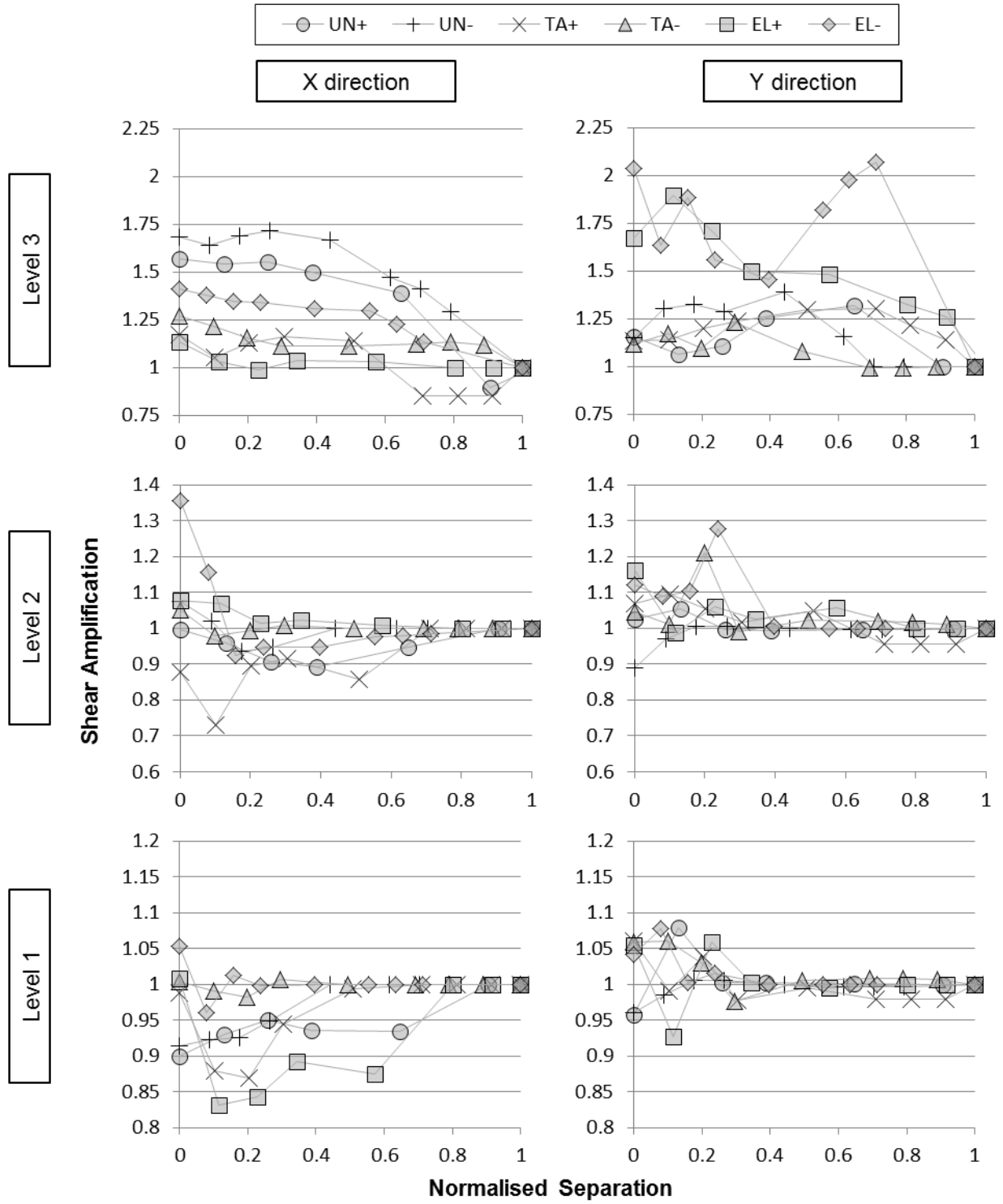

Figure 8.15 Interstorey shear amplification in Building 2. Note that different vertical scales are used at each floor level

The remaining building elements are assessed using the maximum recorded ductilities. Figure 8.16 presents the maximum member ductilities corresponding to building movement in the X direction. Building 1 is more sensitive to pounding effects in comparison to Building 2. Recalling the values of α in Table 8.3, this is expected at Level 1 and Level 2 but not at roof level. This discrepancy highlights a drawback of the simplified calculations since total building mass is not factored into the computations. Building 2's ductilities only significantly increase at

separations greater than 0, while approximately 50% of Building 1's actions have been reduced by pounding. If the buildings have a normalised separation of 0.5 or greater, pounding induced demands differ from the NC records by less than 28%.

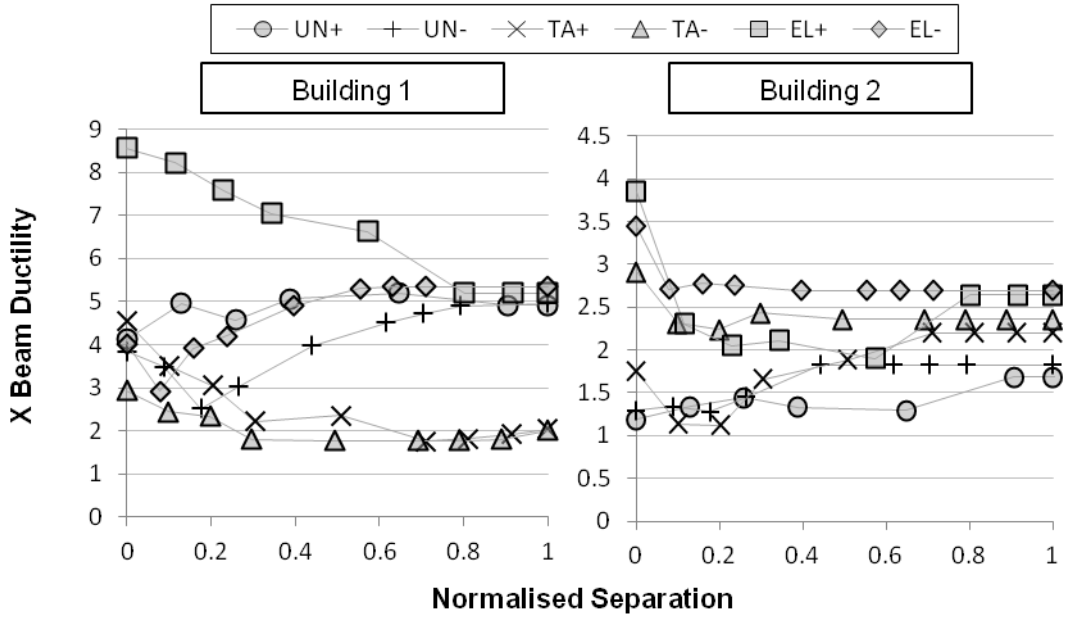

Figure 8.16 Beam ductility due to movement in the X direction

Other Building 1 member ductilities are presented in Figure 8.17. Building 2's corresponding data is not reported since very little yielding occurred in those members. Beam ductilities due to Y axis movement have either reduced or have not changed as a result of pounding. However, column ductilities (recorded as the maximum from both the X and Y directions) are amplified by up to 75% and reduced by up to 25% as a result of pounding. These effects reduce with increasing separation.

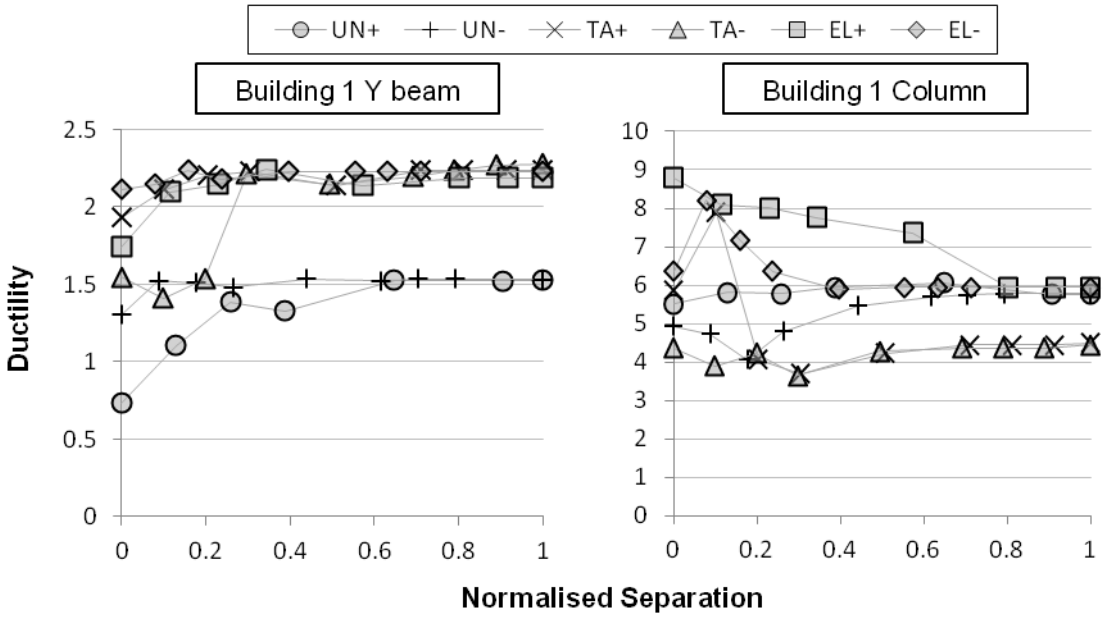

Figure 8.17 Building 1 ductilities. Left: Beam ductility due to movement in the Y direction. Right: Column ductilities

Finally, the maximum ductilities recorded by Beam A and Beam B are presented in Figure 8.18. The presented data is incomplete because yielding did not occur in every record. The observed trends are similar to those presented in Figure 8.16, although in Beam A and Beam B, pounding causes even more notable reductions in ductility demand.

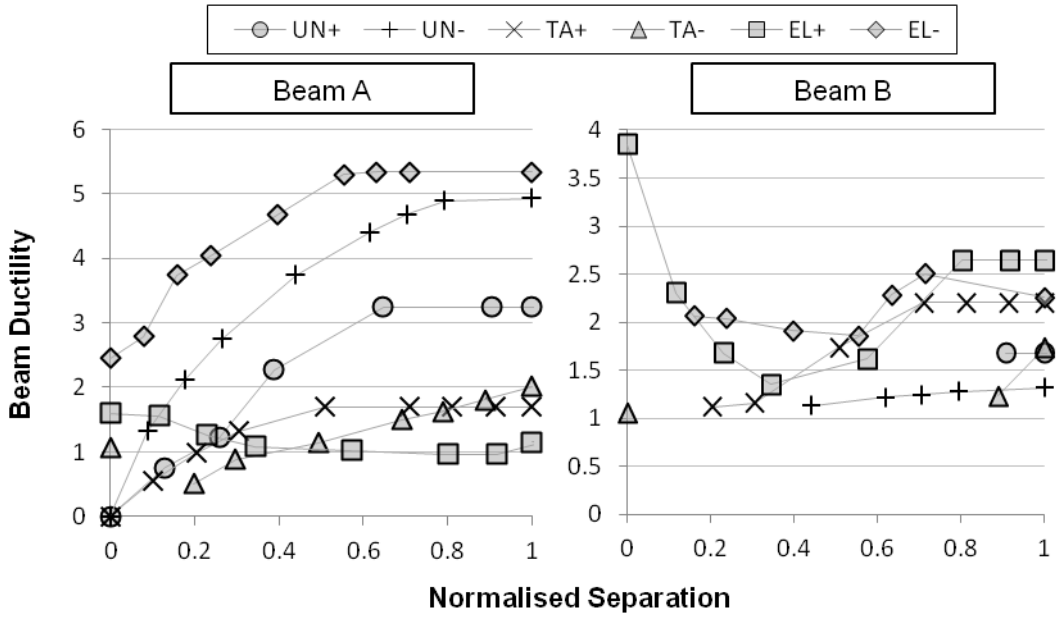

Figure 8.18 Ductilities recorded at Beam A and Beam B

Generally, global damage is observed to be most strongly affected at 0 mm separation, with ductilities being amplified by up to 125 percentage points. As separations increase, this sensitivity decreases. At normalised separations greater than 0.5 actions are generally (but not always) within 25% of the NC values.

8.4.4 Local Damage Sensitivity to Building Separation

As noted in Chapter 6, the trends between local damage and global damage can differ markedly. Three different forces are produced by the 3D contact elements; axial load (contact force), horizontal friction, and vertical friction. The comparative magnitudes of these forces are presented in Figure 8.19. In this figure, the maximum force values from a single analysis are then averaged across all separations for that particular ground motion. As is expected, the largest force occurs in the axial direction of the collision element. On average, the horizontal friction force is approximately one third the axial loading. Vertical friction forces are an order of magnitude smaller than either the horizontal or axial loads. This result indicates that excluding vertical friction from pounding analyses would not significantly affect the analyses' results.

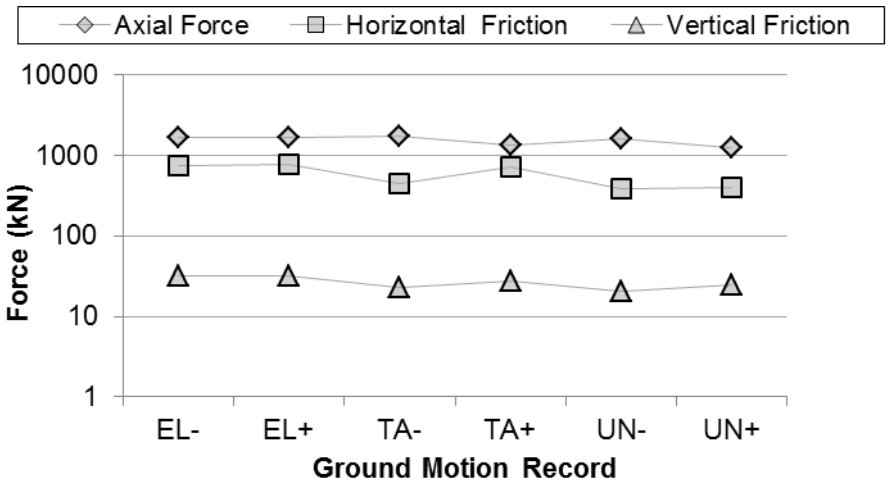

Figure 8.19 Average force magnitudes for contact element actions. Axial force applied along the X axis, horizontal friction along the Y axis, and vertical friction along the Z axis

The maximum axial contact forces are presented for each record in Figure 8.20. Level 2's contact force is larger than Level 3's force. Level 1 also records larger forces than Level 3 at 0 mm separation. This is due to the much larger floor masses at these levels (refer Table 8.2). Contact force reduces with increasing separation at Level 1, but the other levels forces remain reasonably constant. These trends can be more easily observed when both axes are normalised (Figure 8.21). This normalisation is performed in the same manner as shown in Section 6.6.3.

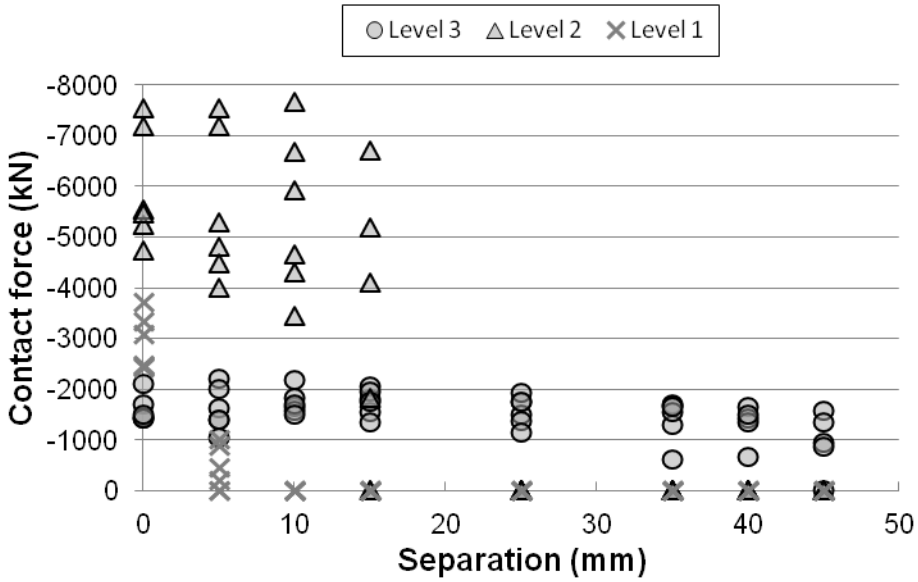

Figure 8.20 Axial contact force results from 3DModel testing

The amplification of contact force at separations greater than zero has reduced in comparison to the 2D analyses (refer Figure 6.22); however, normalised contact forces still remain at approximately 1.0 at normalised separations up to 0.8. Once the normalised separation is greater than 0.9, the maximum contact force approximately halves (although more data is required at this separation to conclusively define this relationship).

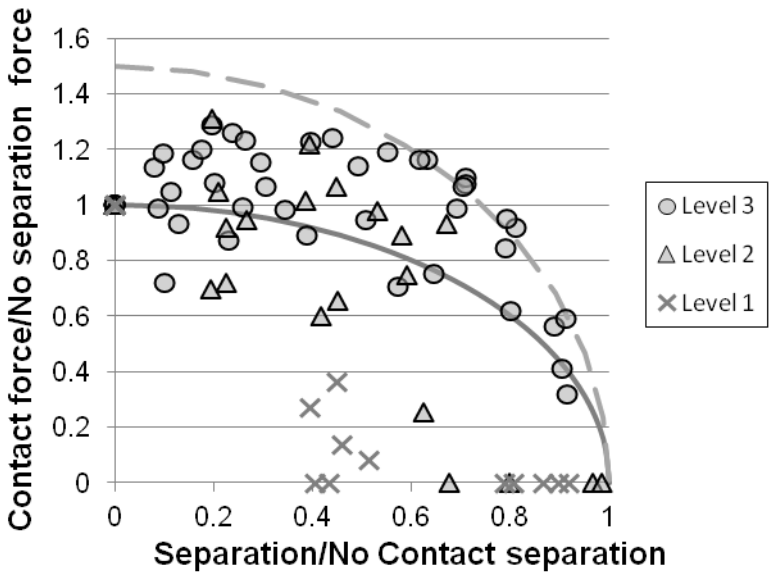

Figure 8.21 Normalised contact force response. Solid line: SDOF prediction. Dashed line: 1.5xSDOF prediction.

In Section 6.6.3, it was determined that collision force can be approximately predicted using the maximum velocities from the NC results for a given ground motion. These velocities were then used to calculate collision force using Equation 3.30. Two alternative prediction methods are tested here: using ground motions' Spectral Velocities (SV) to predict collision force, and using a Pseudo Spectral Velocity (PSV) derived from the New Zealand loadings standard (NZS1170.5 2004). The collision force is calculated assuming that collision occurs when both buildings are moving towards each other at their respective spectral velocities (i.e. an absolute combination):

$$F = 2\frac{SV_1 + SV_2}{\frac{T_1}{m_1} + \frac{T_2}{m_2}} \qquad (8.1)$$

where SV = the spectral velocity (or in the case of the loadings standard, the pseudo spectral velocity), T = the diaphragm's axial period, m = the diaphragm's mass. Predictions are made for all three building levels, however it is assumed that velocity linearly decreases with decreasing building height. Thus, Level 2's velocities are assumed to be ⅔ that of Level 3 (and Level 1, ⅓ that of Level 3). The accuracy of these predictions is shown in Figure 8.22.

In this figure, the recorded maximum contact force is divided by the force predicted by each method. As shown in Section 8.1, the maximum recorded contact force is similar to (usually within 10%) the contact force predicted using Equation 3.30. Viewed in this way, Figure 8.22 is a comparison of how accurately the relative velocity at the time of greatest impact can be predicted. A normalised force greater than 1.0 indicates that the prediction underestimated the

collision force. The results are surprisingly consistent given the level of crudeness of the prediction methods.

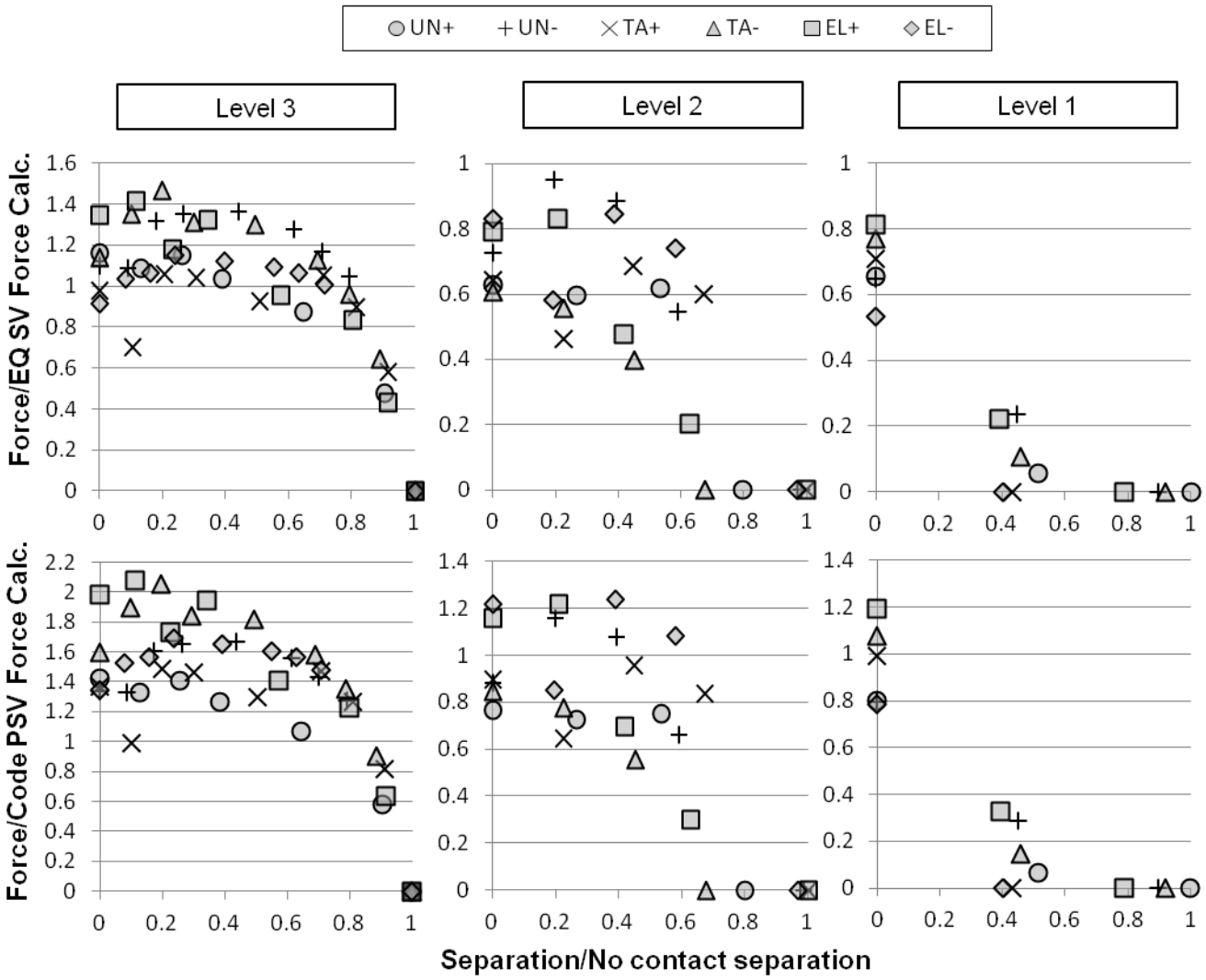

Figure 8.22 Maximum contact force normalised by the force predicted using records' Spectral Velocities (SV) or the NZ loading code's Pseudo Spectral Velocity (PSV).

Predictions using the code's PSV are less accurate than the ground motions' SV. This is expected since the code spectra do not contain information about the specific ground motion being analysed. Figure 8.22 shows a similar relationship to building separation to that seen in Figure 8.21. This suggests that Equation 8.1 could be combined with Equation 3.18 to incorporate the effects of initial building separation on contact force. However, this combination is not performed here since the resulting equation would require additional input parameters that cannot be as easily obtained. It appears that collision force can be reasonably well approximated using either method when modelling low rise buildings.

Comparison of the noted trends between global and local damage measures suggests that these measures are largely independent from each other. Chapter 6 investigated correlations between interstorey shear force and contact force. Here, correlations between maximum ductility and

maximum collision force are investigated (Figure 8.23). Maximum ductilities are observed to increase with increasing collision force, however direct relationships are not obvious. Furthermore, the R^2 values are much less than 1.0 (see Figure 8.23). Local and global damage therefore cannot be inferred from one another and must be individually evaluated.

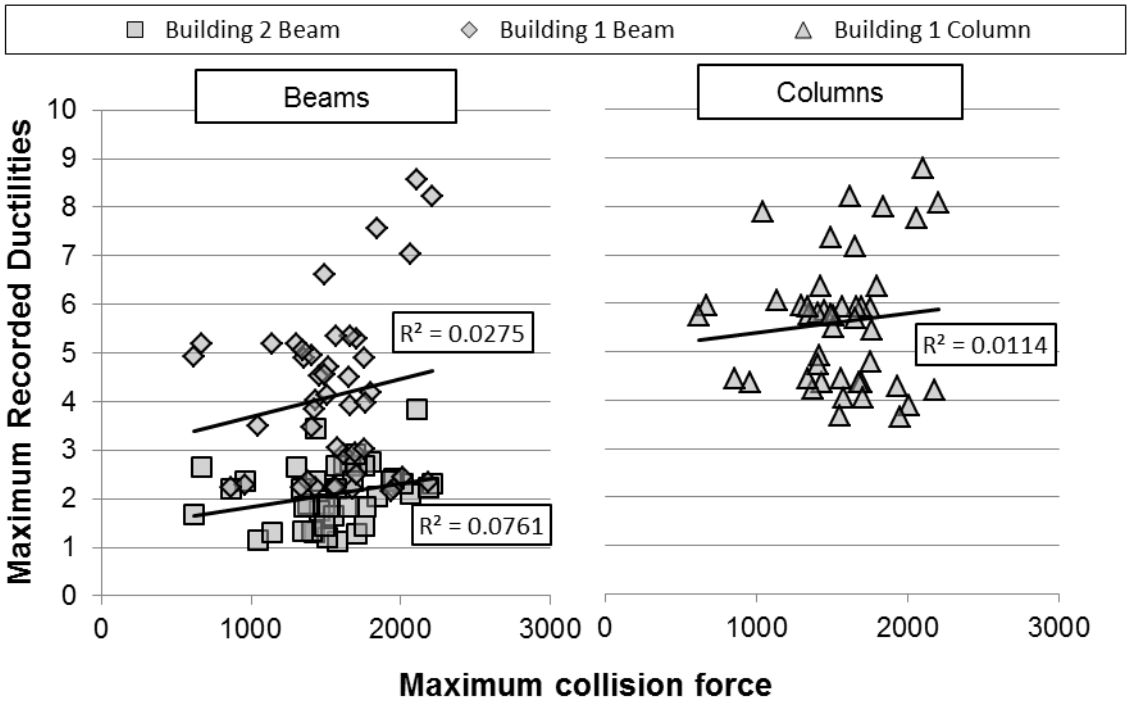

Figure 8.23 Correlations between global and local damage measures

8.4.5 Collision Force Response to Individual Collisions

Finally, the collision force profiles themselves are investigated. The six largest level 2 collisions in the test *EL+05_3DModel* are presented in Figure 8.24. Level 2 is selected since the largest collision forces occur at this level. A total of 11 collisions were recorded at Level 2 during the analysis. Figure 8.24 presents the sum of the axial forces from all the collision elements at Level 2. In this figure, the rate of the initial increase in collision force (at approximately 0.001 seconds) varies significantly between the collisions. This characteristic was not observed in the 2D modelling (Figure 6.5), and can be explained by diaphragm rotation. The two 'steepest' collision forces have negligible relative diaphragm rotation at the time of collision. However, the remaining collisions all present varying degrees of diaphragm rotation before collision. Figure 8.25 illustrates the reason for this stiffness softening.

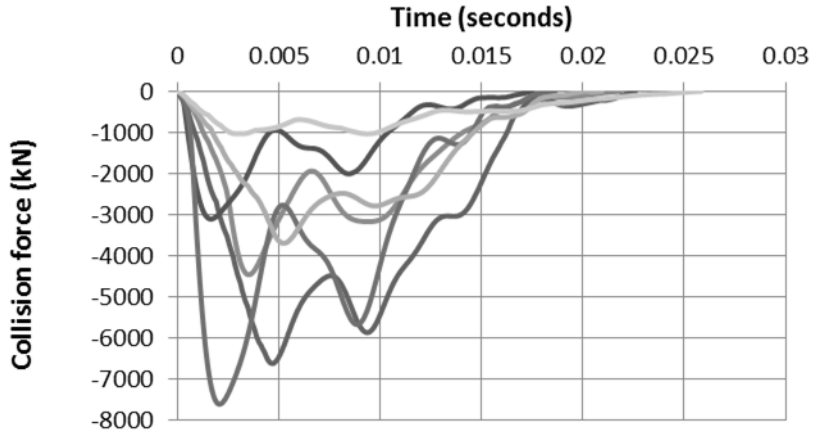

Figure 8.24 Collision profiles of the six largest Level 2 collisions during EL+05_3DModel

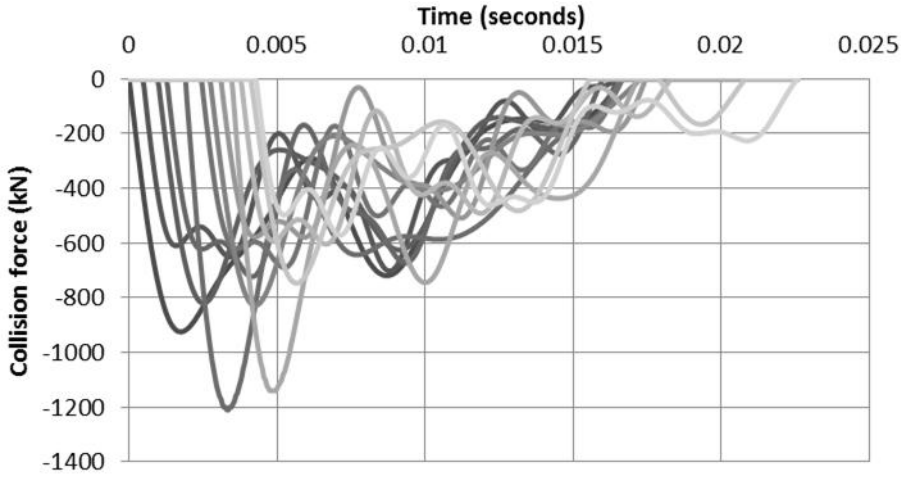

Figure 8.25 Collision affected by diaphragm rotation. Note lighter lines indicate collision elements at higher Y axis ordinates.

The figure shows the force in each collision element at Level 2 for one of the collisions shown in Figure 8.24 (the collision with a minimum force of -6500 kN). The reduced 'stiffness' is caused by a delay in the activation of individual collision elements, due to the diaphragms' rotation and the differing deformations along the interface edge. Level 2 collisions are only expected to last 0.01 seconds (refer Table 8.2), however the last collision element is activated over 0.004 seconds after the first collision element. If this delay is removed from the collision profiles, the collision duration matches that shown in the single collision analysis (Figure 8.2). The two collision elements at the furthest end of the building (i.e. the collision elements with the two largest Y ordinates) usually have longer collision durations. This is attributed to the influence of Building 1's overhang.

Other unique characteristics of 3D collisions can be observed during the smaller collisions. Figure 8.26 shows an example of a 'toe – tip' collision where a collision occurs at one corner of the building, which causes diaphragm rotation and results in a collision occurring at the other corner. The low magnitude of the forces involved means that this phenomenon is unlikely to

affect the recorded displacement and force maxima. Nevertheless, it is a realistic consequence of pounding that cannot be captured by the models in Chapter 6.

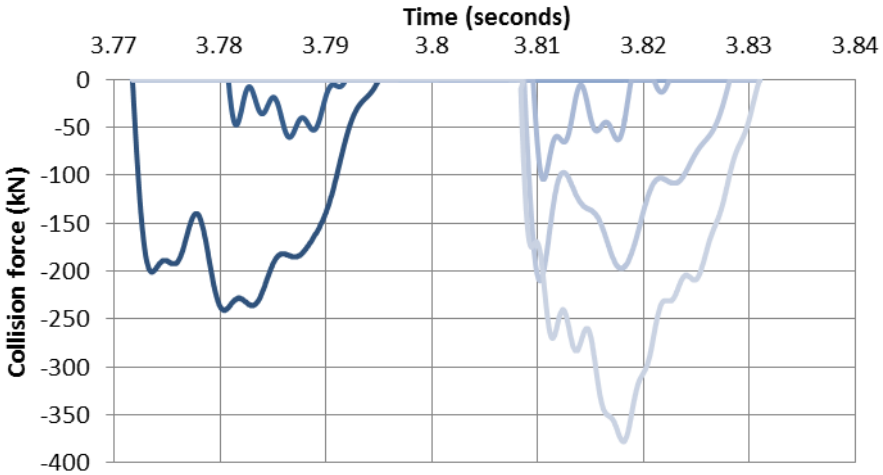

Figure 8.26 'Toe - tip' collision where only the diaphragm's two corners experience collision. Lighter lines indicate collision elements at higher Y axis ordinates

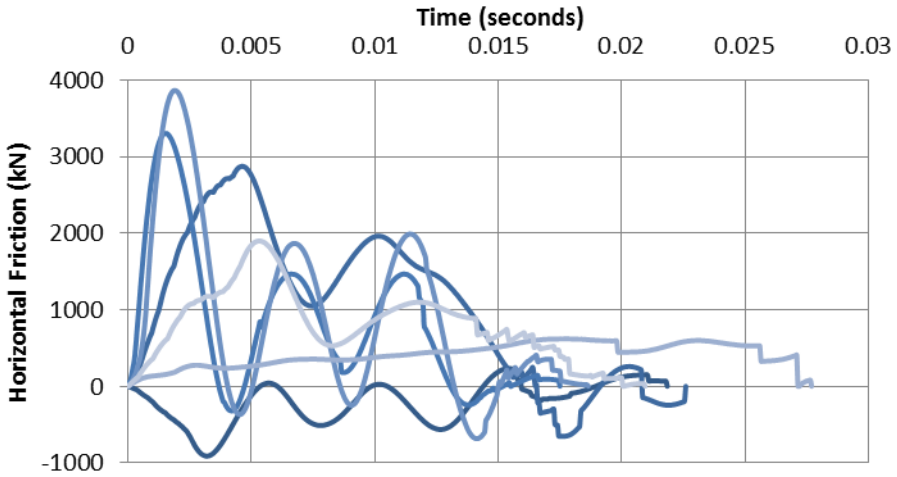

Figure 8.27 Horizontal friction forces at Level 2 during EL+05_3DModel

Frictional forces have also been recorded during these collisions. Figure 8.27 presents the six largest horizontal friction forces that were recorded at Level 2 in *EL+05_3DModel*. As expected, the durations of these forces are the same as or slightly less than that of the axial loads. Sudden jumps in frictional force are observed in some places, particularly at the end of the collisions. This is due to separation or contact of individual contact elements. In reality these force transitions would be much smoother since the friction is controlled by the area undergoing contact. The friction forces in individual contact elements are presented for a single collision in Figure 8.28. Note that the combined force response is shown using a secondary axis. Individual elements tend to oscillate around 0 causing positive and negative friction forces over the collision duration. The six largest vertical friction forces are also presented in Figure 8.29. As previously noted, these forces are considerably smaller than the other actions.

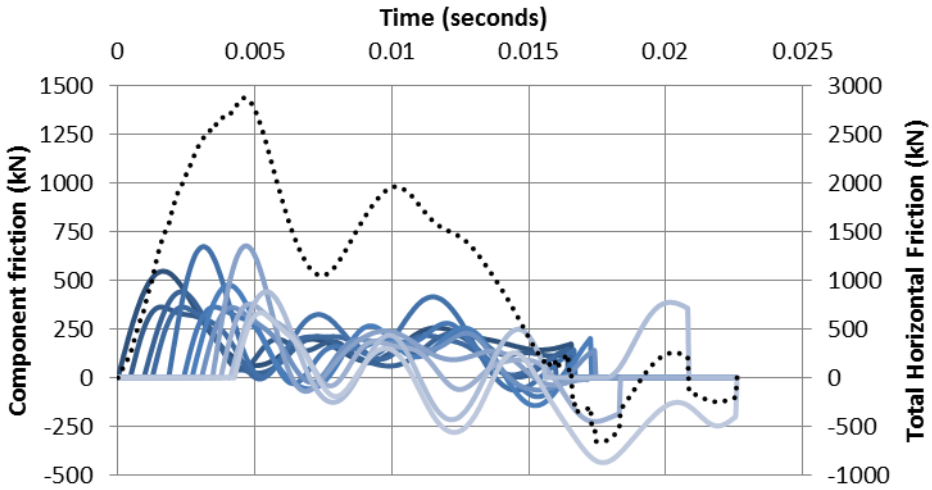

Figure 8.28 Individual collision element horizontal friction forces in EL+05_3DModel. The dotted series shows total horizontal friction.

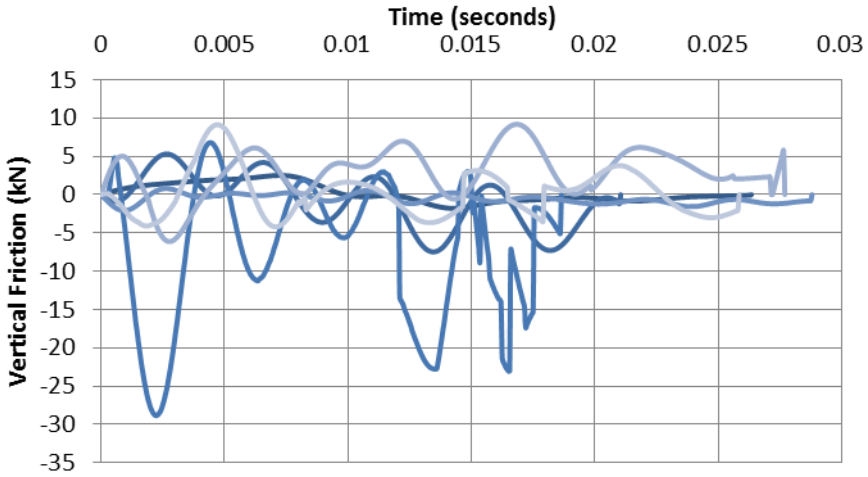

Figure 8.29 Vertical friction forces at Level 2 during EL+05_3DModel

8.5 Comparison with 2D Analysis Methods

As illustrated in Section 8.3, modelling in 2D may be performed in a variety of ways. Two test suites performed here to evaluate the influence of 3D vs. 2D modelling for this specific building configuration. Figure 8.30 illustrates these approaches for a simplified building.

Both 2D models restrict movement to the XZ plane. *2DSlave* uses rigid links to connect the adjacent frames. These rigid links restrict all connected nodes to move with the same X and Z translation and Y direction rotation. *2DSlave* works in a similar way to standard 2D building analysis (with or without pounding modelling). Since all out-of-plane nodes are slaved together in *2DSlave*, the entire building is represented as an equivalent single frame (Figure 8.31). In normal 2D analysis, a single element would be used to model each beam and column in this equivalent frame. However, *2DSlave* uses the original number of elements to explicitly model each element's individual hysteretic. *2DSlave* would produce identical results to normal 2D analysis if a completely elastic building was modelled.

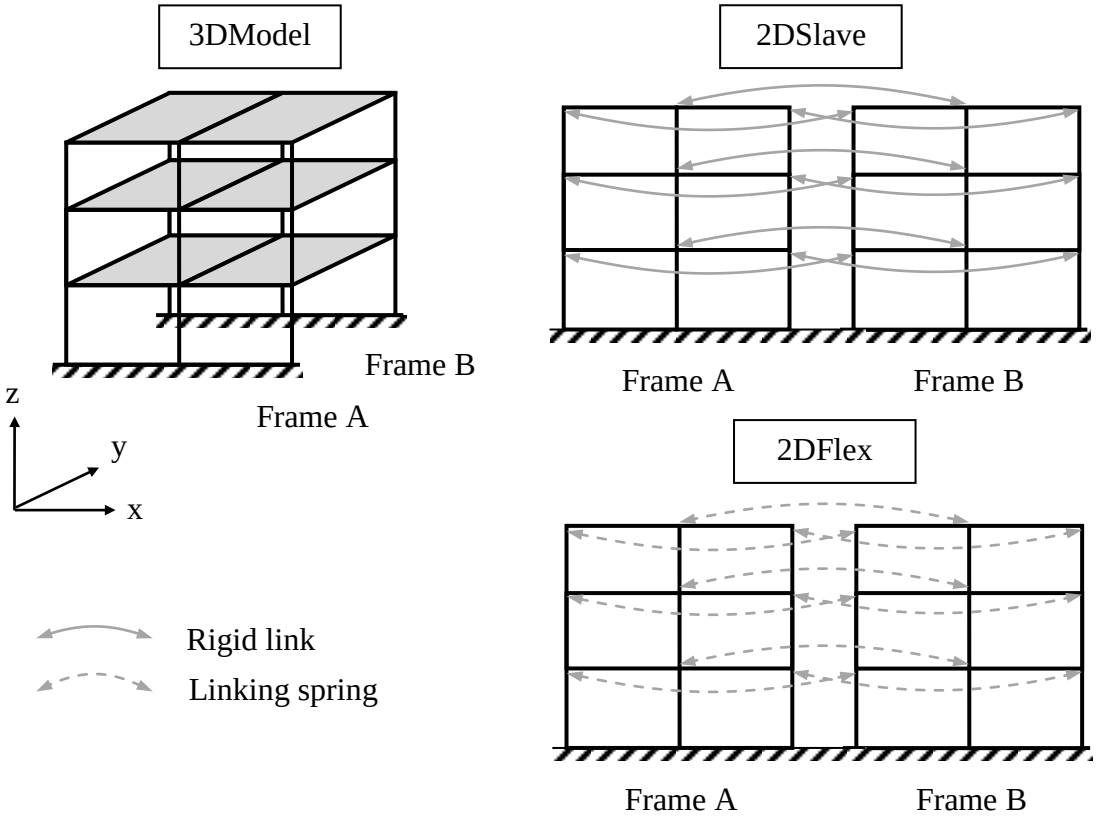

Figure 8.30 Representations of 3D performance in 2D models

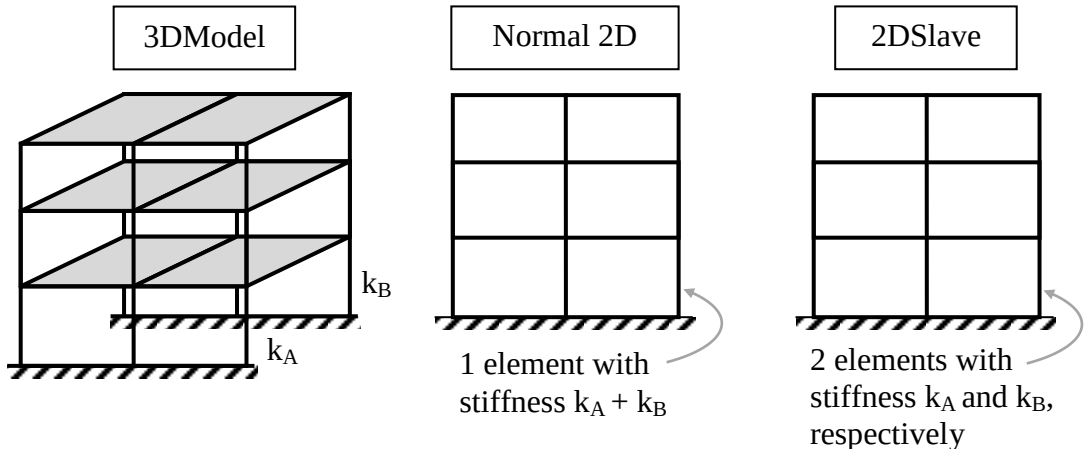

Figure 8.31 Comparison of 2DSlave with standard 2D analysis techniques

2DFlex uses springs representing the interframe stiffness to connect the adjacent frames. These springs should be calibrated so they match in the in-plane stiffness of the diaphragms between adjacent frames. The springs allow adjacent frames to deform differently, enabling a more realistic response. However, torsion still cannot be modelled since the required degrees of freedom are not available in the 2D analysis. To create the 2D models from the existing 3D Ruaumoko models, the following modifications were made:

1. *2DFlex* – the 3D model's movement is restricted to just the 2D directions (X and Z translation, and Y rotation). This allows the interframe stiffnesses to be explicitly modelled using the existing intervening elements.

2. *2DSlave* – in addition to the modifications made in 2DFlex, each node not located in the Y = 0 m plane is rigidly connected to the corresponding node at Y = 0 m.

Note that the configuration of contact elements has not been modified. Thus the same contact stiffnesses are used in all models. In this section the changes in modelled performance is simultaneously presented for *2DFlex* and *2DSlave*.

The reported average and standard deviation of the amplifications in the following sections are slightly less than the actual result for pounding-only analyses. This is because 45 mm building separation is reported for all ground motions, even though two of these records have sufficient separation to not undergo pounding during the record (refer Table 8.5). This reduction is minor since it only affects 2 out of the 36 reported analyses.

8.5.1 Influence on Displacement Envelopes

Changes in the recorded displacement envelopes are evaluated by dividing the recorded 2D values (*2DSlave* & *2DFlex*) by the corresponding values recorded in the 3D analysis (*3DModel*). In this way, results are interpreted in terms of the difference (or variation) from *3DModel*. Figure 8.32 presents the displacements amplifications of Level 3's leftward building envelopes since they recorded the largest differences. *2DFlex*'s displacements are reasonably similar to those recorded in *3DModel*. The differences in building envelope are usually smaller than 10% (six records exceed 10% variation). These differences are seen to generally reduce with increasing normalised separation; however, significant increases occur between normalised separations of 0.2 to 0.4. This region corresponds with the points of highest contact force reported in *3DModel* (Figure 8.21). When the buildings are sufficiently separated to prevent pounding (normalised separation ≥ 1), negligible difference is observed. This indicates that displacements from non-pounding analyses can be accurately predicted using 2D methods.

The results from *2DSlave* present consistently larger variations. Building 1's displacements differ by up to 33% even when no contact occurs. This difference is a consequence of the rigid links, which changes the force distributions in the building frames. For example, the internal frames in Building 1 do not have central columns at Level 2. The external frames do have columns in these locations. Linking the nodes at the top of the columns with the adjacent frame's nodes results in these columns taking more load than occurs in *3DModel*. The significance of these effects is notable in Building 1, but is less apparent in Building 2. No results for the Tabas records are presented for *2DSlave*. This is because model instability occurred in these records, which caused displacements exceeding 10^{256} m within two seconds of the simulation. The source

of this instability appears to be due to the wide range of values in the stiffness matrix. These analyses include very stiff elements, such as the collision element stiffness, in addition to flexible elements such as light weight steel rafters with pin connections at one end. Compilation of these stiffnesses causes the stiffness matrix to include terms over a range of many orders of magnitude, and is known to be a potential source of instability. Fortunately, such instabilities can be easily identified when they occur.

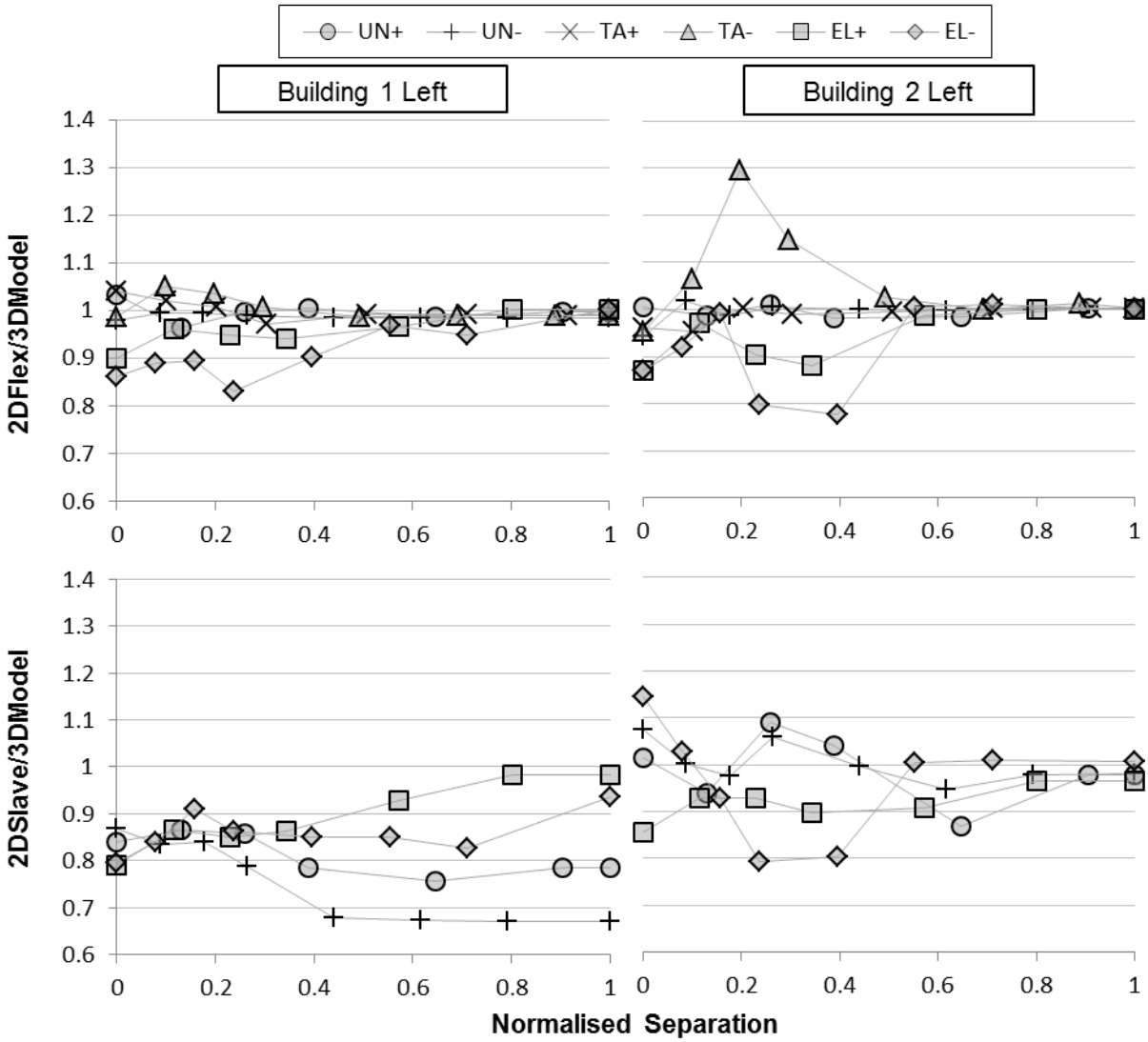

Figure 8.32 Front frame displacement magnifications in 2D models at Level 3.

The rear frames' (the building frames located at the greatest Y ordinates) normalised displacements are presented in Figure 8.33. *2DSlave* displays even greater variations in the rear frame results. This result is expected since the rear frames are located at the source of plan irregularity between the two buildings. *2DFlex*'s front and rear frames display similar levels of displacement variation. No comparisons with *3DModel*'s Y axis can be performed since the 2D models exclude these degrees of freedom.

If displacement predictions are the only parameter of interest in a pounding analysis, *2DFlex* may provide adequate accuracy. Individual records cause variations of up to 30%; however the vast majority of displacements are within 10% of the *3DModel* predictions. *2DSlave* values are too unreliable for any accurate displacement predictions.

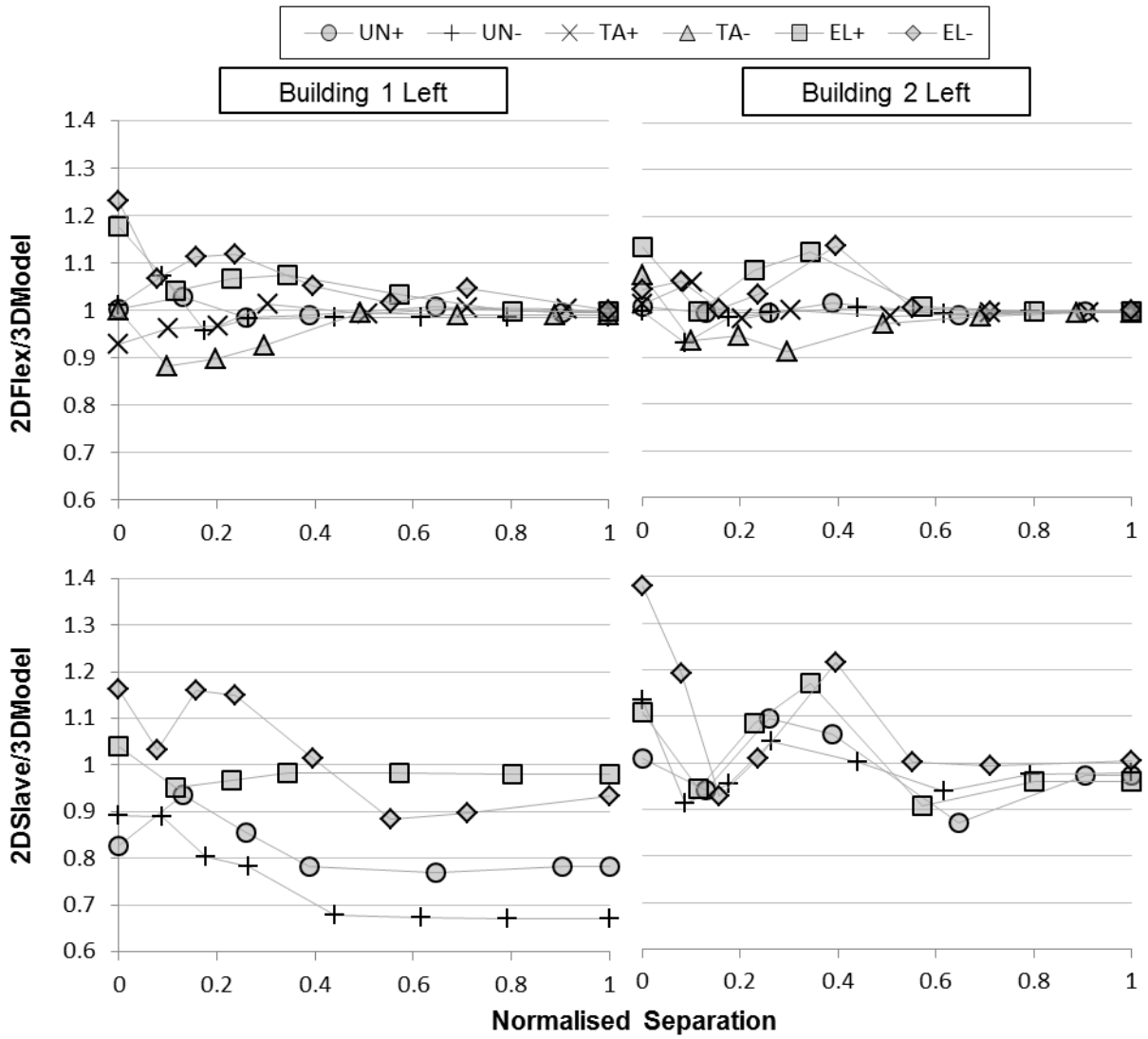

Figure 8.33 Rear frame displacement differences in 2D models at Level 3.

8.5.2 Influence on Global Damage Demand

Building 2's normalised shears are presented in Figure 8.34. Note that *2DFlex* uses a different y axis scale than *2DSlave*. In both tests, Level 3 shows the greatest sensitivity to the modelling approach. This is again attributed to the low magnitude of shears at Level 3. Shear variation is less than 10% for all *2DFlex* records but exceeds 10% at all levels in the *2DSlave* records.

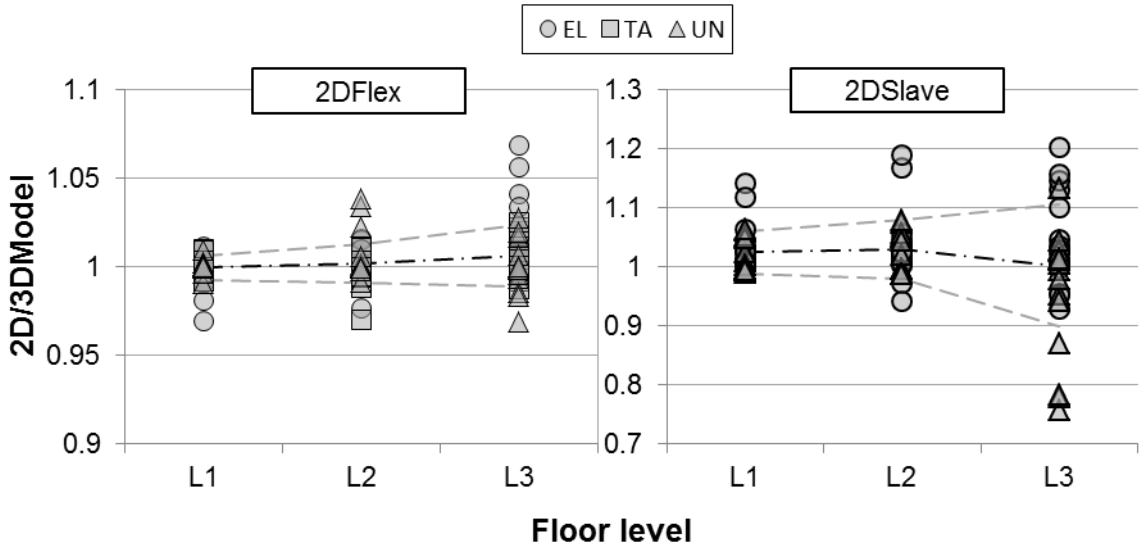

Figure 8.34 Differences in shear maxima resulting from 2D modelling. Line series indicate mean and standard deviation.

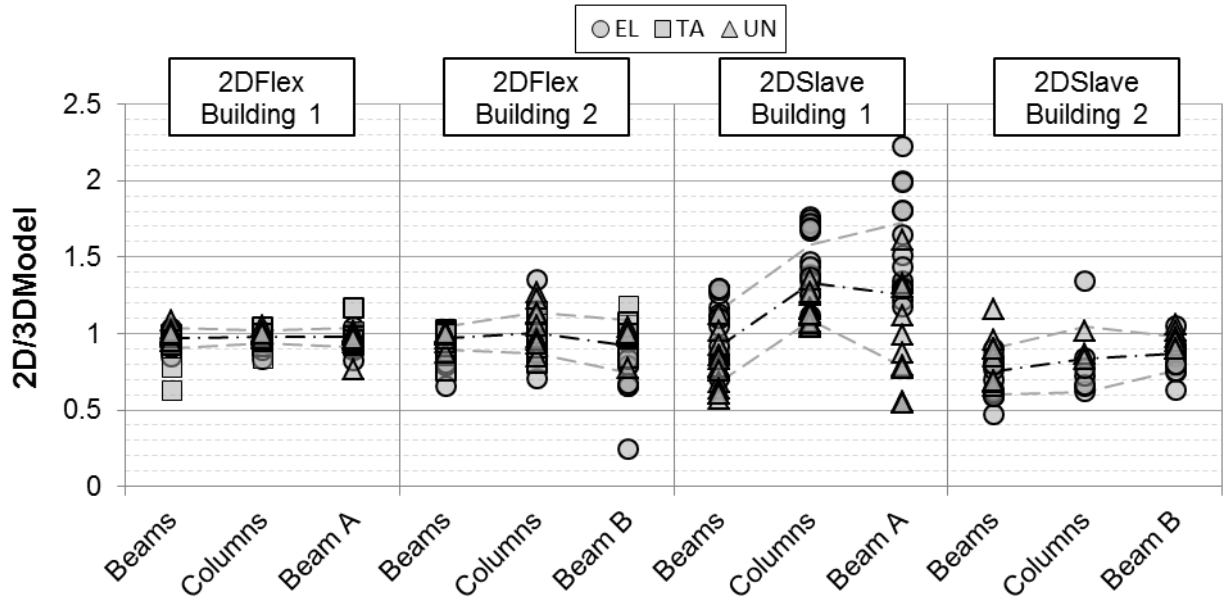

Figure 8.35 Differences in ductility maxima resulting from 2D modelling. Line series indicate mean and standard deviation.

The effect of 2D modelling on ductility is presented in Figure 8.35. Maximum ductilities are much more sensitive to model changes than shear maxima. Average ductility differences remain within 10% for *2DFlex*; however individual records under report ductilities by as much as 70%. *2DSlave* does not produce reliable global damage measures. *2DFlex* models may provide suitable shear and ductility results providing a suite of records are being analysed. Multiple analyses reduce the influence of any individual variations on design decisions.

8.5.3 Influence on Local Damage Demand

Contact force is even more sensitive to the modelling approach. Figure 8.36 presents the difference in contact force at all levels. *2DSlave* shows multiple records with normalised forces of 0. This indicates that no collisions occurred in *2DSlave* while collisions did occur in

3DModel. Collision force variation is greater in the lower floors. This cannot be attributed to differences in collision force magnitude since Level 3 actually has the lowest collision forces (and thus highest sensitivity to small changes in the force) due to the roofs' comparatively low masses. This trend is more likely to be a result of greater velocity sensitivity at the lower floors, since greater velocities are present higher in the buildings. However, this theory cannot be confirmed with the presented data. Vertical friction forces presented even higher errors, however the magnitudes of these forces are sufficiently low that they may be ignored. Collision forces are not reliably predicted by either 2D model.

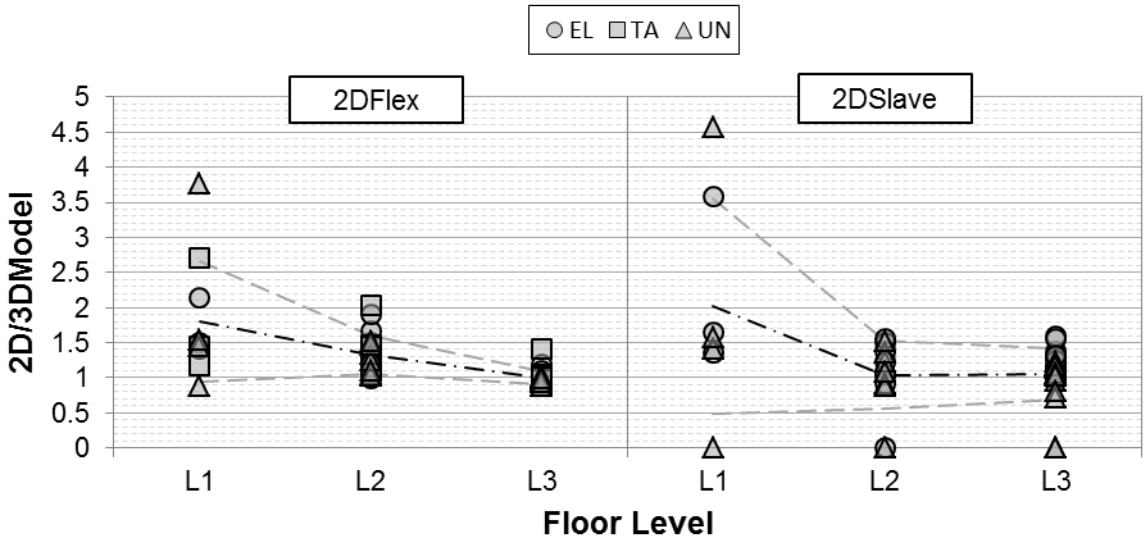

Figure 8.36 Collision force sensitivity to 2D modelling approaches. Line series indicate mean and standard deviation.

8.6 Effects of Rigid Diaphragms

Previous researchers modelling 3D pounding usually used rigid diaphragms in their models. The significance of this selection is investigated by comparing the response of rigid diaphragms (test *3DRigid*) with the flexible diaphragm results presented previously (test *3DModel*).

8.6.1 Influence on Displacement Envelopes

Figure 8.37 presents the X axis displacement envelope sensitivity for the front and rear frames of both buildings. Note the change of legend in this figure; each series is identified in terms of building separation (in mm). These series were previously identified by ground motion record. This change allows easier identification of the building separations that cause the largest errors. Displacement variation differs significantly between the two frame locations in each building. Greater variation is expected at the rear frames due to the diaphragm overhang; however, this is not always reflected in the results. The rightward displacement envelope of Building 1 is significantly less sensitive than the other envelopes. The reason for this is not readily apparent. Recorded displacements are overestimated in *3DRigid* by up to 50%, and underestimated by up

to 30%. However, when the averaged results are considered the displacement variations lie within ±10%. This dispersion is greater than that observed in *2DFlex*. Thus, suitably accurate displacement results can be obtained if the average of many (≈20) analyses is used.

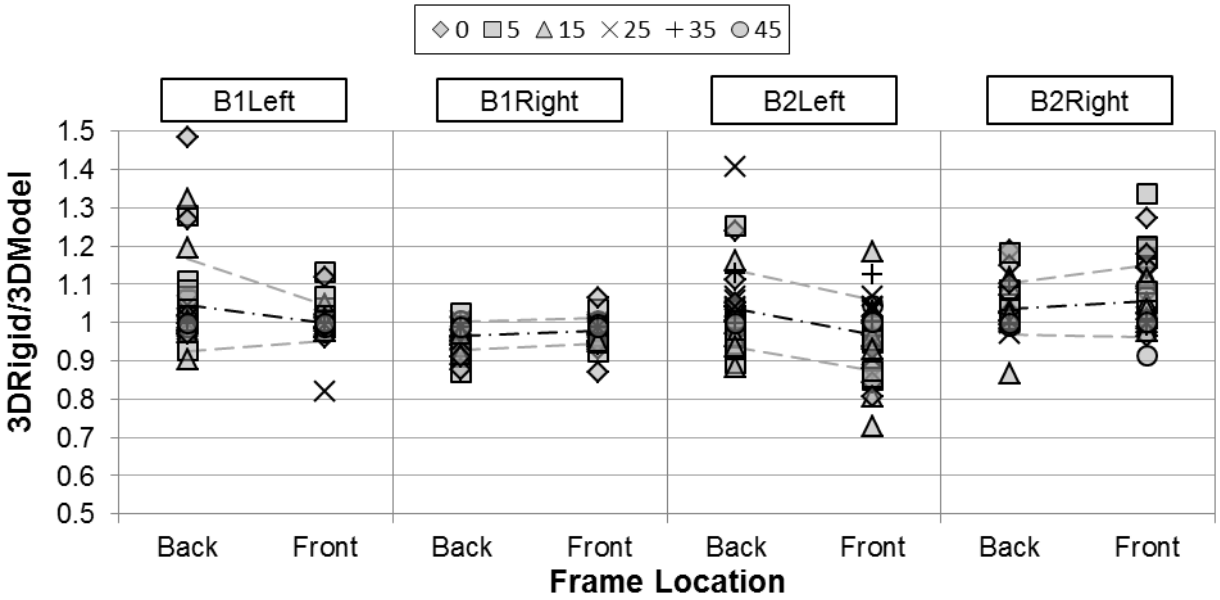

Figure 8.37 Level 3 X axis displacement envelope sensitivity to diaphragm flexibility

Y axis displacements present similar trends to the X axis results. NC results are omitted from the figures in this and the following sections. This is because these analyses are primarily focused on the pounding performance of the systems. However, the NC X axis and Y axis displacements were all within 1.5% of the flexible diaphragm results.

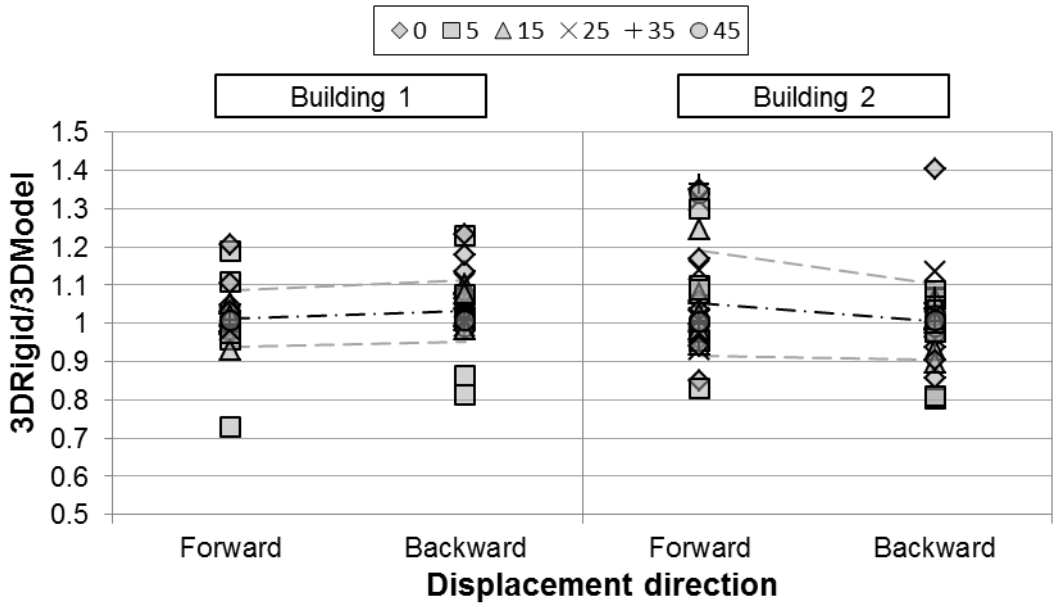

Figure 8.38 Level 3 Y axis displacement envelope sensitivity to diaphragm flexibility. 'Forward' indicates negative movement along the Y axis

8.6.2 Influence on Global Damage Demand

Interstorey shear amplifications are presented in Figure 8.39. Shear forces are generally overestimated by the rigid diaphragm models. Building 1's X direction shear amplifications are observed to be suppressed due to the extensive yielding in the building's columns. Y axis shears are affected more than the X axis shears at all floor levels. This is attributed to the behaviour of the horizontal friction forces during contact and is discussed in the next section.

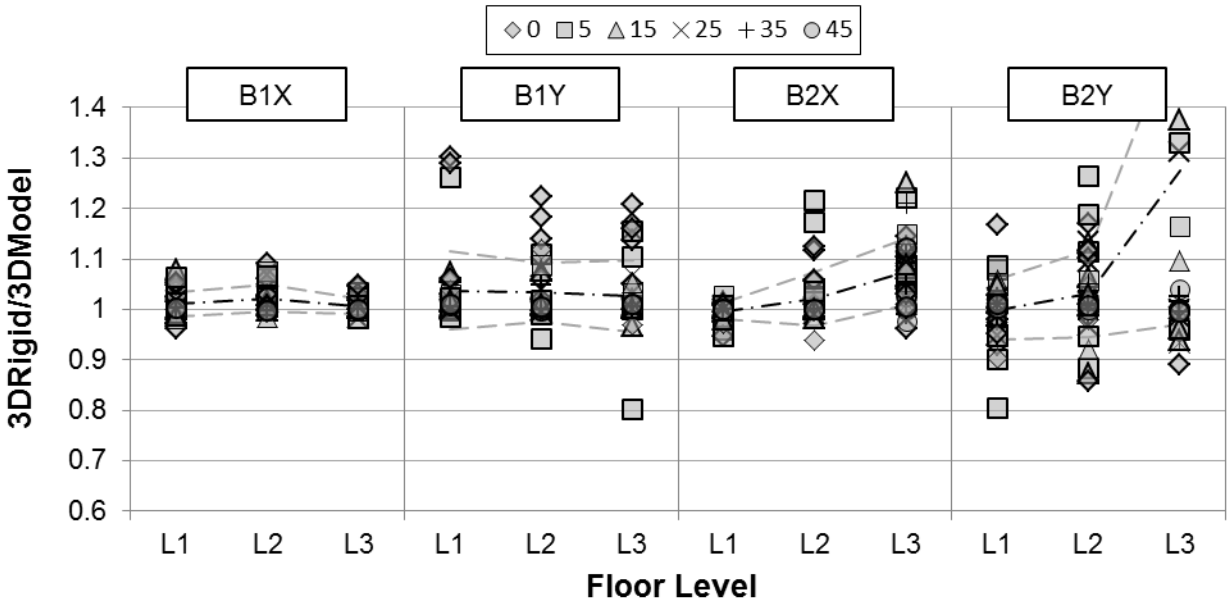

Figure 8.39 Effect of diaphragm flexibility on interstorey shears

Y axis sensitivity is also more pronounced in the beam ductilities (Figure 8.40). Ductilities can be greatly affected by diaphragm rigidity. Building 2's maximum column ductilities are greatly overestimated by *3DRigid*. The members with the maximum ductilities recorded in Building 2's columns are located at the four corners of Level 3. When Level 3 is modelled with diaphragm flexibility, much of this load is transferred through the more flexible perimeter columns. When Level 3 is rigid however, more load is directly transferred to the stiffer corner columns which increases the critical building demand. Building 1 does not present a similar trend because its critical column ductilities occur at Level 2, which has much stiffer diaphragms.

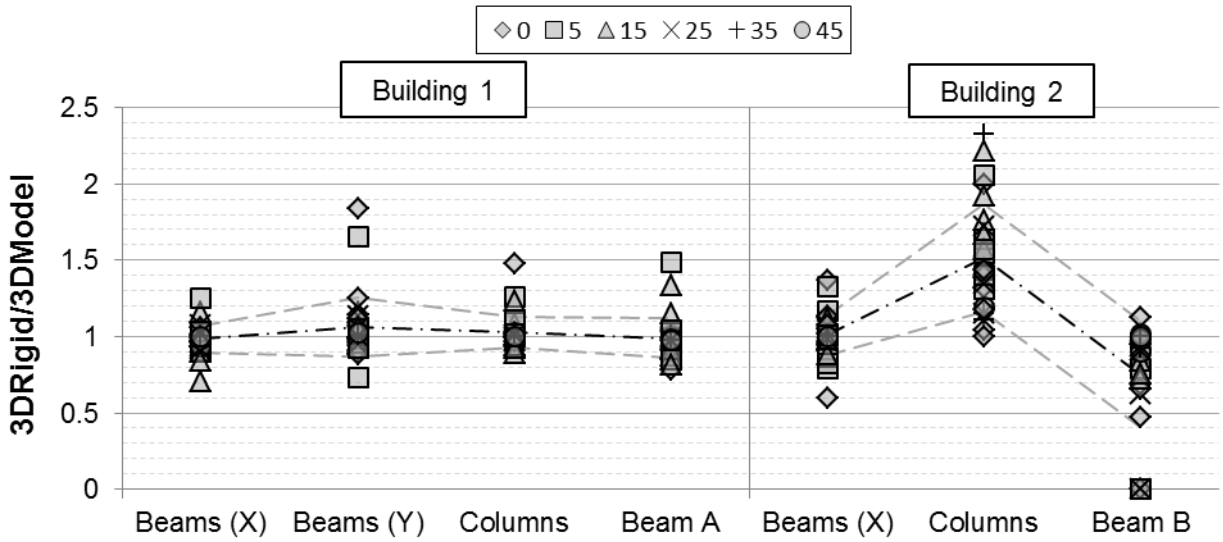

Figure 8.40 Effect of diaphragm flexibility on building ductilities

8.6.3 Influence on Local Damage Demand

As previously discussed, rigid diaphragms' contact forces are determined by the contact element stiffnesses and do not reflect the actual force expected during a collision (Section 3.2.5). However, the effect of rigid diaphragms on friction forces is not immediately apparent. Figure 8.41 presents the amplifications of maximum contact force and maximum friction force due to diaphragm rigidity. Level 1 is not reported because the relevant data was accidently omitted from the recorded results. In *3DModel*, collisions only occur at Level 1 for the 0 and 5 mm separations, so the data loss was minor.

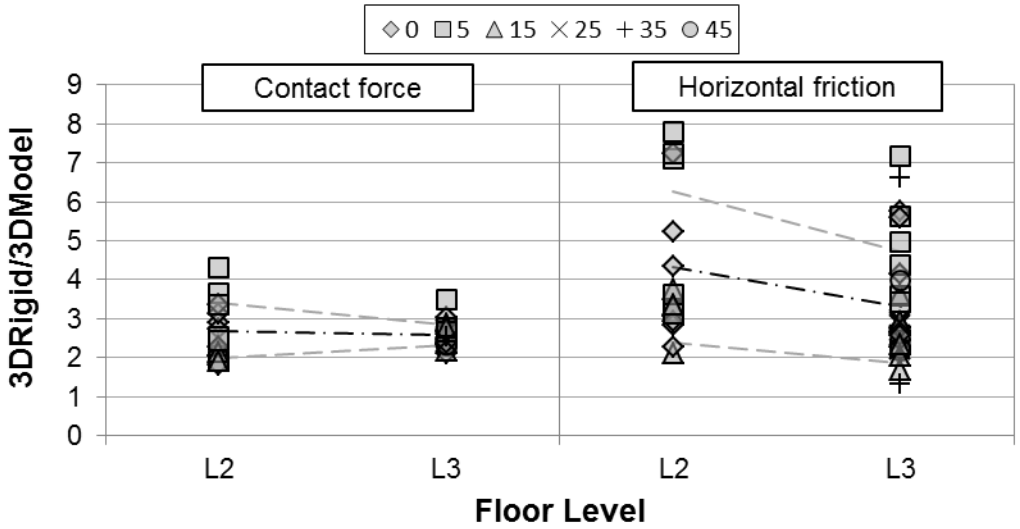

Figure 8.41 Effect of diaphragm flexibility on contact force and friction force

The friction force variations are considerably higher than those of the contact force. This is because the total friction force is found by summing the friction forces reported at each contact element. When a flexible diaphragm is modelled, individual contact elements' maximum friction forces occur at different times (refer Figure 8.28). However, when rigid diaphragms are

modelled, all friction maxima occur simultaneously. In more practical terms, rigid diaphragms overestimate contact friction because they assume complete and immediate participation of both diaphragms' masses. In reality friction load transfer involves a shearing force that travels through each diaphragm as a wave.

8.7 Collision Damping in 3D Models

The significance of additional contact-specific damping is tested using the damped Kelvin element. The plasticity index backbone curve for this configuration is presented in Figure 8.42. In this figure, the percentage of critical damping is calculated in a different way than in 2D. Equation 2.10 is still used; however, Mass 1 and Mass 2 refer to the immediately adjacent node masses (in 2D, these masses referred to the total mass of Building 1 and Building 2, respectively). Assigning the mass in this manner results in the viscous damping being allocated in proportion to the contact elements' tributary width. This makes the approach consistent with the manner of assigning collision element stiffness (i.e. the tributary width method in Section 7.4).

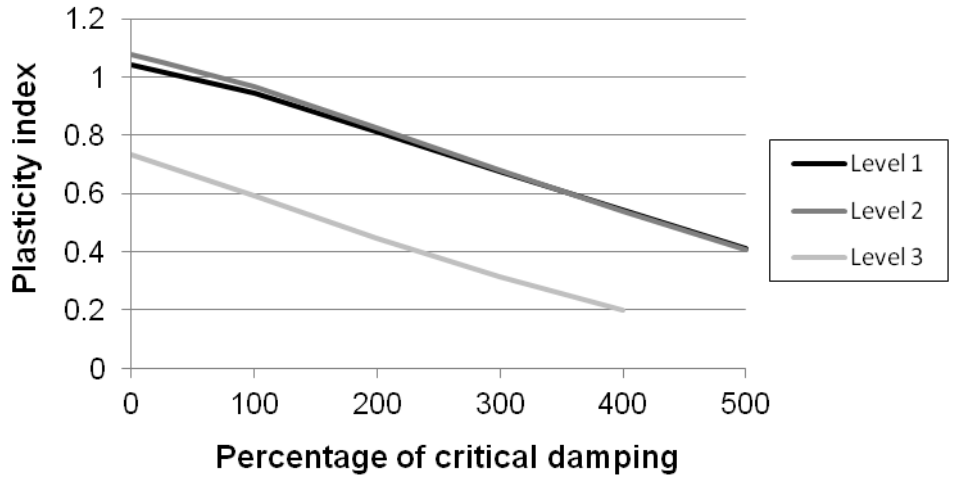

Figure 8.42 Plasticity index backbone calculated for the building configuration *3DModel*

Level 3 displays a backbone significantly less than 1.0 when no damping is present. This is due to the abrupt changes in stiffness at Level 3. Building 2's Level 3 diaphragm is relatively flexible, but stiff beams are located at regular intervals across the floor. These changes in stiffness cause more internal oscillation in both Level 3 diaphragms after a collision. Level 1 and Level 2 show almost identical backbone curves since the buildings' diaphragms are very similar at these levels.

In the 2D analyses (Section 6.9), the collision plasticity was investigated using a plasticity index of 0.85. Figure 8.42 shows that this value cannot be achieved in these analyses at Level 3. A value of 0.65 is selected instead to be consistent across all diaphragms. The resulting contact

parameters are presented in Table 8.6. Since energy loss due to diaphragm oscillation is already accounted for, a plasticity index of 0.65 is considered to be low.

The plasticity index values for Level 3 (the roof) are misleading. While e_{eff} is reported for r = 1, this plasticity index was never actually achieved in any analysis (see Figure 8.42). This means that the damping applied at Level 3 is much less effective. In effect, the damping at Level 3 has gone from r = 0.73 to r = 0.65. However, adopting a lower value of r for the damped model would reduce Level 1 and 2 to plasticity indexes substantially less than 0.4.

Table 8.6 Damped 3D diaphragm properties

Floor number	*e_{eff} (elastic, r = 1)*	*e_{eff} (r = 0.65)*	*ζ (%) for r = 0.65*
3	*0.910*	0.592	58
2	*0.561*	0.364	323
1	*0.564*	0.367	320

8.7.1 Influence on Displacement Envelopes

The X axis displacement envelopes are not markedly affected by the collision plasticity (Figure 8.43). Two analyses record variations greater than 10%, and all averaged values present almost no variation. Y axis displacement results are not presented here, but also show less than 10% difference in all records except one. This insensitivity can be partially attributed to the small effective change in plasticity index. However, relatively little sensitivity was also noted in the 2D damping tests (Section 6.9).

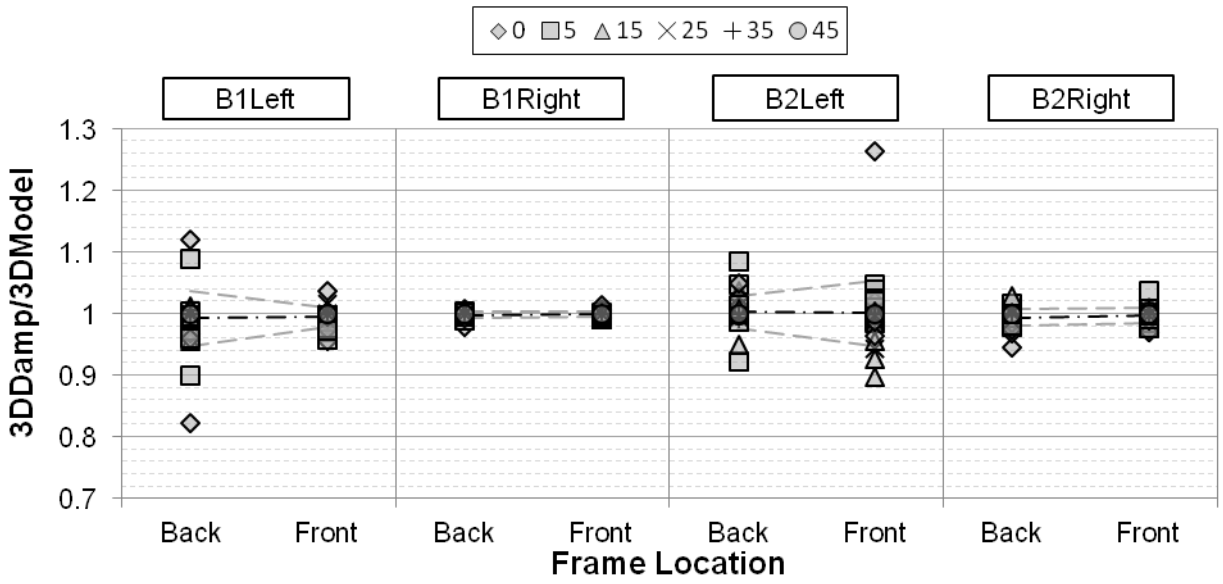

Figure 8.43 Level 3 X axis displacement sensitivity to diaphragm damping

8.7.2 Influence on Global Damage Demand

Greater sensitivity is observed in the Y axis shear results (Figure 8.44). However, these magnifications are significantly smaller than those observed in *3DRigid*. Averaged values of shears across all records are all within 2% of *3DModel*. Averaged ductilities also lie within 5% of *3DModel* values (Figure 8.45). The global demand parameters are insensitive to the modelled collision-specific damping, provided that averaged values from multiple ground motions are used.

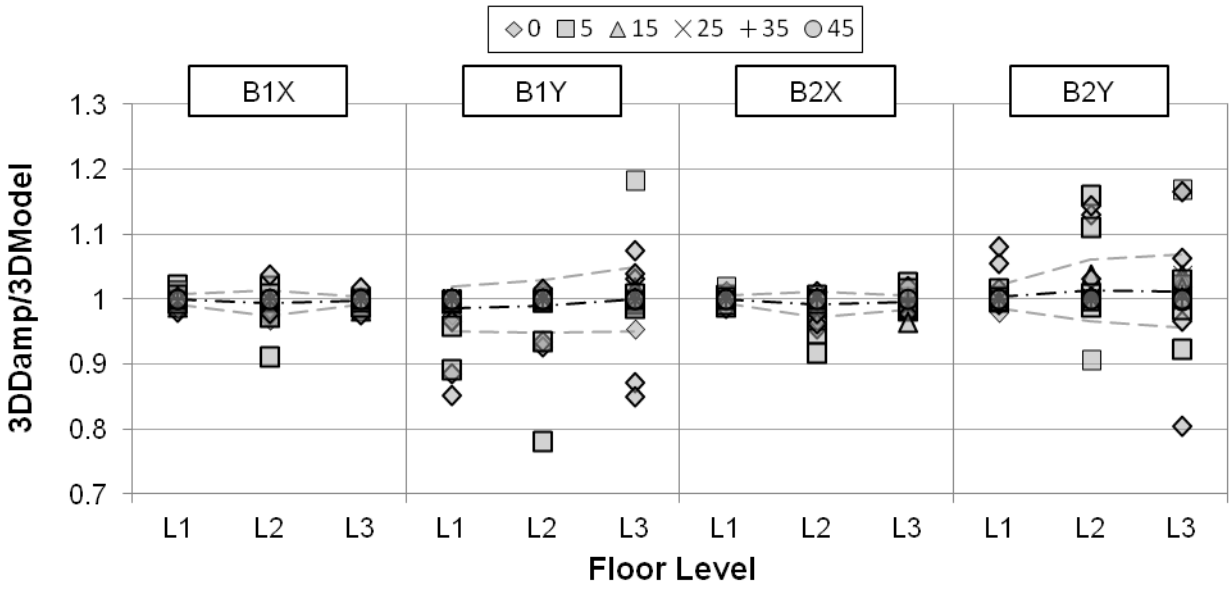

Figure 8.44 Shear force amplification due to collision damping

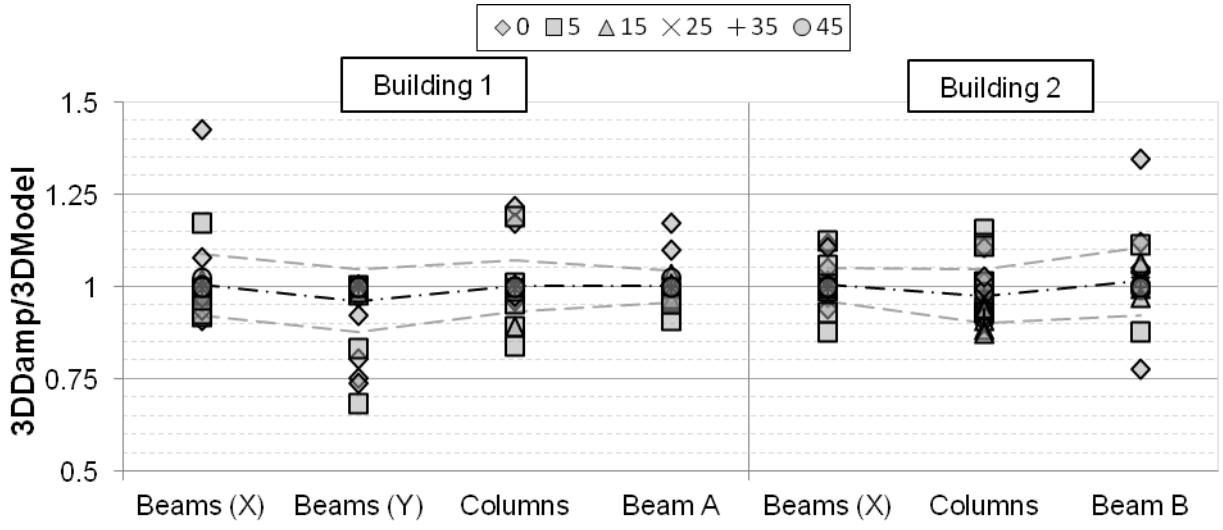

Figure 8.45 Ductility amplification due to collision damping

8.7.3 Influence on Local Damage Demand

The damped Kelvin element significantly changes the collision force profile during collision. This change prevents any meaningful comparison of contact force, so such comparisons are not made here. Instead, Figure 8.46 presents the amplification of maximum horizontal friction force. Friction forces are dependent upon contact load, so these results also record greater variations.

However, in comparison to other models, the averaged response is also very similar to the *3DModel* response. As has been noted in other sections, Level 1's local response is the most sensitive to model changes, while Level 3 is the least sensitive.

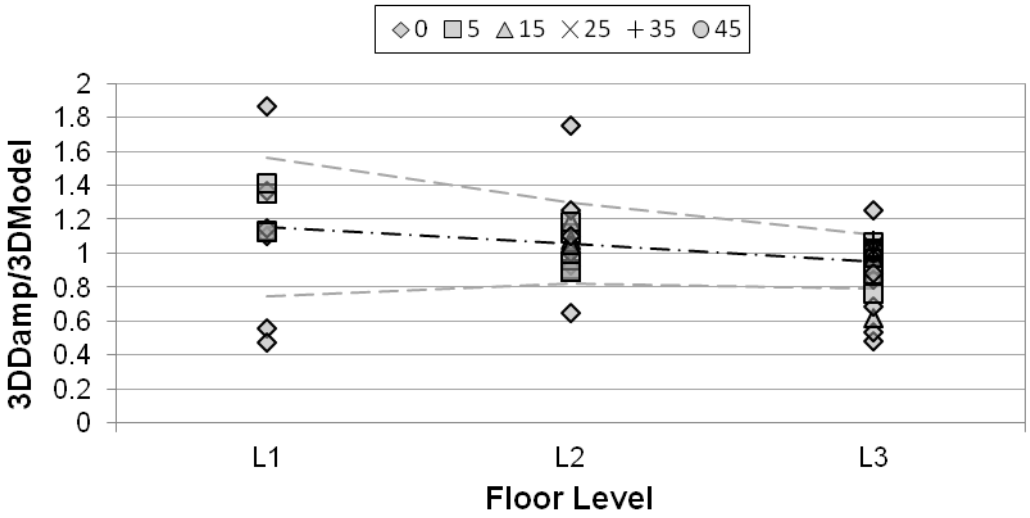

Figure 8.46 Horizontal friction force amplification due to collision damping

Minimal differences in displacement, global damage and local damage are observed due to the added collision plasticity. This level of insensitivity is surprising since multiple collision properties have been changed markedly. It is possible this insensitivity is unique to the low rise (first mode dominated) responses investigated here. Definitive statements on this insensitivity would require further testing of other building configurations. The effects of collision damping are dramatically less than that of using rigid diaphragms.

8.8 Eccentric Pounding Configuration

Building 2 is now modified to provide an eccentric pounding load to Building 1 (test *3DModelE*, refer Section 8.3). This was achieved by removing two internal frames from Building 2 (Figure 8.47). The new external frame's properties were set equal to that of the old external frame to maintain the building's symmetricitiy. The change to Building 2's configuration causes minor changes (less than 3%) to the building's periods. The modified Building 2 is hereby termed Building 2A to distinguish it from the original version. This new configuration is used to investigate the significance of eccentric loading on 2D and rigid diaphragm predictions. Revised collision element properties are presented in Table 8.7 and Table 8.8.

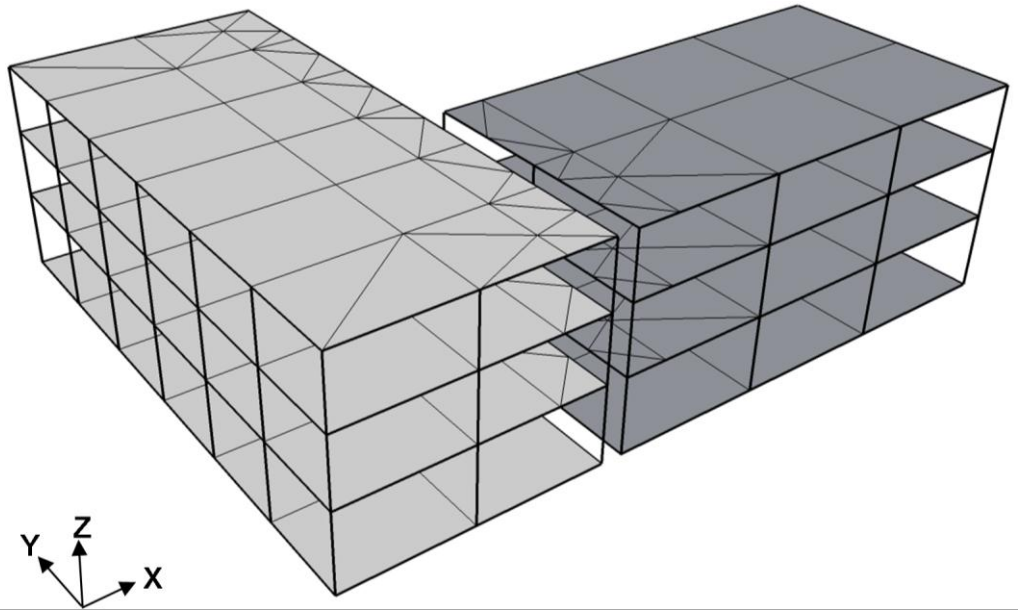

Figure 8.47 Building configuration selected to induce eccentric pounding load. Refer to Figure 8.6 for original configuration

Table 8.7 Eccentric pounding 3D model colliding floor properties

	Building 1			*Building 2A*			*Ratio*	
Level	***Mass***	***Axial Stiffness***	***Axial Period***	***Mass***	***Axial Stiffness***	***Axial Period***	***Mass***	***Axial Period***
	Tonne	*kN/m*	*sec*	*Tonne*	*kN/m*	*sec*	*-*	*-*
Roof	*150*	*927,196*	*0.022*	*34*	*187,093*	*0.027*	*4.41:1*	*0.82:1*
Level 2	*338*	*11,958,185*	*0.010*	*264*	*2,853,104*	*0.019*	*1.28:1*	*0.53:1*
Level 1	*321*	*12,184,738*	*0.010*	*264*	*3,002,291*	*0.019*	*1.22:1*	*0.53:1*

Table 8.8 Eccentric pounding calculated floor collision properties

	Building 1		*Building 2A*		*Collision Properties*	
Level	***Lumped Mass α***	***Distributed Mass α***	***Lumped Mass α***	***Distributed Mass α***	e_{eff}	***Secondary collisions***
Roof	*0.185*	*0.158*	*0.815*	*0.699*	*0.715*	*Yes*
Level 2	*0.438*	*0.296*	*0.562*	*0.379*	*0.350*	*Yes*
Level 1	*0.451*	*0.305*	*0.549*	*0.371*	*0.351*	*Yes*

8.8.1 Response of Building 2A with No Contact (NC)

Since Building 1 has not been modified, its no contact results are the same as were reported in Section 8.4.1. Building 2A's no contact response is presented below. Graph scaling is consistent with the figures presented in Section 8.4.1 to allow direct comparison. Building displacements, shears and ductilities are presented in Figure 8.48, Figure 8.49 and Figure 8.50, respectively.

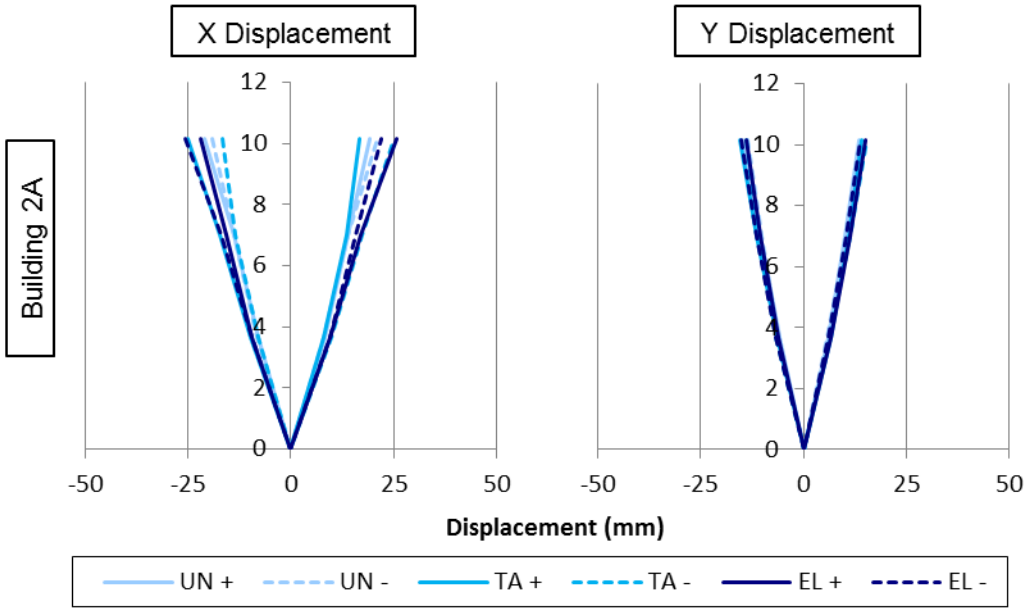

Figure 8.48 Building 2A displacement envelopes

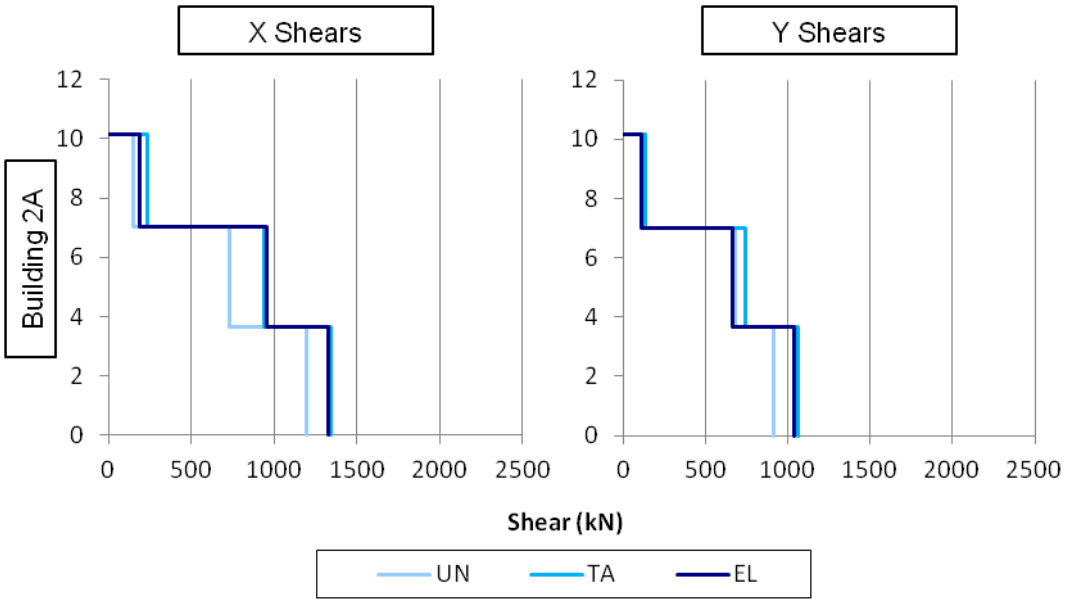

Figure 8.49 Building 2A interstorey shear envelopes

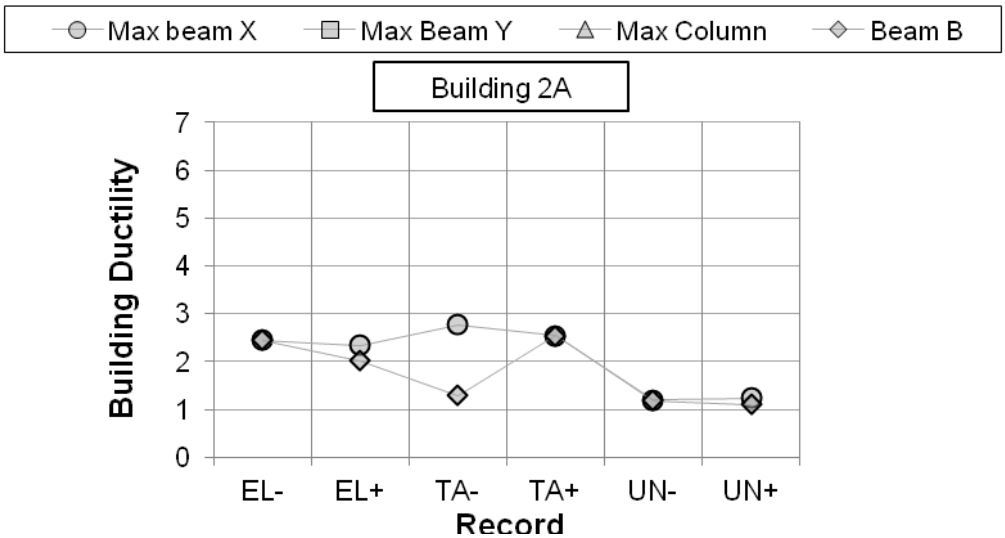

Figure 8.50 Building 2A maximum recorded ductilities

Building 2A's displacements and ductilities remain very similar to those shown for Building 2. This similarity is beneficial since any differences observed in the pounding responses can be more confidently attributed to the change in the buildings' geometry. The interstorey shears have reduced since the seismic weight of the building has also reduced.

8.8.2 Displacement Sensitivity to Building Separation

Since torsional actions are expected in this configuration, displacements were recorded at three locations on Building 1, the front frame, the nodes aligned with the rear frame of Building 2A, and the rear frame. The front frames' actions are presented first in Figure 8.51. The displacement amplifications are similar to that observed in *3DModel*. Individual ground motions show both amplification and de-amplification of the Buildings' displacements, depending upon the specific building separation (for example, record TA- produces amplifications and de-amplifications in Building 1 left and Building 2A left). This further highlights the complex nature of the consequences of pounding. Displacement amplifications are again noted to generally reduce with increasing building separation, however exceptions do exist.

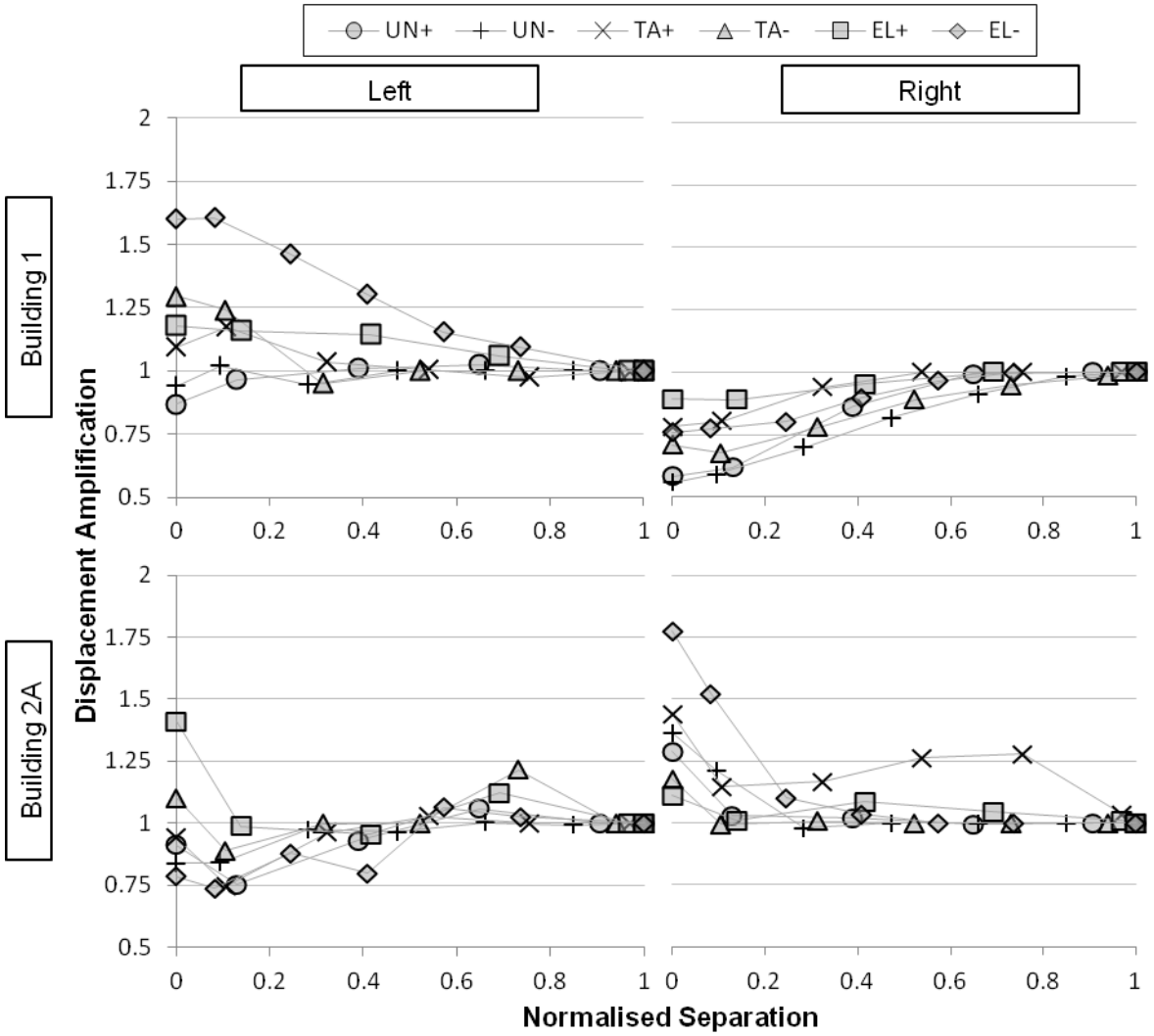

Figure 8.51 Front frame x axis displacement sensitivity to building separation

The displacement envelopes observed in different buildings' frames are shown in Figure 8.52 and Figure 8.53. These figures are also remarkably similar to those presented in *3DModel*. This is surprising since more building rotation (and hence more displacement difference in the frames) is expected in the eccentric pounding case. However, Building 2A is half the length of Building 2 so these displacement differences occur over a smaller intervening distance. Displacement sensitivity in the Y direction is greater in *3DModelE* than *3DModel* (Figure 8.54), but smaller than that of the X direction. This indicates that torsional collision does change transverse (Y direction) loading, but its sensitivity is less than that in the direction of pounding.

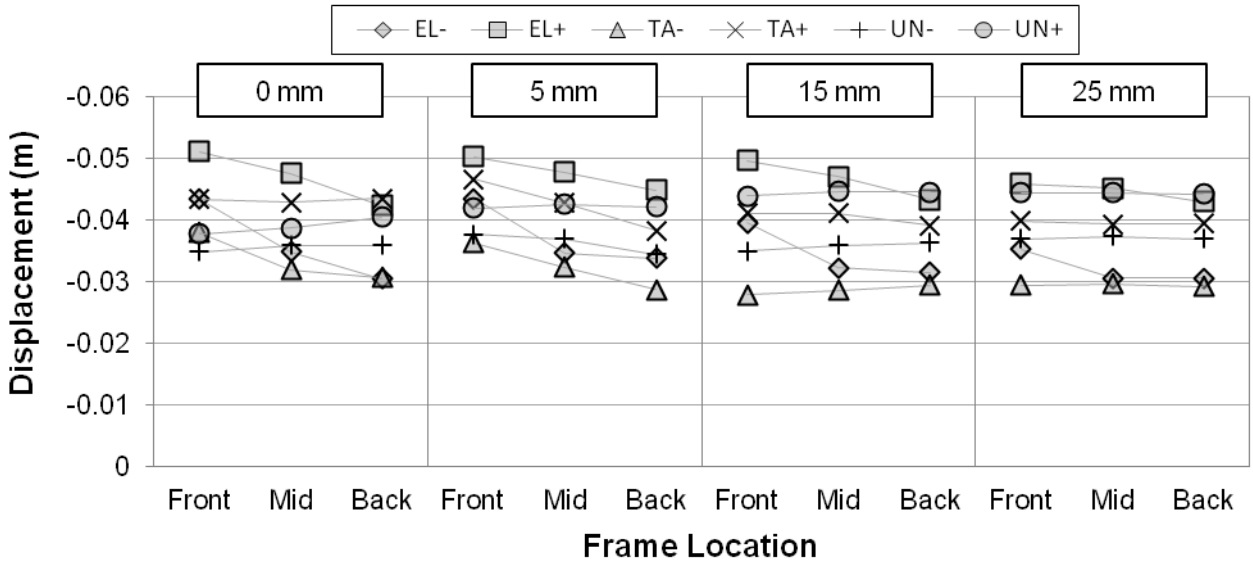

Figure 8.52 Building 1 left displacement envelopes at Level 3. Mid denotes the nodes aligned with the back frame of Building 2A . Building separations indicated with boxed numbers

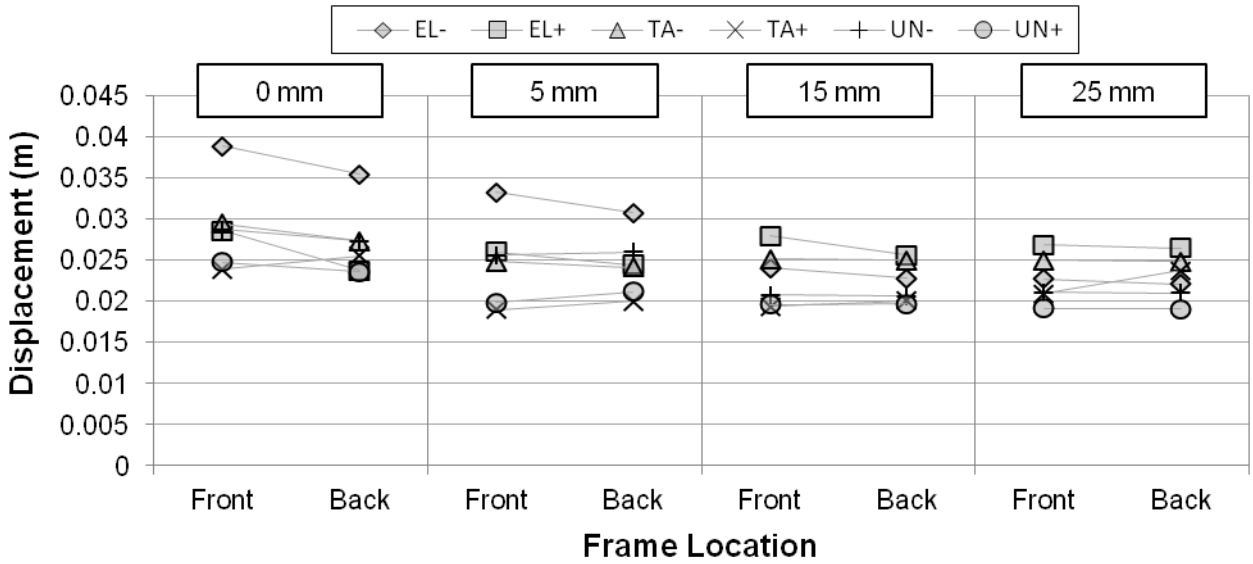

Figure 8.53 Building 2A right displacement envelopes at Level 3. Building separations indicated with boxed numbers

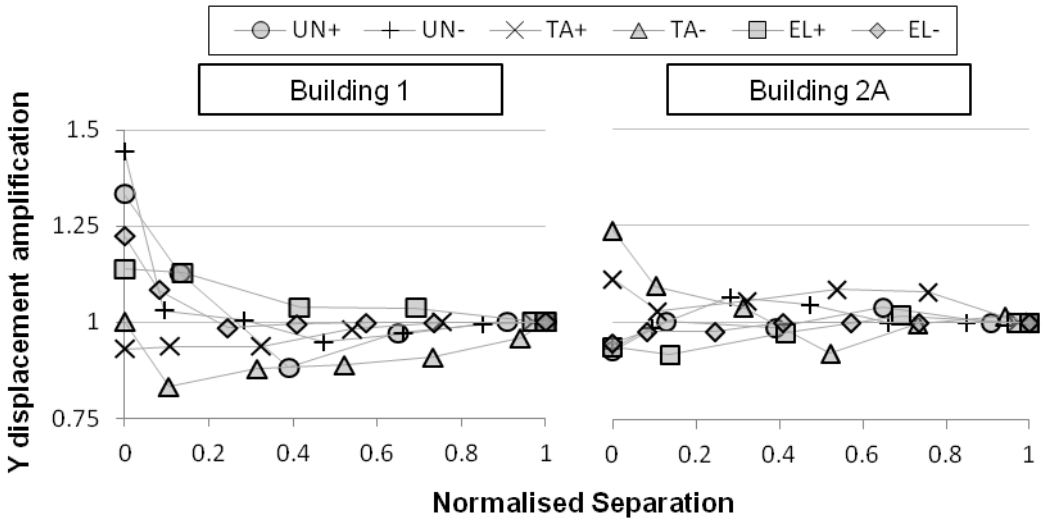

Figure 8.54 Y axis maximum absolute displacement amplifications

8.8.3 Global Damage Sensitivity to Building Separation

3DModelE's building interstorey shears and ductilities display very similar trends to those noted for *3DModel*. The new model's degree of sensitivity to building separation varies from slightly less to slightly more than that presented in Section 8.4.3, and is generally within 10% of the reported values. Since the observed trends are so similar to previous results, they are not reproduced here.

The similarity in global damage amplifications regardless of building eccentricity is not unprecedented. Similar conclusions were drawn by Wang and Chau (2008) and Leibovich et al. (1996) for simplified building systems (see Section 2.4.1). However, since only two eccentricities have been investigated in this section, conclusive statements about this relationship would be premature.

8.8.4 Local Damage Sensitivity to Building Separation

Local damage also presents similar trends to those presented in Section 8.4.4. However, Figure 8.55 is included because force amplifications exceed 2.0 in some analyses. These are the largest force amplifications reported in any model tested in this project. The relationship between normalised collision magnitude and normalised separation is consistent with previous observations. The trend line obtained by multiplying the SDOF prediction by 1.5 appears to be a good upper bound predictor for the majority of the performed analyses in 3D (see also Figure 8.21). However, different multipliers were found to give accurate predictions in the 2D models. This 1.5 multiplier therefore cannot be recommended for general predictions without further testing.

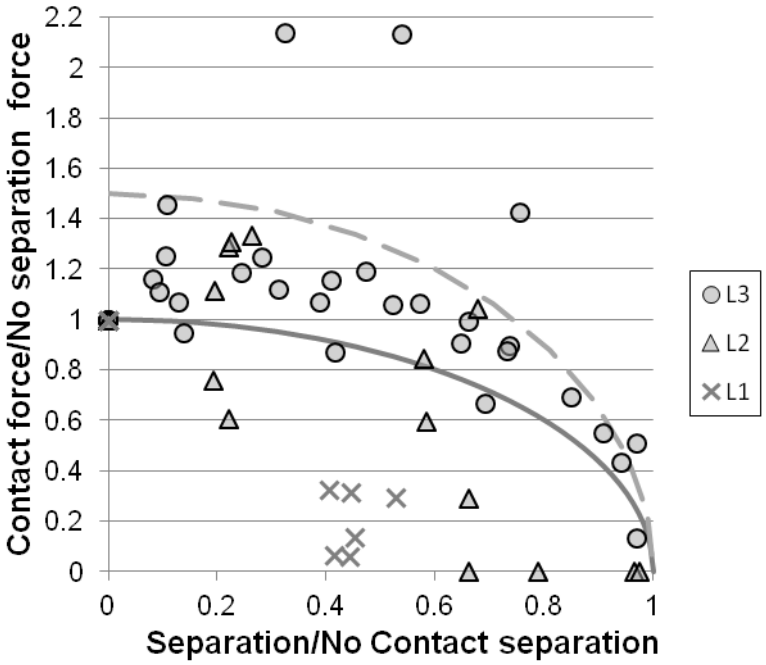

Figure 8.55 Normalised contact force in test 3DModelE. Solid line: SDOF prediction. Broken line: 1.5x SDOF prediction

8.9 Effects of 2D Analysis for Eccentric Configuration

The effect of modelling a torsional building configuration using 2D modelling techniques is assessed using *2DSlaveE*. An eccentric equivalent of *2DFlex* is not performed, since it is considered to be a much rarer modelling technique. *2DSlave* has already been noted as an inaccurate modelling method (Section 8.5). However, here it is of interest to see whether building eccentricity significantly increases the recorded variations.

8.9.1 Influence on Displacement Envelopes

The displacement sensitivity to *2DSlaveE* is presented in Figure 8.56. The effect of the nodal slaving is apparent in these results; in *2DSlaveE*, Building 1's displacements have been reduced by about 10%, while Building 2A's displacements have increased by approximately 10%. *2DSlaveE* does not accurately predict the displacement response of this building configuration. However, these values are again similar to those presented in *2DSlave* (*2DSlave*'s corresponding data is presented in Figure 8.32 using a different format). *2DSlaveE* does show higher displacement sensitivity, however values are generally within 15% of *2DSlave* (the maximum difference between *2DSlave* and *2DSlaveE* is 31%).

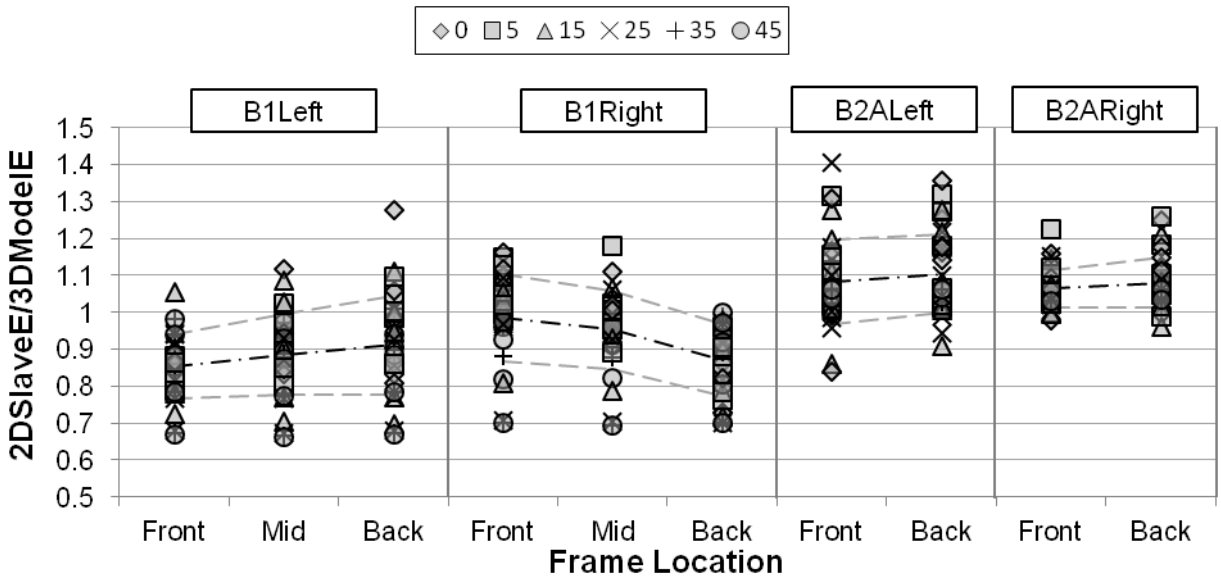

Figure 8.56 Displacement sensitivity to 2D modelling.

8.9.2 Influence on Global Damage Demand

Interstorey shear force is universally over-predicted by *2DSlaveE* (Figure 8.57). Building 1's amplifications change significantly with height. The lower shear amplifications at Level 3 is attributed to column yielding at this level. Building 2A's shears are over-predicted by an average of 5%. On average, conservative interstorey shear demands are predicted by *2DSlaveE*.

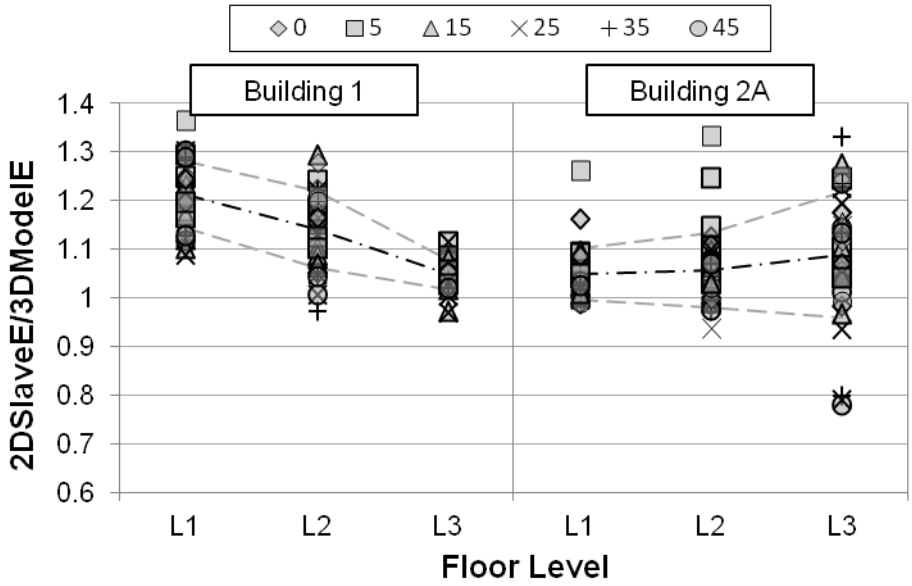

Figure 8.57 Interstorey shear sensitivity to 2D modelling

The maximum ductilities are more sensitive to the modelling method change (Figure 8.58). Building 1's ductilities are generally over-predicted, and show wide dispersion (all Building 1 standard deviations exceed 0.2). Building 2A's beam ductilities are significantly underestimated by *2DSlaveE*. Curiously, the amplification of the ductilities show different trends to the displacement amplifications (where Building 1 is under-predicted and Building 2A is over-

predicted). As expected, all global damage predictions have been significantly changed by the 2D modelling.

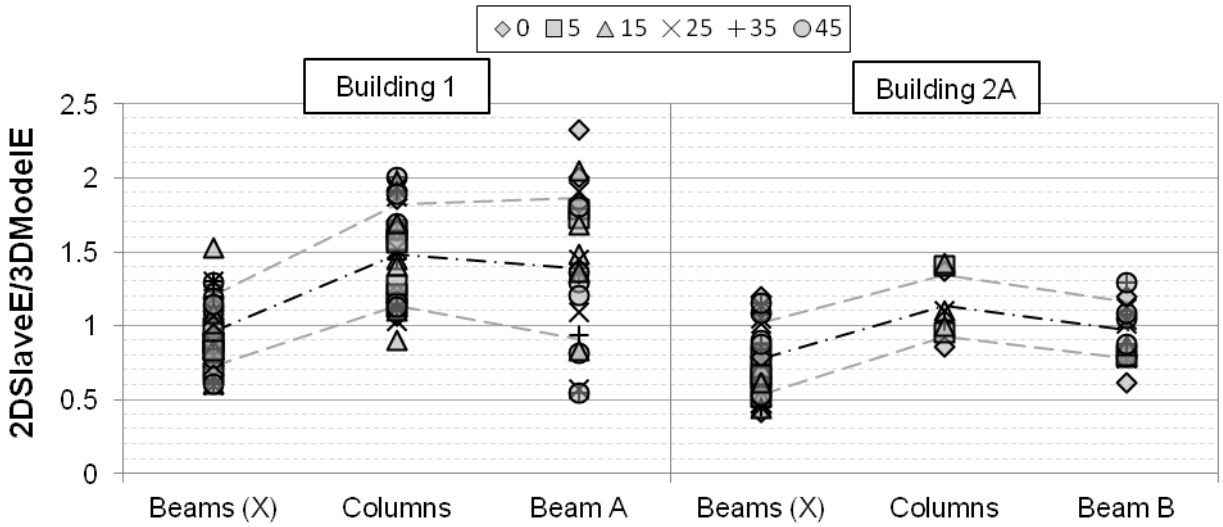

Figure 8.58 Ductility sensitivity to 2D modelling

8.9.3 Influence on Local Damage Demand

Local damage is similarly affected by 2D modelling (Figure 8.59). The presented contact force amplification varies widely, and many *2DSlaveE* analyses predict no collision, when the corresponding *3DModelE* did (this is indicated in the figure with normalised collision forces of 0 magnitude). Contact force is not well predicted by 2D modelling at any floor level. If accurate contact force data is required, 3D analysis is necessary.

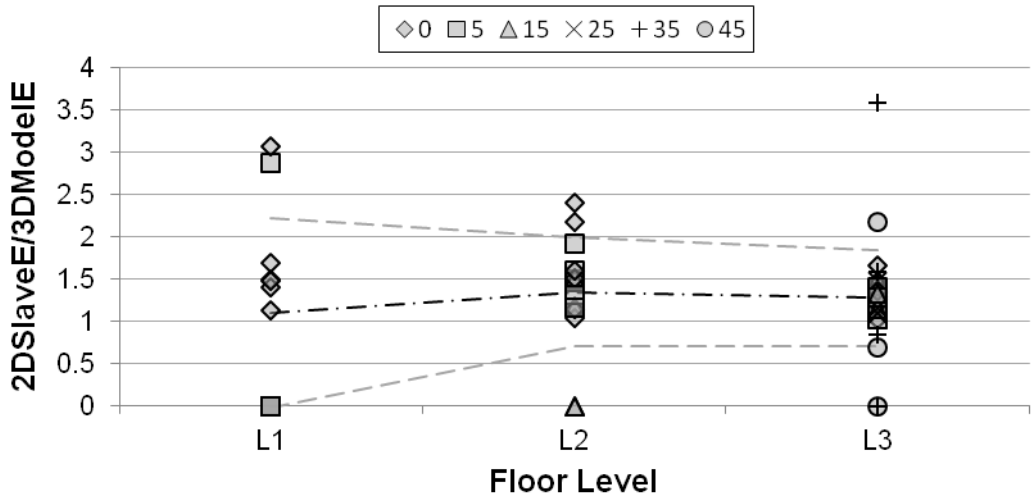

Figure 8.59 Collision force sensitivity to 2D modelling

8.10 Effects of Rigid Diaphragms for Eccentric Configuration

Finally, the effects of rigid diaphragms are considered for the eccentric building configuration. As with the previous sections, NC results are not presented here. It is noted that the effects of

rigid diaphragms are minimal when pounding does not occur (maximum recorded differences are as follows - displacements: 1.5%, shears: 2.5%, and ductilities: 5%).

8.10.1 Influence on Displacement Envelopes

Figure 8.60 presents the X direction displacement sensitivity to the rigid diaphragm modelling. In Building 1 the rear frame is most affected by this change, where the movement away from Building 2A is over-predicted, while the opposite direction is under-predicted. This result is expected since the portion of diaphragm between frames 'Mid' and 'Back' is effectively acting as a cantilever during a building collision (see Figure 8.47). The rigid diaphragm modelling also causes greater deflections away from Building 1 in Building 2A. These differences are generally observed to increase with decreasing building separation. The displacement differences presented here are greater than those observed between *3DRigid* and *3DModel*. This indicates that eccentric collision requires floor flexibility to be modelled when accurate displacement envelopes are required.

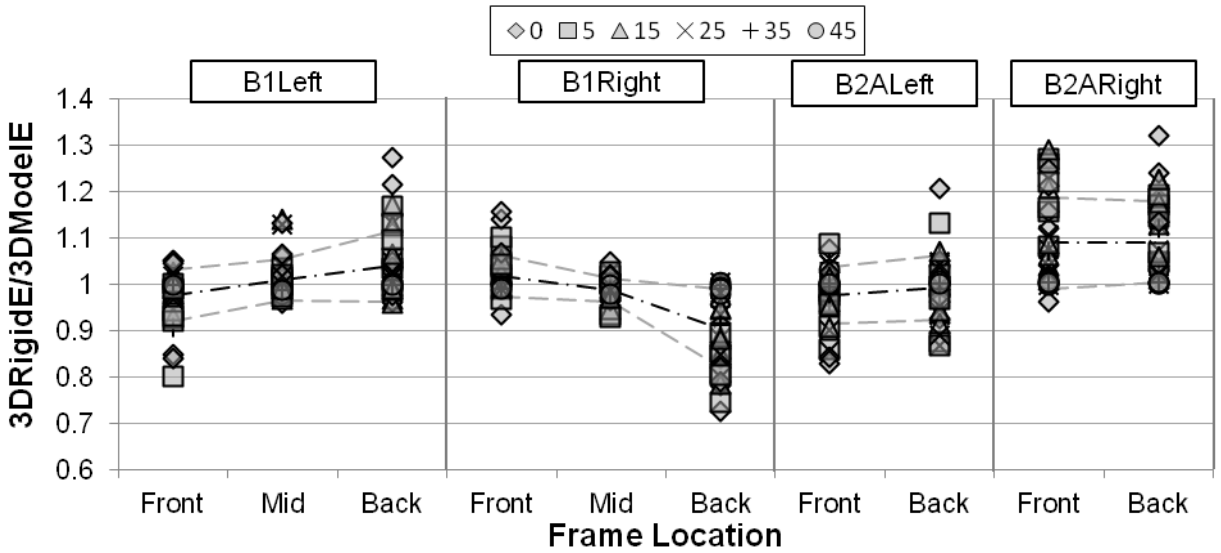

Figure 8.60 X direction Level 3 displacement amplification for test 3DRigidE

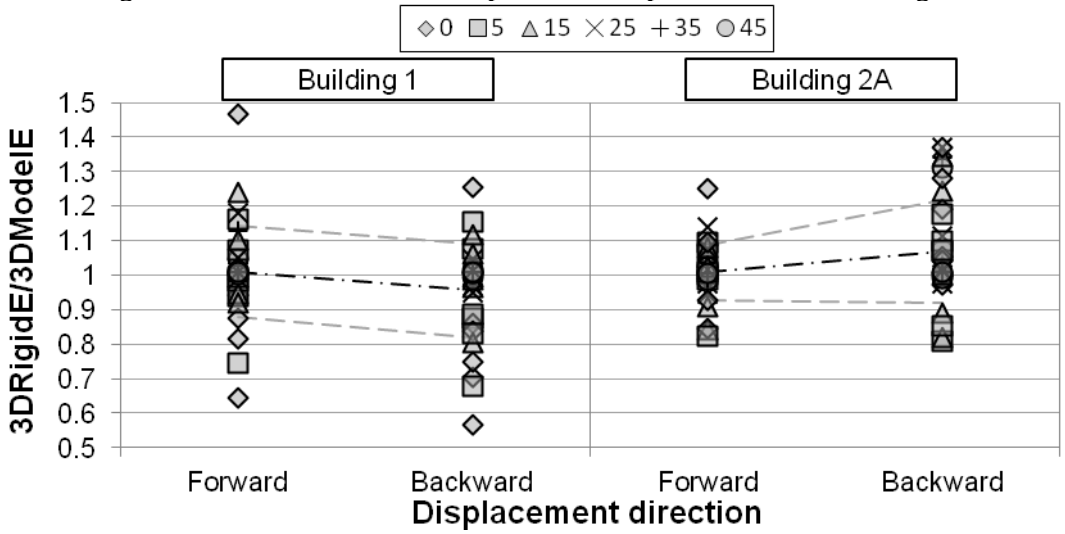

Figure 8.61 Y direction displacement sensitivity to rigid diaphragms

Y axis displacement sensitivity is displayed in Figure 8.61. The distribution of these results is greater than that observed for the X axis, however this distribution occurs approximately evenly either side of *3DModelE* (i.e. the amplifications and deamplifications are approximately balanced). This means that while individual displacement results differ by as much as 50%, averaged results are within 6% that predicted in *3DModelE*. While it is difficult to observe in the figure, these results also generally increase in accuracy with increasing building separation. Y axis displacement amplifications are marginally more sensitive in the eccentric configuration when compared to the original configuration (i.e. *3DRigid/3DModel*).

8.10.2 Influence on Global Damage Demand

Building interstorey shears are presented in Figure 8.62. As was also observed in the *3DRigid* model, Y axis actions are much more sensitive to floor rigidity than the X axis. This is again attributed to the complete and immediate participation of the floor masses during any contact friction (see Section 8.6.3).

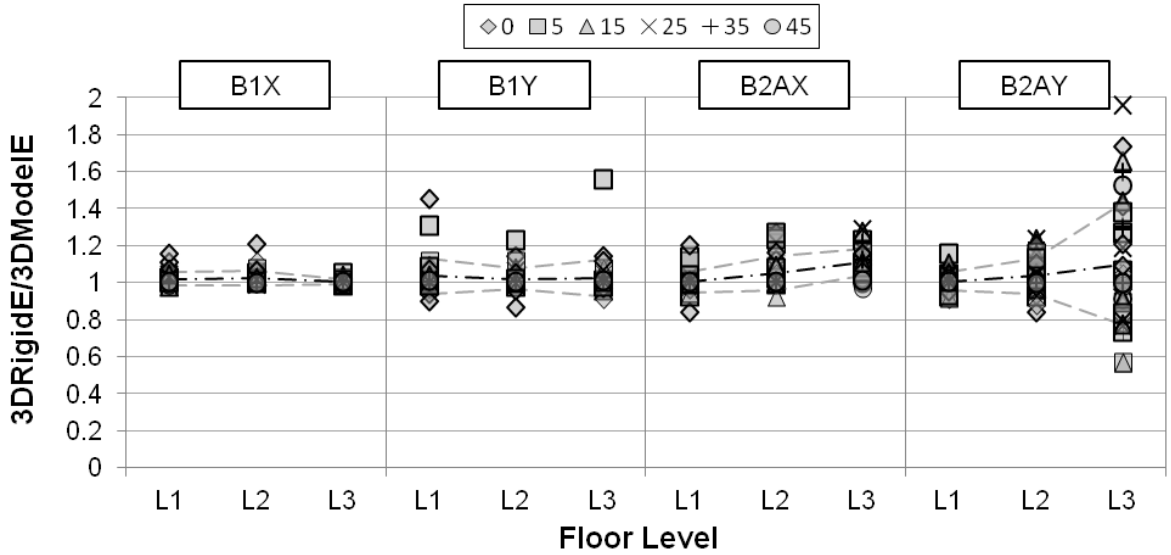

Figure 8.62 Interstorey shear sensitivity to rigid diaphragm modelling

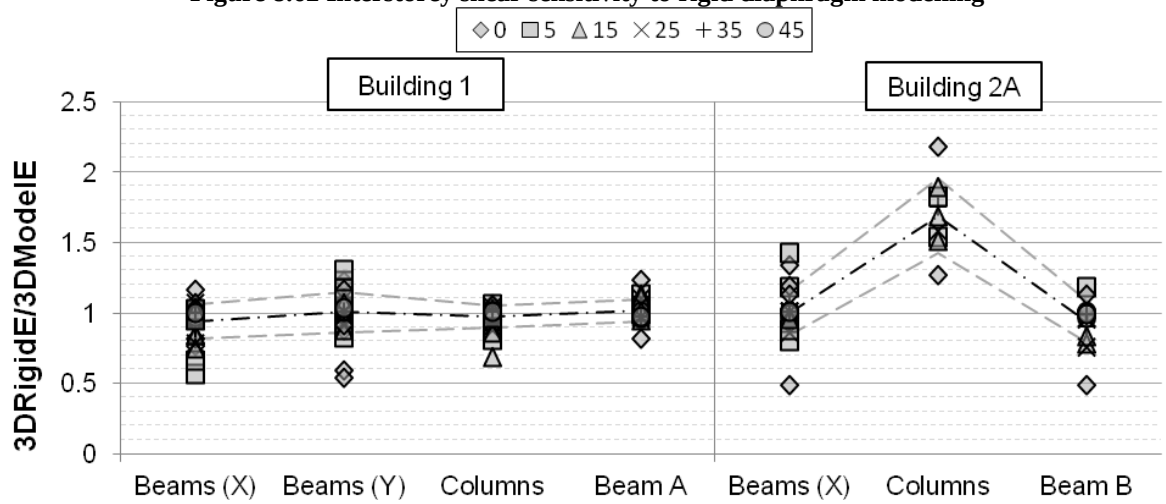

Figure 8.63 Ductility sensitivity to rigid diaphragm modelling. Broken lines show result averages (black line) and averages ± one standard deviation (grey lines)

The ductility amplifications (Figure 8.63) show wider variance than the shear amplifications. Building 2A's column ductilities are highly sensitive to the diaphragm modelling change due to the change in load transfer mechanism in the roof (see Section 8.6.2). The eccentric pounding configuration has not greatly increased the sensitivity of these global parameters.

8.10.3 Influence on Local Damage Demand

Contact force is known to be highly sensitive to diaphragm flexibility; however, results are presented here to illustrate how large this discrepancy can be. Figure 8.64 shows the force amplification for the contact force and horizontal friction. These results are again similar to *3DRigid* (Figure 8.41). Note that two outliers are not shown for Level 3's horizontal friction. These points record amplifications of 12 and 18. Reliable contact forces cannot be obtained from rigid diaphragm models at any floor level.

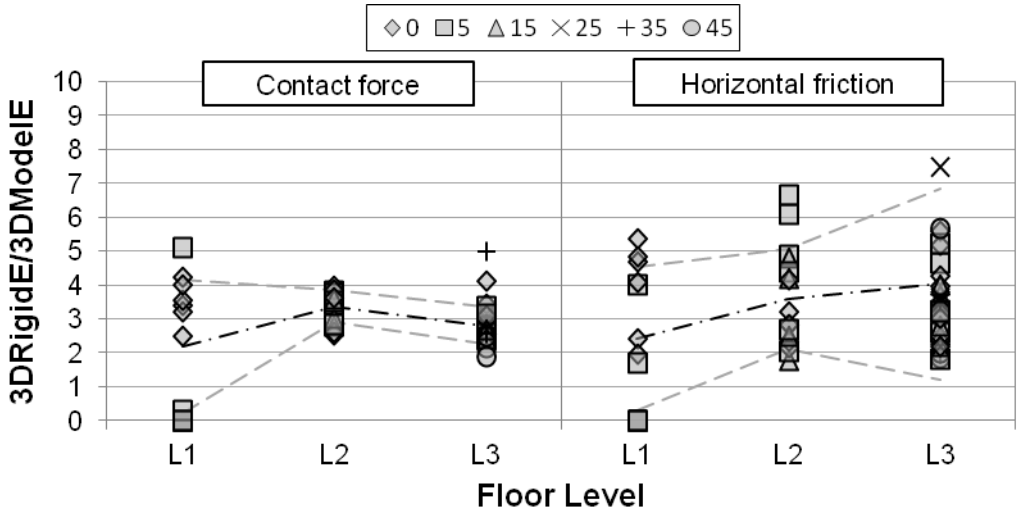

Figure 8.64 Contact force sensitivity to rigid diaphragm modelling

8.11 The Suitability of Modelling Pounding in 2D

Based on the results presented in this chapter, recommendations can be made on when pounding can be appropriately modelled in 2D. Two factors affect the suitability of 2D pounding modelling; the symmetry of each individual building, and the symmetry of the entire configuration when pounding occurs. Here it is assumed that both buildings are perfectly symmetrical. 2D pounding model suitability is summarised in Table 8.9 for *2DSlave* and *2DFlex*. These recommendations assume that the secondary component of the ground motion (the Y direction) has no affect on the response of the buildings in the primary direction (X direction). *2DFlex* was found to provide useful results in all tested configurations. However, as previously stated, *2DFlex* requires nearly as much data input as a full 3D analysis. This method's usefulness is therefore limited.

Table 8.9 Comparison of 2D models' suitability for representing pounding response

Configuration type	*2DSlave*	*2DFlex*
Perfectly symmetrical collision	*Not suitable*	*Perfect prediction of response*
Minor asymmetry in collision (see Figure 8.6)	*Not suitable*	*Global damage is suitably predicted if the average of multiple analyses is used*
Significant asymmetry in collision (see Figure 8.47)	*Not suitable*	*Untested*

Other 2D modelling methods do exist. The 2D method used in Chapter 6 (modelling the stiffest frames that undergo collision) is only useful in very specific circumstances. Each frame must accurately represent the overall response of its respective building (as shown in Table 8.4, this was not the case for the configuration considered here). Furthermore, the tributary width of the mass participating in collision for each building must be equal (see Figure 5.14). These requirements severely limit the usefulness of such modelling.

The 2D models used in this project have been selected because they can predict the demands of individual members in each building. It is possible to model at a coarser scale, where only the gross response of interstorey element is considered (for example, see 'Normal 2D' in Figure 8.31). In these analyses, the interstorey shear is usually of the greatest interest. Once an analysis is performed, the demands on different members can be assigned using their relative stiffnesses. The difficulty with this approach is calibrating the interfloor responses in the coarse model. While elastic response can be reasonably accurately predicted, the non-linear response of the elements cannot. Individual element's hysteretic responses are significantly simplified for such analyses. However, assuming this calibration can be successfully achieved, it is expected that this form of modelling would provide similar model accuracy to *2DSlave*.

8.12 Conclusions

The following conclusions are drawn based on the results presented in Chapter 8:

1. The fundamental properties of a 3D floor/floor collision without any building rotation can be predicted with reasonable accuracy using the simplified calculations developed in previous chapters.
2. Building displacement and global damage amplifications due to pounding reduce approximately linearly with increasing building separation. However, local damage initially increases with increasing building separation. Even at separations 80% of that needed to prevent pounding, collision forces are approximately equal to these recorded at zero separation.

3. 3D analysis captures collision behaviour not observed in 2D analysis. ‘Toe-tip’ collisions, and collision ‘stiffness softening’ are noted as consequences unique to 3D modelling of pounding interactions.
4. Eccentric pounding configurations can cause torsional building response, even if both buildings are perfectly symmetrical and do not have any torsional vulnerability.
5. 2D analyses can provide reasonable accuracy if multiple ground motions are tested and local damage is not of interest. However, floor flexibility is necessary in the models since rigid slaving introduces significant additional error.
6. Rigid floor models introduce significant error to individual analyses. However, if many analyses are performed, the averaged values of global damage are generally consistent with the results including diaphragm flexibility. Local damage cannot be accurately predicted in rigid floor models.
7. The addition of collision damping to the modelled 3D pounding analyses causes surprisingly little change to the buildings’ responses. It is believed that this is at least partially caused by the changing flexibility within each buildings’ roofs. If the observed trends were also observed in other models, collision-specific plasticity models could be disregarded in future modelling.
8. Increasing building eccentricity generally increases the effects of building pounding. However, this increase was observed to be comparatively small in the tested models. 3D modelling is required to adequately capture the response of buildings with eccentric pounding loads.
9. Parameter sensitivity to pounding can be reliably predicted. The considered parameters are listed in order of increasing sensitivity here; building displacement, interstorey shear, member ductility, and contact forces.

Chapter 9 Analysis of Collisions with Columns

Related papers

Cole G, Dhakal R, Carr AJ, and Bull D (2010), *Distributed Mass Effects on Building Pounding Analysis*, 9th US National and 10th Canadian Conference on Earthquake Engineering. 2010: Toronto, Canada

Chapter 3 to Chapter 8 dealt exclusively with floor/floor collision. While this approach was necessary to understand the most basic form of building collision, floor/column collisions are known to usually cause more devastating damage to building configurations. In particular, buildings susceptible to floor/column collision risk failure of their impacted columns. This could cause global failure of the building's gravity system.

Chapter 9 specifically addresses the modelling of floor/column collisions. The development of a simplified floor/column modelling method mirrors that used to develop the floor/floor model. No theoretical derivation of collision force or duration is attempted due to the governing problem's complexity; however Euler – Bernoulli and Timoshenko beam theories are used to determine the elastic column response to impulse. These detailed models are then used to determine a suitably accurate simplified model when considering a single collision. The adopted model is applied to modified versions of the 3D building configurations presented in Chapter 5.

This thesis focuses on reinforced concrete columns. This is because reinforced concrete (RC) columns are more common in New Zealand buildings than steel columns. It is believed that steel columns could be modelled in a similar manner; however, each steel column's likely failure mechanism would require specific assessment before any pounding analysis was performed.

9.1 Existing Column/Floor Collision Research

Karayannis and Favvata have previously performed detailed modelling of floor/column collisions (Section 2.5.5). However, the investigations presented here differ in a number of ways. Karayannis and Favvata (2005a; 2005b) modelled their collisions using a specialised column element designed to accurately model the column's flexural capacity and plastic hinge length. In the analyses performed here, attention is focused on the shear capabilities of the column (for reasons that will become apparent). Furthermore, the analyses presented here consider collisions along the entire height of each column. Karayannis and Favvata modelled collision only at the topmost point of their smallest building. This approach was found to be acceptable for collisions between buildings of greatly differing heights. However, the models considered here use buildings with very similar heights, so the model method must be reassessed. Finally, the

modelling methods presented here are developed based upon theoretical and numerical considerations that have not been presented in the literature to date.

9.2 Idealized Floor/Column Response to a Single Collision

Under normal seismic loading, columns are primarily loaded by the relative movement of the floors immediately above and below their position. Loading of this type is usually modelled using Euler – Bernoulli beam theory (Chopra 2007). However, if a column suffers direct collision, the significantly smaller duration of this loading causes an intricate interaction that may not be adequately captured by the above theory.

To the author's knowledge, no experimental data exists for collision between RC columns and floors. However, blast loadings feature similarly small durations of loading and have been previously investigated. Blast loadings experiments and simulations have identified multiple issues that may also affect pounding structures (Low and Hao 2002). Specifically, the modelling of blast loading requires more accurate modelling than the standard Euler – Bernoulli beam theory. This is because the column's shear deformation and the rotational inertia of the column's section affect the overall dynamic response of the element. Strain rate effects also affect the material properties of the column. Finally, and most importantly, the hierarchy of failure can change within the column.

Blast investigations have shown that columns can fail in shear, when a flexural failure is predicted using pseudo-static analysis (Low and Hao 2002). Furthermore concrete columns can fail in direct shear rather than the conventional shear failure (diagonal tension strut failure). The issues of direct shear have not been investigated for pounding buildings to the author's knowledge. As further investigation into this particular complication is too onerous to be performed here, it is noted that that columns could fail in direct shear and thus the direct shear or 'shear friction' capacity should be evaluated when considering any floor/column collision.

The importance of shear force in floor/column collisions can be approximately evaluated by comparing the ratio of column moment and shear set during design to the demand ratio caused by pounding loading. Here the impacted column behaviour is approximated as a single column with completely rigid supports. When a column's flexural and shear capacities are designed, they are typically assumed to perform in a column sway mechanism (Figure 9.1). This leads to an approximate column moment/shear capacity ratio of L/2. However, if a floor/column collision occurs, the applied loading causes a different capacity ratio which depends upon a/L. A sufficiently large change in this ratio can cause the column's hierarchy of failure to change. This

difference in capacity ratio increases as the value of a/L reduces; however, even the maximum value of a/L = 0.5 causes the capacity ratio to halve. This behaviour suggests shear failure is the likely failure mechanism of floor/column collisions.

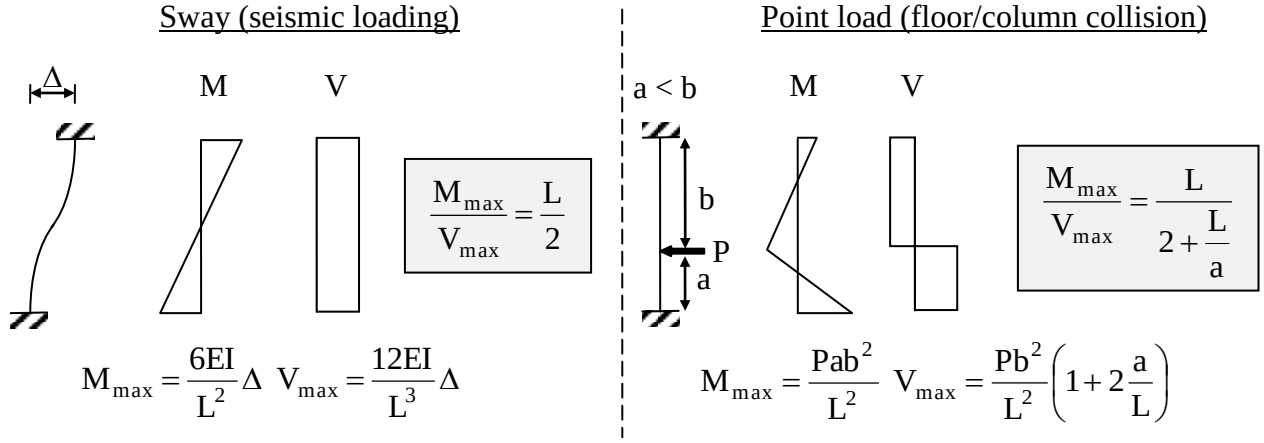

Figure 9.1 Moment/shear demand ratio due to various loadings. Left: sway demands assumed during design. Right: Floor/column collision point load demands.

Strain rate effects on column impact are not considered in this thesis, this is because the 'normal' column properties are required for the majority of the analysis while no collision occurs. Furthermore, detailed strain rate data for the considered collision scenarios is not currently accessible. If strain rate effects were to be included, a modelling method would be required which could identify high strain rate loading and adjust relevant parameters as necessary. The effects of such modelling are recommended as a subject of future research.

Since shear loading must be accurately represented in floor/column analysis, the numerical performance of columns with and without shear deformations and rotational inertias are tested to determine their influence on pounding configurations.

9.2.1 Euler – Bernoulli and Timoshenko Beam Models

Prismatic frame element modelling with shear deformation and rotational inertia is characterised by Timoshenko beam theory (Chopra 2007):

$$\rho A\frac{\partial^2 u}{\partial t^2} + EI\frac{\partial^4 u}{\partial x^4} - \rho A r^4\left(1 + \frac{E}{\kappa G}\right)\frac{\partial^4 u}{\partial x^2 \partial t^2} + \frac{(\rho A)^2 r^2}{\kappa G A}\frac{\partial^4 u}{\partial t^4} = F(x,t) \quad (9.1)$$

where u = transverse beam displacement, I = beam second moment of area, ρ = beam mass density, E = Young's modulus, G = shear modulus, A = beam area, r = beam radius of gyration, F(x,t) = any externally applied force and κ is a constant representing the nonuniform shear stress distribution in the beam's section. The left hand side of this equation can also be described by its four terms. From left to right, they are the beam's; translational inertia, flexural stiffness, shear

deformation, and rotational inertia. It is known that the last two terms in this equation are only significant in two specific situations (Chopra 2007);

1. When there is a high beam depth to length ratio (deep beams)
2. When a beam is subjected to very high frequency excitation

For the case of floor/column pounding, the aspect ratio of a typical column excludes the first criteria in all but very rare configurations. However, it is possible that the second condition is met. A floor colliding with a column may excite frequencies that require Timoshenko beam theory for accurate response prediction. High frequency excitation excites higher modes in the modelled beam. These modes have larger coefficients on the rotational inertia and shear deformation terms when compared to the translational inertia and flexural stiffness terms (i.e. the ratio of the second two terms to the first two terms increases with increasing mode). Thus Timoshenko beam theory may be necessary for the modelling of floor/column collisions.

When Timoshenko beam theory is not required, the Euler – Bernoulli equation is found by removing the last two terms;

$$\rho A \frac{\partial^2 u}{\partial t^2} + EI \frac{\partial^4 u}{\partial x^4} = F(x,t) \qquad (9.2)$$

Both the above equations assume completely elastic column response. In reality, concrete deviates from truly elastic response almost immediately. This means that neither equation will predict a concrete column's response with complete accuracy. Nevertheless, comparison between Euler – Bernoulli and Timoshenko beam theories provides insight into the important parameters that influence the column response. The significance of the model differences is assessed using Equation 9.1 and Equation 9.2 for two impact scenarios.

9.2.2 Characterising an Arbitrary Column Impact

Column (or beam) impact is modelled by providing an initial velocity to a section of a pin – pin beam. Two scenarios are tested; an initial velocity at mid-span, and an initial velocity at 0.6 m from the support. The 0.6 m spacing is selected since it is approximately equal to the likely beam depth. At distances less than ~0.6 m, it may be possible for the collision force to create a direct load path from the point of impact to the nearest support (i.e. a compression strut at approximately 45 degrees within the beam depth), which is not modelled here. The equations are modelled in Ruaumoko for the layout shown in Figure 9.2.

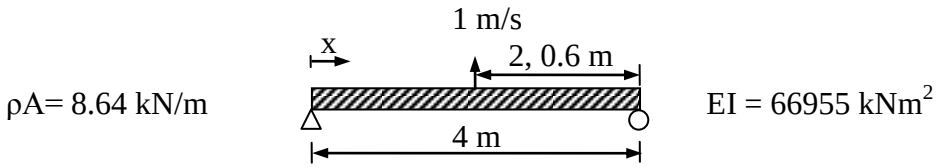

Figure 9.2 Pin - pin beam subjected to a transverse impulse

For each scenario (i.e. mid-span and near-support), Ruaumoko models are run with and without the combined effects of rotational inertia and shear stiffness. These models approximate the distributed mass of the beam using 100 flexural elements (101 nodal point masses). The initial impulse is created by applying a high magnitude force for a very small duration. The impulse of this load is calibrated to give momentum to the loaded node which equates to 1 m/s. However, the node may never reach this velocity since some proportion of the impulse is transferred to the adjacent nodes in the first few instants of modelling.

Figure 9.3 and Figure 9.4 show snapshots of the beam deflections at the time that the maximum overall displacement was recorded. The equivalent scaled static deformation for a point load at each impulse location is also presented (i.e. the shown static deformation shape corresponds to a static load applied at the impulse location). The two beam theories show differing displacement profiles at maximum deflection: the Timoshenko beam can be seen to possess higher mode effects in its displacement profiles, while the Euler-Bernoulli beam is relatively straight. The time that this maximum deflection is achieved also differs between the models (see Figure 9.5). However, the profiles are similar in both shape and magnitude. The displacement profiles are notably different to what is expected for a static loading. In particular, the near support loading shows negative deflections in some sections of the beam, which is not predicted for a static load.

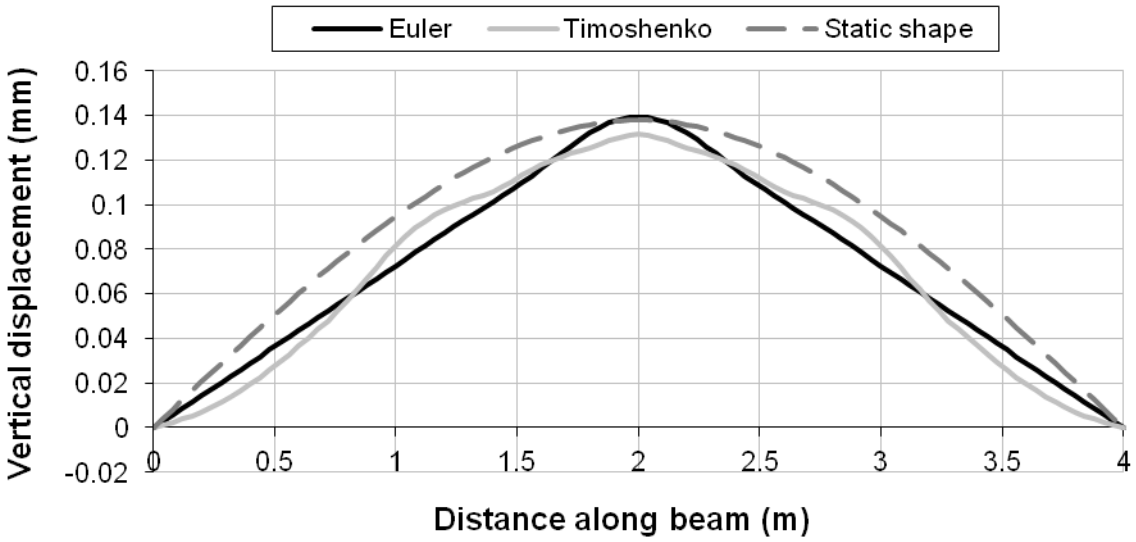

Figure 9.3 Displacement profiles at maximum displacement after mid-span loading.

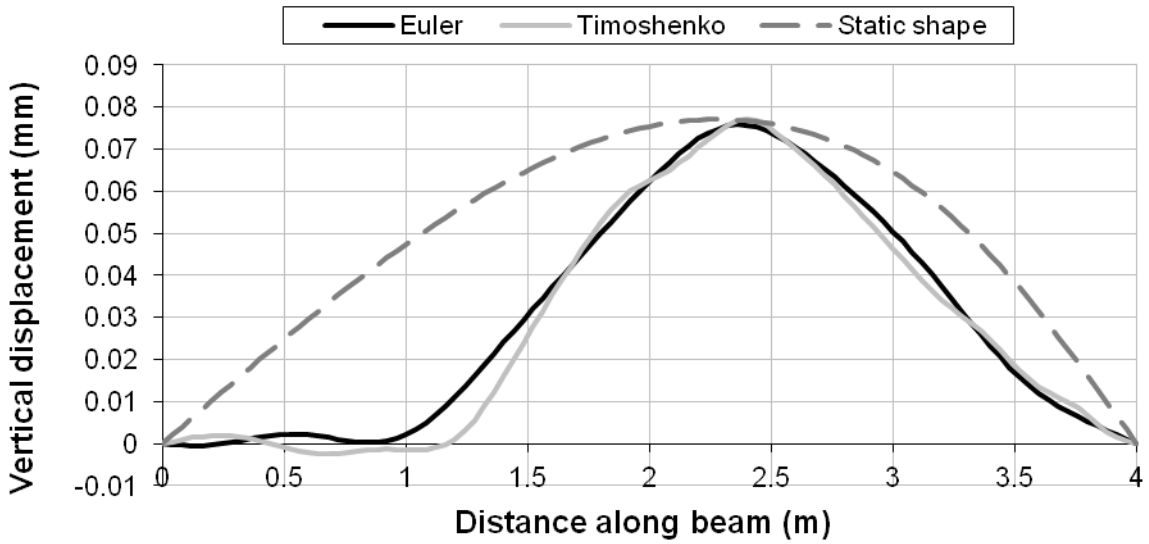

Figure 9.4 Displacement profiles at maximum displacement after near support loading (the loading is applied 3.4 m along the beam).

Results can also be analysed in the time domain. The response of the points of maximum deflection (x = 2 m for mid-span and x = 2.4 m for near-support) are presented in Figure 9.5 Once again the results are noted to be similar but distinct. Note time plots are shown until just past maximum deflection. After this point, the deflections pass back through the origin. The beam then continues to oscillate with a constant period (no damping has been applied). In both tests, the Timoshenko solution results in a slightly longer response period. This can be attributed to the presence of the beam's rotational inertia.

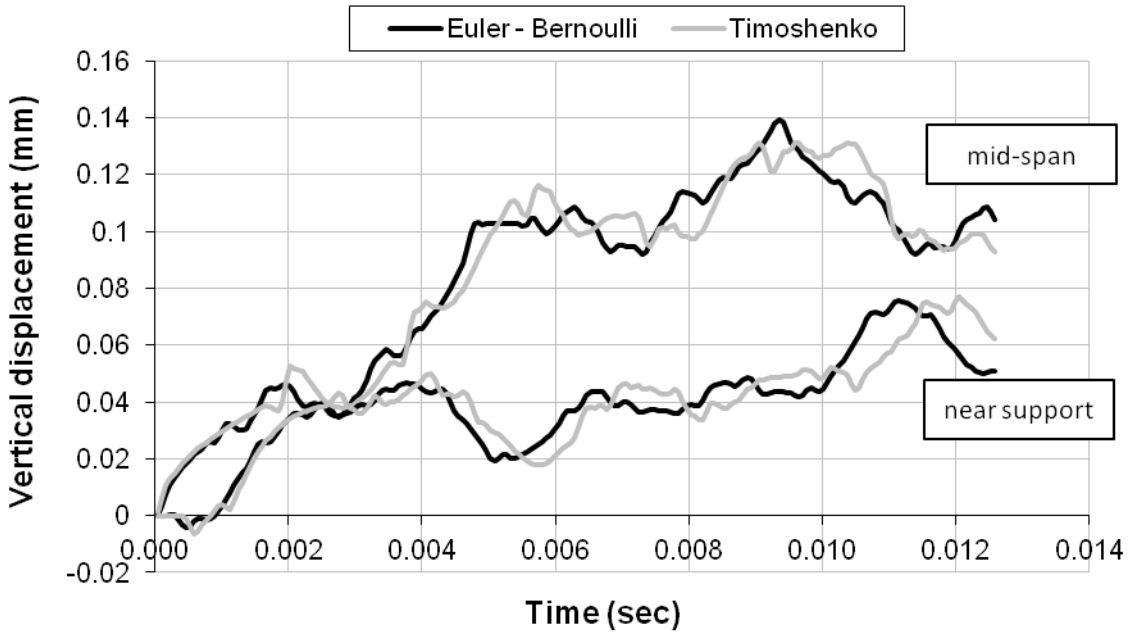

Figure 9.5 Beam deflections during the first 0.013 seconds at the point of maximum deflection

The mid-span configuration is now considered in detail to illustrate the significance of the selection of beam theory. The near-support beam behaviour is similar and is not presented here. The chaotic and seemingly arbitrary displacement response of Figure 9.5 may be at least

conceptually understood by close inspection of the first few instants after the excitation is initiated. These results are presented for the Timoshenko beam (Figure 9.6).

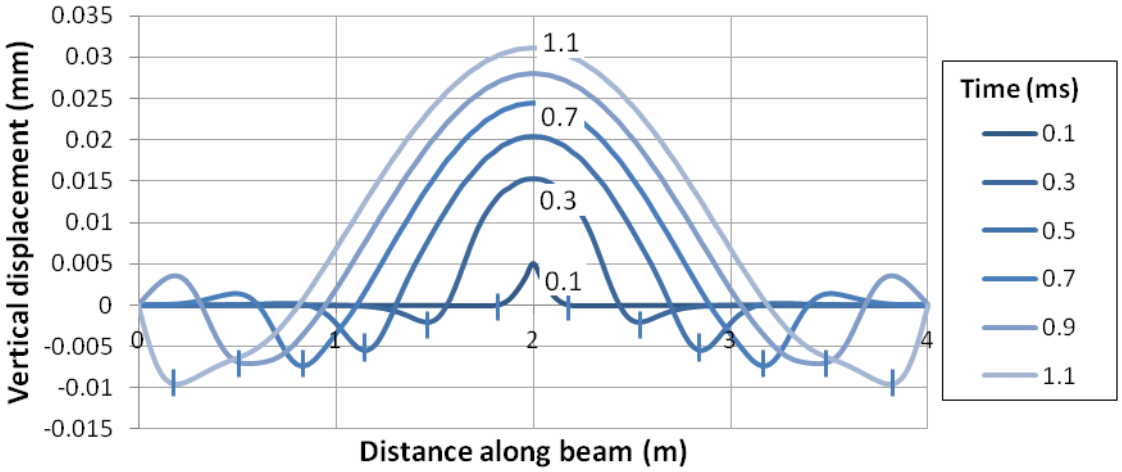

Figure 9.6 Snapshots of beam displacements during the first 1.1 ms of mid-span loading. Impulse wave fronts indicated with vertical lines.

The impulse excitation causes a positive (upwards) translation of the beam. However, many points on the beam are observed to displace down prior to the actual translational wave. This negative deflection is caused by the beam's continuity requirements. The requirements of continuity affect the rest of the beam much sooner than the actual translation at mid-span (that is, continuity affects the beam's deflections much earlier than the main displacement impulse wave). The impulse wave reaches the supports at approximately 1.1 milliseconds, however the effects of continuity are observed to reach the supports as early as 0.7 ms. The continuity effects are reflected by the pinned supports, which creates more complicated beam deflections. This is first apparent at 1.1 milliseconds, where a small 'kink' in the impulse bell shape is observed just behind the impulse wave front. As more time passes, the continuity and impulse waves continue to reflect at the supports creating the complex displacement shapes observed in Figure 9.5. Figure 9.7 presents an alternate visualisation of both beam models displacement responses, until just after maximum displacement is achieved.

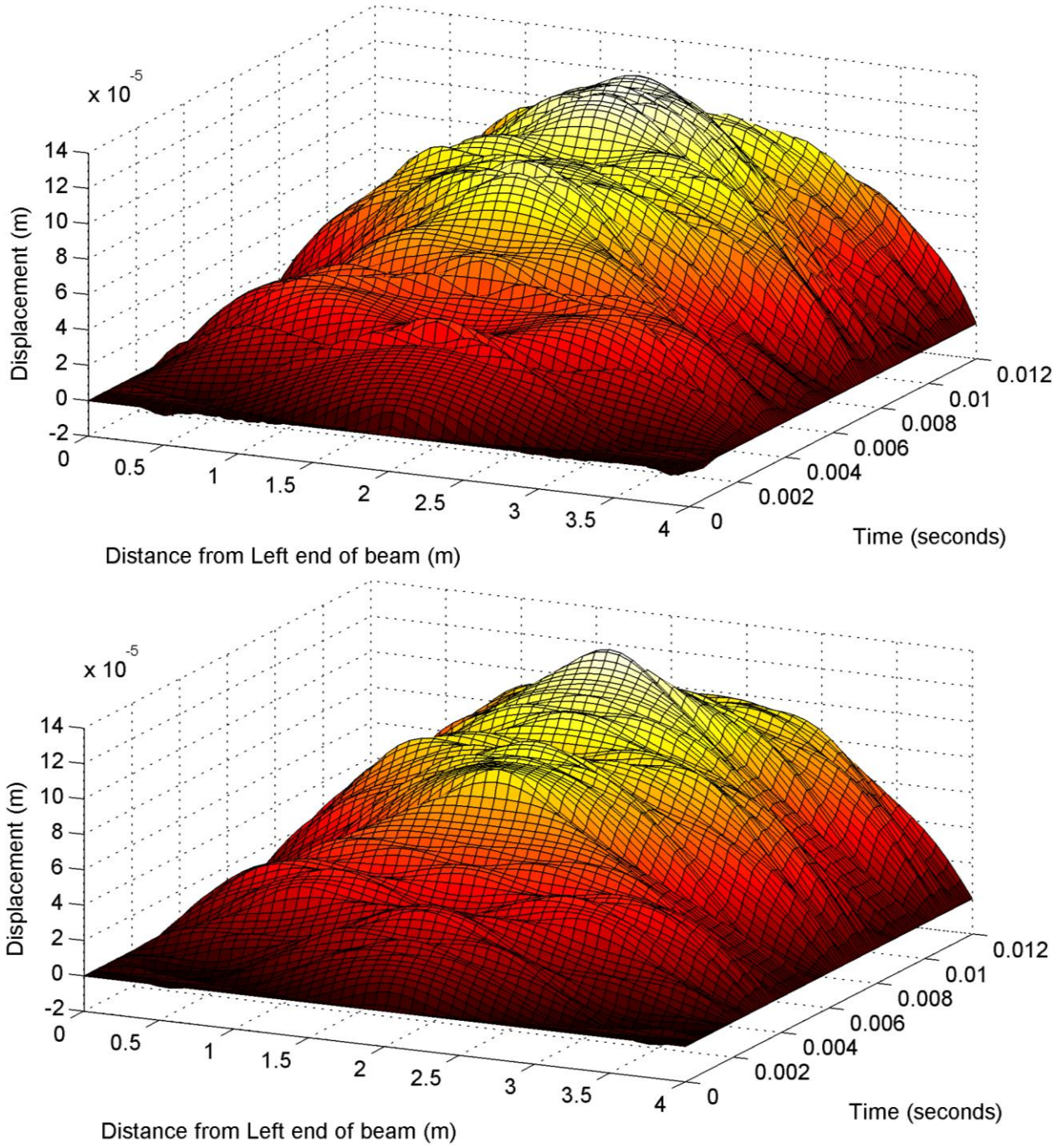

Figure 9.7 3D representation of displacements due to mid-span loading. Top: Timoshenko beam. Bottom: Euler - Bernoulli beam.

While the displacement response of the beam is important, the beam's shear force is more critical since shear capacity is likely to determine when the beam fails. The shear results of both beam models are presented for mid-span loading in Figure 9.8. Shear loadings notably differ between the two models. The Timoshenko results initially show an orderly wave propagation along the beam, however this breaks down after approximately 5 ms when other waves create more complicated interactions. The Euler – Bernoulli beam records a much faster transfer of shear. This is attributed to the lack of rotational inertia in the model. The difference in the maximum shears induced at the beam's supports is of greater concern. These values vary from

119 kN (Euler – Bernoulli) to 178 kN (Timoshenko). However, the durations of these shears are very small (less than 1 ms). Note that the presented time scale is different to that used in Figure 9.7. This has been done to emphasize the differences between the two methods.

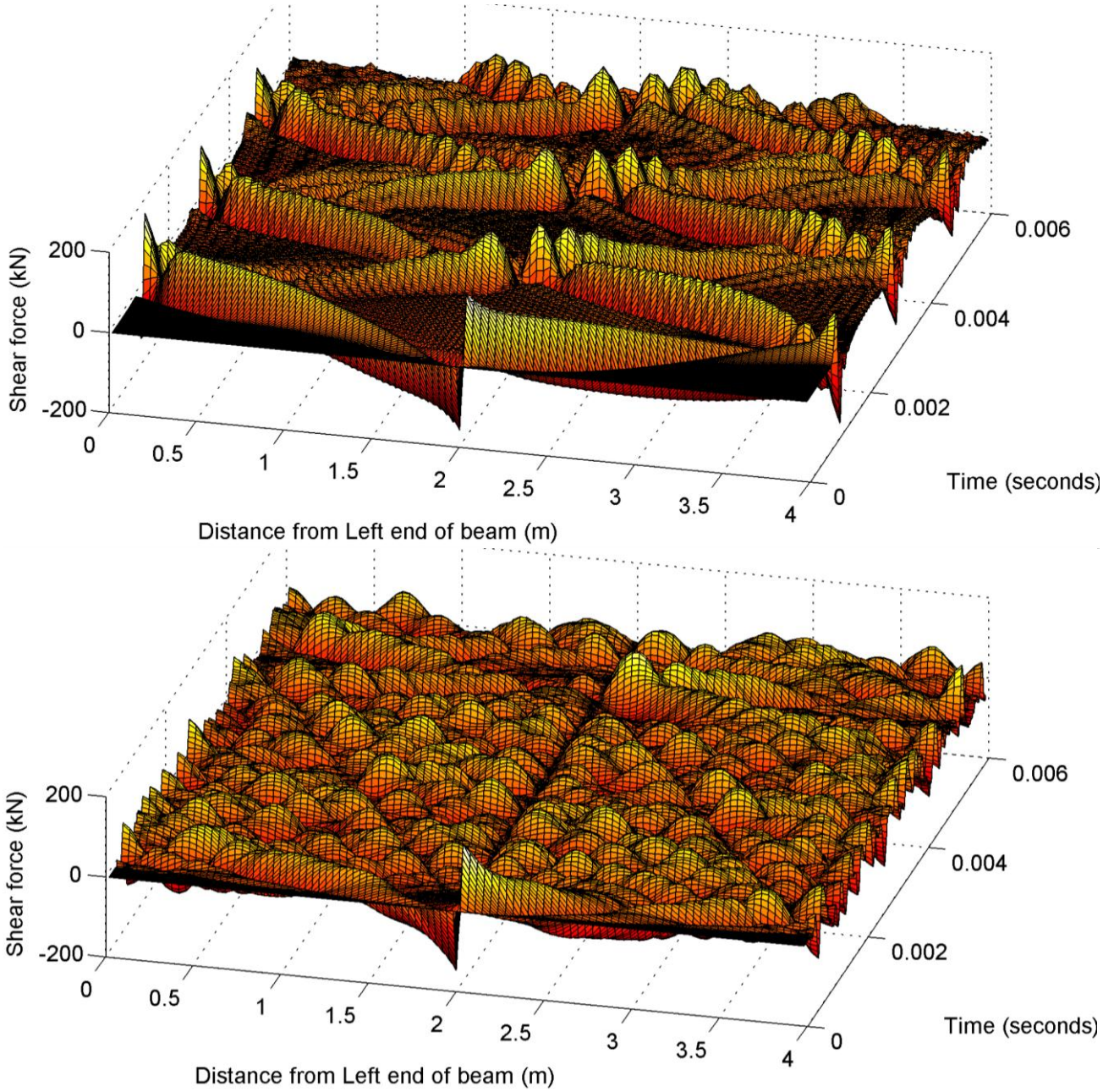

Figure 9.8 3D representation of shear loads due to mid-span loading. Top: Timoshenko beam. Bottom: Euler - Bernoulli beam.

The above analyses are useful in understanding the beam's response; however, a configuration that is more representative of pounding is required to assess the specific modelling requirements for floor/column pounding. This is performed in the following section.

9.2.3 Characterising Floor/Column Impact

A reliable model of floor/column collision is required as an intermediate step in developing simplified models. This section determines the 'accurate' model which is used as the benchmark

for subsequent model simplifications. Since shear loading was sensitive to the adopted beam theory in the previous section, a Timoshenko model using 100 column elements is selected for the accurate floor/column model. However, many other parameters still require definition. In addition to the model configuration, a collision element stiffness and suitable floor model must also be selected. Figure 9.9 shows the selected physical configuration and the selected model representation of floor/column collision.

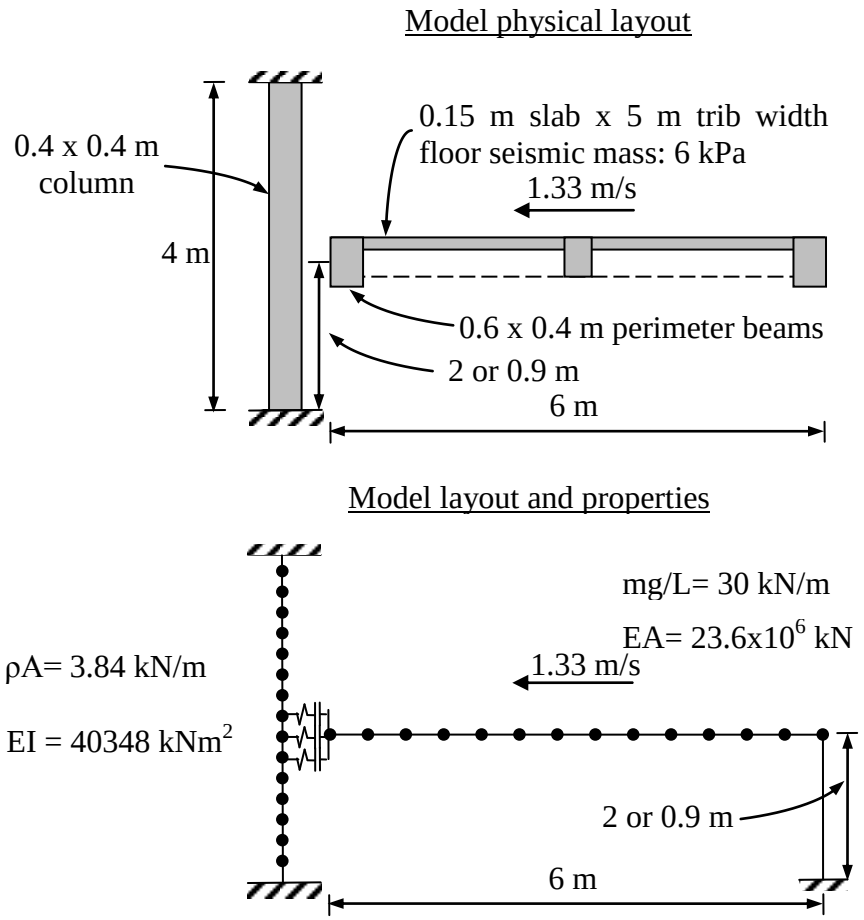

Figure 9.9 Column/floor test model

Perimeter beams are included in the model because they provide contact over a length of the column, rather than just a single point of contact loading. To reduce model complication, the stiffnesses and masses of this beam system are not modelled within the diaphragm and thus do not affect wave propagation. The perimeter beams are assumed to remain perfectly vertical throughout the collision. The diaphragm is also fixed in the vertical and rotational directions and thus provides a completely translational excitation to the adjacent column. For the purposes of this initial modelling, the floor/column collision is assumed to uniformly compress the diaphragm over the entire tributary width of the floor. This assignment is reassessed later.

Again, two scenarios are considered in the modelling; a collision at mid-span and a collision near the bottom of the column (called near-base). Note the wireframe column on the right hand side

of Figure 9.9 has a nominal stiffness and is provided only to meet the requirements of Ruaumoko (that is the structure is connected to the ground). No modal damping is applied in the model. For the initial testing, the number of diaphragm elements is set to the number of column elements. This restriction was used to reduce the number of required analyses and is checked in Section 9.3.4.

The final parameter requiring quantification is the collision element stiffness. As in the floor/floor collision case, this parameter is determined via numerical investigation.

Collision element stiffness is again defined in terms of γ (Equation 2.20). When modelling large numbers of elements in each diaphragm, the most accurate response for floor/floor collisions was found to be $\gamma = 0.1$ (Section 4.2). Here, values of $\gamma = 10$, 1.0, 0.1 and 0.01 were tested for floor/column collisions. Initially γ was defined in terms of the adjacent floor element stiffness. Alternative collision element stiffness definitions are investigated in Section 9.3.6.

9.2.4 Prediction of Floor/Column Loads

An approximate prediction of column shears for the presented models (Figure 9.9) can be made by assuming the collision responds like a pseudo static interaction. If the column and floor are both assumed to be stationary when the maximum column deformation is achieved, an equivalent static point load, P, can be found by equating the floor's kinetic energy (prior to collision) with the column's strain energy (at maximum deformation):

$$\begin{aligned} \frac{1}{2}mv^2 &= \frac{1}{2}k\Delta^2 \\ &= \frac{1}{2}k\left(\frac{P}{k}\right)^2 \\ P &= v\sqrt{mk} \end{aligned} \qquad (9.3)$$

where $P = k\Delta$, m = floor mass, k = column stiffness, Δ = column deformation and v = floor velocity at onset of collision. The derivation assumes that no strain energy is present in the floor at the time of maximum column deformation. While this is likely to be a suitable approximation for mid-span loadings, the equivalent point load will be overestimated when collision occurs near the base. Column shears can be calculated based upon the predicted equivalent point load. Figure 9.10 presents the equations for shear force for a built-in beam with a point load applied at an arbitrary location. Using the parameters defined in Figure 9.10, the column stiffness is:

$$k = \frac{3EIL^3}{a^3 b^3} \tag{9.4}$$

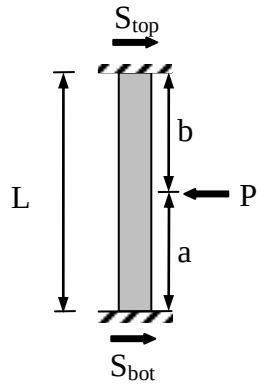

$$S_{top} = P\left(\frac{a}{L}\right)^2\left(1+2\frac{b}{L}\right)$$

$$S_{bot} = P\left(\frac{b}{L}\right)^2\left(1+2\frac{a}{L}\right)$$

Figure 9.10 Reactions and column stiffness for point load at an arbitrary height

Substituting the column reactions and Equation 9.4 into Equation 9.3 provides:

$$S_{top} = \left(\frac{a}{L}\right)^2\left(1+2\frac{b}{L}\right)v\sqrt{\frac{3EIL^3}{a^3b^3}m} \tag{9.5}$$

$$S_{bot} = \left(\frac{b}{L}\right)^2\left(1+2\frac{a}{L}\right)v\sqrt{\frac{3EIL^3}{a^3b^3}m} \tag{9.6}$$

Once again the collision force is found to be directly proportional to collision velocity. Using Equation 9.5 and Equation 9.6, predictions of shear force for the 'accurate' models (as defined at the beginning of Section 9.2.3) are presented in Table 9.1. These values have been calculated using a = 2 m and 0.9 m for the mid-span and near-base models, respectively. Note that Δ is the deflection at the point of the applied load, not necessarily the maximum deflection of the column.

Table 9.1 Predicted properties of accurate models

	S_{top} kN	S_{bot} kN	k kN/m	P kN	Δ mm
Mid-span	*994*	*994*	*121,000*	*1,990*	*16.4*
Near base	*440*	*2,970*	*356,700*	*3,410*	*9.56*

The stiffness (k) calculated in Equation 9.4 may be considered to be an 'effective impact' stiffness. This is because the calculated stiffness is dependent upon the location of the collision. The column can therefore be effectively stiffened by changing the location of the impact. The effect of this stiffness change is considered further in later sections.

The presented method may also be used in more realistic models of floor/column pounding. However, the error in these predictions will substantially increase. For example, consider collision between a modified version of the 2D model presented in Section 5.2.5 (Figure 9.11). Floor/column collisions occur over the height of the building interface (five in total). To simplify this process, each floor/column collision is considered separately. However, even considering only the top collision presents complexity. The velocity, v, must represent the relative velocity of the two buildings. This is difficult to accurately determine because the column is connected to two floors, each with differing velocities. An approximate value can be obtained using:

$$v = v_c - \left(v_a \left(\frac{b}{L} \right) + v_b \left(\frac{a}{L} \right) \right) \qquad (9.7)$$

where a, b and the floor velocities v_a, v_b and v_c are defined in Figure 9.11. This model assumes that velocities v_a and v_b do not change during the collision. Furthermore, no allowance of the strain energy of colliding floor's columns is made. These approximations all act to overestimate the collision forces in the column.

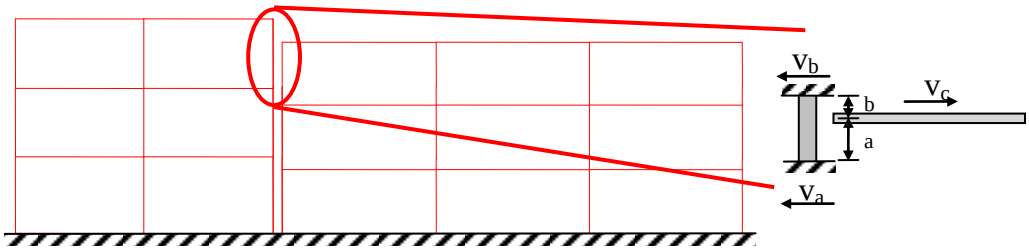

Figure 9.11 Simplified prediction of floor/column loadings for the topmost collision point

The previously presented floor/floor collision predictions also assumed that the buildings' columns do not affect the collision response. However, in floor/floor collisions this assumption is more valid because the collision duration is shorter and the deformations of the floors are very small. In contrast, floor/column collisions can cause relatively large displacements in the impacted column. For example, the following section shows impacted column displacements of ~15 mm (Figure 9.12). This magnitude of displacement is sufficient to cause considerable additional load in the other columns that do not suffer impact at this floor level. This effect would reduce the loading demand on the impacted column. Making realistic collision force predictions may be possible by revising the assumptions and simplifications presented here. This is left as a subject for future research. While the proposed method may provide only approximate results for actual floor/column building configurations, the formulation is still instructive in indicating important collision parameters.

9.2.5 Accurate Mid-span Model

The selection of γ for floor/column collision requires considerations similar to those used in selecting γ for floor/floor collision (Section 4.2.3). γ must be large enough to prevent material overlap, but small enough to avoid unduly large oscillations in the collision force results. Since this selection process is very similar to that shown previously, only the most accurate results are presented here. In the mid-span model, the most accurate results were obtained when $\gamma = 0.1$.

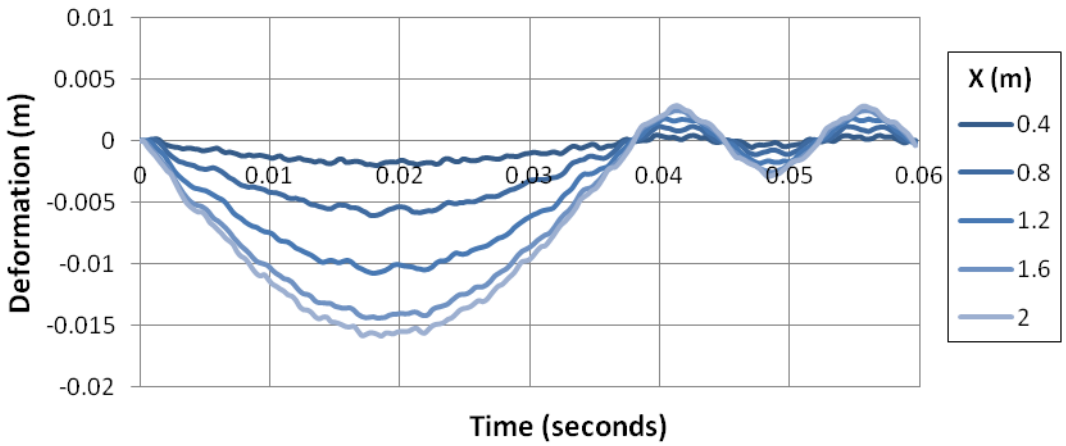

Figure 9.12 Deformation of specific column locations. X indicates distance from column base. Column response is symmetric around X = 2 m.

Figure 9.12 presents the displacement response of the column. These displacements significantly differ to that of the single impulse loading (Figure 9.5). The displacements' response in time is approximately sinusoidal, while the single impulse loading's response was much more complex. This difference is due to the ongoing contact of the floor and the column during the collision (the floor/column contact lasts approximately 0.038 seconds). After this contact the column continues to oscillate with a reduced magnitude. Displacements are only presented for the bottom half of the column since the model is symmetric about the column mid-height.

The overall shape of the column deformations is presented in Figure 9.13 for various times during collision. The presented time contours show the same displacement shape with changing magnitudes over the duration of the collision. The maximum displacement shape also matches the displacement shape predicted by a static loading. This observation may have important implications for pseudo-static analysis methods of floor/column contact. If the maximum column deformation shape is similar to the static deformation shape (for a point load applied at the floor height on the column), then the assumed column strain energy in the pseudo-static analysis will be accurate. This will result in more accurate predictions of column demands.

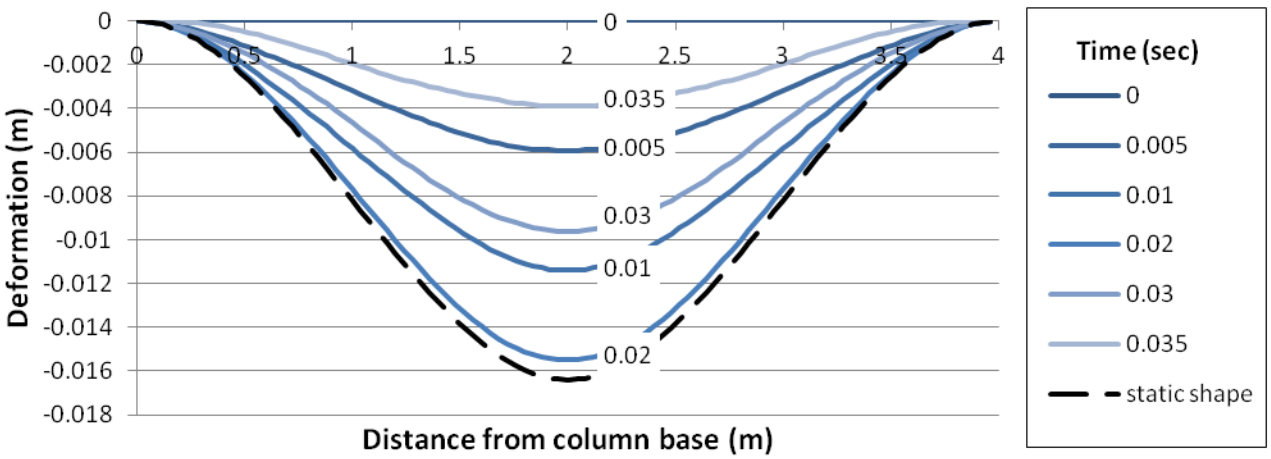

Figure 9.13 Column displacements during collision.

The column shears (Figure 9.14) show a similar sinusoidal response to that observed in the column displacements. Short oscillations are also observed that increase the shear force by 500 to 1000 kN. The duration of these peaks is typically in the order of 0.001 seconds. When reporting maximum shears, these small duration spikes are not included. Instead maximum shear is determined by averaging the shears between the point of loading and the nearest support. It is possible that averaging these peaks underestimates the shear loads on the column. However, as the considered columns are concrete, these peaks would be likely to be smoothed out by concrete micro-cracking and other material non-linearities. In Figure 9.14, shears are presented for $0 \leq X \leq 2$ m, since shears are anti-symmetric about X = 2 m.

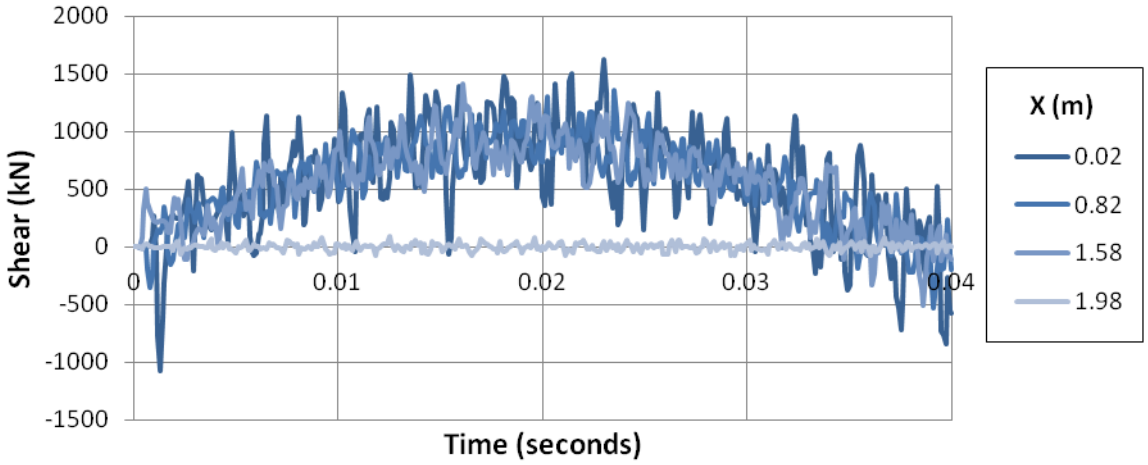

Figure 9.14 Column shears from mid-span floor collision. X indicates distance from column base.

The maximum and minimum averaged shears were recorded as 1010 and -1010 kN, respectively. These values agree excellently with the predictions in Table 9.1. At X = 1.98 m, almost no shear force is recorded. This is because this point of the column is within the zone of contact of the perimeter beam (see Figure 9.9).

Finally, the contact force is presented in Figure 9.15. The presented collision force is obtained by summing the collision forces of the fifteen contact elements. Two processes can be observed in

the results. In the first 0.0025 seconds, the initial collision loading is caused primarily by the column's inertia. After this point, the column moves at approximately the same speed as the impacting floor. However, as the column displaces its stiffness begins to slow the column, bringing it back into contact with the floor. This second collision can be averaged into an approximately sinusoidal shape, which is also seen in the displacement and shear results. This sinusoid has an approximate magnitude of 2000 kN, in agreement with Table 9.1.

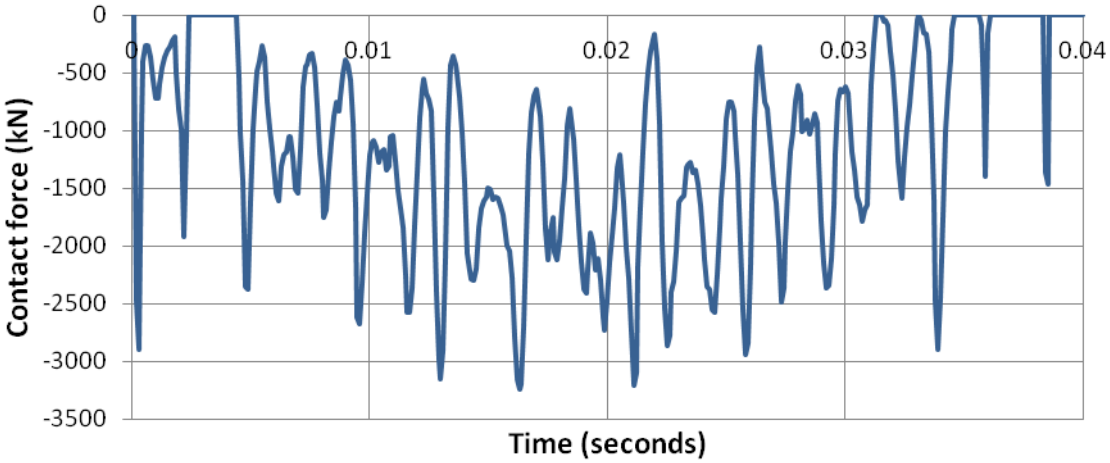

Figure 9.15 Collision force resulting from mid-span floor collision

9.2.6 Accurate Near-base Model

The mid-span model is actually likely to be the least critical floor/column collision situation since shear loads are minimised. For the near-base model, $\gamma = 1$ was found to be the most appropriate model of the floor/column collision. The results of the near-base model are more complex than the mid-span model and are presented below.

Figure 9.16 presents the column displacements during the collision (collision duration = 0.0174 seconds). This time the location of maximum static deformation differs significantly to the recorded column shape. This difference is attributed to the column's inertia. The difference in static and dynamic deformation shapes indicates that collision shears predictions will be less accurate than observed in the mid-span modelling. However, the displacement of the column at the point of loading (0.9 m from column base) is accurately predicted.

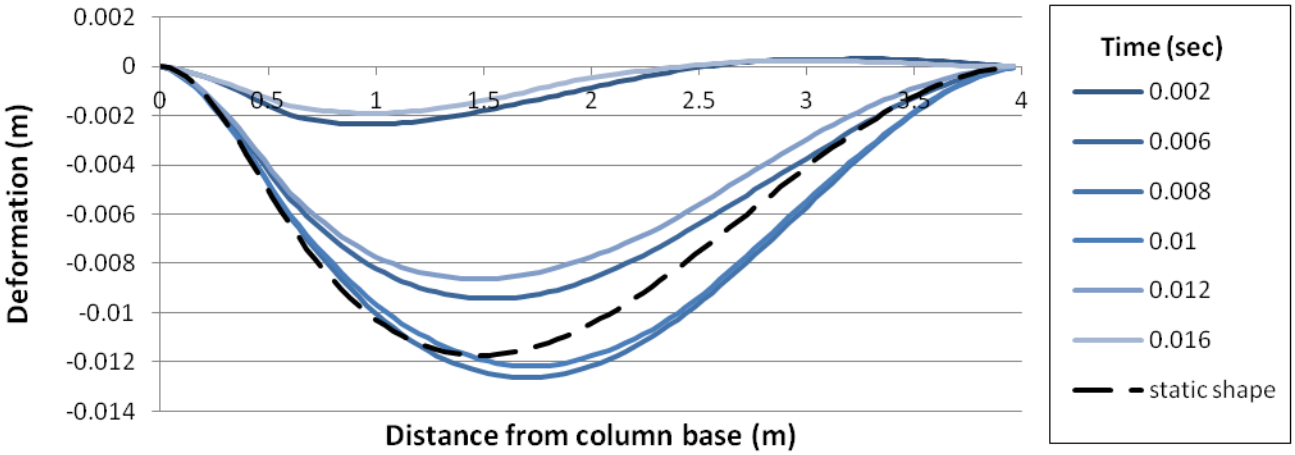

Figure 9.16 Near-base displacement profiles at specified times.

Column shears are presented in Figure 9.17. The presented column positions fall into three categories; below the contact zone (X = 0.02, 0.5 m), within the contact zone (X = 0.7, 1.18 m) and above the contact zone (X = 2.38, 3.98 m). As expected, most shear loading occurs below the contact zone. The maximum averaged shear in this region is 3740 kN (Equation 9.6 predicted 3970 kN). However, the loadings within the contact zone are approximately the same as the loadings above the contact zone. This can be explained by considering the deformation patterns of the column (Figure 9.18). Due to the shape of the column as it deforms, the bottom of the beam actually applies the majority of the loading to the column over the duration of the collision. This results in the elements within the contact zone behaving as if they were above the contact zone.

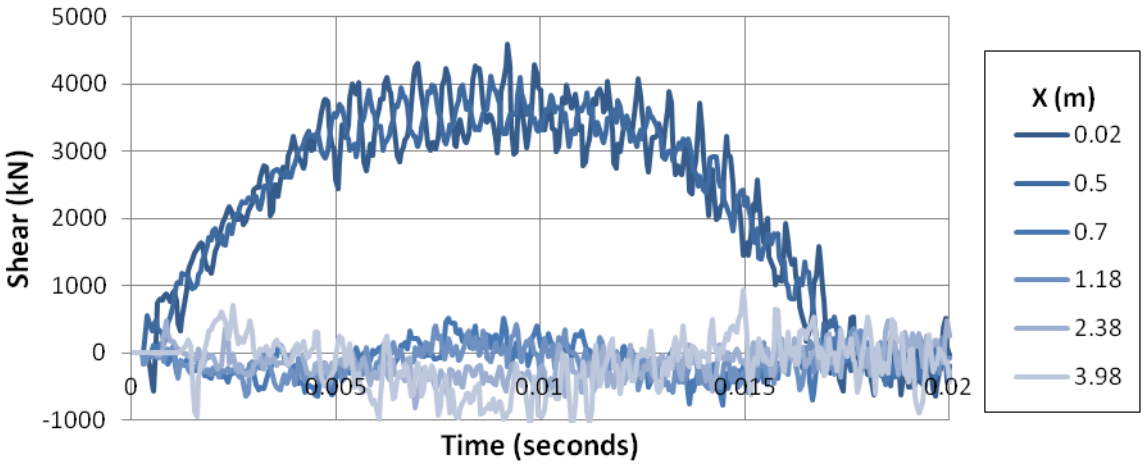

Figure 9.17 Near-base column shear loadings at specific column locations.

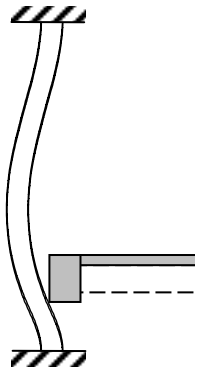

Figure 9.18 Exaggerated column deformation resulting from near-base collision

The deformation shape of the column causes the location of the contact force centroid to change over the course of the collision. This can be explained in terms of the total collision force (Figure 9.19). In the first 0.001 seconds, the process of momentum transfer occurs in the same manner as the mid-span collision. Over this time, the contact force centroid is in the middle of the contact zone (i.e. 0.9 m from the column base). At 0.0009 seconds, the deformations of the column cause the contact force centroid to move. By 0.0011 seconds, the centroid is located at the bottom of the contact zone (0.6 m from the column base), since only the bottommost contact element is still in contact. Near the end of the collision (at 0.0165 seconds) other collision elements do also experience contact, however the duration of these contacts are very small (approximately 0.0002 seconds long).

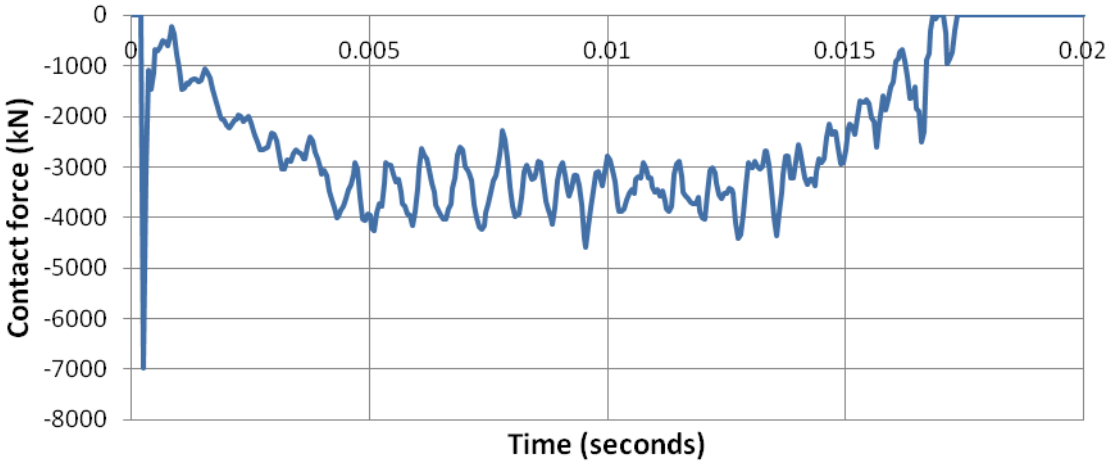

Figure 9.19 Total collision force resulting from near-base collision

The movement of the contact centroid requires reassessment of the values used for a and b in Equation 9.6. The prediction options are presented in Table 9.2. Shear loads are most accurately predicted by the beam mid-height predictions for this particular case. However, confirmation of this result would be necessary for other models with differing beam heights and locations before this was recommended as best practise.

Table 9.2 Predicted floor/column collision properties based upon loading point

	S_{top} kN	S_{bot} kN	k kN/m	P kN	Δ mm
Loading at beam mid-height (a = 0.9 m, b = 3.1 m)	*-440*	*3,970*	*356,700*	*3,410*	*9.56 @ 0.9 m*
Loading at beam base (a = 0.6 m, b = 3.4 m)	*-330*	*5,120*	*912,500*	*5,460*	*5.98 @ 0.6 m*
Recorded values	*-410*	*3,740*	*-*	*-*	*9.26 @ 0.9 m* *6.25 @ 0.6 m*

9.3 Simplified Floor/Column Model Development

Attention is now turned to the minimum modelling conditions required to model a floor/column collision at an acceptable level of accuracy. Specifically, the minimum number of column elements and the most appropriate selection of γ are to be determined. Results from two column configurations (mid-span and near base) are compared to those obtained from the 'accurate' models (Section 9.2.5 and Section 9.2.6).

9.3.1 Model Naming Conventions

Tests in the following sections are named using the following format:

[*value of* γ] [M/S/C] [*number of column elements*]

Where M = mid-span loading, S = 'split' near-base loading and C = 'closest' near-base loading. Definitions of the 'split' and 'closest' models are provided in Section 9.3.3.

9.3.2 Mid-span Floor/Column Collision

The performance of the models for the mid-span collision is measured in terms of the following seven properties. The list is ordered with decreasing importance

1. Column shear
2. Maximum column moment at the supports
3. Maximum column moment at the point of impact
4. The maximum displacement of the diaphragm at collision interface (during the collision)
5. The maximum displacement of the column at collision interface (during the collision)
6. Velocity of the diaphragm after collision
7. Collision duration

Column shear and column maximum moments are most important as these properties determine any failure of the column. Typically, this also affects the entire gravity carrying structural system since complete column failure is likely to cause partial or total building failure. The next most important parameter is diaphragm displacement since this affects the shears in the adjacent building (due to interstorey drift). Diaphragm displacement is partially determined by the column displacement at the point of impact. As seen in previous chapters, the velocity of the diaphragm can be used to calculate floor momentum after collision, while collision duration is still important but has less effect on the overall building response.

All results are presented in this section as percentage variations relative to the accurate model from Section 9.2.5. A model is considered to be suitably accurate if it records variations of less than 10% for all considered parameters. Test model values are shown in Table 9.3. The definition of the number of column elements is further complicated by the modelled beam depth of the colliding diaphragm. Figure 9.20 presents the adopted column layouts for the various models. The column element number refers to the number of elements outside the collision zone. The number of elements within the collision zone is selected to provide the same approximate nodal spacing as used outside the collision zone.

Table 9.3 Test model values for mid-span floor/column collision

γ	*column element number*
10, 1, 0.1	*10 , 4, 2*

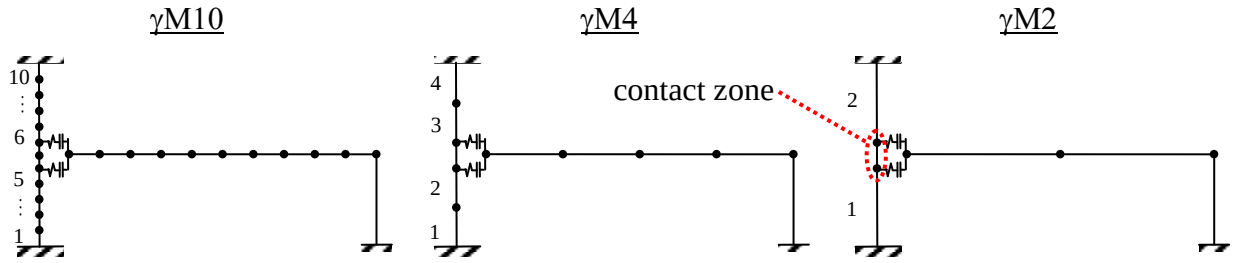

Figure 9.20 Mid-span collision model layouts

Maximum column moment and shear force are presented in Figure 9.21. The shear force is anti-symmetric and the moment is symmetric around the collision point, so only actions below the point of loading are presented. The ten element and four element models show increasing accuracy with decreasing γ. Test of 0.01M10 and 0.01M4 were also performed, however both tests recorded variations in excess of 10% for multiple parameters and are not included in the figure. Reduction in the number of column elements generally decreases shear and moment

accuracy. In particular, all two column element models result in variations greater than 10%, which indicates their unsuitability as representative models.

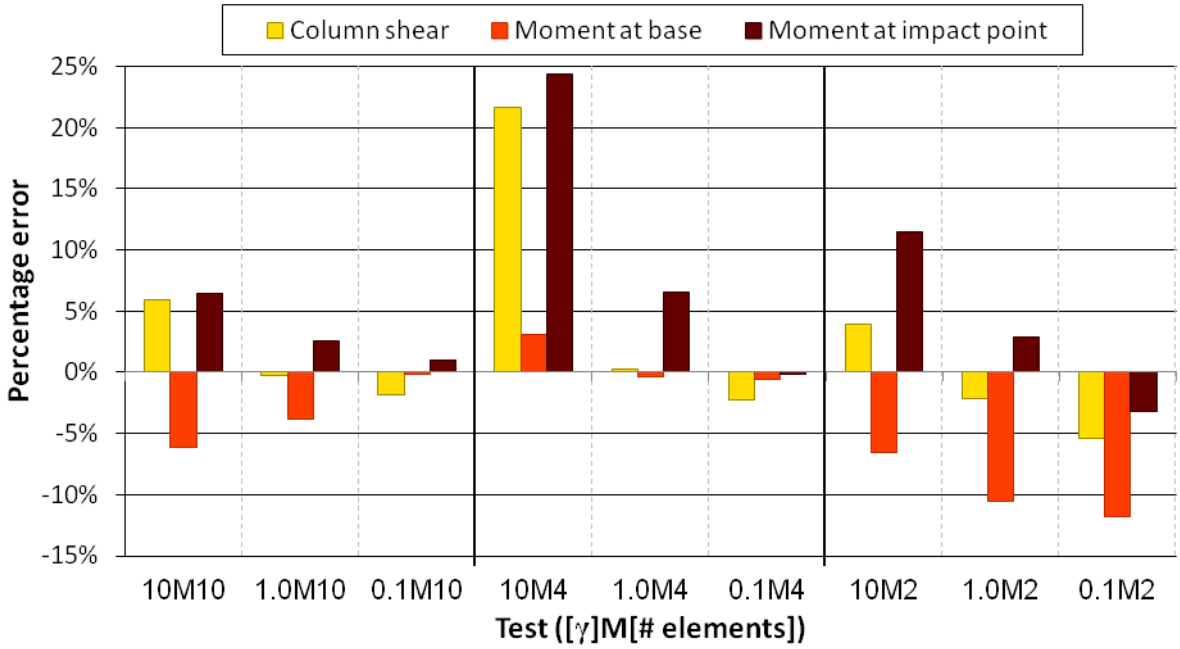

Figure 9.21 Column shear and moment variation for mid-span collision

The maximum collision displacements are presented in Figure 9.22. Generally, the models provide very accurate displacement results, however larger variation appears in models with $\gamma = 0.1$. Displacement variation does not appear to be sensitive to the number of elements except for the $\gamma = 0.1$ case, where decreasing elements results in increasing diaphragm displacement difference. This is because the softer contact requires a greater relative penetration to produce the same level of compressive force.

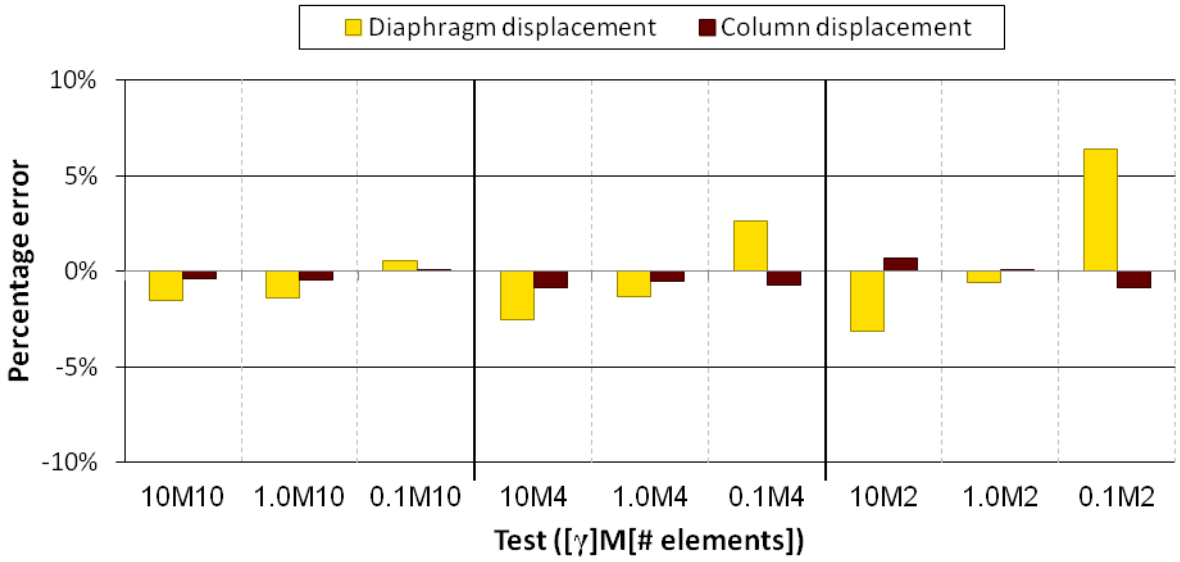

Figure 9.22 Maximum deflections for mid-span collision

Figure 9.23 presents the remaining two properties. Diaphragm post collision velocity is well predicted by all models, however collision duration predictions vary widely between models. The variation in the collision durations is less than 10% for all models except 0.1M2.

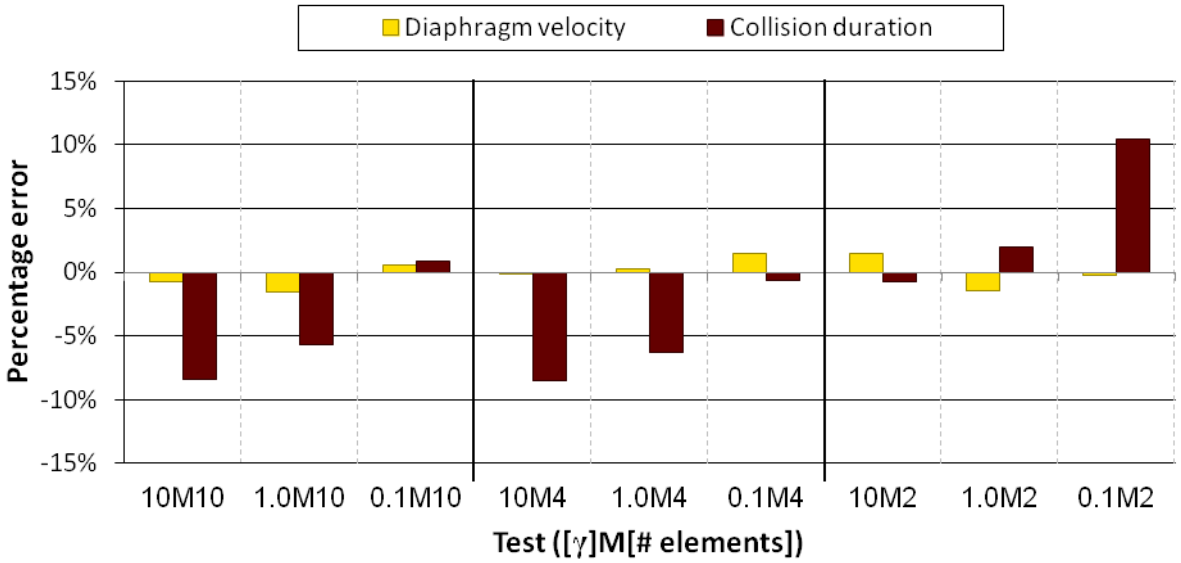

Figure 9.23 Post collision diaphragm velocity and collision duration for mid-span collision

Assessment of the accuracy of the presented models is considered in terms of modelling complexity (i.e. the number of column elements). In the 10 element case, all presented values of γ provide sufficiently accurate results (all parameters are reported with less than 10% variation). Of these tests, 0.1M10 provides the greatest accuracy. When four column elements are used, both 1.0M4 and 0.1M4 models are acceptable, while the two element cases all exceed 10% in at least one parameter. However, final selection of the modelling method first requires consideration of collisions at other locations on the column.

9.3.3 Near-base Floor/Column Collision

The properties determined in the previous section will not necessarily be valid for near-base collisions. The near-base collision is much more likely to excite higher modes in the column due to the asymmetrical loading point, and both shear force and moment profiles change considerably. With this in mind, the near-base case is checked independently of the mid-span case. Obviously a consistent result between the two cases is preferable.

The performance of the models for the near-base collision is measured in the same manner to that of the mid-span model. Moments and shears are no longer the same above and below the point of contact, however the loadings above the point of contact are not critical for the column (i.e. maximum moment and maximum shear occur immediately below the collision point). The

impulse that is sent to the top support is significant since that determines the change in velocity of the top diaphragm. This parameter is considered later in this section.

The location of the point of impact provides new modelling issues not seen in the mid-span case. If the column nodes are evenly distributed across the height of the column, the edges of the collision zone may not necessarily coincide with a node. Two approaches are investigated in this section;

1. "Split" – indicated in testing with 'S'. The middle column node is positioned in the collision zone. The nodes above and below this node are then evenly distributed in the remaining space. If there are an odd number of elements in the column, the extra element may be placed either side of the collision zone.
2. "Closest" – indicated in testing with 'C'. The column node closest to the collision zone is positioned at the point of impact. The nodes above and below this node are then evenly distributed in the remaining space.

The accurate solution with 100 elements already had nodes at 0.6 m and 1.2 m (which corresponds to the locations of the beam edges), so no element redistribution was required. Figure 9.24 demonstrates the two above methods for a generalized point of impact. In this figure, and in the following analyses, an extra node is added to define either the top or the bottom of the contact zone.

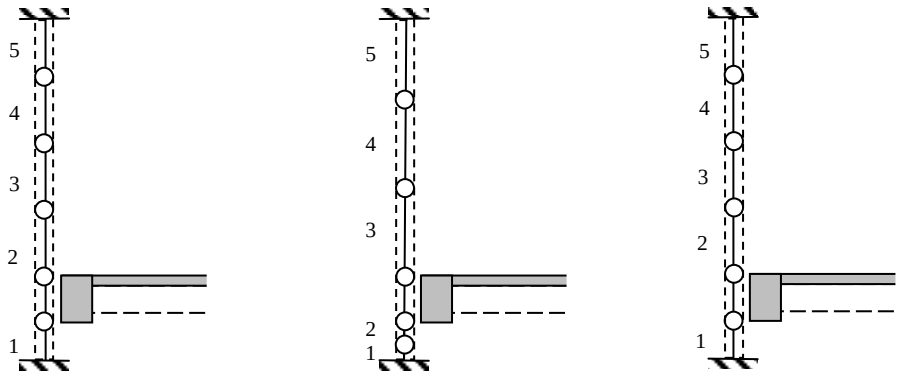

Figure 9.24 Column mass distribution options

Splitting the elements evenly either side of the contact point provides a more accurate mass distribution in the region of high shear, while using the closest node ensures a more even mass distribution over the height of the column.

A total of 12 tests are performed in this section (Table 9.4). The mid-span tests have already shown that the two column element models have insufficient accuracy. These elements are not

tested in the near-base models. Once again, a variation of 10% (from that of the accurate model) is considered to be the threshold of acceptable accuracy.

Table 9.4 Tested near-base models

γ	*mass distribution*	*column element number*
10, 1, 0.1	*Split (S), Closest (C)*	*10 , 4*

Results are presented for the 10 and 4 column element models separately (Figure 9.25 and Figure 9.26). The ten element results are considered first. Post collision velocity and collision duration are not shown in Figure 9.25 but record less than 2% difference for the γ = 10 and 1.0 models. Little change in variation is observed between the Closest and Split modelling methods. Greater sensitivity is observed when changing γ, with γ = 0.1 recording variations exceeding 10% for multiple parameters. However, little difference is observed between the γ = 10 and γ = 1 results.

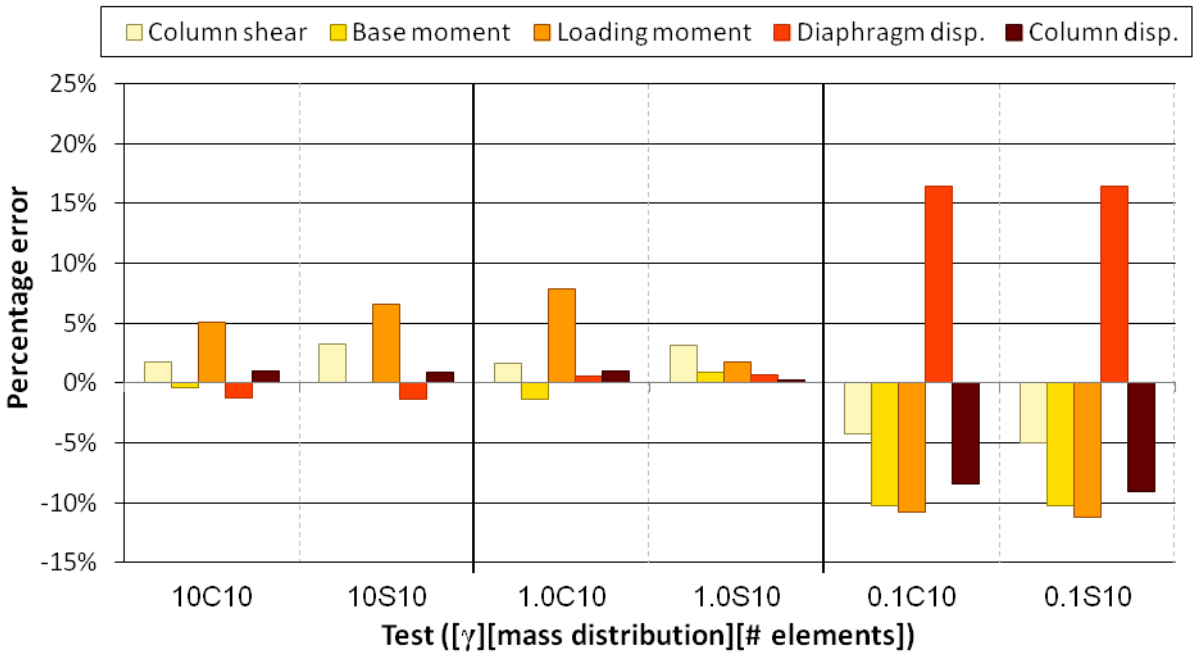

Figure 9.25 Important parameter variations for 10 column element models

The four column element models show more sensitivity in the selection of γ (Figure 9.26). γ = 1.0 provides the most accurate results over the considered parameters. The 'Closest' modelling method is marginally more accurate than the 'Split' method for γ = 1.0, however this difference is negligible. Post collision velocity and collision duration variations remain within 5% for the γ = 10, 1.0 models.

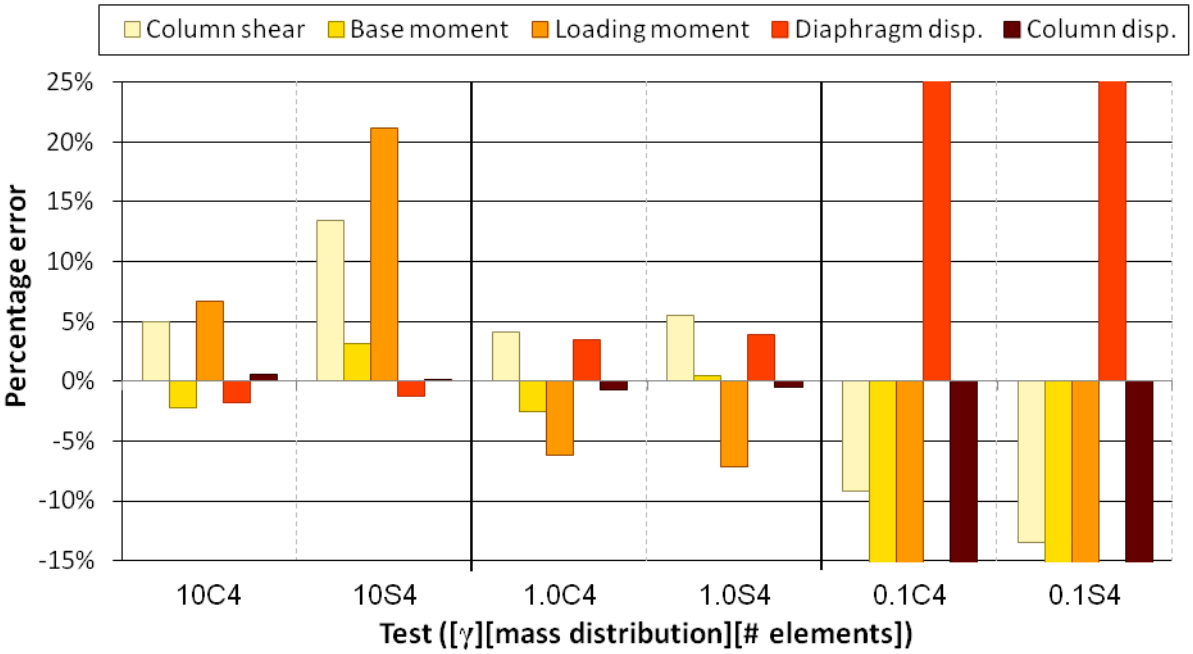

Figure 9.26 Important parameters variations for 4 column element models

As stated at the beginning of this section, shear and moment above the point of contact do not provide meaningful information if only a maximum value is reported. This is because the critical actions occur below this point on the column. Instead, the primary concern regards the momentum transfer (or impulse) to the floor above the point of contact. This may be found by integrating the shear plot of the topmost column element over the duration of the collision. Figure 9.27 presents the shear plots which are to be integrated.

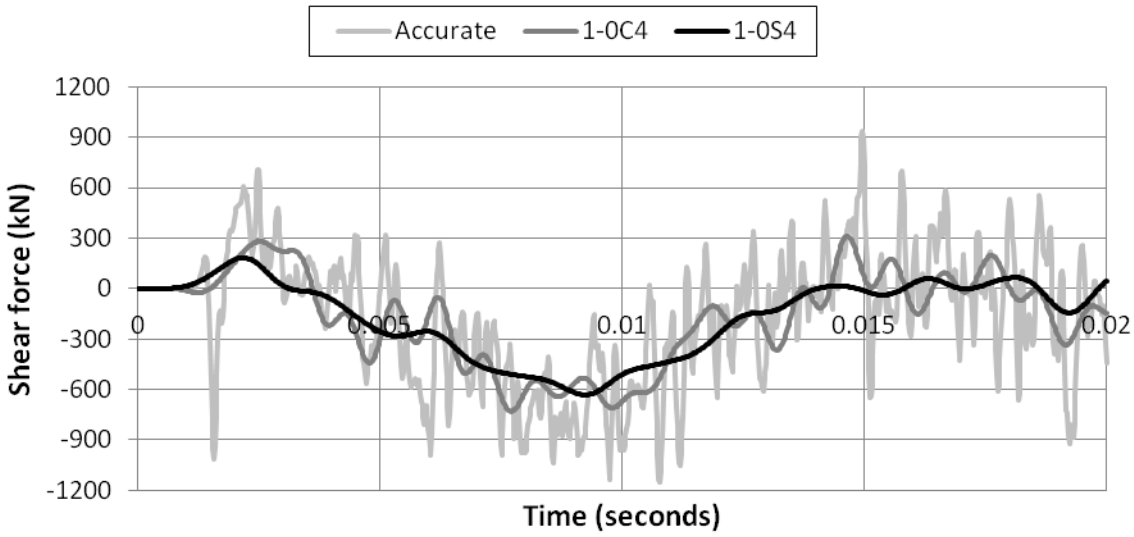

Figure 9.27 Top support shear loading during collision

While the maximum and minimum shear forces are not well captured, the overall response is reasonably similar. The impulses recorded from these records are presented in Table 9.5. These values are suitably accurate for simplified modelling.

Table 9.5 Impulse error from simplified near-base models

Test name	*Impulse (kN·s)* *($m\Delta v = F\Delta t$)*	*% error*
Accurate	*-3.34*	-
1.0C4	*-3.42*	*2.4%*
1.0S4	*-3.34*	*0.1%*

Considering just the near-base models, both 1.0C4 and 1.0S4 provide reasonably accurate results. Either model is suitable for this type of column collision.

9.3.4 Effect of Differing the Number of Diaphragm Elements

The preceding sections constrain the number of diaphragm elements to be equal to the number of column elements. The effects of removing this restriction are investigated below. The model naming format is adjusted to reflect the new parameters under consideration:

[*number of column elements*] [M/C] [*number of diaphragm elements*]

where M = mid-span model and C = near-base 'closest' model. 12 tests were performed for each of the mid-span and near-base models. These tests used 10 and 4 column elements with 10, 4, 2 and 0 diaphragm elements (where 0 elements corresponds to a perfectly rigid diaphragm). Test *2M4* is also included to investigate whether increasing the number of diaphragm elements can reduce the column modelling requirements. The results for the 4 column element tests, and *2M4* are presented below.

Figure 9.28 presents the mid-span collision results. Once again, the test parameters are listed in decreasing importance from left to right. While the sensitivities of individual parameters accuracies are different, the overall accuracy of the mid-span predictions is reasonably insensitive to changes in the number of diaphragm elements. The four column element models remain within the target 10% variation from the accurate model. However, the two column element case does exceed 10% variation and is considered to be unsuitable for modelling.

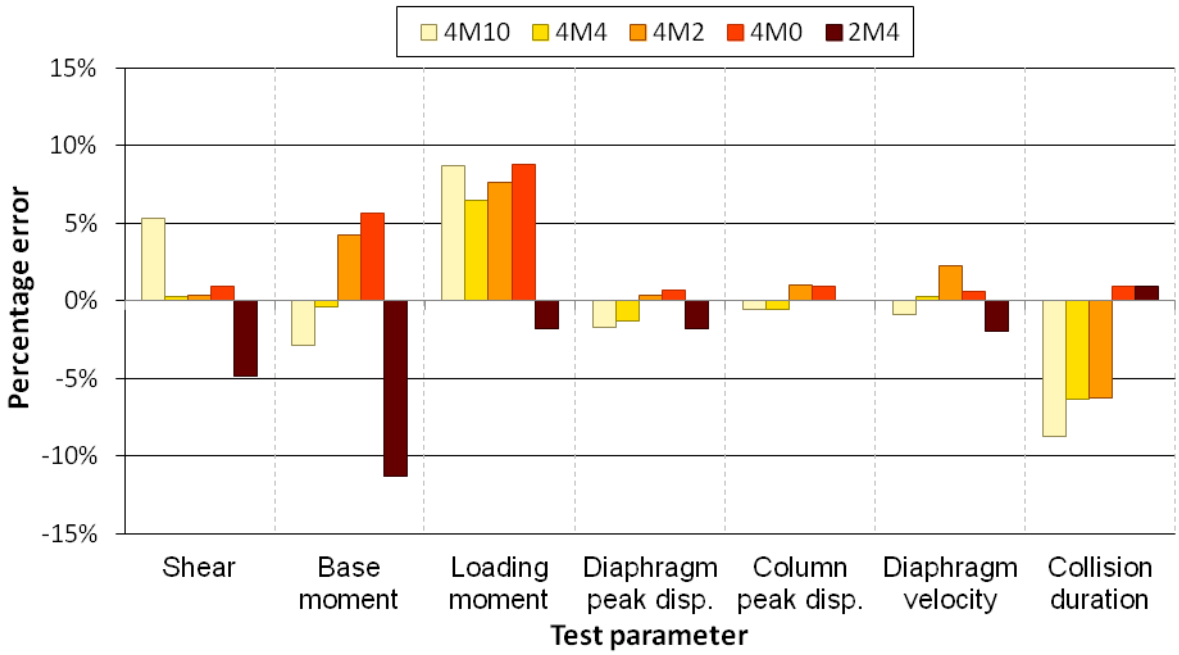

Figure 9.28 Effect of differing diaphragm element number on mid-span collision

The near base collision shows a much higher dependency on the number of diaphragm elements (Figure 9.29). This is especially noticeable in the peak displacement of the diaphragm. The four column element tests' accuracy generally decreases with decreasing element number. The zero element error is approximately twice that of the 2 element error. The two element error is, in turn, approximately twice that of the 4 element error. These errors are directly attributable to the contact element stiffness (since γ is set at 1.0). A softer contact allows a greater relative penetration of the two nodes defining the contact element. The lower stiffness increases the collision duration, and increases the diaphragm's peak displacement during the collision. Model *4C0* reports differences that exceed 10%, while *4C2*'s displacement records 9.6% variation.

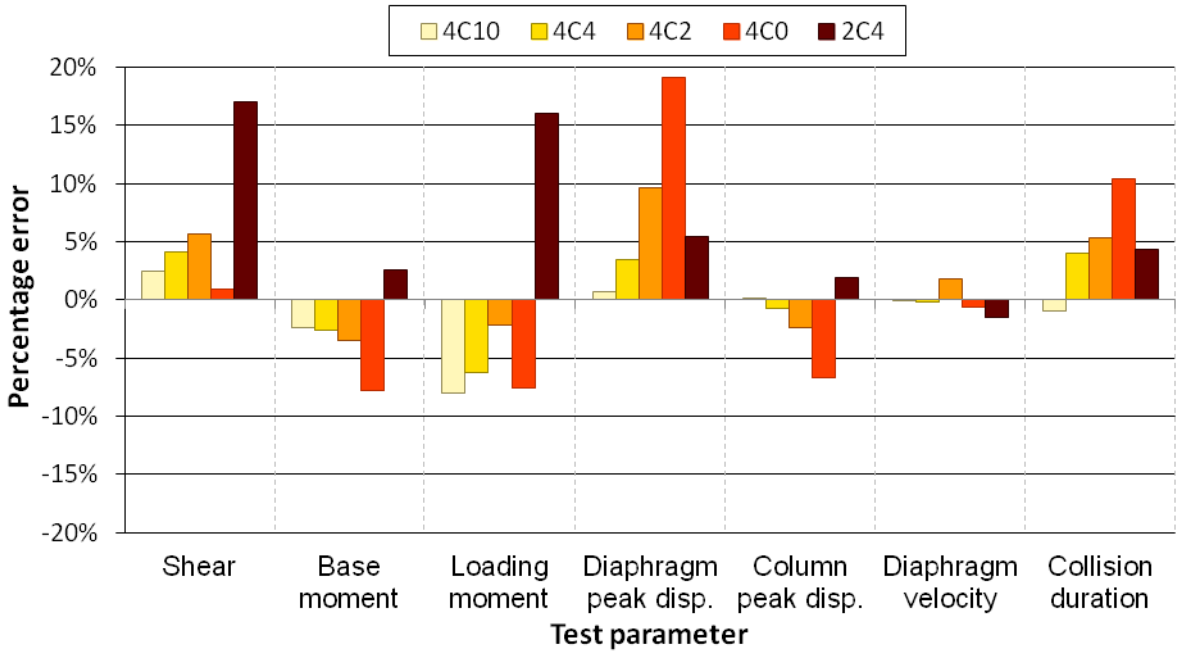

Figure 9.29 Effect of differing diaphragm element number on near-base collision

As with case *2M4*, case *2C4* was also included in the analysis suite. The reported variations for *2C4* exceed acceptable tolerances. Similar levels of variation were also observed for model *2C10*.

Based upon the considerations of this section, floor/column collision is modelled using four column elements and more than two diaphragm elements. This criterion is actually more stringent than that used for floor/floor collision (where two elements per diaphragm is suitable). This can be attributed to two factors:

1. The adopted floor/column model assumes a rigid column base connection. In reality the base of the column is attached to another floor, or a foundation system. In both cases, these elements introduce further flexibility into the system.
2. The floor/floor collision system was optimised for various parameter maxima using multiple time histories for a simplified building model (Section 4.3). However, the floor/column interaction has been optimised using a single collision.

Further testing with more detailed models could be performed to address the above issues. However, these tests are not performed here. This is because the modelling requirements determined in this section can be simply applied into current non-linear time history programs. Further optimisation beyond this point would provide minimal additional benefit. It is also noted that the analyses performed in Chapter 8 use more than two elements per floor. In these models, this is a result of the building geometry rather than any contact modelling requirements.

9.3.5 Effect of Shear Stiffness and Rotational Inertia

The beginning of this chapter (Section 9.2) was primarily concerned with the differences between Timoshenko and Euler-Bernoulli beam predictions. In the simplified analyses (Section 9.3.2 to Section 9.3.4) shear stiffness and rotational inertia were included in all column elements and nodes. These additional modelling requirements attempt to more accurately emulate the Timoshenko beam (Equation 9.1). However, not all software programs model shear stiffness or rotational inertia. The effects of removing these aspects of the model are considered for two models: *4M4*, and *4C4*. The results for *4M4* are presented in Figure 9.30.

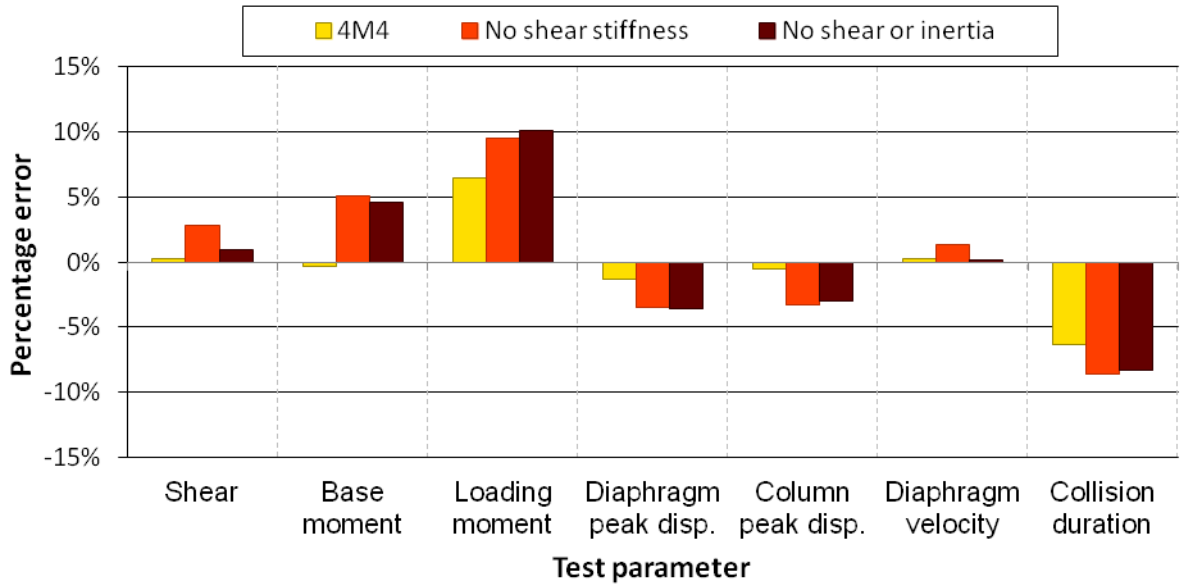

Figure 9.30 Influence of shear stiffness and rotational inertia on mid-span collision results

Removing shear stiffness notably decreases the accuracy of the reported parameters. Variations increase by up to 5 percentage points. The effect of rotational inertia is less marked, and sometime even results in smaller variations (in comparison to the 'no shear stiffness' results). The effect of shear stiffness is even more pronounced for *4C4* (Figure 9.31). Similar trends were also observed for *10C10* when shear stiffness and inertia were removed.

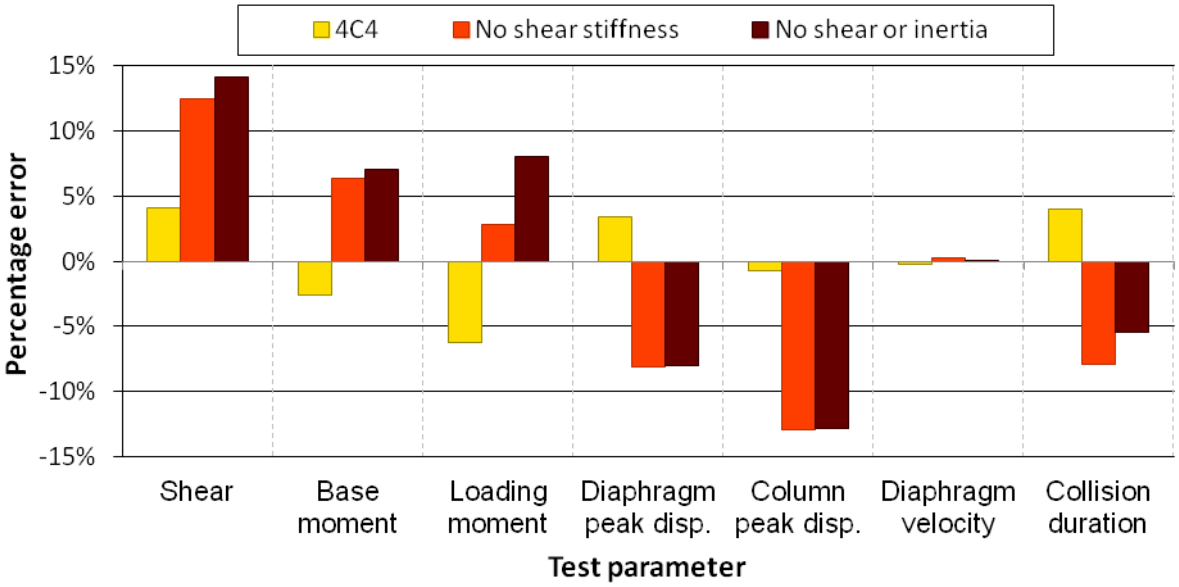

Figure 9.31 Influence of shear stiffness and rotational inertia on near-base collision results

In order to test the time sensitivity of these results, a new model was assessed where a constant force was applied to the diaphragm throughout the collision. In these circumstances the column undergoes a much longer collision. Removing shear stiffness and inertia in these tests did not significantly affect parameter maxima. This indicates that the shear stiffness sensitivity is a result of the short duration of the impact, which agrees with the theory presented in Section 9.2.1.

Based upon the above tests, it is recommended that any floor/column collision modelling is performed with elements that include shear stiffness effects. Rotational inertia is less important but should also be included where possible.

9.3.6 Reassessing the Definition of Collision Element Stiffness

The previous sections in this chapter calculate γ based upon the adjacent diaphragm's element stiffness. This approach assumes that the column stiffness is not important in determining an appropriate collision element stiffness. Furthermore, defining the collision element stiffness in this way is inconsistent with the approach used in floor/floor collisions. This is because the floor/floor collision element stiffness is defined using the diaphragm with the more flexible element stiffness. However, the floor/column collision element stiffness is currently defined using the more rigid elements involved in the collision (i.e. the diaphragm elements). Alternative definitions of the collision element stiffness are considered in this section.

Three alternatives for calculating collision element stiffness are considered here. The first method uses the flexural stiffness of two column elements in place of the diaphragm's axial stiffness (Figure 9.32). This approach is the column equivalent to the method proposed by Watanabe and Kawashima (2004) for floor/floor collisions (refer Section 2.2.4). Note that this alternative method uses Γ rather than γ to define the ratio between the frame element stiffness and the collision element stiffness. This is done to distinguish between the two methods.

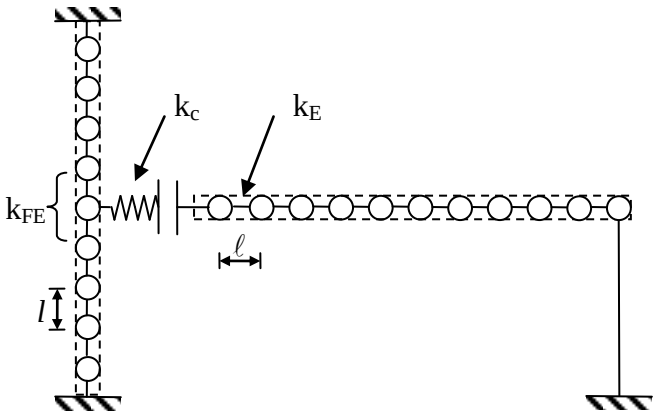

10 element model layout

Typical k_c calculation;

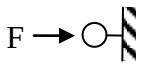

$$F = k_E \Delta = \frac{EA}{\ell} \Delta$$

$$k_c = \gamma k_E = \gamma \frac{EA}{\ell}$$

Alternate k_c calculation;

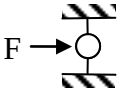

$$F = k_{FE} \Delta = \frac{24EI}{l^3} \Delta$$

$$k_c = \Gamma k_{FE} = \Gamma \frac{24EI}{l^3}$$

Figure 9.32 Element stiffness evaluation for determining k_c

Determining the flexural stiffness of an individual element is dependent on the rotation and translation of both ends of the element. In order to simplify the calculation, the stiffness is obtained assuming the following; a mid-span point load is applied on a beam two elements long with fixed ends (the beam is assumed to be infinitesimally thin).

The suitability of this method can be assessed without performing any further tests. This is done by calculating the equivalent value of γ supposing that $\Gamma = 1$ was used to set the collision element stiffness (i.e. $k_c = k_{FE}$):

$$\gamma = \frac{k_c}{k_E} = \frac{k_{FE}}{k_E} = \frac{24EI}{l^3} \times \frac{\ell}{EA} \tag{9.8}$$

This equation is then used to plot the equivalent γ values for the tests performed in Section 9.2.3 (Table 9.6).

Table 9.6 Equivalent value of γ if collision element stiffness was set using $\Gamma = 1$

column element number	*equivalent γ*
100 (accurate)	*208*
10	*2.08*
4	*0.15*
2	*0.083*

These equivalent values of γ are already known to perform poorly from these existing tests. For example the one hundred element case performs poorly for $\gamma = 10$ because of high oscillation in the contact force. A higher stiffness, such as $\gamma = 208$, amplifies this effect. Furthermore, the four element case showed highly undesirable properties for $\gamma = 0.1$, so the suggested value of $\gamma = 0.15$ is also unsuitable. Thus, for the general case, equating the collision stiffness to the column elements' flexural stiffness does not increase model accuracy.

The second alternative method uses the static stiffness of the entire column (Equation 9.4) to define the collision element stiffness (Figure 9.33). However, this approach can also be dismissed without further modelling. This is because the proposed method does not consider the number of elements within the diaphragm, which means k_c should be constant regardless of the diaphragm element count. This suggests that if the 100 element model is optimised at $\gamma = 1$ (as is the case for the near-base model), then the 10 element model should be optimised at $\gamma = 10$, and the four element model should be optimised at $\gamma = 25$. Inspection of the results of the near-base model (Section 9.3.3) shows these predictions to be incorrect.

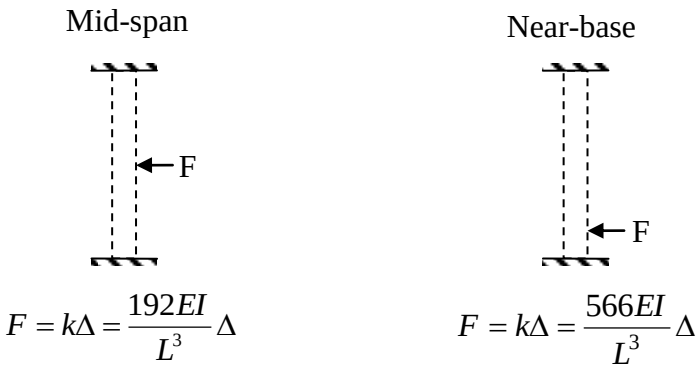

Figure 9.33 Column stiffness to loadings applied in modelled tests

The column stiffness is more likely to become important for defining the collision element stiffness when the magnitude of the column stiffness is similar to that of the collision element. This is because of the requirement for no material overlap during collision. As the collision gets closer to the base (or top) of the column, the column's stiffness greatly increases. The stiffnesses of the models considered thus far are presented in Table 9.7. With the exception of the 2 element model, which has already been ruled out, the collision element stiffness is significantly greater than the column stiffness. When the column stiffness's magnitude is similar to that of the collision element stiffness, the definition of the collision element stiffness may require reassessment. This is considered in Section 9.3.7.

Table 9.7 Comparative stiffnesses of collision elements and impacted column

	Column stiffness (kN/m)	***10 element k_c (kN/m)***	***4 element k_c (kN/m)***	***2 element k_c (kN/m)***
Mid-span	*121,000*	*39,300,000*	*15,700,000*	*7,860,000*
Near-base	*357,000*	*39,300,000*	*15,700,000*	*7,860,000*

The final alternate method implicitly models the collision response of the column within the contact element itself. This is done by using two contact elements that are directly connected to the floor above and below the contact point, respectively (Figure 9.34). If the floors are assumed to not have any rotational flexibility, the overall stiffness of this collision is known (Equation 9.4) and the proportions of load transferred to the floor above and the floor below are also known (Equation 9.5 and Equation 9.6). These relationships are shown in Figure 9.34 and can be used to provide the following collision element stiffnesses:

$$k_{c,top} = \frac{3EIL}{ab^3}\left(1+2\frac{b}{L}\right) \qquad (9.9)$$

$$k_{c,bot} = \frac{3EIL}{a^3 b}\left(1 + 2\frac{a}{L}\right) \tag{9.10}$$

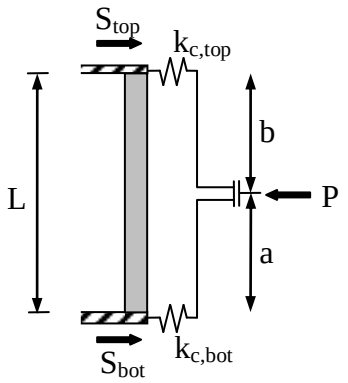

$$\frac{k_{c,top}}{k} = \frac{S_{top}}{P} = \left(\frac{a}{L}\right)^2\left(1 + 2\frac{b}{L}\right)$$

$$\frac{k_{c,bot}}{k} = \frac{S_{bot}}{P} = \left(\frac{b}{L}\right)^2\left(1 + 2\frac{a}{L}\right)$$

$$k_{c,top} + k_{c,bot} = k = \frac{3EIL^3}{a^3 b^3}$$

Figure 9.34 Definitions of contact elements without explicit column collision modelling. Left: contact element configuration. Right: known relationships used to calculate $k_{c,\,top}$ and $k_{c,\,bot}$.

This method models the impacted column in the standard manner (i.e. a single flexural element without any collision modelling). However, this approach also means that the effects of collision on the column are not reproduced. Since the impacted column is generally the element of most interest, this method has little practical use for the pounding analyses considered here.

The alternative contact stiffness assignment methods presented in this section are not as suitable as the previously presented method. However, evaluating the column stiffness is useful for indicating whether the collision will act as primarily a floor/column or a floor/floor collision. The transition between floor/column and floor/floor collision is considered further in the next section.

9.3.7 Transitioning Between Floor/Column and Floor/Floor Collisions

While floor/column and floor/floor collisions involve two different processes, it is useful to consider how collisions change from one behaviour to another. This is particularly significant for evaluation of the contact element stiffness in each situation. Consider an expanded model which includes the flexibility of the floors above and below the column of interest (Figure 9.35). As the vertical offset between floors reduces, the stiffness of the column (k_{col}) increases (see Equation 9.4). When the column stiffness becomes equal to the below floor's diaphragm element stiffness, both buildings' floors will experience deformations due to contact and will essentially respond as per a floor/floor collision. In this circumstance load is still transferred through the column in shear, however the primary collision mechanism is momentum transfer between the two floors. A similar process will also occur for a collision between a particularly stiff column and a particularly flexible diaphragm.

This transition can be predicted by approximating the column element stiffness assuming the column has completely built in supports (refer Figure 9.10). This approach will overestimate the column stiffness; however, collision floor deformation is also likely to become significant before $k_{col} = k_c$. These two effects at least partially counteract each other, so $k_{col} = k_c$ is selected as a representative boundary between primarily column deformation and primarily floor deformation.

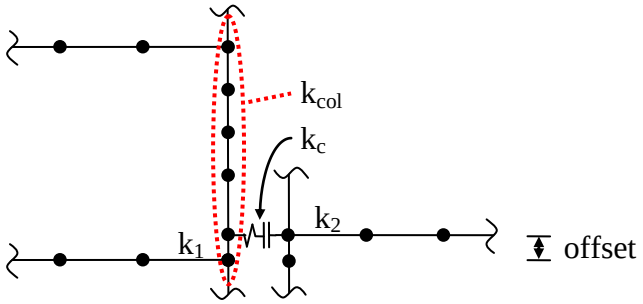

Figure 9.35 Elements in floor/column collision when the floors are slightly offset. k_1 and k_2 each represent the axial stiffness of one diaphragm element. k_{col} = the overall stiffness of the column and k_c = collision element stiffness. In this figure, beams and diaphragms are assumed to be infinitesimally shallow

When deformation occurs primarily in the colliding floors, k_c should be calculated considering the properties of each floor. This is because the collision is essentially floor/floor. The process for defining floor/column collision element stiffness can be modified to:

$$k_c = \begin{cases} k_2 & \text{for } k_{col} < \min[k_1, k_2], \\ \min[k_1, k_2] & \text{for } k_{col} \geq \min[k_1, k_2] \end{cases} \qquad (9.11)$$

However, unlike floor/floor collisions, k_1 and k_2 are not calculated using Equation 2.20. This is because floor/column collisions only compress the impacted floor over the width of the column, (Figure 9.36). Similarly, the floor below an impacted column receives load from the impacted column. This reduced zone of contact affects the stiffness of the diaphragms during collision. In comparison, floor/floor collisions cause an approximately uniform floor compression over the entire length of the buildings' width. The transition between these two states occurs abruptly when the height of the impacted floor's perimeter beam's soffit is the equal to or less than the height of the floor below the impacted column (see Figure 9.38).

Figure 9.36 Plan view at impacted floor height of areas in contact during floor/floor and floor/column collisions

One method of calculating the floor/column collision element stiffness is to calculate an effective width, w_{eff}, of the slab which directly undergoes compression during collision. As shown in Figure 9.37, the compression zone is assumed to expand at 45 degrees over the length of the first diaphragm element. If a compression zone overlaps with another compression zone for an adjacent column, each zone is considered to have reached its maximum width in that direction. The compression zone can also be restrained by a building boundary (as shown for the top column in Figure 9.37). The effective width is calculated as the centroidal distance from the column centreline to the extent of the compression zone in each direction.

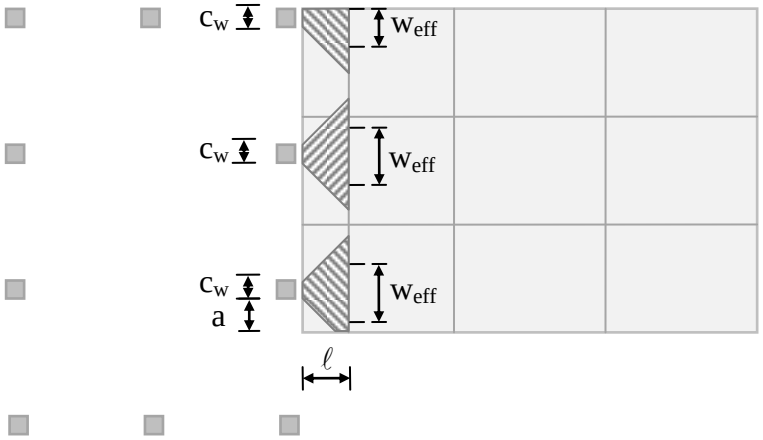

$$w_{eff} = c_w + \frac{\ell}{2}$$

$$w_{eff} = c_w + \ell$$

$$w_{eff} = c_w + \frac{\ell}{2} + \frac{\frac{a}{2} \times \frac{1}{2} a^2 + a \times \left(a\left(\ell - a\right)\right)}{\frac{1}{2} a^2 + a \times \left(a\left(\ell - a\right)\right)}$$

$$k = \frac{E t w_{eff}}{\ell}$$

Figure 9.37 Plan view at impacted floor height of effective slab widths activated in floor/column collision

Beams oriented in the direction of the compression may also be compressed during collision. Here beam axial stiffness is included in the contact element stiffness if the beam is within 1.5 column widths (c_w) of the column centreline. This boundary has been relatively arbitrarily defined, and could be refined with further investigation.

The above method may appear to be a departure from the $\gamma = 1$ philosophy tested earlier in the chapter. However, the method actually more accurately predicts the adjacent element stiffness that is experienced in a collision within the model. This means that setting the collision stiffness (k_c) to the stiffness defined in Figure 9.37 is directly compatible with the approach used in previous testing.

In total, three distinct phases can occur as the vertical offset between two floors reduces. This is summarised in Table 9.8 and Figure 9.38. Type a or type b collisions may not occur depending on the relative stiffnesses of the column and the surrounding diaphragms. However, type c collisions always occur when the vertical offset reduces sufficiently.

Table 9.8 Characteristics of floor/column and floor/floor collisions

Type	Primary deformation mode	Calculation of k_c	Floor tributary width	Method of identification
a	*column deformation*	$k_c = k_2$	w_{eff} *(Figure 9.37)*	$k_{col} < min[k_1, k_2]$, *offset > rigid end block*
b	*floor deformation extending from impacted columns*	$k_c = min[k_1, k_2]$	w_{eff} *(Figure 9.37)*	$k_{col} \geq min[k_1, k_2]$, *offset > rigid end block*
c	*floor deformation over building length*	$k_c = min[k_1, k_2]$	w_i *(Figure 7.15)*	*offset ≤ rigid end block*

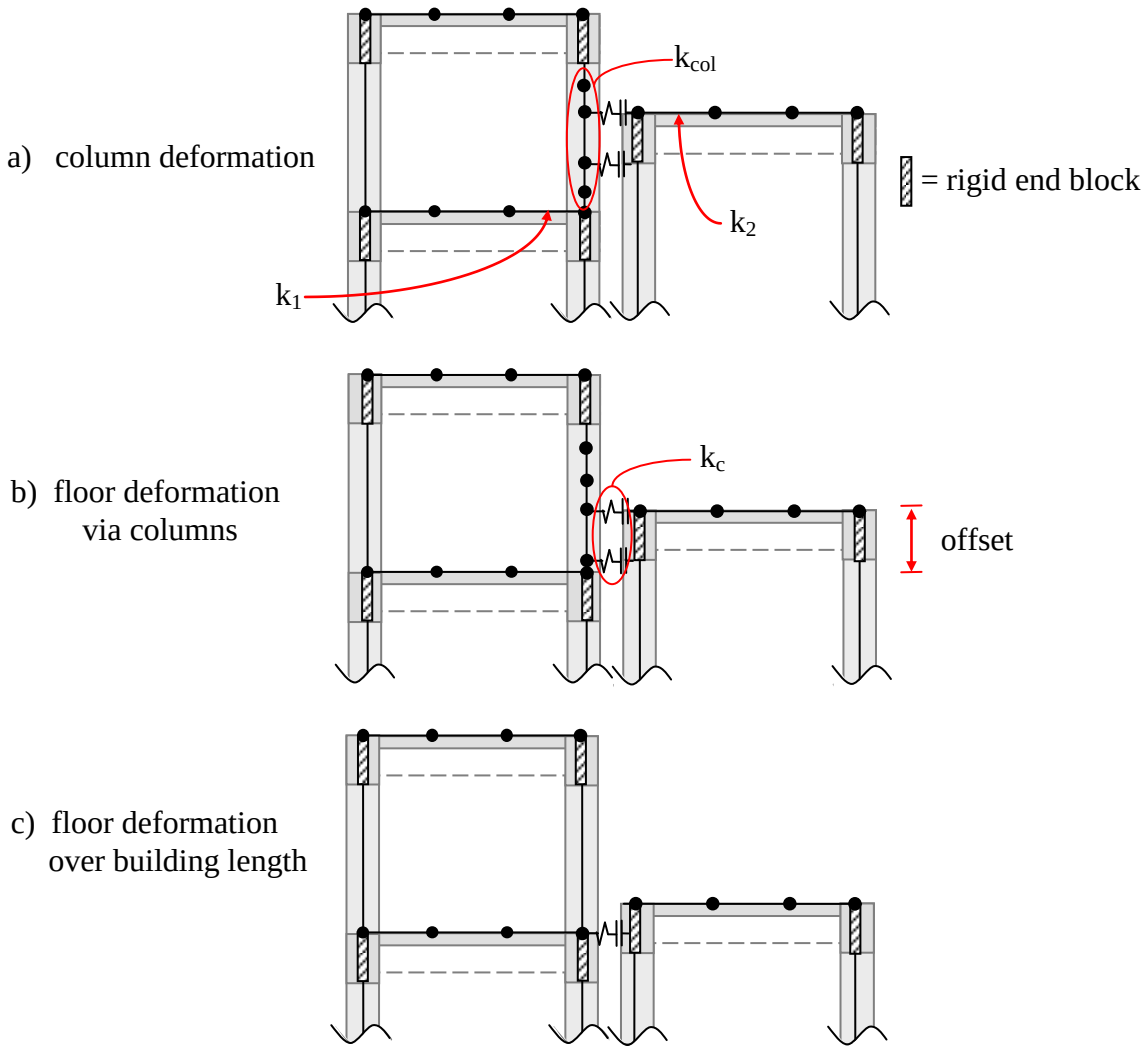

Figure 9.38 Transition between floor/column and floor/floor collision. In this figure, the model layout is overlain over the physical layout it represents.

9.3.8 Modelling Column Plasticity

Floor/column collisions increase the number of possible locations of plastic hinges in a column. Figure 9.39 illustrates the plastic hinge locations for an example building. The plastic hinge length determines the relationship between an element's rotation and curvature at a given end. In

all presented modelling, the plastic hinge length has been set at half the column depth (measured in the direction of collision loading). When floor/column collisions are considered, the heights of the colliding floors can cause insufficient space for two plastic hinges to develop in the available space. In this circumstance the column hinges associated with building sway are modelled preferentially. This is because any collision in such a configuration is much more likely to cause shear failure than flexural failure. Note that modelling of the second floor/column collision (involving the left hand building's lower floor and the right hand building's column) is not shown here for clarity.

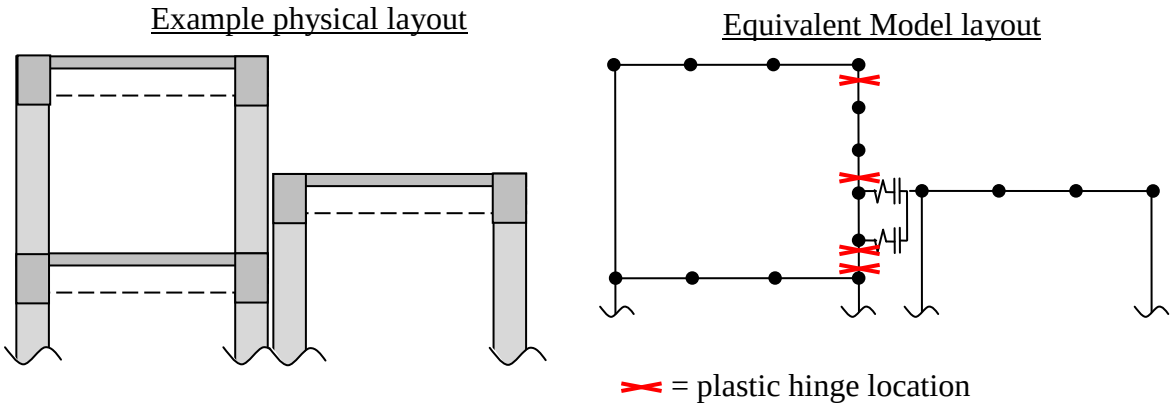

Figure 9.39 Plastic hinge locations for floor/column modelling

Columns vulnerable to floor/column collision are modelled using the hysteresis described in Section 5.3.6. This is done to remain consistent with the other columns in the model. More detailed hysteresis models could be introduced; however this would require parameter calibration and would contribute little to the collision interaction. This is because column shear is the primary parameter of interest in the following sections.

9.3.9 Floor Plasticity in Floor/Column Collisions

Floor/column collisions also cause damage to the impacted floor. This damage is more localised than in floor/floor collisions due to the localised floor impact zones. This aspect of floor/column collision is not considered further in this thesis. This is because the floor damage is unlikely to materially contribute to the column failure mechanism.

9.3.10 Conclusions

Based on the results of the tests in Section 9.3, the following conclusions are drawn:

1. A generic column collision model must be appropriate for a collision occurring at any point over the height of the column.
2. The behaviour of a collision may vary drastically depending on the collision's location.

3. Collision stiffness equal to the adjacent floor axial element stiffness provides the most accurate results in the simplified models (i.e. $\gamma = 1$).
4. The two proposed column mass distribution methods produce similar results, however the 'closest' method is selected for all subsequent analysis.
5. The number of axial elements in the floor does affect the accuracy of model results. At least four column elements and more than two diaphragm elements are required for acceptably accurate results.
6. Removing shear stiffness significantly affects key parameters. Shear stiffness should be included in columns that are subjected to pounding. Rotational inertia terms also increase model accuracy; however, their omission does not critically affect overall results.

9.4 Performance of Column Collision Models in 3D

Detailed 3D modelling of floor/column collisions is performed in this section. 2D analysis has not been performed since the performance of the impacted columns is the primary focus of these analyses. Suppose that one column was to be used as a 'representative' impacted column, all other impacted columns would need to have identical properties (such as column stiffness and column flexural capacity), with identical tributary widths in the opposing floor. This situation will occur in only the most idealised situations, and is not representative of the model considered here (refer Figure 9.42).

Since each column is required to be modelled separately, the detail needed to create a fully 3D model is readily available, so the more advanced analysis is adopted. However, 2D modelling may be useful when developing simplified modelling predictions for floor/column collisions (for example, extending on the ideas presented in Section 9.2.4). Simplified floor/column models are not developed further in this thesis, but may be of interest to other researchers.

Two building configurations with floor/column pounding are investigated here to show an example application of the modelling methods recommended earlier in this chapter.

9.4.1 Building Configurations

The tested building configurations were created by modifying *3DModel*. Additional column elements were added to every column that may suffer impact, in accordance with the recommendations of Section 9.3 (Figure 8.6). Floor/column pounding configurations were created by raising the height of all floors of Building 2. Building 2 was raised 1.81 m to create the *mid-span* model, and 1.2 m to create the *near-floor* model. As was briefly described in Section 10.2.2, some floor separation is maintained in the *near-floor* model to prevent the

formation of any localised strut action within the impacted column (Figure 9.40). This is because the potential load path shown in Figure 9.40 cannot be modelled with the adopted flexural element. If this configuration was to be modelled, it is expected that a fine mesh of finite elements would be necessary. This is beyond the scope of the modelling presented here.

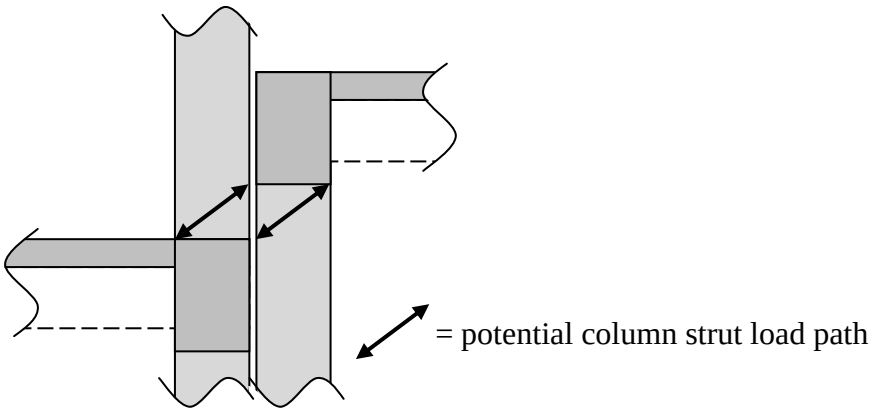

Figure 9.40 Possible load transfer mechanism when floors are slightly offset

The locations of floor/column collisions are shown in Figure 9.41. The reported percentages in this figure indicate the percentage of the overall clear span of each column segment. Note that the mid-span model does not cause collision at exactly mid-span in each column due to uneven building floor spacing. Instead, the change in building height was optimised to get the closest fit to mid-span collision. The full 3D layout of the *mid-span* model is also shown in Figure 9.42.

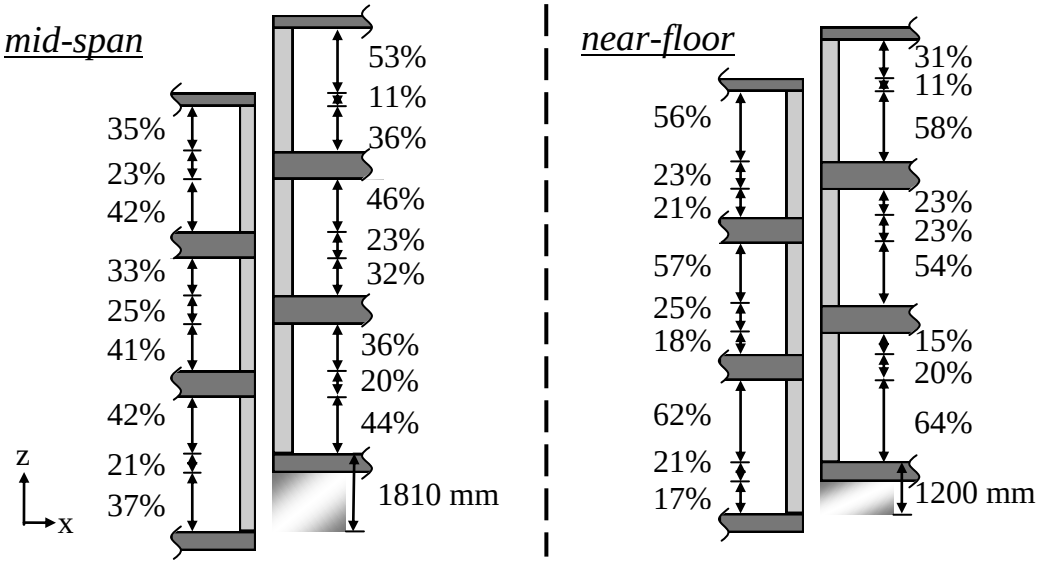

Figure 9.41 Elevation of floor/column collision locations. Percentages indicate the proportion of clear column span of each section. Dark grey shading indicates beam depth at each floor.

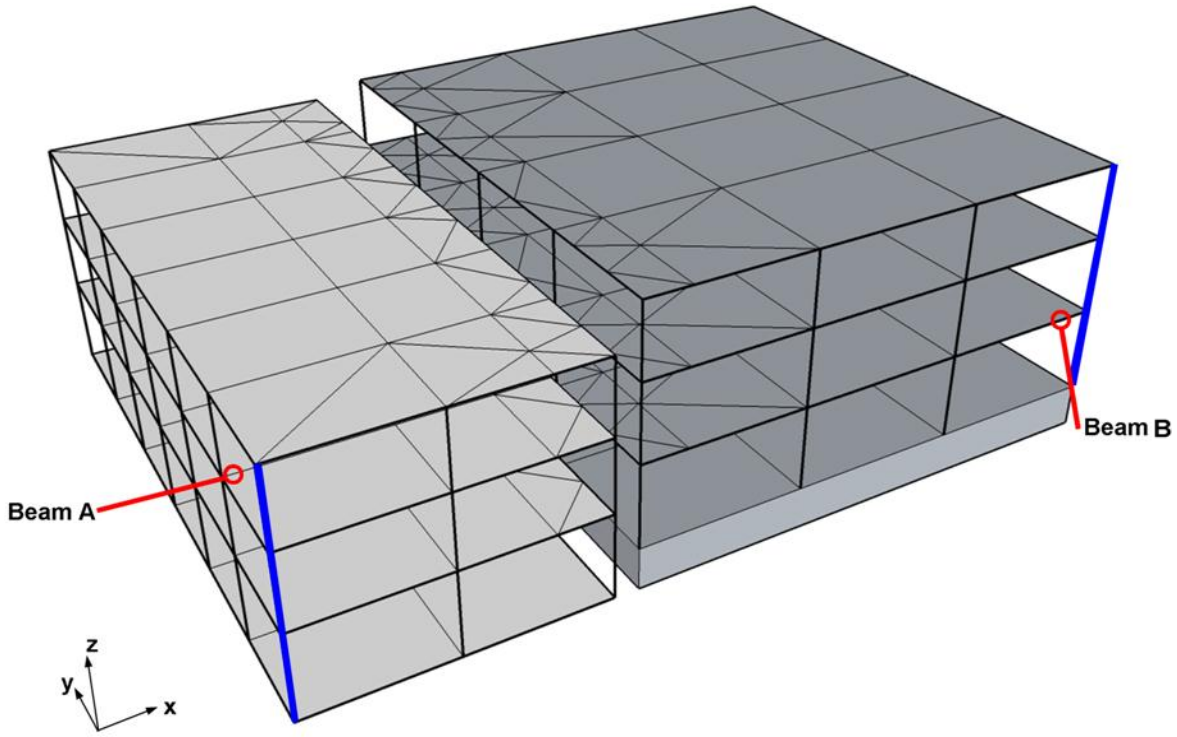

Figure 9.42 Mid-span floor/column model configuration. Thick lines indicate points where floor displacements were recorded. Circled members indicate locations of ductility recordings.

Apart from the modifications stated above, Building 1 and Building 2 are unchanged from the 3D floor/floor modelling. This means that the no contact (NC) response of the buildings is the same as previously reported in Section 8.4.1. However as the position of Building 2 has changed, the separations required to prevent pounding have also changed (Table 9.9). The reported values represent the required distances to prevent collision between the roof level of Building 1 and Building 2's columns at that height. The results of these two models are considered separately in the following two sections.

Table 9.9 Separations required to prevent pounding in analysed records (mm)

	mid-span		*near-floor*	
	'+' orientation	*'-' orientation*	*'+' orientation*	*'-' orientation*
El Centro (EL)	*37.1*	*56.1*	*38.9*	*58.0*
Tabas (TA)	*38.8*	*43.5*	*41.7*	*45.5*
La Union (UN)	*33.8*	*51.5*	*35.1*	*52.9*

9.5 Floor/Column Models – Mid-span Collision

In floor/column collisions, the most likely cause of structural collapse is through failure of the impacted columns. Since column performance is so crucial, the demands on impacted columns are considered first in this section. Global effects from floor/column pounding are investigated later.

9.5.1 Mid-span Collision Influence on Local Damage

In order to be able to accurately identify impacted columns, each column is labelled according to its floor level and frame. This is illustrated in Figure 9.43 and Figure 9.44. Figure 9.43 labels columns according to the floor immediately above their location.

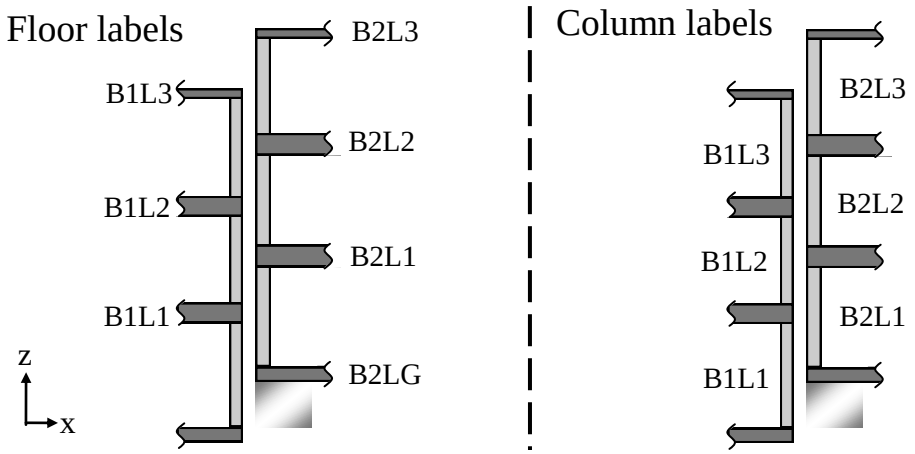

Figure 9.43 Elevation of column labelling according to floor number

In Figure 9.44 Building 2's impacted columns are obscured by Building 2's floor, and are indicated instead by the beams that connect with these columns at the edge nearest to Building 1. In both buildings, the properties (such as stiffness, shear strength and flexural strength) of the corner columns (columns 1A, 1G, 2A and 2E) differ from the internal column along the impacted edge. To clearly present the column actions, only the results of select columns are presented. The following columns are used (ordered with increasing Y ordinate): 1A, 2A, 1B, 2B, 2D, 1F, 2E. The remaining columns' actions are expected to be intermediate values of these results. For example, column 1E is not included since its column properties are the same as column 1F, and its actions will be within the results of columns 1B and 1F.

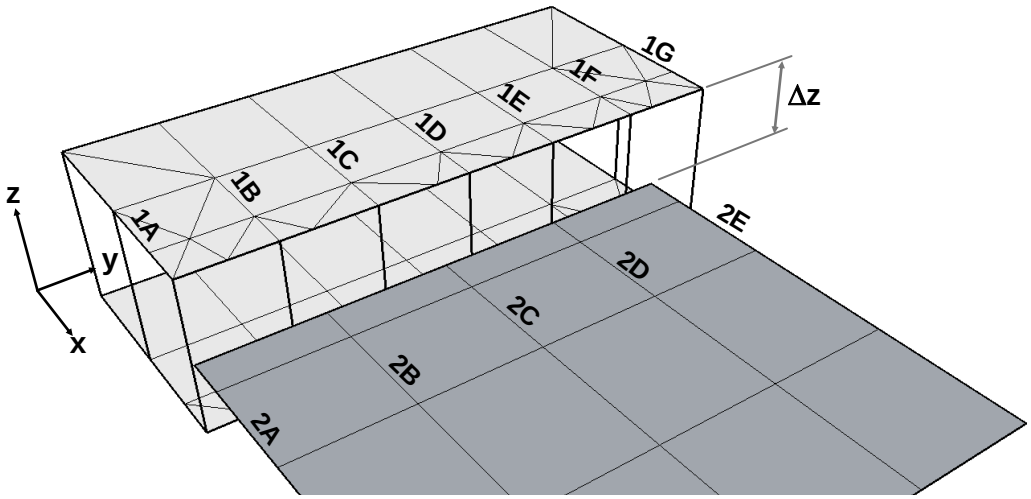

Figure 9.44 Column layout over impacted area. Only Level 2 and Level 3 of Building 1, and Level 2 of Building 2, are shown.

Figure 9.45 presents the amplification of maximum column shear. This value has been normalised by the maximum shear in the NC results for each ground motion. The columns are ordered in decreasing height. Each column level has either three or four data points for each ground motion, corresponding to the number of recorded frame locations in the considered building (for example, B2L3 has four data points: 2A, 2B, 2D, 2E).

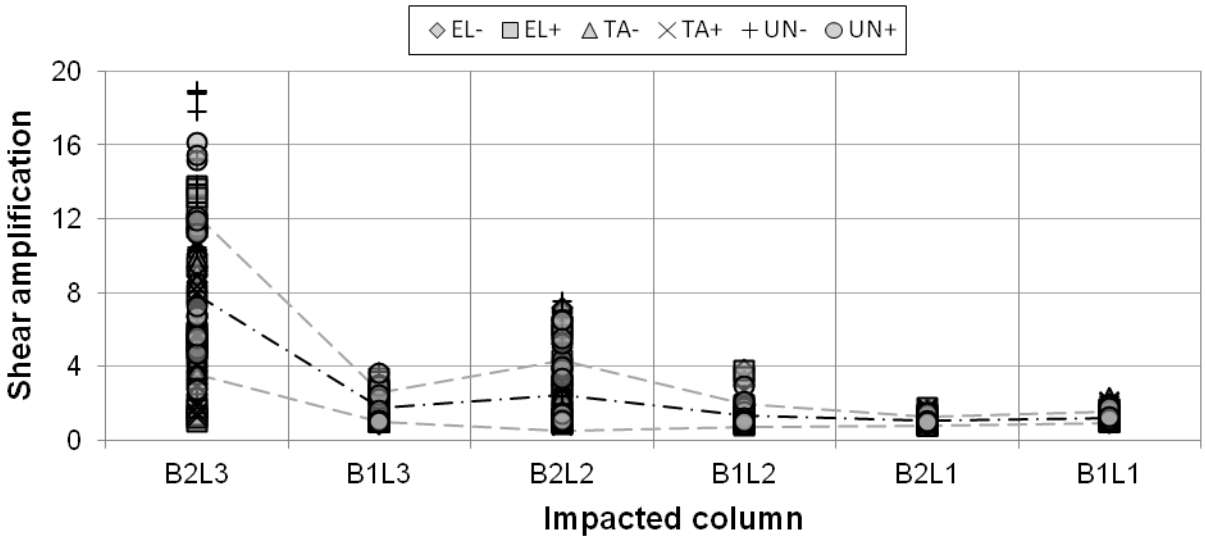

Figure 9.45 Shear amplification in mid-span collision. Columns ordered in decreasing height

The most severe shear increase occurs in the columns at B2L3. This effect is a combination of B2L3 being the highest location of impact, in addition to being the location of lowest shear force in the NC results. The shear amplifications generally reduce with decreasing height. B1L3 was less sensitive than B2L2 to column pounding because the columns at B2L2 are significantly stiffer than those at B1L3. This indicates two key parameters that influence impacted column demands; column stiffness and column height.

The shear amplification results may be also categorised according to frame location (Figure 9.46). In this figure, three data points exist for each ground motion. These correspond to Level 3, Level 2 and Level 1. The mean and standard deviation are also included to show the relative sensitivity of each frame. The data is ordered with increasing Y ordinate. This corresponds to viewing the columns in the YZ plane in Figure 9.44. If all columns had the same stiffness, the maximum shear amplifications would be expected at the corners of Building 2. This is because any torsion in either building would compress the corner columns more than the edge columns. However, in Building 1 the corner columns are stiffer than the other columns, and in Building 2 the corner columns are more flexible. This has led to the internal columns of Building 2 being the most adversely affected by floor/column collision. This again indicates the significance of column stiffness on pounding sensitivity.

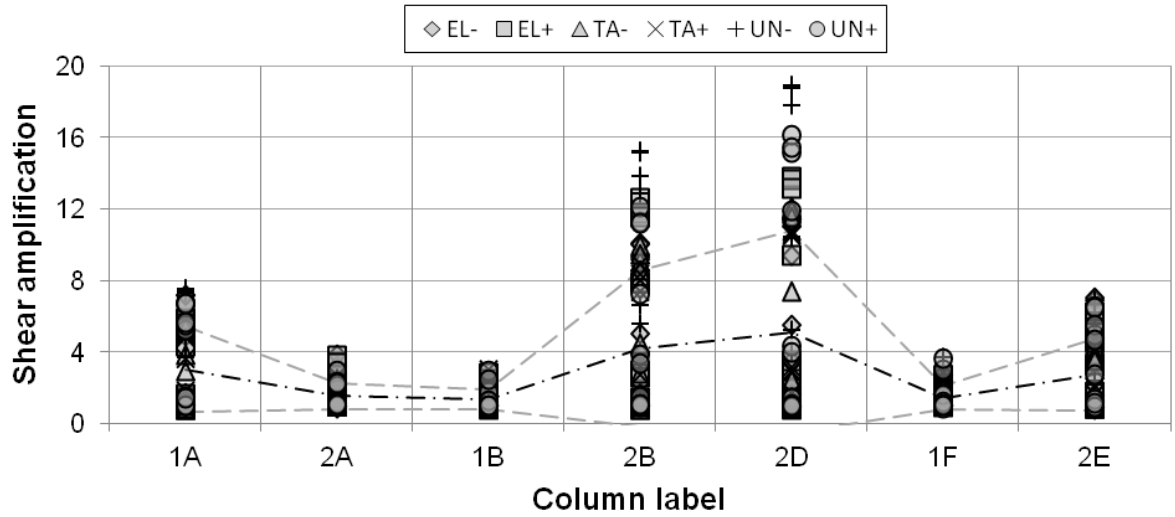

Figure 9.46 Shear amplification of mid-span model. Amplifications categorised by column location

Columns have exceeded their shear capacities at two levels in Building 2 (no shear capacities were exceeded in Building 1). Figure 9.47 presents the shear loadings normalised by the shear capacities of both of these column levels. Shear capacity is dependent upon axial load. For the purposes of these analyses, axial load has been assumed to be equal to the axial load calculated prior to applying the ground motion. It is possible that more detailed calculations would show that the column's capacities have not been exceeded. However, Figure 9.47 illustrates that impacted columns shear capacity may be critical even in mid-span configurations, which are considered to be the least shear-critical (refer Section 9.2) floor/column collision configuration. As stated in this chapter's introduction, the direct shear capacities could also potentially be exceeded. However, in the *mid-span* analyses shear loading was found to be considerably less than all column's direct shear capacities.

The shape of the results of B2L3 in Figure 9.47 is also noteworthy. Here the separations are normalised by the separation required to prevent contact *at the stated columns*. This differs from the normalisations used in other figures, since they use the separation required to prevent contact *anywhere in the buildings*. This normalisation is used to be comparable with the local floor/floor results in previous chapters. The trends shown in this graph are similar to those observed in the contact force of floor/floor collisions. While Figure 9.46 shows column shear amplifications of up to 18, the shear capacity is only exceeded by approximately 20%. This reflects the low level of shear demands in these particular buildings when no pounding is present (recall that the ground motions are scaled for the 1/25 year event). B2L2 shows a faster drop in demand with increasing separation. This is also consistent with the lower floor's floor/floor response. The trend observed in B2L3 is investigated further in Figure 9.48.

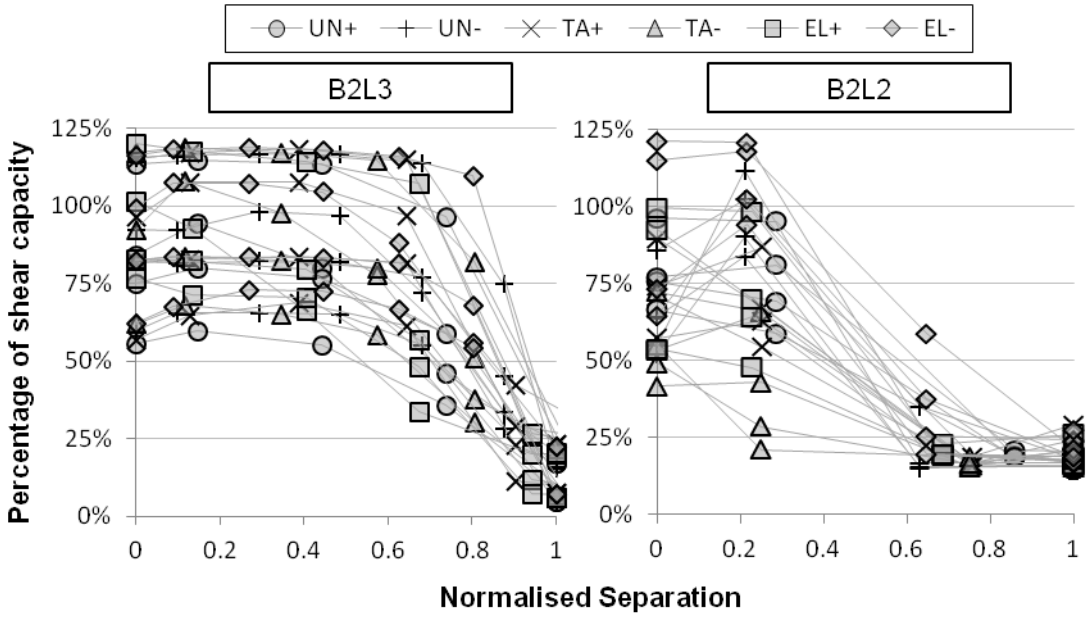

Figure 9.47 Percentage of shear capacity as a function of floor separation

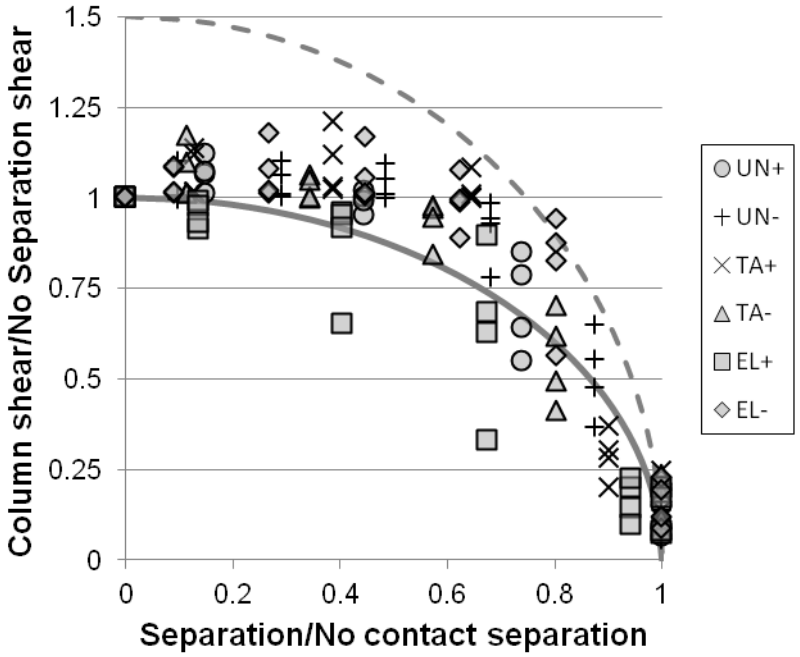

Figure 9.48 Normalised shear force in columns at B2L3. Shear is normalised by the column shear when no separation is present. Solid line: SDOF idealisation. Dashed line: 1.5x SDOF idealisation.

In this figure, the column shears are normalised by the column shears when no separation is present. The shear demands are very well (but unconservatively) predicted by the simplified SDOF model proposed in Section 3.1.2. Note that the values tend to approximately 0.2, not 0, when normalised separation is 1.0. This is because shear demand still occurs when the buildings do not experience pounding, whereas floor/floor contact force reduces to zero when no pounding occurs.

The maximum ductility of each recorded column is presented in Figure 9.49. Absolute values (not amplifications of NC results) are shown in order to allow comparisons with the maximum

allowable curvature ductility of $\mu_\phi = 12$. While floor/column collision has increased ductility demands, they are still well within the stated limits. This further highlights the importance of considering the shear demands when modelling floor/column pounding.

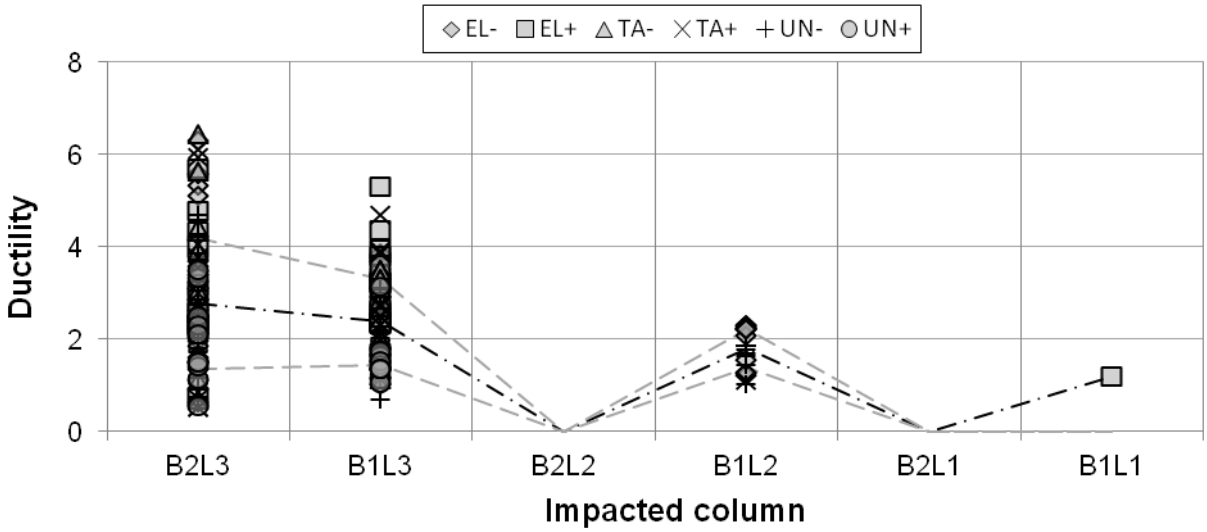

Figure 9.49 Column ductility in mid-span collision. Amplifications ordered by decreasing floor height

The final aspect of local damage that is considered here is the force experienced by the impacted floors (Figure 9.50). These values correspond to the maximum force experienced by the entire floor over the course of the collision. This means that the reported force is the sum of the contact forces in the contact elements of each column. Presenting the data in this way allows direct comparison to 3D floor/floor collision (Figure 8.20). Note that the legend refers to the floor location (not the column location, refer Figure 9.43).

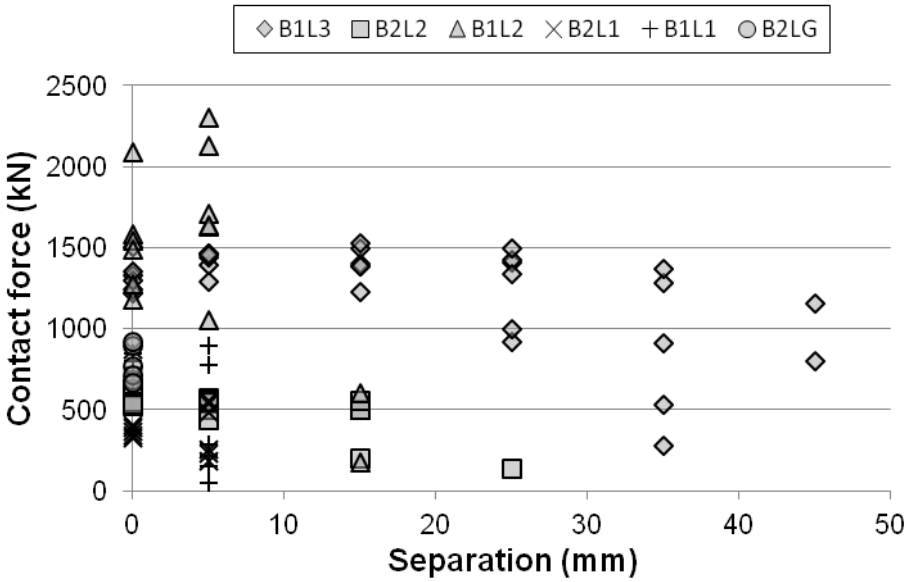

Figure 9.50 Maximum collision force recorded at each floor. Floors ordered from highest to lowest

The *mid-span* contact force is approximately one quarter that reported for *3DModel*. This result is expected since the process of the column deflecting increases the collision duration while decreasing the maximum force (keeping the change in momentum approximately constant).

Similar trends are observed in the reduction of contact force with increasing separation, particularly at the topmost point of contact between the buildings (B1L3). This further indicates the usefulness of Equation 3.17.

9.5.2 Mid-span Collision Influence on Global Damage

The effects of floor/column collision on the remainder of Building 1 and Building 2 can be assessed in a similar manner to that adopted in Section 8.4. However, the observed trends in the *mid-span* model are largely similar to those presented in Section 8.4. In the interests of brevity, only the key aspects are discussed below. The figures showing the global building response of the *mid-span* model are included in Appendix L.

Displacement amplification trends are particularly close to those presented previously. While the results are not identical, the reported amplitudes are similar magnitudes to that shown in Section 8.4.2. However, some displacement amplification plots do not linearly reduce with increasing separation. For example, Building 1's normalised Y displacements are approximately constant between normalised separations of 0.2 to 0.7. Nevertheless, the trends observed in previous sections are also valid here.

The results for the relative displacement between front and back frames (indicating torsion) are also very similar to the floor/floor results. This is perhaps unsurprising, since the floor/floor and floor/column analyses both cause load to be transferred between the buildings at similar plan locations, which causes similar levels of building torsion.

The amplification of shear in Building 2 does show minor differences (Building 1 is not reported since many of these columns have performed inelastically). In order to look at interstorey shear in the floor/column models, it is necessary to leave out any columns that suffer direct impact. This is because the impacted columns have major shear amplifications due to the transfer of the impact load to their connecting floors (as shown in the previous section). The effect this omission has on the overall interstorey shear should be relatively minor. The *mid-span* model causes significantly less amplification at Level 3, in comparison to the floor/floor model. This reduction at Level 3 can be partially explained by the energy dissipation that occurs in the plastic hinges formed in the impacted columns.

Finally, the recorded building ductilities are also similar to those presented in Section 8.4.3. Notable exceptions include the X direction ductilities of Building 2 increasing by approximately 50 percentage points, and non-linear reduction of amplifications with increasing separation. The

similarity of these results indicates that the global processes of momentum transfer remain similar to the floor/floor model (i.e. *3DModel*), despite the change in the nature of the collision.

9.6 Floor/Column Models – Near-floor Collision

The *mid-span* model represents a very specific building configuration. In the author's experience, low rise buildings do not usually have floors that are positioned at the mid-span of adjacent building's columns. This is because buildings typically use very similar interstorey height spacings. Low rise buildings are much more likely to have floors that are only slightly offset from each other. This type of building configuration is investigated using the *near-floor* model. The floor offsets of this building configuration are shown in Figure 9.41.

9.6.1 Near-floor Collision Influence on Local Damage

Figure 9.51 presents the shear amplification resulting from floor/column pounding. As noted in Section 9.5.1, this type of figure presents all recorded impacted column data so multiple data points are plotted for each individual analysis. The trends of Figure 9.51 differ significantly to the equivalent *mid-span* results (Figure 9.45). The amplifications observed in columns in the upper levels of Building 2 (B2L3 and B2L2) have reduced, while the maximum amplifications of the upper levels of Building 2 (B1L3 and B1L2) are more than double that of the *mid-span* results.

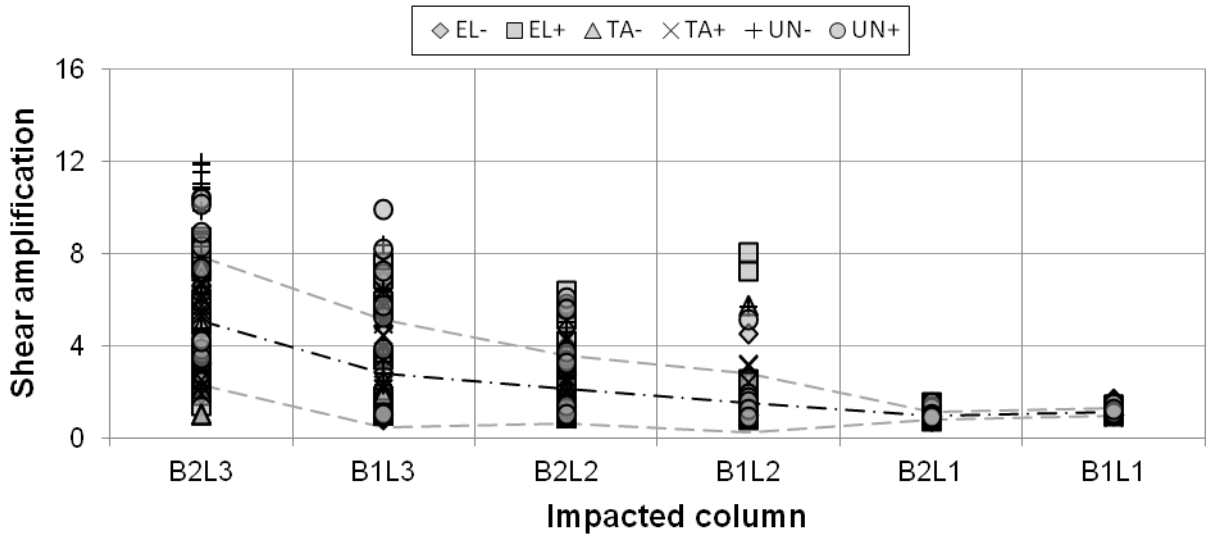

Figure 9.51 Shear amplification in near-floor collision. Columns ordered in decreasing height

This change in behaviour was not anticipated, but can be explained in terms of the change in column stiffness which was caused by the change in Building 2's floor heights. In the *mid-span* configuration, both B1L3 and B2L3 had at least 35% minimum clear span before any impact loading was applied (Figure 9.52). However, in the *near-floor* configuration B2L3 columns have at least 31% clear span, while B1L3 columns have a minimum of 21%. This significantly raises

the stiffness of these columns during collision. Despite the columns in Building 1 having smaller cross sections than the corresponding columns in Building 2, the effective impact stiffness of these columns causes a more even distribution of load between the two buildings' impacted columns.

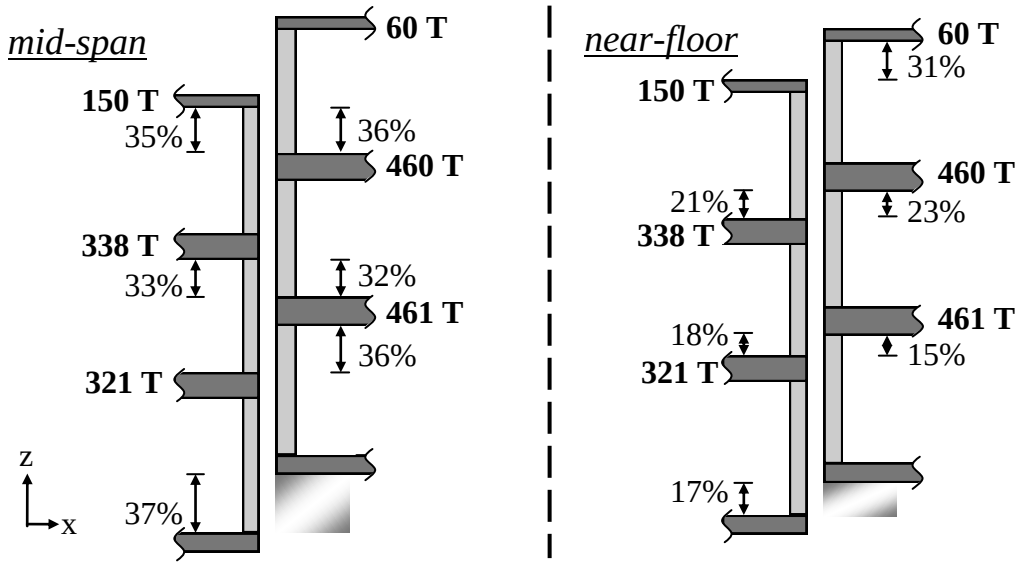

Figure 9.52 Column layouts for mid-span and near-floor models including floor mass

The mass of each floor also contributes to this change in shear loading. In the *mid-span* model, B2L3 columns primarily cause load transfer between a 150 T and a 460 T floor (Figure 9.52). However, in the *near-floor* configuration the interaction primarily occurs between a 150 T and a 60 T floor. This reduction in mass corresponds to a reduction in these columns' shear demands. This result shows that collision shears are not solely dependent on the effective column stiffness. A direct comparison between the *mid-span* and *near-floor* column shears is presented in Figure 9.53. This comparison is made by summing all six ground motion's maximum shears to provide a representative measure of the difference in shear demand. The test with maximum shear demand is dependent upon the considered building. The simplified modelling methods presented previously do not capture this effect, which limits their usefulness. Figure 9.53 once again demonstrates the highly nonlinear relationship between increasing building separation and impact column response. Normalised shears and separations are presented for B2L3 in Appendix L.

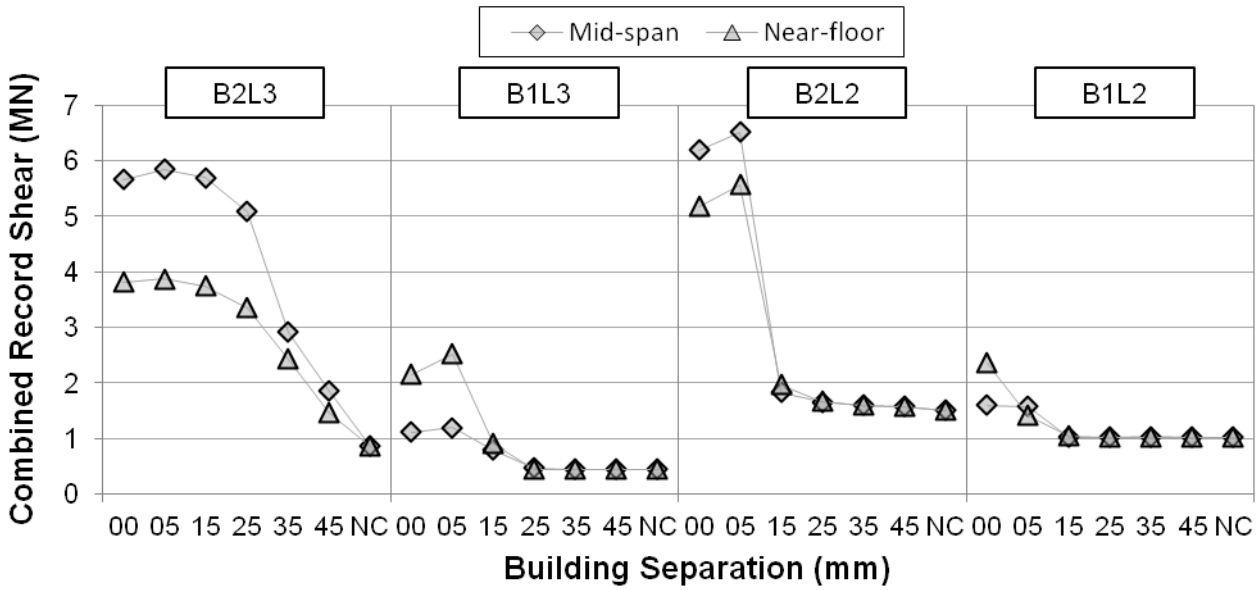

Figure 9.53 Comparison of mid-span and near-floor column shear demands. The vertical axis presents a sum of the maximum shear forces recorded in each of the six tested ground motions

The data can again be rearranged so it is sorted according to the Buildings' frame locations (Figure 9.54). This figure is also significantly different from the equivalent *mid-span* plot (Figure 9.46). Frames 1A and 2E show similar magnifications; however frames 2B and 2D maximum amplifications have significantly reduced, while frames 2A, 1B and 1F have all approximately doubled. These results suggest that as building offset reduces, the cross sectional area of these columns become less influential on the effective column stiffness during a collision. Instead, the relative height of the impact point on the free span governs the effective collision column stiffness. This appears to cause more evenly distributed shear demands between the buildings' impacted columns. However, further testing would be necessary to confirm the generality of these trends.

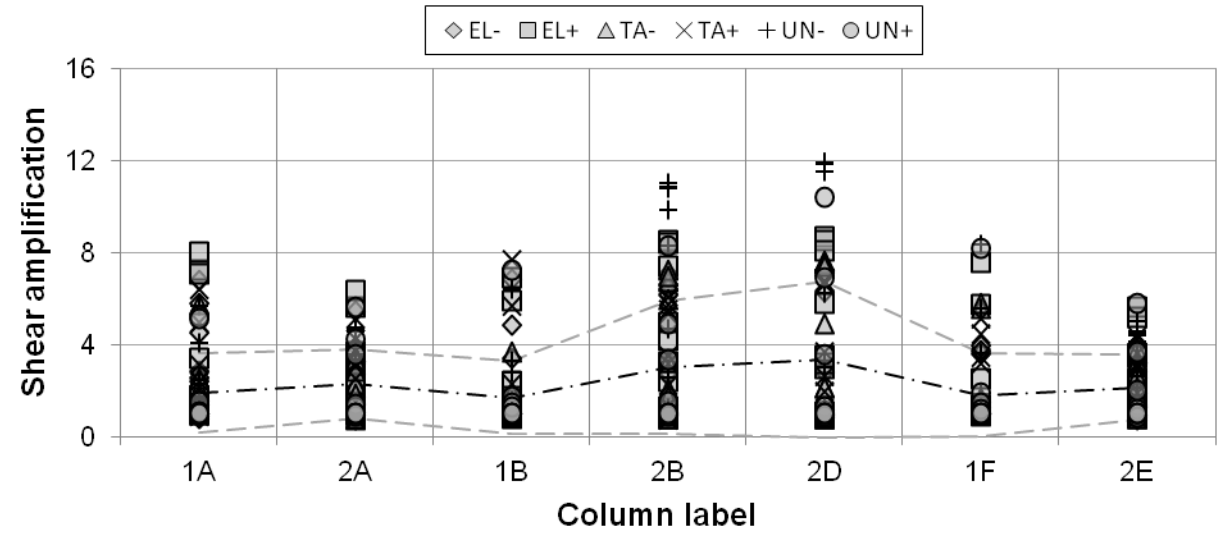

Figure 9.54 Shear amplification of near-floor model. Amplifications categorised by column location

Some of the implications of this 'impact shear sharing' can be observed in Figure 9.55, which shows column demand normalised by column capacity. Column capacity is greatly exceeded in

B1L3 columns, and is also exceeded in a few cases at B1L2 and B2L2. This result shows that the topmost impacted columns are not the critical components in the modelled system. This result is significant in light of previous results by Karayannis and Favvata (2005), which stated that only the topmost point of collision was important for floor/column collisions between buildings of significantly differing heights. This result does not contradict that of Karayannis and Favvata (since the buildings considered here are almost the same height), however it does demonstrate that their findings are not applicable over all possible floor/column collision configurations.

In the presented analyses, simulation was not stopped when a column's capacity was exceeded. It is therefore possible that B1L2 and B2L2 columns would not actually be exceeded as predicted, since it is likely that at least partial building collapse would have already occurred in Building 1 at Level 3. Any collapse would substantially change the response of that building, so the adopted model's subsequent predictions are most likely incorrect.

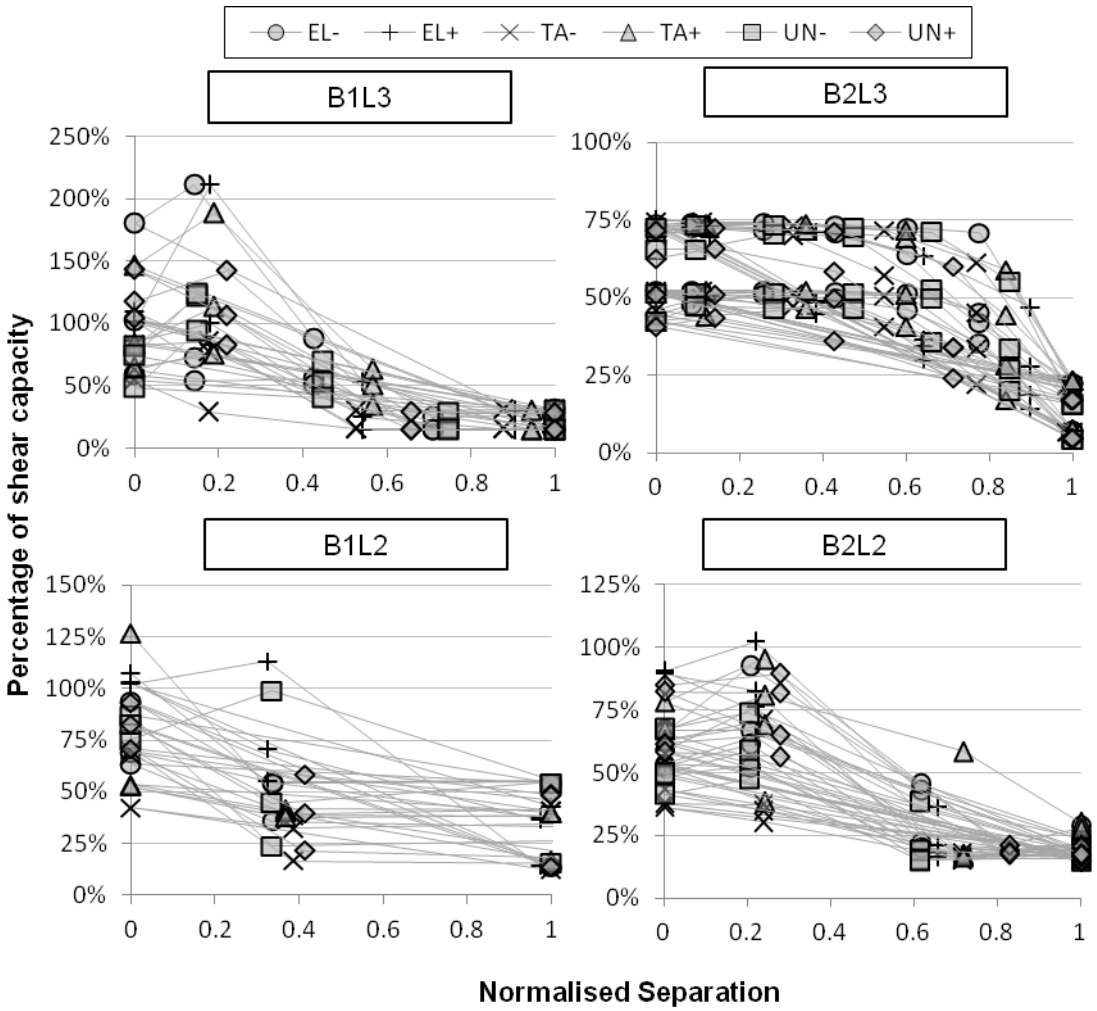

Figure 9.55 Percentage of shear capacity as a function of (normalised) separation. Separation is normalised by the separation required for no collision to occur in the considered columns. Data for the top four floors is shown.

As with the *mid-span* model, each floor is normalised by a different 'no contact' separation in Figure 9.55. This makes the results comparable with the normalisation of floor/floor contact force results (for example, Figure 8.21). Column direct shear capacities were not exceeded in any of these analyses (see Section 9.2). B2L3 columns again show similar trends between normalised floor separation and impacted column shear loading to that of floor/floor collision. The lower levels' demands drop more rapidly, however this is also consistent with the results of the lower levels in floor/floor collision (refer Figure 8.21). This general shape of local demand drop off with increasing separation appears to be universal for any local damage measure.

Impacted column ductility has also reduced in Building 2 and increased in Building 1 (Figure 9.56). However, these changes are much less pronounced than those observed in column shear results. As observed in the *mid-span* results, no columns have exceeded the stated column ductility capacity from Section 5.2.9. The lower levels of Building 2 suffer particularly little inelastic action, with B2L2 columns only recording one inelastic result.

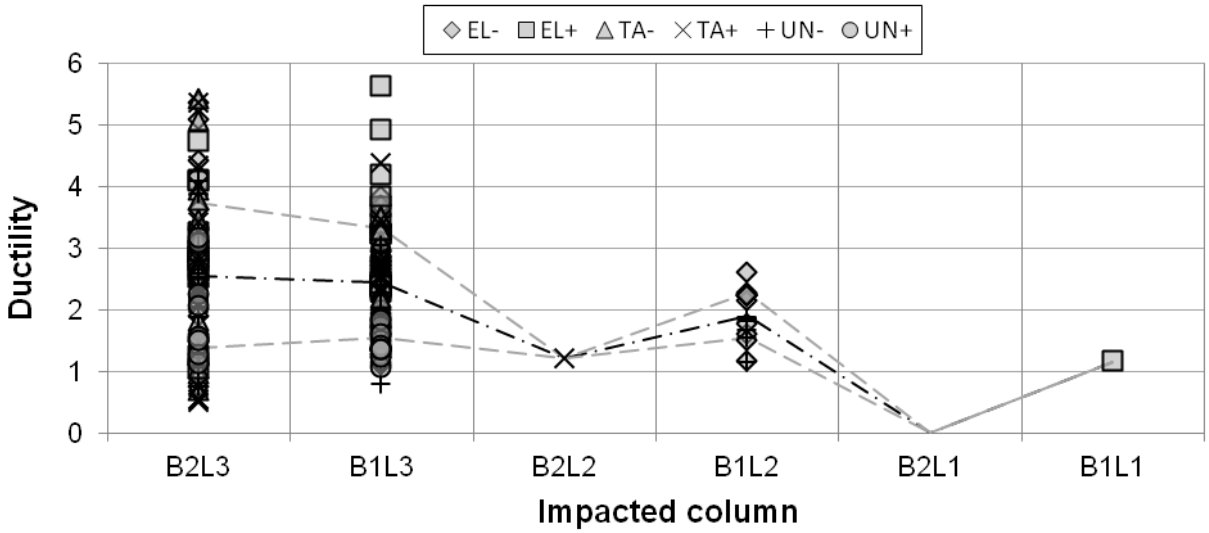

Figure 9.56 Column ductility in near-floor collision. Amplification classified by floor height

Finally, the collision force experienced by the impacted floors is documented in Figure 9.57. The trends observed in Section 9.2.5 and 9.2.6 suggests that the contact forces in the *near-floor* models would be notably greater than the corresponding *mid-span* results. This is based on the floors being closer to the ends of the columns, which increases the columns' effective impact stiffness. However, the maximum recorded contact forces are actually less than that shown in Figure 9.50. The impact loads on the upper floors of Building 1 have reduced (B1L3 ΔF_{max} = -130 kN, B2L3 ΔF_{max} = -360 kN), while the impact loads on the upper floors of Building 2 have increased (B2L2 ΔF_{max} = 340 kN, B2L1 ΔF_{max} = 100 kN). No notable overall increase in floor loading has been observed. These observations are consistent with the shear results (see Figure 9.53), but would not be predicted by the simplified models proposed in Section 9.2.4. This

implies that more sophisticated techniques would be necessary for accurate predictions of floor/column performance.

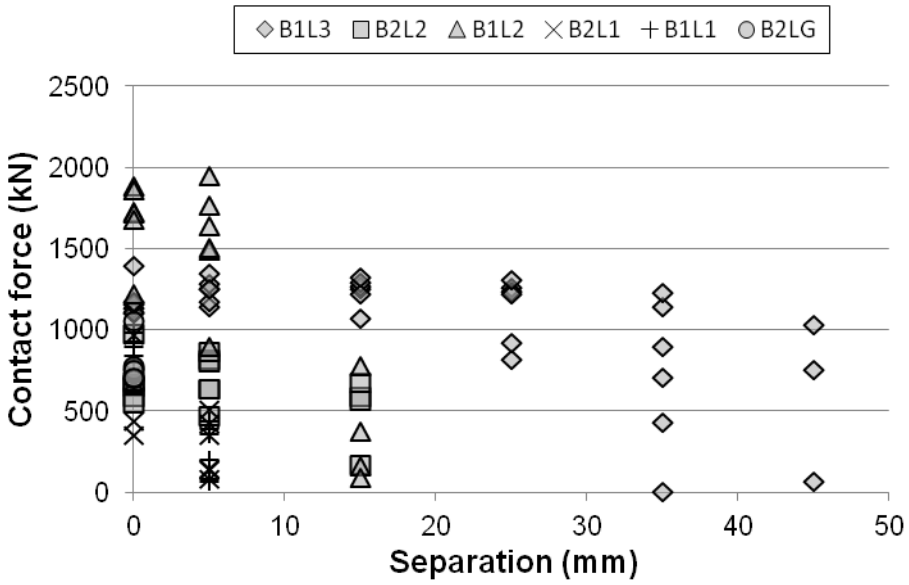

Figure 9.57 Maximum collision force recorded at each floor. Floors ordered from highest to lowest

9.6.2 Near-floor Collision Influence on Global Damage

Global damage is similar to that reported for *mid-span* in Section 9.5.2. While building displacements envelopes and member ductilities do differ from the mid-span results, the overall trends are the same as previously noted. This result makes sense since the *near-floor* ($\Delta z = 1.2$ m, refer Figure 9.44) configuration is an intermediate building layout between the *mid-span* ($\Delta z = 1.81$ m) and floor/floor models ($\Delta z = 0$ m). Additional figures on the global effects of the *near-floor* tests are included in Appendix L.

9.7 Conclusions

The following conclusions are drawn based on the investigations and results presented in Chapter 9:

1. Timoshenko and Euler-Bernoulli beam theories can predict significantly differing shear loading demands when a sudden impulse is applied to a beam
2. Column demands can be approximately predicted when the impacted column is modelled as a single flexural element with fully rigid supports. This result suggests that column demands may also be able to be predicted for more realistic floor/column collision models. Investigation into this possibility is recommended for future research.
3. The simplest floor/column modelling method with acceptable inaccuracy was found to include the following properties:

a. four column elements in each impacted column. The impacted column elements should include modelling of shear stiffness effects,
b. more than two axial diaphragm elements in the impacting floor,
c. contact element stiffness set using Table 9.8

4. The transition between purely floor/column collision and purely floor/floor collision can be categorised into three phases:
    a. collision where deformation occurs primarily in the impacted columns,
    b. collision where deformation primarily occurs in one or more floors, but the buildings' perimeter beams do not come into direct contact with each other during collision,
    c. floor/floor collision where perimeter beams do come into direct contact with each other during collision.
5. Shear amplification of an individual column is dependent upon that column's effective column impact stiffness as well as the stiffness of the other columns undergoing impact. The height of the impact on each column affects the effective column impact stiffness and therefore also affects shear amplification and contact force.
6. The relationship between shear amplification in the impacted column and normalised separation is very similar to that observed in the contact force for floor/floor collision. These trends can be predicted using Equation 3.17.
7. In the tested building configurations, global building response to floor/column collision is very similar to that of floor/floor collisions. This similarity is attributed to the nearly identical plan locations of force transfer between the two modelled buildings.
8. Columns that have their shear capacities exceeded in the *mid-span* model do not necessarily have their shear capacities exceeded in the *near-floor* model, despite the *near floor* model being considered to cause higher column shear demands. This highlights the highly sensitive nature of columns undergoing impact.

Chapter 10 Analysis of Collisions with Walls

Walls are the final structural element to be considered for pounding in this thesis. The scope of this chapter is somewhat reduced in comparison to the chapters on floor/floor and floor/column collision. A detailed simulation of wall collision is presented, however simplified models are not considered here. This decision is based upon a number of factors:

Firstly, out-of-plane wall modelling is itself a complicated problem. Any simplified models developed here would be specific to the type of plate finite element used in the models. In contrast, floor/floor and floor/column model development used common element types that are likely to be readily available in multiple structural analysis programmes. As is shown in this chapter, walls collision performance is relatively insensitive to collision element definition. This means that key parameters, such as mesh size, are more likely to be governed by finite element considerations rather than contact-specific concerns. This issue limits the general applicability of any results developed here.

Wall collision modelling is also considerably more difficult to model using Ruaumoko. This is because Ruaumoko's post processing abilities are focused on nodal and line element data. When area elements are used, nodes' finite element stresses must be manually averaged from all adjacent elements. While this can be (and has been) done, it considerably increases the amount of time required to compile the relevant data.

Finally, any researcher considering the effects of wall collisions is unlikely to actually want a highly simplified model. In most normal applications out-of-plane wall response is assumed to be negligible and not modelled at all. When out-of-plane wall actions are considered, the desired level of detail is likely to be much higher than equivalent column or floor collision models.

As simplified models are of dubious value in this circumstance, the objectives of this chapter differ from those considering floor/floor and floor/column collision. The objectives of this chapter are:

1. To provide recommendations for the stiffness of contact elements in wall/wall collision
2. To demonstrate the response of two walls that experience an out-of-plane wall/wall collision in order to illustrate the fundamental processes governing this form of collision.

These objectives are addressed in the following sections.

10.1 Existing Wall Collision Research

To the author's knowledge, no building wall/wall pounding research has been published to date. This may be at least partially attributed to the lower earthquake building deflections observed in wall buildings. Moment resisting frame buildings move more during earthquakes and have suffered multiple dramatic failures in previous earthquakes, yet even floor/column collisions have received little research attention (Section 9.1).

Out-of-plane wall failure due to collision is, however, a legitimate and current concern for many New Zealand buildings. Specifically, adjacent unreinforced masonry buildings without any separation exist in most New Zealand towns and cities. These configurations have the potential to catastrophically fail due to collision in even a moderate seismic event. Analytical tools to model such processes provide a rational method to quantify the seriousness of this risk.

10.2 Idealized Wall Response to a Single Collision

Wall response is characterised in this section by first considering an arbitrary collision on a beam like structure. This is done to assess the significance of shear stiffness for typical wall geometries and to verify the performance of the selected finite element. Two wall/wall collision scenarios are then modelled using these elements.

The dynamic out of plane response of area elements is usually addressed using plate theory. Ruaumoko provides the 'hybrid stress type 2' element for plate modelling (hereafter referred to as the hybrid element). Hybrid elements allow the stress equilibrium conditions between finite elements to be relaxed (Pian and Tong 1972). However, the energy resulting from any boundary overlap or gap is measured, and the total energy of each element is conserved. This results in more accurate stress results, while displacements are only accurately known along the edges of each element. The hybrid element is adopted for all plate modelling in this section.

10.2.1 Characterising an Arbitrary Wall Impact

To check the reliability of the hybrid element in Ruaumoko, two test analyses were performed (Figure 10.1). This section presents the results of the *mid-span* test; however the observed trends were also present in the *near-support* model. A model of a column similar to that tested in Section 9.2.2 was used to compare the column's responses using frame elements with that using hybrid elements. The test configuration and analysis properties are presented in Figure 10.1 and Table 10.1, respectively.

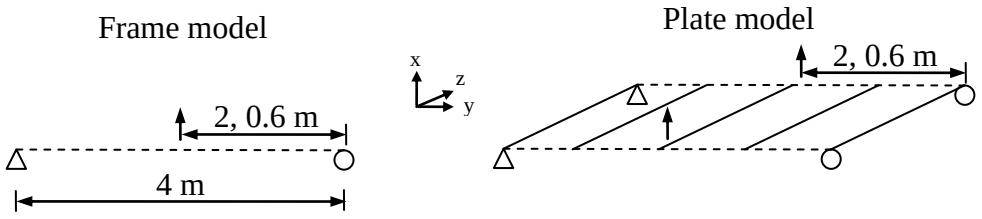

Figure 10.1 Arbitrary collision test of hybrid finite element

Table 10.1 Properties of arbitrary collision test

Dimensions	*4 m long x 1 m wide x 0.05 m thick*
Element number	*100*
Excited node velocity	*7.2 m/s*
Material density	*24 kN/m^3*
Young's modulus	*27898 MPa*
Poisson's ratio	*0.2*

Each configuration (*mid-span* and *near-support*) was run with three different models; frame with shear stiffness, frame without shear stiffness, and plate without shear stiffness. A working plate model including shear stiffness was not available at the time of modelling. In these tests, the thickness to beam span ratio is much smaller than that used in the column tests (Section 9.2.2). This difference reflects the smaller thickness of walls, which typically range between 50 and 200 mm, whereas columns' thicknesses are generally greater than 400 mm. Walls are also much wider than columns (by definition), which results in different stress distributions. These differences reduce the importance of the shear stiffness terms in the Timoshenko beam. The reduction in shear stiffness' importance can be observed in the mid-span displacement response of the column (Figure 10.2). The effect of the shear stiffness term on the frame elements is almost completely negligible. The hybrid element configuration also presents very similar results, although some change in natural frequency of the column is present.

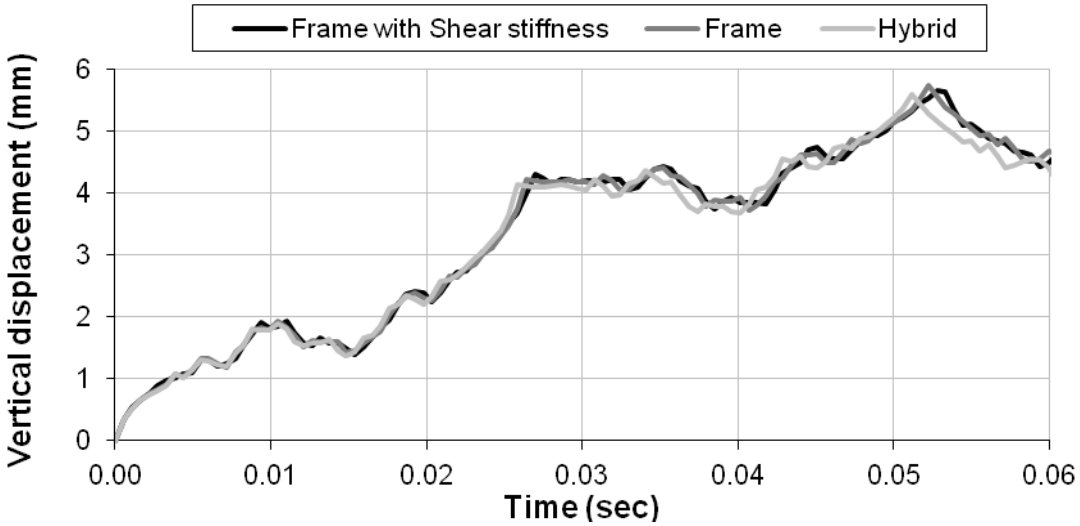

Figure 10.2 Mid-span displacement due to mid-span loading

Moving from column to wall cross section geometry also changes the likely hierarchy of failure. Whereas columns are likely to fail in shear, walls can be vulnerable to both shear and moment failure. This is evident from the calculations of section stresses. Bending capacity is based upon the section modulus (width × depth^2 ÷ 6) whereas shear capacity is based upon the cross sectional area (width × depth). As the depth of a section reduces, flexural capacity drops at a faster rate than shear capacity. Both moment and shear envelopes are presented below (Figure 10.3 and Figure 10.4).

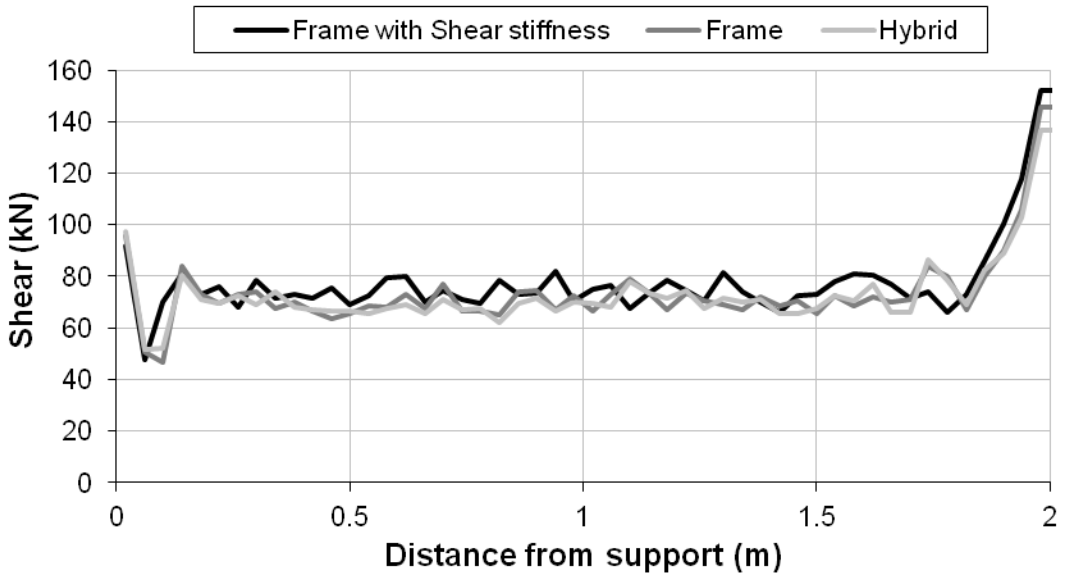

Figure 10.3 Maximum shears along beam as a result of mid-span excitation. Note that the beam is symmetrical about mid-span

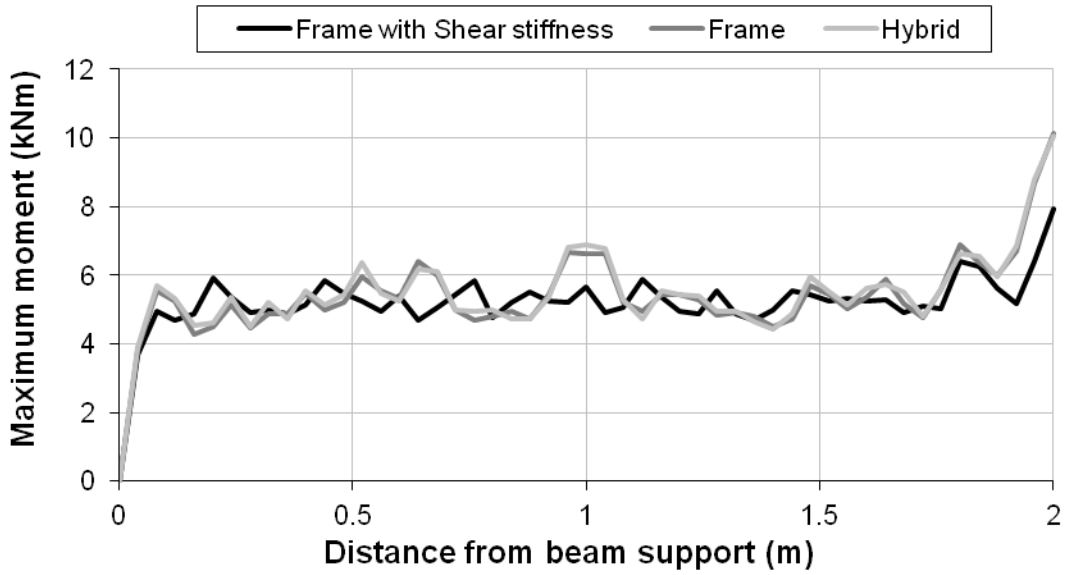

Figure 10.4 Maximum moment envelope due to mid-span excitation

The presented moment and shear accuracies are not adequate to be used to define the acceptable accuracies for simplified models. However, for the effects considered here (sensitivity to

collision element stiffness and general trends resulting from collision), the presented accuracies are acceptable. Obviously, a hybrid stress model including shear stiffness would still be preferable if it was available.

10.2.2 Calibration of Wall/Wall Collision Element Stiffness

As with floor/floor or floor/column collision, wall/wall collision requires a method of calibrating each collision element's stiffness. Any collision element (used in either floor/floor, floor/column, or wall/wall) can be broadly classified according to the horizontal stiffness of the colliding building components. In total, three types of collision exist: hard vs. hard, hard vs. soft, and soft vs. soft collisions.

The hard/soft classification refers to the stiffness of one colliding building at the location that a collision is anticipated. The relevant stiffness acts along the line of action of the potential impact force. Hard building elements have significant stiffness in the direction of the impact force and include floors, or walls that are loaded in plane. Hard building elements commonly have distributed mass, which results in some level of axial oscillation after a collision. Soft buildings elements have little stiffness at the point of collision in the collision direction, and include walls acting out-of-plane and columns. Soft elements do not cause significant axial oscillation, as any significant mass is distributed in directions other than the line of action of the collision force.

All three collision element types (hard vs. hard, hard vs. soft, and soft vs. soft) can be present when a wall collides with a larger wall (Figure 10.5).

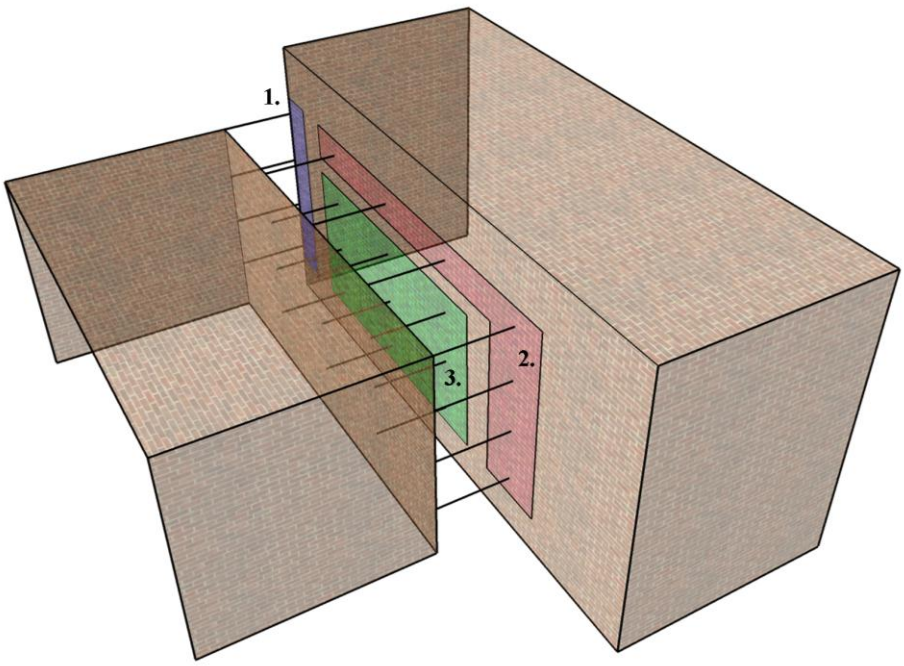

Figure 10.5 Collision element types present when a wall collides with a large wall. Type 1 (blue) = hard vs. hard, Type 2 (red) = hard vs. soft, Type 3 (green) = soft vs. soft

The classification of contact elements in the above manner is useful because it provides guidance on the appropriate selection of contact element stiffness for walls. This guidance is based upon the analogous situations found previously in floor/floor and floor/column collisions. The suggested contact element stiffnesses are summarised in Table 10.2.

Table 10.2 Recommended contact element stiffnesses based on contact classification

Collision type	***Previously analysed analogous configuration***	***Suggested collision element stiffness***
Hard vs. hard	*floor/floor*	*equal to softer adjacent element axial stiffness ($\gamma = 1.0$)*
Hard vs. soft	*floor/column*	*equal to the adjacent axial element stiffness ($\gamma = 1.0$)*
Soft vs. soft	*?*	*?*

Soft vs. soft collision is the only classification not previously considered in earlier testing. Here it is proposed that the hardest axial element stiffness adopted over the perimeter of the contact surface is also used for the soft vs. soft collisions. In Figure 10.5, this would mean the Type 3 contact elements would use the same stiffness as the Type 1 contact elements (these values are generally similar to Type 2 contact elements stiffnesses). This selection is based upon the following considerations:

1. A consistent contact element stiffness is applied across the contact element surface. This allows simple definition of the contact element members.
2. No other appropriate element stiffnesses are readily available to help characterize the contact.
3. Soft vs. soft collisions do not cause the same numerical instability issues as found in hard vs. hard collisions. This is because the axial oscillations caused in hard vs. hard collisions are not important in soft vs. soft collisions. Essentially, a soft vs. soft collision models collision between two lumped masses. Some of the issues discussed in the chapters considering floor/floor collision are therefore circumvented.

Confirming the insensitivity of wall/wall models to the collision stiffness of soft vs. soft collisions requires numerical testing. Tests are performed for two building configurations; collision of two walls of equal size, and collision of walls with differing height and length.

10.2.3 Accurate Equal Wall Model – Stiffness Calibration

The simplest possible wall collision involves two buildings with identical wall dimensions. The adopted mesh for this model is presented in Figure 10.6.

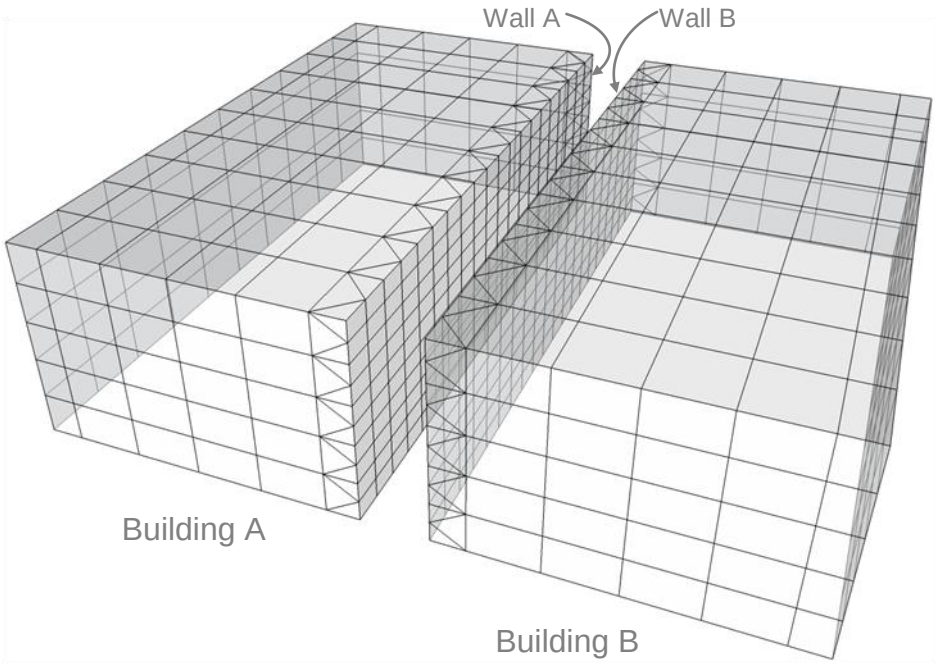

Figure 10.6 Finite element layout of the equal wall model.

Note that no building separation is present in the actual model, however separation is shown in the figure to show the selected wall mesh size. Collision elements are also omitted from this figure but are positioned between each wall node undergoing collision. The key properties of the model are presented in Table 10.3 and Table 10.4.

Table 10.3 Shared building properties for equal wall collision

Property	*Value*	*Property*	*Value*
Building dimensions	*10 x 5 x 3 m*	*Poisson's ratio (of all elements)*	*0.2*
Roof thickness	*150 mm*	*Roof Young's modulus*	*29171 MPa*
Collision wall thickness	*75 mm*	*Young's modulus (all walls)*	*11668 MPa*
Other wall thickness	*50 mm*		

Table 10.4 Differing building properties for equal wall collision

	Building A	*Building B*
Roof seismic weight	20.3 kN/m^2	16.2 kN/m^2
Wall unit weight (all walls)	30 kN/m^3	24 kN/m^3
Building period	0.09 sec	0.08 sec

The wall elements' Young's modulus is reduced to 40% of that in the roof slab. This is to account for the loss of concrete (or masonry) section stiffness that is generally caused by out-of-plane motion during seismic excitation. The two single storey buildings have mirrored geometry, with a refined mesh along the collision surface. Each node on Wall A is connected to the corresponding node on Wall B by a collision element.

Some simplification of the collision wall boundary conditions was required to perform this modelling. With the exception of the walls' bases, the perimeters of both collision walls are modelled with a 'knife edge' boundary (meaning moments do not get transferred to the adjacent walls). This simplification removes the need for side walls to be modelled as plate elements, which permits the use of triangular elements on the side walls (the available triangle elements cannot model plate actions). The use of triangle elements enables a coarser finite element mesh in the rest of the building, which greatly reduces the computational difficulty of the problem. The thin wall thickness of the side walls justifies this modelling choice since little moment can be realistically transferred across these building interfaces.

A collision between the two buildings is created by releasing Building A's roof from an initial displacement. This configuration was subjected to four tests with varying stiffnesses for the 'soft vs. soft' collision elements. Here the model proposed in Section 10.2.2 is labelled as $\gamma = 1$. This is because the stiffness is set as equal to the adjacent element stiffness of the hardest surrounding collision element stiffnesses, which is consistent with the approaches of previous chapters. The remaining tests are labelled $\gamma = 10$, $\gamma = 0.1$ and $\gamma = 0$ (i.e. no soft vs. soft collision elements are present). These tests correspond to soft vs. soft collision element stiffnesses of ten times, one tenth times, and zero times the proposed model, respectively.

Results are presented in terms of mid-wall and top-of-wall deflections, mid-wall moments, and top-of-wall shears. These locations are indicated in the inset diagrams in Figure 10.7 to Figure 10.10. Moments are not presented for the top and sides of the colliding walls since they have pinned connections. The first 0.15 seconds of wall interaction is considered here, during which three collisions occur (at 0.03, 0.075 and 0.13 seconds). The displacement response (Figure 10.7 and Figure 10.8) shows almost no sensitivity to the contact element stiffness. However, removing the contact elements does cause a noticeable change in the mid-wall displacements. The additional contact caused by including contact elements at soft vs. soft collisions increases the positive deflection of Wall B, and also decreases the negative deflection of Wall A.

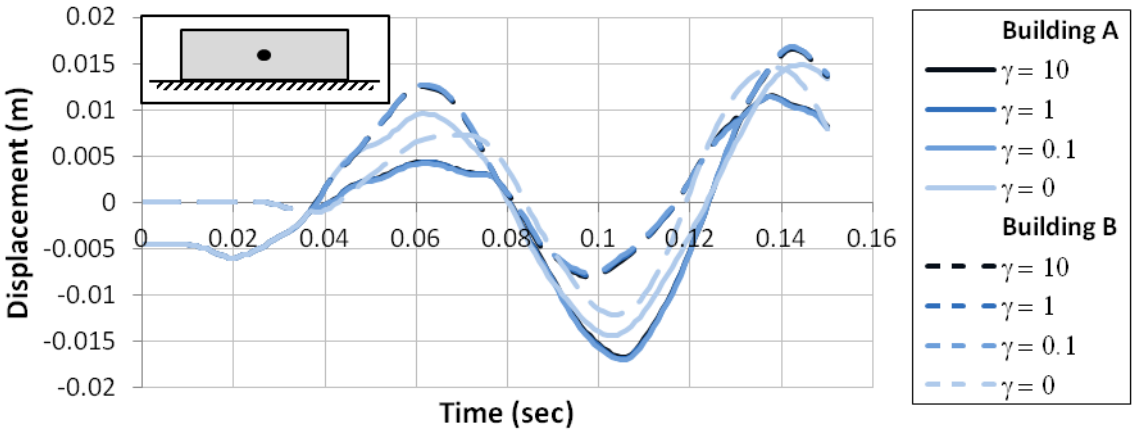

Figure 10.7 Mid-wall deflection sensitivity to soft vs. soft collision element stiffness

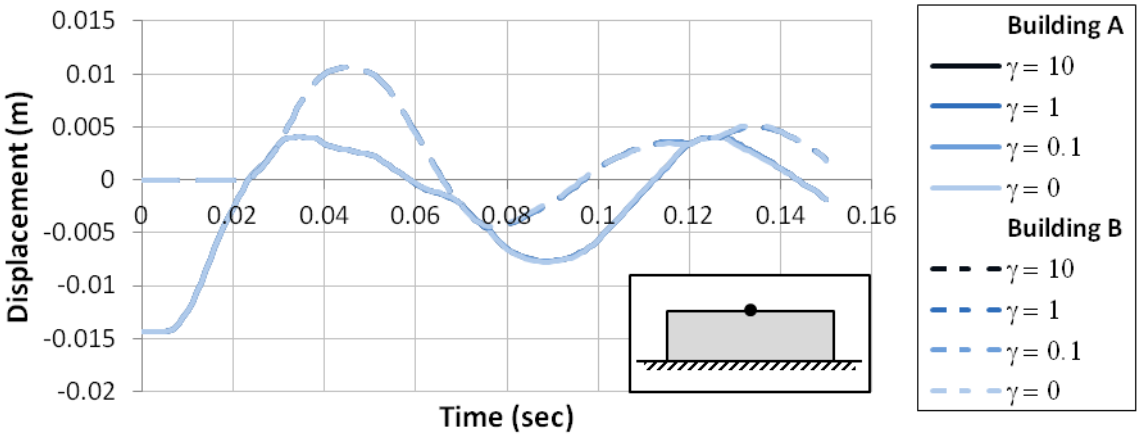

Figure 10.8 Top-of-wall deflection sensitivity to soft vs. soft collision element stiffness

When considering just the top of the collision walls, the displacement responses are insensitive to all contact element stiffness selections. This result indicates that detailed modelling of wall collisions does not affect the other elements present in either colliding structure. This result is unsurprising since the movement of the buildings is primarily controlled by the stiff perimeter walls either side of the collision zone, rather than the collision walls themselves.

The moment response of the centre of Wall A is presented in Figure 10.9. M_{xx} moments are presented. This corresponds to a horizontal moment vector in the plane of the wall, which causes vertical flexural stresses. M_{yy} moments are not presented here, but display similar trends. The flexural stresses are not significantly affected by the changes in γ. When the contact elements are removed, the flexural stresses remain similar, but do notably deviate from the other results. Wall B's flexural stresses also display similar trends to those discussed above.

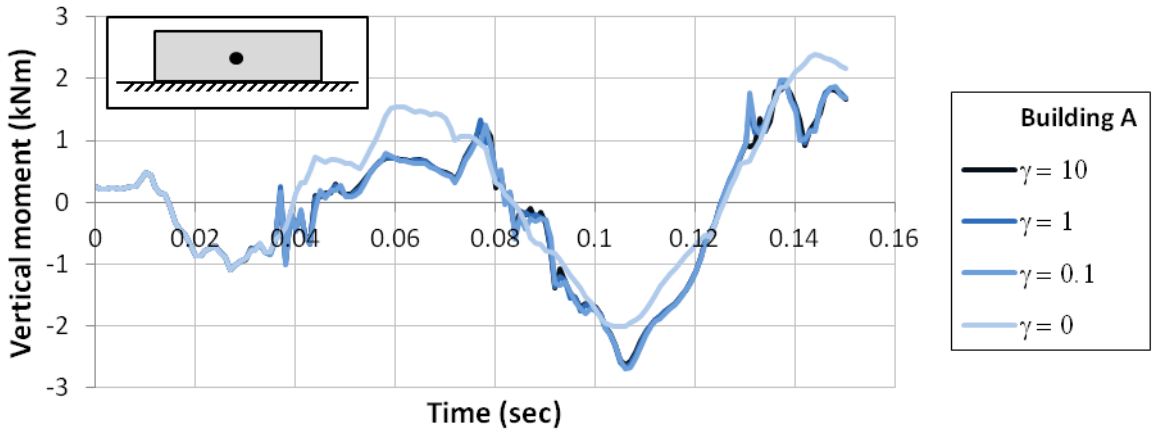

Figure 10.9 Wall A mid-wall, out-of-plane moment results about the horizontal axis.

Finally, Wall A's top-of-wall shear forces are presented in Figure 10.10. These forces correspond to the change in M_{xx} between adjacent vertical elements. The shear results are the most sensitive to changes in the soft vs. soft element stiffness. However, these differences are still small. Once again, removal of soft vs. soft elements causes similar but noticeably different results.

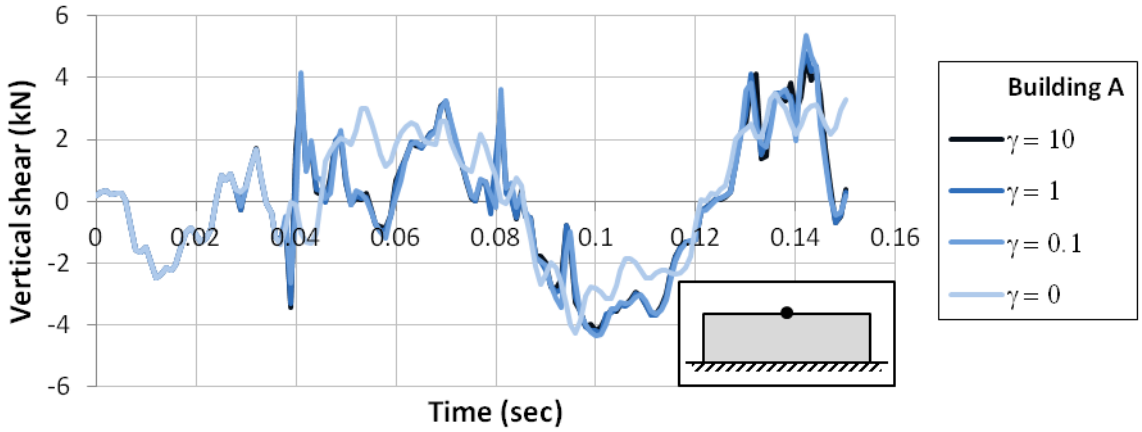

Figure 10.10 Top-of-wall shear force sensitivity to collision element stiffness

γ = 1 is selected for the accurate equal wall model. This is the most desirable definition since it is consistent with the approaches used for soft vs. hard and hard vs. hard collisions.

10.2.4 Accurate Equal Wall Model – Collision Behaviour

This section presents in detail the wall displacement response observed in the equal wall model. This information is present in order to better understand the process of wall/wall collisions.

The time dependent displacements of the wall are most effectively presented as an animation. Since this cannot be presented in the thesis, snapshots of each collision wall's out-of-plane displacements are shown in Figure 10.11 to Figure 10.13.

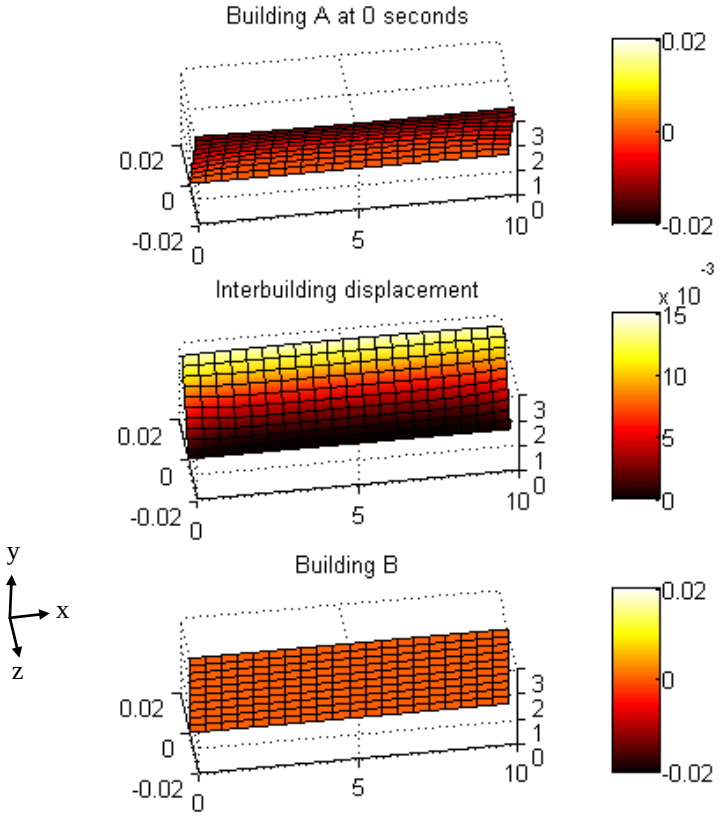

Figure 10.11 Wall displacements (m) at time of release. X and Y axes correspond to distance along, and distance up the considered wall, respectively. The Z axis shows out of plane deflections

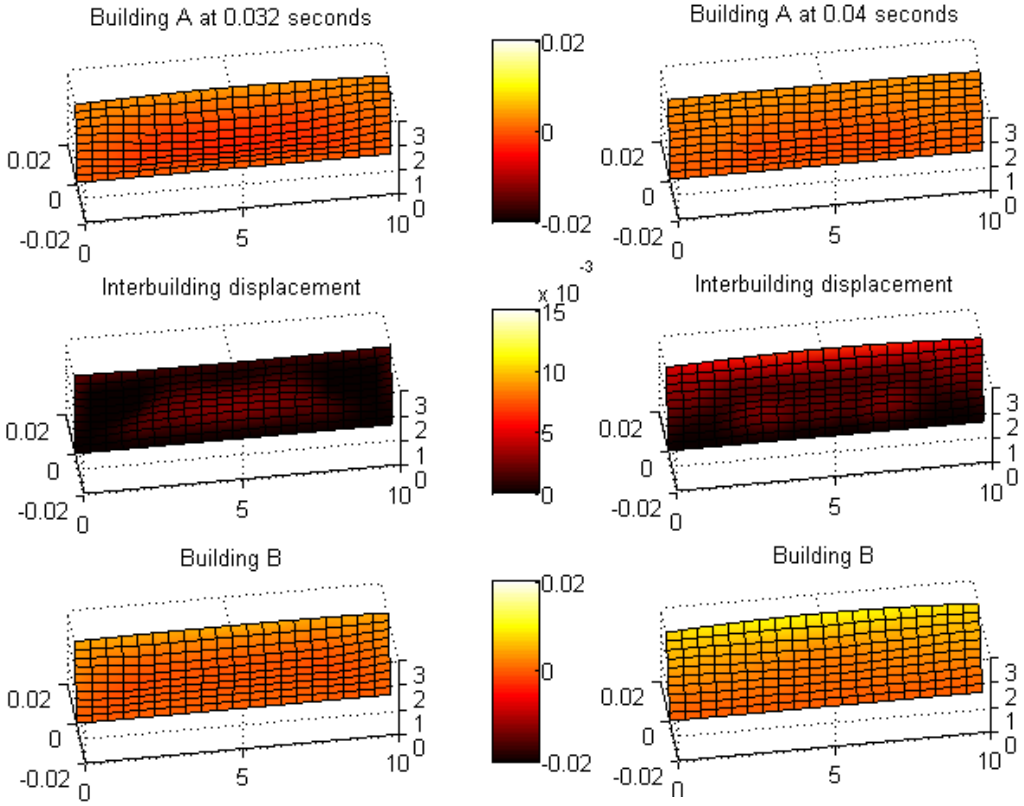

Figure 10.12 Wall displacements (m) at 0.032 and 0.04 seconds after release

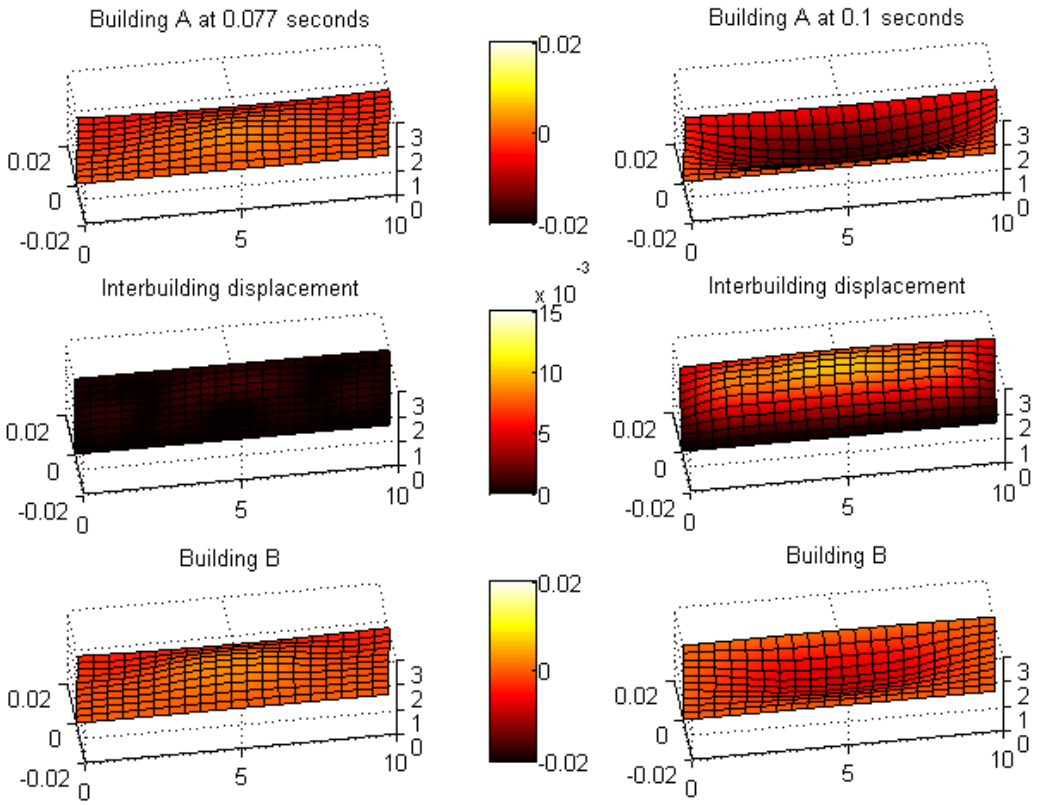

Figure 10.13 Wall displacements (m) at 0.077 and 0.1 seconds after release

A total of five snapshots of the two colliding walls are presented. Each snapshot plots Building A's wall displacements, the interbuilding wall displacements and Building B's wall displacements. The out-of-plane displacements are plotted on the plots' z axes (into the page) and range between -0.02 to 0.02 meters. The x and y axes correspond to distance along and distance up the wall being considered. The interbuilding wall displacement illustrates the separation of the two walls (i.e. Building B displacement minus Building A displacement). This displacement corresponds to the axial displacement of the contact element located at the considered point. When separation is zero, the two walls are in contact. The interbuilding wall displacement also utilises a different colour scale, so black indicates wall contact.

At time = 0 seconds (Figure 10.11), Building A is released from a static force separating the top of the two walls by 12 mm. Building A has negative displacements since the wall has been pulled back, however the interbuilding displacement is positive since the gap between the walls has widened. Building B is unaffected.

Wall collisions start almost instantaneously just above the bottom of the wall since the separation due to the static load at this height is negligible. The contact spreads quickly up the sides and then across the top of the wall, due to the stiff wall and floor elements supporting these points (Figure 10.12, Left). The central nodes of the wall contact later due to their comparatively small out-of-plane stiffness (Figure 10.12, Right). Another contact involving nearly all of the walls'

contact elements occurs as Building A's wall attempts to move away from Building B (Figure 10.13, Left). This contact is caused by Building B's shorter natural period. The peak displacements of both walls occur after this second collision (Figure 10.13, Right). While it is not apparent in the presented results, the maximum wall displacements are caused by the superposition of at least two out-of-plane wall modes.

While the equal wall model presents a complex response to collision, its fundamental method of transferring momentum actually occurs between the perimeter walls either side of the collision zone. The collision response of walls is much more important when one wall is bigger than its impacted neighbour. This is investigated in the next section.

10.2.5 Accurate Unequal Wall Model – Stiffness Calibration

The unequal wall model is based upon the equal wall model. Building B's dimensions are modified to 20 x 5 x 4.2 m, which changes the building's natural period to 0.164 seconds. All other building properties remain as detailed in Table 10.3 and Table 10.4. The new element configuration is presented in Figure 10.14, with contact elements omitted for clarity. The walls are modelled with zero separation, however the buildings are displayed with some separation to show the element configuration.

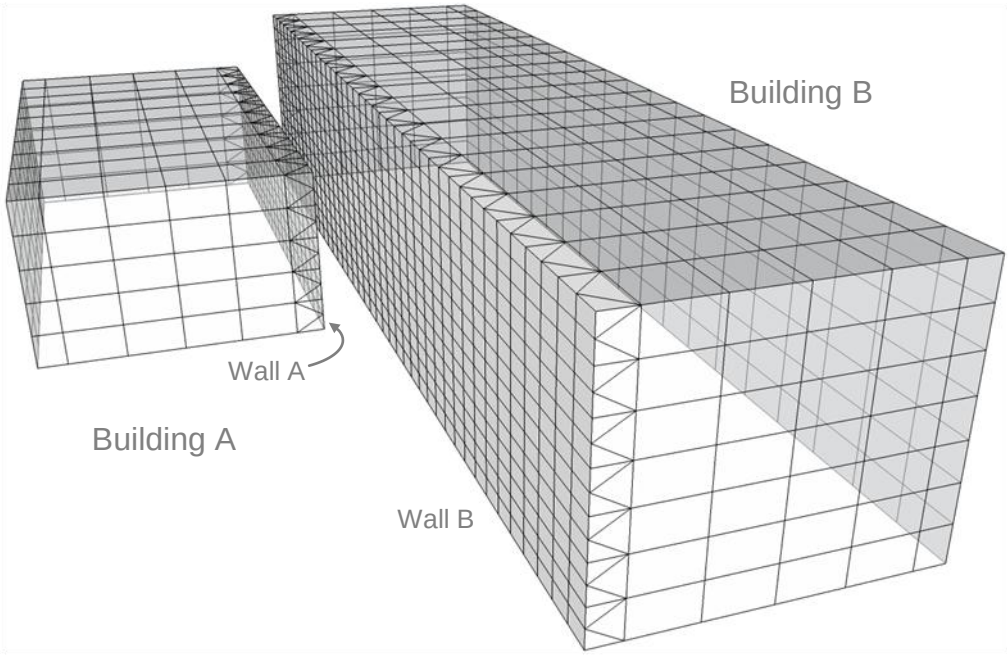

Figure 10.14 Element configuration for collision of uneven walls

Figure 10.15 presents the displacement results for the centre of Wall A, and its corresponding position on Wall B. Increasing or reducing the collision element stiffness by an order of magnitude causes almost no change to wall displacements. However, neglecting internal wall contact does notably change the mid wall displacement response, especially after the contact at

0.12 seconds. The displacements of the corners of each wall are found to be insensitive to whether the internal wall contacts are modelled or not. This is because the displacements of these points are governed by the contacts between the in-plane walls and/or floors. Displacements were also compared at the top right corner of Wall A. However, this point was found to be completely insensitive to whether soft vs. soft collision elements were modelled.

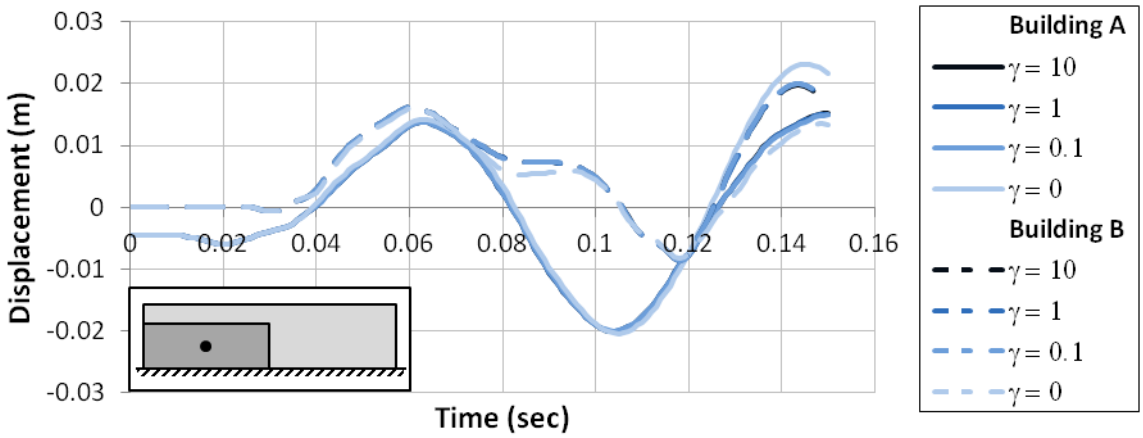

Figure 10.15 Out-of-plane displacement sensitivity to collision element stiffness

The moment results present similar trends. Figure 10.16 displays the horizontal shear stresses in the mid-height of the right side of Wall A. Once again omitting the soft vs. soft collisions entirely causes a noticeable change in response. This difference is most noticeable after the second collision at approximately 0.1 seconds.

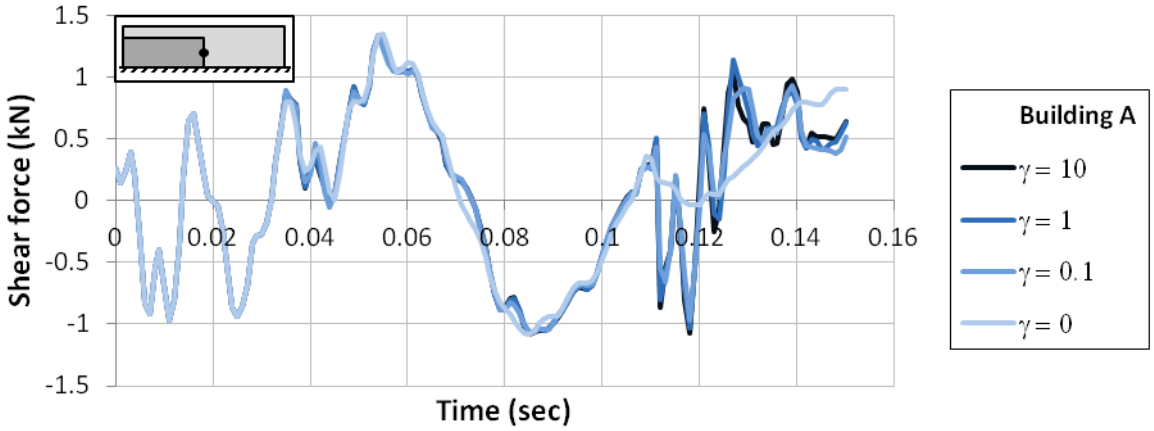

Figure 10.16 Horizontal shears at mid-height of Building A's right wall

The horizontal moments in Wall B at the location corresponding to the mid-height of Wall A is presented in Figure 10.17. These moments correspond to bending about a vertical axis in the plane of the wall. Even in this location, the response of the collision is controlled by the soft vs. hard collision element stiffnesses. Little sensitivity is seen in variation of soft vs. soft collision stiffnesses. This indicates that the soft vs. soft collision elements do not affect the global

response of the buildings. Based on these results, $\gamma = 1.0$ is again found to be the most suitable assignment of collision element stiffness. There is very little difference between the results for $\gamma = 1.0$ and $\gamma = 10$ or $\gamma = 0.1$, however $\gamma = 1.0$ provides a consistent method of stiffness assignment with that of hard vs. hard, and hard vs. soft collision.

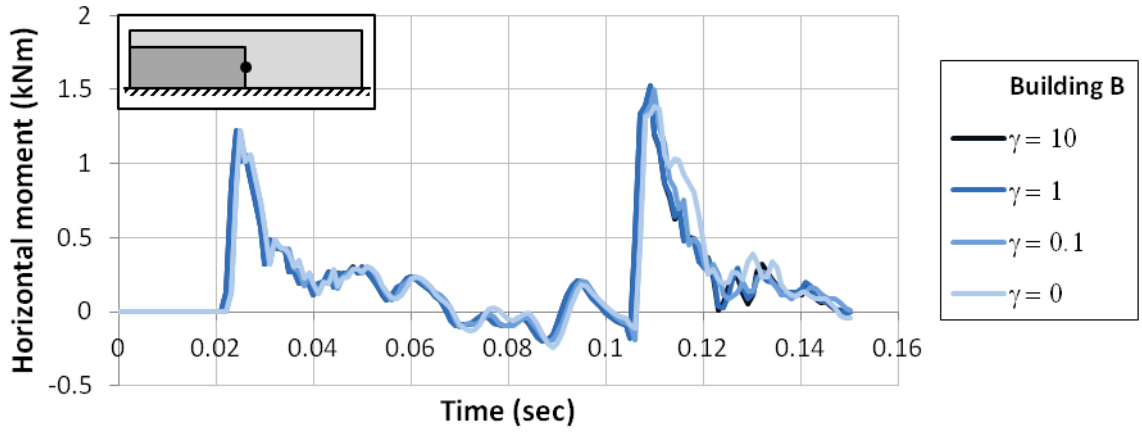

Figure 10.17 Horizontal moments in Building B. Measured location corresponds to the mid-height of Building A's right wall.

10.2.6 Accurate Unequal Wall Model – Collision Behaviour

Finally, a more detailed description of the unequal wall collision behaviour is presented. The increased wall dimensions causes Building B's collision wall to become notably more flexible than the equal wall model. This additional flexibility subtlety changes the nature of the first contact between the walls. The collision still initiates at approximately 0.022 seconds with contact occurring around the perimeter of Building A's wall (Figure 10.18, Left). However some parts of the wall do not make contact with Building B during this collision. This is due to the contact in other areas of the wall transferring sufficient momentum to push Wall B away. In the initial collision, the bottom 0.6 m of the walls remains in contact for approximately 0.5 seconds (Figure 10.18, Right). This contact is significantly longer than that of the top section of wall, and reduces the demand moment caused by momentum transfer between the two walls.

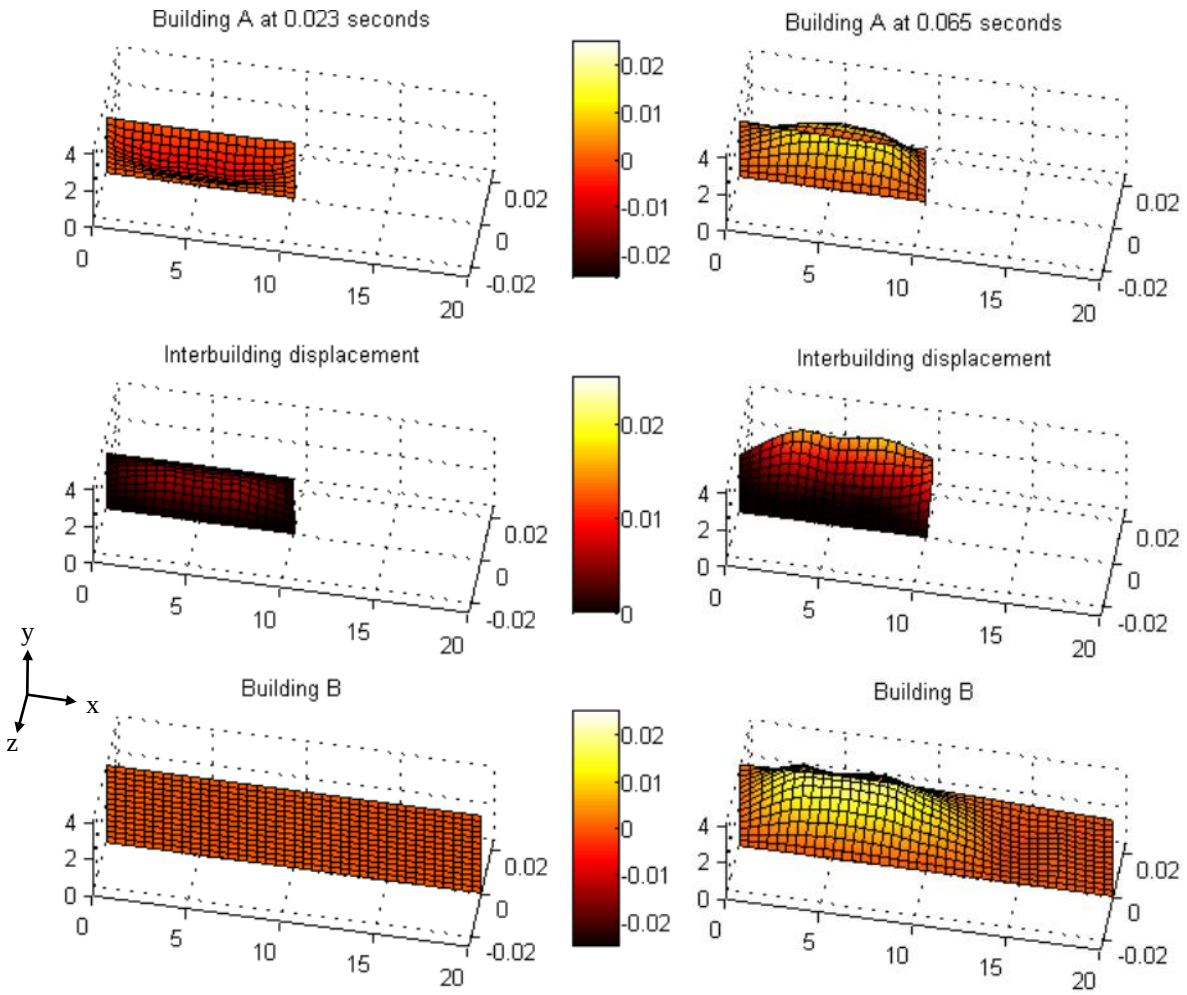

Figure 10.18 Snapshots of collision of two unequal walls at 0.023 and 0.065 seconds

The second collision occurs at approximately 0.1 seconds and creates a very different response (Figure 10.19, Left). The contact again begins with the perimeter of the wall. However, because both walls are in motion and are moving towards each other, all nodes on Wall A collide with their corresponding nodes on Wall B. Since the walls are in contact over a wide area, the walls' displacements are the same at this time (Figure 10.19, Right). The displacement patterns are not symmetric, due to the asymmetric positioning of Building B.

Throughout the recorded history, the second half of Wall B (between 10 and 20 meters) is not significantly affected by the wall collisions. The overall orientation of the wall does twist a little, however this response is minimised due to the large torsional stiffness in both buildings. The largest effect observed in this half of the wall was the maxima of a second mode wave which ran horizontally across the wall. While this effect is apparent, its significance on the overall wall response is minor.

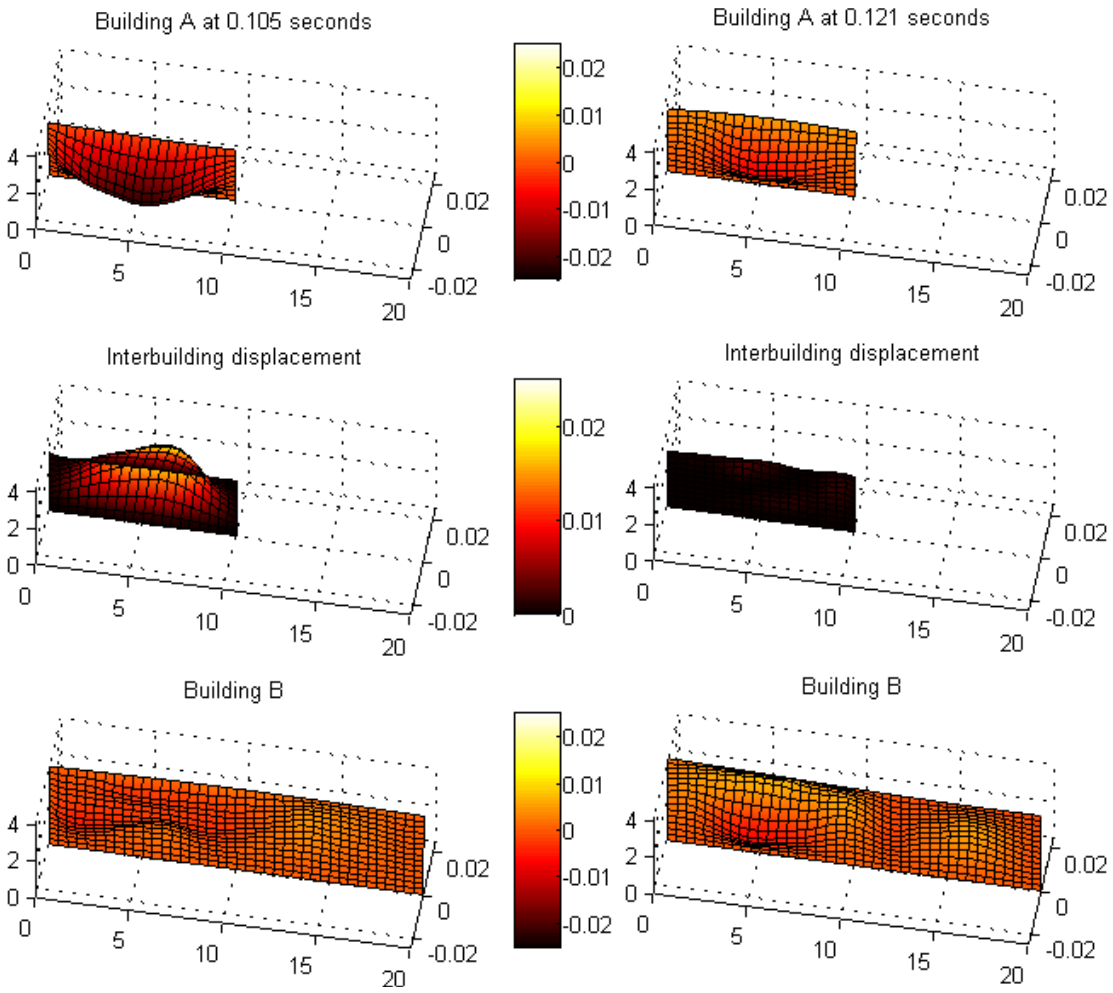

Figure 10.19 Snapshots of collision of two unequal walls at 0.105 and 0.121

Further analysis of the considered wall/wall collisions (such as showing how flexural and shear stresses propagate through each wall during collision) is not presented here. This is because the fundamental properties of wall/wall collision are considered to be well characterised by the responses that have been illustrated in previous figures. As the objectives of this work have been achieved (see the beginning of this chapter), further detailed wall/wall collision analysis is left as a subject for future research.

10.3 Conclusions

The following conclusions are drawn based on the results presented in Chapter 10:

1. Wall/wall configurations are less sensitive than floor/column configurations to shear stiffness. However, the effects of wall shear stiffness can still be significant for shear and moment results
2. Wall/wall collision elements can be broadly categories as either hard vs. hard, hard vs. soft or soft vs. soft collisions. Categorising in this manner is useful since the definition of collision element stiffness can be obtained from analogous floor/floor or floor/column situations.

3. Soft vs. soft collisions do not have an analogous collision configuration that has been already considered. It is recommended that these elements' stiffnesses be set equal to the stiffest contact element on the contact area's perimeter.
4. Soft vs. soft collision elements are not required if the capacities of the impacted walls are not of interest. This is because the majority of the momentum transfer during the collision occurs at locations of hard vs. hard or hard vs. soft collision elements.
5. Wall/wall collision causes a complex response in both walls. Different sections of the walls experience impact at different times. This response could be investigated in even more detail; however, such investigation is left as a subject for future research.

Chapter 11 Conclusions and Recommendations

This final chapter summarises the conclusions and key contributions of this project to the field of building pounding analysis. Particular focus is placed on the recommended analysis methods that have been developed throughout the thesis (Section 11.2). Limitations of the presented research (Section 11.3) and the opportunities for further research (Section 11.4) are also presented.

11.1 Conclusions and Key Contributions

This section presents the key advancements to the field of building pounding provided in this thesis. The most significant conclusions from the thesis are presented first. This is followed by a section of 'key contributions' which presents the primary elements of new understanding that have resulted from this work. Further, more detailed conclusions are available in the final sections of each chapter (excluding Chapter 1).

11.1.1 Conclusions

The following conclusions are drawn based upon the research presented throughout this thesis. The chapter where each conclusion was made is also identified to aid reference.

1. Severe pounding damage resulting in building collapse is rare, but has occurred in multiple earthquakes. While factors have been identified that greatly increase the risk of collapse due to pounding damage, further understanding of this phenomenon is necessary to design effective mitigation measures for existing buildings. [Chapter 2].
2. Building floor/floor collision can be modelled as the impact of two distributed masses. The predictions obtained using this model differs from those obtained using the traditionally adopted lumped mass models. The effect of this difference may be explicitly stated by considering the post collision velocities that are predicted by each method. This also produces a method by which distributed mass predictions may be emulated in lumped mass models. [Chapter 3].
3. Multiple methods can be developed to model energy dissipation during a distributed mass collision. However, all considered methods have drawbacks which limit their application. While viscous diaphragm damping is the most generally suitable model, researchers can select from any of the presented methods depending upon their specific modelling requirements. A general method to calibrate these elements for any considered building configuration has also been presented. [Chapter 4].
4. When building pounding is modelled, multiple modelling parameters require reassessment. In particular, the adopted time step and modal damping scheme may

significantly influence model predictions. Rayleigh modal damping is not recommended when modelling pounding. [Chapter 5].

5. While performing 2D analysis of pounding, interstorey shears were observed to increase by an average of 10% at roof level. High magnitude collision forces were also recorded, and maximum forces were found to remain approximately constant regardless of building separation (providing a collision occurred). Soil structure interaction was also found to significantly affect the predicted displacement and contact force results. However, interstorey shears were not notably changed. [Chapter 6].
6. Modelling of pounding in 3D introduces additional complexity to the adopted contact elements. Contact element stiffness was found to be most appropriately assigned in proportion to each contact element's tributary width. More complicated modelling methods were also explored but were not adopted. [Chapter 7].
7. The methods of collision prediction developed in Chapter 3 are found to predict the response of 3D floor/floor collision with reasonable accuracy when building rotation is not involved in collision. [Chapter 8].
8. When only minor building eccentricity is present in a model, reasonably accurate predictions of 3D building performance can be made using 2D modelling techniques. However, the average building amplifications of multiple ground motions are necessary to achieve this accuracy, and local damage information is not reliable. Floor flexibility must be included in these models since rigid slaving introduces significant additional errors. [Chapter 8].
9. Increasing building eccentricity generally increases the effects of pounding. However, this increase was observed to be reasonably small in the tested models. Eccentric building pounding requires 3D modelling to be accurately predicted. [Chapter 8].
10. Floor/column collision greatly increases the shear demand on the impacted columns. While ductility is also affected, column shear capacity is usually found to be the critical component. However, global building response is similar to that found to floor/floor collision. This is attributed to the near identical plan locations of force transfer between the two modelled buildings. [Chapter 9].
11. Depending on the relative height of adjacent floors, collision can be purely floor/column, a combination of floor/floor and floor/column, or purely floor/floor. The transitions between these types of response depend on the relative stiffness of the floors and columns involved in the collisions. [Chapter 9].

12. The calibration of many contact elements for out-of-plane wall/wall collision modelling can be performed using existing floor/floor and floor/column rules. This is because the response at each contact node has similar axial characteristics to the previously investigated models. A calibration method for the one situation that has not been previously addressed is developed. However this element is found to not significantly affect the global building response of either building. [Chapter 10].

11.1.2 Key Contributions and Findings

This section states the key findings and themes of this project. This list differs from the conclusions because the items are not restricted to observations from single chapters, and instead focus on more holistic observations about the nature of pounding.

The fundamental processes governing floor/floor collision – The end-on-end collision of two floors results in shock waves that propagate through each floor. Modelling this collision as the impact of two infinitely rigid floors (termed lumped masses) misrepresents the processes involved in floor/floor collision and can result in incorrect predictions of building performance. Two methods to include wave propagation in floor/floor collision models (the explicit modelling of floor diaphragms and the equivalent lumped mass element) have been developed and tested. Tools that compare the effects of these models against lumped mass modelling have also been developed. The level of inelasticity present in these collisions is difficult to quantify; however, the developed models provide parameters that allows the user to specify the expected level of collision plasticity. Using these models and tools, researchers can explicitly quantify the effects of diaphragm wave propagation on floor/floor collision.

Global building response vs. local element response resulting from pounding – Pounding damage causes two distinct types of building response and damage. Damage is firstly caused in the building components that come into direct contact with the adjacent building during a collision (local damage). The remaining building elements can also suffer damage, or can be beneficially affected, as a result of the momentum transfer that occurs between the two buildings during collision (global damage). Measures of global building response include; interstorey shear, member curvature ductility away from the point of collision, and maximum displacement envelopes. Local element response depends on the specific building configuration, but includes the impacted floors, columns and/or walls. Local damage can also usually be assessed by inspecting the contact force recorded in the collision element.

The two phenomena respond differently when the initial building separation is adjusted, and are not strongly correlated to one another. In the tests performed in this thesis, the effects of global building response are typically greatest when zero building separation is present, and usually reduce with increasing building separation. As separation increases to the point where no building collision occurs, the global building response returns to the response predicted when no other buildings are modelled. However, local element actions were found to generally increase with increasing separation over a specific range. Building separations up to 80% of that required to prevent building collision were found to cause similar local element responses to buildings with zero separation. The differences in global and local behaviour mean that they must be investigated separately and not inferred from the response of the other.

Low rise buildings' vulnerability to pounding – This thesis emphasizes the effects of pounding on buildings with three storeys or less. Buildings with favourable geometries (such as well distributed structural elements in plan with no major vertical irregularities), but poor seismic performance (such as buildings designed before building codes required capacity design for seismic loads) are used for all analyses. Previous researchers have almost exclusively investigated the pounding potential of much taller buildings. Low rise buildings with pounding potential are common in many New Zealand towns and cities. Analyses of the modelled low rise buildings have predicted failure of building elements in multiple floor/column collision configurations. Building member failure was only predicted for floor/floor pounding when the ground motion amplitude was increased (test *2xPGA*). However, many floor/floor analyses showed increased member demands due to pounding, indicating the buildings' vulnerability to pounding in larger excitations. It was found that low rise buildings can suffer partial or complete building collapse as a direct result of building pounding.

Additional quantitative data on the effects of building pounding – While the tests performed in this thesis are limited to a few building configurations, a significant amount of data has been generated which describes the change in building response caused by pounding. Global building responses were observed to be remarkably similar for floor/column and floor/floor collision configurations, and are described together here. Building interstorey shear was observed to be amplified and de-amplified due to pounding, depending on the specific building configuration and ground motion. Interstorey shear loads were in most cases 30% – 40% greater than the shears of the buildings without pounding. In a few records, the shear increased by over 100%. Maximum member curvature ductilities from pounding analyses were similarly affected.

Floor/floor collision forces as great as 8 MN were recorded during pounding. However, collision force is dependent upon the mass of each colliding object, so this value could change significantly for other building configurations. In floor/column collisions, impacted columns' shears were as much as 18 times larger than the corresponding shears with no pounding. This level of shear increase frequently exceeds the impacted columns' shear capacity. The data in this thesis is not sufficiently broad to generalise to all buildings, however it does indicate approximate magnitudes of the response change that may be expected from pounding for similar configurations.

The significance of column stiffness in floor/column collision – The increase in shear demand on a specific column undergoing floor/column impact is affected by that column's effective impact stiffness, but is also affected by the effective impact stiffness of other columns undergoing impact at the same time. A larger effective impact stiffness causes greater shear amplification in the considered column. A column's effective impact stiffness describes the stiffness of the column when subjected to a point load at the expected location of collision. This property can be approximately evaluated by assuming the column has fully rigid supports at the top and bottom of its clear span. The effective stiffness is dependent upon the location of collision in addition to the properties of the impacted column. These properties make it possible for the location of the most vulnerable columns to change when the impact location is modified.

Recommended pounding modelling techniques - The primary output of this thesis involves recommendations for how pounding should be modelled in analysis. Modelling of floor/floor, floor/column and floor/wall configurations have been developed separately, but follow a similar modelling philosophy. The following section summarises the modelling techniques recommended in this thesis for a variety of possible analysis problems.

11.2 Recommended Pounding Modelling Techniques

Table 11.1 and Figure 11.1 summarise the recommended techniques for modelling building pounding in various situations. All these models use the Kelvin element to represent contact between objects. In this table, 'rigid end block' refers to the depth of the perimeter beam on the impacted floor. Note that in-plane wall collision is considered to be functionally equivalent to floor/floor collision (see Section 10.2.2). All the presented models can incorporate additional collision-specific energy dissipation through the use of the plasticity index, r. Calibration of a specific damping model's plasticity index is described in Section 4.11.

Table 11.1 Summary of recommended modelling methods for various building configurations

Collision type	Case	Collision element stiffness (k_C)	Width of diaphragm (w) for k_C calculation	Number of elements in impacted component
Floor/floor	Detailed model	$k_c = \min[k_1 , k_2]$	w = sum of half the distance to the next contact element in each direction	At least two axial elements in each floor
	Equivalent lumped mass model	$k_C = \frac{\frac{m_1 m_2}{m_1 + m_2}\left(\frac{\pi}{T_1}\right)^2}{1-\zeta^2}$ $\zeta = \frac{-\ln(e_{eff})}{\sqrt{\pi^2 + (\ln(e_{eff}))^2}}$ $e_{eff} = r\left(2\frac{\left(\frac{m_1}{m_2}+1\right)}{\frac{T_2 m_1}{T_1 m_2}+1} - 1\right)$ $T_i = \sqrt{\frac{diaphragm\,mass}{diaphragm\,stiffness}}$ m_i = *diaphragm mass* r = *plasticity index*	N/A	No axial elements in each floor (alternatively, all axial floor elements are completely rigid)
Floor/Column	$k_{col} < \min[k_1, k_2]$ & a > rigid end block	$k_c = k_1$	w = sum of the centroidal distance assuming 45° spread of load in each direction	At least three axial elements in each floor, at least four flexural elements with shear stiffness in each column
	$k_{col} \geq \min[k_1, k_2]$ & a > rigid end block	$k_c = \min[k_1, k_2]$		
	a ≤ rigid end block	Equivalent to floor/floor collision		
Wall collision	out-of-plane hard vs. hard collision	Equivalent to floor/floor collision	Equivalent to floor/floor collision	At least three axial elements in each floor/wall
	out-of-plane hard vs. soft collision	Equivalent to floor/column collision	Equivalent to floor/column collision	Equivalent to floor/column collision
	out-of-plane soft vs. soft collision	Use largest k_c from wall perimeter	N/A	Determined by out-of-plane wall modelling requirements
	in-plane collision	Equivalent to floor/floor collision	Equivalent to floor/floor collision	At least three axial elements in each floor/wall

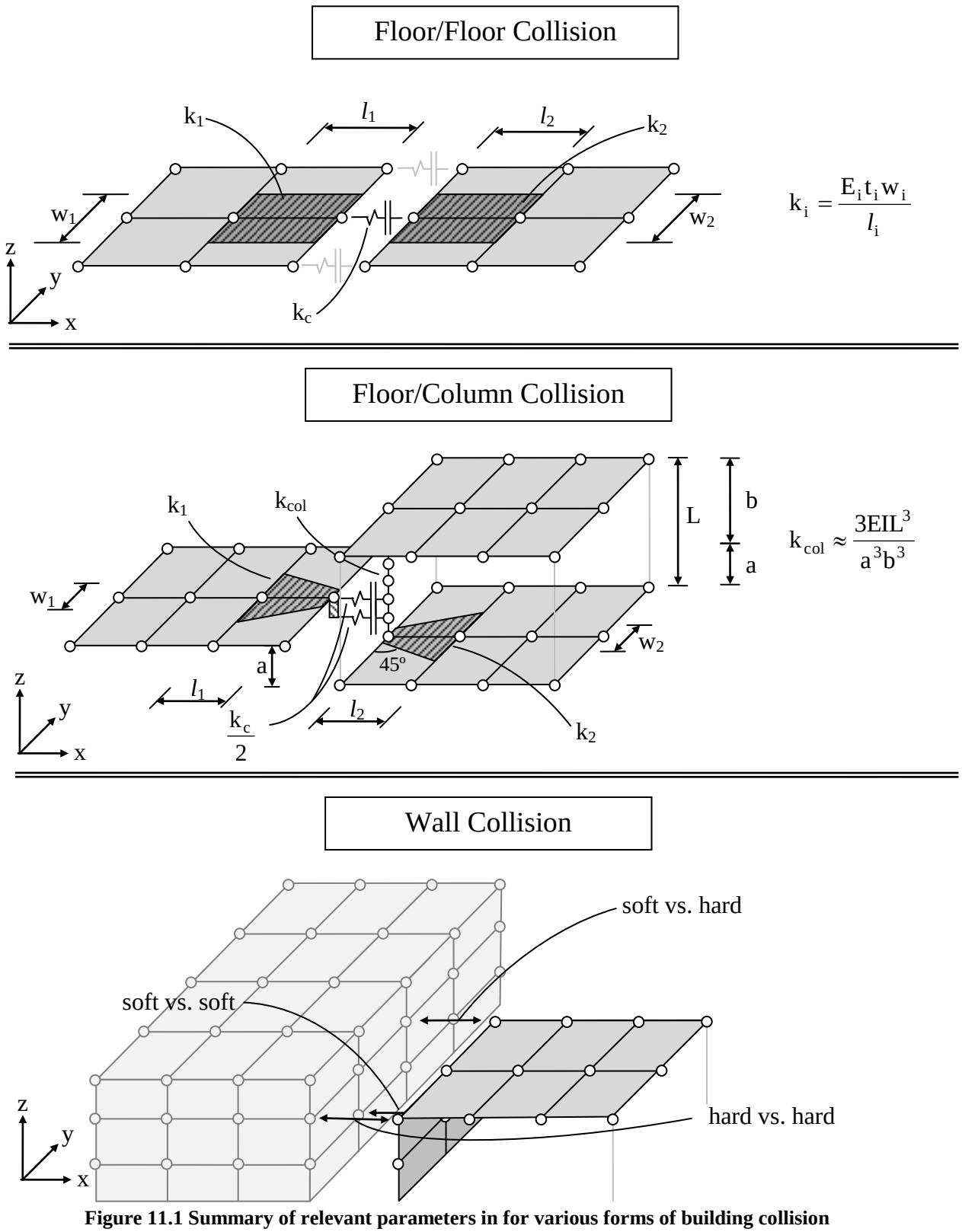

Figure 11.1 Summary of relevant parameters in for various forms of building collision

11.3 Research Limitations

The applicability of the presented research is primarily limited by the lack of supporting experimental evidence, the potential for errors within the adopted software and the small number of modelled buildings. While considerable time has been spent by multiple parties checking the implementation of Ruaumoko algorithms, the possibility of error within the presented analyses

(whether in the program or the individual models) must be acknowledged. The simplest way to address this potential error source is comparison with experimental data. However, experiments also require a further time investment that is not possible here. The small variety of buildings considered in this project is an inevitable consequence of the available time and computing power. The adopted modelling approach enabled in-depth analysis of the modelled buildings configurations; however, it also limited the types of buildings that could be investigated. This does leave some fragility in the results, since there is a chance that these buildings respond atypically to pounding (compared to other low rise buildings). However, the adopted models were selected with considerable care to address this issue, so the risk is considered to be small.

Other more specific limitations of the adopted modelling methods are listed throughout this thesis (most of these limitations are discussed in Chapter 5). Limitations include:

1. Modelling of soil-structure interaction using comparatively simple models.
2. Assuming that building collisions behave primarily elastically.
3. Various idealisations of building member hystereses.

Each of these limitations has been necessary to perform the presented analyses, and their likely effects have been discussed within the text. However, they are reiterated here to emphasize these potential error sources. Future investigations into any of these aspects could further improve the modelling of pounding buildings.

11.4 Avenues for Future Research

Despite the extensive previous research that has been performed investigating building pounding, many topics would benefit from further attention. The following list highlights topics of particular interest and relevance to the subjects discussed in this thesis. These topics are roughly listed in order of decreasing importance.

Physical testing of floor/column impact – Chapter 9 makes numerous assumptions about the performance of floor/column collisions because experimental data is not available. Physical testing of floor/column collision could provide confirmation of the column failure mechanism (flexural failure, traditional shear failure, or direct shear failure), in addition to quantifying strain rate effects for this type of collision. It is envisaged that such testing could be performed using a physical specimen similar to the model shown for floor/column collision in Figure 11.1, where the floor causing collision is suspended with cables. Impact could be initiated by pulling the floor back and then releasing it, effectively creating an impact ‘pendulum’. Testing in this manner would also show the damage suffered by the floor during collision. It is also possible that

testing in this manner could verify whether column damage can be predicted using simplified analysis methods. Alternatively, column damage could be investigated by using a drop hammer onto a horizontal column. In such circumstances care must be used to ensure the floors' response can be accurately approximated using a point mass.

Detailed modelling of soil-structure-interaction in pounding modelling – Section 6.8 illustrates that pounding modelling is sensitive to soil structure interaction. Given this sensitivity, a more thorough modelling of the soil would bring additional insight and accuracy to pounding analyses. Ideally such work should be undertaken by researchers with a background in the dynamic analysis of soil, in order to compliment the primarily structural focus of the present thesis.

Detailed evaluation of energy loss during collision – As discussed in Section 2.2, energy dissipation during collision has not been accurately defined to date. The majority of previous experiments use spherical objects to calculate impact energy loss. However, both floor/floor and floor/column collisions usually involve the collision of two flat surfaces. It is hoped detailed experimentation in this area could provide appropriate values for the coefficient of restitution (e) and plasticity index (r). It is also possible that such experimentation would show that e and r can not accurately predict energy dissipation. If such experiments were performed, characterisation of the contact coefficient of friction would also be beneficial.

Numerical testing of common New Zealand building pounding situations – New Zealand cities frequently have building configurations with one or more low rise buildings that could be subjected to pounding during an earthquake. Monte – Carlo testing of typical New Zealand buildings would provide a much better understanding of the risk New Zealand buildings face from pounding. Data on floor accelerations due to pounding would also be useful to assist in quantifying damage to building contents. The above information would be particularly useful to the New Zealand engineering community since many of these buildings are currently undergoing retrofit. This topic was initially intended to be covered in this thesis; however, time constraints restricted the testing to a single building configuration.

Simplified prediction methods of pounding damage – Practising engineers are primarily interested in quickly quantifying the likely affects of pounding on a given building. While equations governing some aspects of pounding behaviour is produced in this thesis, they typically rely on non-linear time history analyses be performed. The one prediction equation proposed in this thesis (Equation 8.1) is promising, however it requires further verification. The

development of prediction methods that do not require detailed modelling would be of great benefit to the engineering community.

Detailed modelling of pounding between masonry buildings - Appendix A shows that much of the observed pounding damage in the Christchurch earthquakes occurred between masonry buildings. Detailed analysis of masonry structures has not been performed in this thesis because of the complexity of accurately modelling masonry as a material. However, further information about how masonry responds to impact is an important issue that potentially affects many New Zealand structures. Ideally such work would be performed by a researcher with a background in masonry performance using the modelling recommendations of this thesis.

Intra-building pounding consequences – As discussed in Section 1.3.3, pounding between elements within buildings has not been investigated in this project. However, damage has been previously documented (Figure 1.6) inside buildings as a result of collision between building elements. Investigation into the consequences of exceeding buildings' internal seismic separations could be useful, especially for buildings with particularly valuable contents (such as hospitals).

References

AIR. (1999). "Findings of the Air Post-Disaster Field Investigation Team; the Izmit Earthquake." from http://www.air-worldwide.com/_Public/NewsData/000136/Izmit_part2.pdf.

AIR. (2009). "Observations from the Magnitude 6.3 L'Aquila Earthquake." from www.air-worldwide.com/PublicationsItem.aspx?id=17228.

Anagnostopoulos, S. A. (1988). Pounding of Buildings in Series During Earthquakes. *Earthquake Engineering & Structural Dynamics* **16**(3): 443-456.

Anagnostopoulos, S. A. and Spiliopoulos, K. V. (1992). Investigation of earthquake induced pounding between adjacent buildings. *Earthquake Engineering & Structural Dynamics* **21**(4): 289-302.

Anagnostopoulos, S. A. (1995). Earthquake induced pounding: state of the art. *Proceedings, 10th European Conference on Earthquake Engineering; pp. 897-905*, A. A. Balkema, Rotterdam.

Anagnostopoulos, S. A. (1996). Building pounding re-examined: how serious a problem is it? *Eleventh World Conference on Earthquake Engineering; 1996*, Pergamon, Elsevier Science Ltd , [Oxford, England].

Anagnostopoulos, S. A. (2004). Equivalent viscous damping for modeling inelastic impacts in earthquake pounding problems. *Earthquake Engineering & Structural Dynamics* **33**(8): 897-902.

Anagnostopoulos, S. A. and Karamaneas, C. E. (2008a). Use of collision shear walls to minimize seismic separation and to protect adjacent buildings from collapse due to earthquake-induced pounding. *Earthquake Engineering & Structural Dynamics* **37**(12): 1371-1388.

Anagnostopoulos, S. A. and Karamaneas, C. E. (2008b). Collision Shear Walls to Mitigate Seismic Pounding of Adjacent Buildings. *14 WCEE: 14th World Conference on Earthquake Engineering Conference Proceedings*. Beijing, China.

Arnold, C. (1989). *The seismic design handbook*. New York, Van Nostrand Reinhold.

ASCE31 (2003). Seismic Evaluation of Existing Buildings. Reston, Virginia, American Society of Civil Engineers (ASCE).

Athanassiadou, C. J., Penelis, G. G. and Kappos, A. J. (1994). Seismic response of adjacent buildings with similar or different dynamic characteristics. *Earthquake Spectra* **10**(2): 293-317.

Azevedo, J. and Bento, R. (1996). Design criteria for buildings subjected to pounding. *Eleventh World Conference on Earthquake Engineering; 1996*, Pergamon, Elsevier Science Ltd , [Oxford, England].

Bentz, E. C. (2000). Response 2000, Reinforced Concrete Section Analysis using the Modified Compression Theory. Toronto, University of Toronto.

Berg, G. V. and Degenkolb, H. J. (1973). Engineering lessons from the Managua earthquake. *Managua, Nicaragua Earthquake December 23 1972*. New York, American Iron and Steel Institute. **5-21**.

Bertero, V. V. and Collins, R. G. (1973). Investigation of the failures of the Olive View stairtowers during the San Fernando earthquake and their implications on seismic design, Earthquake Engineering Research Center. **EERC 73-26**.

Bertero, V. V. (1986). Observations on Structural Pounding. The Mexico Earthquakes—1985: Factors Involved and Lessons Learned, Mexico City, Mexico, ASCE, New York, NY, USA.

Bi, K., Hao, H. and Chouw, N. (2011). Influence of ground motion spatial variation, site condition and SSI on the required separation distances of bridge structures to avoid seismic pounding. *Earthquake Engineering & Structural Dynamics* **40**(9): 1027-1043.

Building Act (2004). New Zealand, http://www.legislation.govt.nz. **Public Act 2004 No. 72**.

Carr, A. J. and Moss, P. J. (1994). Impact between buildings during earthquakes. *Bulletin of the New Zealand National Society for Earthquake Engineering* **27**(2): 107-113.

Carr, A. J. (2007). *Volumes 1-5: Ruaumoko manual*. Christchurch, University of Canterbury.

Chau, K. T. and Wei, X. X. (2001). Pounding of structures modelled as non-linear impacts of two oscillators. *Earthquake Engineering and Structural Dynamics* **30**(5): 633-651.

Chau, K. T., Wei, X. X., Guo, X. and Shen, C. Y. (2003). Experimental and theoretical simulations of seismic poundings between two adjacent structures. *Earthquake Engineering & Structural Dynamics* **32**(4): 537-554.

Chau, K. T., Wei, X. X., Shen, C. Y. and Wang, L. X. (2004). Experimental and Theoretical Simulations of Seismic Torsional Poundings between Two Adjacent Structures. *13 WCEE: 13th World Conference on Earthquake Engineering Conference Proceedings*, Venue West Conference Services Ltd , Suite 645 - The Landing, 375 Water Street, Vancouver, B.C , V6B 5C6, Canada.

Chopra, A. K. (2007). *Dynamics of Structures: Theory and Applications to Earthquake Engineering*. New Jersey, Prentice Hall.

Chouw, N. and Schmid, G. (1995). Influence of soil-structure interaction on pounding between buildings during earthquakes. *Proceedings, 10th European Conference on Earthquake Engineering; pp. 553-558*, A. A. Balkema, Rotterdam.

Chouw, N. (2002a). Influence of soil-structure interaction on pounding response of adjacent buildings due to near-source earthquakes. *Japanese Society of Civil Engineers Journal of Applied Mechanics* **5**: 543 - 553.

Chouw, N. (2002b). *Analysis of pounding responses of soil-structures system to near-source earthquakes*. Beijing, Science Press Beijing.

Chouw, N. and Hao, H. (2005). Study of SSI and non-uniform ground motion effect on pounding between bridge girders. *Soil Dynamics and Earthquake Engineering* **25**(7-10): 717-728.

Cole, G. L., R. P. Dhakal, Carr, A. J. and Bull, D. K. (2009), *The Effect of Diaphragm Wave Propagation on the Analysis of Pounding Structures*. Computational Methods in Structural Dynamics and Earthquake Engineering 2009: Rhodes, Greece.

Cole, G. L., R. P. Dhakal, Carr, A. J. and Bull, D. K. (2009b), *The Significance of Lumped or Distributed Mass Assumptions on the Analysis of Pounding Structures.* 13th Asia Pacific Vibration Conference, 2009: Christchurch, New Zealand.

Cole, G. L., Dhakal, R. P., Carr, A. J. and Bull, D. K. (2010). *Interbuilding pounding damage observed in the 2010 Darfield earthquake*. Bulletin of the New Zealand Society for Earthquake Engineering **43**(4): 382 - 386.

Cole, G. L., R. P. Dhakal, Carr, A. J. and Bull, D. K. (2010b), *Distributed Mass Effects on Building Pounding Analysis*, in 9th US National and 10th Canadian Conference on Earthquake Engineering. 2010: Toronto, Canada

Cole, G. L., Dhakal, R. P., Carr, A. J. and Bull, D. K. (2010c). *Building pounding state of the art: Identifying structures vulnerable to pounding damage*. New Zealand Society for Earthquake Engineering Annual Conference (NZSEE 2010). Wellington, New Zealand: paper P11.

Cole, G. L., R. P. Dhakal, Carr, A. J. and Bull, D. K. (2010d). *Comparing Contact Elements' Abilities to Model Critical Pounding Problems*. Asia Conference on Earthquake Engineering (ACEE 2010). Bangkok, Thailand.

Cole, G. L., R. P. Dhakal, Carr, A. J. and Bull, D. K. (2011) *An Investigation of the Effects of Mass Distribution on Pounding Structures*. Earthquake Engineering & Structural Dynamics, 2011. **40**(6)

Cole, G. L., R. P. Dhakal, A. J. Carr and D. K. Bull (2011b). *Case studies of observed pounding damage during the 2010 Darfield earthquake*. Pacific Conference on Earthquake Engineering (PCEE 2011). Auckland, New Zealand: paper 173.

Cole, G. L., R. P. Dhakal and D. K. Bull (2011c). *Adjacent building hazard – how poorly performing buildings endanger neighbouring buildings' occupants*. Pacific Conference on Earthquake Engineering (PCEE 2011). Auckland, New Zealand: paper 170.

Cole, G. L., Dhakal, R. P., Carr, A. J. and Bull, D. K. (2011d). Bridge and building pounding damage observed in the 2011 Christchurch Earthquake. *Bulletin of the New Zealand Society for Earthquake Engineering* **44**(4): 334 - 341.

Cole, G. L., Dhakal, R. P. and Turner, F. M. (2012). Building pounding damage observed in the 2011 Christchurch earthquake. *Earthquake Engineering & Structural Dynamics* **41**(5): 893-913.

Cole, G., Dhakal, R., Carr, A. J. and Bull, D. (2012b). *The influence of pounding on member demands in low rise buildings*. New Zealand Society for Earthquake Engineering Annual Conference (NZSEE 2012). Christchurch, New Zealand**:** paper 026.

Conoscente, J. P., Hamburger, R. O. and Johnson, J. J. (1992). Dynamic analysis of impacting structural systems. *Proceedings of the Tenth World Conference on Earthquake Engineering; pp. 3899-3903*, A. A. Balkema, Rotterdam.

Cooper, M., Carter, R. and Fenwick, R. (2011). *Interim Report*, New Zealand Royal Commission.

Cousins, J. and McVerry, G. H. (2010). Overview of strong motion data from the Darfield earthquake. *Bulletin of the New Zealand Society for Earthquake Engineering* **43**(4): 222 - 227.

Davis, R. O. (1992). Pounding of buildings modelled by an impact oscillator. *Earthquake Engineering & Structural Dynamics* **21**(3): 253-274.

Dimitrakopoulos, E., Kappos, A. J. and Makris, N. (2009a). Dimensional analysis of yielding and pounding structures for records without distinct pulses. *Soil Dynamics and Earthquake Engineering* **29**(7): 1170-1180.

Dimitrakopoulos, E., Makris, N. and Kappos, A. J. (2009b). Dimensional analysis of the earthquake-induced pounding between adjacent structures. *Earthquake Engineering & Structural Dynamics* **38**(7): 867-886.

Dimitrakopoulos, E., Makris, N. and Kappos, A. (2010a). Dimensional analysis of the earthquake-induced pounding between inelastic structures. *Bulletin of Earthquake Engineering*: 1-19.

Dimitrakopoulos, E., Makris, N. and Kappos, A. J. (2010b). Dimensional Analysis of the Earthquake Response of a Pounding Oscillator. *Journal of Engineering Mechanics* **136**(3): 299-310.

Dizhur, D., Ismail, N., et al. (2010). Performance of unreinforced and retrofitted masonry buildings during the 2010 Darfield earthquake. *Bulletin of the New Zealand Society for Earthquake Engineering* **43**(4): 321 - 339.

Dizhur, D., Ingham, J., et al. (2011). Performance of masonry buildings and churches in the 22 February 2011 Christchurch earthquake. *Bulletin of the New Zealand Society for Earthquake Engineering* **44**(4): 279-296.

Dong, P. (2003). Effect of varying hysteresis models and damage models on damage assessment of r/c structures under standard design level earthquakes obtained using a new scaling method. *Civil Engineering*. Christchurch, University of Canterbury. **Doctorial Thesis**.

Elanshai, A. S., Kim, S. J., Yun, G. J. and Sidarta, D. (2007). The Yogyakarta earthquake of May 27, 2006, Mid-America Earthquake Center. **07- 02**.

Evans, N. and Wells, J. (2008). "Gisborne Earthquake Impacts on Buildings and Lifelines." Retrieved 27/01/2011, from http://db.nzsee.org.nz/2008/Pres2.4.pdf.

Favvata, M. J. and Karayannis, C. G. (2008). Non-linear static versus dynamic analyses for the interaction of structures. *7th European Conference on Structural Dynamics, EURODYN*. Southampton**:** E218.

Filiatrault, A. and Folz, B. (1992). Nonlinear earthquake response of structurally interconnected buildings. *Canadian Journal of Civil Engineering* **19**(4): 560-572.

Filiatrault, A., Cervantes, M., Folz, B. and Prion, H. (1994). Pounding of buildings during earthquakes: a Canadian perspective. *Canadian Journal of Civil Engineering* **21**(2): 251-265.

Filiatrault, A. and Cervantes, M. (1995). Separation between buildings to avoid pounding during earthquakes. *Canadian Journal of Civil Engineering* **22**(1): 164-179.

Filiatrault, A., Wagner, P. and Cherry, S. (1995). Analytical prediction of experimental building pounding. *Earthquake Engineering & Structural Dynamics* **24**(8): 1131-1154.

Filiatrault, A., Wagner, P. and Cherry, S. (1996). An experimental study on the seismic pounding of buildings. *Eleventh World Conference on Earthquake Engineering; 1996*, Pergamon, Elsevier Science Ltd , [Oxford, England].

Ford, C. R. (1926). *Earthquakes and Building Construction*. Auckland, Whitcombe and Tombs Ltd.

Garcia, D. L. (2004). Separation distance necessary to prevent seismic pounding between adjacent structures. *Department of Civil, Structural and Environmental Engineering*. Buffalo, State University of New York at Buffalo. **Doctorial Thesis**.

Geonet. (2011). "New Zealand Earthquake Report - Feb 22 2011." Retrieved 06/05/2011, 2011, from http://www.geonet.org.nz/earthquake/quakes/3468575g.html.

Gillies, A. G., Anderson, D. L., et al. (2001). The August 17, 1999, Kocaeli (Turkey) earthquake — lifelines and preparedness. *Canadian Journal of Civil Engineering* **28**: 881-890.

Gledhill, K., Ristau, J., et al. (2010). The Darfield (Canterbury) Earthquake of September 2010: Preliminary Seismological Report. *Bulletin of the New Zealand Society for Earthquake Engineering* **43**(4): 215 - 221.

Goldsmith, W. (1960). *Impact: the theory and physical behaviour of colliding solids*. London, E. Arnold.

Google. (2011). "Google Maps New Zealand." Retrieved 28/03/2011, 2011, from http://maps.google.co.nz/.

Govil, S. and Singhal, A. (1991). Damage reduction with controlled seismic pounding. *Soil Dynamics and Earthquake Engineering V*, Computational Mechanics Publications and Elsevier Applied Science, Southampton, England, and London: pp. 627-638.

Guo, A., Li, Z. and Li, H. (2008). Experimental Study of Highway Bridges with Pounding Effects Subject Bi-Directional Earthquake Excitations. *14 WCEE: 14th World Conference on Earthquake Engineering Conference Proceedings*. Beijing, China.

Guo, A., Li, Z., Li, H. and Ou, J. (2009). Experimental and analytical study on pounding reduction of base-isolated highway bridges using MR dampers. *Earthquake Engineering & Structural Dynamics* **38**(11): 1307-1333.

Hadi, N. S. and Uz, M. E. (2009). Improving the dynamic behaviour of adjacent buildings by connecting them with fluid viscous dampers. *COMPDYN: Computational Methods in Structural Dynamics and Earthquake Engineering*. Rhodes, Greece.

Hao, H. (1998). A parametric study of the required seating length for bridge decks during earthquake. *Earthquake Engineering & Structural Dynamics* **27**(1): 91-103.

Hao, H. and Zhang, S.-R. (1999). Spatial ground motion effect on relative displacement of adjacent building structures. *Earthquake Engineering & Structural Dynamics* **28**(4): 333-349.

Hong, H. P., Wang, S. S. and Hong, P. (2003). Critical building separation distance in reducing pounding risk under earthquake excitation. *Structural Safety* **25**(3): 287-303.

ICCPDC, INCERC and IPCT (1978). The Romania, 4 March 1977, earthquake and its effects on strucutres *CO.P.I.S.E.E International congress on earthquake protection of construction in seismic areas*. Bucharest.

Jagiasi, A. R. and Kasai, K. (1996). Estimate and control of relative displacement between adjacent structures.

Jankowski, R. (2004). Non-Linear Viscoelastic Model of Structural Pounding. *13 WCEE: 13th World Conference on Earthquake Engineering Conference Proceedings*, Venue West Conference Services Ltd , Suite 645 - The Landing, 375 Water Street, Vancouver, B.C , V6B 5C6, Canada.

Jankowski, R. (2005). Non-linear viscoelastic modelling of earthquake-induced structural pounding. *Earthquake Engineering & Structural Dynamics* **34**(6): 595-611.

Jankowski, R. (2006). Pounding force response spectrum under earthquake excitation. *Engineering Structures* **28**(8): 1149-1161.

Jankowski, R. (2008). Earthquake-induced pounding between equal height buildings with substantially different dynamic properties. *Engineering Structures* **30**(10): 2818-2829.

Jankowski, R. (2009). Non-linear FEM analysis of earthquake-induced pounding between the main building and the stairway tower of the Olive View Hospital. *Engineering Structures* **31**(8): 1851-1864.

Jankowski, R. (2010). Experimental study on earthquake-induced pounding between structural elements made of different building materials. *Earthquake Engineering & Structural Dynamics* **39**(3): 343-354.

Jankowski, R. (2012). Non-linear FEM analysis of pounding-involved response of buildings under non-uniform earthquake excitation. *Engineering Structures* **37**(0): 99-105.

Jeng, V., Kasai, K. and Maison, B. F. (1992). A spectral difference method to estimate building separations to avoid pounding. *Earthquake Spectra* **8**(2): 201-223.

Jeng, V. and Kasai, K. (1996). Spectral Relative Motion of Two Structures due to Seismic Travel Waves. *Journal of Structural Engineering* **122**(10): 1128-1135.

Jeng, V. and Tzeng, W. L. (2000). Assessment of seismic pounding hazard for Taipei City. *Engineering Structures* **22**(5): 459-471.

Karayannis, C. G. and Favvata, M. J. (2005a). Earthquake-induced interaction between adjacent reinforced concrete structures with non-equal heights. *Earthquake Engineering & Structural Dynamics* **34**(1): 1-20.

Karayannis, C. G. and Favvata, M. J. (2005b). Inter-story pounding between multistory reinforced concrete structures. *Structural Engineering and Mechanics* **20**(5): 505-526.

Kasai, K., Jeng, V., et al. (1992). Seismic pounding effects -- survey and analysis. *Proceedings of the Tenth World Conference on Earthquake Engineering; pp. 3893-3898*, A. A. Balkema, Rotterdam.

Kasai, K., Jagiasi, A. R. and Jeng, V. (1996a). Inelastic vibration phase theory for seismic pounding mitigation. *Journal of Structural Engineering* **122**(10): 1136-1146.

Kasai, K., Jagiasi, A. R. and Maison, B. F. (1996b). Survey and analysis of building pounding during 1989 Loma Prieta earthquake. *Eleventh World Conference on Earthquake Engineering; 1996*, Pergamon, Elsevier Science Ltd , [Oxford, England].

Kasai, K. and Maison, B. F. (1997). Building pounding damage during the 1989 Loma Prieta earthquake. *Engineering Structures* **19**(3): 195-207.

Komodromos, P., Polycarpou, P. C., Papaloizou, L. and Phocas, M. C. (2007). Response of seismically isolated buildings considering poundings. *Earthquake Engineering & Structural Dynamics* **36**(12): 1605-1622.

Kramer, S. L. (1996). *Geotechnical Earthquake Engineering*. Upper Saddle River NJ, Prentice Hall.

Lavan, O. (2009). Contact Analysis in the Mixed Lagrangian Framework. *COMPDYN 2009*. M. Papadrakakis, N. D. Lagaros and M. Fragiadakis. Rhodes, Greece.

Lavelle, F. M. and Sues, R. H. (1992). Seismic pounding retrofits for closely spaced buildings. *Proceedings of the Tenth World Conference on Earthquake Engineering; pp. 5367-5372*, A. A. Balkema, Rotterdam.

Leibovich, E., Rutenberg, A. and Yankelevsky, D. Z. (1996). On eccentric seismic pounding of symmetric buildings. *Earthquake Engineering & Structural Dynamics* **25**(3): 219-233.

Leibovich, E. and Rutenberg, A. (1998). *Symmetric and eccentric seismic pounding of yielding building structures*. Technion, Israel Institute of Technology.

Lin, J. H. and Weng, C. C. (2001). Probability analysis of seismic pounding of adjacent buildings. *Earthquake Engineering and Structural Dynamics* **30**(10): 1539-1557.

Lindsay, B., Li, B., Chouw, N. and Butterworth, J. W. (2011). *Seismic pounding of bridge superstructures at expansion joints*. Pacific Conference on Earthquake Engineering (PCEE 2011). Auckland, New Zealand: paper 155.

Lopez-Garcia, D. and Soong, T. T. (2009). Evaluation of current criteria in predicting the separation necessary to prevent seismic pounding between nonlinear hysteretic structural systems. *Engineering Structures* **31**(5): 1217-1229.

Low, H. Y. and Hao, H. (2002). Reliability analysis of direct shear and flexural failure modes of RC slabs under explosive loading. *Engineering Structures* **24**(2): 189-198.

Luco, J. E. and De Barros, F. C. P. (1998). Optimal damping between two adjacent elastic structures. *Earthquake Engineering & Structural Dynamics* **27**(7): 649-659.

Mahmoud, S. and Jankowski, R. (2009). Elastic and Inelastic Multi-Storey Buildings Under Earthquake Excitation with the Effect of Pounding. *Journal of Applied Sciences (Faisalabad)* **9**(18): 3250-3262.

Maison, B. F. and Kasai, K. (1990). Analysis for type of structural pounding. *Journal of Structural Engineering* **116**(4): 957-977.

Maison, B. F. and Kasai, K. (1992). Dynamics of pounding when two buildings collide. *Earthquake Engineering & Structural Dynamics* **21**(9): 771-786.

Masroor, A. and Mosqueda, G. (2012). Experimental simulation of base-isolated buildings pounding against moat wall and effects on superstructure response. *Earthquake Engineering & Structural Dynamics*: *early view*. DOI: 10.1002/eqe.2177

Matsumoto, T. and Kawashima, K. (2008). Effect of Pounding on the Seismic Performance of Continuous Buildings. *14 WCEE: 14th World Conference on Earthquake Engineering Conference Proceedings*. Beijing, China.

Mouzakis, H. P. and Papadrakakis, M. (2004). Three dimensional nonlinear building pounding with friction during earthquakes. *Journal of Earthquake Engineering* **8**(1): 107-132.

Muthukumar, S. and DesRoches, R. (2004). Evaluation of Impact Models for Seismic Pounding. *13 WCEE: 13th World Conference on Earthquake Engineering Conference Proceedings*. Vancouver, Canada.

Muthukumar, S. and DesRoches, R. (2006). A Hertz contact model with non-linear damping for pounding simulation. *Earthquake Engineering & Structural Dynamics* **35**(7): 811-828.

NZ Police. (2011). "List of deceased." Retrieved 14/06/2011, 2011, from http://www.police.govt.nz/list-deceased.

NZS1170.5 (2004). Structural Design Actions. *Part 5: Earthquake Actions - New Zealand*. Wellington, Standards New Zealand.

NZS1900.8 (1964). Model building bylaw. *Chapter 8: Basic design loads*. Wellington, Standards New Zealand.

NZS3101 (2006). Concrete Structures Standard. *Part 1 - The Design of Concrete Structures.* Wellington, Standards New Zeland.

NZS4203 (1976). General structural design and design loadings for buildings. Wellington, Standards New Zealand.

NZSEE (1996). Assessment and Improvement of the Structural Performance of Buildings in Earthquakes, New Zealand Society of Earthquake Engineers.

Ohami, K., Otani, S. and Abe, S. (2008). Seismic Retrofit by Connecting to Adjacent Building. *14 WCEE: 14th World Conference on Earthquake Engineering Conference Proceedings*. Beijing, China.

Pallett, P., Gorst, N., Clark, L. and Thomas, D. (2002). Friction resistance in temporary works materials. *Concrete* **36**(6): 12-12.

Pantelides, C. P. and Ma, X. (1996). Nonlinear seismic pounding of inelastic structures. *Eleventh World Conference on Earthquake Engineering; 1996*, Pergamon, Elsevier Science Ltd , [Oxford, England].

Pantelides, C. P. and Ma, X. (1998). Linear and nonlinear pounding of structural systems. *Computers and Structures* **66**(1): 79-92.

Papadrakakais, M., Apostolopoulou, C., Zacharopoulos, A. and Bitzarakis, S. (1996). Three Dimensional Simulation of Structural Pounding During Earthquakes. *Journal of Engineering Mechanics* **122**(5): 423-431.

Papadrakakis, M., Mouzakis, H., Plevris, N. and Bitzarakis, S. (1991). Lagrange multiplier solution method for pounding of buildings during earthquakes. *Earthquake Engineering & Structural Dynamics* **20**(11): 981-998.

Papadrakakis, M. and Mouzakis, H. P. (1995). Earthquake simulator testing of pounding between adjacent buildings. *Earthquake Engineering & Structural Dynamics* **24**(6): 811-834.

Penzien, J. (1997). Evaluation of building separation distance required to prevent pounding during strong earthquakes. *Earthquake Engineering & Structural Dynamics* **26**(8): 849-858.

Pian, T. H. H. and Tong, P. (1972). Finite Element Methods in Continuum Mechanics. Advances in Applied Mechanics. Y. Chia-Shun, Elsevier. **Volume 12:** 1-58.

Polycarpou, P., Papaloizou, L., Mavronicola, E. and Komodromos, P. (2008). Numerical Simulation Of Seismically Isolated Buildings Considering Poundings With Adjacent Structures. *14 WCEE: 14th World Conference on Earthquake Engineering Conference Proceedings*. Beijing, China.

Raheem, S. E. A. (2006). Seismic pounding between adjacent building structures. *Electronic Journal of Structural Engineering* **6**: 66-74.

Rahman, A. M. (1999). Seismic Pounding of Adjacent Multiple-Storey Buildings Considering Soil-Structure Interaction and Through Soil Coupling. *Department of Civil Engineering*. Christchurch, University of Canterbury. **Doctorial thesis**.

Rahman, A. M., Carr, A. J. and Moss, P. J. (2000). Structural pounding of adjacent multi-storey structures considering soil flexibility effects.

Rahman, A. M., Carr, A. J. and Moss, P. J. (2001). Seismic pounding of a case of adjacent multiple-storey buildings of differing total heights considering soil flexibility effects. *Bulletin of the New Zealand Society for Earthquake Engineering* **34**(1): 40-59.

Rezavandi, A. and Moghadam, A. S. (2007). Experimental and numerical study on pounding effects and mitigation techniques for adjacent structures. *Advances in Structural Engineering* **10**(2): 121-134.

Rezavani, A. and Moghadam, A. S. (2004). Using Shaking Table to Study Different Methods of Reduceing Effects of Buildings Pounding During Earthquake. *13 WCEE: 13th World Conference on Earthquake Engineering Conference Proceedings*, Venue West Conference Services Ltd , Suite 645 - The Landing, 375 Water Street, Vancouver, B.C , V6B 5C6, Canada

Rosenblueth, E. and Meli, R. (1986). *The 1985 earthquake : causes and effects in Mexico City*.

Salem, Y. S. (2006). Mitigation of Building Pounding using Energy Dissipation Devices. *Civil Engineering*. Irvine, University of California. **Doctorial thesis**.

Salem, Y. S. and Feng, M. (2008). Shake Testing of Frame Structures Retrofitted with Viscous Dampers to Mitigate Seismic Pounding. *14 WCEE: 14th World Conference on Earthquake Engineering Conference Proceedings*. Beijing, China.

Schmid, G. and Chouw, N. (1992). Soil-structure interaction effects on structural pounding. *Proceedings of the Tenth World Conference on Earthquake Engineering; pp. 1651-1656*, A. A. Balkema, Rotterdam.

Shakya, K., Wijeyewickrema, A. C. and Ohmachi, T. (2008). Mid-Column Seismic Pounding of Reinforced Concrete Buildings in a Row Considering Effects of Soil. *14th World Conference on Earthquake Engineering: Innovation Practice Safety*, International Association for Earthquake Engineering.

Shakya, K. and Wijeyewickrema, A. C. (2009). Mid-Column Pounding of Multi-Story Reinforced Concrete Buildings Considering Soil Effects. *Advances in Structural Engineering* **12**(1): 71-85.

Sinclair, K. M. (1993). The response of multi-storey frames to seismic pounding. *Civil Engineering*. Christchurch, University of Canterbury. **Masters Thesis**.

Sozen, M. A. and Roesset, J. (1976). Structural damage caused by the 1976 Guatemala earthquake, University of Illinois at Urbana-Champaign. **Civil Engineering Studies, Structural Research Series No. 426**.

Spiliopoulos, K. V. and Anagnostopoulos, S. A. (1992). *Earthquake induced pounding in adjacent buildings*, Madrid, Spain, Publ by A.A. Balkema, Rotterdam, Neth.

Stavroulakis, G. E. and Abdalla, K. M. (1991). Contact between Adjacent Structures. *Journal of Structural Engineering* **117**(10): 2838-2850.

Stratta, J. L. and Wyllie, L. A. (1979). Friuli, Itally earthquakes of 1976. Oakland California, Earthquake Engineering Research Institute Reconnaissance Report.

Takeyama, K. (1973). Earhtquake response of a building collided with a neighbouring building. *Proc. 5th world conference on earhtquake engineering*. Rome**:** 2211-2214.

Tande, S. N. and Shinde, D. N. (2008). Optimal Seismic Response of Adjacent Coupled Buildings with Dampers. *14 WCEE: 14th World Conference on Earthquake Engineering Conference Proceedings*. Beijing, China.

Tubaldi, E., Barbato, M. and Ghazizadeh, S. (2012). A probabilistic performance-based risk assessment approach for seismic pounding with efficient application to linear systems. *Structural Safety* **36–37**(0): 14-22.

ULIEGE (2007). Analysis of hammering problems. Stage 2. *LessLoss Project: Risk Mitigation for Earthquakes and Landslides Integrated Project, Sixth Framework Programme Project No. GOCE-CT-2003-505488, Sub Project 7 - Techniques and methods for vulnerability reduction*, LESSLOSS.

Valles-Mattox, R. E. and Reinhorn, A. M. (1996). Evaluation, prevention and mitigation of pounding effects in building structures. *Eleventh World Conference on Earthquake Engineering; 1996*, Pergamon, Elsevier Science Ltd , [Oxford, England].

Valles, R. E. and Reinhorn, A. M. (1997). *Evaluation, prevention and mitigation of pounding effects in buildings structures*, National Center for Earthquake Engineering Research.

van Mier, J. G. M., Pruijssers, A. F., Reinhardt, H. W. and Monnier, T. (1991). Load-Time Response of Colliding Concrete Bodies. *Journal of Structural Engineering* **117**(2): 354-374.

Walker, A. F. and Dhakal, R. P. (2009). Assessment of material strain limits for defining plastic regions in concrete structures. *Bulletin of the NZ Society of Earthquake Engineering* **42**(2): 86-95.

Wang, L. X. and Chau, K. T. (2008). Chaotic Seismic Torsional Pounding between two Single-story Asymmetric Towers. *14th World Conference on Earthquake Engineering: Innovation Practice Safety*, International Association for Earthquake Engineering.

Wang, S. S. and Hong, H. P. (2006). Quantiles of critical separation distance for nonstationary seismic excitations. *Engineering Structures* **28**(7): 985-991.

Watanabe, G. and Kawashima, K. (2004). Numereical Simulation of Pounding of Bridge Decks. *13 WCEE: 13th World Conference on Earthquake Engineering Conference Proceedings*, Venue West Conference Services Ltd , Suite 645 - The Landing, 375 Water Street, Vancouver, B.C , V6B 5C6, Canada.

Westermo, B. D. (1989). The dynamics of interstructural connection to prevent pounding. *Earthquake Engineering & Structural Dynamics* **18**(5): 687-699.

Wilson, E. L. and Penzien, J. (1972). Evaluation of Orthogonal Damping Matrices. *International Journal of Numerical Methods in Engineering* **4**: 5-10.

Wolf, J. P. (1994). *Foundation vibration analysis using simple physical models*. Englewood Cliffs, NJ, PTR Prentice Hall.

Wood, P., Robins, P. and Hare, J. (2010). Preliminary Observations of the 2010 Darfield (Canterbury) Earthquakes: An Introduction. *Bulletin of the New Zealand National Society for Earthquake Engineering* **43**(4): i - iv.

Ye, K., Li, L. and Zhu, H. (2009). A note on the Hertz contact model with nonlinear damping for pounding simulation. *Earthquake Engineering & Structural Dynamics* **38**(9): 1135-1142.

Yu, Q. K. and Gonzalez, D. (2008). Lessons Learned from the October 15, 2006 Hawaii Earthquake and the August 15, 2007 Peru Earthquake. *14th World Conference on Earthquake Engineering: Innovation Practice Safety*, International Association for Earthquake Engineering.

Zhu, P., Abe, M. and Fujino, Y. (2002). Modelling three-dimensional non-linear seismic performance of elevated bridges with emphasis on pounding of girders. *Earthquake Engineering & Structural Dynamics* **31**(11): 1891-1913.

Appendix A The Christchurch Earthquakes

This appendix was originally intended to be a chapter in the main body of the thesis, and is formatted as such. References cited in this appendix are listed with the rest of the thesis' references. This section has been moved to the appendices because it deals with issues only tangentially related to the central subject of this thesis.

Related papers

Cole, G. L., R. P. Dhakal, et al. (2010). *Interbuilding pounding damage observed in the 2010 Darfield earthquake*. Bulletin of the New Zealand Society for Earthquake Engineering 43(4): 382 - 386.

Cole, G. L., R. P. Dhakal, A. J. Carr and D. K. Bull (2011). *Case studies of observed pounding damage during the 2010 Darfield earthquake*. Pacific Conference on Earthquake Engineering (PCEE 2011). Auckland, New Zealand: paper 173.

Cole, G. L., R. P. Dhakal and D. K. Bull (2011). *Adjacent building hazard – how poorly performing buildings endanger neighbouring buildings' occupants*. Pacific Conference on Earthquake Engineering (PCEE 2011). Auckland, New Zealand: paper 170.

Cole, G. L., Dhakal, R. P., Carr, A. J. and Bull, D. K. (2011). Bridge and building pounding damage observed in the 2011 Christchurch Earthquake. *Bulletin of the New Zealand Society for Earthquake Engineering* **44**(4): 334 - 341.

Cole, G. L., Dhakal, R. P. and Turner, F. M. (2012). Building pounding damage observed in the 2011 Christchurch earthquake. *Earthquake Engineering & Structural Dynamics* **41**(5): 893-913.

During the course of research for this thesis, multiple moderate to large earthquakes occurred in the Canterbury region. Pounding damage surveys were performed after each of the two largest magnitude earthquakes. This chapter presents the results of these surveys. The content presented in this chapter is largely reproduction of selected papers stated above. The modifications of these papers include reformatting to suit the thesis, minor additions of content, and rearranging of sections to provide better comparisons between the earthquakes. It is intended that this section will provide further clarification of the risks posed by pounding buildings to existing building stock.

A.1 Recent Canterbury Seismicity

At 4:35am on the 4th of September 2010, a M_w 7.1 earthquake occurred approximately 40 km west of Christchurch (Gledhill et al. 2010). Widespread but generally low-moderate level damage was reported throughout the Canterbury region. No fatalities were reported, however this may be largely attributed to the early morning timing of the earthquake. Nevertheless, unreinforced masonry (URM) buildings performed badly and resulted in multiple partial building failures (Wood et al. 2010).

A second significant earthquake occurred at 1:51pm on the 22nd of February 2011. While this earthquake had a lower magnitude (M_L 6.3, M_w 6.3), its epicentre was located within 10 km of

Christchurch city (Geonet 2011). This earthquake caused significantly more damage to Christchurch's building stock and resulted in collapse of two multi-storey reinforced concrete buildings, as well as many URM buildings (Dizhur et al. 2011). At least 181 people died in the earthquake (NZ Police 2011).

The extent of observed pounding damage was also significantly greater in the second earthquake. As the two events were separated by a significant period of time, they are reported individually. The two survey methods differ due to the differing earthquake intensities and method refinements. The second survey is also more comprehensive. In the remainder of this thesis, the first and second earthquakes will be referred to as the 'Darfield earthquake' and the 'Christchurch earthquake', respectively. Other earthquakes also occurred during this timeframe, including large aftershocks on 26th December 2010 (M_w 4.7) (Cooper et al. 2011) and 13th June 2011 (M_w 6.0) (Geonet 2011). However, these events had a lesser effect on buildings and consequently no additional surveys were performed specifically for these events.

A.2 Darfield Earthquake

This section describes the pounding damage from the September 4th Darfield earthquake. The text in this section was written prior to the Christchurch earthquake, so no comparison to the Christchurch earthquake is made in this section.

A.2.1 Survey Method

Building pounding damage was specifically investigated in Christchurch's central business district (CBD) on Thursday September 9th, five days after the Darfield earthquake. Pounding damage was qualitatively surveyed throughout the CBD, in an area roughly bordered by Gloucester St, Madras St, St Asaph St and Oxford Tce (Figure A.1). A comprehensive survey could not be conducted in this area due to building demolition, road cordons and available resources. However, exterior building pounding damage was examined and documented when observed. As the survey was limited to external damage, no account of intrabuilding pounding damage was made. The presented figures include wide angle, panoramic photography. While panoramic photos present more building configuration detail, some image distortion is caused. The photographed buildings have flat facades, however the panorama effect creates the illusion of a curved face. All panoramic images are identified in their captions.

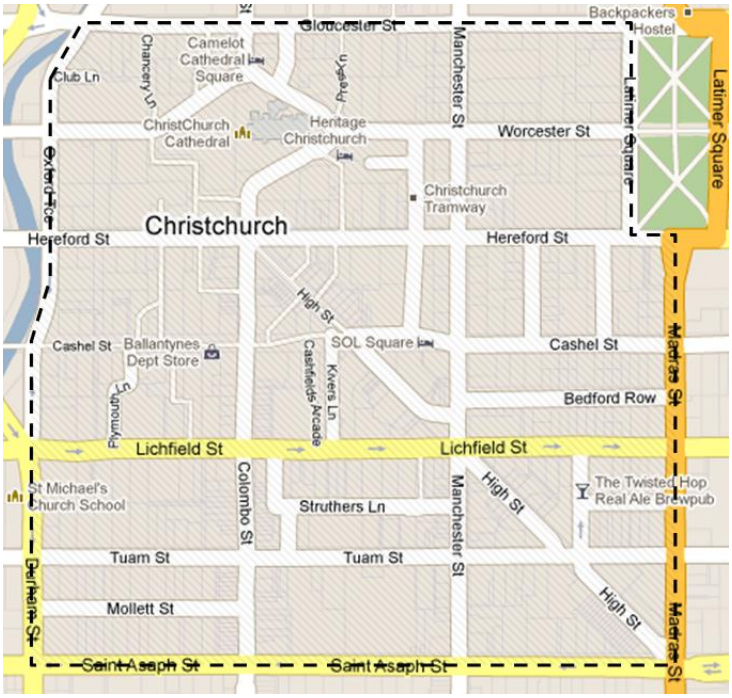

Figure A.1 limits of survey performed after the Darfield Earthquake. Map source (Google 2011)

A.2.2 General Observations

Few of the buildings in the CBD showed signs of pounding damage. Very crude estimates suggest roughly 5% of surveyed buildings were affected by pounding in some manner. Frequently the observed damage could also be attributed to other aspects of the building configuration. In particular, damage to parapets was not attributed to pounding unless other evidence was present. While the pounding damage was typically minor or absent (Figure A.2), the damage patterns often demonstrated the initiation of mechanisms that would lead to building failure under further seismic activity. All moderate to serious pounding damage observed occurred in URM buildings. Concrete buildings typically displayed only localised spalling damage.

Figure A.2 Minor pounding damage. Left: Spalled concrete at building interface. Right: Glazing damage (highlighted) predominately located at the roof of the adjacent buildings.

The observed damage was typically attributable to both pounding and URM construction. The central building in Figure A.3 suffered damage from both adjacent buildings, including loss of decorative cladding on the left face. The damage to the masonry wall of the taller building is primarily attributable to the URM construction but pounding is likely to be a significant secondary factor. Parapet collapse also occurred along the length of this wall.

Figure A.3 Loss of decorative cladding, and damage to masonry wall partly due to pounding. Left: panoramic image Right: Magnification of damage at the left building interface.

Adjacent facades where one facade protruded relative to its neighbour frequently suffered noticeable local pounding damage at the exposed corners (Figure A.4). This configuration had not been previously identified as critical for pounding. Pounding damage of this type may be particularly severe if timber diaphragms are present in the protruding structure since they will provide little lateral support to the affected wall.

Figure A.4 Damage to wall resulting from stepped facade

Buildings with observed pounding damage were typically two to four storeys tall. This is likely to be due to the large number of URM structures built within this storey range (Figure A.5).

Figure A.5 Pounding damage between two four storey structures Left: panoramic image. Right: Magnification of damage to top of right structure.

Adjacent buildings with greatly differing total heights displayed surprisingly little damage. Figure A.6 shows the most severe damage observed between buildings differing by three or more storeys. While the level of damage is low, the location of this damage is critical. Both buildings suffered damage to their vertical structural elements and not their horizontal elements. Since lateral loading is generally not considered at this location in any structure, and special detailing for inelastic behaviour due to such loading is unlikely to be present, this could potentially lead to brittle collapse in a larger event.

Figure A.6 Minor damage resulting from pounding buildings of greatly differing heights. Left: panoramic image. Right: Magnification of damage at the building interface.

A.2.3 Unique Pounding Damage

The most pronounced pounding damage observed within the CBD was located on High St (Figure A.7). Pounding occurred between two URM buildings of three and four storeys,

respectively. No building separation was present. While the damage was severe, it was also relatively localised. Two factors seem to have significantly contributed to the local failure: The brittle nature of the unreinforced masonry, and the position of the relatively strong window lintel. The location of the lintel immediately above the parapet of the adjacent building, and the relative strength of the lintel created a highly brittle configuration. Using the known dimensions of the brick units as a scale, the top of the damaged masonry's displacement is estimated as 70 mm. Broken bricks fell into the resulting gap between the two buildings, which is likely to have contributed to this displacement. The lintel was also damaged to a lesser extent. Other damage was also noted in the left hand building including partial failure of the wall not affected by pounding. However, this damage is attributed primarily to the building's URM construction.

Figure A.7 Top floor pounding damage. Left: Building configuration. Right: Magnification of damage.

Less severe but still notable damage also occurred on Cashel St. Figure A.8 displays the central two of four consecutive buildings with zero separation. Damage was confined to the interface between the two buildings. However significant masonry crushing was noted at the first floor. Some of the noted damage may be a result of the momentum transfer from the external buildings. No damage was observed at the top of the second floor. No other buildings in the CBD were observed to have this form of masonry crushing.

Pounding damage was not restricted to Christchurch CBD, two notable examples located further afield are presented in Figure A.9 and Figure A.10. These buildings were observed eight days after the CBD survey, while undertaking other research. Figure A.9 displays the local damage caused by a single fence in Woolston. The adjacent building to the left suffered no apparent damage. Figure A.9 illustrates how a seemingly trivial addition to a building may have serious repercussions for the structural system. Figure A.10 is also attributed to pounding, although the photo was taken after some demolition work was performed. The damage to the right structure

was amplified by the roof height of the left structure, which acted as a localised hammer on the failed wall. Both the first and second floor were significantly damaged. Other damage is also found throughout the building, which is attributable to the URM construction. While major cracking was observed in the external walls, none collapsed. Pounding is considered to have significantly contributed to the illustrated failure.

Figure A.8 Local crushing of brick between buildings. Left: panoramic image. Right: Magnification of damage between buildings at the first floor.

Figure A.9 Pounding damage resulting from adjacent fence

Figure A.10 Damaged masonry structure in Kaiapoi. Right: Magnification of damaged building interface

A.2.4 Comparison to Previously Identified Pounding Prone Characteristics

After the survey, the observed pounding damage was qualitatively compared to the six pounding prone building characteristics presented in Section 2.1.5. A brief comment is made on the prevalence each of these characteristics in the Darfield event.

1. **Floor/column or floor/wall pounding**. Much of the observed pounding damage occurred between adjacent buildings with differing floor heights (see Figure A.5 to Figure A.7, Figure A.9, and Figure A.10). Buildings with floor/column pounding generally suffered more damage than buildings with floor/floor pounding. However, floor/floor pounding damage was also observed (Figure A.3, Figure A.8).

2. **Adjacent buildings with greatly differing mass**. Differing building mass was not considered to have significantly contributed to any pounding damage in the Darfield event.

3. **Building subject to torsional actions arising from pounding**. This characteristic was not extensively investigated. Some torsional interaction may have occurred between the buildings in Figure A.6 and Figure A.10. However, it is not believed that torsion significantly contributed to pounding damage in this event.

4. **Similar buildings in a row with no separation**. Multiple buildings in series performed very well. Usually damage is expected on the buildings at either end of a row, however this was not observed in this earthquake. Damage to buildings within the row was sometimes observed when adjacent buildings had differing numbers of storeys.

5. **Buildings with significantly differing total heights**. Only one case was observed where pounding damage was attributed total building height difference (Figure A.6). As previously stated, this damage was minor.

6. **Buildings made of brittle materials**. URM was found to be the defining characteristic of pounding damage in this earthquake. All moderate to large pounding damage was found in URM buildings.

A.2.5 Building Configurations without Obvious Pounding Damage

Numerous building configurations where pounding may be expected due to their close relative proximity actually showed no external damage when inspected. This may be attributed to the low spectral response for buildings with short natural periods (Cousins and McVerry 2010). In particular, three to four storey wall structures were not generally greatly excited. However, taller buildings have been excited to approximately design basis earthquake levels. Lack of pounding damage in taller buildings can be partially attributed to the low number of tall buildings immediately neighbouring other tall buildings in Christchurch CBD, and the presence of seismic separation between tall building's towers and their surrounding podiums. Other factors affecting pounding damage include the direction of the strong motion shaking, and the relatively short duration of large intensity excitation.

A.3 Christchurch Earthquake

This section describes the pounding damage observed after the 22nd February Christchurch earthquake. Comparisons between this earthquake and the Darfield event are made in Section A.3.4.

A.3.1 Survey Method

On the 16th and 17th of March 2011, a detailed street survey of pounding damage was performed. Although debris removal and isolated building demolition were undertaken prior to the survey, the majority of Christchurch buildings remained largely unaffected by these actions. The survey was performed by walking the streets highlighted in Figure A.11 and externally inspecting each building for symptoms of pounding damage. The exclusion zone could not be accessed due to cordons. Any evidence of pounding damage was photographed and the building location, number of storeys, and building material noted. Each building was rated for severity of pounding damage and the level of confidence that pounding was responsible for the observed damage. Demolished or collapsed buildings were also noted. Once the survey was complete, the total

number of surveyed buildings was determined using Google Street View, and aerial photography from Google Maps (Google 2011). A total of 376 buildings were inspected during the survey.

Figure A.11 Surveyed streets. Streets that were surveyed are highlighted. Shaded areas next to streets indicate demolished or collapsed buildings as at 16/03/2011. Original map source (Google 2011)

Observed pounding damages to buildings were subdivided into six categories (Table A.1). These categories were adapted from the pounding damage measures used previously by Kasai and Maison (1997), with modifications to reflect the type of damage observed in Christchurch. Because buildings were only inspected externally, the cause of the observed damage could not always be definitively determined. While utmost care was taken to interpret the cause of building damage based on engineering judgement, the author accepts that these judgements were based on incomplete evidence in some cases. In an attempt to quantify this uncertainty, two categories of confidence level were adopted (Table A.2). Examples of each damage and confidence category are displayed in Figure A.12. The adopted icons are also displayed in every scenario presented in this section to inform the reader of the authors' classification in each case.

Table A.1 Adopted damage categories

Icon	Damage level	Description of pounding damage
	0	**None**: Building involved in pounding, however no evidence of damage found
	1	**Minor damage**: Damage to non-structural elements, or isolated hairline cracking
	2	**Damage at contacts**: Local spalling or crushing damage at the interface between buildings, or substantial damage or collapse of parapets
	3	**Significant damage**: cracks greater than 1 mm extending along load paths or present in multiple locations on the building
	4	**Partial collapse**: Loss of a façade or similar sized component

	5	**Complete building collapse**: Collapse of a building storey or greater damage

Table A.2 Adopted confidence levels

Icon	Confidence level	Description
	Low	Evidence of pounding is present, however pounding may only be a secondary factor for the observed level of damage. Alternatively, specific details of damage are unavailable due to collapse or demolition
	High	Damage follows load paths that indicate building collision, or damage patterns are consistent with pounding damaged structures observed in previous earthquakes

As of February 2011, the Christchurch CBD predominantly consisted of low rise structures with very little separation. A small survey of 51 buildings was performed on a segment of Colombo St between Armagh St and Tuam St to obtain a fair understanding of the distribution of Christchurch CBD buildings in terms of height, material and building separation. The results are presented in Table A.3. Building separation was not recorded when a building was on the end of a street. For example, if a block contained five buildings, four building separations were recorded. While this survey is too small to provide accurate statistics, it provides some idea of Christchurch's building makeup at the time of the Christchurch earthquake.

Figure A.12 Examples of damage and confidence classifications

Table A.3 Colombo street building characteristics

Storeys	1	2	3	4	5	6	7	8	9	10	>10
#	*2*	*33*	*7*	*4*	*0*	*1*	*2*	*0*	*0*	*1*	*2*
%	4%	65%	14%	8%	0%	2%	4%	0%	0%	2%	4%

Material	URM	Concrete	Steel	Timber
#	*23*	*23*	*3*	*2*
%	45%	45%	6%	4%

Separation	0 mm	1 – 50 mm	51 – 100 mm
#	*37*	*2*	*1*
%	93%	5%	3%

The sheer number of Christchurch buildings with no building separation merits consideration. A minimum building separation has been specified in the New Zealand code since 1964 (NZS1900.8 1964), however the majority of the assessed buildings predate this. Because most of these buildings are stiff low rise structures, the term 'pounding' may be inappropriate. Pounding implies that buildings collide with one another with some relative velocity. However it is likely in many Christchurch building configurations that separation never occurred, and thus no relative velocity ever existed. Damage can still occur in these situations due to momentum transfer between buildings, and grinding between building interfaces. Thus, some of the observed building damage may be more accurately termed as 'building interaction'. However this distinction has not been investigated further.

Pounding is known to also have potentially beneficial effects for buildings (Anagnostopoulos and Spiliopoulos 1992). A central building can transfer some of its earthquake load demand to adjacent buildings, and the interaction of adjacent walls can cause some level of energy dissipation. However, these effects have not been investigated in this survey. This is because evidence of the beneficial effects is significantly more difficult to identify from external building inspection. The survey also includes data from both inter-building pounding and intra-building pounding. However, only two examples of intra-building pounding were recorded. It is expected that more intra-building pounding occurred, however internal building inspection would be necessary to find this type of damage. Internal building inspections could not be performed at the time of the survey due to safety concerns, and the limited time available in the central city.

A.3.2 General Observations

This section describes general building pounding damage, and damage characteristics that were observed in multiple instances.

Typical URM Pounding Damage

Low rise masonry wall buildings were typically most severely damaged by pounding at the highest point of collision (Figure A.13a). This collision point frequently coincided with a window arch, sometimes causing masonry units to fall from the lintel or arch. Cracking frequently included nearby parapet sections. Collision between lower floors typically presented significantly less damage, and normally presented only hairline cracks. Some local crushing was observed where the floors collided. The severity and extent of damage was frequently observed to be markedly different between buildings involved in the same collision. Buildings which collided with shorter neighbours also commonly suffered local damage in the storey immediately above the collision in the bay closest to the building interface.

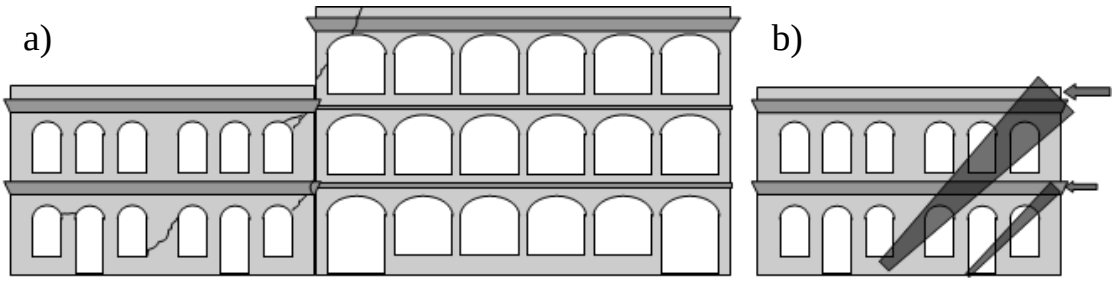

Figure A.13 Damage to URM buildings. a) Typical pounding damage. b) Idealized masonry strut damage.

An approximate idealisation of observed masonry pounding damage is presented in Figure A.13b, where the width of each shaded zone indicates approximate severity of damage and the arrows denote floor collision points of the adjacent building. The observed damage patterns can be described as a wall shear failure, or an approximately 45 degree compression strut. In practice the angle of damage may be significantly shallower, since the failure load path is affected by the wall openings. Loads are typically transferred horizontally across the top of any openings, which decreases the overall angle of the strut. Damage progressively lessens from the point of collision, however local damage may be amplified in stiffer lateral load resisting elements, or at weaknesses such as the top of windows.

Figure A.14 presents an example of the observed strut mechanism where damage has been caused by the impact of three floors in the adjacent building. During the Christchurch earthquake, the top floor of the adjacent building collapsed, however its effects are still evident on the building shown in the figure. The severity of the damage within the considered building is directly correlated to the floor each strut extends from. The primary strut associated with the collision of the adjacent building's top floor is notably more damaged than the secondary strut. The tertiary strut has only minor damage. While other buildings presented less pronounced damage of this form, only four buildings presented multiple struts similar to that of Figure A.14. Examples of typical pounding damage to URM buildings are presented in Figure A.15.

Figure A.14 Damage associated with compression struts (panoramic image). Struts from the impact of three floors of an adjacent building are highlighted.

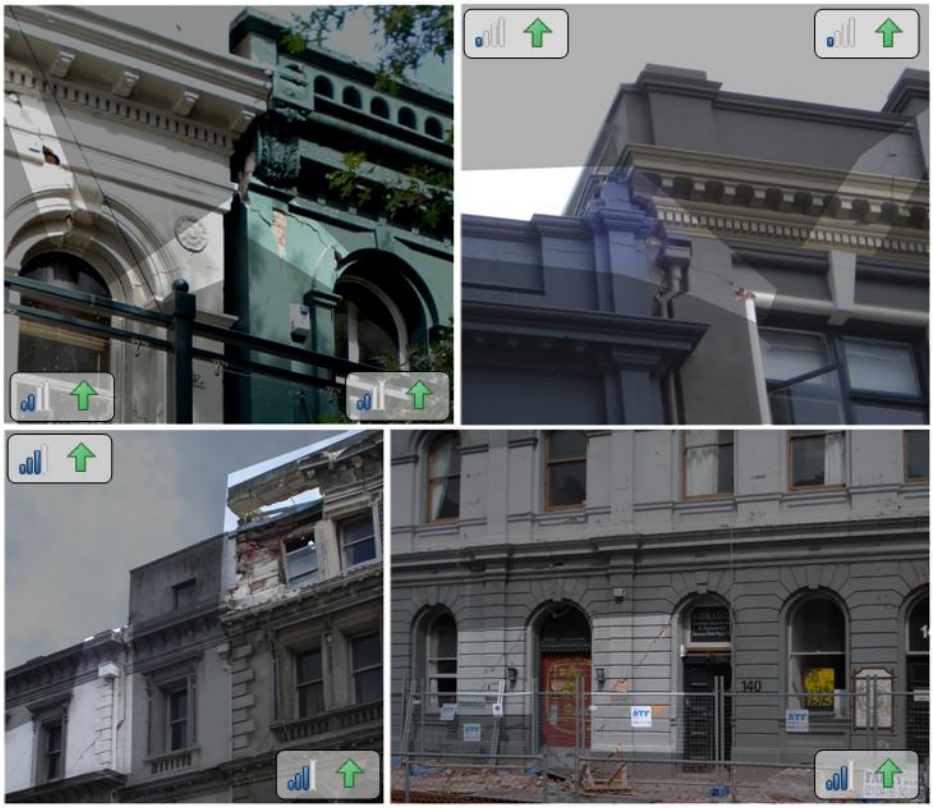

Figure A.15 Examples of URM damage. Top: cracking from collision points to windows. Bottom: cracking in stiff elements below the point of collision.

Damage due to separation details

Some buildings that did provide sufficient separation suffered even more substantial damage due to the presence of strong and stiff flashings in the building separations (Figure A.16). Solid timber infill used to support flashings between buildings caused concentrated collision areas. This concentration of contact area amplifies the damage potential due to pounding loads. In some instances the flashings failed and fell off the building. For high rise buildings, the weight and

length of the flashing can present a high risk falling hazard to surrounding pedestrians. In some cases flashing details were found to be sufficiently stiff and strong to cause failure of the surrounding buildings' structural elements. Five instances of separation covers transferring pounding forces were observed in the survey.

Figure A.16 Damage caused by poor separation cover detailing.

Buildings crushed by pounding

Buildings located between two more massive buildings can also be susceptible to global crushing (Figure A.17). In the presented case, crushing or buckling of the concrete elements at roof level appears to have caused failure of the facade. The failed facade was constructed in concrete, which was rarely observed to fail elsewhere in the CBD. Three instances of similar global crushing were observed in the survey. While this form of damage was uncommon, it also appears to be one of the most damaging forms of pounding. Failures of this type can endanger nearby pedestrians and greatly increase the likelihood of building collapse.

Figure A.17 Concrete facade failure due to building crushing between two other buildings. Left: Building overview. Centre and right: details at collision locations

Damage to stepped facades

Adjacent facades where one facade protruded relative to its neighbour frequently suffered severe damage along the protruding interface. This form of damage was also identified after the

Darfield earthquake (Figure A.4), however the observed damage was more severe in the Christchurch earthquake (Figure A.18). Two instances of stepped facade pounding damage were observed during the survey.

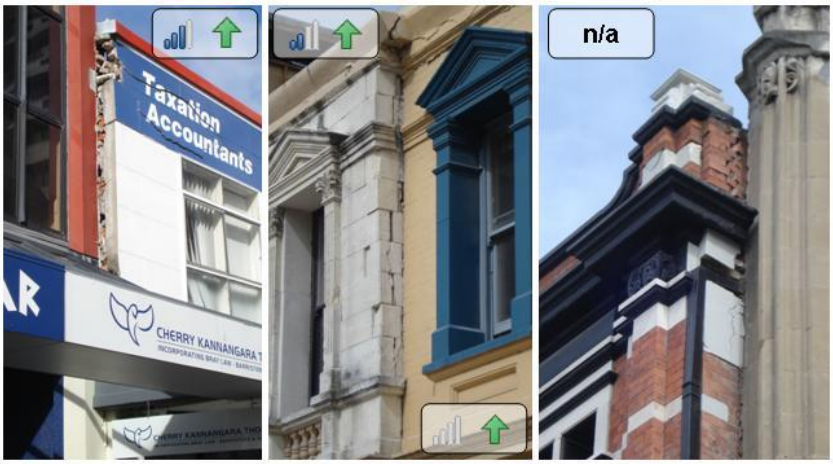

Figure A.18 Stepped facade damage. The right example is not categorised as it lies outside the survey area

Damage at collision points

The crushing of elements in locations where collision occurs can occasionally be severe, even when no damage is observed in the rest of the building. Two such cases are shown in Figure A.19. In these cases, the damage is curiously located close to the base of the structure. In the top example of Figure A.19, this can be explained by the solid timber infill between the structures that stops at the height of the concentrated damage. However, the bottom example does not have an obvious explanation. Similar crushing was also noted in the Darfield earthquake (Figure A.8). Four instances of significant isolated collision point damage were observed in the survey.

Figure A.19 Local damage at point of collision. Left: building configuration with collision location highlighted (panoramic image top left). Right: damage details.

Failure plane extending over multiple buildings

Occasionally, failure planes were observed to extend between separate buildings. These failure patterns indicate that load and momentum transfer did occur between adjacent buildings. Three cases of damage in one building extending across the interface to the next building were observed in the survey. Examples of this type of damage are shown in Figure A.20. Note that the right example has partial collapse of each building out of shot, which has caused the level 4 damage rating.

Figure A.20 Failure planes extending over two buildings. (Right photo courtesy of Colin Monteath, Hedgehog House)

A.3.3 Unique Pounding Damage

This section describes individual instances of pounding damage that presented unique and notable pounding damage.

Damage to a single storey building due to pounding

Single storey buildings do not usually experience severe pounding damage. This can be primarily attributed to the typically low amount of mass in the roof structure. However, the one storey building presented in Figure A.21 (neighbouring a four storey building) did suffer significant pounding damage. Shear cracking occurred in one direction between the window panels. Approximately 10 mm building separation was present; however this was not sufficient to prevent contact. The damage in the concrete block piers progressively lessened the further they were located from the building interface. While the four storey building is extensively damaged, the damage was not primarily caused by pounding. It is rated as level zero damage. This example is presented to illustrate that even very low rise buildings can be susceptible to pounding damage.

Figure A.21 Damage to single storey building from pounding. Top: Building configuration (panoramic image). Bottom: Damage details and building separation.

Damage over the height of the building interface

While most cases of pounding damage displayed localised damage at the adjacent building's floor level, more distributed damage throughout the interacting surface was also observed. Significant pounding damage was present over the full height of the building interface shown in Figure A.22. Although only one case was observed to be this severe, it highlights the possible extent of pounding damage at the building interface.

Figure A.22 Pounding damage over height of the building interface. Left: Building interface (panoramic image). Right: Details of ground level damage

Effect of existing retrofit strategies on pounding damage

Retrofits of existing Christchurch buildings prior to the Darfield earthquake rarely considered the possibility of pounding damage. The much stronger and stiffer adjacent building in Figure A.23 appears to have significantly contributed to the wall failure at the building interface, despite the existing retrofit. The steel portal frame retrofit shown in Figure A.23 was actually installed prior to the construction of the adjacent building. However, this damage demonstrates that common retrofit techniques, which often do not specifically address pounding, are frequently not adequate in pounding situations. Level 2 pounding damage was recorded at this location after the Darfield event (Dizhur et al. 2010).

Figure A.23 Damage to URM building in the Christchurch earthquake. Left: building configuration. Right: Damage at building interface.

A.3.4 Comparison of Darfield and Christchurch Pounding Damage

Sixteen buildings from inside and outside the survey area were externally investigated after the 4th of September Darfield event and again after the 22nd February Christchurch event. The performance of five of these buildings are scrutinized here to investigate whether building performance in smaller seismic events may provide indications as to which buildings are susceptible to major pounding damage in a large event.

Configuration 1

Figure A.24 presents pounding damage to a row of buildings observed after the Darfield earthquake (see also Figure A.2). Pounding damages from the Christchurch earthquake are presented for the same buildings in Figure A.17. After the Darfield earthquake, only glazing damage and some minor spalling were noted between the four storey and two storey buildings. No damage was present at other building interfaces. No indication of facade instability was apparent. Prior to the Darfield earthquake, this specific set of buildings were identified as

pounding prone due to the large number of adjacent buildings with no separation. However, even using hindsight after the 2011 event, specific prediction of the observed failure would be extremely difficult.

Figure A.24 Pounding damage after the Darfield earthquake. Left: Building configuration. Right: interface building detail

Configuration 2

Figure A.25 displays two URM buildings that suffered significant damage. After the Darfield earthquake, the smaller masonry building in Figure A.25 was noted to be leaning onto its neighbour. A gap of approximately 50 mm existed at ground level, however the buildings were in contact at the roof level of the smaller building. Damage after the 2011 event is too extensive to be confidently attributed to pounding, however building interaction definitely occurred in this instance. This building was identified as highly susceptible to pounding after the Darfield earthquake due to the building's lean and its masonry construction.

Figure A.25 Damage to URM buildings. Left: After Darfield earthquake. Right: after February earthquake

Configuration 3

The Darfield earthquake caused minor damage to the buildings shown in Figure A.26. Minor local spalling was observed between the central and rightmost buildings. However, this damage was located at the mid height of the central building's columns. After the Darfield event, it was concluded that the central building was susceptible to collapse in a larger event due to the hinging potential of the interface column (Figure A.6).

Figure A.26 Collision of buildings of considerably differing height. Top: panoramic image after the Darfield event (the left building is predominately outside the field of view). Bottom: details of damage after the Christchurch earthquake and probable load transfer mechanism.

In the Christchurch event collapse did not occur, however significant damage did occur. The right interface of the central building displays significant spalling damage, although the columns have not formed hinges. This lack of mechanism is attributed to the strength of the right building's wall (Figure A.26, bottom right). This wall appears to have transferred the loads from the right building's floors to the floor of the central building, preventing further damage to the central building's columns at the building interface. However, this load transfer also appears to have negatively affected the interface between the central building and the left building. The

central building's column at this location has fractured at the top and the bottom of the window (Figure A.26, bottom left). This column has moved approximately 30 mm due to interaction with the left building. The column adjacent to the moved column displays damage consistent with force transfer from the taller rightmost building. While significant pounding damage was predicted for this building configuration, the exact nature of the damage was not anticipated.

Configuration 4

Figure A.27 shows a series of 2-3 storey URM buildings without any separation. The pounding damage observed in these buildings varied significantly between the two earthquake events.

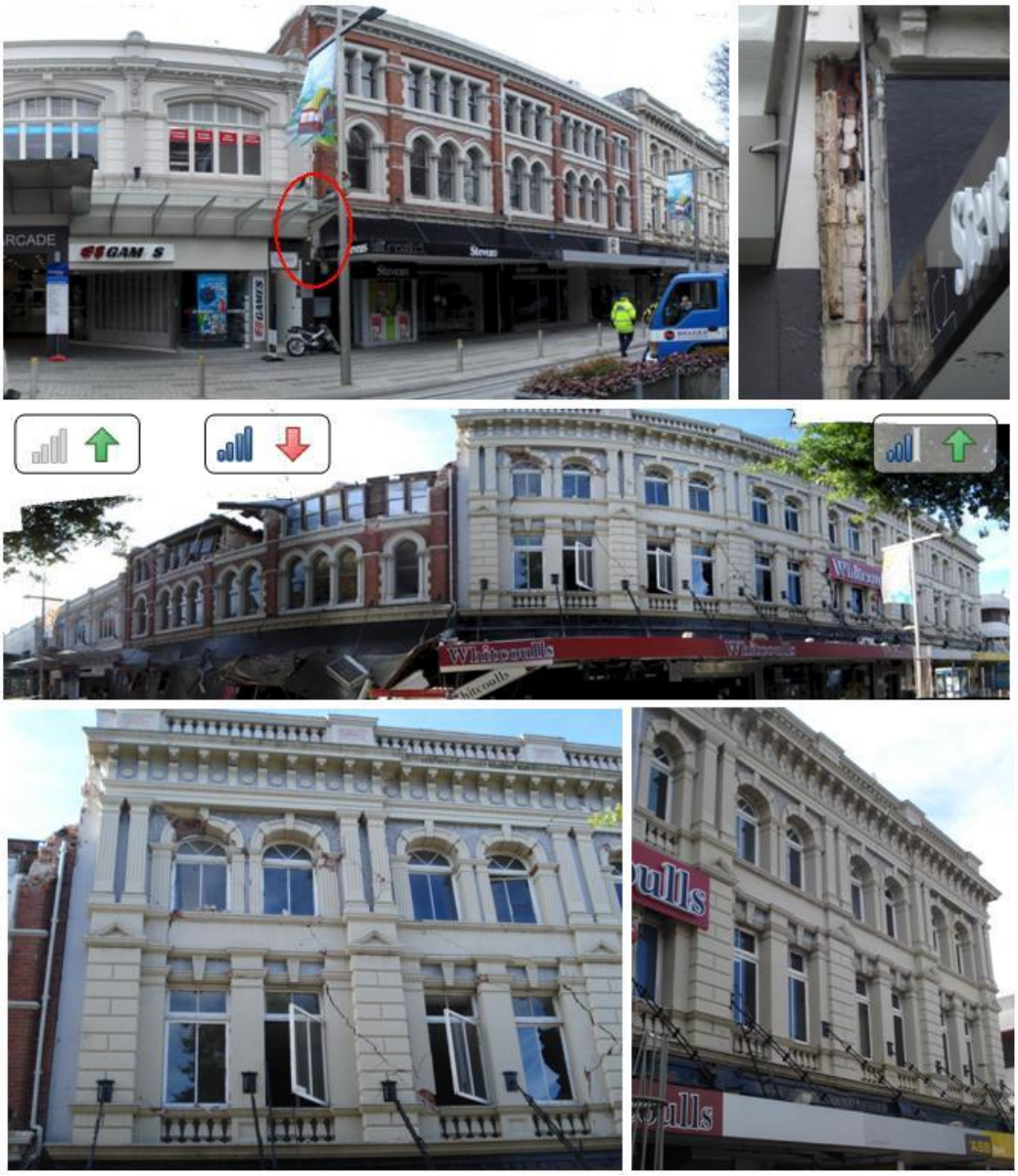

Figure A.27 Pounding damage to masonry buildings. Top Right: Damage after the Darfield earthquake (panoramic image). Top Left: Detail of damage. Centre: Damage after February earthquake (panoramic image). Bottom left: damage at collision point. Bottom right: minor damage at opposite end of the building.

The damage observed after the Darfield event comprised only masonry crushing between the leftmost building and the central building. No external damage was observed between the

rightmost building and the central building. However, the February event caused insignificant additional damage to the crushed masonry. Damage was instead concentrated on the interface of the rightmost and central buildings. It is difficult to determine whether the central building facade collapse was due to collision, however the rightmost building showed strong evidence of pounding damage (see also Figure A.8, Figure A.14). Spalling occurred at the collision point of the rightmost building, and extensive shear cracks propagated from this point to the ground, as previously discussed. Inspection of the opposite half of this building revealed only vertical cracking. Once again pounding damage in a bigger event was anticipated but the exact nature of the damage could not be foreseen.

Configuration 5

In one case, interaction between buildings in a row was found to contribute to partial collapse of multiple buildings. In the buildings shown in Figure A.28, only moderate pounding damage was documented after the Darfield earthquake (Figure A.3).

Figure A.28 Pounding damage to masonry buildings. Top: damage after the Darfield event (panoramic image). Bottom: damage after the February event (photo courtesy of Colin Monteath, Hedgehog House).

Figure A.29 and Figure A.30 present damage at the respective building interfaces, which illustrate how the damage progressed during the Christchurch earthquake. While pounding cannot be definitively stated as the primary cause of the observed collapses, the extent of the facade collapse runs between locations of previously identified pounding damage. The leftmost building interface appears to contain a shared party wall. Whether interaction between these two

buildings can strictly be attributed to pounding depends on the original designs of the two buildings. However, the other building interfaces do not appear to be connected. Collapse of these buildings in a level of shaking similar to that experienced in the Christchurch earthquake could be reasonably predicted given the level of damage observed in the Darfield event.

Figure A.29 Detail A: damage at the leftmost building interface. Coloured areas indicate common points of reference between the photos. Left photos display floor one damage, right photos display roof level damage. Top: After the Darfield earthquake. Bottom: After the Christchurch earthquake (photos courtesy of Colin Monteath, Hedgehog House).

Figure A.30 Detail B: damage between the two central buildings. Coloured circles indicate common points of reference between the photos. Left: After the Darfield event (note the major cracking at the adjoining perpendicular wall). Right: After the Christchurch event (photo courtesy of Colin Monteath, Hedgehog House).

A.3.5 Survey Statistics

A total of 376 buildings were surveyed for pounding damage following the Christchurch earthquake. A can be seen in Table A.4, 22–32% of these buildings were found to be involved in pounding in some manner, with 6–12% of buildings suffering serious (level 3 or higher) damage due to pounding. Including the 'low confidence' cases, the survey identified 119 buildings that were involved in 52 separate pounding instances. This data is also presented with cumulative totals in Figure A.31.

Table A.4 Total number of buildings with observed pounding damage

	Number of observed buildings			Percentages		
	↑	↓	↑+↓	↑	↓	↑+↓
	31	4	35	8%	1%	9%
	13	5	18	3%	1%	5%
	17	3	20	5%	1%	5%
	19	7	26	5%	2%	7%
	4	14	18	1%	4%	5%
	0	2	2	0%	1%	1%
Totals	**84**	**35**	**119**	**22%**	**9%**	**32%**

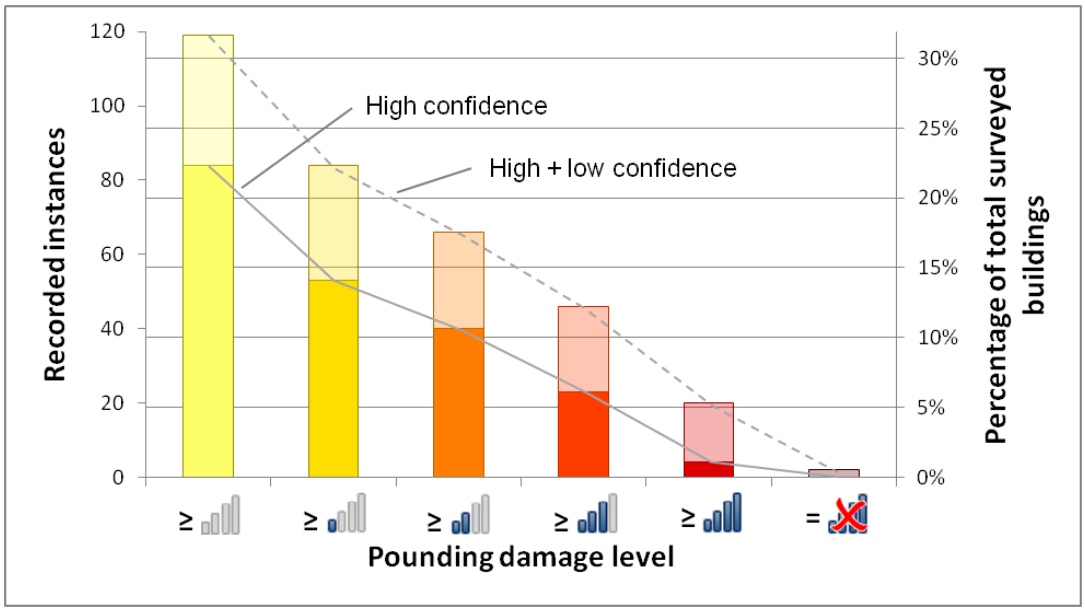

Figure A.31 Cumulative pounding damage totals for the Christchurch earthquake. Full colour: high confidence. Half colour: High + low confidence

The gathered pounding damage data can also be analysed in terms of the number of storeys and building materials of each building (Figure A.32). Both high confidence and the combined high and low confidence figures are presented. Some inaccuracy is expected in these results as the building material had to be determined from only external inspection. Over 90 % of level 3 or

higher damage occurred in masonry structures. The low numbers of observed pounding damage in steel and timber structures reflect their relative scarcity within the Christchurch CBD. Figure A.32 also presents the data in terms of number of storeys. The majority of buildings involved in pounding were two or three storeys. This is primarily due to a high proportion of two and three storey buildings within the CBD, although the majority of URM buildings also lie within this storey range.

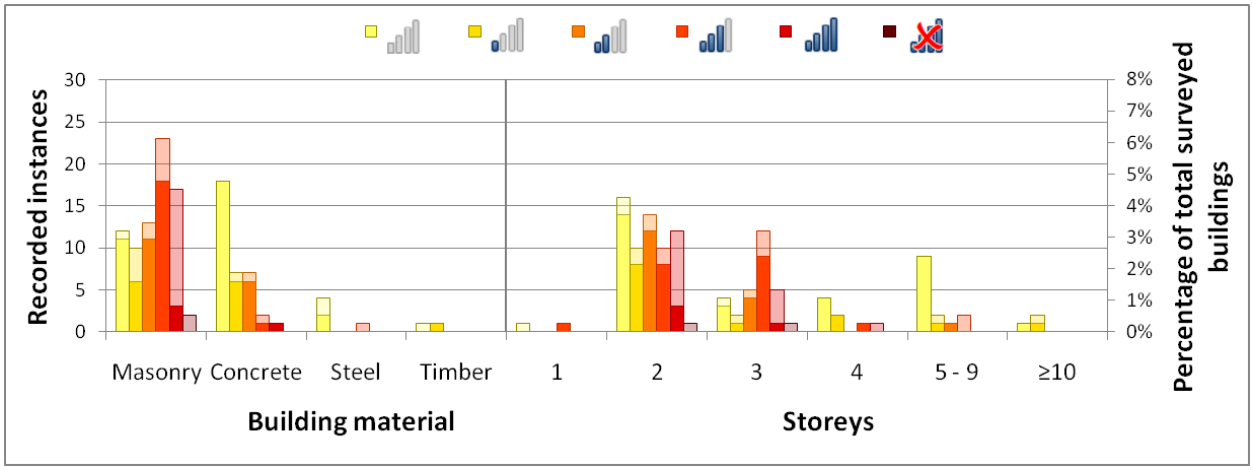

Figure A.32 Pounding damage by building material and number of storeys. Full colour: High confidence. Half colour: high + low confidence

A.3.6 Comparison to Previously Identified Pounding Prone Characteristics

Each of the 52 pounding scenarios was quantitatively assessed for each critical pounding vulnerability, which were determined by the following criteria:

1. **Floor/column or floor/wall pounding**. Floor/column pounding was considered to exist if floor heights differed by more than the depth of the flooring system. The depth of the system was estimated since no internal inspections were performed.

2. **Adjacent buildings with greatly differing mass**. A mass imbalance was considered to exist if the ratio of building floor areas was greater than 2. Floor size was estimated using aerial photos. The number of storeys was not considered when making this assessment.

3. **Buildings subject to torsional actions arising from pounding**. A pounding configuration was considered to be torsional if one building extended twice the length of the collision interface and no other buildings were present over the remaining length.

4. **Buildings in a row with no separation (Bookend effect)**. Pounding involving multiple buildings was identified wherever pounding damage was observed on more than two adjacent buildings.

5. **Buildings with significantly differing total heights**. Buildings whose heights differed by more than two storeys were considered to be significantly different.

6. **Buildings made of brittle materials**. A pounding configuration was noted as brittle if one of the damaged buildings was constructed of unreinforced masonry. Modern concrete buildings were not classified as brittle.

The frequency of each pounding vulnerability is presented in Figure A.33. Many pounding scenarios presented multiple critical pounding vulnerabilities. However, it is considered that some of these vulnerabilities may be over reported. For example, some buildings which met the criteria for torsional pounding did not present any external damage that suggested significant torsion had occurred. It is difficult to refine the criteria used for identifying torsional buildings with the current level of knowledge on this specific pounding characteristic.

Brittle buildings is the most prevalent pounding vulnerability observed in the Christchurch earthquake. This problem is amplified by the absence of separation between most brittle buildings. Lack of building separation also exists in many other New Zealand cities, which may be vulnerable in future events.

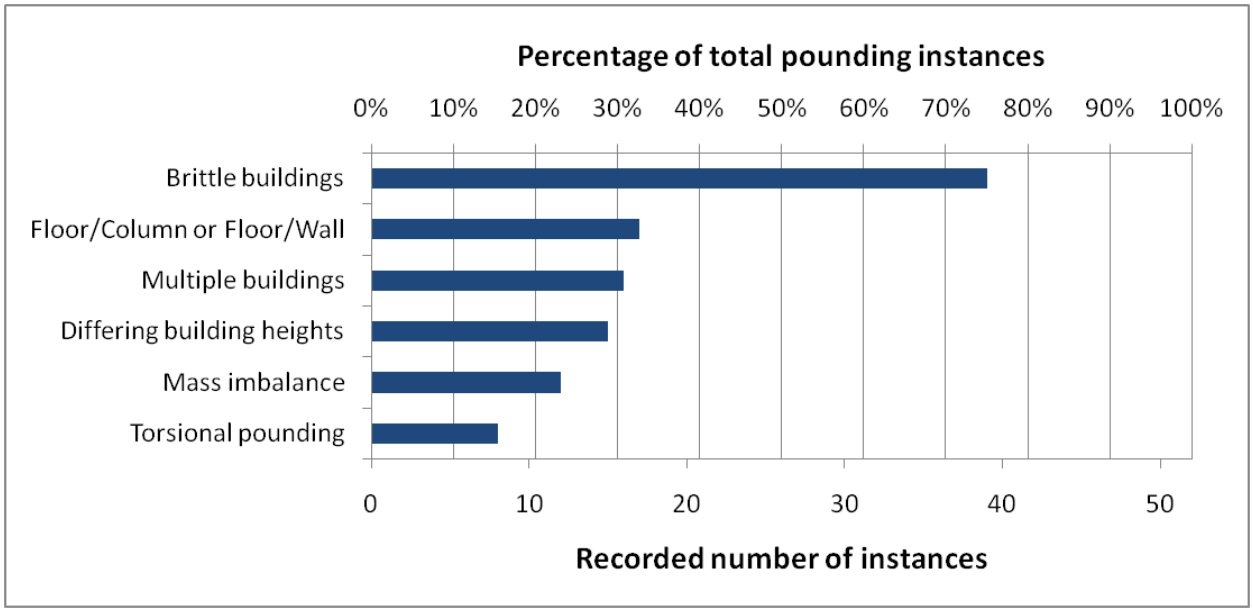

Figure A.33 Frequency of critical pounding vulnerabilities (including high and low confidence results)

Characteristics that are not represented in Figure A.33 include the relative strength and stiffness of adjacent buildings. The influence of relative stiffness has been extensively investigated analytically in terms of overall building response (for example, Anagnostopoulos and Spiliopoulos 1992; Dimitrakopoulos et al. 2009b). However, it has been observed in the Christchurch earthquake that damage to individual elements at the building interface is also

strongly affected by relative building strength and stiffness (for example, Figure A.23). It is feasible to identify stiffness and strength differences between adjacent buildings during pre-earthquake seismic evaluations if plans or on-site surveys can be conducted to develop estimates of those building characteristics. Further research may be able to define reasonable thresholds of strength and stiffness differences beyond which unacceptable levels of pounding-related damage will occur.

A.4 Adjacent Building Failure

As discussed in Section 1.3.2, building damage resulting from failure of adjacent buildings was frequently observed after both earthquakes. In the Christchurch earthquake, the data collection was primarily concerned with building pounding. However in the Darfield event, some information on adjacent building failure was also collected.

Figure A.34 Examples of masonry failure affecting neighbouring buildings

Figure A.35 Examples of parapet failure onto adjacent buildings

Figure A.34 illustrates two examples of the failure of URM buildings in Christchurch city in the Darfield earthquake, while Figure A.35 displays parapet failure from the same event. These

types of failure were frequently observed in the Darfield event (Dizhur, Ismail et al. 2010), despite the relatively low excitations of buildings in this period range (Cousins and McVerry 2010). The failures in these examples had a devastating effect on their neighbouring buildings. When the URM walls failed, the masonry units typically fell outwards towards other buildings. This behaviour is attributed to the partial restraint provided by the roof and other walls of the failing building that prevent large wall sections falling inwards. Parapet failure also frequently results in masonry units falling outside the building envelope, but is more likely to fall in longer continuous sections.

Damage to the adjacent building typically involves local or global failure of the roof structure due to falling debris. Failure of this form is often sudden and provides little to no warning to the building's occupants, other than the shaking of the earthquake itself. Taller adjacent buildings may instead suffer damage to walls from adjacent flying debris. However, wall damage is typically less severe because the loading caused by the dislodged debris is predominantly in the plane of the wall. Small commercial buildings within and immediately surrounding the CBD are considered to be highly vulnerable to adjacent building failure. Throughout the CBD, little space exists between adjacent buildings due to the high value of the surrounding land. While some residential buildings may also be at risk from neighbouring buildings, they are relatively infrequent. This is due to the comparatively large sections residential buildings typically occupy, which allows much greater separation between adjacent buildings.

Based on observations from the Darfield earthquake, the buildings most at risk from adjacent building failure typically have little to no building separation and are shorter than the adjacent building by at least one storey. Smaller adjacent buildings at a greater risk due to the debris falling at a higher velocity onto their roofs. Single storey timber buildings with light weight roofing are particularly vulnerable. Small, lightweight buildings typically perform well in earthquakes and usually incur little or no structural damage from the earthquake ground motion. The safety of the occupants in this type of structure is thus primarily endangered by their neighbouring buildings.

Figure A.36 Risk posed by falling masonry to pedestrians

Figure A.37 Risk posed by falling masonry to traffic

Falling debris also affects public access routes, including pedestrian footpaths and roading (Figure A.36, Figure A.37). Members of the public who happen to be walking or driving by an URM building or unrestrained parapet are at a similar level of risk to occupants of neighbouring buildings. The issue of public safety is further complicated because the risk to any *one* individual is low. This is because of the low probability that a specific person will be next to a specific at risk building when a large earthquake occurs. Informing every local individual about such a low risk is therefore inappropriate. However, the probability that *any* person will be next to a specific at risk building during an earthquake is considerably higher. Thus this issue is a valid concern for the communities that surround buildings with URM or unrestrained parapets.

Adjacent building failure is presented here because it is believed this hazard to be largely overlooked. While the seismic vulnerability of URM buildings is commonly recognised, the repercussions for people in the immediate vicinity of these buildings are not widely acknowledged. There are also many common issues relating adjacent building failure and pounding damage. The remediation of the hazard typically requires communication and

cooperation of multiple building owners and engineers. Further investigation of adjacent building failure is strongly recommended, but is not performed in this dissertation.

A.5 Discussion

This section details three issues that arose while analysing the presented data.

A.5.1 Comparison of pounding prevalence to other earthquakes

The reported frequency of pounding damage in both events may appear to be anomalously high when compared to other reconnaissance reports. Many earthquake reconnaissance reports have no mention or little mention of pounding damage. This discrepancy is attributed to a number of factors.

1. As discussed in Section 2.1, pounding is a relatively niche topic, and can be easily overlooked when it is one of many contributing factors to building damage. The two other pounding specific surveys that have been performed after major earthquakes have all reported notably higher extents of pounding damage than general reconnaissance reports.

2. Pounding damage is highly dependent upon the existing building stock. The high frequency of buildings with zero separation and URM construction within Christchurch has increased the likelihood of pounding damage. This damage also significantly differs to what may be expected in large overseas cities, such as Taipei (Jeng and Tzeng 2000) in which pounding between high rise buildings is more likely.

3. The pounding damage reported in Christchurch includes all levels of damage. If the presence of pounding damage was only investigated for buildings suffering complete collapse, only two buildings would be reported. The inclusion of all damage levels is intended to present a more complete picture of how pounding affects buildings.

4. The bounds of each survey area do not include all buildings in Christchurch CBD. The survey covers buildings within the core CBD where there is a high frequency of little to no building separation. If the survey area had been extended to include the city outskirts, the percentage of reported pounding damaged buildings in the Christchurch event would drop significantly. The extents of this survey were selected to appropriately present the risk to buildings with little to no building separation.

A.5.2 Prediction of pounding damage

Identification of pounding-prone buildings is a key step in mitigating pounding hazards. Predictions of specific damage patterns are very difficult without detailed dynamic modelling, however pounding-prone building configurations can be identified with a quick external visual inspection. In the Christchurch event, buildings without any of the six pounding weaknesses (Section A.3.6) suffered only minor to moderate pounding damage. Buildings with level 3 or higher damage contained at least one critical pounding vulnerability. The only exception to this suffered level 3 damage as a result of poor detailing. Two characteristics in particular were observed to greatly increase pounding risk during the Christchurch event: the presence of brittle URM buildings, and the presence of four or more buildings in a row without separation. In the Darfield earthquake, buildings in a row were observed to perform very well. It is possible that an excitation threshold exists where multiple buildings in a row becomes more detrimental than beneficial, however further evidence would be required to provide a definitive statement on this issue.

Severe pounding damage has typically affected buildings already identified to be structurally deficient. Many of these buildings would have been considered "earthquake prone" according to the New Zealand Building Act 2004 prior to the Darfield earthquake. In general, modern (circa 1990s) buildings have not suffered significant (level 3 or higher) pounding damage in this event. This can be attributed to the presence of seismic gaps, the presence of ductility at potential collision points and the relative scarcity of these buildings within the survey area. The primary pounding risk to these buildings comes from poorly detailed separation covers.

A.5.3 Implications for other towns and cities

The observed pounding damage can be considered to be a reasonable representation for other cities with unreinforced masonry buildings with no separation. In addition to numerous other towns and cities, New Zealand's capital Wellington is known to have a substantial number of 1–2 storey URM buildings without separation. The recommendations proposed in the following section are considered to be applicable to most cities with similar building configurations worldwide.

A.6 Recommendations

The following recommendations are made based upon the observations of building pounding damage in the Christchurch earthquakes.

A.6.1 Construction of new buildings

Enforce the existing building separation specifications: Most building codes prescribe a minimum building separation using either absolute (ABS) or square root sum of the squares (SRSS) combination methods. These methods produce an overall minimum separation by combining the calculated deflections for both buildings that may come into contact. In New Zealand, clause 7.4.1 of NZS1170.5:2004 requires a minimum building separation to be calculated using deflections from the ultimate limit state event and combined using the absolute combination method. However, it is the authors' understanding that this specific clause is not strictly enforced. Building owners have a financial incentive to optimise the use of their land, and look to minimise any gap requirements. This earthquake has demonstrated that the lack of separation is a primary contributor to the widely observed pounding damage. Less evidence exists on the efficacy of gaps smaller than that specified by the codes. However, in the absence of further information, it is recommended that this clause be strictly enforced for all new buildings within New Zealand. It is further recommended that other seismically active countries review the enforcement of their respective building separation requirements.

Ensure adequate detailing of separation flashings: Multiple examples of building element failures were observed to be caused by the infill of building separations. Failures of some separation flashings were also observed to create additional falling hazards. Infilling building separations with stiff and strong materials entirely defeats the purpose of building separation. Separation flashings should be designed with a rigid connection to one building only, and comprise either a crushable material or rest on the front of the adjacent building facade. Other rigid elements, such as the fence presented in Figure A.9, should be designed in a similar manner. These details are not commonly designed by structural engineers so relevant information needs to be provided to the architectural community on this specific hazard. Furthermore standards that evaluate building separations, such as ASCE 31 (2003), should encourage practitioners to inspect the separations to check for local elements that may connect the buildings.

A.6.2 Existing buildings

Retrofit of existing URM buildings: Over 90% of buildings severely damaged by pounding were constructed of masonry. When URM buildings are retrofitted, special consideration of pounding damage is recommended. The factors that increase pounding risk have been presented (Section A.3.6), and can be identified on site. The topmost point of collision between buildings is the most likely point of damage and should be considered in detail. The use of retrofit

techniques that adhere bricks together, such as glass fibre wraps, is recommended to prevent explosive failure of masonry units when building collision occurs.

Replace infilled separation flashings: As described for new buildings above, existing separation flashings that have solid infill, such as timber, should be replaced with flashings that will not transfer seismic load in the event of an earthquake.

A.7 Conclusions

The following conclusions are drawn from the investigations performed in A.

1. Pounding was observed in the Darfield and Christchurch earthquakes to occur rarely when compared to the total affected building stock. However, damage that was specifically attributable to building pounding was observed in each event.

2. Pounding in the Darfield event severely affected only URM buildings.

3. Minor 'non-structural' elements between buildings, such as building flashings, can significantly damage important structural elements if they are not appropriately designed.

4. Pounding damage from each earthquake was assessed in terms of previously identified factors that increase pounding vulnerability. In both events, floor/column pounding and brittle materials were found to be the most common factors present where significant pounding damage occurred.

5. The ability to predict pounding damage was briefly assessed. All buildings that were severely damaged by pounding in these events possessed at least one of the previously established critical pounding vulnerabilities. However, the extent and nature of pounding damage was not easy to predict.

6. Adjacent building failure can also cause partial failures of buildings as a direct result of neighbouring failures. While this hazard is not considered further in this thesis, it is recommended as a subject for future research.

Appendix B Graphical Records of Pounding Damaged Buildings

The following photos and diagrams were collected during the production of this thesis. The year, location and magnitude of each earthquake are stated. The source of the presented information is listed before each case. If no source is listed, the source is the same as the immediately preceding case. Note pounding damage from the Christchurch earthquakes is not presented here.

1921 Santa Barbara M_w 6.8

Source: (Ford 1926)

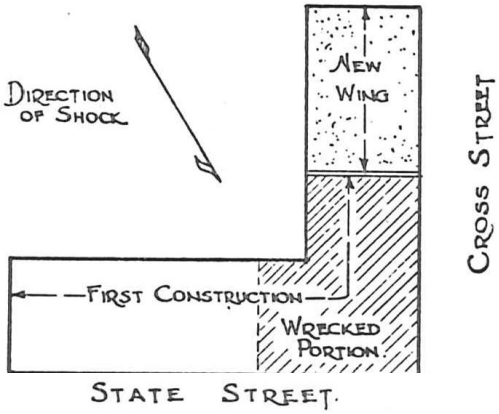

Pounding damage was noted between the original 1913 building a 1923 extension, constructed with zero separation. "*The shock, which lasted for fifteen seconds, evidently set up different vibrations in the two portions of the structure and the new wing acted as a battering ram on the stiffer or corner portion of the old building causing total collapse of the corner.*" Poor construction is also listed as a contributory cause.

1971 San Fernando M_w 6.6

Source: (Bertero and Collins 1973)

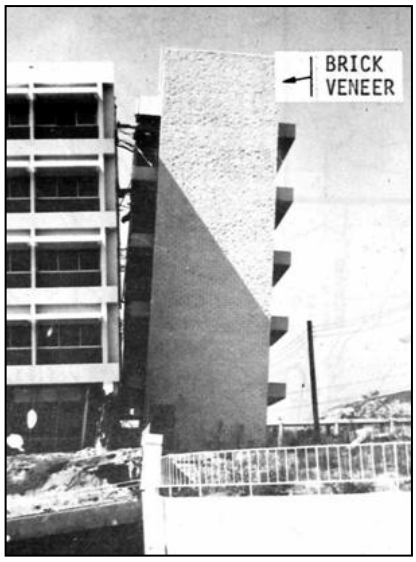

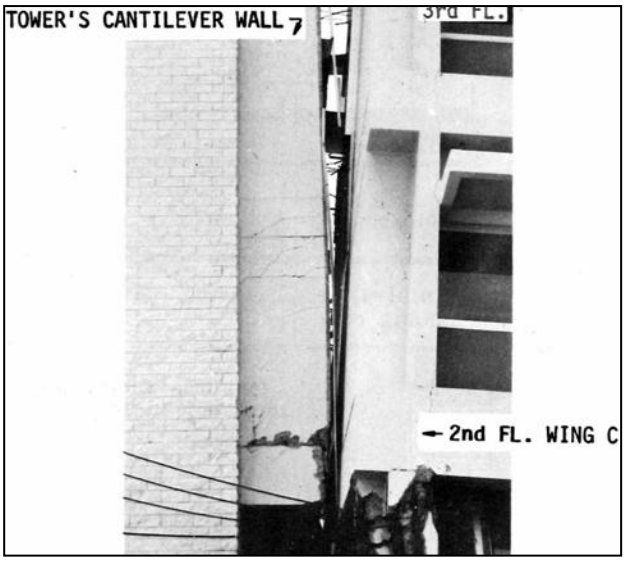

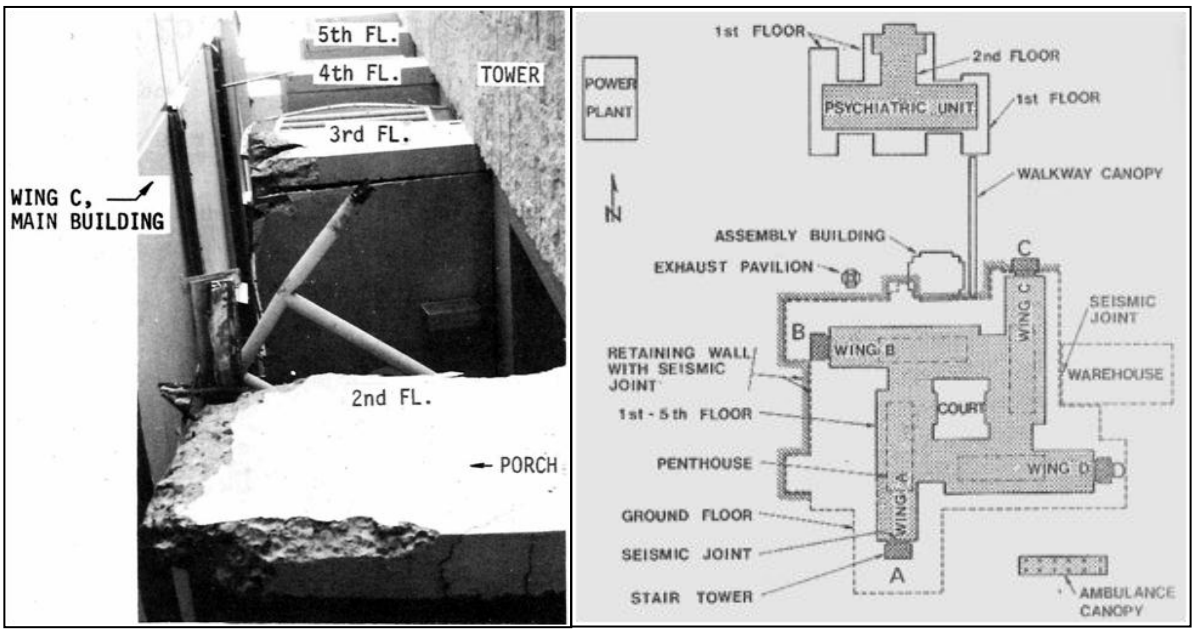

Damage between main hospital building and a seismically separate stair tower. The most severe pounding damage is note at floors 2 and 3. Permanent relative deflection is also apparent

1985 Mexico City M_w 8.0

Source: (Bertero 1986)

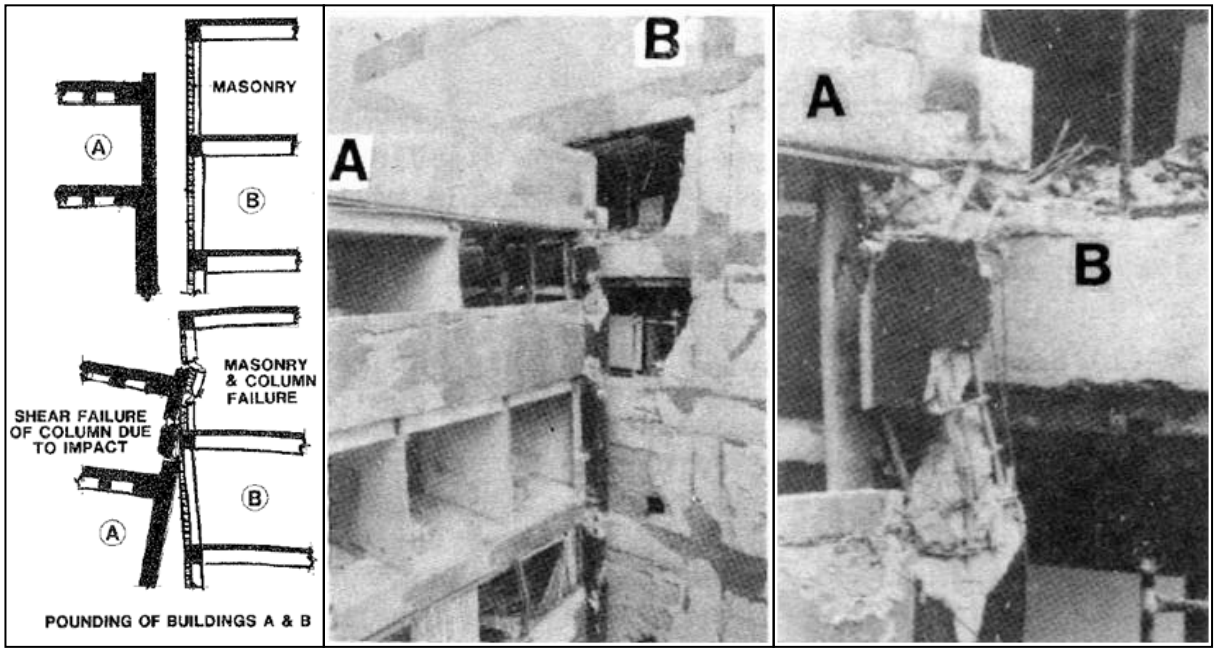

Masonry and column failure as a result of collision. Left: Schematic of damage mechanism. Centre: Building configuration. Right: Magnification of column damage in top storey of shorter building.

Multiple units of almost identical construction. Centre and right, details showing permanent relative deflections, both away from adjacent building (Centre) and into adjacent building (Right)

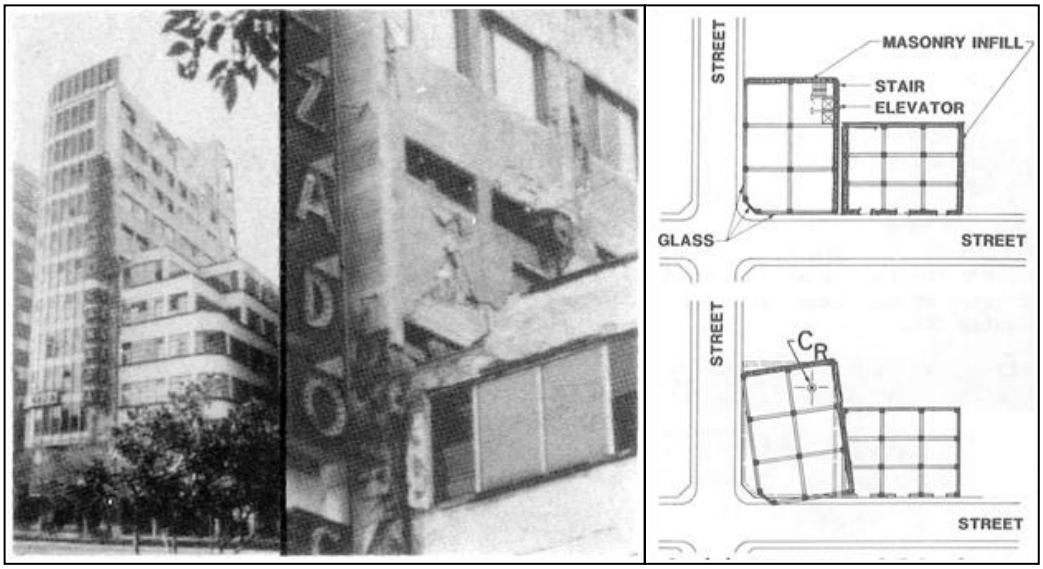

Pounding damage resulting from torsional building response.
Source: http://www.livescience.com/php/multimedia/imagegallery/igviewer.php?gid=16

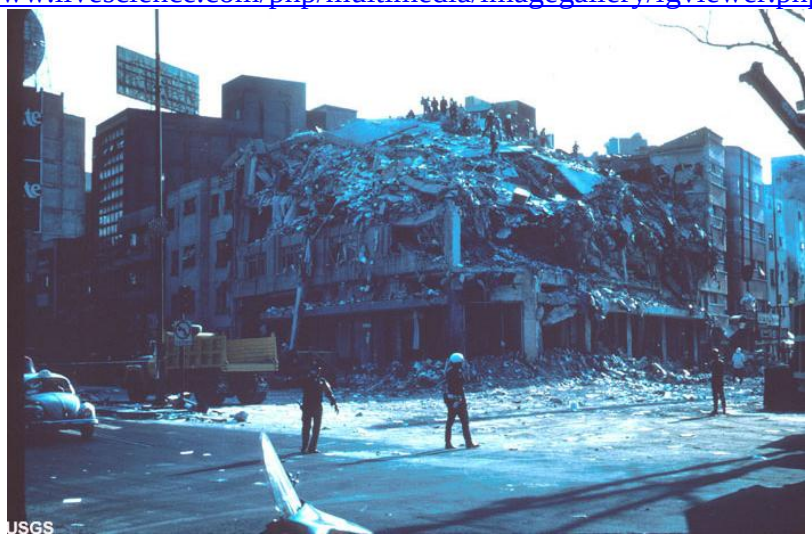

Partial collapse of building. This damage was attributed to pounding, however this could not be independently verified.

Source: http://www.smate.wwu.edu/teched/geology/eq-Mexico.html

Collapse of top floors of a flexible building due to collision with smaller and more rigid buildings located either side of the building.

Pounding damage between three buildings due to differing overall heights. Note the rightmost building was not vertical after the earthquake, as a result of this pounding damage. Left: Building configuration. Right: Magnification of damage between the central and rightmost buildings.

1989 Loma Prieta M_w 6.9

Source: (Kasai and Maison 1997)

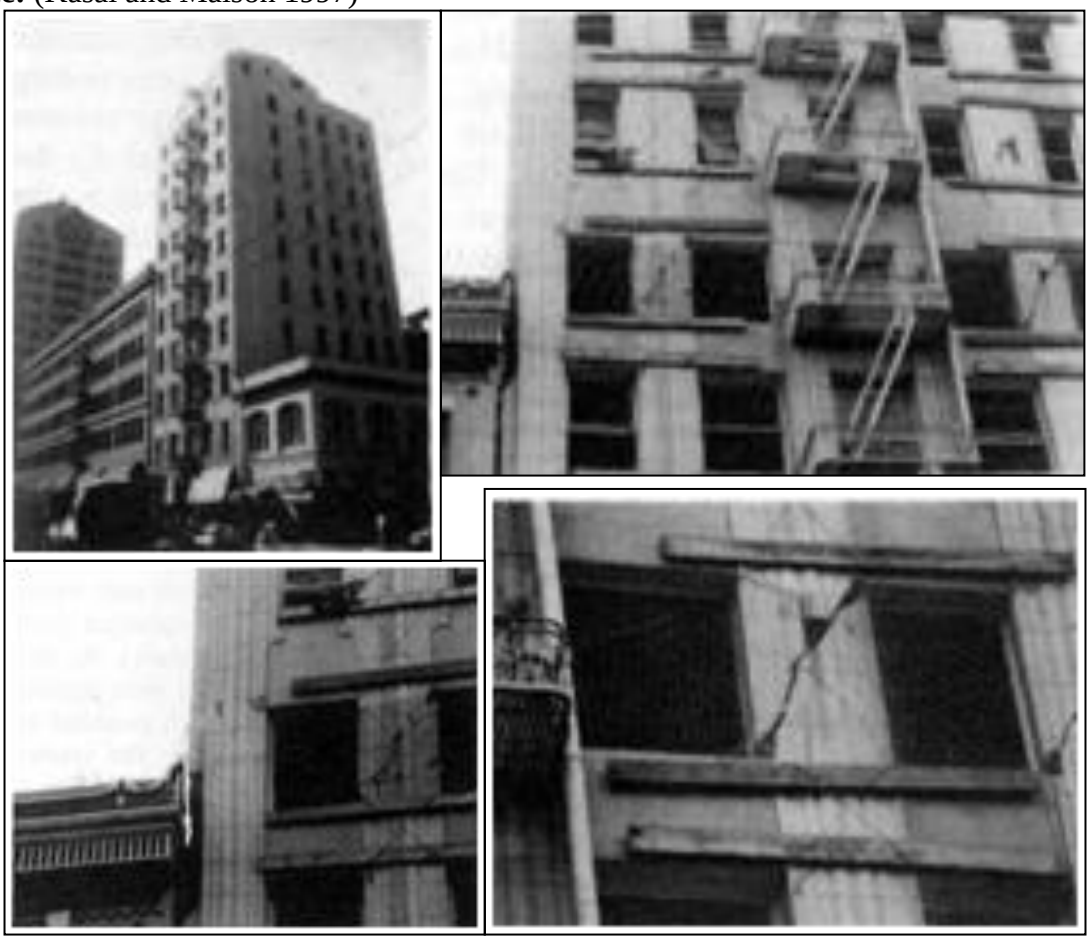

Pounding damage due to pounding induced torsion and greatly differing overall heights. Note the diagonal cracks are significantly more pronounced in one direction as a result of the collision. Clockwise from top left: Building configuration, point of collision, column damage above point of collision, damage at point of impact.

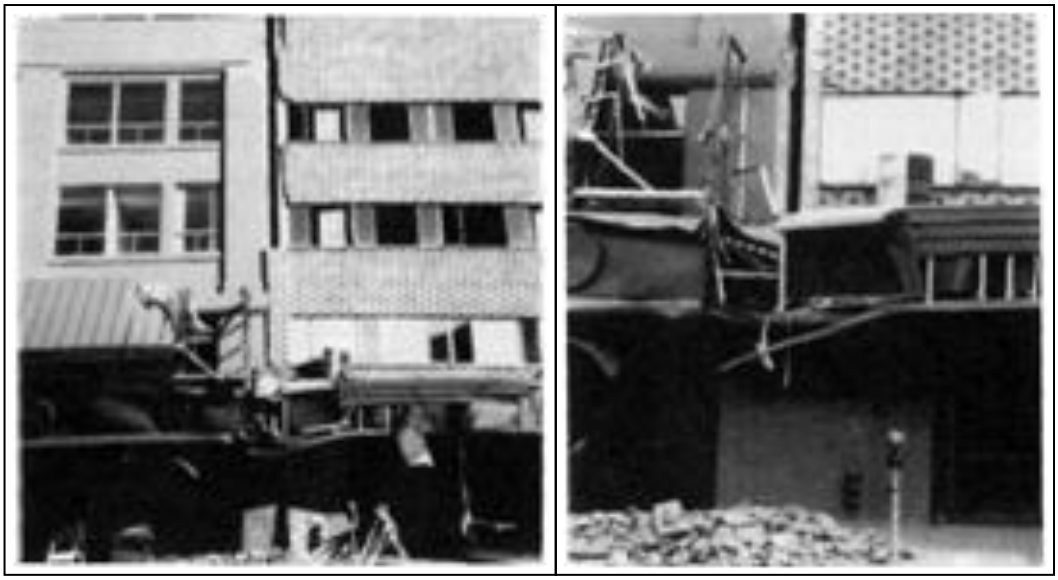

Consequences of facade pounding damage on the footpath below. Left: Building configuration. Right: damage to pavement as a result of falling debris.

Pounding damage due to differing overall building heights. The severe masonry damage resulted in the removal of this section of the building after the earthquake. Pounding damage was also present the entire length of the building contact.

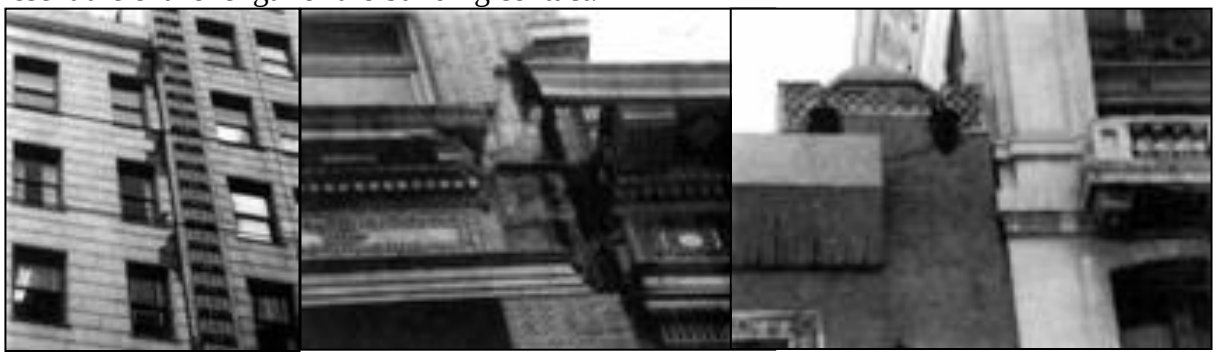

Three examples of minor or superficial pounding damage. Damage affects facade or parapets but does not affect the integrity of the structure.

1999 Izmit M_w 7.4

Source: (AIR 1999)

No supplemental information available. It is likely that local soil conditions have contributed to collision.

Source: http://www.world-housing.net/whereport1view.php?id=100031

Wall failure due to pounding damage between a two and a six storey structure.

2001 Nisqually M_w 6.8

Source: http://www.eeri.org/mitigation/image-gallery?g2_itemId=28049&g2

Low rise pounding damage. Left: Building configuration. Right: Magnification of damage.

Source: http://nsmp.wr.usgs.gov/data_sets/20010228_1/20010228_seattle_pics.html

Minor pounding damage. Left: building configuration. Right: Magnification of damage.

2006 Yogyakarta M_w 6.3

Source: (Elanshai et al. 2007)

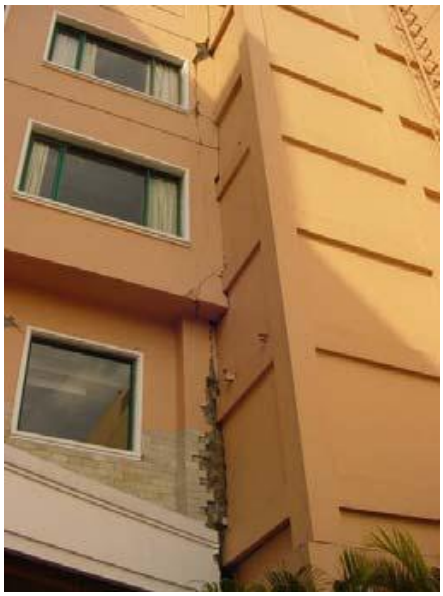

Minor pounding damage at seismic separation.

2007 Peru M_w 8.0

Source: (Yu and Gonzalez 2008)

Minor damage at seismic separation in a hospital. Pounding occurred between the wings of the hospital and the elevator tower.

2007 Gisbourne M_w 6.3

Source: (Evans and Wells 2008)

Damage between two two-storey masonry buildings. Left; external photo of impacted wall. Right: Internal damage.

2008 Wenchaun M_w 7.9

Source: (Wang and Chau 2008)

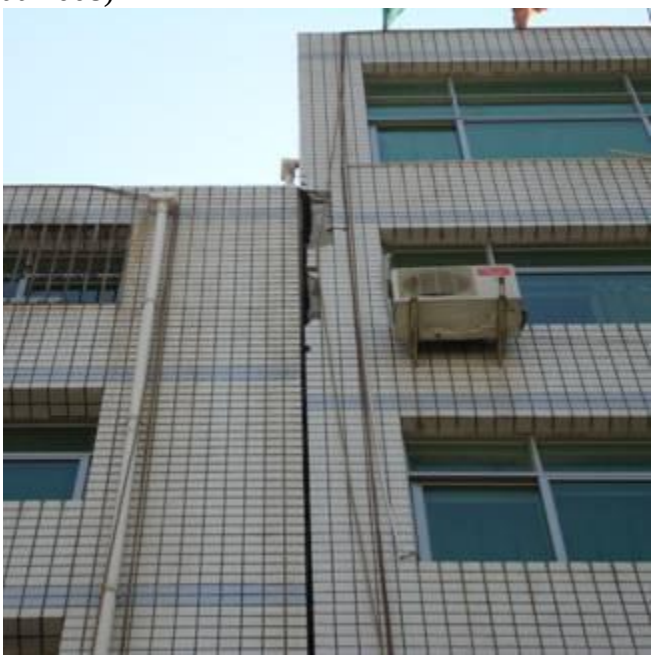

Superficial pounding damage.

2009Wenchaun M_w 6.3

Source: (AIR 2009)

Significant pounding damage between two low rise structures. Damage is concentrated at the second floor of the taller building.

2010Haiti M_w 7.0

Source: Fierro, E. (2010) Title page - *Engineering Earthquake Practice*. National Information Centre of Earthquake Engineering 4(2) www.nicee.org

It is unclear whether pounding damage occurred before or after collapse of the central building. However, significant damage at the point of impact in the rightmost building is apparent.

Appendix C Derivation of Stereo Mechanics

The post collision velocities of two colliding point masses are calculated below using known pre-collision velocities, the mass of each object and a specified degree of collision plasticity.

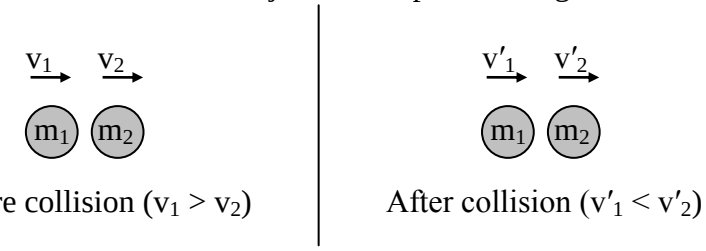

Before collision ($v_1 > v_2$) | After collision ($v'_1 < v'_2$)

Collision plasticity is characterised using the coefficient of restitution, e. The coefficient of restitution is defined as the ratio of the restitution impulse and the approach impulse during contact.

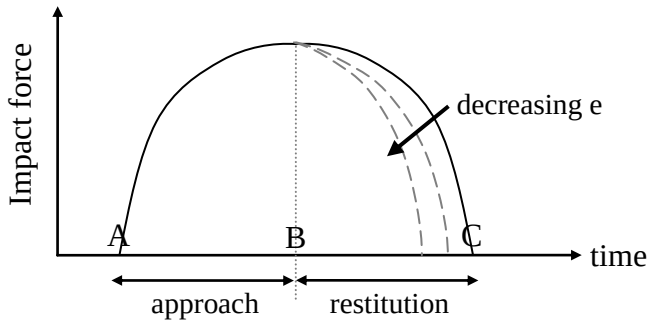

The momentum of each particle can be presented at three moments in time:

Time	Mass 1 momentum	Mass 2 momentum
Before collision	$p_{1A} = m_1 v_1$	$p_{2A} = m_2 v_2$
During collision, when there is no relative velocity between m_1 and m_2	$p_{1B} = m_1 v_n$	$p_{2B} = m_2 v_n$
After collision	$p_{1C} = m_1 v'_1$	$p_{2C} = m_2 v'_2$

Where v_n is the 'common normal velocity' and describes the velocity at which both point masses move at the time during the collision when there is no relative velocity. Since the total momentum of the system does not change:

$$m_1 v_1 + m_2 v_2 = (m_1 + m_2) v_n = m_1 v'_1 + m_2 v'_2$$

Thus

$$v_n = \frac{m_1 v_1 + m_2 v_2}{m_1 + m_2} = \frac{m_1 v'_1 + m_2 v'_2}{m_1 + m_2}$$

The impulse exerted on each point mass can be calculated by just considering that mass. Furthermore, by Newton's second law, the impulse exerted on one mass is equal and opposite to the impulse exerted on the other mass. The momentum of each particle can be related by the definition of e.

$$e = \frac{\Delta p_{\text{restitution}}}{\Delta p_{\text{approach}}} = \frac{p_{1C} - p_{1B}}{p_{1B} - p_{1A}} = \frac{p_{2B} - p_{2C}}{p_{1B} - p_{1A}} = \frac{m_2 v_n - m_2 v'_2}{m_1 v_n - m_1 v_1}$$

By substituting for the v_n in terms of the initial velocities in the denominator, and for v_n in terms of the final velocities in the numerator, v_n can be removed:

$$e = \frac{m_2\left(\frac{m_1v_1' + m_2v_2'}{m_1 + m_2}\right) - m_2v_2'}{m_1\left(\frac{m_1v_1 + m_2v_2}{m_1 + m_2}\right) - m_1v_1} = \frac{m_2(m_1v_1' + m_2v_2') - (m_1 + m_2)m_2v_2'}{m_1(m_1v_1 + m_2v_2) - (m_1 + m_2)m_1v_1}$$

$$= \frac{m_2m_1v_1' + m_2{}^2v_2' - m_1m_2v_2' - m_2{}^2v_2'}{m_1{}^2v_1 + m_1m_2v_2 - m_1{}^2v_1 - m_2m_1v_1} = \frac{m_2m_1(v_1' - v_2')}{m_2m_1(v_2 - v_1)}$$

$$e = \frac{(v_1' - v_2')}{(v_2 - v_1)}$$

Thus e is a ratio of the final relative velocity and the initial relative velocity. To find v'_2 in terms of the initial velocities, both v_n terms are substituted in terms of the initial velocities (into the equation at the bottom of the previous page).

$$e = \frac{\Delta p_{\text{restitution}}}{\Delta p_{\text{approach}}} = \frac{m_2\left(\frac{m_1v_1 + m_2v_2}{m_1 + m_2}\right) - m_2v_2'}{m_1\left(\frac{m_1v_1 + m_2v_2}{m_1 + m_2}\right) - m_1v_1}$$

$$= \frac{m_2(m_1v_1 + m_2v_2) - (m_1 + m_2)m_2v_2'}{m_1(m_1v_1 + m_2v_2) - (m_1 + m_2)m_1v_1}$$

$$= \frac{m_2(m_1v_1 + m_2v_2) - (m_1 + m_2)m_2v_2'}{m_2m_1(v_2 - v_1)}$$

$$m_1(v_2 - v_1)e = (m_1v_1 + m_2v_2) - (m_1 + m_2)v_2'$$

$$v_2' = \frac{m_1v_1 + m_2v_2}{m_1 + m_2} - \frac{m_1e(v_2 - v_1)}{m_1 + m_2}$$

$$= \frac{m_1v_1}{m_1 + m_2} + \frac{m_2v_2}{m_1 + m_2} - \frac{m_1e(v_2 - v_1)}{m_1 + m_2}$$

$$= \frac{m_1v_1}{m_1 + m_2} + \frac{(m_1 + m_2)v_2}{m_1 + m_2} - \frac{m_1v_2}{m_1 + m_2} - \frac{m_1e(v_2 - v_1)}{m_1 + m_2}$$

$$= \frac{m_1v_1}{m_1 + m_2} + v_2 - \frac{m_1v_2}{m_1 + m_2} - \frac{m_1e(v_2 - v_1)}{m_1 + m_2}$$

$$= v_2 - \frac{m_1(v_2 - v_1)}{m_1 + m_2} - \frac{m_1e(v_2 - v_1)}{m_1 + m_2}$$

$$v_2' = v_2 - (1 + e)\frac{m_1}{m_1 + m_2}(v_2 - v_1)$$

The expression for v'_1 can be found in a similar manner by taking $\Delta p_{\text{approach}}$ in terms of the impulse on mass 2, and $\Delta p_{\text{restitution}}$ in terms of mass 1. This gives:

$$v_1' = v_1 - (1 + e)\frac{m_2}{m_1 + m_2}(v_1 - v_2)$$

Appendix D Solution of Wave Equation for a Distributed Mass vs. a Rigid Barrier

Using the boundary conditions and initial conditions presented in Section 3.1.1, the wave equation is solved below. The defining properties of this collision are also identified.

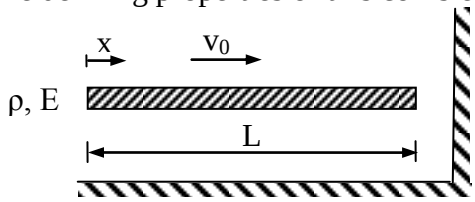

$$\frac{\partial^2 u(x,t)}{\partial t^2} = v^2 \frac{\partial^2 u(x,t)}{\partial x^2} \qquad where \;\; v^2 = \frac{E}{\rho}$$

$$E\frac{\partial u(0,t)}{\partial x} = 0 \qquad u(L,t) = 0 \qquad u(x,0) = 0 \qquad \frac{\partial u(x,0)}{\partial t} = v_0$$

Solve using separation of variables:

$$u(x,t) = X(x)T(t)$$

Substituting into the governing equation provides:

$$\frac{d^2T}{dt^2} + \lambda v T = 0 \qquad and \qquad \frac{d^2X}{dx^2} + \lambda^2 X = 0$$

Which has the following solutions:

$$T(t) = A\cos\lambda v t + B\sin\lambda v t \qquad X(x) = C\cos\lambda x + D\sin\lambda x$$

Applying boundary conditions:

$$D = 0 \qquad \lambda_n = \frac{(2n-1)\pi}{2L}$$

Which produces the general solution:

$$u(x,t) = \sum_{n=1}^{\infty} \cos\lambda_n x\left(A_n \cos\lambda v t + B_n \sin\lambda v t\right)$$

Applying initial conditions and solving the infinite Fourier series:

$$\sum_{n=1}^{\infty} A_n = 0 \qquad B_n = \frac{2v_0(-1)^{n+1}}{\lambda_n{}^2 vL}$$

Therefore the complete solution is:

$$u(x,t) = \sum_{n=1}^{\infty} \frac{2v_0(-1)^{n+1}}{\lambda_n{}^2 vL}\cos(\lambda_n x)\sin(\lambda_n v t)$$

$$\frac{\partial u(x,t)}{\partial t} = \sum_{n=1}^{\infty} \frac{2v_0(-1)^{n+1}}{\lambda_n L}\cos(\lambda_n x)\cos(\lambda_n v t)$$

$$\frac{\partial^2 u(x,t)}{\partial t^2} = \sum_{n=1}^{\infty} \frac{2v_0(-1)^{n} v}{L}\cos(\lambda_n x)\sin(\lambda_n v t)$$

$$f(x,t) = E\frac{\partial u(x,t)}{\partial x} = \sum_{n=1}^{\infty} \frac{2v_0(-1)^{n} E_1}{\lambda_n vL}\sin(\lambda_n x)\sin(\lambda_n v t)$$

Inspection of the solution for u(x,t) provides the duration of the collision

$$\sin(\lambda_n v t) = 0 \quad when \quad \lambda_n v t = \pi$$

Substituting for λ_n and knowing that n =1 corresponds to the fundamental mode gives:

$$\frac{(2n-1)\pi}{2L} vt = \pi$$

thus

$$t = \frac{2L}{v}$$

Therefore the duration of the collision is the time for the impact wave to travel the length of the rod and back again.

Alternatively, the solution may be placed in dimensionless form. This can be achieved by making the following substitutions:

$$\mathrm{T} = \frac{v}{L}t \qquad \mathrm{X} = \frac{x}{L} \qquad \varepsilon_n = (2n-1)\frac{\pi}{2} \qquad u(\mathrm{X},\mathrm{T}) = \frac{v_0 L}{v} U(\mathrm{X},\mathrm{T})$$

$$\mathrm{v}(\mathrm{X},\mathrm{T}) = \mathrm{v}_0 \mathrm{V}(\mathrm{X},\mathrm{T}) \qquad \mathrm{a}(\mathrm{X},\mathrm{T}) = \frac{\mathrm{v}_0 v}{L}\mathrm{A}(\mathrm{X},\mathrm{T}) \qquad f(\mathrm{X},\mathrm{T}) = \frac{\mathrm{E}\mathrm{v}_0}{v}\mathrm{F}(\mathrm{X},\mathrm{T})$$

Thus

$$U(\mathrm{X},\mathrm{T}) = 2\sum_{n=1}^{\infty} \frac{(-1)^{n+1}}{\varepsilon_n{}^2} \cos(\varepsilon_n \mathrm{X}) \sin(\varepsilon_n \mathrm{T})$$

$$\mathrm{V}(\mathrm{X},\mathrm{T}) = 2\sum_{n=1}^{\infty} \frac{(-1)^{n+1}}{\varepsilon_n} \cos(\varepsilon_n \mathrm{X}) \cos(\varepsilon_n \mathrm{T})$$

$$\mathrm{A}(\mathrm{X},\mathrm{T}) = 2\sum_{n=1}^{\infty} (-1)^n \cos(\varepsilon_n \mathrm{X}) \sin(\varepsilon_n \mathrm{T})$$

$$\mathrm{F}(\mathrm{X},\mathrm{T}) = 2\sum_{n=1}^{\infty} \frac{(-1)^n}{\varepsilon_n} \sin(\varepsilon_n \mathrm{X}) \sin(\varepsilon_n \mathrm{T})$$

Presentation in this form is useful since these functions are independent of v_0.

Appendix E Initial Acceleration Solution of Wave Equation for a Distributed Mass vs. Rigid Barrier

This solution process is similar to Appendix D, but differs in initial conditions. This derivation is known to deviate from the standard mathematical solutions for PDEs, because usually acceleration initial conditions cannot be applied. However, comparisons with numerical solutions have shown complete agreement. It is assumed that this approach is mathematically acceptable for some reason unknown to the author.

Using the boundary conditions and configuration presented in Appendix D, the initial conditions are changed to:

$$\frac{\partial u(x,0)}{\partial t} = v_0 \qquad \frac{\partial^2 u(x,0)}{\partial t^2} = a_0$$

The general solution is identical to Appendix D:

$$u(x,t) = \sum_{n=1}^{\infty} \cos \lambda_n x \left(A_n \cos \lambda \nu t + B_n \sin \lambda \nu t\right)$$

Applying initial conditions provides:

$$A_n = \frac{2a_0(-1)^n}{{\lambda_n}^3 \nu^2 L} \qquad B_n = \frac{2v_0(-1)^{n+1}}{{\lambda_n}^2 \nu L}$$

However, as no displacement initial condition has been applied, this solution does not give u(x,0) = 0. This is adjusted by adding a constant to the solution

$$u(x,t) = E + \sum_{n=1}^{\infty} \cos \lambda_n x \left(A_n \cos \lambda \nu t + B_n \sin \lambda \nu t\right)$$

Applying u(x,0) = 0 gives:

$$E = \sum_{n=1}^{\infty} \frac{2a_0(-1)^{n+1}}{{\lambda_n}^3 \nu^2 L} \cos \lambda_n x$$

Equations of the form Acos(ωt) + Bsin(ωt) can be simplified into Rsin(ωt +ϕ). Applying this simplification gives:

$$R = \sqrt{A^2 + B^2} = \frac{2v_0(-1)^{n+1}}{{\lambda_n}^2 \nu L} \sqrt{1 + \left(\frac{a_0}{\lambda_n w_0}\right)^2}$$

$$\phi = \tan^{-1}\left(\frac{A}{B}\right) = \tan^{-1}\left(\frac{-a_0}{\lambda_n w_0}\right)$$

Thus the solution for displacement is:

$$u(x,t) = \sum_{n=1}^{\infty} \cos \lambda_n x \frac{2v_0(-1)^{n+1}}{{\lambda_n}^2 \nu L} \left(\sqrt{1 + \left(\frac{a_0}{\lambda_n w_0}\right)^2} \sin\left(\lambda \nu t + \tan^{-1}\left(\frac{-a_0}{\lambda_n w_0}\right)\right) + \frac{a_0}{\lambda_n w_0} \right)$$

This can also be made dimensionless, however one new term is required:

$$\gamma = \frac{a_0 L}{w_0}$$

This term indicates the relative strength of the initial acceleration compared to the initial velocity. The following substitutions are also required to provide the dimensionless solution:

$$\mathrm{T} = \frac{\nu}{L} t \qquad \mathrm{X} = \frac{x}{L} \qquad \varepsilon_n = (2n-1)\frac{\pi}{2} \qquad u(\mathrm{X},\mathrm{T}) = \frac{v_0 L}{\nu} U(\mathrm{X},\mathrm{T})$$

$$v(X,T) = v_0 V(X,T) \qquad a(X,T) = \frac{v_0 \nu}{L} A(X,T) \qquad f(X,T) = \frac{E v_0}{\nu} F(X,T)$$

Thus:

$$U(X,T,\gamma) = 2\sum_{n=1}^{\infty} \frac{(-1)^{n+1}}{\varepsilon_n{}^2} \cos(\varepsilon_n X) \left[\sqrt{1+\left(\frac{\gamma}{\varepsilon_n}\right)^2} \sin\left(\varepsilon_n T - \tan^{-1}\left(\frac{\gamma}{\varepsilon_n}\right)\right) + \frac{\gamma}{\varepsilon_n} \right]$$

$$V(X,T,\gamma) = 2\sum_{n=1}^{\infty} \frac{(-1)^{n+1}}{\varepsilon_n} \cos(\varepsilon_n X) \sqrt{1+\left(\frac{\gamma}{\varepsilon_n}\right)^2} \cos\left(\varepsilon_n T - \tan^{-1}\left(\frac{\gamma}{\varepsilon_n}\right)\right)$$

$$A(X,T,\gamma) = 2\sum_{n=1}^{\infty} (-1)^n \cos(\varepsilon_n X) \sqrt{1+\left(\frac{\gamma}{\varepsilon_n}\right)^2} \sin\left(\varepsilon_n T - \tan^{-1}\left(\frac{\gamma}{\varepsilon_n}\right)\right)$$

$$F(X,T,\gamma) = 2\sum_{n=1}^{\infty} \frac{(-1)^{n}}{\varepsilon_n} \sin(\varepsilon_n X) \left[\sqrt{1+\left(\frac{\gamma}{\varepsilon_n}\right)^2} \sin\left(\varepsilon_n T - \tan^{-1}\left(\frac{\gamma}{\varepsilon_n}\right)\right) + \frac{\gamma}{\varepsilon_n} \right]$$

Appendix F Solution of the Wave Equation for Two Colliding Distributed Masses

The wave equation is solved below for the collision of two distributed masses. Important parameters in this process are also simplified and non-dimensionalised.

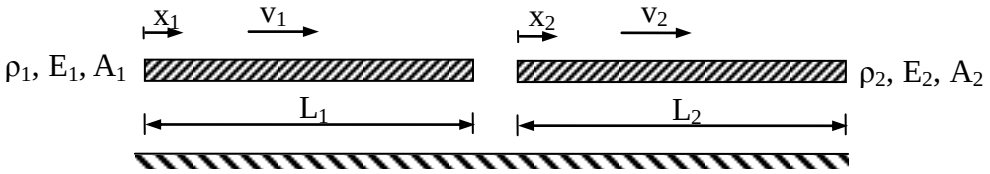

Consider first mass 1:

$$\frac{\partial^2 u_1(x,t)}{\partial t^2} = \nu_1^{\,2}\frac{\partial^2 u_1(x,t)}{\partial x^2} \qquad \text{where } \nu_1^{\,2} = \frac{E_1}{\rho_1}$$

$$E_1\frac{\partial u_1(0,t)}{\partial x} = 0 \qquad u_1(L_1,t) = v_c t \qquad u_1(x,0) = 0 \qquad \frac{\partial u_1(x,0)}{\partial t} = \mathrm{v}_{0,1}$$

As one of the boundary conditions is now non-homogeneous, the solution for $u_1(x,t)$ must be broken into stationary and transient components (ϕ_1 and ψ_1, respectively). ϕ_1 has homogeneous boundary conditions and so D and λ_n are solved in an identical manner to Appendix D. To solve the constants for ψ_1, substitute into the governing wave equation;

$$\frac{\partial^2 \psi_1}{\partial t^2} = \nu_1^{\,2}\frac{\partial^2 \psi_1}{\partial x^2}$$

$$0 = \nu_1^{\,2}\frac{\partial^2 \psi_1}{\partial x^2}$$

Provided the second time derivative is zero. The general solution of this expression is

$$\psi_1 = Ex + F$$

Where E and/or F may be functions of time. Applying the boundary conditions gives

$$\frac{\partial \psi_1(0,t)}{\partial x} = 0 = E \qquad \psi_1(L,t) = v_c t = F$$

$$\psi_1(x,t) = v_c t$$

Initial conditions must now be solved. Applying the displacement initial condition provides

$$u_1(x,0) = \phi_1(x,0) + \psi_1(x,0) = 0$$
$$= \phi_1(x,0) + 0$$

This has the same solution as Appendix D (A_n=0). This process is applied again to find the velocity initial condition

$$\frac{\partial u_1(x,0)}{\partial t} = \frac{\partial \phi_1(x,0)}{\partial t} + \frac{\partial \psi_1(x,0)}{\partial t} = \mathrm{v}_{0,1}$$
$$= \frac{\partial \phi_1(x,0)}{\partial t} + \mathrm{v}_c$$
$$\mathrm{v}_{0,1} - \mathrm{v}_c = \frac{\partial \phi_1(x,0)}{\partial t}$$

Thus B_n is:

$$B_n = \frac{2(\mathrm{v}_{0,1} - v_c)(-1)^{n+1}}{\lambda_{n,1}^{\,2}\nu_1 L_1}$$

Therefore the full solution is:

$$u_1(x,t) = \mathrm{v_c} t + \sum_{n=1}^{\infty} \frac{2(\mathrm{v}_{0,1} - \mathrm{v}_c)(-1)^{n+1}}{{\lambda_{n,1}}^2 \nu_1 L_1} \cos(\lambda_{n,1} x) \sin(\lambda_{n,1} \nu_1 t)$$

$$\frac{\partial u_1(x,t)}{\partial t} = \mathrm{v_c} + \sum_{n=1}^{\infty} \frac{2(\mathrm{v}_{0,1} - \mathrm{v}_c)(-1)^{n+1}}{\lambda_{n,1} L_1} \cos(\lambda_{n,1} x) \cos(\lambda_{n,1} \nu_1 t)$$

$$\frac{\partial^2 u_1(x,t)}{\partial t^2} = \sum_{n=1}^{\infty} \frac{2(\mathrm{v}_{0,1} - \mathrm{v}_c)(-1)^{n} \nu_1}{L_1} \cos(\lambda_{n,1} x) \sin(\lambda_{n,1} \nu_1 t)$$

$$f_1(x,t) = E_1 \frac{\partial u(x,t)}{\partial x} = \sum_{n=1}^{\infty} \frac{2(\mathrm{v}_{0,1} - \mathrm{v}_c)(-1)^{n} E_1}{\lambda_{n,1} \nu_1 L_1} \sin(\lambda_{n,1} x) \sin(\lambda_{n,1} \nu_1 t)$$

Similarly, by changing the ends of the boundary conditions, the solution for mass 2 is

$$u_2(x,t) = \mathrm{v_c} t + \sum_{n=1}^{\infty} \frac{2(\mathrm{v}_{0,2} - \mathrm{v}_c)}{{\lambda_{n,2}}^2 \nu_2 L_2} \sin(\lambda_{n,2} x) \sin(\lambda_{n,2} \nu_2 t)$$

$$\frac{\partial u_2(x,t)}{\partial t} = \mathrm{v_c} + \sum_{n=1}^{\infty} \frac{2(\mathrm{v}_{0,2} - \mathrm{v}_c)}{\lambda_{n,2} L_2} \sin(\lambda_{n,2} x) \cos(\lambda_{n,2} \nu_2 t)$$

$$\frac{\partial^2 u_2(x,t)}{\partial t^2} = \sum_{n=1}^{\infty} \frac{2(\mathrm{v}_{0,2} - \mathrm{v}_c)(-1)^{n} \nu_2}{L_2} \sin(\lambda_{n,2} x) \sin(\lambda_{n,2} \nu_2 t)$$

$$f_2(x,t) = E_2 \frac{\partial u_2(x,t)}{\partial x} = \sum_{n=1}^{\infty} \frac{2(\mathrm{v}_{0,2} - \mathrm{v}_c) E_2}{\lambda_{n,2} \nu_2 L_2} \sin(\lambda_{n,2} x) \sin(\lambda_{n,2} \nu_2 t)$$

And the duration of the collision is now the lesser of:

$$t_1 = \frac{2L_1}{\nu_1} \qquad t_2 = \frac{2L_2}{\nu_2}$$

Note these expressions are only valid until the lesser of t_1 and t_2 is reached.

The solutions may be placed in dimensionless form. This can be achieved by making the following substitutions.

$$\mathrm{T}_m = \frac{\nu_m}{L_m} t \qquad \mathrm{X}_m = \frac{x}{L_m} \qquad \varepsilon_n = (2n-1)\frac{\pi}{2} \qquad \Psi_m = \frac{\mathrm{v}_c}{\mathrm{v}_{0,\mathrm{m}}}$$

$$u_m(\mathrm{X}_m, \mathrm{T}_m, \Psi_m) = \frac{\mathrm{v}_{0,m} L_m}{\nu_m} U_m(\mathrm{X}_m, \mathrm{T}_m, \Psi_m) \qquad \mathrm{v_m}(\mathrm{X}_m, \mathrm{T}_m, \Psi_m) = \mathrm{v}_{0,\mathrm{m}} \mathrm{V_m}(\mathrm{X}_m, \mathrm{T}_m, \Psi_m)$$

$$\mathrm{a_m}(\mathrm{X}_m, \mathrm{T}_m, \Psi_m) = \frac{\mathrm{v}_{0,m} \nu_m}{L_m} \mathrm{A_m}(\mathrm{X}_m, \mathrm{T}_m, \Psi_m) \qquad f_m(\mathrm{X}_m, \mathrm{T}_m, \Psi_m) = \frac{E \mathrm{v}_{0,\mathrm{m}}}{\nu_m} \mathrm{F_m}(\mathrm{X}_m, \mathrm{T}_m, \Psi_m)$$

Thus

$$U_1(\mathrm{X}_1, \mathrm{T}_1, \Psi_1) = \Psi_1 \mathrm{T}_1 + 2(1-\Psi_1) \sum_{n=1}^{\infty} \frac{(-1)^{n+1}}{{\varepsilon_n}^2} \cos(\varepsilon_n \mathrm{X}_1) \sin(\varepsilon_n \mathrm{T}_1)$$

$$\mathrm{V}_1(\mathrm{X}_1, \mathrm{T}_1, \Psi_1) = \Psi_1 + 2(1-\Psi_1) \sum_{n=1}^{\infty} \frac{(-1)^{n+1}}{\varepsilon_n} \cos(\varepsilon_n \mathrm{X}_1) \cos(\varepsilon_n \mathrm{T}_1)$$

$$\mathrm{A}_1(\mathrm{X}_1, \mathrm{T}_1, \Psi_1) = 2(1-\Psi_1) \sum_{n=1}^{\infty} (-1)^{n} \cos(\varepsilon_n \mathrm{X}_1) \sin(\varepsilon_n \mathrm{T}_1)$$

$$\mathrm{F}_1(\mathrm{X}_1, \mathrm{T}_1, \Psi_1) = 2(1-\Psi_1) \sum_{n=1}^{\infty} \frac{(-1)^{n}}{\varepsilon_n} \sin(\varepsilon_n \mathrm{X}_1) \sin(\varepsilon_n \mathrm{T}_1)$$

mass two's values are:

$$U_2(X_2, T_2, \Psi_2) = \Psi_2 T_2 + 2(1-\Psi_2)\sum_{n=1}^{\infty} \frac{1}{\varepsilon_n^{\,2}} \sin(\varepsilon_n X_2)\sin(\varepsilon_n T_2)$$

$$V_2(X_2, T_2, \Psi_2) = \Psi_2 + 2(1-\Psi_2)\sum_{n=1}^{\infty} \frac{1}{\varepsilon_n} \sin(\varepsilon_n X_2)\cos(\varepsilon_n T_2)$$

$$A_2(X_2, T_2, \Psi_2) = -2(1-\Psi_2)\sum_{n=1}^{\infty} \sin(\varepsilon_n X_2)\sin(\varepsilon_n T_2)$$

$$F_2(X_2, T_2, \Psi_2) = 2(1-\Psi_2)\sum_{n=1}^{\infty} \frac{1}{\varepsilon_n} \cos(\varepsilon_n X_2)\sin(\varepsilon_n T_2)$$

Appendix G Calculating Velocities in a Collision of Two Distributed Masses considering Momentum

The results of the wave equation may be found by only physical considerations and application of conservation of momentum. Such a derivation is presented below:

When two distributed masses collide, a shockwave travels through each mass, which then reflects at the free end before coming back to the collision interface. The velocity of the wave front may be different in each mass, and the masses may be of different length. This results in a differing axial 'collision' period. Consider a specific point on one of the masses, the forces acting on this particle are equal until the wave front passes its location. An instantaneous velocity change occurs as the wave front passes, after which the internal forces are changed but again balanced. Since the wave front can pass through each point twice during the course of a collision, a particle may move at one of three velocities v_i, v_c and v'_i. If the collision is assumed to elastic, the impulse of the wave front does not degrade. This means that the change in velocity that occurs when the wave front first passes is equal to the change in velocity when the reflected wave front passes again;

$$(v_c - v_i) = (v'_i - v_c)$$

$$v_c = \frac{v'_i + v_i}{2}$$

Now consider three instances in time where two distributed masses collide; the onset, the half way point, and the completion of the collision. In the example shown below $T_1/T_2 = ¾$.

	Mass 1 momentum	Mass 2 momentum
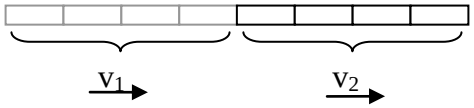	$m_1 v_1$	$m_2 v_2$
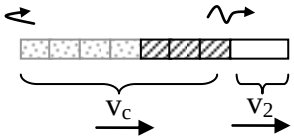	$m_1 v_C$	$m_2\left(\frac{T_1}{T_2}v_C + \left(1-\frac{T_1}{T_2}\right)v_2\right)$
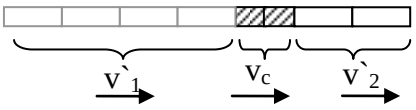	$m_1 v'_1$	$m_2\left(\left(2\frac{T_1}{T_2}-1\right)v'_2 + 2\left(1-\frac{T_1}{T_2}\right)v_C\right)$ $= m_2\left(\frac{T_1}{T_2}v'_2 + \left(1-\frac{T_1}{T_2}\right)v_2\right)$

From these values the impulse (change in momentum) between each time point is;

	Momentum Change	Mass 1	Mass 2
Approach	Intermediate - Initial	$m_1(v_c - v_1)$	$m_2\left(\frac{T_1}{T_2}(v_C - v_2)\right)$
Restitution	Final - Intermediate	$m_1(v'_1 - v_C)$	$m_2\left(\frac{T_1}{T_2}(v'_2 - v_C)\right)$

As the two masses are only interacting with each other, the impulse from Mass 1 must be equal and opposite to the impulse of Mass 2. This result can be used to find the intermediate velocity v_c both in terms of initial velocities and final velocities.

	Approach	Restitution
Initial expression	$m_1(v_c - v_1) = -m_2\left(\frac{T_1}{T_2}(v_C - v_2)\right)$	$m_1(v_1' - v_C) = -m_2\left(\frac{T_1}{T_2}(v_2' - v_C)\right)$
Rearranging for v_c	$v_C = \frac{m_1 v_1 + m_2 \frac{T_1}{T_2} v_2}{m_1 + m_2 \frac{T_1}{T_2}}$	$v_C = \frac{m_1 v_1' + m_2 \frac{T_1}{T_2} v_2'}{m_1 + m_2 \frac{T_1}{T_2}}$

The expression for v_c in terms of initial velocities matches the expression derived directly from the wave equation (Equation 3.1).

A relationship between initial and final velocities can be found by equating Mass 1's approach impulse to Mass 1's restitution impulse. This approach is valid because the wave front is known not to degrade, and the approach and restitution phases last an equal time interval. This means that the impulse of the first half of the collision is equal to the impulse of the second half of the collision.

$$m_1(v_c - v_1) = m_1(v_1' - v_c)$$

$$v_c - v_1 = v_1' - v_c$$

Substitute Left Hand Side (LHS) v_c in terms of initial velocities and Right Hand Side (RHS) in terms of final velocities;

$$\frac{m_1 v_1 + m_2 \frac{T_1}{T_2} v_2}{m_1 + m_2 \frac{T_1}{T_2}} - v_1 = v_1' - \frac{m_1 v_1' + m_2 \frac{T_1}{T_2} v_2'}{m_1 + m_2 \frac{T_1}{T_2}}$$

$$\frac{m_1 v_1 + m_2 \frac{T_1}{T_2} v_2 - m_1 v_1 - m_2 \frac{T_1}{T_2} v_1}{m_1 + m_2 \frac{T_1}{T_2}} = \frac{m_1 v_1' + m_2 \frac{T_1}{T_2} v_1' - m_1 v_1' - m_2 \frac{T_1}{T_2} v_2'}{m_1 + m_2 \frac{T_1}{T_2}}$$

$$\frac{m_2 \frac{T_1}{T_2}(v_2 - v_1)}{m_1 + m_2 \frac{T_1}{T_2}} = \frac{m_2 \frac{T_1}{T_2}(v_1' - v_2')}{m_1 + m_2 \frac{T_1}{T_2}}$$

$$(v_2 - v_1) = (v_1' - v_2')$$

$$v_2' = v_1' + v_1 - v_2$$

Using this result, and equating the expressions for v_c in terms of initial and final velocities from the previous table provides;

$$\frac{m_1 v_1 + m_2 \frac{T_1}{T_2} v_2}{m_1 + m_2 \frac{T_1}{T_2}} = \frac{m_1 v_1' + m_2 \frac{T_1}{T_2}\left(v_1' + v_1 - v_2\right)}{m_1 + m_2 \frac{T_1}{T_2}}$$

$$\left(m_1 + m_2 \frac{T_1}{T_2}\right) v_1' = m_1 v_1 - m_1 \frac{T_1}{T_2} v_1 + 2 m_2 \frac{T_1}{T_2} v_2$$

$$\left(m_1 + m_2 \frac{T_1}{T_2}\right) v_1' = m_1 v_1 + m_1 \frac{T_1}{T_2} v_1 - m_1 \frac{T_1}{T_2} v_1 - m_1 \frac{T_1}{T_2} v_1 + 2 m_2 \frac{T_1}{T_2} v_2$$

$$v_1' = v_1 + 2 \frac{m_2 \frac{T_1}{T_2}}{m_1 + m_2 \frac{T_1}{T_2}} \left(v_2 - v_1\right)$$

Similarly

$$v_2' = v_2 + 2 \frac{m_1 \frac{T_2}{T_1}}{m_2 + m_1 \frac{T_2}{T_1}} \left(v_1 - v_2\right)$$

However, while all of Mass 1 moves at v'_1 at the end of the collision, only part of Mass 2 moves at v'_2 (see the first table in this appendix). The average velocity of Mass 2 may be found by considering the momentum of Mass 2 at the end of the collision;

$$m_2 v_2'' = m_2 \left(\frac{T_1}{T_2} v_2' + \left(1 - \frac{T_1}{T_2}\right) v_2 \right)$$

Substituting for v'_2 provides

$$v_2'' = v_2 + 2 \frac{1}{\frac{T_2}{T_1} + \frac{m_2}{m_1}} \left(v_1 - v_2\right)$$

These equations match the results in Appendix F derived from classical wave theory

Appendix H Sample Calculations for Model Production

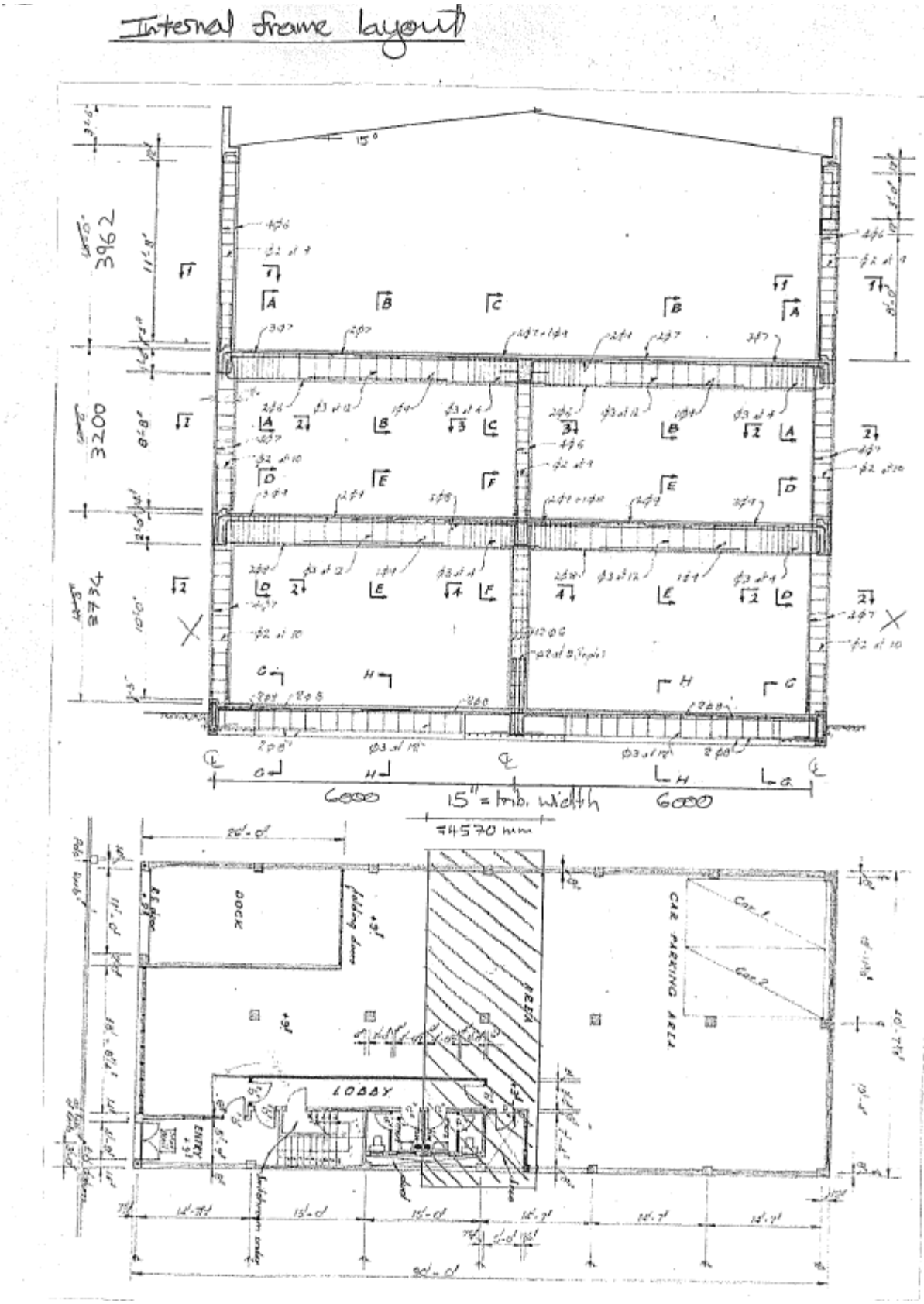

No. OF QUESTION

Internal frame model

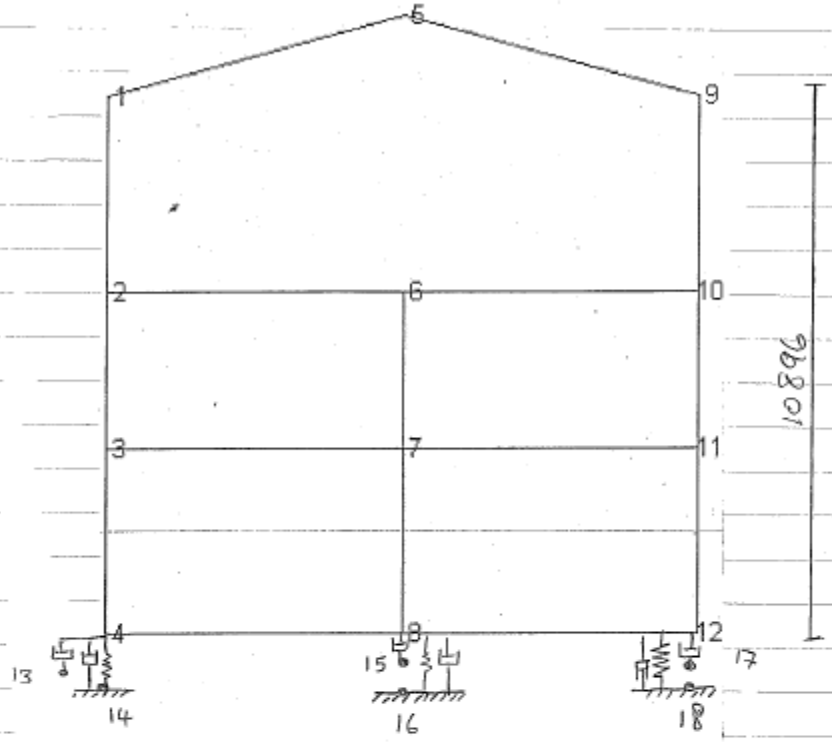

circled number
= Section number

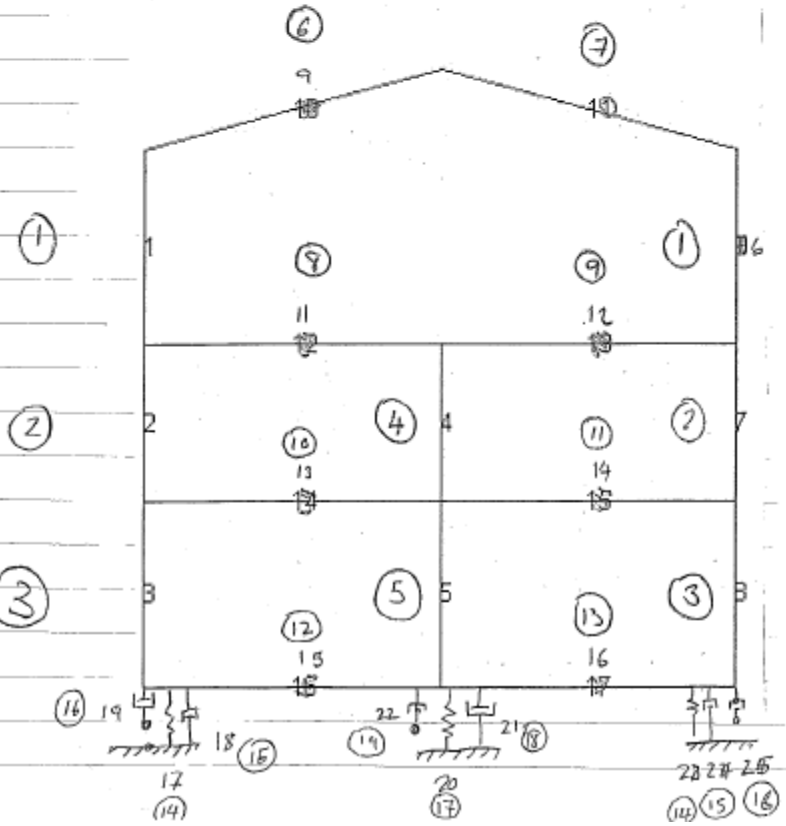

Element Sections

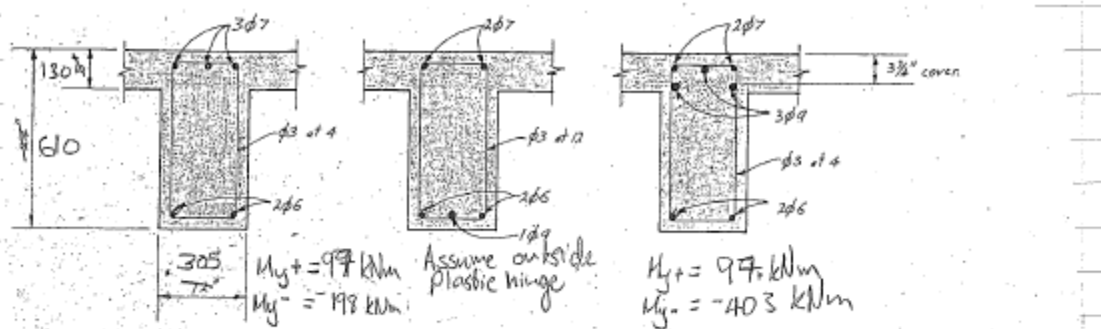

Extra width = 0.61 c.s.
Extra steel = 2#3

Extra width = 0.61 m c.s.
Extra steel = 4#3

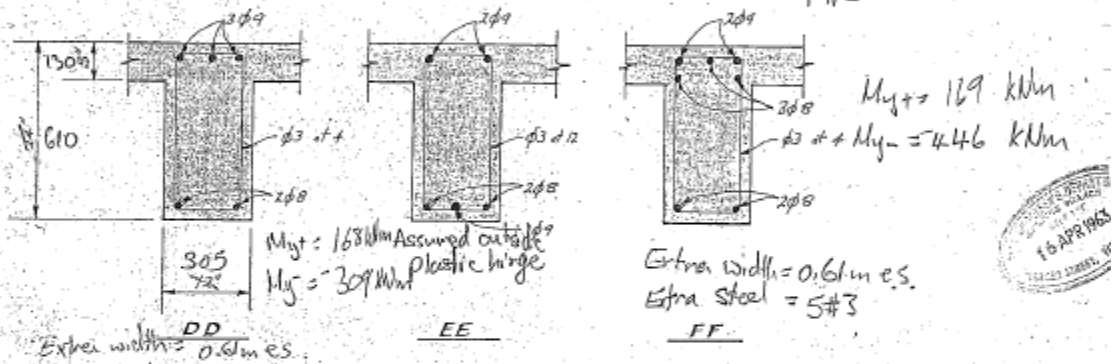

Extra width = 0.61 m c.s.
Extra steel = 1#5

Extra width = 0.61 m c.s.
Extra steel = 5#3

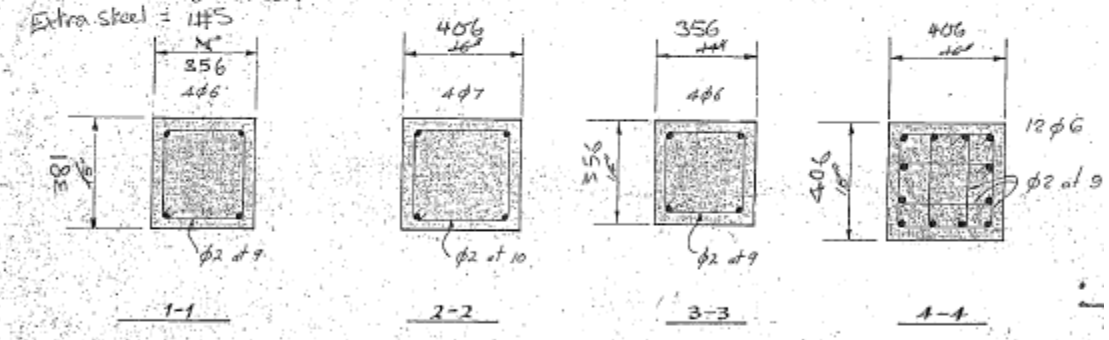

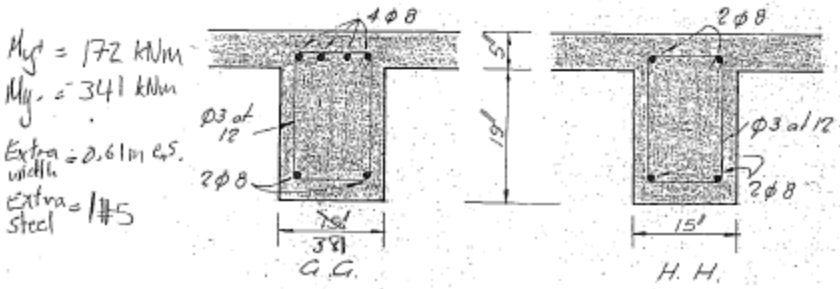

Calculate beam & column properties & capacities

Section 7.1.1 from NZSEE Guidelines:
Probable steel yield strength = 300 MPa (part e)
Probable concrete strength = 1.5x nominal (part f)
Original (nominal) strength is not specified ∴ assume $f'_{c(nom)} = 30$ MPa
→ $f'_c = 30 \times 1.5 = 45$ MPa

Steel yield	300 MPa
Concrete compressive strength	45 MPa

flexural strength reduction factor = 1.0 (part f)
shear strength reduction factor = 0.85 (part f)

From NZS3101:

$$E_c = 3320\sqrt{f'_c} + 6900 = 29\,171 \text{ MPa} \quad \text{(CL 5.2.3)}$$

For section capacity calculations. When modelling in Ruaumoko, an average stiffness is more appropriate thus

$$E_c = 3320\sqrt{(f'_c + 10)} + 6900 = 31\,522 \text{ MPa} \quad \text{(CL 5.2.3)}$$

Strength	$E_c = 29\,171$ MPa
modelling	$E_c = 31\,522$ MPa

Beam effective slab widths (NZS3103)

Compression slab contribution: (CL 9.3.1.2)
The strength of a section shall include a compression contribution from the slab not exceeding the smaller of:

1. 8 x min slab thickness = $8 \times 127 = 1.016$ m
2. The beam depth = 0.610 m
3. clear distance between adjacent beams $\times \left(\frac{d_{beam}}{d_{beam} + d_{adj\,beam}}\right) = 4.267 \times \frac{0.61}{2 \times 0.61} = 2.134$

∴ Compression contribution of slab extends **0.61 m** either side of beam

Note that 50% of this value is used in I_{cr} (CL 9.3.1.3)

Slab reinforcement contribution to beam (NZS3101 CL. 9.3.14, 9.4.1.6.1)

The strength of a section shall include a tension steel contribution from the slab not exceeding the smaller of:

1. The beam depth = 0.61 m
2. 8 x min slab thickness = 1.016 m
3. clear dist between adjacent beams $\times \left(\frac{d_{beam}}{d_{beam} + d_{adj\,beam}}\right) = 2.134$ m
4. Beam span ÷ 8 = $6/8 = 0.75$ m
5. distance from slab edge to considered section x 1.5 = 0.610 m

OF TION steel reinforcement in adjacent 0.61 m of slab

#3@15"crs 2 #3 3/4" from TOE = 2x71 = 142 mm²

#5@11"crs 3 #5 5-3/4" from TOE = 3x200 = 600 mm²

However, the additional steel strength may not exceed 10% of the total flexural tensile strength of the beam. Additional steel is stated next to beam section illustrations.

Calculate beam I_g and A

Only two beam geometries exist. Sections A – F:

	B	D	A=BD	y	Ay	$I_{xo}=\frac{BD^3}{12}$	y-ȳ	$A(y-\bar{y})^2$
Flange	610	130	79300	65	5.155×10^6	111.7×10^6	168	2.238×10^9
Web	305	610	186050	305	56.745×10^6	5769.1×10^6	72	0.964×10^9
			265350		61.9×10^6	5.881×10^9		3.202×10^9

$$\bar{y}=\frac{\Sigma Ay}{\Sigma A}=\frac{61.1\times10^6}{265350}=233\text{ mm}$$

$$I_{xx}=I_{xo}+A(y-\bar{y})^2=5.881\times10^9+3.202\times10^9=9.083\times10^9\text{ mm}^4$$

Section G-H:

	B	D	A=BD	y	Ay	$I_{xo}=\frac{BD^3}{12}$	y-ȳ	$A(y-\bar{y})^2$
Flange	610	130	79300	65	5.155×10^6	111.7×10^6	179	2.541×10^9
Web	381	610	232410	305	70.885×10^6	71066×10^9	61	865×10^6
			311710		76.04×10^6	7.318×10^9		3.406×10^9

$$\bar{y}=\frac{\Sigma Ay}{\Sigma A}=\frac{76.64\times10^6}{311710}=244\text{ mm}$$

$$I_{xx}=I_{xo}+A(y-\bar{y})^2=7.318\times10^9+3.406\times10^9=10.724\times10^9\text{ mm}^4$$

Beam Properties

Not used in Ruaumoko. Axial forces assume complete slab participation. Used in S.W. Calculation

NZS3101 Table C6.6

NZS3101 cl 9.3.9.3.3

Section	A_g	I_g	$0.4I_g$	M_y^{+ve}	M_y^{-ve}	A_g+A_{slab}	A_{shear}
A	265350	9.083×10^9	3.633×10^9	97	-198	740500	173850
B	265350	9.083×10^9	3.633×10^9	—	—	740500	173850
C	265350	9.083×10^9	3.633×10^9	97	-403	740500	173850
D	265350	9.083×10^9	3.633×10^9	168	-369	740500	173850
E	265350	9.083×10^9	3.633×10^9	—	—	740500	173850
F	265350	9.083×10^9	3.633×10^9	169	-446	740500	173850
G	311710	10.724×10^9	4.290×10^9	172	-341	776980	21770
	mm^2	mm^4	mm^4	kNm	kNm	mm^2	

Roof steel section: 12"x5"x32 lb RSJ.

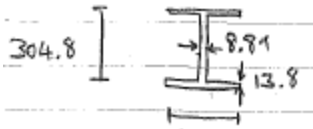

$A_g = 9.26\ in^2$
$= 5974\ mm^2$

32 lb/foot = 14.51 kg/ft
= 45.6 kg/m
= 0.467 kN/m

$I_g = 215.8\ in^4$
$= 89.82 \times 10^6\ mm^4$

$M_y^{+ve} = M_y^{-ve} = fZ = 300 \times \frac{89.82 \times 10^6}{304.8/2} = 177\ kNm$

Beam Hysteresis modelling

Beam hysteresis is modelled using the modified Takeda rule (rule 4) with $\alpha = 0.5$ and $\beta = 0$, as recommended by Dong 2003. See also Thorden modeling assumptions document in 'Study Summaries'.

Column properties

Section	A_g	I_g	α	N_{min}	N_{Bal}	M_{Bal}	N_{max}	$\frac{M_{Bal}}{M_{cr}}$
1-1	135636	1.432×10^9	0.4	-6350	-2845	274	340	0.6
2-2	154686	2.125×10^9	0.4	-7320	-3245	364	465	0.6
3-3	126736	1.339×10^9	0.4	-5956	-2659	257	340	0.6
4-4	164800	2.264×10^9	0.46	-8260	-3654	414	1022	0.6
	mm^2	mm^4	mm^4	kN	kN	kNm	kN	

Note: I_g is used as elastic stiffness in model as stiffness adjustment occurs in hysteresis model.

Defn of α:

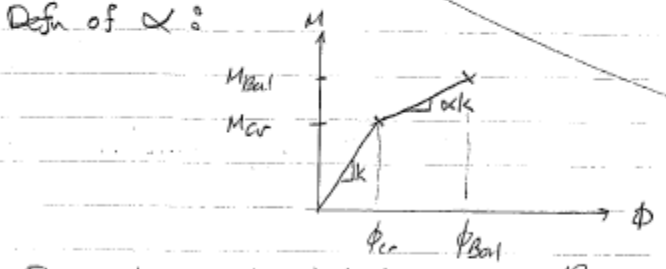

Properties calculated using Response 2000 (using elasto-plastic steel)
$\frac{M_{Bal}}{M_{cr}}$ calculated from response curves M_{cr} is balance moment at first cracking

$$\alpha = \frac{\left(1 - \frac{M_{Bal}}{M_{cr}}\right)}{\frac{\phi_y E I_g}{M_y} - \frac{M_{Bal}}{M_{cr}}}$$

where ϕ_y is taken from response

α and $\frac{M_{Bal}}{M_{cr}}$ rounded to nearest S.f.

Column Hysteresis Modelling

All columns are modelled using the Revised Takeda hysteresis with allowance for M-N interaction (rule 57) with

$\alpha = \beta = 0.4$, $\gamma = 0.5$, $\Delta = 0$, $\phi = 1$, FCRP = FCRN = 0.6

IOP = 0. Ruaumoko, M-N interaction type 2 is selected. Other models may be more suited to type 7 (refer Ruaumoko 3D manual, pg 45)

Seismic Mass properties (NZS1170.1)

Diagonal mass matrix to be used in Ruaumoko. Self weight and remaining seismic mass is assigned in member properties when the weights are distributed. Similarly, Q+G loadings are applied in member properties when distributed.

Self weight of sections:

Concrete unit weight = 24 kN/m³ Steel unit weight = 76.9 kN/m³

Self weight per linear metre of section = γA_g ← Does not include full slab for beam sections

Additional Self weight

Roof level:

Note SDL & Q added to translational D.O.F only

Roof additional deadload:

7 no 8" x 2" timber beams/rafter = 4.6 kN/m³ × 200×50 × 45570×10⁻⁹ (section, trib length)

= 0.2102 kN = 0.035 kN/m

Assume galv corrugated sheeting = 0.12 kPa × 4.57 = 0.548 kN/m

Assume ceiling cladding gypsum plaster = 0.13 kPa × 4.57 = 0.594 kN/m

SDL Roof 1.177 kN/m

Q = 0 as non trafficable roof ($\psi_c = 0$)

2nd floor:

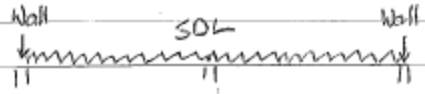

Masonry wall SDL - 11" cavity blockwork - 2" cavity

9" × 140" × (25.4)² × 4570 × 1×10⁻⁹ × 24 = 8.9 kN

(Thickness, Height, inch→mm, trib width, mm³→m³, γ)

Assume this mass is associated with the floor it bounds on

Additional Slab SDL

130 × (4570 − 610×2) × 24 × (1×10⁻³)² = 10.5 kN/m

(Slab thickness; included as S.W.; mm→m)

Assume ceiling attatched to underside = 0.594 kN/m (see roof calc)

SDL floor 11.1 kN/m

Live load

Assume area is used as offices $q = 3.0$ kPa

Calculate ψ_A assuming contributions from all floors (assuming bottom columns are critical)

$$\psi_A = 0.3 + \frac{3}{\sqrt{A}} = 0.3 + \frac{3}{\sqrt{2 \times 4.57 \times 12}} = 0.586$$

$$Q = 3 \times 0.586 = 1.76 \text{ kPa}$$

$$UDL = 1.76 \times 4.57 = 8.04 \text{ kN/m}$$

Seismic mass $= G + \psi_E Q = G + 0.3Q$

$= G + 0.3 \times 8.04$ kN/m

Seismic Mass = G + 2.412 kN/m

Load combination $= G + E_u + \psi_c Q = G + E + 0.4Q$

$= G + E + 3.22$ kN/m

Live Load = 3.22 kN/m

1st floor:

Taken as equal to second floor weights

2nd floor:

Taken as equal to second floor weight. Mass assigned as normal since it may affect SSI. Loads not applied as they are directly transfered to soil.

Notes:

Plastic hinge length $L_p = 0.5h$, as per NZSEE guidelines, and Priestly & Park 1987.

Loads from modelled members inputs as initial fixed end moments. Loads coming from other masses (ie live load, other members) input as static loads.

UDL FEM:  $= \frac{wL}{2}, \frac{wL^2}{12}, \frac{wL^2}{12}, \frac{wL}{2}$

Axial tension & compression beam yield values obtained from Response 2000

L OF STION Additional Loads (+Weights)

Apply weights to vertical & horizontal DoF

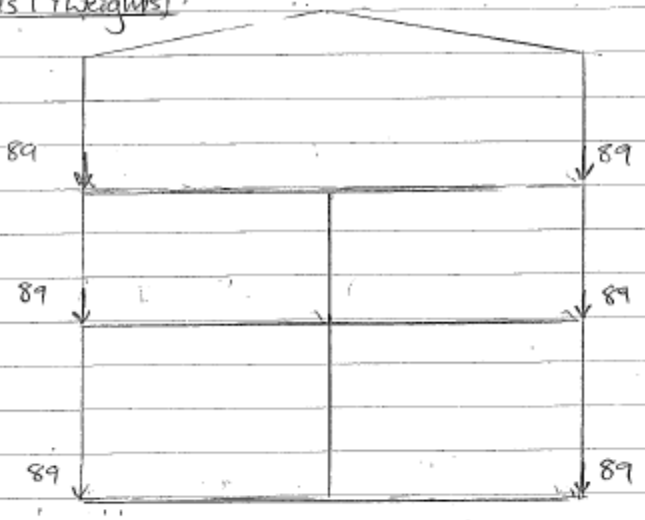

Foundation modelling

Plan:

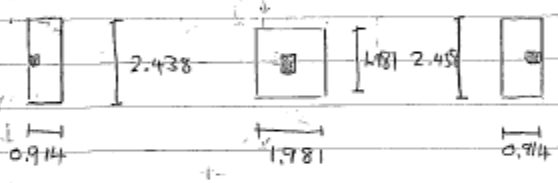

External Foundations: (from Soil Modelling Method in Study Summaries)

$r_0 = \sqrt{\frac{A_0}{\pi}} = \sqrt{\frac{0.914 \times 2.438}{\pi}} = 0.8422$ m $C_s = 290$ m/s $G = 175$ MPa $\nu = 0.3$

General model:

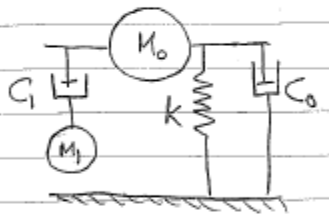

$C_0 = \frac{r_0}{C_s} \gamma_0 K$

$C_1 = \frac{r_0}{C_s} \gamma_1 K$

$M_0 = \frac{r_0^2}{C_s^2} \mu_0 K$

$M_1 = \frac{r_0^2}{C_s^2} \mu_1 K$

where $k, \gamma_0, \gamma_1, \mu_0$ & μ_1 differ for horizontal, vertical & rocking actions

	K	γ_0	γ_1	μ_0	μ_1	C_0	C_1	M_0	M_1
Horiz	694000	0.66	\	\	\	1330	\	\	\
Vert	842000	0.8	0.31	\	0.368	1960	758	\	2610
Rock	398000	\	0.39	\	0.322	\	451	\	1510
	kN/m					kNs/m	kN s/m		kg

N Central foundation $r_0 = \sqrt{\frac{A_0}{\pi}} = \sqrt{\frac{1.981^2}{\pi}} = 1.18\ m$

	k	γ_0	γ_1	μ_0	μ_1	G_0	G_1	M_0	M_1
Horiz	97000	0.66	\	\	\	2610	\	\	\
Vert	1180000	0.8	0.31	\	0.368	3840	1490	\	7190
Rock	1095000 kN/m	\	0.39	\	0.322	\	1740 $kN\frac{s}{m}$	\	5840 kg

Beam Axial yield values:

Sections	Tension Yield	Compression yield
All	1667 (kN)	-33323 (kN)

Assumed steel for all sections:

12 x #3

15 x #5

2 x #6

3 x #7

Appendix I Sample Ruaumoko 3D Input File for 2D Analysis

The following sample file has been included to allow the interested reader to be able to reproduce all aspects of the 2D pounding modelling performed in this thesis. This input may be properly interpreted with either the Ruaumoko manuals or with Ruaumoko3D software. Note two columns have been used to present this data to save space. Where the input data exceeds the available column width, a '_' character has been added with the remaining data placed on the following line. To run the presented data within Ruaumoko, this operation would need to be reversed.

```
2D frame analysis
 2 1 1 2 0 0 0 0 1 0 2
 44 73 43 20 1 2 9.81 5 5 1.00E-04 15 1.5228
 0 100 0 3 0.1 0.1 0.1
 1 0 0 0 1 0
 5 5 0.0001

NODES 0 3

 1   0     10.161  0   0 0 0 0 0 0
 2   0     6.934   0   0 0 0 0 0 0
 3   0     3.734   0   0 0 0 0 0 1
 4   0     0       0   1 0 0 0 0 1
 5   6     10.161  0   0 0 0 0 0 0
 6   6     6.934   0   0 0 0 0 0 0
 7   6     3.734   0   0 0 0 0 0 1
 8   6     0       0   1 0 0 0 0 1
 9   12    10.161  0   0 0 0 0 0 0
 10  12    6.934   0   0 0 0 0 0 0
 11  12    3.734   0   0 0 0 0 0 1
 12  12    0       0   1 0 0 0 0 1
 13  0     -0.005  0   1 0 1 1 1 0
 14  0     -0.01   0   1 1 1 1 1 1
 15  6     -0.005  0   1 0 1 1 1 0
 16  6     -0.01   0   1 1 1 1 1 1
 17  12    -0.005  0   1 0 1 1 1 0
 18  12    -0.01   0   1 1 1 1 1 1
 19  12.1  7.011   0   2 1 1 1 1 1 10
 20  12.1  3.658   0   2 1 1 1 1 1 11

 21  13    10.161  0   0 0 0 0 0 0
 22  13    7.011   0   0 0 0 0 0 0
 23  13    3.658   0   0 0 0 0 0 0
 24  13    0       0   1 0 0 0 0 0
 25  20.14 10.161  0   0 0 0 0 0 0
 26  20.14 7.011   0   0 0 0 0 0 0
 27  20.14 3.658   0   0 0 0 0 0 0
 28  20.14 0       0   1 0 0 0 0 0
 29  27.28 10.161  0   0 0 0 0 0 0
 30  27.28 7.011   0   0 0 0 0 0 0
 31  27.28 3.658   0   0 0 0 0 0 0
 32  27.28 0       0   1 0 0 0 0 0
 33  34.42 10.161  0   0 0 0 0 0 0
 34  34.42 7.011   0   0 0 0 0 0 0
 35  34.42 3.658   0   0 0 0 0 0 0
 36  34.42 0       0   1 0 0 0 0 0
 37  13    -0.005  0   1 0 1 1 1 0
 38  13    -0.01   0   1 1 1 1 1 1
 39  20.14 -0.005  0   1 0 1 1 1 0
 40  20.14 -0.01   0   1 1 1 1 1 1
 41  27.28 -0.005  0   1 0 1 1 1 0
 42  27.28 -0.01   0   1 1 1 1 1 1
 43  34.42 -0.005  0   1 0 1 1 1 0
 44  34.42 -0.01   0   1 1 1 1 1 1

ELEMENTS

 1 1 1 2 0 0 Z
 2 2 2 3 0 0 Z
 3 3 3 4 0 0 Z
 4 1 5 6 0 0 Z
 5 2 6 7 0 0 Z
 6 3 7 8 0 0 Z
 7 1 9 10 0 0 Z
 8 2 10 11 0 0 Z
 9 3 11 12 0 0 Z
 10 4 1 5 0 0 Z
 11 4 5 9 0 0 Z
 12 5 2 6 0 0 Z
 13 6 6 10 0 0 Z
 14 7 3 7 0 0 Z
 15 8 7 11 0 0 Z
```

16 9 4 8 0 0 Z
17 9 8 12 0 0 Z
18 10 4 13 0 0 Z
19 11 4 13 0 0 Z
20 12 4 14 0 0 Z
21 13 4 14 0 0 Z
22 10 8 15 0 0 Z
23 14 8 15 0 0 Z
24 15 8 16 0 0 Z
25 16 8 16 0 0 Z
26 10 12 17 0 0 Z
27 11 12 17 0 0 Z
28 12 12 18 0 0 Z
29 13 12 18 0 0 Z

30 17 21 22 0 0 Z
31 18 22 23 0 0 Z
32 19 23 24 0 0 Z
33 20 25 26 0 0 Z
34 21 26 27 0 0 Z
35 22 27 28 0 0 Z
36 20 29 30 0 0 Z
37 21 30 31 0 0 Z
38 22 31 32 0 0 Z
39 17 33 34 0 0 Z
40 18 34 35 0 0 Z
41 19 35 36 0 0 Z
42 23 21 25 0 0 Z
43 24 25 29 0 0 Z
44 25 29 33 0 0 Z
45 26 22 26 0 0 Z
46 27 26 30 0 0 Z
47 28 30 34 0 0 Z
48 29 23 27 0 0 Z
49 30 27 31 0 0 Z
50 31 31 35 0 0 Z
51 32 24 28 0 0 Z
52 32 28 32 0 0 Z
53 32 32 36 0 0 Z
54 33 24 38 0 0 Z
55 34 24 38 0 0 Z
56 35 24 37 0 0 Z
57 36 24 37 0 0 Z
58 37 28 40 0 0 Z
59 38 28 40 0 0 Z
60 35 28 39 0 0 Z
61 39 28 39 0 0 Z
62 37 32 42 0 0 Z
63 38 32 42 0 0 Z
64 35 32 41 0 0 Z
65 39 32 41 0 0 Z
66 33 36 44 0 0 Z
67 34 36 44 0 0 Z
68 35 36 43 0 0 Z
69 36 36 43 0 0 Z

70 40 9 21 0 0 Z
71 41 19 22 0 0 Z
72 42 20 23 0 0 Z
73 43 12 24 0 0 Z

PROPS
1 Beam "Level 2 columns"
1 2 0 0 2 57 0 0 0 1
31522000 (31522000/2.4) 0.145 0 0.00199_
0.00153 0.13 0.128 0 0 3.48
0.305 0 0.305 0
1 1 0.01 0.01
0.203 0.203 0.178 0.178
3.48 0 0 0 0 1
0 0 1.5 1 0
-6865 -2363 349 303 465
0.4 0.4 0.5 0 1 0.6 0.6 0
0.4 0.4 0.5 0 1 0.6 0.6 0
0.4 0.4 0.5 0 1 0.6 0.6 0
0.4 0.4 0.5 0 1 0.6 0.6 0

2 Beam "Level 1 columns"
1 2 0 0 2 57 0 0 0 1
31522000 (31522000/2.4) 0.145 0 0.00199_
0.00153 0.13 0.128 0 0 3.48
0.61 0 0.61 0
1 1 0.01 0.01
0.203 0.203 0.178 0.178
3.48 0 0 0 0 1
0 0 1.5 1 0
-6865 -2363 349 303 465
0.4 0.4 0.5 0 1 0.6 0.6 0
0.4 0.4 0.5 0 1 0.6 0.6 0
0.4 0.4 0.5 0 1 0.6 0.6 0
0.4 0.4 0.5 0 1 0.6 0.6 0

3 Beam "GND Level columns"
1 2 0 0 2 57 0 0 0 1
31522000 (31522000/2.4) 0.201 0 0.00276_

```
0.0041 0.185 0.181 0 0 4.82
 0.559 0 0.559 0
 1 1 0.01 0.01
 0.248 0.248 0.203 0.203
 4.82 0 0 0 0 1
 0 0 1.5 1 0
 -9609 -3267 492 573 697
 0.4 0.4 0.5 0 1 0.6 0.6 0
 0.4 0.4 0.5 0 1 0.6 0.6 0
 0.4 0.4 0.5 0 1 0.6 0.6 0
 0.4 0.4 0.5 0 1 0.6 0.6 0

 4 Beam "Top roof beam"
 1 1 0 0 2 4 0 0 0 0
 31522000 (31522000/2.4) 0.108 0 0.000336_
0 0.0941 0 0 0 2.59
 0.203 0.203 0 0
 0.01 0.01 0.01 0.01
 0.153 0.153 0 0
 0 -2.59 0 0 0 1
 240 -4860 0 0 2 1
 35 -35 0 0
 35 -35 0 0
 0.5 0 1 2

 5 Beam "Left level 2 beam"
 1 1 0 0 2 4 0 0 0 0
 31522000 (31522000/2.4) 0.428 0 0.00287 0_
0.145 0 0 0 (4.01+21.75)
 0.203 0.203 0 0
 0.01 0.01 0.01 0.01
 0.305 0.305 0 0
 0 (-4.01-22.34+13.4) 0 0 0 1
 914 -19300 0 0 2 1
 160 -215 0 0
 160 -351 0 0
 0.5 0 1 2

 6 Beam "Right Lvl 2 beam"
 1 1 0 0 2 4 0 0 0 0
 31522000 (31522000/2.4) 0.428 0 0.00287 0_
0.145 0 0 0 (4.01+21.75)
 0.203 0.203 0 0
 0.01 0.01 0.01 0.01
 0.305 0.305 0 0
 0 (-4.01-22.34+13.4) 0 0 0 1
 914 -19300 0 0 2 1
 160 -351 0 0
 160 -215 0 0
 0.5 0 1 2

 7 Beam "Left Lvl 1 beam"
 1 1 0 0 2 4 0 0 0 0
 31522000 (31522000/2.4) 0.417 0 0.00219 0_
0.145 0 0 0 (3.74+17.8)
 0.203 0.203 0 0
 0.01 0.01 0.01 0.01
 0.28 0.28 0 0
 0 (-3.74-18.4+9.49) 0 0 0 1
 649 -18800 0 0 2 1
 83 -135 0 0
 82 -209 0 0
 0.5 0 1 2

 8 Beam "Right Lvl 1 beam"
 1 1 0 0 2 4 0 0 0 0
 31522000 (31522000/2.4) 0.417 0 0.00219 0_
0.145 0 0 0 (3.74+17.8)
 0.203 0.203 0 0
 0.01 0.01 0.01 0.01
 0.28 0.28 0 0
 0 (-3.74-18.4+9.49) 0 0 0 1
 649 -18800 0 0 2 1
 82 -209 0 0
 83 -135 0 0
 0.5 0 1 2

 9 Beam "Ground beam"
 1 1 0 0 2 4 0 0 0 0
 31522000 (31522000/2.4) 0.341 0 0.00287 0_
0.159 0 0 0 (4.08+8.35)
 0.203 0.203 0 0
 0.01 0.01 0.01 0.01
 0.305 0.305 0 0
 0 -4.08 0 0 0 1
 374 -15300 0 0 2 1
 65 -75 0 0
 65 -75 0 0
 0.5 0 1 2

 10 Spring "Outer foundation SSI tail spring"
 1 69 0 0 0 0
 1.00E+05 0 0 0 0 1.00E+05 0 1.00E-05_
1.00E-05
 1.00E+08 1.00E+08 1.00E+08 1.00E+08_
1.00E+08 1.00E+08
```

1.00E+08 1.00E+08 1.00E+08 1.00E+08_
1.00E+08 1.00E+08
1.00E-02

11 Damper "Outer foundation SSI tail damper
0 524 0 0 0 216 216

12 Spring "Outer foundation SSI spring"
1 0 0 0 0 0
700000 576000 576000 0 229000 229000

13 Damper "Outer foundation SSI damper
0 1352 918 918 0 0 0

14 Damper "Inner foundation SSI tail damper
0 758 0 0 0 451 451

15 Spring "Inner foundation SSI spring"
1 0 0 0 0 0
842000 693000 693000 0 398000 398000

16 Damper "Inner foundation SSI damper
0 1956 1328 1328 0 0 0

17 Beam "Roof external columns (E2)"
1 2 0 0 2 57 0 0 0 1
31522000 (31522000/2.4) 0.208 0 0.003635_
0.003635 0.191 0.191 0 0 5.01
0.406 0 0.406 0
1 1 0.01 0.01
0.229 0.229 0.229 0.229
5.01 0 0 0 0 1
0 0 1.5 1 0
-10097 -3426 578 578 867
0.4 0.4 0.5 0 1 0.6 0.6 0
0.4 0.4 0.5 0 1 0.6 0.6 0
0.4 0.4 0.5 0 1 0.6 0.6 0
0.4 0.4 0.5 0 1 0.6 0.6 0

18 Beam "Level 1 external columns (E1)"
1 2 0 0 2 57 0 0 0 1
31522000 (31522000/2.4) 0.208 0 0.003635_
0.003635 0.191 0.191 0 0 5.01
0.66 0 0.66 0
1 1 0.01 0.01
0.229 0.229 0.229 0.229
5.01 0 0 0 0 1
0 0 1.5 1 0
-10060 -3477 559 575 852
0.4 0.4 0.5 0 1 0.6 0.6 0
0.4 0.4 0.5 0 1 0.6 0.6 0
0.4 0.4 0.5 0 1 0.6 0.6 0
0.4 0.4 0.5 0 1 0.6 0.6 0

19 Beam "Gnd external columns (EG)"
1 2 0 0 2 57 0 0 0 1
31522000 (31522000/2.4) 0.208 0 0.003635_
0.003635 0.191 0.191 0 0 5.01
0.66 0 0.66 0
1 1 0.01 0.01
0.229 0.229 0.229 0.229
5.01 0 0 0 0 1
0 0 1.5 1 0
-10326 -3481 590 615 1161
0.4 0.4 0.5 0 1 0.6 0.6 0
0.4 0.4 0.5 0 1 0.6 0.6 0
0.4 0.4 0.5 0 1 0.6 0.6 0
0.4 0.4 0.5 0 1 0.6 0.6 0

20 Beam "Roof internal column (I2)"
1 1 2 0 2 2 0 0 0 1
2E+08 (200000000/2.6) 0.0103 0 8.82E-06_
0.000331 0.00497 0 0 0 0.79
0.406 0 0.406 0
1 1 0.01 0.01
0.0762 0.0762 0.229 0.229
0.79 0 0 0 0 1
3090 -3090 0 0 0 0
3090 -3090 0 0 0 0

21 Beam "Level 1 internal columns (I1)"
1 2 0 0 2 57 0 0 0 1
31522000 (31522000/2.4) 0.232 0 0.004041_
0.004993 0.212 0.214 0 0 5.57
0.66 0 0.66 0
1 1 0.01 0.01
0.229 0.229 0.254 0.254
5.57 0 0 0 0 1
0 0 1.5 1 0
-12362 -3895 739 930 2276
0.4 0.4 0.5 0 1 0.6 0.6 0
0.4 0.4 0.5 0 1 0.6 0.6 0
0.4 0.4 0.5 0 1 0.6 0.6 0
0.4 0.4 0.5 0 1 0.6 0.6 0

22 Beam "Gnd internal columns (IG)"
1 2 0 0 2 57 0 0 0 1
31522000 (31522000/2.4) 0.232 0 0.004041_
0.004993 0.212 0.214 0 0 5.57
0.66 0 0.66 0
1 1 0.01 0.01
0.229 0.229 0.254 0.254
5.57 0 0 0 0 1
0 0 1.5 1 0
-12027 -3878 719 863 1889
0.4 0.4 0.5 0 1 0.6 0.6 0
0.4 0.4 0.5 0 1 0.6 0.6 0
0.4 0.4 0.5 0 1 0.6 0.6 0
0.4 0.4 0.5 0 1 0.6 0.6 0

23 Beam "Left roof beam"
1 1 0 0 2 4 0 0 0 0
31522000 (31522000/2.4) 0.124 0 0.00068 0_
0.112 0 0 0 2.98
0.229 0 0 0
0.01 0.01 0.01 0.01
0.203 0 0 0
0 -2.98 0 0 0 1
240 -5580 0 0 2 1
40 -40 0 0
40 -40 0 0
0.5 0 1 2

24 Beam "Central roof steel rafter"
1 1 0 0 2 4 0 0 0 0
31522000 (31522000/2.4) 0.124 0 0.00068 0_
0.112 0 0 0 2.98
0 0 0 0
0.01 0.01 0.01 0.01
0.203 0 0 0
0 -2.98 0 0 0 1
240 -5580 0 0 2 1
40 -40 0 0
40 -40 0 0
0.5 0 1 2

25 Beam "Right roof steel rafter"
1 1 0 0 2 4 0 0 0 0
31522000 (31522000/2.4) 0.124 0 0.00068 0_
0.112 0 0 0 2.98
0 0.229 0 0
0.01 0.01 0.01 0.01
0.203 0 0 0
0 -2.98 0 0 0 1
240 -5580 0 0 2 1
40 -40 0 0
40 -40 0 0
0.5 0 1 2

26 Beam "Left level 2"
1 1 0 0 2 4 0 0 0 0
31522000 (31522000/2.4) 0.574 0 0.004435 0_
0.22 0 0 0 (5.62+28.6)
0.229 0.229 0 0
0.01 0.01 0.01 0.01
0.33 0.33 0 0
0 (-5.62-28.6+17.3) 0 0 0 1
717 -25800 0 0 2 1
133 -270 0 0
100 -409 0 0
0.5 0 1 2

27 Beam "Centre level 2"
1 1 0 0 2 4 0 0 0 0
31522000 (31522000/2.4) 0.574 0 0.004435 0_
0.22 0 0 0 (5.62+28.6)
0.229 0.229 0 0
0.01 0.01 0.01 0.01
0.33 0.33 0 0
0 (-5.62-28.6+17.3) 0 0 0 1
718 -25800 0 0 2 1
100 -409 0 0
100 -409 0 0
0.5 0 1 2

28 Beam "Right level 2"
1 1 0 0 2 4 0 0 0 0
31522000 (31522000/2.4) 0.574 0 0.004435 0_
0.22 0 0 0 (5.62+28.6)
0.229 0.229 0 0
0.01 0.01 0.01 0.01
0.33 0.33 0 0
0 (-5.62-28.6+17.3) 0 0 0 1
717 -25800 0 0 2 1
100 -409 0 0
133 -270 0 0
0.5 0 1 2

29 Beam "Left level 1"
1 1 0 0 2 4 0 0 0 0
31522000 (31522000/2.4) 0.574 0 0.004435 0_

0.22 0 0 0 (5.62+28.6)
0.229 0.229 0 0
0.01 0.01 0.01 0.01
0.33 0.33 0 0
0 (-5.62-28.6+17.3) 0 0 0 1
881 -25800 0 0 2 1
133 -411 0 0
137 -468 0 0
0.5 0 1 2

30 Beam "Centre level 1"
1 1 0 0 2 4 0 0 0 0
31522000 (31522000/2.4) 0.574 0 0.004435 0_
0.22 0 0 0 (5.62+28.6)
0.229 0.229 0 0
0.01 0.01 0.01 0.01
0.33 0.33 0 0
0 -5.62 0 0 0 1
882 -25800 0 0 2 1
137 -468 0 0
137 -468 0 0
0.5 0 1 2

31 Beam "Right level 1"
1 1 0 0 2 4 0 0 0 0
31522000 (31522000/2.4) 0.574 0 0.004435 0_
0.22 0 0 0 (5.62+28.6)
0.229 0.229 0 0
0.01 0.01 0.01 0.01
0.33 0.33 0 0
0 -5.62 0 0 0 1
881 -25800 0 0 2 1
137 -468 0 0
133 -411 0 0
0.5 0 1 2

32 Beam "Ground beams"
1 1 0 0 2 4 0 0 0 0
31522000 (31522000/2.4) 0.556 0 0.003457 0_
0.202 0 0 0 (5.18+28.6)
0.229 0.229 0 0
0.01 0.01 0.01 0.01
0.305 0.305 0 0
0 -5.62 0 0 0 1
841 -25000 0 0 2 1
160 -262 0 0
160 -262 0 0
0.5 0 1 2

33 Spring "External foundation spring"
1 0 0 0 0 0
730000 601000 601000 0 259000 259000

34 Damper "External foundation damper"
0 1470 998 998 0 0 0

35 Spring "Low stiffness tie spring"
1 69 0 0 0 0
10000000 0 0 0 0 10000000 0 0.000001_
0.000001
1E+08 1E+08 1E+08 1E+08 1E+08 1E+08
1E+08 1E+08 1E+08 1E+08 1E+08 1E+08
0.01

36 Damper "External foundation monkey tail"
0 570 0 0 0 254 254

37 Spring "Internal foundation spring"
1 0 0 0 0 0
860000 708000 708000 0 424000 424000

38 Damper "Internal foundation damper"
0 2040 1386 1386 0 0 0

39 Damper "Internal foundation monkey tail"
0 791 0 0 0 490 490

40 Contact "Contact element"
1 5 550000 0 0 0 0 0 0
1E+08 -1E+08 1
1 -1 0

41 Contact "Contact element"
1 5 2250000 0 0 0 0 0 0
1E+08 -1E+08 1
1 -1 0

42 Contact "Contact element"
1 5 2200000 0 0 0 0 0 0
1E+08 -1E+08 1
1 -1 0

43 Contact "Contact element"
1 5 1800000 0 0 0 0 0 0
1E+08 -1E+08 1
1 -1 0

```
WEIGHTS
 1 (7.1+21.8+13.35) (7.1+21.8+13.35)_
(7.1+21.8+13.35) 0 0 0
 2 45.9 45.9 45.9 0 0 0
 3 32.5 32.5 32.5 0 0 0
 4 0 0 0 0 0 0
 5 (14.6+43.5+26.7) (14.6+43.5+26.7)_
(14.6+43.5+26.7) 0 0 0
 6 0 0 0 0 0 0
 7 0 0 0 0 0 0
 8 0 0 0 0 0 0
 9 (7.1+21.8+13.35) (7.1+21.8+13.35)_
(7.1+21.8+13.35) 0 0 0
 10 45.9 45.9 45.9 0 0 0
 11 32.5 32.5 32.5 0 0 0
 12 0 0 0 0 0 0
 13 0 14.7 0 4.2 0 4.2
 14 0 0 0 0 0 0
 15 0 25.6 0 10.6 0 10.6
 16 0 0 0 0 0 0
 17 0 14.7 0 4.2 0 4.2
 18 0 0 0 0 0 0

21 17.6 17.6 17.6 0 0 0
22 51.4 51.4 51.4 0 0 0
23 51.4 51.4 51.4 0 0 0
24 51.4 51.4 51.4 0 0 0
25 25.4 25.4 25.4 0 0 0
26 0 0 0 0 0 0
27 0 0 0 0 0 0
28 0 0 0 0 0 0
29 25.4 25.4 25.4 0 0 0
30 0 0 0 0 0 0
31 0 0 0 0 0 0
32 0 0 0 0 0 0
33 17.6 17.6 17.6 0 0 0
34 51.4 51.4 51.4 0 0 0
35 51.4 51.4 51.4 0 0 0
36 51.4 51.4 51.4 0 0 0
37 0 16.7 0 0 5.18 5.18
38 0 0 0 0 0 0
39 0 27.3 0 0 11.8 11.8
40 0 0 0 0 0 0
41 0 27.3 0 0 11.8 11.8
42 0 0 0 0 0 0
43 0 16.7 0 0 5.18 5.18
44 0 0 0 0 0 0

LOADS
 1 0 (-7.1-21.8-13.35) 0 0 0 0
 2 0 (-45.9-40.2) 0 0 0 0
 3 0 (-32.5-28.5) 0 0 0 0
 4 0 -73 0 0 0 0
 5 0 (-14.6-43.5-26.7) 0 0 0 0
 6 0 -80.4 0 0 0 0
 7 0 36.9 0 0 0 0
 8 0 -146 0 0 0 0
 9 0 (-7.1-21.8-13.35) 0 0 0 0
 10 0 (-45.9-40.2) 0 0 0 0
 11 0 (-32.5-28.5) 0 0 0 0
 12 0 -73 0 0 0 0
 13 0 0 0 0 0 0
 14 0 0 0 0 0 0
 15 0 0 0 0 0 0
 16 0 0 0 0 0 0
 17 0 0 0 0 0 0
 18 0 0 0 0 0 0
21 0 -17.6 0 0 0 0
22 0 (-51.4-61.8) 0 0 0 0
23 0 (-51.4-61.8) 0 0 0 0
24 0 (-51.4-102) 0 0 0 0
25 0 -25.4 0 0 0 0
26 0 -124 0 0 0 0
27 0 -124 0 0 0 0
28 0 -204 0 0 0 0
29 0 -25.4 0 0 0 0
30 0 -124 0 0 0 0
31 0 -124 0 0 0 0
32 0 -204 0 0 0 0
33 0 -17.6 0 0 0 0
34 0 (-51.4-61.8) 0 0 0 0
35 0 (-51.4-61.8) 0 0 0 0
36 0 (-51.4-102) 0 0 0 0
37 0 0 0 0 0 0
38 0 0 0 0 0 0
39 0 0 0 0 0 0
40 0 0 0 0 0 0
41 0 0 0 0 0 0
42 0 0 0 0 0 0
43 0 0 0 0 0 0
44 0 0 0 0 0 0
EQUAKE 15CentroP.acc
 3 1 0.01 1 0 0 0 1
```

Appendix J Calculation of Fundamental Lumped Parameter Model Values for SSI

For each foundation, five parameters must be calculated for each considered direction of motion. The equations presented below are taken from Wolf (1994) and have been used to model SSI in the 2D models.

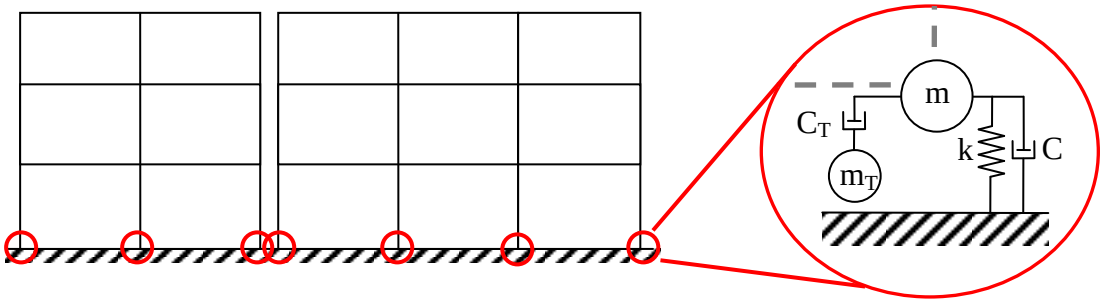

Where

$$C = \frac{r_0}{c_s}\gamma K \qquad C_T = \frac{r_0}{c_s}\gamma_T K \qquad M = \left(\frac{r_0}{c_s}\right)^2 \mu K \qquad M_T = \left(\frac{r_0}{c_s}\right)^2 \mu_T K$$

And r_0 is the equivalent rigid disk radius. The dimensionless constants are found using:

	Static stiffness K	Dimensionless coefficients of Damping γ	Damping γ_T	mass μ	mass μ_T
Horizontal	$\frac{8G_{max}r_0}{2-\nu}$	$0.78-0.4\nu$	-	-	-
Vertical	$\frac{4G_{max}r_0}{1-\nu}$	0.8	$0.34-4.3\nu^4$	$\nu<\frac{1}{3}$ 0 $\nu>\frac{1}{3}$ $0.9\left(\nu-\frac{1}{3}\right)$	$0.4-4\nu^4$
Rocking	$\frac{8G_{max}{r_0}^3}{3(1-\nu)}$	-	$0.42-0.3\nu^2$	$\nu<\frac{1}{3}$ 0 $\nu>\frac{1}{3}$ $1.6\left(\nu-\frac{1}{3}\right)$	$0.34-0.2\nu^2$

Appendix K Rules for Node/Node 3D Contact Element

This following diagrams display the proposed eccentricities that were to be used to calculate the moments at each node. Each node is classified as a finite, semi-infinite or infinite contact surface. If the lateral movement exceeds the contact surface, contact does not occur. For example, if the considered collision node is half way along the collision interface, then this point will always experience collision regardless of building offset (within practical limits). This node is modelled with an infinite collision surface. A semi-infinite surface corresponds to the corner of a floor slab, while a finite surface corresponds to a column.

The presented scenarios are designed to calculate the centroid location of the collision force relative to the left hand node (node K). Note that K- and L- are negative numbers since the positive axis is defined as vertically up. This element is discussed within the main text in Section 7.3.1. Note that the column vs. column configuration is considered to have 0 cases because although column/column collision is possible, there is very little mass in either object. Collision of this form is therefore considered to be a secondary effect.

Possible collision configurations

Layout						
Number of cases	1	3	5	1	3	0
Description	continuum vs. continuum	end/corner vs. continuum	end/corner vs. end/corner	column vs. continuum	column vs. end/corner	column vs. column

Diaphragm vs diaphragm collisions (NB down is positive, x_3 measured from K to L)

continuum vs. continuum (1 case)

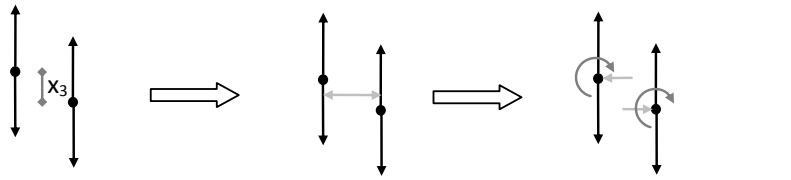

Centroid = $x_3/2$ Internal actions Equivalent nodal loads

end/corner vs. continuum (3 cases)

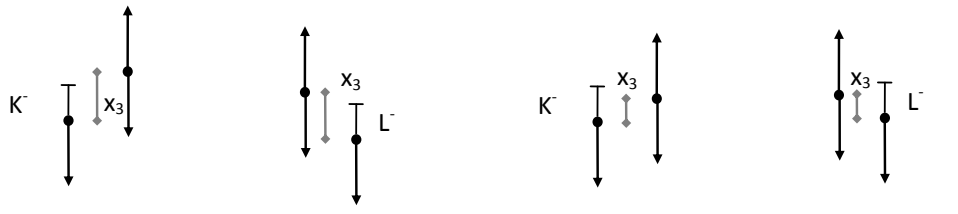

If $x_3 < K^-$ If $x_3 > -L^-$ If $x_3 > K^-$ If $x_3 < -L^-$

Centroid = $(K^-)/2$ Centroid = $(x_3+x_3+L^-)/2$ Centroid = $x_3/2$ Centroid = $x_3/2$

Case A Case B Case C

end/corner vs. end/corner (same end) (3 cases)

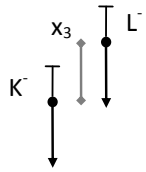

If $x_3 < K^-$

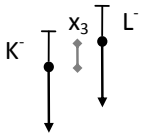

If $x_3 > K^-$

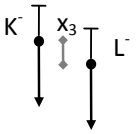

If $x_3 < -L^-$

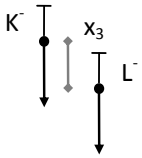

If $x_3 > -L^-$

Centroid = $(K^-)/2$ — Case A

Centroid = $x_3/2$ — Case B

Centroid = $x_3/2$ — Case B

Centroid = $(x_3+x_3+L^-)/2$ — Case C

end/corner vs. end/corner (opposite ends) (2 cases)

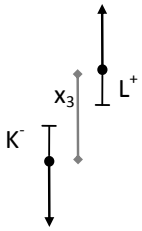

If $x_3 < K^- - L^+$

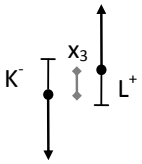

If $x_3 > K^- - L^+$

No collision — Case A

Centroid = $(K^-+x_3+L^+)/2$ — Case B

Diaphragm vs column collisions

column vs. continuum (1 case)

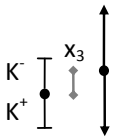

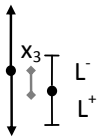

Centroid = $(K^- + K^+)/2$ Centroid = $(L^- + L^+)/2 + x_3$

Case A (with switch on x_3 term)

column vs. end/corner

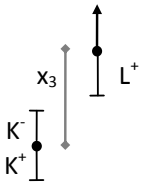

If $x_3 + L^+ < K^-$

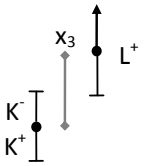

If $K^+ > x_3 + L^+ >= K^-$

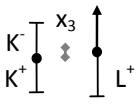

If $x_3 + L^+ >= K^+$

No collision — Case A

Centroid = $(K^-+x_3+L^+)/2$ — Case B

Centroid = $(K^-+K^+)/2$ — Case C

Appendix L Supplementary Figures for Chapter 9

The figures presented here relate to the analyses performed in Chapter 9. Each test suite is presented separately.

Test *mid-span*

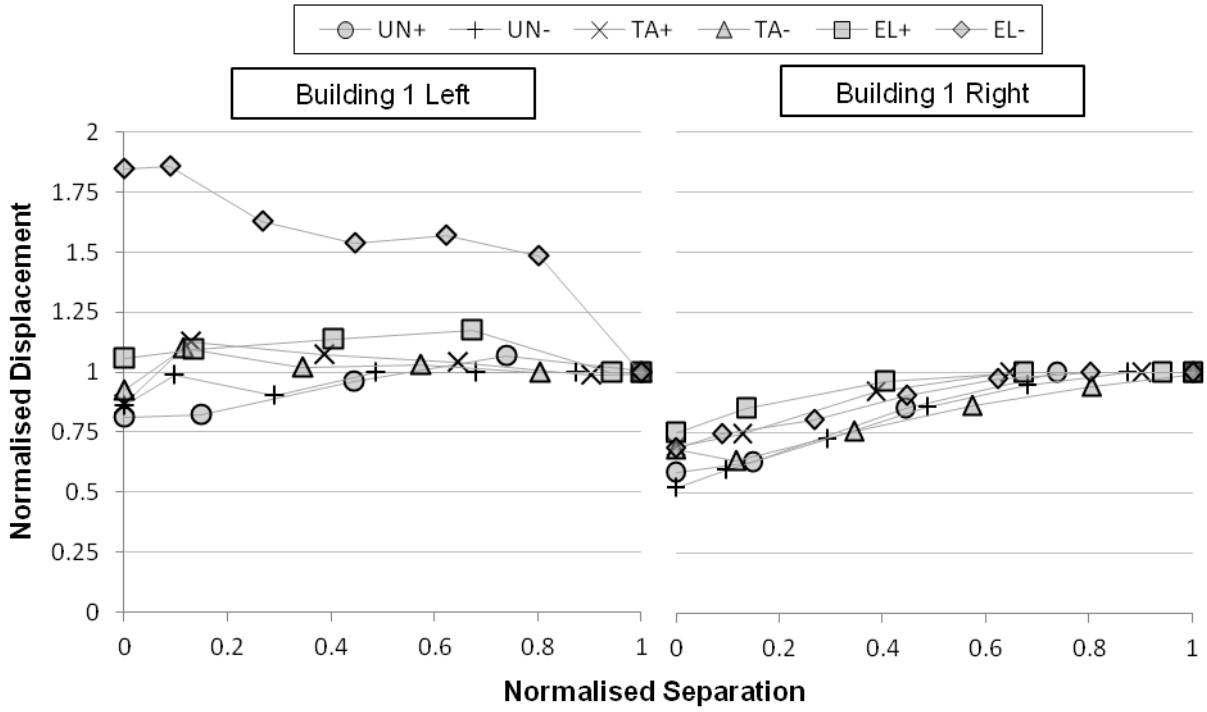

Building 1 X direction displacement amplifications at Level 3

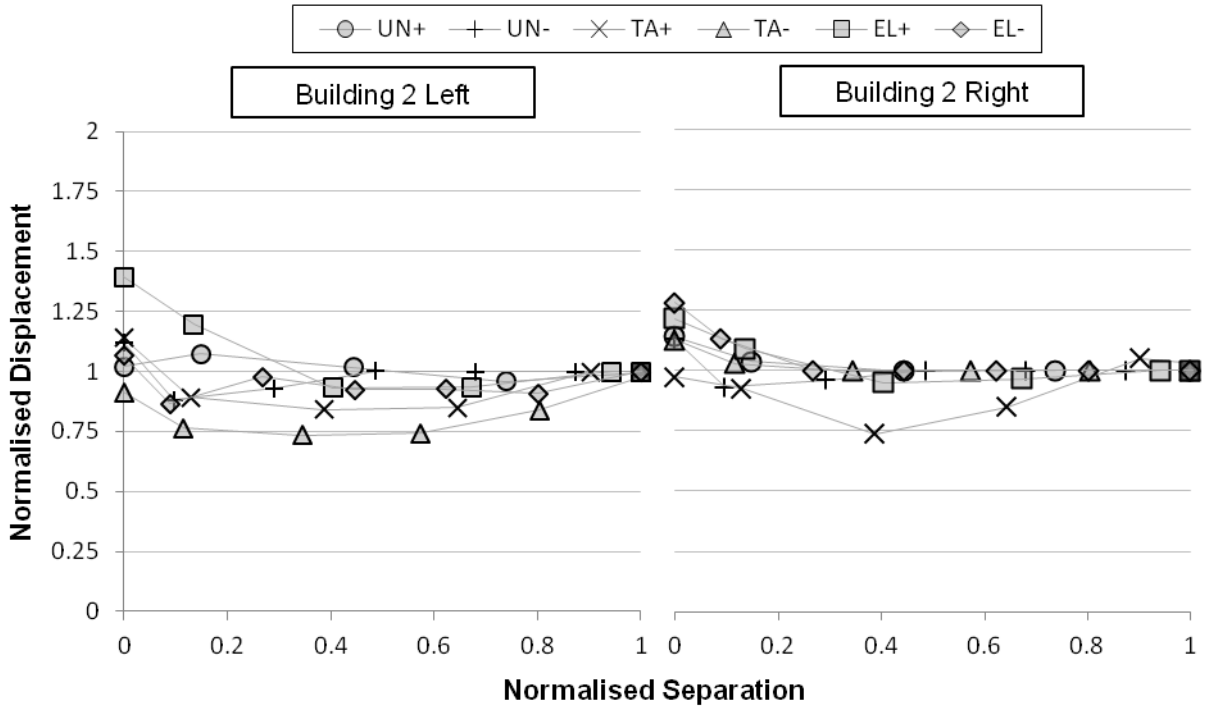

Building 2 X direction displacement amplifications at Level 3

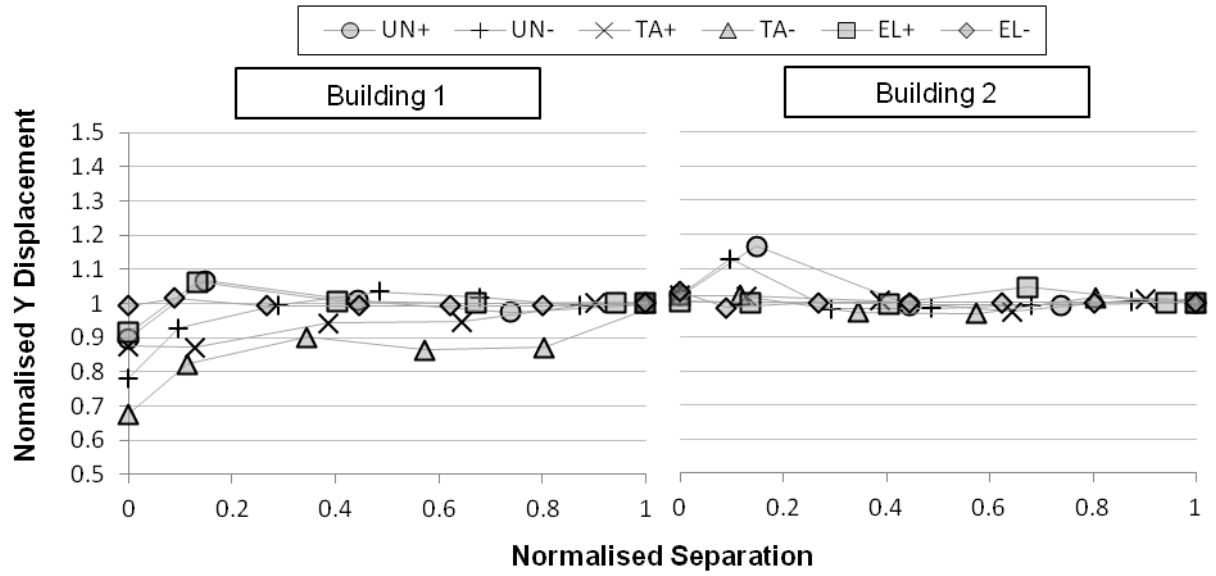

Maximum Level 3 Y displacement amplifications due to floor/column pounding

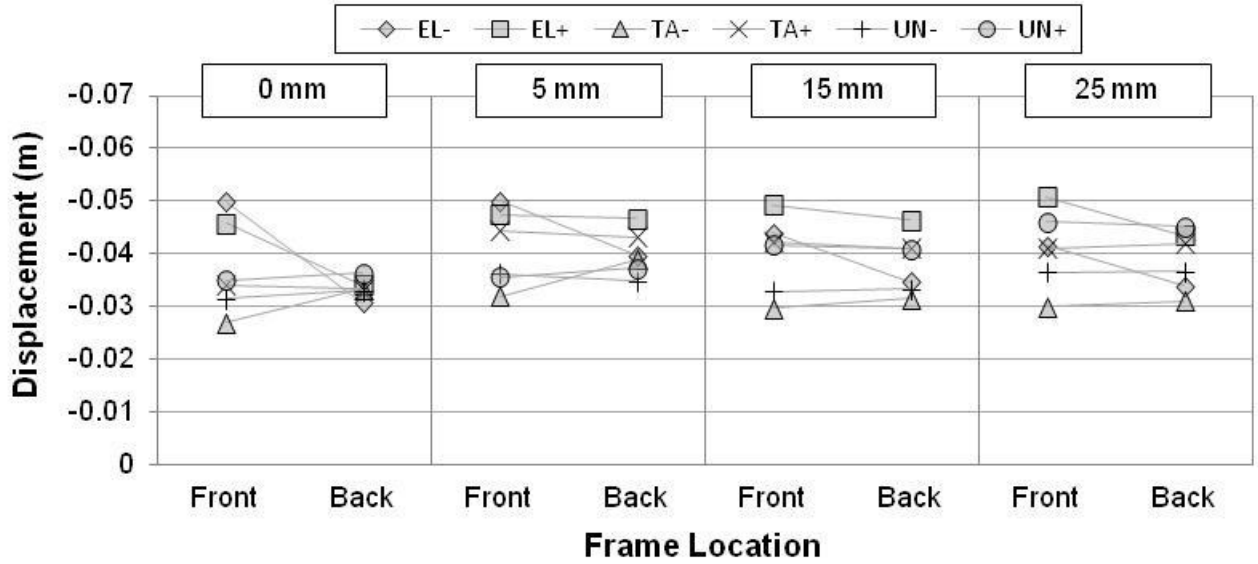

Building 1 left displacement envelopes at front and rear building frames. Building separations indicated with boxed numbers

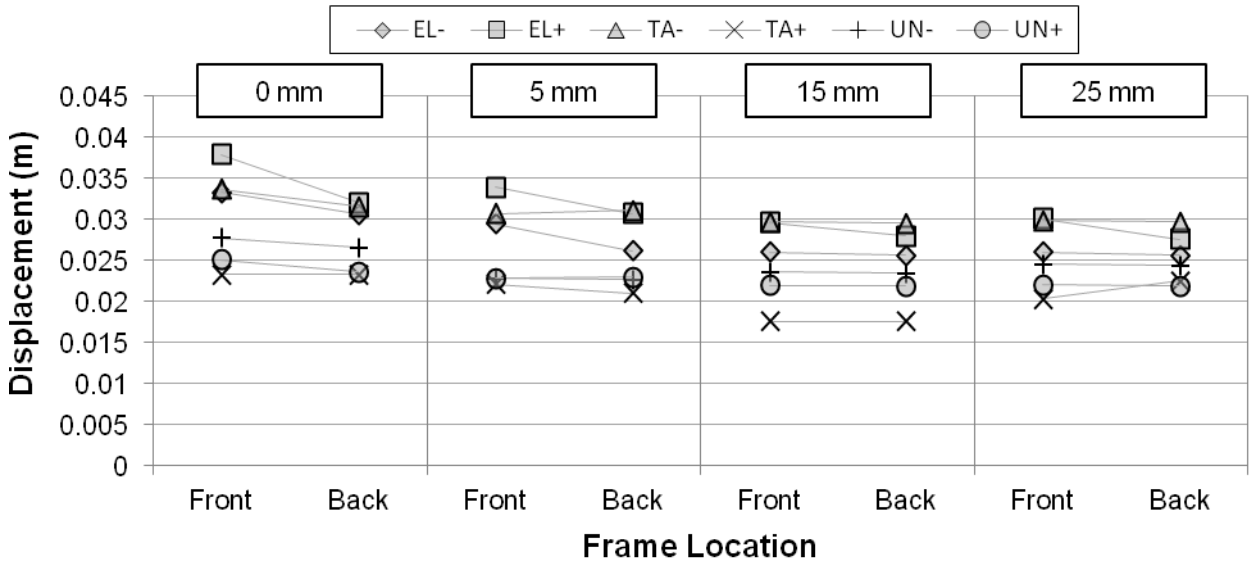

Building 2 right displacement envelopes at front and rear building frames. Building separations indicated with boxed numbers

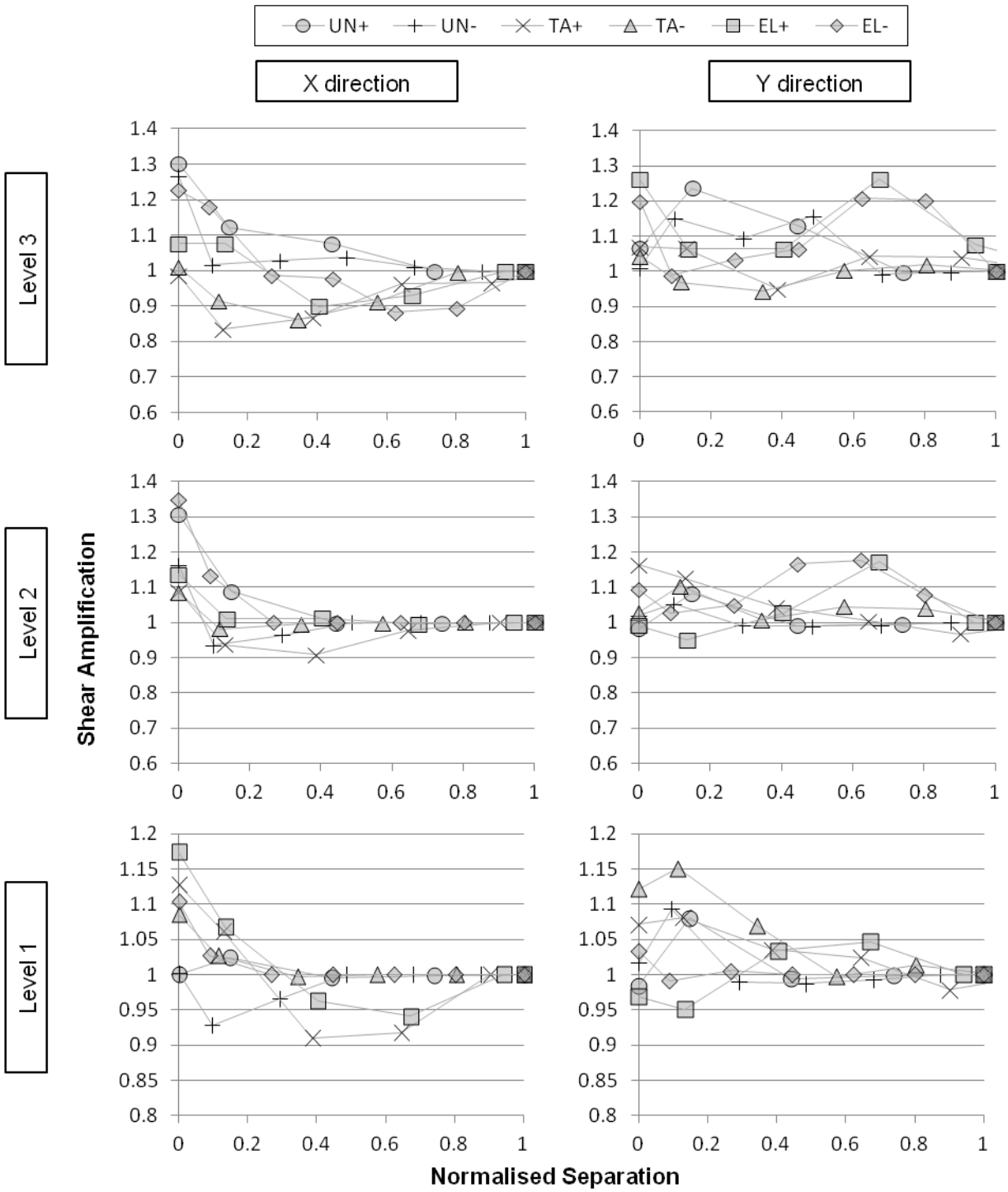

Interstorey shear amplification in Building 2. Note that different vertical scales are used at each floor level

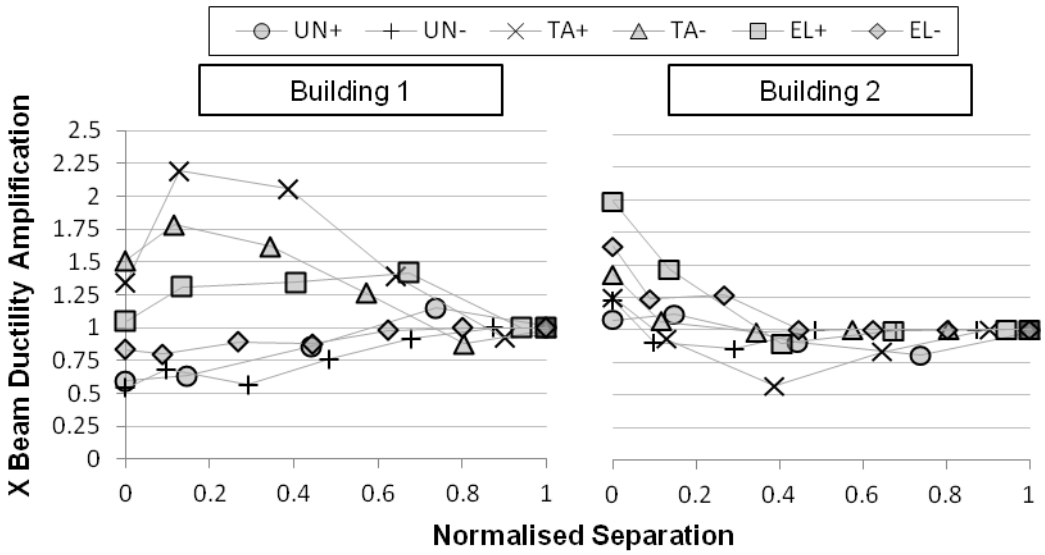

Beam ductility amplifications due to movement in the X direction

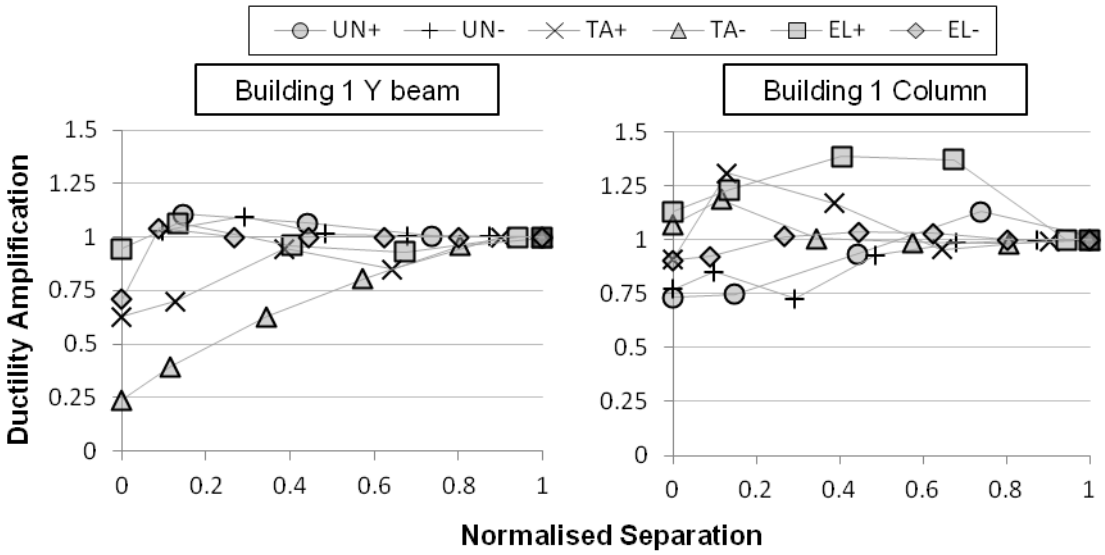

Building 1 ductility amplifications. Left: Beam ductility due to movement in the Y direction. Right: Column ductilities

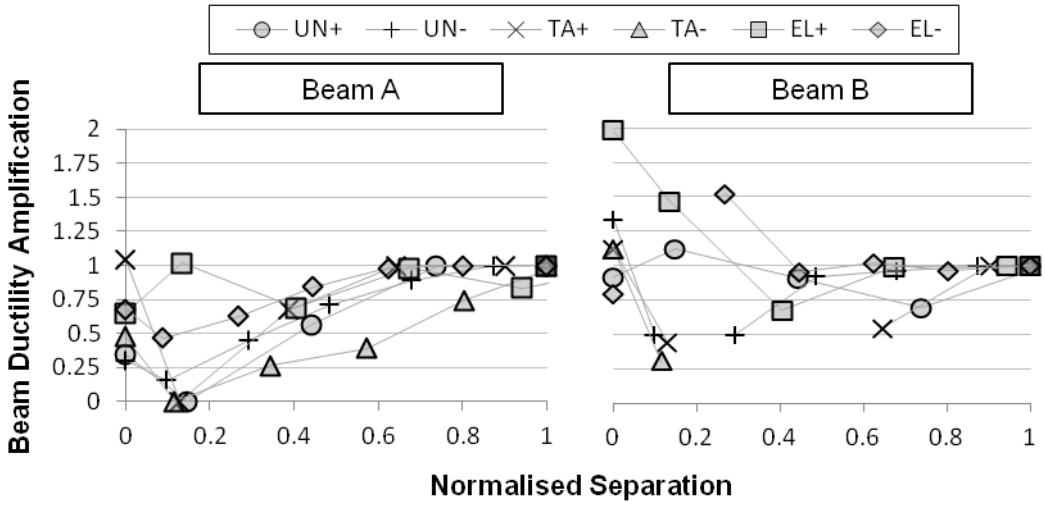

Ductility amplification of Beam A and Beam B. Refer Figure 9.42 for location

Test *near-floor*

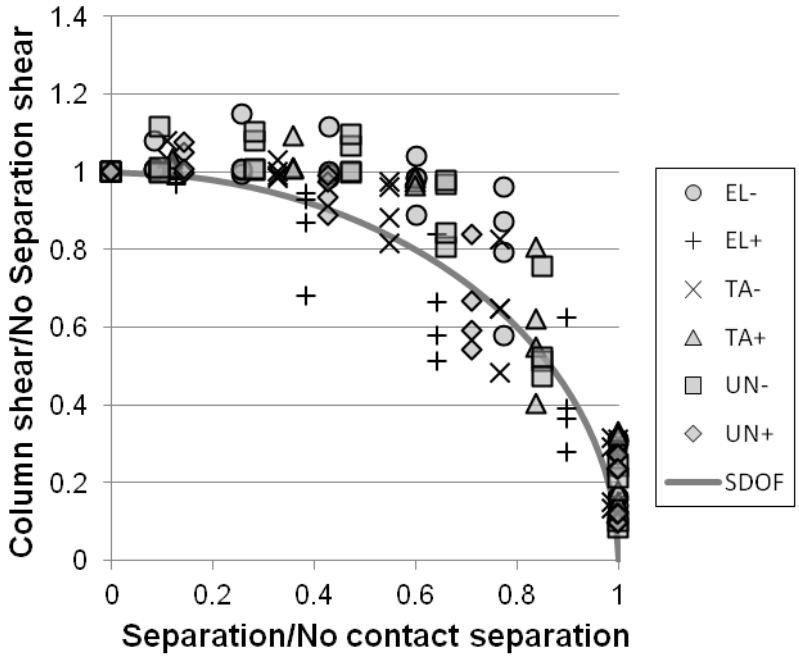

Normalised shear force in columns at B2L3. Shear is normalised by the column shear when no separation is present.

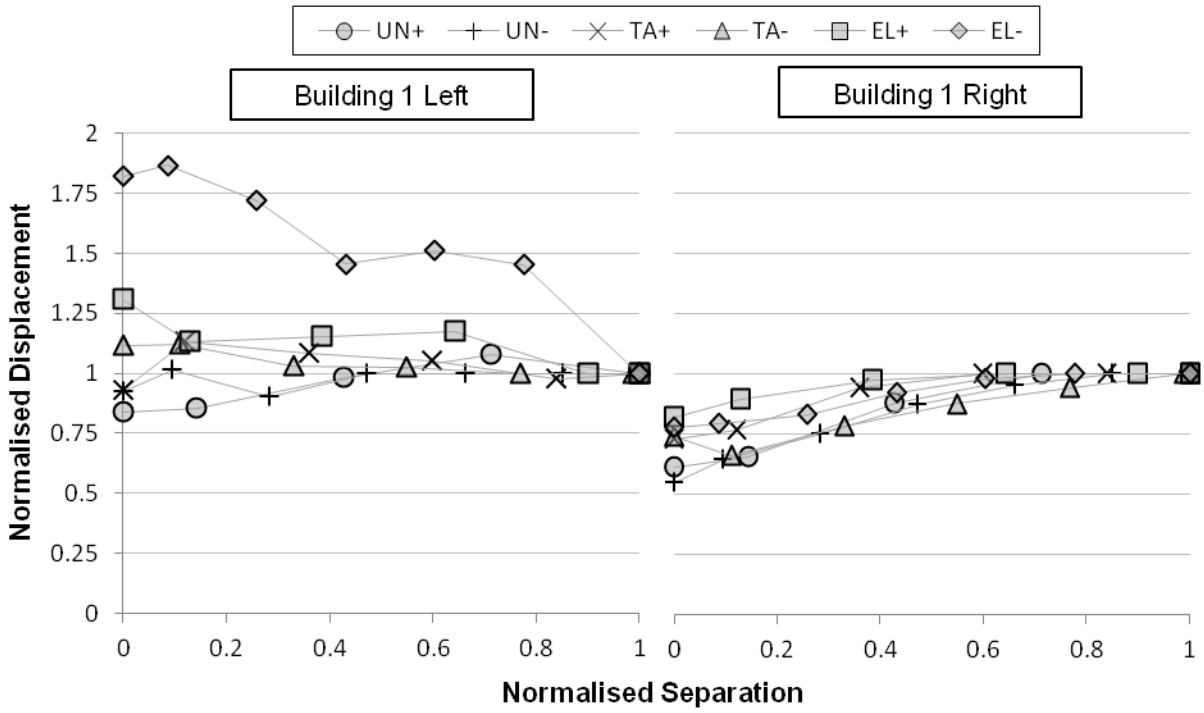

Building 1 X direction displacement amplifications at Level 3

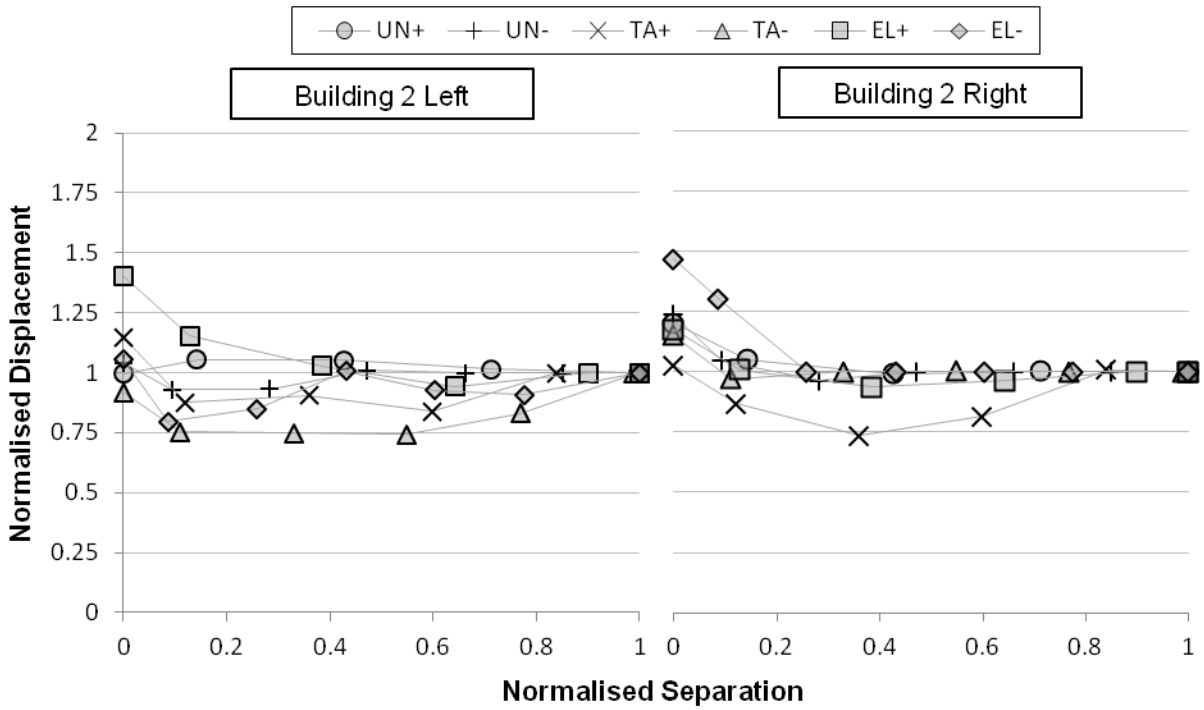

Building 2 X direction displacement amplifications at Level 3

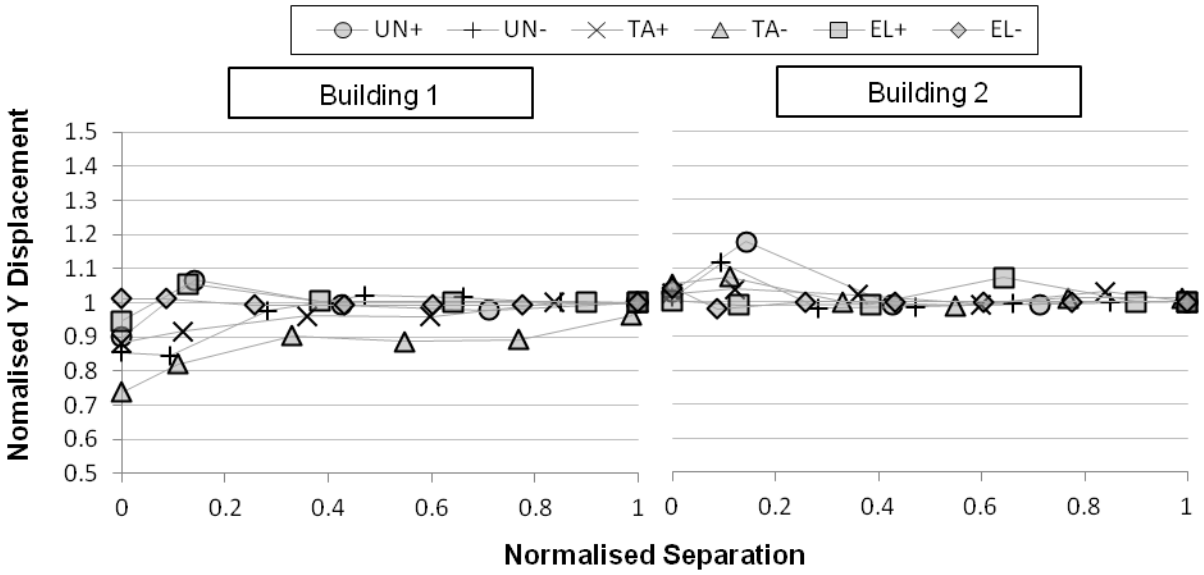

Maximum Level 3 Y displacement amplifications due to floor/column pounding

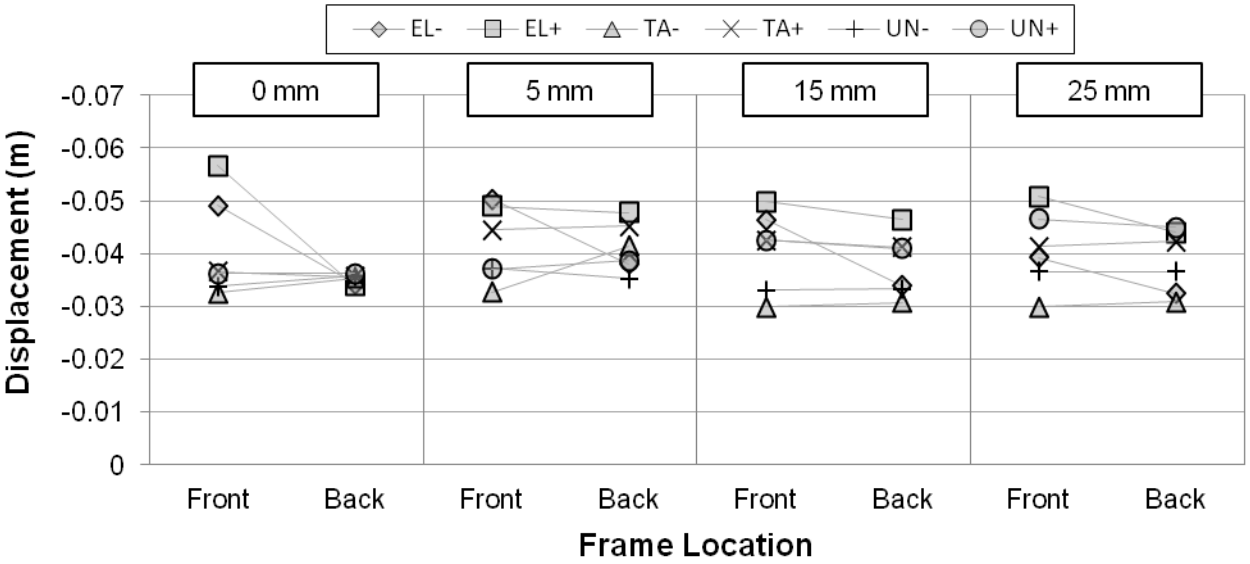

Building 1 left displacement envelopes at front and rear building frames. Building separations indicated with boxed numbers

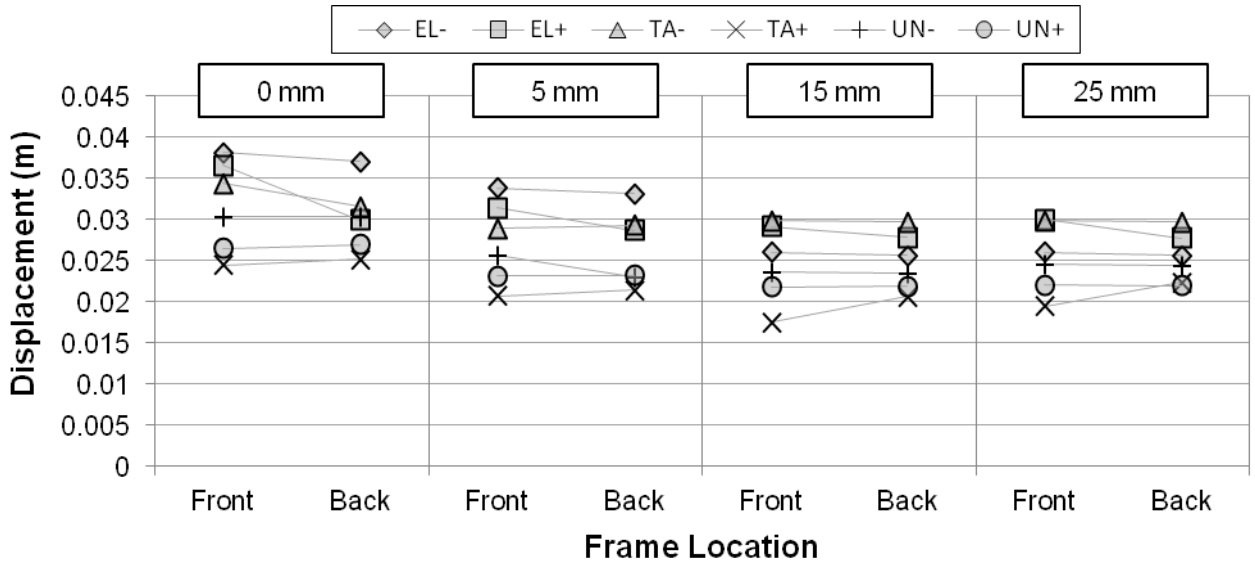

Building 2 right displacement envelopes at front and rear building frames. Building separations indicated with boxed numbers

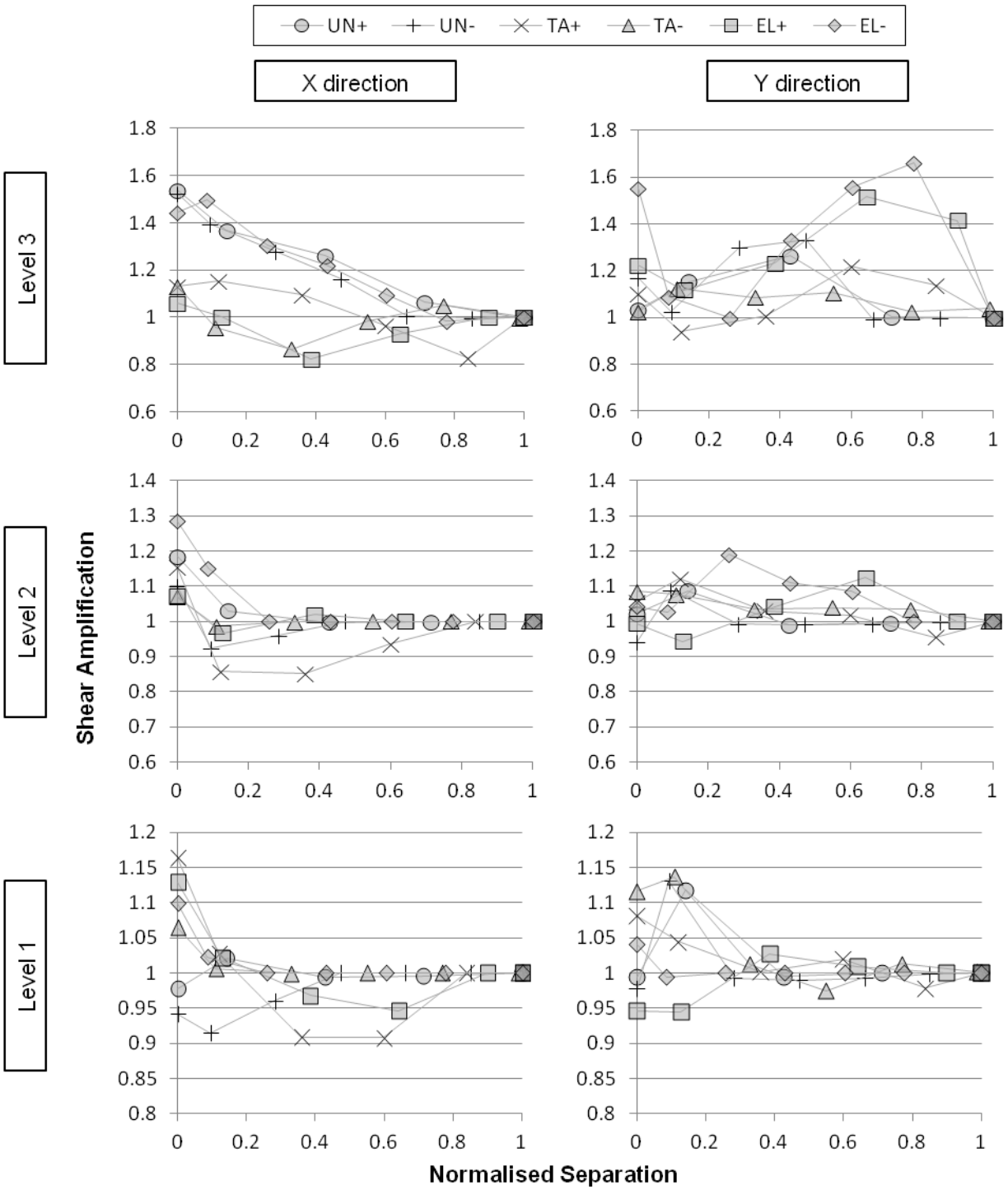

Interstorey shear amplification in Building 2. Note that different vertical scales are used at each floor level

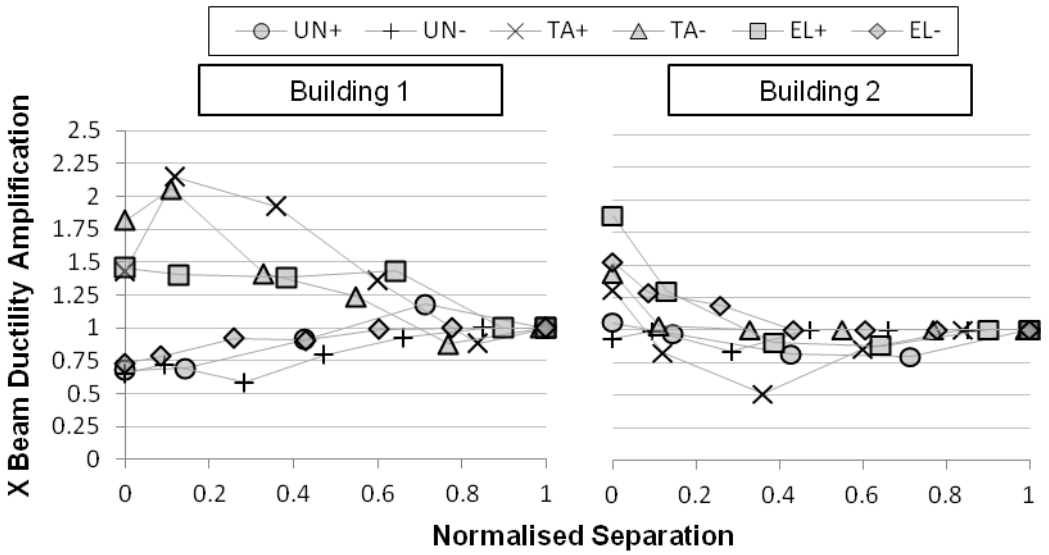

Beam ductility amplifications due to movement in the X direction

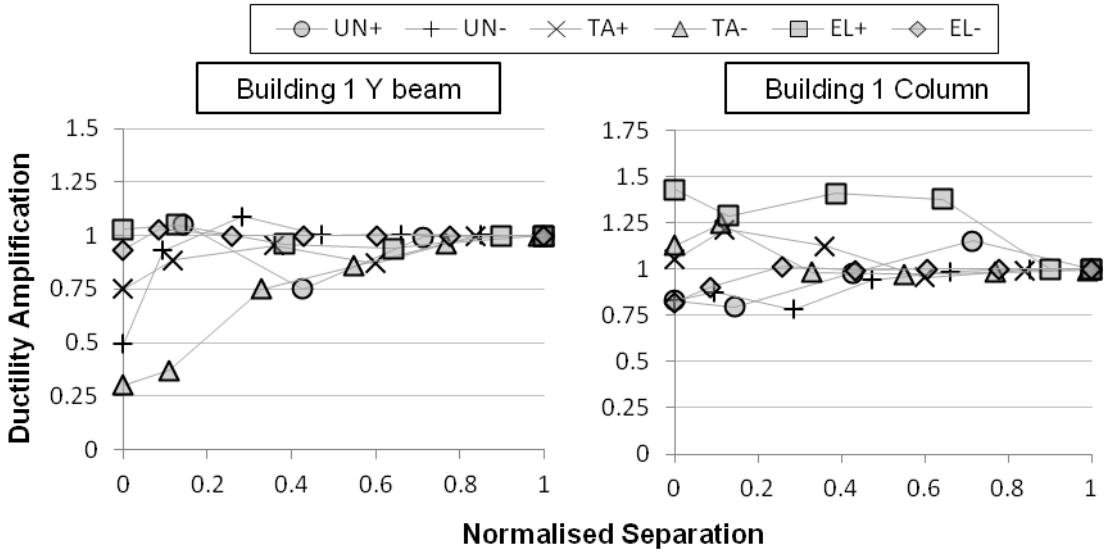

Building 1 ductility amplifications. Left: Beam ductility due to movement in the Y direction. Right: Column ductilities

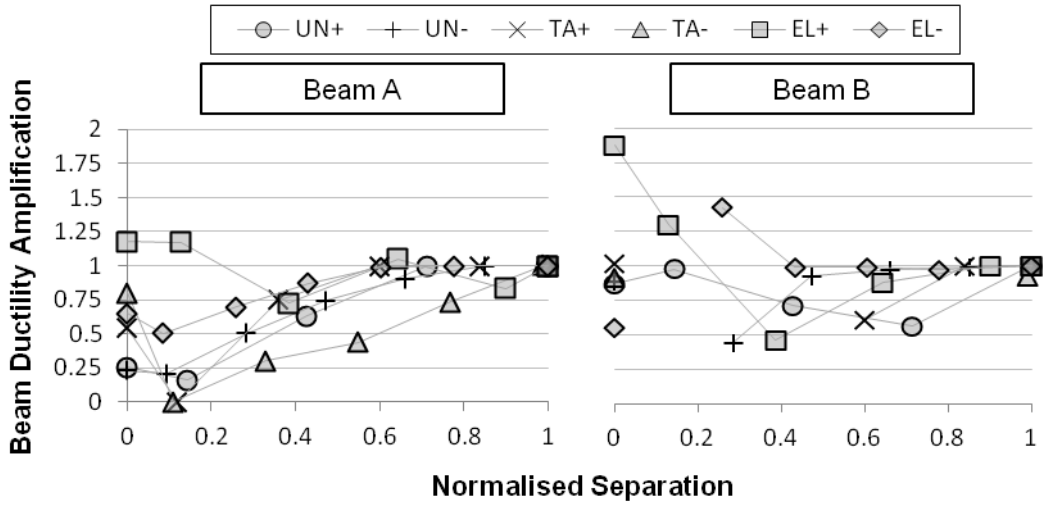

Ductility amplification of Beam A and Beam B. Refer Figure 9.42 for beam locations